Synthesis and evaluation of unique liposomal formulations as a targeted drug delivery system for the management of breast cancer

By

Aliesha Moudgil

10BB18J26025

A thesis submitted to the
Academy of Scientific & Innovative Research
for the award of the degree of
DOCTOR OF PHILOSOPHY
in

SCIENCE

Under the supervision of

Dr. Bhushan P. Chaudhari

CSIR- National Chemical Laboratory, Pune

Academy of Scientific and Innovative Research
AcSIR Headquarters, CSIR-HRDC campus
Sector 19, Kamla Nehru Nagar,
Ghaziabad, U.P. – 201 002, India

December 2023

Certificate

This is to certify that the work incorporated in this Ph.D. thesis entitled, **"_Synthesis and evaluation of unique liposomal formulations as a targeted drug delivery system for the management of breast cancer_"**, submitted by **_Aliesha Moudgil_** to the Academy of Scientific and Innovative Research (AcSIR), in partial fulfillment of the requirements for the award of the Degree of _Doctor of philosophy in Science_, embodies original research work carried-out by the student. We, further certify that this work has not been submitted to any other University or Institution in part or full for the award of any degree or diploma. Research material(s) obtained from other source(s) and used in this research work has/have been duly acknowledged in the thesis. Image(s), illustration(s), figure(s), table(s) etc., used in the thesis from other source(s), have also been duly cited and acknowledged.

Aliesha Moudgil   Dr. Bhushan P. Chaudhari

21/12/2023   21/12/2023
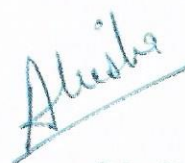
(Student)   (Supervisor)

Statements of academic integrity

I, *Aliesha Moudgil*, a Ph.D. student of the Academy of Scientific and Innovative Research (AcSIR) with Registration No. *10BB18J26025* hereby undertake that, the thesis entitled *"Synthesis and evaluation of unique liposomal formulations as a targeted drug delivery system for the management of breast cancer"* has been prepared by me and that the document reports original work carried out by me and is free of any plagiarism in compliance with the UGC Regulations on *"Promotion of Academic Integrity and Prevention of Plagiarism in Higher Educational Institutions (2018)"* and the CSIR Guidelines for *"Ethics in Research and in Governance (2020)"*.

Signature of the Student

Date: 21/12/2023

Place: Pune

It is hereby certified that the work done by the student, under my supervision, is plagiarism-free in accordance with the UGC Regulations on *"Promotion of Academic Integrity and Prevention of Plagiarism in Higher Educational Institutions (2018)"* and the CSIR Guidelines for *"Ethics in Research and in Governance (2020)"*.

Signature of the Supervisor

Name: Dr. Bhushan P. Chaudhari

Date: 21/12/2023

Place: Pune

I dedicate this thesis to my late Grandparents, my loving family, my supervisor, Dr. Bhushan P. Chaudhari, my partner, Abhinav Pandey, and my brother, Dhruve Moudgil.

For their blessings, love, and unwavering support

tenure in NCL, in the fair days, or when I was reading the difficult chapters of my life. He was an attentive listener, a perfect confidant, an actual counselor, and a genuine partner. I am indebted to him for keeping me sane and lending his ears to all my end of the day talks. He has made a real difference in my life, and I owe him a huge chunk of what I am today.

I greatly thank my friend Eshita Sharma, who always gripped my hand on rainy and sunny days. I am deeply indebted to my friend Ms. Priya Singh for being there when I needed someone the most and who has always steered me on the right path and helped me selflessly and unconditionally. I wouldn't be here if it weren't for her. Nitish Arya, my classmate and my bench mate right from childhood, has always had my back and guided me throughout my Ph.D. tenure, be it the technical details or life. I appreciate the support and timely help of Mr. Anil Negi, the chemistry teacher at St. Thomas School, Pauri, for helping me with the calculations.

I can only repay my teachers from kindergarten once my Ph.D. A million thanks to them, who contributed to shaping my personality and aura. I can't thank them enough. Last but not least, my Grandparents, who were a fountainhead of values instilled in me. It was their farfetched dream, which I could translate into reality. I owe them a lot and will always seek their heavenly blessings.

Abbreviations

Abbreviations	Full form
TME	Tumor microenvironment
DCIS	Ductal carcinoma in situ
LCIS	Lobular carcinoma in situ
IC-NST	Invasive ductal carcinoma-not otherwise specified type
HR	Hormone receptors
ER	Estrogen receptors
PR	Progesterone receptors
HER 2	Human epidermal growth factor receptor 2
TNBC	Triple negative breast cancer
CK	Cytokeratins
EGFR	Epidermal growth factor receptors
PIK3CA	Phosphatidylinositol-4,5-bisphosphate 3-Kinase, Catalytic Subunit Alpha
MAP3KI	Mitogen-activated protein kinase inhibitor
XBP1	High X-box binding protein
GATA3	GATA binding protein 3
FOXA1	Forkhead Box A1
TP 53	Tumor protein 53
MDM2	Mouse double minute 2
ATM	Ataxia Telangiectasia Mutated
FGFR1	Fibroblast growth factor receptor 1
APOBEC	Apolipoprotein B mRNA Editing Catalytic Polypeptide-like
RB1	Retinoblastoma 1
BRCA 1	Breast cancer gene 1
FOXM1	Forkhead box M1
IARC	International Agency for Research on Cancer
WHO	World health organization
HDI	Human development index

ASR	Age-specific incidence rates
CHEK2	Checkpoint kinase-2
PTEN	Phosphatase and tensin homolog
STK11	Serine/threonine kinase
PI3K	Phosphoinositide-3-kinase
CDH1	Cadherin 1
ROS	Reactive oxygen species
CT	X ray computed tomography
MRI	Magnetic Resonance Imaging
PET	Positron Emission Tomography
FISH	Fluorescence in situ hybridization
IHC	Immunohistochemistry
MDR	Multidrug resistance
P-gp	P-glycoprotein
ABC	ATP-binding cassette
MRP	MDR-associated protein
DOX	Doxorubicin
BCRP	Breast cancer resistant protein
HIF-1	Hypoxia induced factor-1
PTX	Paclitaxel
DTX	Docetaxel
FDA	Food and Drug Administration
CHOL	Cholesterol
PE	Phosphatidylethanolamine
Tc	Phase transition
MLVs	Multilamellar vesicles
ULVs	Unilamellar vesicles
RES	Reticuloendothelial system
SUVs	Small unilamellar vesicles
LUVs	Large unilamellar vesicles
DPPC	1,2 dipalmitoylphosphatidylcholine

PEG	Polyethylene glycol
IV	Intravenous route
RBF	Round bottom flask
%EE	Percentage encapsulation efficiency
Ig	Immunoglobulin
HDL	High density lipoproteins
LDL	Low density lipoproteins
EPR	Enhanced permeation and retention effect
MPS	Monophagocytic system
ECM	Extracellular matrix
EDTA	Ethylenediaminetetraacetic acid
DSPE-mPEG2000	1,2-Distearoyl-sn-glycero-3-Phosphoethanolamine methoxy polyethylene glycol-2000
DSPC	1,2-Distearoyl-sn-glycero-3-Phosphotidylcholine
DOPC	1,2-Dioleoyl-sn-glycero-3-phosphocholine
DOTAP	1,2-Dioleoyl-3-trimethylammonium propane
DSPG	1,2-Distearoyl-sn-glycero-3-phosphoglycerol
DPPC	1,2-Dipalmitoyl-sn-glycero-phosphatidylcholine
CUR	Curcumin
Bcl-2	B-cell lymphoma 2
Bak	Bcl-2 homolog antagonist killer
Bax	Bcl2 associated x protein
VEGF	Vascular endothelial growth factor
FOL	Folate
CET	Cetuximab
FRs	Folate receptors
EDB	Extradomain-B fibronectin
ICAM-1	Intracellular adhesion molecule-1
M6P	Mannose-6-phosphate
IGF	Insulin growth factor
EGF	Epidermal growth factor

NIR	Near InfraRed
CPP	Cell penetrating peptide
BCSC	Breast cancer stem cells
CSCs	Cancer stem cells
TPGS	D-a-tocopheryl polyethylene glycol 1000 succinate
MUC-1	Mucin-1
GLUT5	Glucose transporter-5
scFv	Single chain fragment antibody
PC	L-α Phosphatidylcholine
CHEMS	Cholesteryl hemmisuccinate
DSPE-PEG2000-FOL	1,2-Distearoyl-sn-glycero-3-Phosphoethanolamine polyethylene glycol-2000- FOL
DSPE-PEG2000-COOH	1,2-distearoyl-sn-glycero-3-phosphoethanolamine-N-[carboxy(polyethylene glycol)-2000
EDC	1-Ethyl-3-(3-dimethylaminopropyl) carbodiimide
NHS	N-hydroxysuccinimide
RBF	Round bottom flask
RPMI-1640	Rosewell Park Memorial Institute- 1640
DMEM	Dulbecco's Modified Eagle Medium
MTT	3-(4,5-Dimethylthiazol-2-yl)-2,5-Diphenyltetrazolium Bromide
DMSO	Dimethyl sulfoxide
PBS	Phosphate buffer saline
DLS	Dynamic Light Scattering
PDI	Polydispersity Index
% DL	Percentage drug loading
TEM	Transmission electron microscopy
HRTEM	High-resolution transmission electron microscopy
FTIR	Fourier transform infrared spectroscopy
TGA	Thermogravimetric analysis
DSC	Differential scanning colorimetry

% BE	Percentage binding efficiency
BSA	Bovine serum albumin
FACS	Fluorescence activated cell sorting

Table of Contents

Chapter 4: Optimization, Synthesis and Characterization of drug loaded liposomes

Chapter 4A: Optimization, Synthesis and Characterization of CUR loaded liposomes

Chapter 4B: Optimization, Synthesis, and Characterization of DOX loaded liposomes

Chapter 5: Optimization, Synthesis, and Characterization of targeted drug Loaded liposomes

Chapter 5A: Optimization, Synthesis, and Characterization of FOL tagged liposomes

Chapter 5B: Optimization, Synthesis, and Characterization of CET tagged liposomes

Chapter 5C: Optimization, Synthesis, and Characterization of FOL-CET tagged drug loaded liposomes

Chapter 6: Optimization, Synthesis, and Characterization of pH responsive liposomes

Chapter 7: *In vitro* efficacy studies

Chapter 8: Conclusion and Future prospects

Copy of the SCI indexed Publication (emanating from thesis)

List of Tables

Chapter 5C: Optimization, Synthesis, and Characterization of FOL-CET tagged drug loaded liposomes

Chapter 6: Optimization, Synthesis, and Characterization of pH responsive liposomes

Chapter 7: *In vitro* efficacy studies

List of Figures

Chapter 4: Optimization, Synthesis, and Characterization of drug loaded liposomes

Chapter 4A: Optimization, Synthesis, and Characterization of CUR loaded liposomes

Chapter 5C: Optimization, Synthesis, and Characterization of FOL-CET tagged drug loaded liposomes

Chapter 6: Optimization, Synthesis, and Characterization of pH responsive liposomes

ABSTRACT

Chapter 1: Introduction and Review of Literature

The International Agency for Research on Cancer (IARC) (World Health Organization) reported 19.3 million new cancer cases and 10 million deaths in 2020 worldwide, with breast cancer acquiring the first position with 2.3 million cases (11.7% of the new cancer cases) (International agency for research on cancer, 2021). India reported 1,324,413 new cancer cases in India in 2020, with 178,361 breast cancer cases in females (13.5%) and 90,408 deaths (International Agency for Research on Cancer, 2020).

Breast cancer has four molecular subtypes (Prat et al., 2015): Luminal A subtype has an estrogen receptor (ER)+/progesterone receptor (PR)+/Human epidermal growth factor receptor (HER2) 2-profile; Luminal B breast cancer has an ER+/PR+/HER2+ profile (Tsang and Tse, 2020) (Weigelt et al., 2010); HER2 enriched subtype overexpresses HER2 and genes related to the HER2 pathway (Kumar et al., 2015) (Reis-Filho and Pusztai, 2011); and the triple negative breast cancer (TNBC) subtype has an ER-/PR-/HER2 – profile is the most aggressive type with a high relapse rate, has the worst prognosis, and is responsive to chemotherapy (Schnitt, 2010).

Breast cancer treatment comprises a combination of therapeutic modalities, including surgery and radiotherapy under localized treatment and chemotherapy under systemic therapy. Chemotherapy is responsible for poor quality of life, non-specific accumulation causing systemic or organ-specific toxicity, higher injectable doses due to multi drug resistance (MDR) of the cancer cells, and low bioavailability of the hydrophobic drugs. Nanotechnological interventions efficaciously acknowledge these fallouts.

Liposomes are U.S. Food and Drug Administration (FDA) approved nanocarriers analogous to the cell membranes and are biocompatible, biodegradable, and non-immunogenic. We can encapsulate the hydrophobic drugs in the lipid bilayer and the hydrophilic drugs in the aqueous core (Madni et al., 2014). Liposomes protect drugs from metabolic degradation, enhance the pharmacokinetic properties of the drugs, engender a prolonged and sustained drug release profile, reduced drug dosages, and improved the drug's half-life and therapeutic index (Garg and AK Goyal, 2014) (Goyal et al., 2005).

Curcumin (CUR) has a pleiotropic effect on cancer cells and chemo sensitizer attributes (Yallapu et al., 2012). Doxorubicin (DOX) is the most effective chemotherapeutic drug that inhibits the action of topoisomerase II and impedes the DNA repair mechanism (Thorn et al., 2011). The Folate receptors (FRs) are overly expressed on the TNBC cells to suffice the folate (FOL) needs of the highly proliferating cells to meet the heightened DNA synthesis (Zhang et al., 2014). Epidermal growth factor receptors (EGFRs) are also overly expressed in the TNBC cells and contribute to cell proliferation, differentiation, invasion, and metastasis (Hsu and Hung, 2016).

Statement of the problem

A poly (sodium 4-styrene sulfonate) coated liposomal formulation encapsulating CUR and attaching DOX to the polymer surface showed higher anticancer activity in the MCF-7 cells (Sheena et al., 2018). A CUR and celecoxib co-loaded liposomal formulation functionalized with hyaluronic acid and TAT-NBD (TN) peptide when combined with a DOX encapsulated liposomal formulation functionalized with TN peptide was efficacious against the 4T1 cells (Liu et al., 2020). CUR and DOX co-loaded liposomes functionalized with PEG-polyethylenimine linked to Herceptin were effective against the HER2+ SKBR3 cells (Lin et al., 2019).

The extensive literature review suggested an absence of dual ligand tagged liposomal formulations with FRs and EGFRs not exploited to treat breast cancer, especially TNBC. Studies showcasing the efficacy against breast cancer are also limited, especially for the treatment of the TNBC subtype. We proposed a liposomal formulation encapsulating CUR in the lipid bilayer and DOX in the aqueous core surface functionalized with FOL against FRs and CET against the EGFRs. We then investigated the efficacy of various liposomes on MCF-7, a hormone receptor positive cell line, and MDA-MB-231, a TNBC cell line.

We hypothesized that the FOL-CET CUR-DOX liposomes should exhibit a better uptake and anticancer effect on the MDA-MB-231 cell line, and the pH responsive counterparts should be more efficacious than the non-responsive counterparts. Thus, we proposed the following objectives for the study:

1. Optimization, Synthesis, and Characterization of plain liposome.

2. Optimization, Synthesis, and Characterization of drug loaded liposomes.

3. Optimization, Synthesis, and Characterization of ligand tagged drug loaded liposomes against Breast cancer.

4. In vitro efficacy studies.

Chapter 2: Materials and Methods

We followed the following protocols for the synthesis and characterization of liposomes.

2.1 Synthesis of liposomes

We synthesized liposomes using the thin film hydration technique employing L-alpha phosphatidylcholine (PC) and cholesterol (CHOL). The passive loading technique encapsulated CUR and DOX by adding CUR in the thin film formation step and DOX in the thin film hydration step. FOL tagged liposomes were synthesized by adding 1, 2 distearoyl-sn-glycero-phosphoethanolamine- Polyethylene glycol (2000)-FOL (DSPE-PEG2000-FOL) in the thin film formation step; CET tagged liposomes were synthesized by adding 1, 2 distearoyl-sn-glycero-phosphoethanolamine- Polyethylene glycol (2000)-COOH (DSPE-PEG2000-COOH) in the thin film formation step and thereafter tagging CET by the carbodiimide chemistry.

2.2 Characterization of liposomes

We characterized the liposomes for hydrodynamic diameter, polydispersity index (PDI), and zeta potential by the dynamic light scattering (DLS) technique. Transmission electron microscopy (TEM) and high-resolution transmission electron microscopy (HRTEM) determined the particles' morphology. The % encapsulation efficiency (%EE) was calculated by quantifying the drugs in the liposomes by the UV-Vis spectrophotometer. The % drug loading (%DL) was calculated. The functional groups were determined by the Fourier transform infrared spectroscopy (FTIR), and the thermal stability was determined by the Thermogravimetric analysis (TGA) and Differential scanning colorimetry (DSC). The Bradford assay quantified CET.

2.3 *In-vitro* studies

The colloidal stability of the formulations was tested by storing them at 4°C and recording the hydrodynamic diameter, PDI, and zeta potential values at determined time intervals. Drug release studies were carried out by dialysis method. The uptake of the formulations was tested on the MCF-7 and MDA-MB-231 cell lines and quantified by the Fluorescence-activated cell sorting (FACS) technique. The MTT assay tested the cell viability.

Chapter 3: Optimization, Synthesis, and Characterization of plain liposomes

We investigated varied process parameters of the thin film formation step and intrinsic factors to determine their effect on the liposomal specifications. We observed that the thin film formation step controlled the nature of the lipid layer. We optimized 240 RPM rotation speed, 700 mm of Hg of reduced vacuum pressure, and 2 ml chloroform to construct a thin and uniform lipid layer on the RBF wall. The thin film hydration step determined the particle specifications, and we optimized 270 RPM of rotation speed with PBS for 1 h to obtain a smaller and monodisperse population. The subsequent downsizing step also controls the particle specifications, and we optimized a single 100 nm polycarbonate membrane and 10 extrusion passes. The intrinsic factors controlled both the particle specifications and the nature of the lipid layer, and we optimized 10 mg/ml of lipids for a uniform lipid layer, a 7:3 molar ratio of the PC: CHOL, and 1 mole% of DSPE-mPEG2000.

The hydrodynamic diameter, PDI, and zeta potential of the liposomes were 129.57±7.36, 0.06±0.03 and -24.84 ±0.67 mV, respectively; for PEGylated liposomes, it was 119.94±1.23, 0.1±0.002 and -7.55±0.53 mV respectively. The HRTEM images at 100 and 20 nm magnification display spherical particles with smooth surfaces. The peaks in the FTIR spectra of both formulations shift for the hydrocarbon chain region and the head group regions after the liposomal formation.

We determined the degradation onset temperature of PC, CHOL, and DSPE-mPEG2000 at 182.46, 249.76and 320.91 °C that shifted to 240.78 °C for non-PEGylated liposomes and 248.53 °C for PEGylated liposomes. The DSC thermogram displays an endotherm at 136.7 °C for PC, 151.59

°C for CHOL, and 56.96 °C for DSPE-mPEG2000 (Jangde and Singh, 2016). The melting endotherm displaced to 121.13 °C and 116.68 °C for liposomes and PEGylated liposomes.

Chapter 4: Optimization, Synthesis and Characterization of drug loaded liposomes

Chapter 4A: Optimization, Synthesis and Characterization of CUR loaded liposomes

We investigated the CUR: lipid ratios (wt. /wt.) (1:10, 1:20, 1:30, 1:40, and 1:50) and molar ratio of PC: CHOL (1:1, 3:2, 7:3, 4:1 and 9:1) simultaneously and optimized 1: 50 CUR: lipid ratios (wt. /wt.) and 7:3 molar ratio of PC: CHOL. The highest %EE in the 7:3 molar ratio of lipids corresponds to increased bilayer fluidity with a balanced rigidity (Saengkrit et al., 2014) (Chen et al., 2012). CHOL at lower concentrations decreases the particle size, increasing the size; at higher concentrations, it increases the bilayer rigidity, increasing the particle size (Zarrabi et al., 2021). We excluded the sonication step and optimized 5 extrusion passes in the downsizing step. We optimized 1 mole % of DSPE-mPEG2000 to synthesize the PEGylated CUR liposomes.

CUR liposomes recorded the hydrodynamic diameter, PDI, zeta potential, %EE and %DL at 117.66 ± 5.36 nm, 0.07 ± 0.01, -21.15 ± 1.57 mV, 76.08 ± 2.30 %, and 3.64 ± 0.15 % respectively; for PEGylated CUR liposomes at 122.91 ± 0.65 nm, 0.06 ± 0.01, -10.60 ± 0.87 mV, 78.08 ± 3.30 %, and 3.21 ± 0.27 % respectively. The HRTEM images show spherical particles of CUR and PEGylated CUR liposomes with smooth surfaces. The FTIR analysis confirmed the loading of CUR in the bilayer region (Zarrabi et al., 2021). We recorded the degradation onset temperature for CUR at 253.79 °C, CUR liposomes at 244.49 °C, and PEGylated CUR liposomes at 260.7 °C. The DSC thermogram recorded the endotherm for CUR at 176.55 °C, CUR liposomes at 120.50 °C, and PEGylated CUR liposomes at 94.73 °C.

Chapter 4B: Optimization, Synthesis, and Characterization of DOX loaded liposomes

We varied the DOX concentration (0.05, 0.1, 0.2, and 0.4 mg) and optimized 0.1 mg. In the downsizing step, we optimized 5 extrusion passes for both DOX liposomes and PEGylated DOX liposomes. DOX liposomes recorded the hydrodynamic diameter, PDI, zeta potential, %EE and %DL at 129.79 ± 5.07 nm, 0.08 ± 0.001, -20.49 ± 0.77 mV, 78.24 ± 7.59 %, and 2.31 ± 0.21 % respectively; for PEGylated DOX liposomes at 118.57 ± 5.01 nm, 0.08 ± 0.01, -9.25 ± 1.46 mV,

74.42±2.17 %, and 2.51±0.10 % respectively. HRTEM images at 100 nm magnification for DOX and PEGylated DOX liposomes show spherical structures with smooth surfaces. The FTIR analysis confirmed the loading of DOX in the aqueous core and the water-lipid interface (Mady et al., 2012). We recorded the degradation onset temperature for DOX at 213 °C, DOX liposomes at 227.67 °C, and PEGylated DOX liposomes at 268.88 °C. The DSC thermogram recorded the endotherm for DOX at 50.44 °C, DOX liposomes at 104.97 °C, and PEGylated DOX liposomes at 84.17 °C.

Chapter 4C: Optimization, Synthesis, and Characterization of CUR-DOX loaded liposomes

CUR-DOX liposomes recorded the hydrodynamic diameter, PDI, zeta potential, %EE and %DL at 125.4 ± 3.26 nm, 0.08 ± 0.02, -19.07 ± 3.03 mV, 78.66 ± 2.49 for DOX and 76.82 ± 3.9 % for CUR, and 4.46 ± 0.30 % respectively; for PEGylated CUR-DOX liposomes at 121.51 ± 0.82 nm, 0.09 ± 0.02, -10.20 ± 1.60 mV, 73.32 ± 2.84 for DOX and 77.57 ± 2.94 % for CUR, and 4.25 ± 0.24 % respectively. HRTEM images at 100 nm magnification for DOX and PEGylated DOX liposomes show spherical structures with smooth surfaces. The FTIR analysis confirmed the loading of DOX in the aqueous core, the water-lipid interface, and CUR in the lipid bilayer. We recorded the degradation onset temperature for CUR-DOX liposomes at 264.88 °C and for PEGylated CUR-DOX liposomes at 254.61 °C. The DSC thermogram recorded the endotherm for CUR-DOX liposomes at 92.31 °C and for PEGylated CUR-DOX liposomes at 89.89 °C.

Chapter 5: Optimization, Synthesis, and Characterization of targeted drug Loaded liposomes

Chapter 5A: Optimization, Synthesis, and Characterization of FOL tagged liposomes

We synthesized FOL tagged liposomes and optimized 11 extrusion passes for FOL CUR liposomes, FOL CUR-DOX liposomes, and FOL CUR-DOX liposomes. FOL CUR liposomes recorded the hydrodynamic diameter, PDI, zeta potential, %EE, and %DL at 131.24 ± 3.91 nm, 0.10 ± 0.05, -8.99 ± 1.37 mV, 78.40 ± 2.34 %, and 3.57±1.91% respectively; for FOL DOX liposomes at 128.38 ± 2.10 nm, 0.06 ± 0.01, -6.92 ± 0.41 mV, 79.47 ± 4.75 %, and 2.4±0.15 % respectively; FOL CUR-DOX liposomes at 129.44 ± 0.81 nm, 0.07 ± 0.01, -8.57 ± 0.35 mV, 77.73 ± 3.50 for DOX and 78.46 ± 3.26 % for CUR, 4.49±0.18 % respectively. HRTEM images showed

spherical structures with smooth surfaces. The FTIR analysis confirmed the loading of DOX in the aqueous core and the water-lipid interface, CUR in the lipid bilayer, and tagging of FOL.

Chapter 5B: Optimization, Synthesis, and Characterization of CET tagged liposomes

We synthesized CET tagged liposomes by optimizing 11 extrusion passes after adding DSPE-PEG2000-COOH and thereafter tagged CET. CET CUR liposomes recorded the hydrodynamic diameter, PDI, zeta potential, and %EE at 131.08 ± 0.72 nm, 0.09 ± 0.01, -9.80 ± 0.50 mV, and 79.49 ± 1.6%respectively; for CET DOX liposomes at 141.49 ± 2.9 nm, 0.12 ± 0.02, -9.16 ± 0.44mV, and 76.71 ± 3.18% respectively; CET CUR-DOX liposomes at 126.43 ± 2.59 nm, 0.13 ± 0.03, -10.14 ± 0.64mV, 79.11 ± 2.22for CUR and 75.22 ± 1.78% for DOX respectively. We calculated the % binding efficiency of CET at 87.11 ± 1.99 % for CET CUR liposomes, 85.86 ± 1.96 % for CET DOX liposomes, and 88.14 ± 1.72 % for CET CUR-DOX liposomes. HRTEM images showed spherical structures with smooth surfaces.

Chapter 5C: Optimization, Synthesis, and Characterization of FOL-CET tagged drug loaded liposomes

We synthesized FOL-CET tagged liposomes by optimizing 11 extrusion passes after adding DSPE-PEG2000-COOH and DSPE-PEG2000-FOL and thereafter tagged CET. For FOL-CET CUR liposomes, we recorded the hydrodynamic diameter at 130.90 ± 1.54 nm, PDI at 0.08 ± 0.01, the zeta potential of -9.71 ± 1.08 mV, and the % EE at 79.29 ± 2.96 %; for FOL-CET DOX liposomes, we recorded the hydrodynamic diameter at 129.57 ± 0.67 nm, the PDI at 0.10 ± 0.01, zeta potential of -10.45 ± 0.42 mV and the % EE at 76.47 ± 2.20 %; for FOL-CET CUR-DOX liposomes, we recorded hydrodynamic diameter at 131.38 ± 1.96 nm, the PDI at 0.14 ± 0.01, zeta potential of -10.86 ± 1.22 mV, and the % EE for CUR at 79.00 ± 3.65 and 76.77 ± 2.89 %. The HRTEM images for the three FOL-CET formulations show spherical structures with smooth surfaces. We determined the % BE of CET by the Bradford assay and calculated 87.55 ± 2.74 % for FOL-CET CUR liposomes, 86.96 ± 2.35 % for FOL-CET DOX liposomes and 87.67 ± 1.34 % for FOL-CET CUR-DOX liposomes.

Chapter 6: Optimization, Synthesis, and Characterization of pH responsive liposomes

We synthesized pH responsive counterparts of CUR-DOX liposomes, FOL CUR-DOX liposomes, CET CUR-DOX liposomes, and FOL-CET CUR-DOX liposomes. Upon characterization, we recorded the hydrodynamic diameter < 200 nm, PDI < 0.3, and zeta potential in the neutral range. The FTIR analysis confirmed the loading of DOX in the aqueous core and the water-lipid interface, CUR in the lipid bilayer, and tagging of FOL. We recorded the degradation onset temperature for the lipid at 247.38 ° C and for pH responsive CUR-DOX liposomes at 214.90 ° C; the DSC endotherm for the lipid occurred at 123.08 ° C, for CHEMS at 184.15 ° C, and pH responsive CUR-DOX liposomes at 110.90 ° C.

Chapter 7: *In-vitro* efficacy studies

We established the liposomal formulations' efficacy through stability studies, drug release studies, and cell viability assay and uptake analysis. We recorded protracted stability for 3 months for all the drug loaded liposomes with a 60-70% drug retention. This establishes an excellent colloidal stability of the liposomes. The drug release profiles recorded a biphasic release of the drugs, with an initial rapid release followed by a sustained and prolonged release. CUR follows the Gompertz model, and DOX follows the Weibull model of drug release; both these models are diffusion based models suggesting that the drugs diffuse out of the liposomes.

The uptake analysis shows a higher uptake of the liposomal formulations than the plain drugs by the MCF-7 and MDA-MB-231 cell lines. CET tagged liposomes showed a lower uptake in the MCF-7 cell lines, corresponding to the lower expression of the EGFR receptors. The cell viability analysis showed an equivalent efficacy for DOX in FOL-CET CUR-DOX liposomes to the plain DOX and a higher efficacy for CUR in the FOL-CET CUR-DOX liposomes to the plain CUR in the MCF-7 cell lines. The non-responsive counterparts showed a higher efficacy than the pH-responsive counterparts. In the MDA-MB-231 cell lines, DOX and CUR in FOL-CET CUR-DOX liposomes to the plain drugs, but the pH responsive counterpart showed a higher efficacy than the plain drugs and the non-responsive counterparts.

Chapter 8: Conclusion and Future prospects

We performed a robust optimization of the thin film hydration techniques by identifying various parameters of the thin film formation and hydration steps along with the intrinsic factors. This study facilitates the synthesis of liposomes for drug delivery or other applications by modulating the identified parameters to attain the desired specifications. We optimized various parameters for encapsulating CUR and DOX in the liposomes and FOL and CET for active targeting to synthesize robust formulations per the drug delivery mandates. All the formulations had a hydrodynamic diameter < 200 nm, PDI < 0.3, and successful incorporation of the drugs and ligands.

The *in-vitro* efficacy studies show excellent Colloidal Stability for 3 months with 60-70 % drug retention. The drugs showed a biphasic release that was higher in the acidic pH. The liposomal formulations were effectively taken up by the MCF-7 and MDA-MB-231 cells. The dual tagged and dual drug loaded formulations showed the highest anticancer activity. Thus, our results concur with the hypothesis and confirm that CUR and DOX in a liposomal formulation, when targeted against the FRs and EGFRs, show enhanced anticancer potential against TNBC over the hormones responsive cell lines.

The study undertaken is a proof of concept of the higher efficacy of the FOL-CET tagged and CUR-DOX loaded liposomes on the TNBC cell lines over the hormone responsive cell line. We can further optimize the drug and ligand concentrations based on their efficacy in the cell viability assay and the uptake analysis. Thereafter, these formulations can be tested in animal models. The optimized parameters from this study can be used to develop robust liposomal formulations for precision and personalized treatment.

CHAPTER 1

Introduction and Review of Literature

1.1 Anatomy of breast

The breast, a modified cutaneous exocrine gland, spans from the 2nd to 6th / 7th intercostal space and extends from the lateral margin of the sternum (medially) to the anterior axillary line (laterally) (Ellis and Mahadevan, 2013) (Torácica et al., 2005). The pectoralis major muscle strengthens the breast from underneath, the serratus anterior muscle from the sides, and the upper abdominal oblique muscles from the inferior side; Cooper's ligaments, a fibrous connective tissue, lie perpendicular to the dermis for support (Jesinger, 2014). Skin, subcutaneous tissue, fibroglandular tissue (ducts and lobules), and stroma – stroma includes arteries, veins, lymphatic ducts, nerves, and fat- encompass the mammary glands (Jesinger, 2014).

The glandular tissue or the breast parenchyma constitutes 15-20 lobular units -the morphological and functional unit of the mammary gland- that branch into 20-40 lobules per lobe and 10-100 alveoli per lobule (Lemaine and Simmons, 2013); alveoli have lactocytes, the secretory epithelial cells that produce milk (Ramsay et al., 2005). Interlobular ducts drain each lobe and open into lactiferous ducts that expand into a lactiferous sinus below the areola (Pandya and Moore, 2011) (Figure 1.1). A double layered epithelium lines the mammary glands: the cylindrical/cubic glandular ductal cells form the inner layer that keratinizes in the nipple region, and the myoepithelial cells form the outer layer (Pinamonti and Zanconati, 2018).

The breast has three major arterial routes: the internal thoracic (internal mammary) artery and its branches supply the central and medial breast parenchyma corresponding to 60% of blood supply; the lateral thoracic (external mammary) artery drains the superolateral parenchyma/ upper outer quadrant contributing to 30% of blood supply; the posterior intercostal arteries penetrate through the chest wall and feed the deeply situated central parenchyma (remaining part of the breast) (Pandya and Moore, 2011) (Jesinger, 2014).

The internal thoracic, axillary, and posterior intercostal veins run parallel to the arteries in the deep tissues. The superficial veins traverse the central and peripheral areas from where the blood drains into the internal thoracic and lateral thoracic veins (Van Deventer and Graewe, 2016). The lymphatic system of the breast comprises two major networks: the axillary lymph nodes, with 20-30 lymph nodes draining 75% of the lymph from the breast (Pandya and Moore, 2011), and the internal mammary nodes draining lymph from the deeper areas (Geddes, 2007).
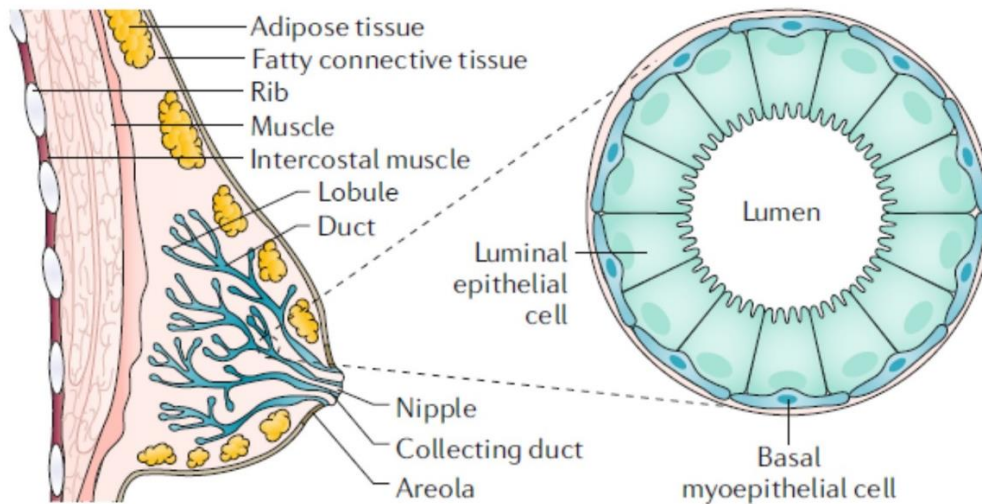
Figure 1.1 Anatomy of the breast (modified from (Harbeck et al., 2019))

Breasts start developing in the 5th week of gestation from mammary ridges at the 4th intercostal space: they form a mammary bud that grows into the chest till 12 weeks and forms 15- 20 secondary buds that form lactiferous ducts and their branches. The mammary glands remain underdeveloped till puberty, comprising only the lactiferous ducts; at puberty, the epithelial cells and connective tissues form under the influence of female estrogen and progesterone (Jesinger, 2014).

1.2 Types of breast cancers

The breast has upper inner, upper outer, lower inner, and lower outer quadrants. Breast carcinomas are adenocarcinomas occurring primarily in the upper outer quadrant, which has more fibroglandular tissue (Lemaine and Simmons, 2013). Breast cancer cells are heterogeneous, differing in morphology, genetics, and biomarkers (at the molecular level). The discrepancy in tumors between individuals is termed intertumor heterogeneity, within the same tumor of an individual as intratumor heterogeneity (Polyak, 2011), at different tumor locations as spatial heterogeneity, and due to tumor progression as temporal heterogeneity (Turashvili and Brogi, 2017).

The disparity in the tumor vasculature, recruitment of immune cells and cancer-associated fibroblasts to different tumor areas, and the cross-talk of the tumor microenvironment (TME) components with the cancer cells (Junttila and De Sauvage, 2013) contribute to this heterogeneity engendering varied clinical outcomes and response to therapy. This

heterogeneity formed the basis for a unified classification scheme of *histology based* and *molecular subtype* based classification systems of breast cancer (Figure 1.2).
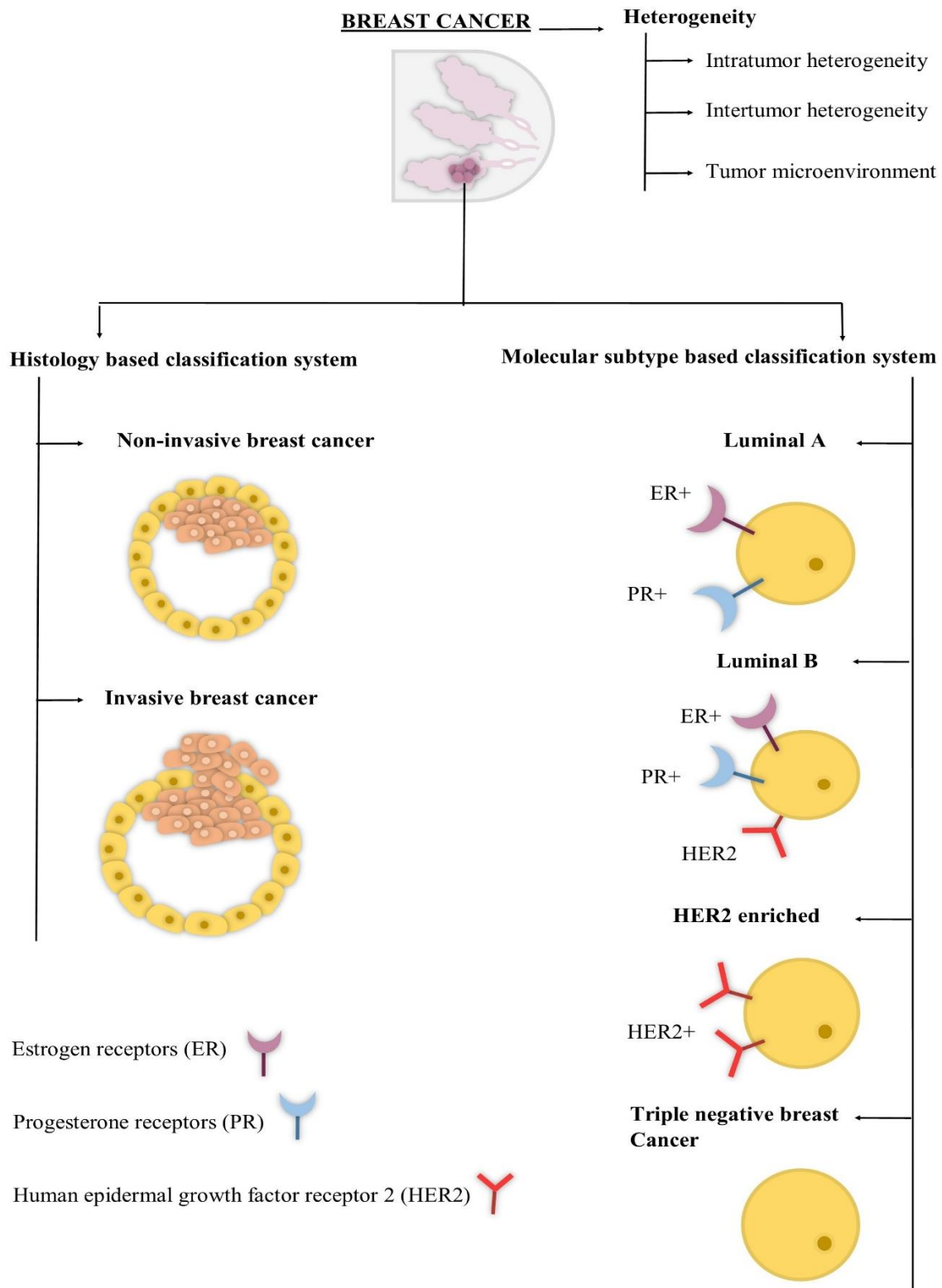
Figure 1.2 Heterogeneity and dichotomous classification of Breast cancer (modified from (Moudgil et al., 2023))

1.2.1 Histology based classification framework

Breast carcinomas arise in either ducts or lobules. They identify as *non-invasive* if the tumors remain within a basement membrane and *invasive* if cancer cells with metastatic phenotype breach the basement membrane and disseminate to distant body parts (Figure 1.3) (Feng et al., 2018). Non-invasive breast cancer bifurcates into *ductal carcinoma in situ* (DCIS) and *lobular carcinoma in situ* (LCIS), originally named after the source of origin, i.e., ducts or lobules, respectively (Sainsbury et al., 1994). But, a remodeled convention proposed that DCIS can also occur in the lobules where enlarged acini present as small ducts.

DCIS is the most prevalent preinvasive condition with typical architectural subtypes: *comedo* DCIS have pleomorphic tumor cells with high grade nuclei and central necrosis; *noncomedo* DCIS are less aggressive with low nuclear grade and without central necrosis; *cribriform* DCIS have gaps or holes in the ducts; *micropapillary* DCIS have bulbous projections without a fibrovascular core; *papillary* DCIS have a true papilla and a fibrovascular core with dead myoepithelial layer (Malhotra et al., 2010). LCIS has lobular structures with discohesive proliferation due to the reduced expression of E-cadherin. It has a uniform monomorphic population of cells with round or oval nuclei in the lobules or ducts (Vinay et al., 2012).

Invasive breast cancer classifies into more than 21 subtypes, of which *invasive ductal carcinoma-not otherwise specified type* (IC-NST) occurs in approximately 70-80% of breast cancers; they appear in any age group, and based on nuclear polymorphism, mitotic index, and glandular/tubular formation are graded from I (well differentiated) to III (poorly differentiated). Since IC-NST is predominant, the histology based classification covers a narrow heterogeneity class and inefficiently defines the patient's prognosis (Viale, 2012) (Vuong et al., 2014).

Invasive lobular carcinoma, the second most recurring kind, corresponds to 10-15 % of breast cancers and is prevalent in older women. The rare invasive types of breast cancers include *mucinous or colloid* invasive breast cancer, where cells assemble in mucin to form a soft textured structure; *tubular* invasive breast cancer has well-built tubular structures with calcifications; *medullary* breast cancer has a softer texture; *papillary* carcinoma has true papilla like structures (Vinay et al., 2012) (Page, 2003) (Provenzano et al., 2018). *Metastatic* breast cancer is the last stage, where breast cancer cells metastasize predominantly to the lymph nodes, brain, bones, liver, and lungs (Malhotra et al., 2010).
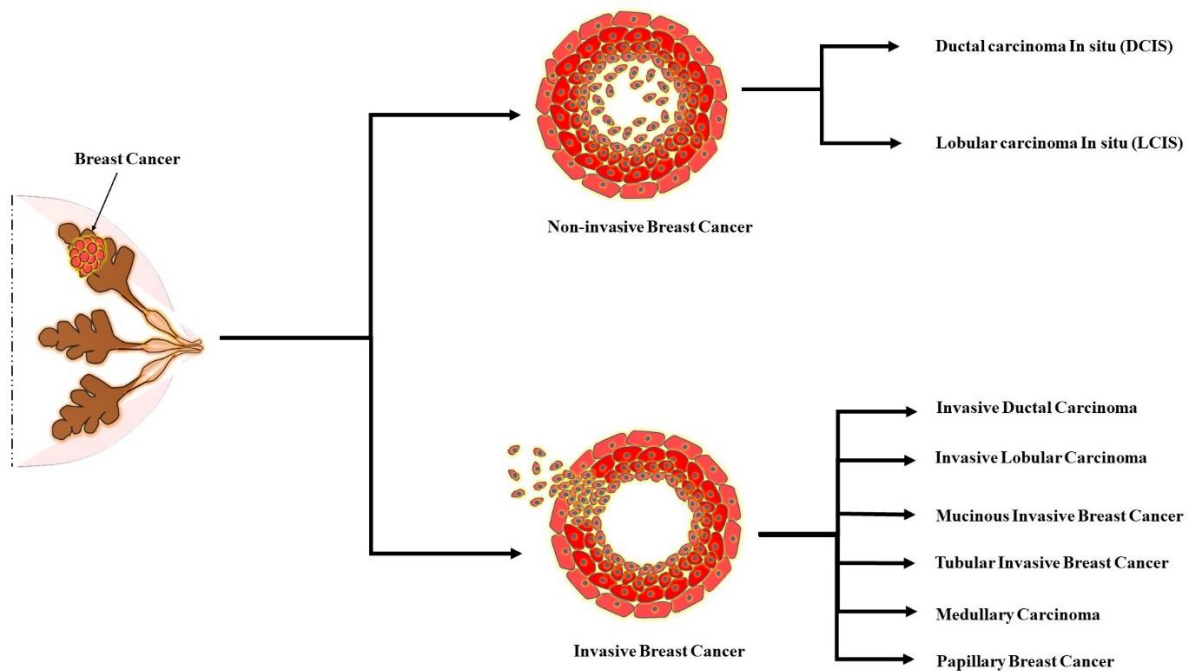
Figure 1.3 Histology based classification of breast cancer (modified from (Moudgil et al., 2022))

1.2.2 Molecular subtype based classification framework

The molecular subtype based classification depends on three hormone receptors (HR), namely, estrogen receptor (ER), progesterone receptor (PR), and human epidermal growth factor receptor 2 (HER 2) (Figure 1.4) (Prat et al., 2015). The *Luminal A* subtype has an ER+/PR+/HER 2- profile, is a low grade type tumor with low ki67 levels, has a good prognosis, and is responsive to hormone therapy; the *Luminal B* subtype has an ER+/PR+/HER 2+ profile, is a high grade type tumor with high ki67 levels, has a poor prognosis, and responds to hormone therapy and chemotherapy (Tsang and Tse, 2020) (Weigelt et al., 2010).

The HER 2 enriched subtype overexpresses HER 2 and genes related to the HER 2 pathway (Kumar et al., 2015a) (Reis-Filho and Pusztai, 2011), has a poor prognosis, and responds to hormonal therapy such as trastuzumab, etc. The triple negative breast cancer (TNBC) subtype has an ER-/PR-/HER 2 – profile, is the most aggressive type with a high relapse rate, has the worst prognosis, and responds to chemotherapy (Schnitt, 2010). Basal like breast cancer is a high grade form of TNBC with upregulated gene expression of basal/myoepithelial cells, cytokeratins (CK) such as CK5 and CK14, epidermal growth factor receptors (EGFR), and has several histological subtypes (Provenzano et al., 2018).
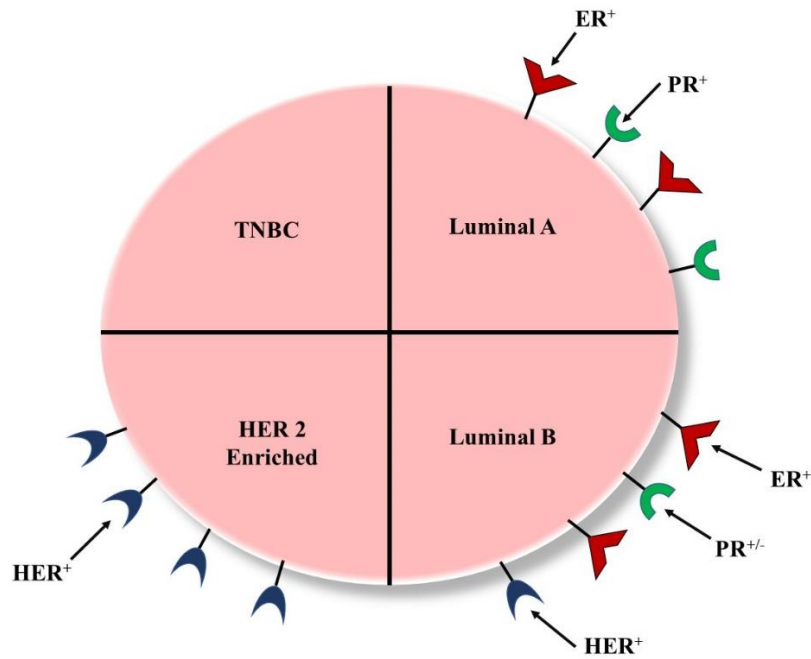
Figure 1.4 Molecular subtype based classification of breast cancer (modified from (Moudgil et al., 2022))

Different molecular subtypes have various morphological and molecular features (Table 1.1) (Weigelt et al., 2008) (Provenzano et al., 2018).

Table 1.1 Histological subtypes and molecular features of the molecular subtypes of breast cancer

Molecular subtype	Histological subtype	Molecular features
Luminal A	IC-NST, classic lobular, tubular, cribriform, mucinous, and neuroendocrine	Phosphatidylinositol-4,5-bisphosphate 3-Kinase, Catalytic Subunit Alpha *(PIK3CA)* mutation, Mitogen-activated protein kinase inhibitor *(MAP3KI)* mutation, high *ER1,* high X-box binding protein *(XBP1),* GATA binding protein 3 *(GATA3)* mutation, and high Forkhead Box A1 *(FOXA1)*
Luminal B	IC-NST, micropapillary and lobular	Tumor protein 53 (TP53) mutation, *PIK3CA* mutation, high Cyclin D1, high Mouse double minute 2 (MDM2), Ataxia

		Telangiectasia Mutated (ATM) loss, high Fibroblast growth factor receptor 1 (FGFR1), and increased genomic instability
HER 2	IC-NST, apocrine, and pleomorphic lobular	High HER 2, TP53 mutation, *PIK3CA* mutation, high FGFR4, high EGFR, Apolipoprotein B mRNA Editing Catalytic Polypeptide-like (APOBEC) mutation, high Cyclin D1, and increased genomic instability
TNBC	IC-NST, medullary, metaplastic, adenoid cystic, and secretory	TP53 mutation, retinoblastoma 1 (RB1) loss, Breast cancer gene 1 (BRCA1) loss, high FGFR2, increased DNA repair proteins, Forkhead box M1 (FOXM1) activation, and increased genomic instability

1.3 Epidemiology of Breast cancer

The International Agency for Research on Cancer (IARC) of the World Health Organization (WHO) reported 19.3 million new cancer cases and 10 million deaths in 2020; breast cancer surpassed lung cancer by bagging 2.26 million cases (11.7% of the new cancer cases) (International agency for research on cancer, 2021). Breast cancer leads in incidence rates in 92 countries, with the second-highest mortality rate in 31 countries (Figure 1.5).

In 2018, Globocan recorded 18.1 million new cancer cases, with 2.1 million breast cancer cases (11.6% of the new cancer cases) and a 6.6% mortality rate (Bray et al., 2018). The year 2012 observed 14.1 million new cancer cases, with 1.7 million breast cancer cases (11.9% of new cancer cases) and 521,900 deaths (Torre et al., 2015). This trend might rise to 3.2 million new cases annually by 2030 (Winters et al., 2017).

Countries with high human development index (HDI) recorded high age-specific incidence rates (ASR) with the lowest mortality rates, but countries with low HDI registered the lowest ASR with high mortality rates (Vogel, 2015). Countries with a lower socioeconomic status report higher mortality rates due to less screening, inefficient treatment (Iacoviello et al., 2020),

inadequate and untimely diagnosis, and lack of consciousness of the disease and its distribution (Ghoncheh et al., 2016). The advanced form of male breast cancer also recorded a 40 % surge from 1975 to 2015, resulting from a dearth of screening and awareness of breast cancer in males (Konduri et al., 2020).

Top cancer per country, estimated number of new cases in 2020, both sexes, all ages (excl. NMSC) a

Breast (92)
Prostate (38)
Lung (23)
Cervix uteri (20)
Liver (6)
Stomach (5)
Oesophagus (1)
Not applicable
No data

Data source: GLOBOCAN 2020
Map production: IARC
(http://gco.iarc.fr/today)
World Health Organization

World Health Organization
© International Agency for Research on Cancer 2020
All rights reserved

Top cancer per country, estimated number of deaths in 2020, both sexes, all ages (excl. NMSC) b

Lung (89)
Breast (31)
Cervix uteri (22)
Liver (16)
Stomach (13)
Prostate (12)
Oesophagus (1)
Colon (1)
Not applicable
No data

Data source: GLOBOCAN 2020
Map production: IARC
(http://gco.iarc.fr/today)
World Health Organization

World Health Organization
© International Agency for Research on Cancer 2020
All rights reserved

Figure 1.5 2020 statistics of global incidence and mortality of breast cancer by IARC-WHO

Globocan reported 1,324,413 new cancer cases in India in 2020, with 178,361 breast cancer cases in females (13.5%) and 90,408 deaths (International Agency for Research on Cancer, 2020). A literature-based meta-analysis from January 1, 1999, to December 31, 2015, covering 17 studies and 7,237 patients reported a 31% prevalence of TNBC, 48 % of HR+, and 27 % of HER 2+ cases in India; the caseload of 28, 34, 30 and 31% in north, south, east and west India showed insignificant difference (Sandhu et al., 2016).

The probable etiology of high TNBC in India includes genetic susceptibility, multiparity, lifestyle, socioeconomic factors, etc. The reported mean age of TNBC in India is 40-55 years, compared to 50-70 years in other countries. TNBC rates are highest in India (27.9%) compared to other countries with highest incidence in Nagpur (43.5%), followed by Srinagar (34.4%), North-East (31.9%), Mumbai (31.1%), Chennai (25.2%), Bengaluru (24.61%), Delhi (24.2%), Pune (23.5%) and Hyderabad (22.8%) (Thakur et al., 2018). India reported the highest prevalence of Luminal A followed by TNBC, Luminal B, and HER 2 enriched (Figure 1.6) – an investigation of 56 cases from May 2012 to April 2014.
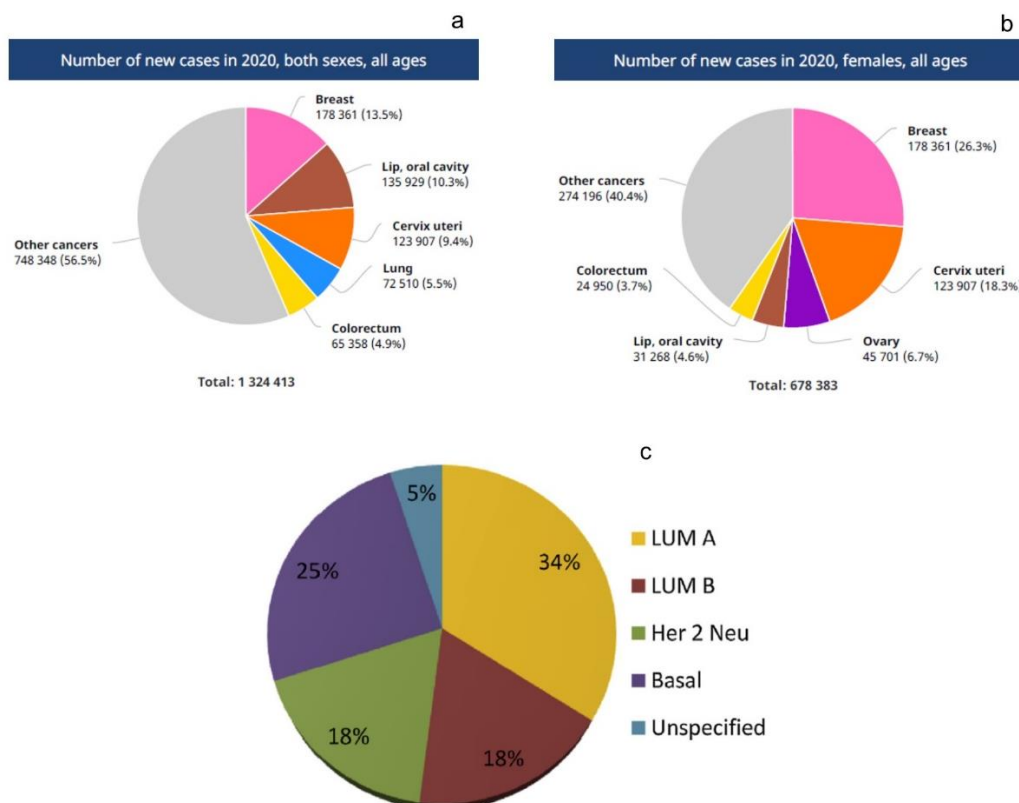
Figure 1.6 IARC statistics of new cancer cases in both sexes in 2020 (a), new cases in 2020 in females (b), and distribution of molecular subtypes in India (c) (Image source: (Kumar et al., 2015)

1.4 Risk factors of breast cancer

Studies report various plausible risk factors for breast cancer (Figure 1.7).

Reproductive factors: Early onset of menarche and delayed natural menopause are independent risk factors that increase estrogen exposure (Macmahon et al., 1973). Hysterectomy (induces artificial menopause) and bilateral oophorectomy before 40 years of age decrease the risk of breast cancer by 75 % at later ages, but after 40 years or natural menopause, this protection is ineffective (Feinleib, 1968).

First full-term pregnancy at a younger age protects against breast cancer over the females that give first birth at 30-35 years of age, and nulliparous women are at the highest risk (Kelsey et al., 1993) -breast cancer was once known as "nun's disease." A meta-analysis showed that every live birth reduces the chance of HR + breast cancer by 11% (Rojas and Stuckey, 2016).

Hormonal factors: Doctors prescribe hormone replacement therapy for menopausal symptoms that also reduces osteoporosis, but a statistical study by the Women's Health Initiative linked breast cancer to estrogen plus progesterone treatment over the estrogen only regimen (Singletary, 2003). The relation between oral contraceptives and breast cancer is a decade long debate, but IARC links the oral dosages of combined estrogen-progestin with breast cancer (Hunter and Sc, 2018).

Demographic factors: Breast cancer is more prevalent in females than males –breast cancer in males accounts for only 1% of the total cases (Gucalp et al., 2019). The upper economic class (sociodemographic risk factor) reports a higher caseload than the lower economic sect (Halka and Stark, 1995). The probability of breast cancer increases with age, saturates at menopause, and further declines or stagnates (Momenimovahed and Salehiniya, 2019).

Genetic factors: Genetic predisposition contributes to 12% of all breast cancers with the inheritance of autosomal dominant BRCA1 and BRCA2 genes in 80-90% of familial breast cancers; TP53 and checkpoint kinase-2 (CHEK2) in less than 10%; and phosphatase and tensin homolog (PTEN), serine/threonine kinase 11 (STK11), and ATM (rare) in less than 1% of all the hereditary breast cancers (Table 1.2) (Vinay et al., 2012).

Table 1.2 Genes associated with breast cancer and their characteristics

Genes	Characteristics
BRCA 1 **BRCA 2**	• Tumor suppressor gene • Autosomal dominant transmittance with a high penetration • Mutations in the BRCA1 gene, located on chromosome 17q, are associated with an increased risk of breast, ovarian, and prostate cancer • Mutations in the BRCA2 genes, located on chromosome 13q, which is an acrocentric chromosome in men, correspond to an increased risk of breast, ovarian, and prostate cancer
p53	• Tumor suppressor gene • Autosomal dominant transmittance • The most commonly mutated gene in breast, colon, lung, ovarian, and brain cancers
PTEN	• Tumor suppressor gene • Expresses a lipid phosphatase regulates the cell cycle, apoptosis, and metastasis.
Phosphoinositide-3-kinase (PI3K)	• The most commonly mutated gene in breast cancer • Expresses lipid kinases that help in cell survival, proliferation, differentiation, and migration
STK11	• Tumor suppressor gene • Regulate cell polarity and mediate apoptosis
Cadherin 1 (CDH1)	• Located on chromosome 16q and encodes E-cadherin • Tumor suppressor gene • It plays a key role in cellular adhesion, cell motility, differentiation, growth, migration, and signalling
ATM	• Located on positions 22 and 23 of chromosome 11 • Encodes a PI3K-related protein kinase that activates cellular responses to DNA double-strand breaks

| **CHEK2** | Positioned at 12.1(22q12.1) Regulates p53 and BRCA 1 |

Breast related factors: China reports that prolonged breastfeeding protects against breast cancer in premenopausal women (Mansfield, 1993) (Kelsey et al., 1993). Breast density positively correlates to breast cancer risk (Nazari and Mukherjee, 2018). Benign breast disease and a strong family history augment the risk (M Román, M J Quintana, J Ferrer, 2017) in premenopausal than in postmenopausal women (Momenimovahed and Salehiniya, 2019).

Lifestyle: The androgenic precursors convert to oestradiol and escalate obesity in premenopausal women, forming a nexus with breast cancer (Miller et al., 2018). The enzymes of the breast tissue transform alcohol to acetaldehyde (a carcinogen) and further to reactive oxygen species (ROS); alcohol also plays a role in the estrogen pathway, thus is a risk factor (Seitz et al., 2012) (Dumitrescu and Shields, 2005). Young females with heavy smoking habits before the first full term pregnancy are highly susceptible to breast cancer (Reynolds, 2013). Reduced vitamin D levels and insufficient physical activity are risk factors for breast cancer (Momenimovahed and Salehiniya, 2019).

Other factors: Areas of massive emissions in the US have high air pollutants and report high breast cancer cases (Wei et al., 2012). Women working night shifts have reduced melatonin levels, which increases reproductive hormone levels and susceptibility to breast cancer (Momenimovahed and Salehiniya, 2019). Women with pre-existing medical conditions who undergo chest radiation are at a higher risk (Halka and Stark, 1995).
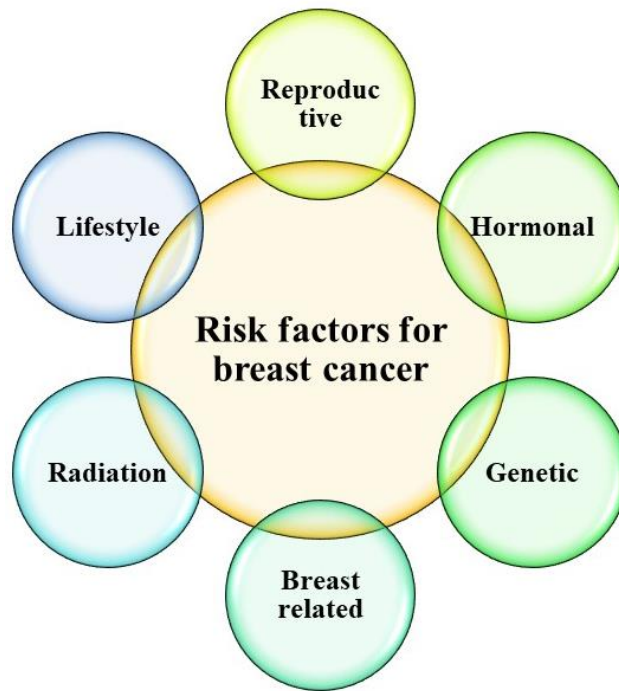
Figure 1.7 Risk factors for breast cancer (modified from (Moudgil et al., 2022))

1.5 Screening and Diagnosis

Early screening and diagnosis of breast cancer are imperative for a favorable prognosis and to prevent relapse. A sequential, well-established protocol practiced for an efficient and accurate diagnosis is as follows (Figure 1.8).

Breast self-exam: Breast self-exam predicates on breast cancer awareness. Females experience high anxiety levels about any breast abnormality that increases needle and excisional biopsies (McCready et al., 2005). A basic knowledge of breast anatomy and periodic changes can circumvent this problem (Rupen Shah, Kelly Rosso, 2014).

Mammography: Mammography is a safe imaging tool that uses low energy X-rays to detect breast abnormalities more efficiently in older women with less dense breasts but can give false negative results in younger women with dense breasts. The advanced versions of full-field digital mammography, computer aided detection, contrast-enhanced mammography, and tomosynthesis have high image quality and better sensitivity to denser breasts (Singh et al., 2008).

Ultrasound: Breast ultrasonography is a cost effective, convenient, and readily available technique employing ultrasound waves in females with dense breasts and in pregnant women.

But, it requires skilled personnel to avoid false positive results due to the non-standardization of the technique (Elmore et al., 2005).

X ray computed tomography (CT): A whole body CT scan identifies the primary tumor and any distant metastasis in a single scan (Wang, 2017). High radiation exposure makes it dangerous and expensive, but reducing the exposure area produces a more excellent contrast and reduces adverse risks (Glick, 2007).

Magnetic Resonance Imaging (MRI): MRI with contrast imaging has high sensitivity for dense breasts and implants and efficiently detects relapse after surgery. But, the high cost, the injectable contrast agent, and the claustrophobic feeling while examining are its significant drawbacks (Andreea et al., 2013).

Positron Emission Tomography (PET): PET is a cutting-edge technology that identifies metastasis and cancer remission and monitors tumor size after treatment. The malignant cells show increased uptake of (18F) 2-fluoro-2-deoxy-D-glucose than the normal cells. PET with CT scan also allows an anatomical construction (Singh et al., 2008) (Andreea et al., 2013).

Biopsy: Biopsy elaborates on cell cytology and histopathology, distinguishes between benign and malignant masses, and establishes the receptor status of cancer cells. It includes fine-needle aspiration cytology and core needle biopsy (Love, 2013) (Nounou et al., 2015).

Genomic and Pathologic Analysis: The in situ hybridization technique identifies the genetic heterogeneity of the tumor cells, and fluorescence in situ hybridization (FISH) ascertains the HER2 status. Gene microarray determines the differential expression of genes in the cancer cells and screens the noncoding RNAs specific to breast cancer to classify the samples based on markers. Pathological analysis of the samples by immunohistochemistry (IHC) and immunofluorescence identify the estrogen, progesterone, HER2, and other markers (Song et al., 2016).
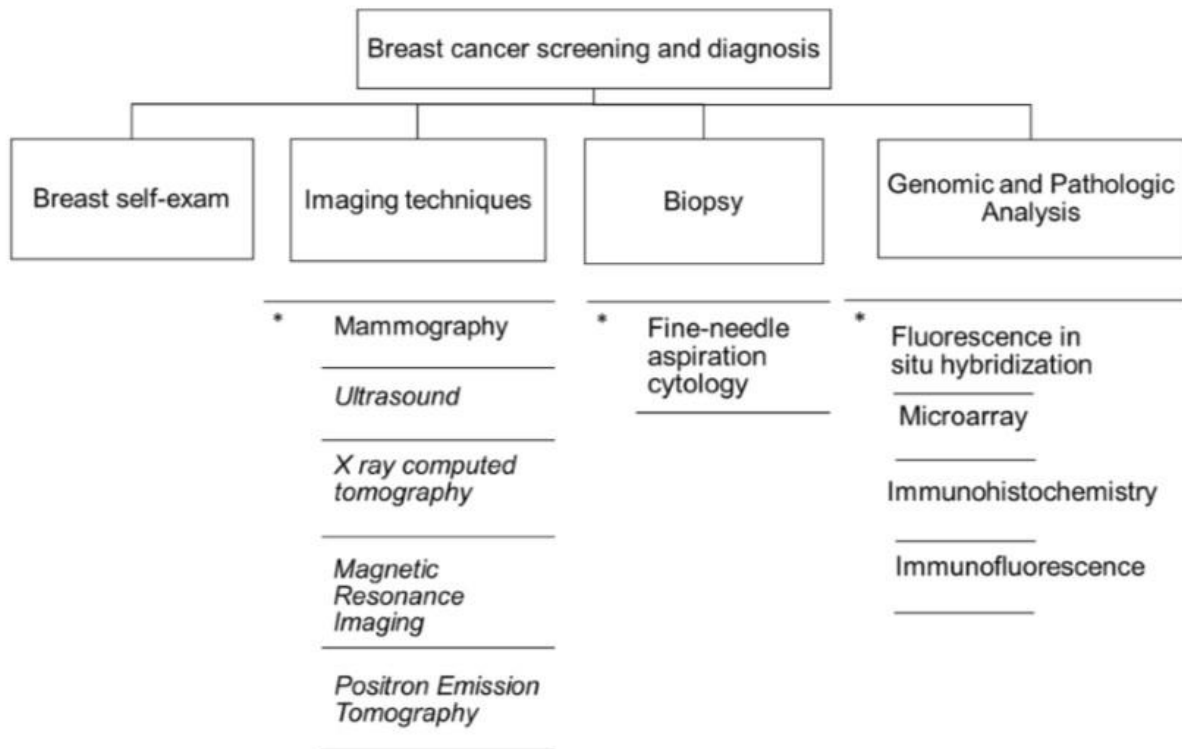
Figure 1.8 Breast cancer screening and diagnosis

1.6 Treatment of breast cancer

The routinely practiced strategies for breast cancer management entail surgery and radiotherapy under localized treatment and chemotherapy under systemic therapy (Figure 1.9). The proposed treatment plan depends on the tumor size, tumor grade, staging, subtype of cancer, hormonal receptors, status of malignancy, metastasis, etc. The complex nature of breast cancer requires a combination of these treatment modalities.

Figure 1.9 Treatment options for breast cancer (Image source: www.google.com)

Surgery: Mastectomy is the removal of the whole breast and is done for relatively large tumors compared to the breast size, for multi focal tumors, and upon the patient's inclination (Shah et al., 2014). *Halsted mastectomy* is the extraction of the whole breast, axillary lymph nodes, and pectoralis major and minor muscles (Cotlar et al., 2003); *modified radial (Patey) mastectomy* is the excision of the whole breast with the axillary lymph nodes and the skin that envelops the tumor area.

Clinical trials support the efficacy of conservative breast surgery (Cardoso et al., 2019): doctors resect the tumor with tumor free margins without excising healthy breast tissue in *Wide local excision or lumpectomy* (Gradishar et al., 2018); surgeons remove the whole quadrant that habitats the tumor in *Quadrantectomy* (Love, 2013) (Gradishar et al., 2018). The preoperative sentinel lymph node investigation supersedes the axillary lymph node excision to determine metastasis of the cancer cells; the axillary lymph node is dissected and biopsied in a node positive disease (Klevos et al., 2017).

Radiotherapy: Radiation therapy reduces cancer relapse and increases survival rates (Klevos et al., 2017). Patients with higher grade tumors and involvement of 4 axillary lymph nodes undergo radiation after mastectomy (Cardoso et al., 2019). Whole-breast radiation therapy is a conventional and routine practice after conservative breast surgery over regional radiation therapy.

Systemic therapy: Systemic therapy encompasses chemotherapy, endocrine, and HER 2 directed therapy. Preoperative chemotherapy shrinks large tumors for easy resection, an approach termed neoadjuvant therapy, and chemotherapy after tumor excision to prevent relapse is termed adjuvant chemotherapy. Patients with HR - cancer respond more effectively to chemotherapy than those with HR+ cancers (Maughan et al., 2010).

Multidrug resistance (MDR) eminently affects breast cancer therapeutics and prognosis (Hait and Yang, 2005) with bifurcations of *intrinsic MDR*, where the cancer cells are innately resistant to the chemotherapeutic drugs and *acquired MDR*, where cancer cells initially respond to chemotherapy but later relapse and acquire a resistant drug phenotype (Videira et al., 2014). The MDR phenotype emanates either by reduced uptake or an elevated removal of the drugs. Breast cancer cells overexpress P-glycoprotein (P-gp), an ATP-binding cassette transporter (ABC-transporters), and MDR-associated protein (MRP1), an efflux pump, that expels drugs

like doxorubicin (DOX); the overexpressed breast cancer resistant protein (BCRP) shows resistance to a broad spectrum of anticancer agents (Wind and Holen, 2011).

Hypoxic breast cancer cells show hypoxia induced chemoresistance when hypoxia induced factor-1 (HIF-1α) interacts with the MDR1 gene that encodes P-gp (Yuan et al., 2016) (Fulfager and Yadav, 2021) and elevates drug efflux. Alteration in the DNA repair mechanism, reduced activity of topoisomerase II (target of DOX), modification in the apoptotic or antiapoptotic pathways (Thomas and Coley, 2003), detoxification of drugs by glutathione or glutathione-S-transferases and cytochrome P450s – inactivation of drugs that require metabolic activation upon injection - (O'Driscoll et al., 2006) also instill MDR in the cancer cells.

Chemotherapy includes drugs of two significant classes, i.e., anthracyclines and taxanes. Anthracyclines were first isolated in the 1960s from Streptomyces species, such as daunomycin from *Streptomyces peucetius*. Adriamycin isolated from *Streptomyces peucetius* var. *caesius* (Fujiwara et al., 2008) has glycosidic compounds with aglycones with a basic structure of 7, 8, 9, 10-tetrahydro-5, 12-napthacene quinone (Vaněk et al., 1977), and the aglycone ring linked to amino sugars in all the anthracyclines. Daunorubicin of daunomycin and DOX or hydroxyl daunomycin of adriamycin are planar structures with a tetracycline ring attached to the amino sugar, mainly daunosamine by a glycosidic bond; the quinone and the hydroquinone groups are the electron donors or electron acceptors (Rabbani et al., 2005).

The anthracyclines interact with the enzyme topoisomerase II, creating double strand breaks in the DNA. The aglycone ring of the drug incorporates within adjacent base pairs, deforming the DNA structure and stabilizing the enzyme (Jasra and Anampa, 2018). After intercalating, hydrophobic interactions and hydrogen bonds develop between the sugar moieties of the bases and the chromophore region of the drug, positioning the sugar moieties of the drug in the minor grooves of the DNA. Anthracyclines degrade enzymatically to produce semiquinone free radicals that convert to hydroxyl free radicals and degrade non-enzymatically to hydroquinone components after conjugating with ferric ions (Hortobágyi, 1997).

Among taxanes, paclitaxel (PTX) and docetaxel (DTX) are commercially available drugs. In 1966, Wani and Wall isolated PTX from *Taxus brevifolia* (Yared and Tkaczuk, 2012), a slow growing pacific yew tree. For conservation reasons, alternative sources of fast growing European yew tree or *Taxus baccata* and DTX, a semi-synthetic drug developed by Sanofi France, were explored (Maloney et al., 2020).

DTX is more soluble than PTX, and both drugs treat a wide range of cancers such as breast, lung, gastric, bladder, prostate, squamous cell carcinoma of the head and neck, Kaposi's sarcoma, etc. (Yared and Tkaczuk, 2012). But these drugs exhibit a broad spectrum of side effects such as hypersensitivity reactions (hypertension, hypotension, anxiety, dyspnea, etc.), neutropenia (bone marrow suppression), arthralgias/myalgias (flu like symptoms), neuropathy, fluid retention, etc. (Cella et al., 2003) (Markman, 2003).

The tubulin heterodimer of α and β subunits form microtubules (Oshiro et al., 2009) that grow and shorten, aiding in cellular processes for cancer cell proliferation and metastasis (Ojima et al., 2016). Taxanes bind to the N-terminal amino acids of the β-subunit of tubulin heterodimer, causing the microtubules to polymerize, preventing the spindle from forming, and inhibiting the metastatic plate blocking mitosis and inducing apoptosis (Rowinsky, 1997).

Endocrine therapy includes tamoxifen, an antiestrogen that competitively inhibits estrogen from binding to the ER. Doctors prescribe this oral medication to pre and postmenopausal patients with ER+/HER2- subtype breast cancer. Doctors prescribe aromatase inhibitors like anastrozole, exemestane, and letrozole to menopausal women to prevent androgens from converting to estrogens (Winer, 2019). Trastuzumab, a HER 2 specific monoclonal antibody (MAb) with chemotherapy, prolongs the survival of HER 2 + patients (David Mankoff, 2016).

The National Cancer Institute approves various drugs and drug combinations to treat and prevent breast cancer (Table 1.3).

Table 1.3 Drugs and drug combinations to prevent and treat breast cancer and combination of drugs ("Drugs Approved for Breast Cancer - NCI," 2023)

	Drug	Function
Approved drugs to prevent breast cancer	**Raloxifene Hydrochloride**	Decreases the risk of invasive breast cancer in high risk post-menopausal women
	Tamoxifen citrate	Decreases the chance of invasive breast cancer after surgery and radiation in ER$^+$ patients

Approved drugs to treat breast cancer	**PTX Albumin-stabilized nanoparticle formulation**	Used alone or in combination to treat relapsed or metastasized tumors after chemotherapy with other drugs
	Anastrozole	For post-menopausal women with early stage HR$^+$ cancer or metastatic cancer
	Capecitabine	Used alone when anthracyclines or taxanes do not work or used in combination
	Cyclophosphamide	Used alone or in combination
	DTX	Used alone or in combination with metastatic breast cancer with no improvement after chemotherapy
	DOX hydrochloride	Used alone or in combination
	Epirubicin hydrochloride	Used alone or in combination after surgery for metastasized cancer
	5-Fluorouracil	To treat breast cancer
	Fulvestrant	Used alone or in combination for post-menopausal women with HR$^+$ and HER2$^-$ advanced cancer
	Gemcitabine hydrochloride	Used alone or in combination when chemotherapy fails
	Trastuzumab	Used alone or in combination for HER2+ cancer
	Letrozole	Used alone or in combination for early stage HR+ cancer
	Methotrexate sodium	Used alone or in combination
	PTX	Used alone or in combination node positive cancer
	Tamoxifen citrate	To treat metastatic cancer
	Vinblastine sulfate	For palliative treatment
Drug combinations for breast cancer	DOX hydrochloride + Cyclophosphamide	
	DOX hydrochloride + Cyclophosphamide + PTX	
	Cyclophosphamide + DOX hydrochloride + Fluorouracil	

| Cyclophosphamide + Methotrexate + Fluorouracil |
| Fluorouracil + Epirubicin hydrochloride + Cyclophosphamide |
| DTX + DOX hydrochloride + Cyclophosphamide |

1.7 Nanotechnology interventions for the treatment of cancer

Chemotherapy results in a poor quality of life, accumulates non-specifically causing systemic or organ specific toxicities, requires higher injectable doses, and exhibits lower bioavailability of the hydrophobic drugs. Nanoparticle based treatment supersedes these fallouts by lowering the drug dosage, reducing non-specific accumulation and toxicities, allowing targeted drug delivery, encapsulating drugs and altering their pharmacodynamic and pharmacokinetic properties, increasing drug accumulation in the tumor area, and releasing the drug in a controlled and sustained manner (Dang and Guan, 2020) (Suri et al., 2007). Nanoparticles such as liposomes, micelles, chitosan nanoparticles, mesoporous silica nanoparticles, dendrimers, solid lipid nanoparticles, polymeric nanoparticles, magnetic nanoparticles, nano gel, etc. show higher efficacy for cancer therapy (Figure 1.10) (He et al., 2016) (Jain, 2005) (Dang and Guan, 2020) (Jafari et al., 2019) (Senapati et al., 2018).

Liposomes   Polymeric micelle   Dendrimer

Polymer-drug conjugate   Mesoporous silica nanoparticles   Magnetic nanoparticles
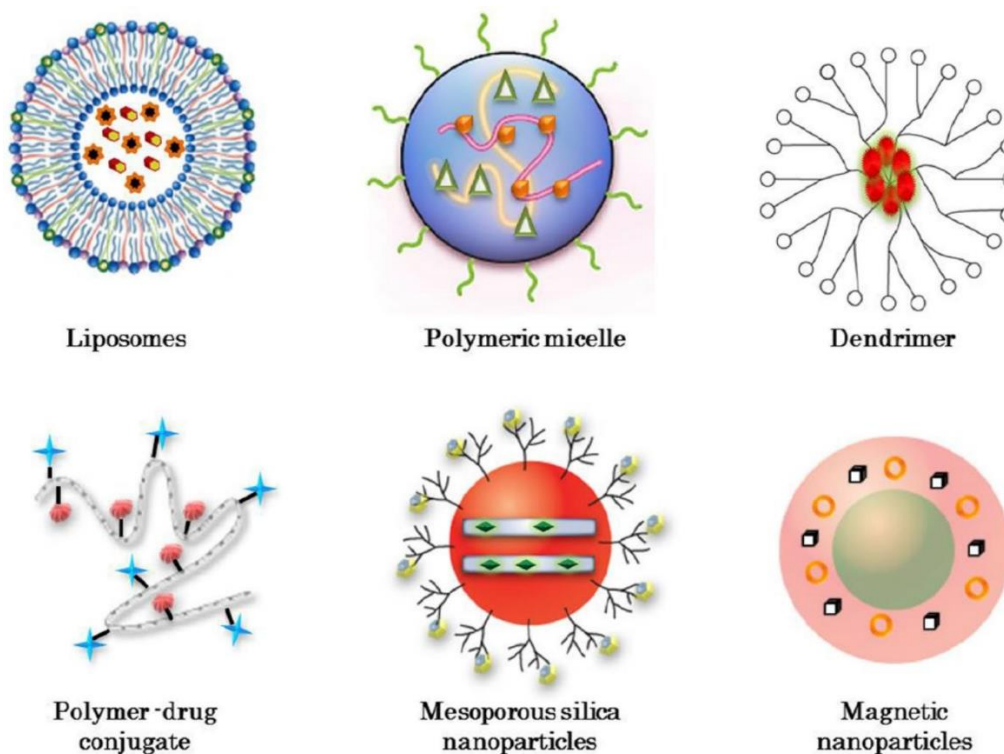
Figure 1.10 Different nanoparticles explored for the treatment of cancer (Image source: Choi et al., 2016)

1.8 Liposomes

Liposomes are U.S. Food and Drug Administration (FDA) approved nanocarriers. Dr. Alec D. Bangham and R. W. Horne discovered some bilayer structures upon negatively staining dry phospholipids in 1961 while examining a new electron microscope at the Babraham Institute in Cambridge (Dua et al., 2012). Previously known as bangosomes, these structures are known today as liposomes, a name coined by Gerald Weismann (Riaz et al., 2018). It constitutes two Greek words, 'Lipos' meaning fat, and 'soma' meaning body (Daraee et al., 2016).

Liposomes have multidimensional applications: in physics and mathematics, they help study the topology of 2D surfaces in 3D space; in biophysics, liposomes help explore cell membranes and associated channels, phase transitions, and permeability; in physical chemistry, liposomes help investigate the colloidal nature, and intra and inter aggregate forces; in chemistry, they help examine artificial photosynthesis, micrcompartmentalization, photochemistry, and catalysis; in biochemistry, liposomes help inspect membrane proteins and in biology cell trafficking, function, excretion, gene delivery etc. (Lasic, 1995). Gregory Gregordiadis was the first to explore liposomes as drug delivery vehicles (Allen and Cullis, 2013).

1.8.1 Structure of Liposomes

Phospholipids constitute a significant portion with cholesterol (CHOL) as a secondary component to form a lipid bilayer that self-encloses into spherical structures (Figure 1.11) (Pandey et al., 2016). The lipid bilayer incorporates hydrophobic drugs, and the enclosed aqueous core or the water–lipid interface contains hydrophilic drugs (Bozzuto and Molinari, 2015).
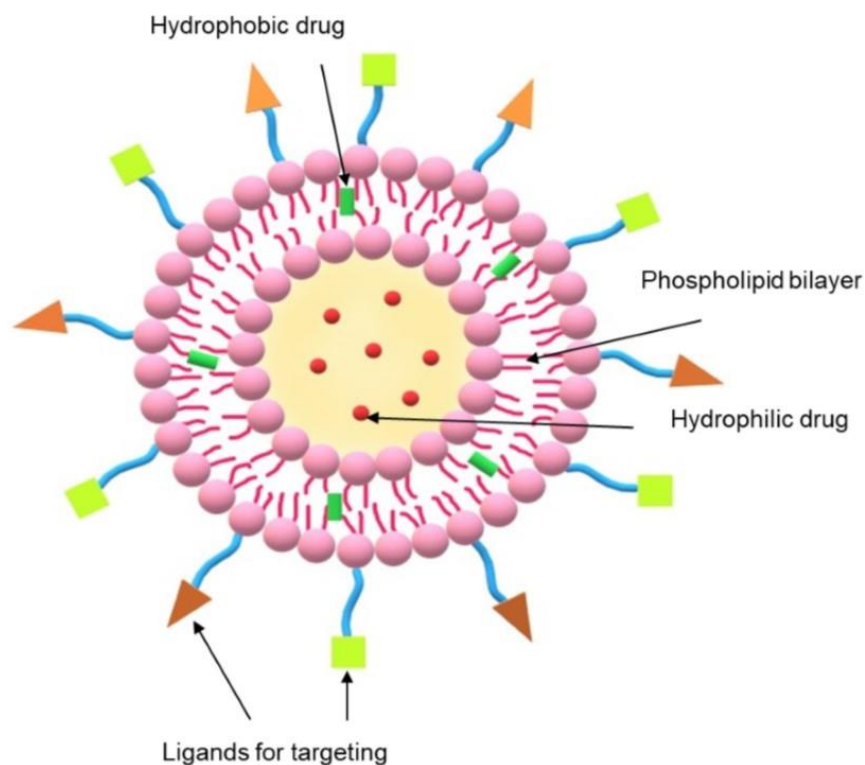
Figure 1.11 Structure of liposomes

Phospholipids form sheets in an aqueous solvent, enclosing themselves to reduce the energy gap between the hydrophobic and hydrophilic phases and maintain a thermodynamic equilibrium; these spherical structures have higher stability due to low surface tension (Figure 1.12). The carboxyl ions of the fatty acyl chains exhibit better electrostatic interactions at neutral pH due to the repulsive forces increasing liposomal stability at the lamellar phase. But, the acidic medium protonates the carboxylic groups, creating unstable liposomes that aggregate and leak their payload (Yadav et al., 2017). Hydrophobic interactions help create liposomes, van der Waals forces keep the hydrocarbon chains together and strengthen the bilayer, and hydrogen bonds and polar interactions between the water molecules of the aqueous medium and polar head groups of the lipid stabilize the liposomes (Bozzuto and Molinari, 2015).
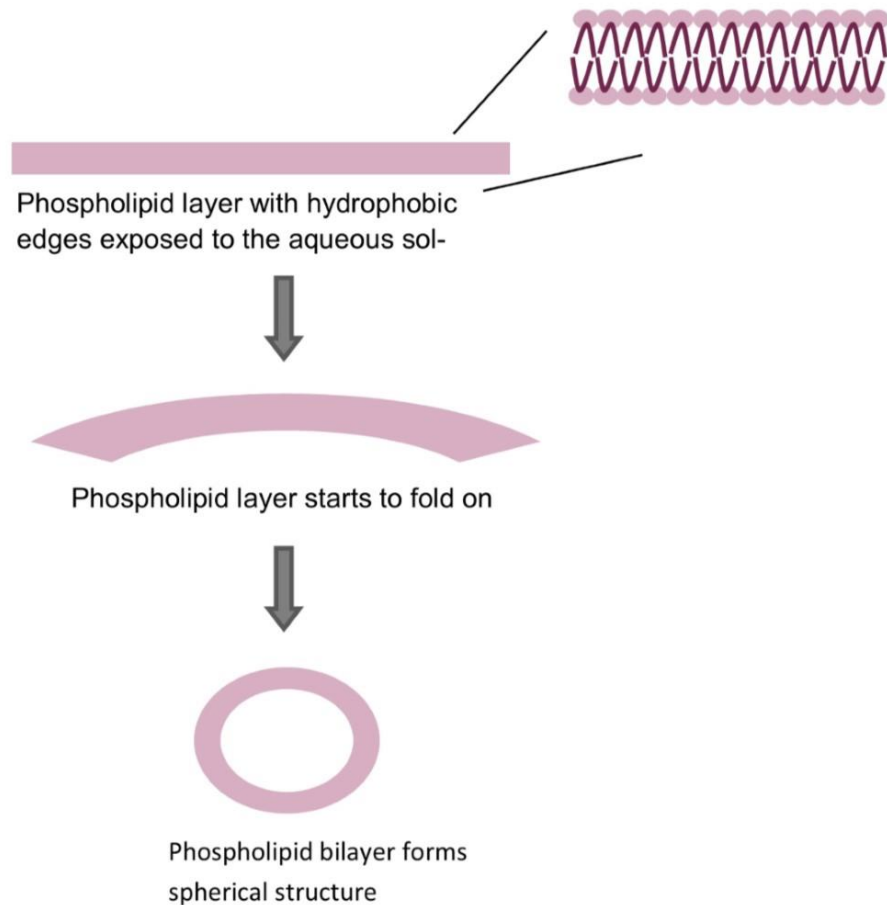
Figure 1.12 Mechanism of liposome formation

Phospholipids are amphipathic molecules with a hydrophilic headgroup linked to a hydrophobic tail by ether, ester, or amide bonds. The ether bonds impart high stability, non-degradability, and a cytotoxic attribute to the liposomes, but ether and amide bonds provide biodegradability and low levels of cytotoxicity to the liposomes (Li et al., 2019). Phospholipids are glycerophospholipids with a glycerol backbone or sphingomyelins with a sphingosine backbone.

Glycerophospholipids, the major phospholipids of the eukaryotic cells, have the first and second carbon of the glycerol moiety esterified to long chain fatty acids, and the third carbon atom esterified to phosphoric acid that is further esterified to organic molecules like choline, serine, inositol, etc. (Li et al., 2015). Phospholipids differ in fatty acyl chain length and level of unsaturation (Drescher and van Hoogevest, 2020), denoted by two numerical values of the number of carbon atoms and the number of *cis*-double bonds (Table 1.4).

Table 1.4 Phospholipids with varied fatty acyl chain lengths and levels of unsaturation

Carbon chain length and level of unsaturation	Name of the phospholipid
C14:0	Myristic acid (tetradecanoic acid)
C16:0	Palmitic acid (hexadecanoic acid)
C18:0	Stearic acid (octadecanoic acid)
C18:1	Oleic acid (octadecenoic acid)
C18:2	Linoleic acid (octadecadienoic acid)
C18:3	α-linolenic acid (octadecatrienoic acid)
C20:0	Arachidic acid (eicosanoic acid)
C20:4	Arachidonic acid (eicosatetraenoic acid)
C22:0	Behenic acid (docosanoic acid)
C22:4	Docosatetraenoic acid
C22:5	Docosapentaenoic acid
C22:6	Docosahexaenoic acid

Natural phospholipids are a mixture of different phospholipids sourced from egg yolk, soybean, and rapeseed, have a higher level of unsaturation, and are cheaper; synthetic phospholipids are composed of a single lipid, are generally saturated, and are more expensive. As a component of bile, phospholipids solubilize cholesterol and fatty acids by forming micelles; as a lipoprotein, they help transport fats between the gut and liver (Drescher and van Hoogevest, 2020); as a lung surfactant, they reduce the surface tension of the air/water interface; as a component of the lipid-calcium-phosphate complex, they help in bone formation, and regulate blood coagulation (R. P. Singh et al., 2017). Structures like micelles, liposomes, and hexagonal phases form in an aqueous environment depending on the shape of the lipid (Table 1.5).

Table 1.5 Structure of phospholipids and shape formed in an aqueous environment

Phospholipid	Shape of lipid	Structure in aqueous medium
Phosphatidylcholine	Inverted cone	Bilayer
Phosphatidylethanolamine (PE)	Cone	Hexagonal
Phosphatidylserine	Cylinder and cone	Bilayer and hexagonal
Phosphatidylinositol	Cylinder	Bilayer

Cardiolipin	Cylinder and cone	Bilayer and hexagonal
Sphingomyelin	Cylinder	Bilayer

CHOL has a steroid backbone with a hydroxyl group (small polar headgroup) inclining towards the hydrophilic headgroup of the phospholipid (Figure 1.13) and a tricyclic ring (hydrophobic region) accommodating within the initial carbon atoms of the fatty acid chains in the bilayer (Vemuri and Rhodes, 1995). The structure and orientation of CHOL enable it to fill the gaps in the bilayer created due to imperfect packing of the lipids.

CHOL prevents the flip flop movement of phospholipids, provides rigidity to the membrane by evading the lipid phase transition (Tc), reduces drug leakage, and prevents the hydrolytic degradation of the lipid bilayer. Thus, CHOL imparts elasticity, stability, and permeability to liposomes. Phospholipids make 55-100 % of the total lipid components, and CHOL constitutes 30-45 % as it cannot form liposomes independently.
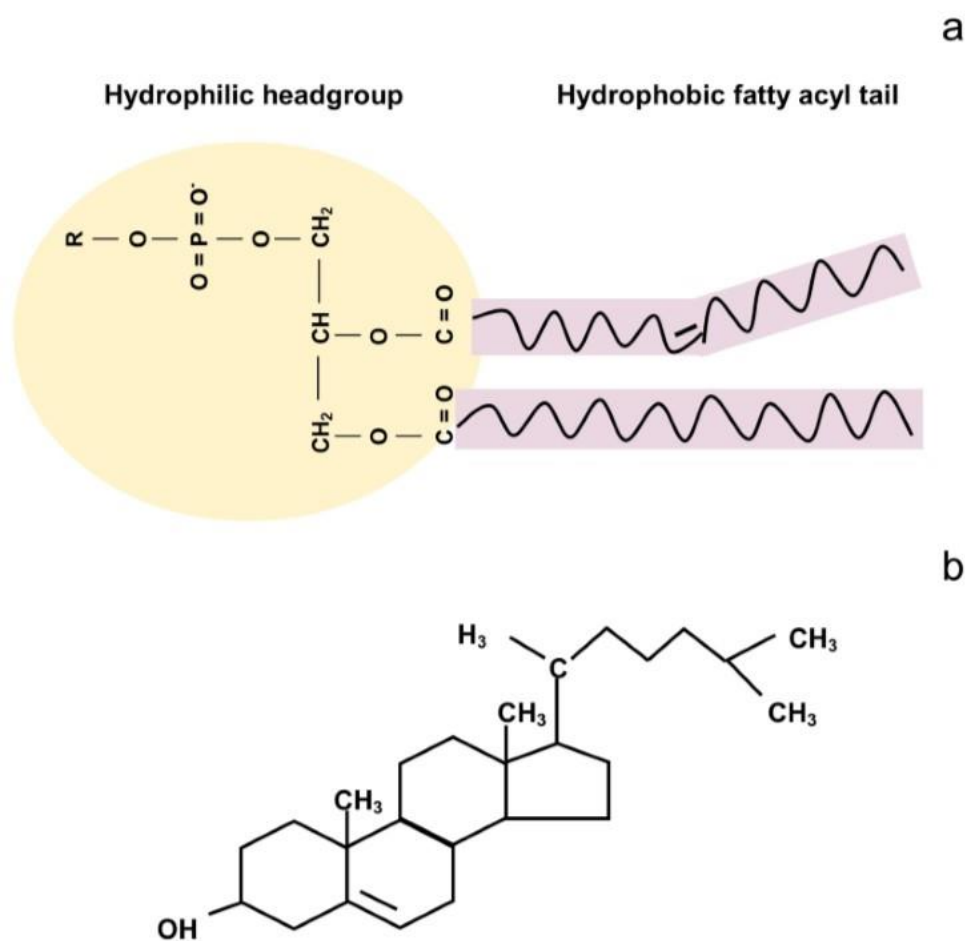
Figure 1.13 Structure of phospholipid and CHOL

1.8.2 Classification of liposomes

Liposomes are classified based on their size, number of bilayers, responsiveness to stimuli, charge, and evolution (Figure 1.14).

Size: Liposomes can be *multilamellar vesicles* (MLVs) and *unilamellar vesicles* (ULVs) based on the number of lipid bilayers and size (Shailesh et al., 2009). MLVs have more than one lipid bilayer with an aqueous cavity enclosed between adjacent layers, have sizes up to 5 μm that enhance drug encapsulation, and show long term stability. However, the reticuloendothelial system (RES) rapidly clears these particles due to their increased sizes, making vehicles efficient against RES-related diseases.

ULVs have a single bilayer and bifurcate into *small unilamellar vesicles* (SUVs) with a 50-100 nm size range and *large unilamellar vesicles* (LUVs) with a 100-250 nm size range (Harrington et al., 2010); RES rapidly clears the LUVs due to larger sizes than the SUVs. MLVs display a slower drug release than ULVs, as every bilayer restricts the movement of the drug.

Responsiveness to stimuli: Stimuli responsive liposomes have two classes of triggers, namely, *intrinsic stimuli* (pH, temperature, redox potential, enzymes) associated with the pathological characteristics of the tumors and *extrinsic stimuli* (temperature, magnetic, light, ultrasound) as artificial and externally applied triggers. *pH responsive liposomes* release drugs in the acidic environment of the TME or the intracellular compartment of cancer cells. They are routinely synthesized with PE and an acidic phospholipid that acts as a stabilizer (Karanth et al., 2007).

The physiological pH stabilizes the pH sensitive liposomes, but the acidic environment displays their fusogenic properties. The negatively charged polymers/peptides/lipids protonate in an acidic medium (5.5 pH in the endosomal compartment is 5.5 and 4.5 pH in the lysosomes), destabilizing the liposomal structure or creating pores and triggering drug release (Voinea et al., 2002). The high redox potential difference between the cancer cells' reducing intracellular space and oxidizing extracellular space and between the normal and cancer cells triggers drug release from the *redox sensitive liposomes*. Glutathione is approximately 100-1000 times higher in the cancer cells than in the blood and by 1000 folds than the extracellular environment of the normal cells, thus creating a high redox potential. Glutathione reduces the disulfide

bonds of the lipids or other components to thiol groups that compromise liposomal integrity, releasing the enclosed drug (Singh et al., 2017).

Enzyme sensitive liposomes are responsive to enzymes such as matrix metalloproteinase and proteinase (Torchilin, 2014) that, upon exposure, disrupt the liposomal integrity to release the drugs. *Thermosensitive liposomes* attain a leaky nature at temperatures (42 °C) higher than the physiological temperature (37 °C) at the cancer site that is pathologically hyperthermic (intrinsic stimuli) or on externally applied heat (extrinsic stimuli). 1,2 dipalmitoylphosphatidylcholine (DPPC) has a Tc temperature of 41 °C and transitions to a leaky morphology under hyperthermia, and lysolipids create pores in the lipid bilayer (Kneidl et al., 2014). External heat increases the intercellular gap between the endothelial cells, dilating the tumor vasculature, increasing blood flow to the tumor site, and increasing liposomal accumulation (Dou et al., 2017).

Magnetic liposomes have a magnetic component (such as iron oxide nanoparticles) encapsulated in the liposomes, showing a therapeutic effect under a magnetic field. *Phototriggerable liposomes* encapsulate a photosensitizer that activates upon irradiation at the near infrared region (700-2500 nm) and generates ROS that adversely affects the target cells - known as photodynamic therapy (Puri, 2013). *Ultrasound sensitive liposomes* are susceptible to the extrinsic stimuli of ultrasound waves that result in the release of the payload (Schroeder et al., 2009).

Charge: Liposomes are negative, positive, or neutral based on the charge of the phospholipid headgroup. *Neutral liposomes* aggregate (devoid of charge), unlike charged liposomes that electrostatically repel each other and increasingly interact with the target cells (Bozzuto and Molinari, 2015). The *cationic* and neutral liposomes activate the immune system and get more rapidly cleared than the *anionic liposomes* (Miller et al., 1998).

Cationic liposomes target and accumulate in the angiogenic cells and inflammation sites (Krasnici et al., 2003) and are majorly used to deliver nucleic acids -as the positively charged lipids interact with the negatively charged nucleic acids. Anionic liposomes formed by lipids like dimyristoyl phosphatidylglycerol or dipalmitoyl phosphatidylglycerol undergo rapid opsonization and elimination by the RES and have toxic side effects but show an increased penetration through the skin (Ogiso et al., 2001).

Evolution: The conventional or *first generation liposomes*, initially composed of naturally derived phospholipids, displayed a shorter blood circulation half-life and instability in plasma (Storm and Crommelin, 1998), but adding CHOL supersedes these drawbacks (Mufamadi et al., 2011). The *second generation liposomes* have hydrophilic polymers like polyethylene glycol (PEG) (PEGylated liposomes) decorated on the surface to synthesize stealth liposomes (Mufamadi et al., 2011). PEG creates a steric barrier that bypasses opsonization, evades the RES, prolongs the blood circulation time, and reduces the clearance rates (Gabizon and Martin, 1997).

PEG also prevents liposomes from aggregating by overcoming the attractive van der Waals forces between the particles. The *targeted liposomes* are remodeled stealth liposomes synthesized by functionalizing the surfaces with ligands (such as antibodies, peptides, carbohydrates, and folic acid) with an affinity towards receptors overexpressed on the target cells (Sercombe et al., 2015). This approach of active targeting allows liposomes to accumulate in the tumor cells in large numbers (Li et al., 2019). *Multifunctional or theranostic* liposomes are actively targeted with anticancer and imaging agents (Riaz et al., 2018).
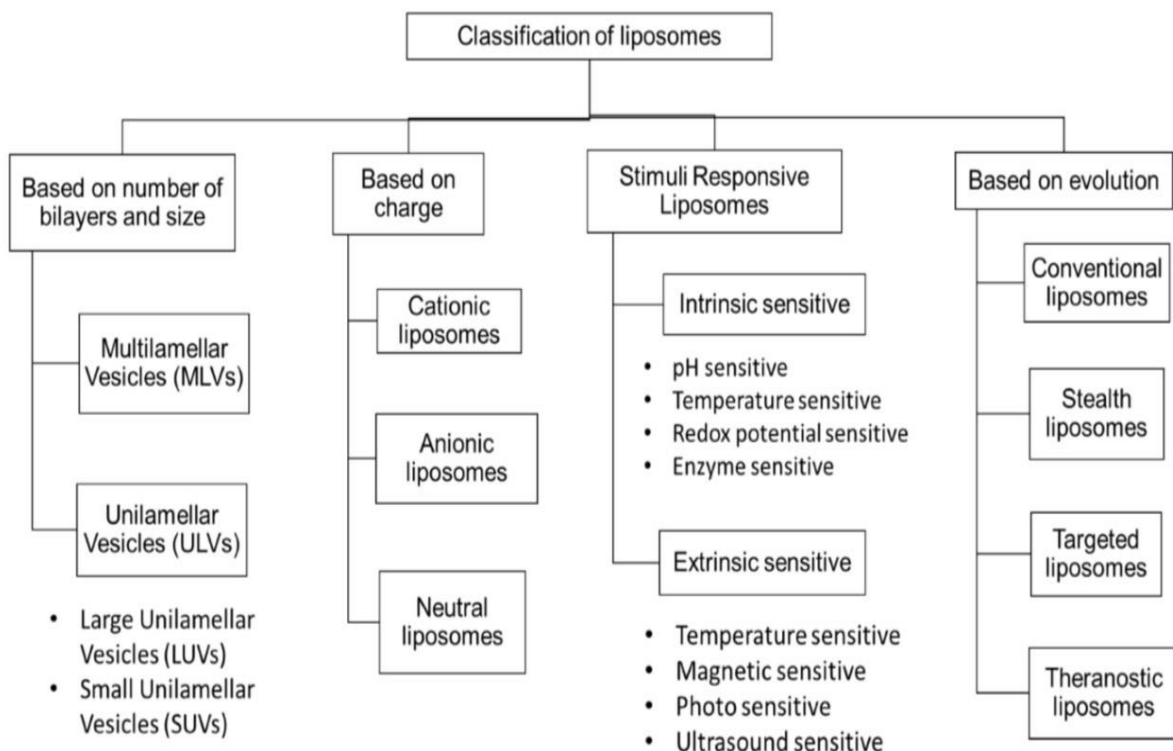
Figure 1.14 Classification of liposome

1.8.3 Advantages of liposomes

Liposomes are analogous to cell membranes and are biocompatible, biodegradable, and non-immunogenic. The amphipathic nature of liposomes allows the hydrophobic drugs to encapsulate in the lipid bilayer and the hydrophilic drugs in the enclosed aqueous core -the majority of the anticancer drugs are lipophilic (Madni et al., 2014). Liposomes protect drugs from metabolic degradation, enhance the pharmacokinetic properties of the drugs- as the pharmacokinetics of the liposomes determine the fate of the drug-, show sustained drug release, reduce the drug dosages, improve the drug half-life, increase the drug efficacy, and improve the therapeutic index of the drug (Garg et al., 2014) (Mishra et al., 2018).

Smaller liposomes evade the immune system effectively, accumulate in the target organs, and reduce systemic toxicities. FDA approves the intravenous route (IV) of liposomes, and researchers have also explored liposomes as inhalers for lung diseases. Researchers avoid the delivery through the oral route to prevent the liposomes from disintegrating by the bile salts. Liposomes significantly reduce the non-target drug accumulation in the heart, liver, kidney, etc., and avoid systemic toxicities, unlike DOX, which engenders cardiotoxicity.

1.8.4 Synthesis of liposomes

Synthesis of liposomes follows three primary techniques (Figure 1.15).

1.8.4.1 *Mechanical method*

***Thin film hydration technique*:** The thin film hydration technique involves two basic steps: organic solvent containing dissolved lipids is evaporated to form a lipid layer on the walls of the round bottom flask (RBF) in the thin film formation step; the lipid layer is hydrated with an aqueous solvent in the thin film hydration step. We can carry out the Synthesis by a rotary evaporator to create a thin film and hydrate the layer by agitating mechanically.

Hand shaken method: In the hand shaken approach, we perform the two steps of the thin film hydration technique by the hand (Ghatage et al., 2017).

Freeze thawing: Preformed liposomes with drugs in close contact are dehydrated, causing the drugs to adhere to the liposomal surface; after hydrating, the liposomes swell and encapsulate these drugs. We can repeat the freezing-thawing many times to ensure an increased drug

encapsulation, but it can also cause SUVs to fuse and produce LUVs (Akbarzadeh et al., 2013) (Ghatage et al., 2017) (Samad et al., 2007).

Sonication: Probe sonication reduces the particle size by converting MLVs to LUVs/SUVs and LUVs to SUVs. This process leaches titanium that requires an additional filtration step, elevates the temperature that adversely affects the liposomal integrity, and the high energy sonication oxidizes and hydrolysis the lipids (Ghatage et al., 2017) -thus carried out on ice. Water bath sonication reduces the particle size but generates a heterogeneous population. It is easier to control the process temperature but requires longer sonication times, affecting liposomal integrity.

Extrusion: Extrusion is a downsizing strategy where we pass liposomes through a polycarbonate membrane of definite pore size or successive membranes with decreasing pore sizes. Extrusion is a reproducible technique that is faster and gentler on the liposomes than other techniques. We can use an automated system of high-pressure extrusion with pressures of up to 250 psi (Panahi et al., 2017) (Vishvakrama and Sharma, 2014).

High pressure homogenization: The French press cell extrusion technique downsizes the MLVs to SUVs by passing the liposomal suspension through an orifice –it is similar to extrusion, but we replace the polycarbonate membranes with an orifice. Microfluidizer supersedes this technique as it is scalable (Vemuri and Rhodes, 1995), and a controlled synthesis procedure where lipids solubilized in alcohol are passed through two aqueous streams in a microfluidic channel to form liposomes (Maherani et al., 2011). This process is repeated many times under a pressure range of 0-200 bar with a heating and cooling component (Wagner and Vorauer-Uhl, 2011).

Proliposome: We coat lipids and drugs on a soluble carrier that forms a flowing material to form liposomes after hydration. It is a cost effective and scalable technique (Dua et al., 2012).

1.8.4.2 *Solvent dispersion method*

Ether injection method: We dissolve lipids in diethyl ether or ether/methanol mixture and slowly inject them into an aqueous solution containing the drug at reduced pressures or upon heating; the organic solvent is then removed under vacuum to form liposomes –the organic solvent should be immiscible in the aqueous solvent for easy removal. But, this technique

synthesizes heterogeneous liposomes, exposes drugs to organic solvents, and creates a highly concentrated liposomal suspension (Ghatage et al., 2017) (Dua et al., 2012).

Ethanol injection method: We solubilize lipids in ethanol are injected them into an excess aqueous solvent containing the drug. This technique forms a heterogeneous population, dilutes the liposomes, ethanol creates an azeotrope with water, resulting in its difficult removal that inactivates the biologically active molecules, and phospholipids show poor solubility in ethanol (Ghatage et al., 2017) (Dua et al., 2012). This technique is easy to scale up and is prevalent in the pharmacological Synthesis of liposomes.

Reverse phase evaporation technique: Phospholipids dissolved in an organic solvent are mixed with excess buffer containing drugs to form a water-in-oil emulsion by mechanical methods like sonication that form inverted micelles; the organic solvent is then removed under reduced pressure that causes phospholipid coated water droplets to aggregate and form a gel like matrix. On further reducing the organic phase, the gel phase converts to a paste of smooth consistency of LUVs. But, the exposure of drugs to organic solvents and the mechanical agitation can denature or cause conformational changes in biological molecules (Akbarzadeh et al., 2013) (Vemuri and Rhodes, 1995) (Dua et al., 2012).

1.8.4.3 *Detergent removal method*

Phospholipids, when solubilized in detergent (non-ionic, anionic, or cationic) containing the drug, form a micellar mixture, followed by removing the detergent by column chromatography, dialysis, filtration, or adsorption on biobeds that increases the density of micelles that causes the lipids to aggregate and create bilayers. This technique is reproducible and produces homogenous liposomes, but the detergent within the liposomes, low concentrations of liposomes and the encapsulated drugs, and colossal time consumption are its major drawbacks (Vishvakrama and Sharma, 2014) (Vemuri and Rhodes, 1995) (Dua et al., 2012).
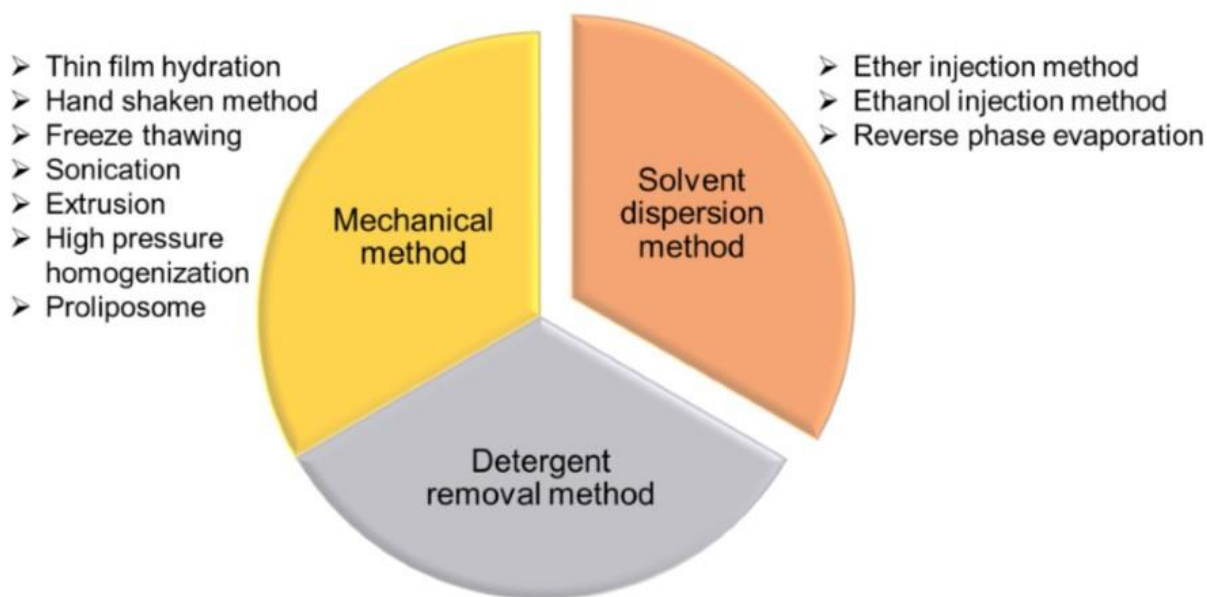
Figure 1.15 Synthesis techniques of liposomes

1.8.5 Loading of drugs in liposomes

We can encapsulate drugs during the synthesis of liposomes in the passive loading technique (Figure 1.16). Researchers use this technique for hydrophobic drugs; in the thin film hydration technique, we add the hydrophobic drug in the thin film formation step. The percentage encapsulation efficiency (% EE) for the hydrophobic drug depends on the lipid concentration, size of liposomes, type of lipids, and drug to lipid ratio.

We can encapsulate the hydrophilic drugs after the synthesis of liposomes by the active loading technique; in the thin film hydration method, we add the hydrophilic drugs in the hydration step. The % EE of hydrophilic drugs is directly proportional to the volume of the aqueous cavity. The lipophilic drugs attain a higher % EE by the passive loading technique, unlike the active loading method for the hydrophilic drugs.
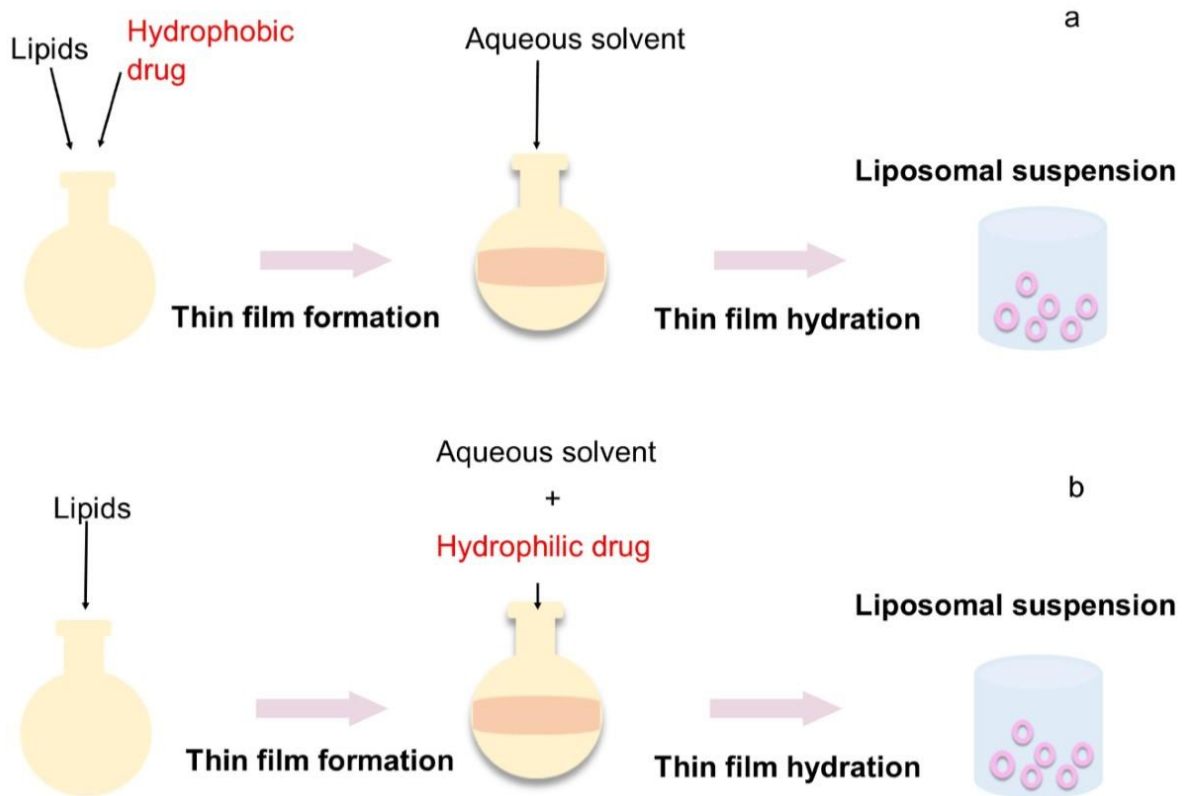
Figure 1.16 Loading technique of drugs in liposomes

In the active loading technique, we create a pH or ion gradient by buffers of specific pH and ion concentrations for anticancer drugs that are weak bases with primary, secondary, or tertiary amine (Figure 1.17). After loading, DOX precipitates in the aqueous cavity, resulting in a higher drug retention. We then exchange the external medium of the liposome with either another buffer or the same buffer with different pH or ionic concentration by dialysis or size exclusion chromatography (Barenholz, 2001) (Gubernator, 2011).
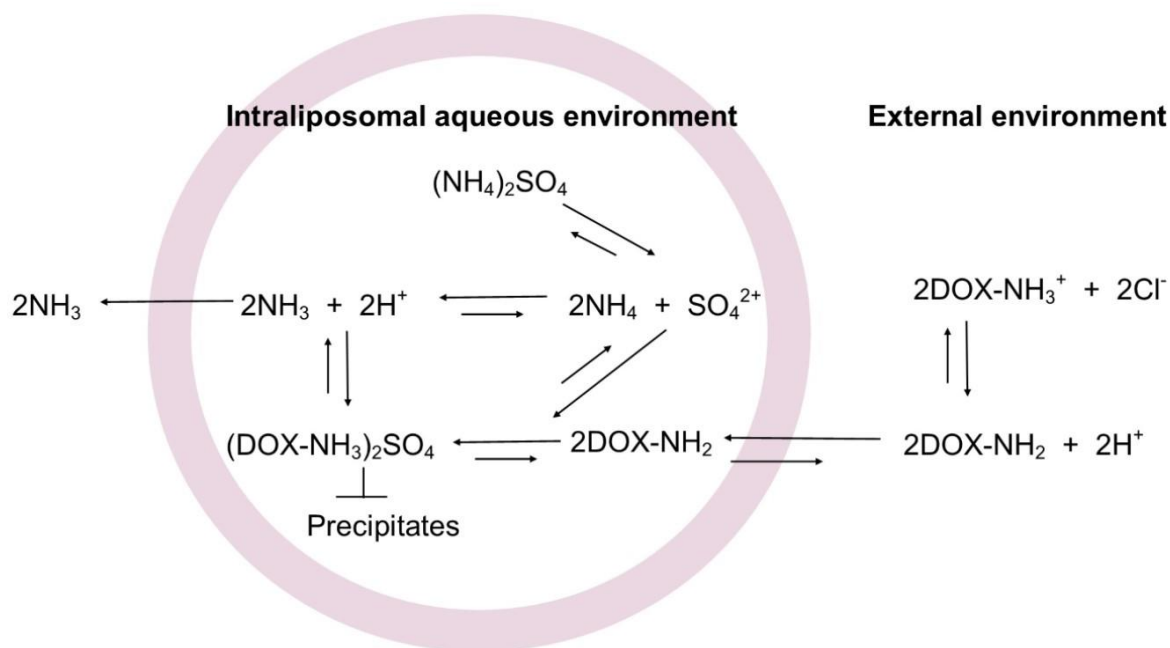
Figure 1.17 Active loading of DOX in liposomes

1.8.6 Fate of liposomes *in vivo*

Plasma proteins/opsonins such as immunoglobulin (Ig), fibronectin, beta 2-glycoproteins, C reactive proteins, beta 2-macroglobulin, and complement proteins cover the liposomal surface by a process of opsonization (Nazeer et al., 2019). Components of the RES (part of the innate immune system) recognize these opsonins and eliminate the foreign bodies (liposomes in this case) by hepatic clearance, metabolizing kupffer cells, and splenic macrophages (Papahadjopoulos, 1996). The liver (largest capacity), spleen, lungs, bone marrow, and lymph nodes are the main sites where liposomes accumulate (Inglut et al., 2020) through large fenestrations of pore size of 100-800 nm in the RES microvasculature (Figure 1.18).

The high density and low density lipoproteins (HDL and LDL) affect liposomal stability by inducing lipid transfer and rearrangement, depleting the lipids, disintegrating the liposomes, and releasing the cargo (Gregoriadis, 1991). Dysopsonins such as human serum albumin and IgA bind to the liposomes, reducing their recognition and phagocytosis by the RES components (Shi et al., 2016). Thus, the rate of clearance by opsonins and masking by the dysopsonins regulate the Fate of liposomes in blood.
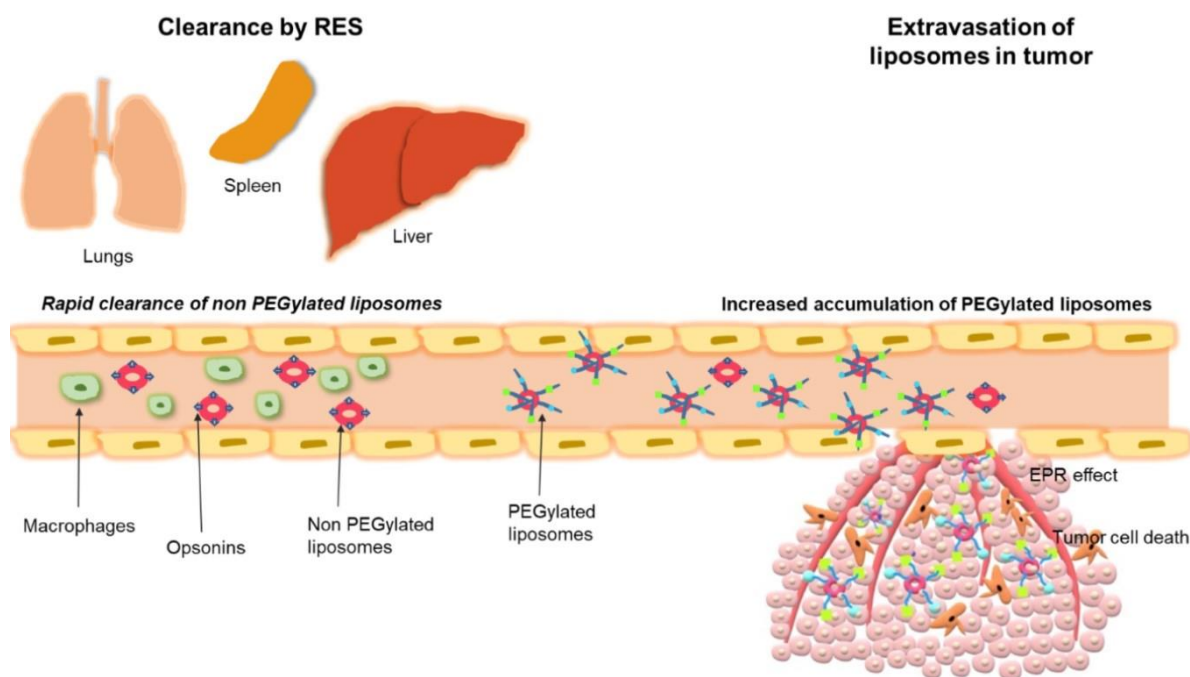
Figure 1.18 Fate of liposomes in the bloodstream

Highly active and growing tumors develop new blood vessels through neovascularization to sustain the highly proliferating cancer cells (Cho et al., 2008). But, this vasculature has an extensive and discontinuous branching with large endothelial fenestrations, allowing molecules up to 4000 KDa to pass and enter the interstitial space. Liposomes that evade the RES accumulate in the tumor due to the defective vasculature and poor lymphatic drainage by the enhanced permeation and retention (EPR) effect (Lila and Ishida, 2017) (Torchilin, 2011).

The EPR effect varies from person to person and from tumor to tumor within the same patient. The width of the tight junctions between the normal endothelial cells is 12-20 nm, which increases to 0.2-1.2 μm in the pathological endothelium due to inflammatory mediators. The normal vasculature has a controlled and balanced vessel growth with a doubling time of approximately 1000 days. But, the tumor vasculature has reduced vessel diameter and extensive branching with a significantly shorter doubling time of 10 days – this property of abnormal vessel growth is known as tortuosity.

The innate characteristics of liposomes also influence their in vivo fate. Liposomes undergo a size dependent opsonization: liposomes in the 0-30 nm size range undergo renal excretion, and liposomes > 30 nm interact with the mono phagocytic system (MPS) components such as macrophages in the liver and spleen –the phagocytic scavengers (Malam et al., 2009);

liposomes in the 50-200 nm size range effectively accumulate in the tumors by the EPR effect but, liposomes < 100 nm show a comparatively reduced opsonization; liposomes ≤ 500 nm pass through the endothelial fenestrations but are readily taken up by the RES.

PEG is biocompatible, non-toxic, has low immunogenicity and antigenicity, and has good excretion kinetics (Inglut et al., 2020) (Torchilin, 2011). Water molecules create hydrogen bonds with the oxygen molecules of PEG to form a tight hydrophilic shell on the liposomal surface, creating a steric barrier that prevents the opsonins from interacting (Lian et al., 2001) (Needham et al., 1992). Opsonization depends on the liposome's size, surface charge, and stability (Gregoriadis and Florence, 1993). High electrostatic charge facilitates the binding of opsonins. CHOL provides rigidity to the liposomes by reducing phospholipid exchange from liposomes to the red blood cells and lipoproteins and prevents the binding of the lipoproteins that destabilize liposomes (Dewhirst and Secomb, 2017).

The lipid's Tc -the temperature at which the lipids transition from an ordered gel phase to a disordered liquid crystalline phase- influences the bilayer fluidity and the liposomal interaction with cells (Bonté and Juliano, 1986). The bilayer fluidity increases at temperatures ≥ Tc as the rotational motion of the fatty acyl chains increases, but CHOL in a ≥ 30 molar % reduces the membrane fluidity. CHOL also modulates the lipid-lipid interaction to maintain an intermediate fluid state by imparting rigidity to the membrane at temperatures > Tc and fluidizing at temperatures < Tc.

Phospholipids with Tc > 37 °C are less fluid at the physiological temperature that reduces drug leakage, and at Tc < 37 °C, the phospholipids form a fluid bilayer with a higher drug leakage. Tc of lipids depends on various factors: the phospholipid head group determines the Tc such that PE has a higher Tc than phosphatidylcholine of the same hydrocarbon chain length due to stronger head group interactions; the higher the length of the acyl chains higher the Tc; the Tc increases with the degree of saturation; naturally occurring phospholipids have a broad and ill-defined Tc than the synthetic phospholipids.

TME and its components also influence liposomal accumulation in the target cells. The extracellular matrix (ECM) of the TME is dense and stiffens than the normal cells, restricting the liposomal movement after extravasation from the vasculature (Mitchell et al., 2017) (Hare et al., 2017).

1.8.7 Targeting approaches and uptake of liposomes

Active targeting: Overexpression of receptors of the normal cells or explicit receptors is a hallmark of cancer cells. These receptors perform metabolic functions to support and sustain the highly proliferating cancer cells. Liposomes tagged with ligands specific to these receptors undergo receptor-mediated endocytosis, accumulating heavily in the target cells (Figure 1.19). The "magic bullets" concept by Paul Ehrlich inspired the active targeting method (Chidambaram et al., 2011).
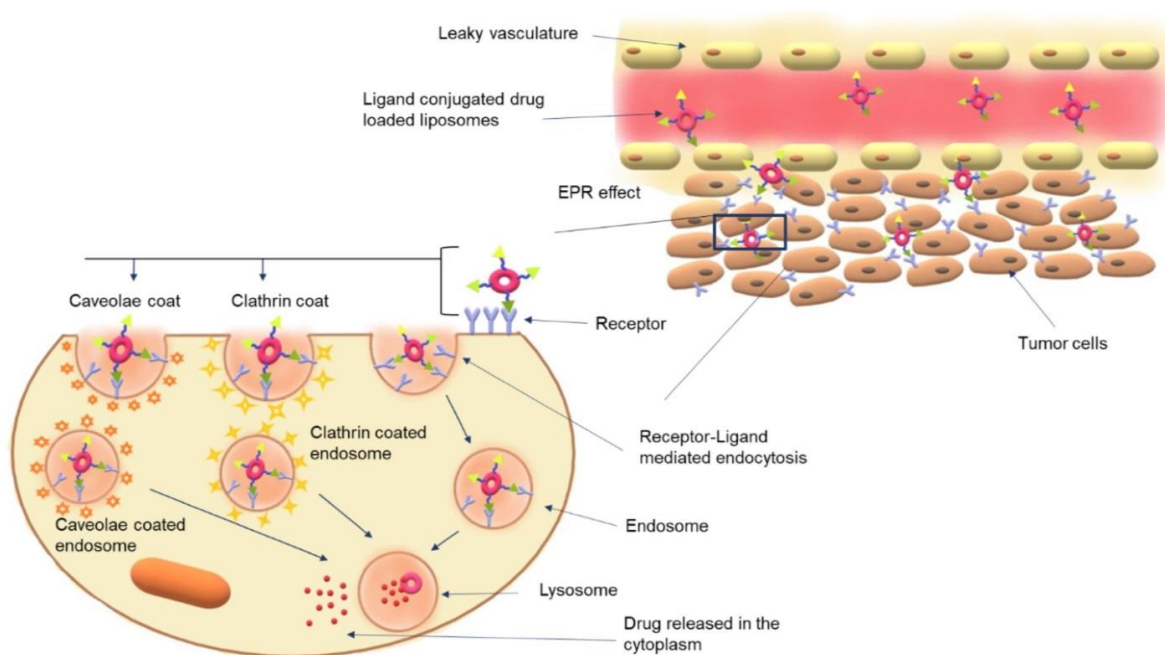
Figure 1.19 Mechanism of active targeting of liposomes (modified from (Moudgil et al., 2023))

Passive targeting: Liposomes accumulate in tumors by the EPR effect due to the leaky vasculature and a poor lymphatic system. Without the assistance of ligands, this uptake method is defined as passive targeting and exploits the tumor's pathological conditions, such as temperature, acidic pH, and specific enzymes (Figure 1.20).
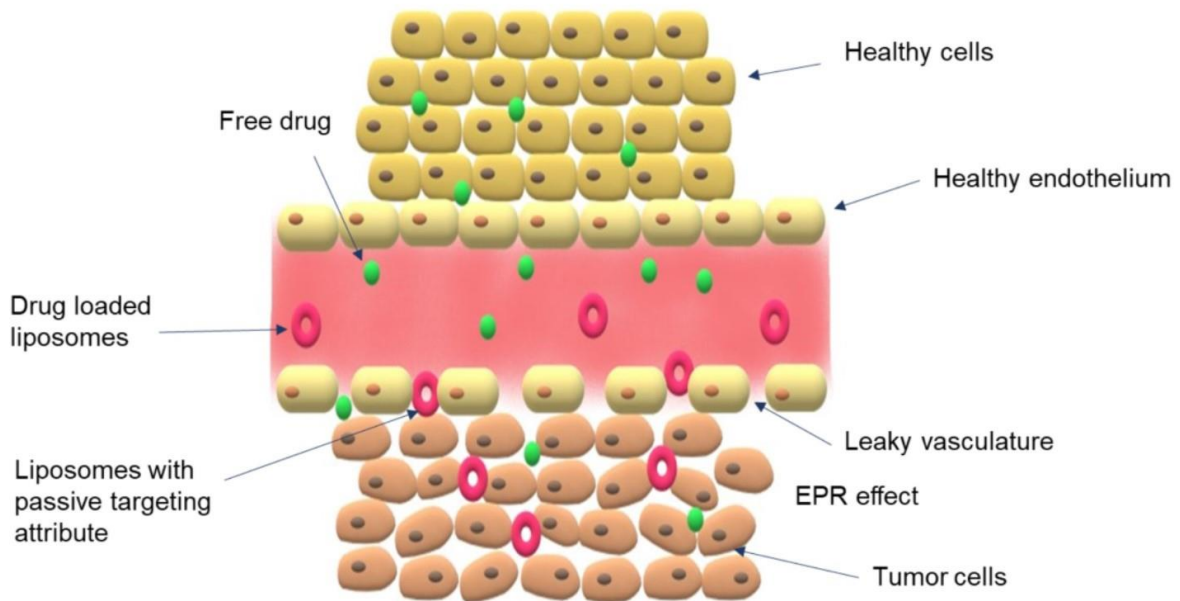
Figure 1.20 Mechanism of passive targeting of liposomes (modified from (Moudgil et al., 2023))

Targeted and non-targeted liposomes reach the tumor areas via passive distribution (Allen et al., 2013). But, the targeted formulations exhibit a comparatively higher uptake by receptor mediated endocytosis (Rahman et al., 2019).

The following mechanisms take up liposomes to reach the target site.

Passive diffusion: When liposomes release the drugs in the TME, the cells take up the drugs by passive diffusion. Hydrophobic drugs remain unchanged after crossing the cell membrane, but hydrophilic drugs use cell membrane transporters for uptake as the cell membrane resists these drugs.

Fusion: Liposomes fuse with the cell membrane and release the payload in the cell (Düzgüneş and Nir, 1999).

Lipid transfer: Lipids of the liposomes interchange with the lipid bilayer of the plasma membrane and release the drug in the cell.

Endocytosis: Cells take up liposomes by the process of endocytosis of various types as follows (Zhao and Stenzel, 2018) (Behzadi et al., 2017).

Phagocytosis: Cells such as macrophages and neutrophils carry out phagocytosis of particles > 500 nm.

Macropinocytosis: In macropinocytosis, the cell membrane forms 0.2-5 µm macropinosomes, engulfing nanoparticles and large extracellular fluid.

Clathrin-mediated endocytosis: This predominant endocytosis pathway bifurcates into non-absorptive and receptor-mediated uptake. In the non-absorptive uptake, interactions such as hydrophobic bonds or electrostatic interactions help the nanoparticles to internalize. In receptor mediated uptake, the coated pits take up the actively targeted liposomes decorated with ligands against receptors overexpressed on the target cells. After that, these nanoparticles follow the endosomal-lysosomal route, where the liposomal components degrade in acid- and enzyme-rich environments, releasing the drug.

Caveolin dependent pathway: The plasma membrane forms a 50-80 nm flask shaped invagination triggered by the caveolin protein engulfing the nanoparticles.

1.8.8 Limitation of liposomes

Liposomal stability is a significant concern. The ester groups in the phospholipid hydrolyze in the presence of acids or bases -the carboxy esters hydrolyze more rapidly than the phosphate esters, and the fatty acyl chains oxidize, which affects the chemical stability; the liposomes aggregate and release the payload that affects the physical stability (Sharma and Sharma, 1997). The free radicals formed delocalize the unpaired electrons, creating breaks in the lipid chain. The unsaturated fatty acyl chains oxidize readily, but the saturated fatty acyl chains oxidize at higher temperatures.

Synthesizing the liposomes in an inert atmosphere (such as nitrogen and argon), storing the liposomes in dark and low temperatures, and adding anti-oxidants like alpha-tocopherol, butyl hydroxyl toluene, and ethylenediaminetetraacetic acid (EDTA) prevents the lipids from oxidizing. Lyophillizing with cryoprotectants (such as trehalose, fructose, lactose, and sucrose) maintains liposomal stability during long term storage; many commercially available liposomal products such as myocet, ambisome, and Amphotech reconstitute in aqueous phase before injection.

Sterilizing liposomes is another major issue. Techniques explored to sterilize liposomes include autoclaving, heat sterilization, γ irradiation, UV irradiation, chemical sterilization, and filtration. Autoclaving requires high temperatures that oxidize, hydrolyze, and induce phase transition of the lipids; the liposomes aggregate, causing the drug to leak and degrade. Heat sterilization causes structural changes in the liposomes, causing drug leakage and oxidation of lipids (Delma et al., 2021).

γ irradiation hydrolyses fragments and peroxidizes the unsaturated lipids; it lowers the medium's pH and oxidizes CHOL (Sakar et al., 2017). UV irradiation poorly penetrates with a low ionizing effect and is ineffective; it peroxidizes the lipids and degrades the encapsulated drug (Abuhanoğlu and Özer, 2014). Chemical sterilization uses ethylene oxide gas that is toxic, carcinogenic, flammable, and explosive. Filtering by aseptic bacterial-free membrane or depth filters of 0.22 µm pore size is the safest method; cellulose acetate, cellulose nitrate, polycarbonate, and polyvinylidene fluoride filters are the most recommended (Singh et al., 2017). Synthesis of the liposomes in aseptic working conditions also ensures sterility.

Many laboratory scale synthesis techniques are non-scalable and non-reproducible, which is a significant challenge for the pharmaceutical production of liposomes. Removing the organic solvents used during synthesis is necessary to curtail any harmful effects on the drugs (Vijay et al., 2010). Synthesizing large scaled ligand targeted liposomes and their characterization constitute a significant challenge. Ligand tagging can be confirmed, but quantifying the ligands on the liposomal surface is difficult. This problem escalates in dual or multi-ligand liposomes (Belfiore et al., 2018). Despite these limitations, liposomal advancements have found ways to overcome them.

1.8.9 FDA approved liposomes

Doxil: Doxil (Doxil in the US and Caelyx outside the US) is a DOX-HCL encapsulated PEGylated liposomal formulation, initially manufactured by Sequus Pharmaceuticals (Lee, 2019), USA for Kaposi's sarcoma, advanced ovarian cancer and multiple myeloma (Bulbake et al., 2017); it is now manufactured by Johnson and Johnson. First approved in 1995 for Kaposi's sarcoma in AIDS patients, Doxil was later approved for metastatic breast cancer (Bobo et al., 2016).

It is 80-100 nm in size (Gregoriadis and Perrie, 2010), composed of a 56:39:5 molar ratio of hydrogenated soy phosphatidylcholine, CHOL, and 1,2-Distearoyl-sn-glycero-3-Phosphoethanolamine methoxy polyethylene glycol-2000 (DSPE-mPEG2000), and has storage stability of 20 months (Chang et al., 2012). Each vesicle encapsulates approximately 15,000 DOX molecules with 90 % encapsulation by the remote loading method using an ammonium sulfate pH gradient.

Lipodox: An imbalance of demand and supply of Doxil in 2011 due to quality control issues led to the shutdown of the manufacturing units, resulting in a temporary import of Lipodox by SunPharma. Lipodox got FDA approval in 2012 and was later approved for breast cancer treatment (Beltrán-Gracia et al., 2019). It is a PEGylated liposomal formulation composed of 1,2-Distearoyl-sn-glycero-3-Phosphotidylcholine (DSPC), CHOL, and PEG with storage stability of 36 months (Chang et al., 2012).

Myocet: Myocet, a registered trademark of Cephalon, is a non-PEGylated DOX encapsulated liposomal formulation. Myocet with cyclophosphamide was initially approved in Europe for metastatic breast cancer (Pillai, 2014). It comprises Egg phosphatidylcholine and CHOL in a 55:45 molar ratio in a 150-190 nm size range (Lee, 2019) (Gregoriadis and Perrie, 2010). It is manufactured by Elan Pharmaceuticals, USA, in a powdered form with a storage stability of 18 months (Chang et al., 2012) (Bulbake et al., 2017).

There are many formulations in the clinical pipeline for the treatment of breast cancer (Table 1.6) (Chang et al., 2012) (Bulbake et al., 2017) (Beltrán-Gracia et al., 2019) (Pillai, 2014) (Stathopoulos and Boulikas, 2012) (Fan and Zhang, 2013).

Table 1.6 Liposomal formulations in the clinical trials

Liposomal formulation	Drug	Components of liposomal formulation
LEP-ETU	PTX	1,2-Dioleoyl-sn-glycero-3-phosphocholine (DOPC) + CHOL + Cardiolipin in 90:5:5 molar ratio
LEM-ETU	Mitoxantrone	DOPC + CHOL + Cardiolipin in 90:5:5 molar ratio
EndoTAG-1	PTX	1,2-Dioleoyl-3-trimethylammonium propane (DOTAP) + DOPC + PTX in 50:47:3 molar ratio

INX-0125	Vinorelbine	Egg sphingomyelin + CHOL in 55:45 molar ratio
Liposome-Annamycin	Annamycin	DSPC + 1,2-Distearoyl-sn-glycero-3-phosphoglycerol (DSPG) + Tween
ThermoDox	DOX	1,2-Dipalmitoyl-sn-glycero-phosphatidylcholine (DPPC) + DSPE-PEG2000 + myristoyl stearyl phosphatidylcholine
Alocrest	Vinorelbine	Sphingomyelin + CHOL
Lipoplatin	Cisplatin	Soy phosphatidylcholine + CHOL + dipalmitoyl phosphatidylcholine glycerol + DSPE-mPEG2000
MM-302	DOX	DSPE + HER 2 + PEG

Researchers explore liposomal technology worldwide for cancer therapy and multiple patents for liposomes as approved drug delivery agents (Table 1.7).

Table 1.7 Approved patents of liposomes for breast cancer

Patent	Patent Number	Reference
Treatment of Breast Cancer	US 9707204B2	(Kliche et al., 2015)
Liposomal curcumin for treatment of cancer	US9283185B2	(Kurzrock et al., 2016)
Use of mitoxantrone hydrochloride liposome for treating breast cancer	US20230078702	(Li et al., 2021)
Treatment of Breast Cancer with Liposomal Irinotecan	US20190142822	(Bayever et al., 2019)
Non-Pegylated liposomal doxorubicin combinations for the treatment of triple negative breast cancer	US20150250723	(Rozencweig et al., 2015)
Use of cationic liposomes, which includes paclitaxel	DK2286794T3	(Teifel et al., 2016)

1.9 Major underlining facts for the study

1. Breast cancer has the highest incidence and high mortality rates worldwide, with the cases anticipated to rise in the future. TNBC, the most aggressive form, is highly invasive, with a high relapse rate and poor prognosis. TNBC cases are growing and are the highest in India compared to other countries.

2. The breast cancer cells are multi drug resistant, causing the chemotherapy to fail. Studies report a higher therapeutic efficacy with the co-delivery of drugs that also acknowledge MDR. DOX is the primary chemotherapeutic drug to treat breast cancer, but it induces cardiotoxicity. Curcumin (CUR) has a pleiotropic effect on cancer and is a chemosensitizer.

3. Liposomes are effective drug delivery vehicles with myriad advantages, and stealth liposomes have increased circulation time and bioavailability. Active targeting also increases the uptake of particles in the cells.

1.10 Major components of the study

1.10.1 CUR

CUR is a yellow phytochemical extracted from the rhizome of *Curcuma longa linn* of the Zingerberaceae family (Sun et al., 2012). CUR (1,7-bis(4-hydroxy-3-methoxy phenyl)-1,6-heptadiene-3,5-dione) is the most active component of turmeric among the other two curcuminoids, namely deoxycurcumin (1,6-heptadiene-3,5-dione, 1-(4 hydroxy-3-methoxyphenyl)-7-(4 hydroxyphenyl) and bisdemethoxycurcumin (1,7 bis (4 hydroxyphenyl)-1-6- heptadiene-3,5-dione) (Feng et al., 2017). Many parts of Asia use CUR as a traditional medicine, which forms the basis of Ayurveda and traditional Chinese medicine.

CUR has many pharmacological activities such as anti-inflammatory (Ji et al., 2012), anti-oxidant (Shindikar et al., 2016), anti-viral, anti-microbial (anti-bacterial and anti-fungal) (Doello et al., 2018), anti-tumor and anti-angiogenesis (Maleki Dizaj et al., 2022), wound healing (Prasad et al., 2014), chemosensitizer (Yallapu et al., 2012), anti-arthritic (Ahmad et al., 2016), anti-amyloid and anti-Alzheimer (Naksuriya et al., 2014), etc. It inhibits telomerase activity and induces apoptosis in leukemia cells; it shows hypocholesterolemic, antiplasmodic, anticoagulant, hepatoprotective, cardioprotective, and lipid peroxidation activity. CUR's biological activity corresponds to the drug's structure (Figure 1.21).

CUR is poorly soluble in water (0.4 µg/ml), resulting in reduced bioavailability, and excretes out rapidly from the body. Upon oral administration in rats, CUR transforms into dihydro and tetrahydro CUR that are poorly absorbed in the intestine; upon IV and intraperitoneal administration, bile metabolizes CUR to glucuronides of tetrahydrocurcumin and hexahydrocurcumin. The urine of healthy male rats showed CUR metabolites, namely tetrahydrocurcumin, dihydrocurcumin, hexahydrocurcumin, and their glucuronic acid derivatives (Feng et al., 2017). Orally administered CUR metabolizes in the intestines and is excreted in feces and urine (Lee et al., 2014). FDA regards CUR as Generally Recognized as Safe drug and is nontoxic even at a 12g/day dose in humans.
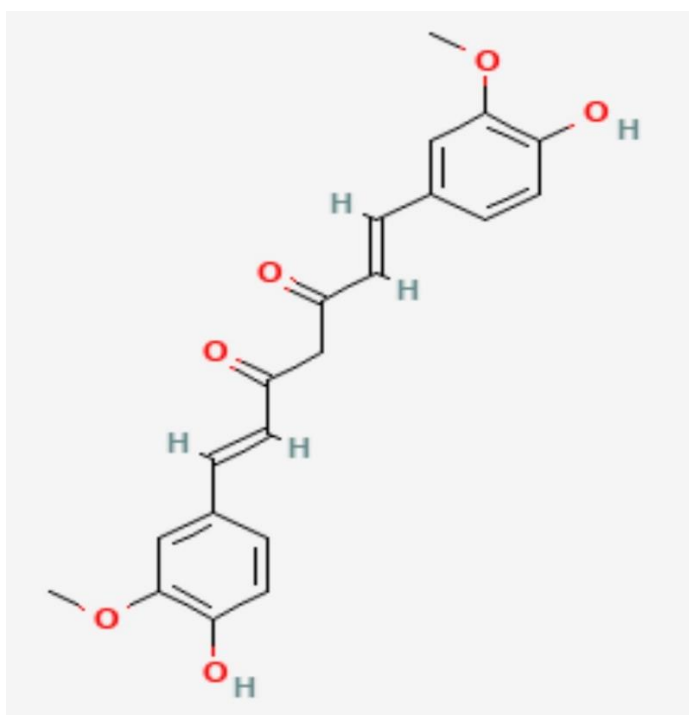
Figure 1.21 Structure of CUR (Image source: pubchem.ncbi.nlm.nih.gov)

CUR has a pleiotropic effect on cancer and acts on its various hallmarks. CUR inhibits NF-κB and subsequently modulates inflammatory cytokines (CXCL1 and CXCL2), matrix metalloproteinase 9, urokinase plasminogen activator and receptor, intercellular adhesion molecule 1 and chemokine receptor 4 promoting to impede tumor progression, metastasis, and invasion. CUR downregulates HER2 and insulin like growth factor receptor-1, increases TNF related apoptosis inducing ligand -induced apoptosis, and inhibits the telomerase activity by the downregulation of telomerase reverse transcriptase (Wang et al., 2016).

CUR also induces apoptosis by regulating p53 expression that activates pro-apoptotic members, namely, B-cell lymphoma 2 (Bcl2), namely Bcl-2 homolog antagonist killer (Bak) and Bcl2 associated x protein (Bax) (Salem et al., 2014); Bak and Bax release cytochrome c from the mitochondria initiating a caspase signaling mechanism for apoptosis. CUR also reduces ki67 and proliferating cell nuclear antigen levels to induce apoptosis.

CUR stimulates c-Jun NH_2-terminal kinase and p38 kinase (members of the mitogen-activated protein kinase (MAPK) pathway) to induce G2/M arrest and apoptosis (Liu and Chen, 2013). It also reduces cyclin D1 activity by binding to CDK4. Studies report that CUR degrades cyclin E (essential for the G1/S progression by binding to the CDK2 and retinoblastoma protein) and increases the expression of CDK inhibitors (such as p53, p21, and p27) in the MCF-7 cells (Wang et al., 2016). CUR stops CDK4 from associating with CDK6, preventing the retinoblastoma protein from phosphorylating to cause G2 arrest. Studies in MCF-7 and MDA-MB-231 cells report that CUR increases the tumor suppressing GSK3β and the loss of the nuclear β catenin, affecting cyclin D1 synthesis and causing G1/M arrest (Song et al., 2019).

CUR prevents the loss of T cells and the immune suppressive chemokine (such as transforming growth factor beta and IL-10) to support the reduced immune system in cancer. CUR increases ROS levels in the cancer cells, initiating an anticancer activity. It is an anti-angiogenic agent as it down-regulates the expression of pro-angiogenic factors such as vascular endothelial growth factor (VEGF) and fibroblast growth factors produced constitutively by cancer cells (Song et al., 2019).

1.10.2 DOX

DOX, an anthracycline, was first extracted from *Streptomyces peucetius var. caesius* but is also chemically synthesized from daunorubicin that differs in a single OH group (Vigevani and Williamson, 1981). DOX has a chemical formula of $C_{27}H_{29}NO_{11}$, molecular weight of 543.5 g/mol and IUPAC name of (7S,9S)-7-[(2R,4S,5S,6S)-4-amino-5-hydroxy-6-methyloxan-2-yl]oxy-6,9,11-trihydroxy-9-(2 hydroxyacetyl)-4-methoxy-8,10-dihydro-7H-tetracene-5,12-dione (Figure 1.22). It is a broad spectrum antineoplastic drug for hematological malignancies and solid tumors such as breast, ovary, uterus, liver, osteosarcomas, Kaposi's sarcoma, thyroid, Hodgkin's lymphoma, and prostate.

DOX is the primary chemotherapeutic drug prescribed either alone or with other drugs. DOX-HCl (red crystalline powder) is the injectable form of DOX. NADPH dependent aldoketoreductase metabolizes DOX into doxorubicinol, a hydrophilic and cytotoxic metabolite, and the NADPH dependent cytochrome reductase metabolizes DOX into doxorubicinone and 7-deoxydoxorubicinone, hydrophobic aglycones and non-cytotoxic metabolites. Approximately 50% of DOX and its metabolites pass out in bile by metabolizing the reducing ketone group to the hydroxyl group, and 25-45% flushes through feces (25-45%) (Speth et al., 1988).
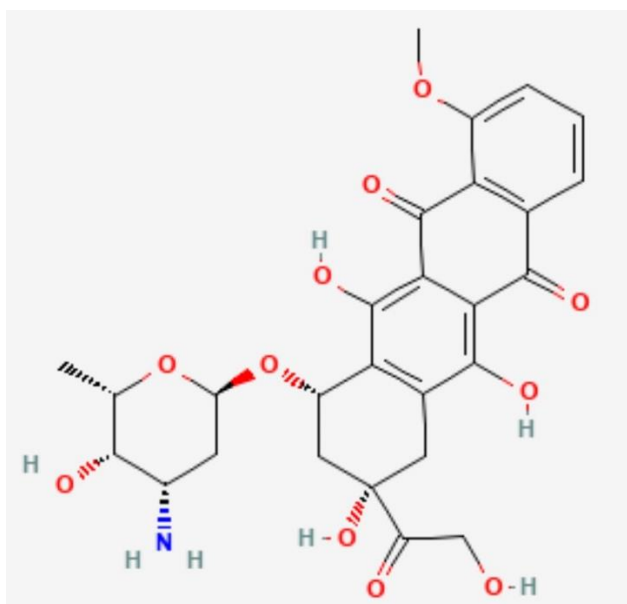
Figure 1.22 Structure of DOX (Image source: pubchem.ncbi.nlm.nih.gov)

DOX intercalates with DNA to interrupt topoisomerase II, interfering with the DNA repair mechanism by cleaving DNA strands and creating double stranded breaks (Rivankar, 2014). DOX generates free radicles that have inhibitory effects on the cell membranes, proteins, and DNA and create oxidative stress that triggers apoptosis (Thorn et al., 2011). Oxidoreductases such as NADH dehydrogenase, NADPH cytochrome P450 reductase, and nitric oxide synthase induce one-electron reduction of DOX, converting it to semiquinone; the molecular oxidization of semiquinone forms superoxide and hydrogen peroxide that creates an oxidative stress. The major limitation of DOX is cardiotoxicity.

1.11 Studies on passive and active CUR-DOX liposomes for breast cancer

We searched for the published studies on search engines such as PubMed and Google Scholar by using keywords such as "DOX," "CUR," "Liposomes," "DOX liposomes," "CUR liposomes," DOX and CUR liposomes," "breast cancer," "active targeting," "receptor-mediated uptake," "Folate (FOL) liposomes" and "Cetuximab (CET) liposomes." We first segregated these studies into drug delivery for breast cancer and other pathological conditions and then further bifurcated them into liposomal based drug delivery and delivery by other nanoformulations.

1.11.1 Studies on CUR-DOX liposomes for breast cancer treatment

Studies report the efficacy of DOX and CUR for various cancers. CUR acknowledges the MDR in the DOX resistant breast cancer cells along with its chemotherapeutic effect. Wen et al. (2019) reported that CUR decreases ABCB4 activity and reverses MDR, resulting in DOX accumulating heavily in MDA-MB-231 and MCF-7 cell lines (DOX resistant) (Wen et al., 2019).

Sheena et al. (2018) synthesized CUR liposomes and functionalized the surface with poly (sodium 4-styrene sulfonate) linked to DOX; this formulation showed a higher cytotoxic effect majorly by apoptosis of the MCF-7 cells (Sheena et al., 2018). Liu et al. (2020) formulated CUR and celecoxib coloaded liposomes surface functionalized with hyaluronic acid, TAT-NBD (TN) peptide, and DOX liposomes surface functionalized with TN peptide. This combination therapy was synergistic with enhanced anticancer activity in the 4T1 cells (Liu et al., 2020). Lin et al. (2019) developed CUR and DOX coloaded liposomes surface functionalized with PEG-polyethylenimine linked to Herceptin to target the HER2 receptors in the HER 2+ SKBR3 cells (Lin et al., 2019).

Studies report the efficacy of CUR and DOX coloaded NPs in treating breast cancer (Table 1.8).

Table 1.8 Studies reporting the efficacy of various CUR-DOX loaded nanoformulations for the treatment of breast cancer

Formulation	Cell lines	Highlights of the study	Reference
Chitosan- Poly(butyl cyanoacrylate) nanoparticles	MCF-7 and MCF-7/ADR	MDR reversal and improved cytotoxicity in the resistant cancer cell lines	(Duan et al., 2012)
Poly(ethylene glycol)-poly(ε-caprolactone) micelles	4T1	Increased uptake of DOX due to CUR and improved cytotoxicity	(Sun et al., 2014)
Core shell nanoparticles composed of heparin forming the shell and poly(L-lactide) grafted polyethyleneimine nanoparticles	4T1	Increased cytotoxicity	(Guo et al., 2014)
Poly(ethylene glycol)-block poly lactide micelles	MCF-7/ADR	MDR reversal and increased tumor accumulation of the micelles	(Lv et al., 2016)
Micelles composed of Hyaluronic acid and vitamin B succinate copolymer	4T1	Synergism between DOX and CUR improved uptake and cytotoxicity of the cancer cells, and MDR reversal	(Ma et al., 2017)
Poly (ε-caprolactone)-b-poly(ethylene glycol)-b poly (ε-caprolactone) linked to DOX by acid susceptible hydrazone linkages, attached to a cell penetrating peptide (CRGDK) to target the neuropilin- receptors	MCF-7/ADR	Inhibition of P-gp and reversal of MDR with increased cytotoxicity	(Yang et al., 2018)

pH sensitive nanoparticles of monomethoxy (polyethylene glycol)-b-P (D, L-lactic-co-glycolic acid) –b-P (L-glutamic acid) polymer	MCF-7 and MDA-MB-231	MDR reversal with increased uptake of DOX in the resistant cell line with improved cytotoxicity	(Yuan et al., 2018)
Magnetic nanocomposite of iron oxide, hydroxyapatite and β-cyclodextrin	MCF-7 and MCF-7/ADR	MDR reversal by CUR and increased DOX accumulation in the cancer cells	(Rastegar et al., 2018)
PEI decorated mesoporous silica nanoparticles	MCF-7R	Enhanced cytotoxicity at lower drug concentrations	(Harini et al., 2019)
Poly ε-caprolactone –co-maleic anhydride-graft- citric acid copolymer micelle	MDA-MB-231	Synergism between DOX and CUR, Improved uptake and cytotoxicity of the cancer cells, and MDR reversal	(Sabzi et al., 2020)
Chitosan coated solid lipid nanoparticles	MCF-7 and MDA-MB-231	MDR reversal by CUR and increased DOX accumulation in the cancer cells	(Abd-Ellatef et al., 2020)
Folic acid-activated chitosan coated metal organic framework of Ni/Ta	MCF-7	Synergism between DOX and CUR that enhanced the cytotoxicity of MCF-7 cells	(Sargazi2, 2022)

These studies suggest the drug combination's efficacy in reversing MDR with increased cytotoxicity. The CUR and DOX combination is still unexplored for breast cancer, especially TNBC, with an absence in the actively targeted formulations.

1.12 Receptors to target for breast cancer

In the last decade, researchers targeted various receptors on breast cancer cells using liposomal formulations (Figure 1.23).

HER 2: HER2 is an integral EGFR family component and a proto-oncogene positioned at chromosome 17q21 (Krishnamurti and Silverman, 2014). It encodes a tyrosine kinase with an extracellular, transmembrane, and intracellular domain without any specific ligand, causing it to form heterodimers with HER 3 to initiate the signal transduction cascade (Brand et al., 2006). HER 2 aids in cellular growth and differentiation and overexpresses in highly aggressive and metastatic cancers (Rubin and Yarden, 2001).

ER: ERs are nuclear hormone receptors with two forms, namely, ERα and ERβ (Burns and Korach, 2012). ERα enhances cellular proliferation under the influence of estrogen, and ERβ opposes ERα acting as anti-proliferative or pro-apoptotic (Huang et al., 2015). Increased cellular proliferation enhances DNA replication and mutations (Shanle and Xu, 2010).

Folate receptors (**FRs**)*:* FRs translocate folic acid in the cells required to synthesize nucleotide bases, amino acids, and other methylated compounds (Hartmann et al., 2007). FRs have two isoforms: FR-α, overexpressed on epithelial cancers, and FR-β, overexpressed on activated macrophages and myeloid leukemia (Zhao et al., 2008).

Integrin receptors: Integrins function in cell growth, cell differentiation, and cell death and aid in metastasis and angiogenesis by mediating cell adhesion to the ECM (Taherian et al., 2011) (Subbaram and Dipersio, 2011). The integrin receptors are heterodimeric transmembrane glycoproteins of α and β subunits that bind to the ECM proteins or other ligands via the extracellular domain and to the cytoskeleton-associated proteins via the intracellular domain.

CD44 receptors: The CD44 receptor is a transmembrane protein and a member of the cell adhesion molecule family that functions in cell adhesion, cell proliferation, and migration (Basakran, 2015). In breast cancer, CD44 aids in cancer progression and metastasis and is associated with poor prognosis (Ouhtit et al., 2018).

Nucleolin receptors: Nucleolin is over expressed in nucleolus that partakes in rDNA transcription, ribosome assembly, and remodeling of nucleolar chromatin in normal cells and regulates proliferation, apoptosis, and metastasis (Chen and Xu, 2016). Breast cancer cells

show a 3-6 fold overexpression of nucleolin receptors over the normal cells (Berger et al., 2015). Nucleolin receptors present on the outer side of the plasma membrane interact with the intracellular actin cytoskeleton (Fujiki et al., 2014).

Mitochondrial targeting: Dequalinium shows specificity to the mitochondria of cancer cells and depreciates the high negative mitochondrial membrane potential, releasing cytochrome C in the cytoplasm that induces apoptosis.

Other receptors: Fibronectin is elemental to ECM that aids in cell adhesion, differentiation, growth, and migration but plays a detrimental role in cell invasion and migration of cancer cells (Fernandez-Garcia et al., 2014). The oncofetal splice variant, extradomain-B fibronectin (EDB), facilitates cancer cell proliferation, angiogenesis, and metastasis (Vaidya et al., 2020). ECM remodels as breast cancer progresses by adding EDB to the fibronectin of the neovessels and the tumor associated ECM.

Neuropilin-1 is a single pass transmembrane glycoprotein regulating tumor growth, invasion, metastasis, and angiogenesis (Cao et al., 2015). EphA2, a transmembrane glycoprotein, is overly expressed in the neovasculature of very aggressive breast cancers (Guo et al., 2015). Chemokine receptor type 4 is essential in metastasis (Guo et al., 2012). Transferrin receptors translocate ferric ions in the cancer cells (Gandhi et al., 2016).

The intracellular adhesion molecule-1 (ICAM-1) is a cell surface glycoprotein that gives a metastatic phenotype to breast cancer (Guo et al., 2016). Mannose-6-phosphate (M6P) bears affinity to the mannose-6-phosphate/insulin like growth factor receptor (M6P/IGF-IIR), overexpressed in breast cancer cells for tumor development and metastasis, that functions to translocate the proteins from either the cell surface to the lysosomes or the trans-Golgi network to the lysosomes (Minnelli et al., 2017).

Figure 1.23 Receptors targeted for breast cancer treatment in a liposomal formulation (modified from (Moudgil et al., 2023))

1.12.1 FRs

FRs are composed of 220-237 amino acids and have four isoforms, namely, FRα, FR β, FRϒ and FR δ. FRα is the most widely studied glycosylphosphatidylinositol anchored cell surface glycoprotein expressed on the apical surface of cells and has a high affinity for 5-methylhydrofolate, the physiological form of FOL. FOL or vitamin B9 are small hydrophilic molecules acting as cofactors for carbon transfer reactions vital for the biosynthesis of nucleotide bases, amino acids, and methylated compounds that are paramount for DNA and RNA synthesis, cellular proliferation, and epigenetic processes (Zhang et al., 2014); folic acid a synthetic form taken as an oral supplement.

FRα has four long (α1, α2, α3, and α6) and two short α-helices (α4 and α5), four short β stands (β1-β4), and many loo regions that are stabilized by eight disulfide bonds to form a tertiary structure (Chen et al., 2013). They are less expressed and restricted to the apical surfaces of organs such as kidneys, lungs, and choroid plexus. After FOL-FR interaction, a lipid raft mediated endocytosis occurs, resulting in an invagination forming early endosomes that fuse with lysosomes to release the FOL.

The immunohistochemical studies establish a higher expression of FRs on TNBC cells over the ER+/PR+ or the HER2+ cells and the lowest in the normal cells. Zhang et al. showed that FRα was more elevated in high histological grade tumors, higher nodal stage, and tumors with high ki67 activity (Zhang et al., 2014). Studies report an upregulation of FRα in 80% of TNBC subtypes that is associated with a poor prognosis. FRs are biomarkers and therapeutic targets for breast cancer.

Normal cells predominantly transport FOL by the ubiquitously expressed low affinity reduced FR, a transmembrane anionic exchanger that cannot translocate folic acid (the oxidized form of FOL). High affinity FRs rarely transport FOL (Meier et al., 2010) that are either seldom expressed on the normal cells or are inaccessible and only expressed on the apical surface of organs such as kidneys, lungs, intestines, retina, placenta, and choroid plexus; in kidneys, the FRs retrieve FOL entered the urine (O'Shannessy et al., 2012).

The high affinity FRs are highly expressed in cancer cells of epithelial origin such as ovarian, breast, colon, kidney, uterine, and lung cancer to meet the demand of highly proliferating cells. These FRs are highly tumor specific compared to normal cells, making them fit for targeted

drug delivery. Proton coupled high affinity FOL transporter is another FR predominantly present in the intestines.

Chen et al. (2018) developed pH sensitive FOL liposomes co-loaded with DOX and Imatinib. Free DOX showed a stronger uptake in the MCF-7 cells than MCF-7/ADR cell lines, but FOL tagged DOX liposomes showed a comparatively stronger uptake in the MCF-7/ADR cells. Imatinib reversed DOX resistance, lowering the IC_{50} values (Chen et al., 2018). Gazzano et al. (2018) formulated FOL tagged liposomes encapsulating nitroxy-DOX; the authors conjugated DOX to nitric oxide releasing groups to reverse MDR by the action of nitric oxide on the P-gp. The targeted formulations accumulated heavily in MDA-MB-231 and TUBO cell lines (resistant cell lines), released high nitrite, and exhibited good nuclear-dependent and mitochondrial dependent cytotoxic activity (Gazzano et al., 2018). Jadia et al. (2018) observed that FOL decked CUR liposomes exhibited increased cytotoxicity against MDA-MB-231 cells with G2/M phase arrest than in MCF-12A (Jadia et al., 2018).

Nguyen et al. (2019) synthesized Folic acid tagged liposomes encapsulating DOX and 7 nm gold nanorods and achieved a synergistic photothermal therapy and chemotherapy in the 4T1 cells. Irradiating at 808 nm triggered the release of DOX from the formulation (Nguyen et al., 2019). Silva et al. (2019) synthesized pH sensitive FOL tagged DOX liposomes that showed higher uptake by the 4T1 cells with increased cytotoxicity than the non-targeted counterparts. The tumor volume decreased by 70%, substantially reducing the pulmonary metastasis foci (de Oliveira Silva et al., 2019).

Deng et al. (2019) synthesized FOL tagged liposomes with long PEG chains that detached when exposed to MMP-2 to reveal FOL and emanated an increased uptake in 4T1 cells and M2-tumor associated macrophages (Deng et al., 2019). Prasad et al. (2019) formulated FOL conjugated DOX liposomes that prevented any premature release of the drug due to Graphene oxide decoration, showed responsiveness to Near InfraRed (NIR) irradiation and pH, resulting in a controlled release, and exhibited a pronounced 4T1 breast tumor regression (Prasad et al., 2019).

Prasad et al. (2020) developed FOL tagged liposomes co-loaded with gold nanoparticles, graphene quantum dots, and DOX for photothermal therapy, chemotherapy, and imaging. Irradiating the formulation at 750 nm generated heat and ROS that reduced the tumor (Prasad et al., 2020). Kong et al. (2020) developed FOL tagged DOX liposomes with light

responsiveness to de-PEGylated liposomes that achieved an uptake by Xenograft MDA-MB-231 in live embryonic zebrafish and a significant cytotoxic activity (Kong et al., 2020).

Yue et al. (2020) developed FOL and octa-arginine polypeptide, a cell penetrating peptide (CPP) tagged liposomes coloaded with DOX and astragaloside. They observed an increased uptake, reduced proliferation, and reversal of DOX resistance in MDA-MB-231/DOX resistant cells (Yue et al., 2020). Lamprou et al. (2021) found that on increasing the concentration of FA (0.1, 0.5, and 1 mol %), the cytotoxic activity of FOL tagged DOX liposomes also enhanced in MDA-MB-231 and 4T1 cells than MCF-7 cells (Lamprou et al., 2021).

Xie et al. (2021) synthesized FOL-chitosan tagged liposomes co-loaded with DOX and erianin, an extract of a Chinese herb, *Dendribium*. The results showed a synergistic action of the free drugs at 2 μM concentration in MCF-7 cells and an antagonistic action in MCF-10A. But, the authors found synergism at a higher concentration of DOX and antagonism exhibited at a lower DOX concentration in MDA-MB-231 cells (Xie et al., 2021). Pradhan et al. (2021) developed FA decorated liposomes encapsulating C1, a synthetic analog of CUR, that efficiently inhibited the breast cancer stem cells (BCSCs) derived from the cancer stem cells (CSCs) of MCF-7 mammosphere and significantly reduced the size of BCSCs enriched MCF-7 mammosphere (Pradhan et al., 2021).

Studies report the efficacy of FOL tagged liposomal formulations for breast cancer (Table 1.9).

Table 1.9 Studies on FOL tagged liposomal formulations for breast cancer treatment

Drug	Formulation	Cell lines	Highlight of the study	Reference
Arsenic trioxide and metal ions (Ni^{2+} and Co^{2+})	FOL -liposomes	MCF-7	Enhanced accretion and cytotoxicity	(Chen et al., 2009)
DTX and quantum dots	d-a-tocopheryl polyethylene glycol 1000 succinate (TPGS) coated theranostic liposomes	MCF-7	Imaging and chemotherapeutic properties	(Muthu et al., 2012)

Gemcitabine	Supramolecular vesicular aggregate of liposomes and polyasparthydrazide co-polymers linked to folic acid	MCF-7	Increased chemotherapeutic activity and complete regression of tumor	(Paolino et al., 2012)
Fluorescein (model drug)	FOL-chitosan coated liposomes	MCF-7	High uptake due to folate mediated endocytosis	(Yang et al., 2013)
PTX	pH sensitive FOL-liposomes	MDA-MB-231 and MCF-7	Pronounced cytotoxic activity	(Barbosa et al., 2015)
PTX conjugated to poly (amidoamine) dendrimers via a cathepsin B-cleavable tetrapeptide	FOL- liposomes	MDA-MB-231 MDA-MB-468 BT-20 T47-D	Increased drug retention and enhanced cytotoxicity and tumor reduction	(Satsangi et al., 2015)
DTX	Liposomes coated with FOL grafted chitosan based thiomer	MDA-MB-231	Increased bioavailability by oral delivery	(Sohail et al., 2016)
Benzoporphyrin derivative monoacid	PEG coated and FOL- liposomes	MDA-MB-231	Photodynamic therapy	(Sneider et al., 2016)
Resveratrol	FOL -liposomes with reduced graphene oxide in the bilayer	MCF-7	Efficient chemotherapy and photothermal therapy upon NIR irradiation	(Hai et al., 2017)

Bleomycin	FOL - liposomes	MCF-7	Increased uptake and pronounced cytotoxicity	(Chiani et al., 2018)
Celastrol and irinotecan	Folic acid - liposomes	MDA-MB-231 and MCF-7	Pronounced uptake and apoptosis	(Soe et al., 2018)
PTX	FOL -pH sensitive liposomes	MDA-MB-231	Enhanced tumor accumulation	(Monteiro et al., 2018)
PTX	Acid cleavable folic acid liposomes and blood brain barrier penetrating peptide dNP2 peptide	4T1	Efficacious targeting with pronounced chemotherapeutic activity	(Li et al., 2018)
Bioactive compounds of *Kappaphycus alvarezii*	FOL - liposomes	MCF-7	Mitochondrial targeting with increased ROS generation	(Baskararaj et al., 2020)
PTX	Glutamic hexapeptide (for bone metastasis) and folic acid modified liposomes	MDA-MB-231	Increased targeting capacity in the *in vitro* and *in vivo* assays and metastatic bone cancer	(Yang et al., 2020)
Cisplatin and gemcitabine	FOL - liposomes	MCF-7	Synergistic anticancer activity	(Pakdaman Goli et al., 2021)
Manganese protoporphyrin	FOL- liposomes	4T1 cells	Sonodynamic therapy	(Chen et al., 2021)

1.12.2 EGFR

EGFR receptors are a member of the ERBB family of receptor tyrosine kinase with an extracellular ligand binding domain, a transmembrane domain, and a cytosolic tyrosine kinase domain. The ligand binding domain can bind to EGF, heparin-binding EGF-like growth factor,

amphiregulin, epiregulin, betacellulin, epigen, and transforming growth factor-α and form homodimers or heterodimers with ERBB2, ERBB3 or ERBB4 (Hsu and Hung, 2016).

The ligand-receptor binding causes the intracellular tyrosine kinase domain to phosphorylate and prompts various signaling pathways such as PI3 kinase, Ras-Raf-MAPK, JNK, and PLCɣ that are involved in multiple metabolic activities such as proliferation, differentiation, apoptosis, survival, migration, adhesion, angiogenesis, etc. (Hsu and Hung, 2016). The overexpression in the expression of these receptors results in the development of breast cancer, and EGFR receptors are overexpressed on the TNBC cells and result in a poor prognosis (Harris et al., 1989). Many therapies target these receptors, namely CET, lapatinib, and gefitinib, but their efficacy has been unsatisfactory (Masuda et al., 2012).

Mamot et al. (2012) synthesized DOX liposomes tagged with Fab' fragments of CET or EMD72000 (matuzumab) that heavily accumulated in MDA-MB-231 and MDA-MB-231 Vb100, the MDR sub cell line unlike. These were equally cytotoxic to free DOX and more than the non-targeted liposomes in the MDA-MB-231 cells but showed a 216 fold higher cytotoxicity than free DOX and non-targeted counterparts in the MDR cell line (Mamot et al., 2012). Tang et al. (2014) developed DOX liposomes tagged with GE11 peptide and observed an intensified accumulation and anticancer activity in the 4T1 cells with 2% PEG and 4% GE11 in the in vitro and in vivo studies (Tang et al., 2014).

Haeri et al. (2016) developed DOX thermosensitive liposomes tagged with either GE11 or Fab' fragment of CET that showed an appreciable uptake and cytotoxicity of the Fab' fragment of CET tagged liposomes in the MDA-MB-456 cells rather than in the MCF-7 cells (Haeri et al., 2016). Su et al. (2017) developed PEG engagers with anti-PEG Fab and anti-EGFR Fv fragments and treated MDA-MB-468 and MDA-MB-231 cells before DOX liposomes. The PEG engagers increased the anticancer activity of DOX liposomes in the in vitro and in vivo studies with xenograft mice models (Su et al., 2017).

Thomas et al. (2019) fabricated DOX liposomes tagged with Indium-111- EGF, which the MDA-MB-468 heavily took over MCF-7 cells. Ultrasound mediated cavitation of microbubbles led to higher extravasation of liposomes and pronounced therapeutic efficacy of the drug and radionuclide (Thomas et al., 2019). Dorjsuren et al. (2020) synthesized citric acid coated iron oxide magnetic nanoparticles and DOX loaded thermosensitive liposomes tagged

with CET. The combination treatment increased the chemotherapeutic efficacy and emanated a photothermal effect in the in vivo studies (Dorjsuren et al., 2020).

Studies report CET-tagged liposomal formulations' efficacy for breast cancer treatment (Table 1.10).

Table 1.10 Studies on CET tagged liposomal formulations for breast cancer treatment

Drug	Formulation	Cell lines	Highlight of the study	References
DOX/ epirubicin/ vinorelbine	Fab' fragments of CET-liposomes	MDA-MB-468	Higher uptake of immunoliposomes	(Mamot et al., 2005)
Mitoxantrone	PEGylated liposomes tagged with EGFR specific Affibody molecules	MDA-MB-468 MDA-MB-231 SKBR3 MCF-7	Increased binding and uptake, and high cytotoxicity in the EGFR overexpressing cell lines	(Beuttler et al., 2009)
siRNA	Liposome-polycation-DNA complex tagged with anti-EGFR Fab'	MDA-MB-231, SK-BR3 and MCF-7	Significant gene silencing	(Gao et al., 2011)
Anti-IGFR kinase inhibitor AG538	Anti-EGFR nanobody-liposomes	MDA-MB-468	Inhibition of the EGFR and IGF-IR pathways	(Van Der Meel et al., 2013)
Celecoxib	CET- liposomes	MDA-MB-468	Higher internalization and cytotoxic effect by the targeted	(Limasale et al., 2015)

FITC labelled ki-67 antibody TUBB-9	Liposomes tagged with Erbitux	MCF-7	Increased uptake of the immunoliposomes, inactivation of ki-67 by irradiation at 490 nm, release of the antibody in the cytoplasm by photochemical internalization	(S. Wang et al., 2016)
siRNA and quantum dots	Anti-EGFR tagged cationic liposomes	MDA-MB-231 and MDA-MB-453	High uptake, gene silencing, and inhibition of tumor growth and metastasis	(M. W. Kim et al., 2019)
Simvastatin	Anti-EGFR tagged liposomes	MDA-MB-231 and MCF-7	Higher apoptosis of the MDA-MB-231 cells	(Matusewicz et al., 2019)
DOX and citric acid coated iron oxide magnetic nanoparticles	CET-thermosensitive liposomes	SKBR-3 and MCF-7	Increased uptake and cytotoxicity in the SKBR-3 cell lines, combined photo-thermal therapy and chemotherapy	(Li et al., 2020)
PTX and piperine	CET-TPGS coated liposomes	MDA-MB-231	Synergism between drugs, high accumulation, and cytotoxicity	(Burande et al., 2020)
CD73 siRNA	GE11 peptide targeted liposomes + liposomal DOX	4T1	Heightened CD73 downregulation by the targeted formulations	(Soleimani et al., 2022)

1.13 Dual Receptor targeting

Researchers explored a few dual functionalized liposomes with different receptor combinations in the last decade to enhance the targeting capacity and the uptake rate. Dual receptor targeting increases the probability of uptake of the particles in the target cells (Figure 1.24).
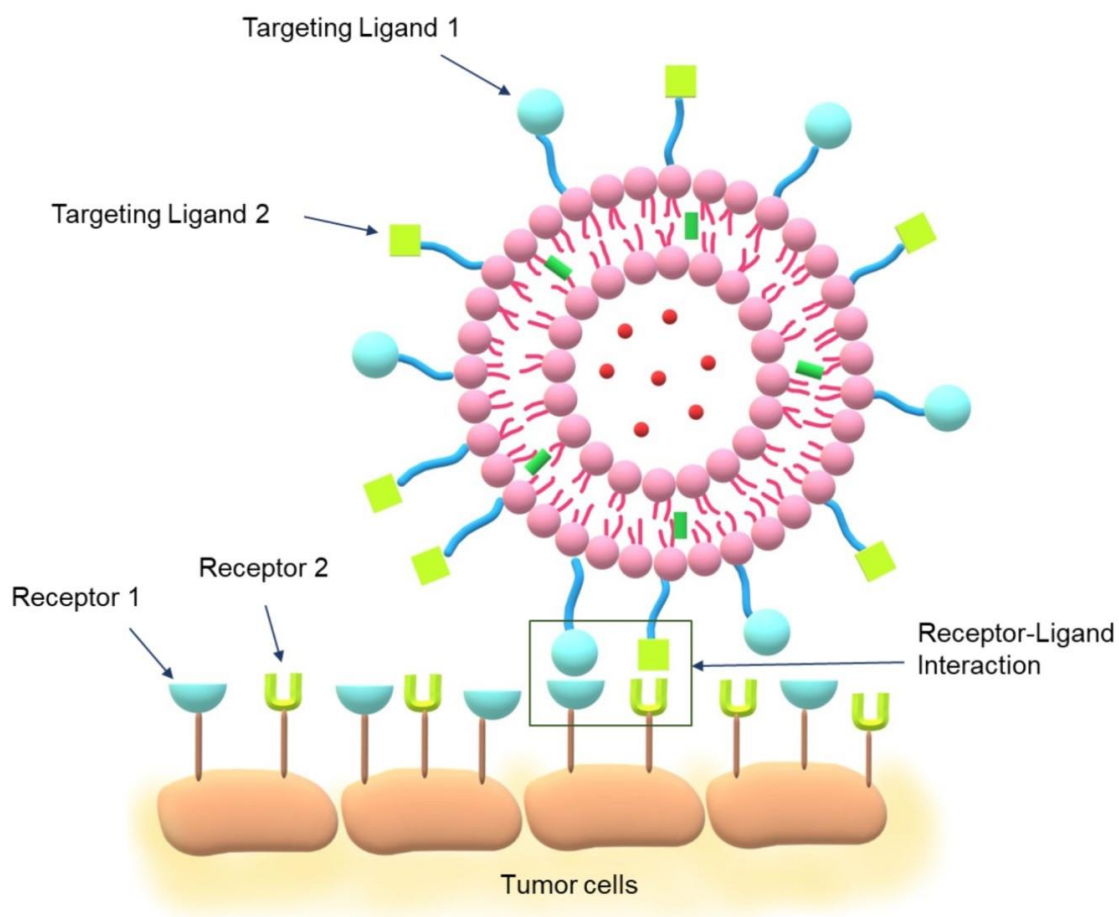
Figure 1.24 Dual receptor targeting of liposomes (modified from (Moudgil et al., 2023))

A few studies report the efficacy of dual targeted liposomes for the treatment of breast cancer with a combination of different ligands and drugs (Table 1.11)

Table 1.11 Studies on dual targeted liposomes

Receptor	Ligand	Drug	Reference
CD44 and mitochondrial targeting	TPGS and HA	PTX and Ionidamine	(Assanhou et al., 2015)
Integrin $\alpha_v\beta_3$ and NRP-1 receptors	dGR linked to octa arginine (R8), a CPP	PTX	(Qiu et al., 2018)
CD44 and mucin-1 (MUC-1)	DNA aptamers for CD44 and MUC-1	DOX	(D. Kim et al., 2019)
Glucose transporter-5 (GLUT5) and integrin $\alpha_v\beta_3$ receptors	Fructose and RGD	PTX	(Pu et al., 2019)
ICAM-1 and EGFR	Antibodies against ICAM-1 and EGFR	DOX	(Guo et al., 2019)

1.13.1 EGFR and FOL targeted liposomes

Tang et al. (2018) formulated lipid coated calcium phosphate nanoparticles encapsulating siRNA and tagged them with EGFR specific single chain fragment antibody (scFv) and folic acid. The dual functionalized liposomes showed a 2.5 and 1.6 folds higher uptake by the MDA-MB-468 cells than by the single targeted scFv and folic acid liposomes, respectively, with enhanced cytotoxic activity in the in vitro and in vivo studies (Tang et al., 2018).

A few studies report the efficacy of FOL and CET tagged nanoparticles in treating various cancers with a higher efficacy (Table 1.12).

Table 1.12 Studies on FOL-CET targeted nanoparticles reported for the treatment of cancer

Formulation	Cancer type	Highlight of the study	Reference
DOX liposomes tagged with folic acid and MAb against EGFR	KB cells	Selective binding to the target cells with improved cytotoxicity	(Saul et al., 2006)

Gold NPs conjugated with CET and anti-FR antibody	Ovarian cancer cells	Increased targeting for ovarian cancer cells (proof of concept)	(Bhattacharyya et al., 2011)
FOL-polyamidoamine dendrimers conjugated with antisense-oligonucleotides against EGFR	C6 glioma cells	Efficient downregulation of the EGFR receptors with reduced tumor growth	(Kang et al., 2010)
DTX loaded Chitosan nanoparticles tagged with CET and FOL	Advanced lung cancer	Increased uptake by caveolae mediated endocytosis and increased cytotoxicity	(Vikas et al., 2021)
CET and FOL tagged Chitosan alginate NPsloaded with cabazitaxel	A-549 lung cancer cells	Increased uptake and improved cytotoxicity	(Vikas et al., 2022)

1.14 Hypothesis and Objectives

To acknowledge the MDR aspect of the breast cancer cells, we aimed to synthesize liposomes encapsulating CUR and DOX and to enhance the uptake of these formulations, we tagged FOL against the FRs and CET against the EGFR receptors on the liposomal surface (Figure 1.25). To synthesize robust, actively targeted liposomal formulations, we intended to optimize the process parameters for liposomal synthesis by the thin film hydration and various intrinsic factors to achieve particle specifications in the drug delivery range (size < 200 nm and PDI < 0.3). We then investigated the efficacy of multiple liposomes on MCF-7, a hormone receptor positive cell line, and MDA-MB-231, a TNBC cell line. We hypothesized the following:

- FOL-CET CUR-DOX liposomes should exhibit a better uptake and cytotoxic activity in the MDA-MB-231 cell line than MCF-7 cell lines as TNBC cells overexpress EGFR receptors and plain drugs (DOX and CUR).

- The pH-responsive liposomal formulations should exhibit enhanced activity compared to non-responsive ones.
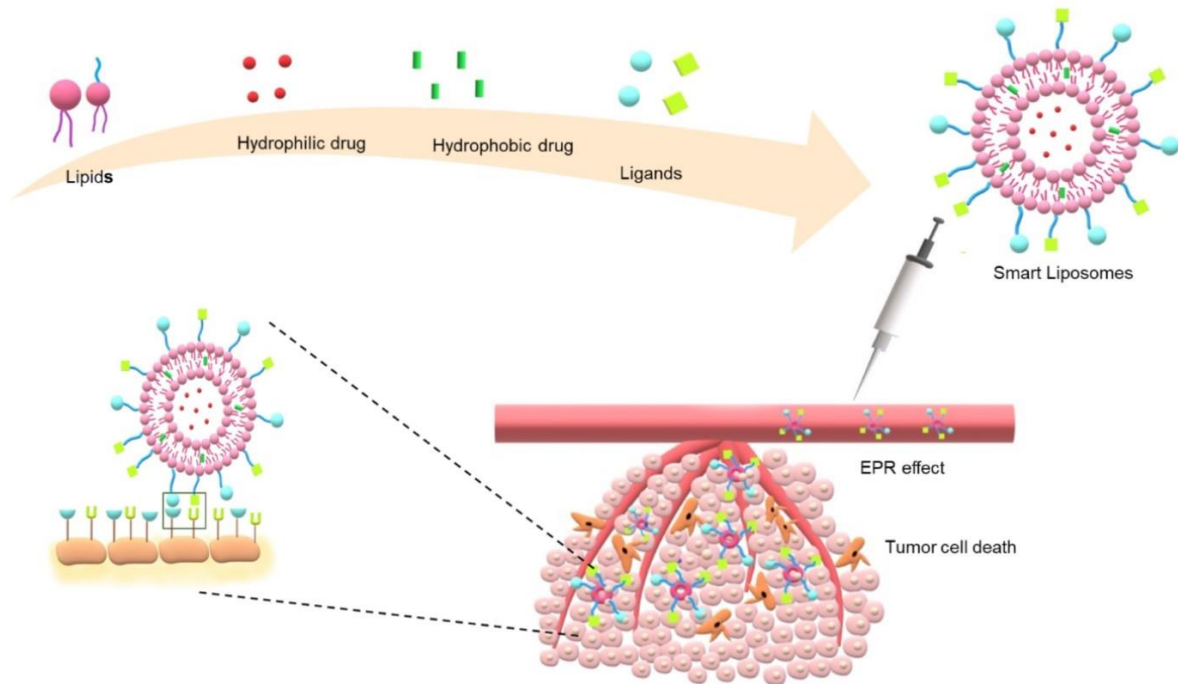
Figure 1.25 Schematics of drug delivery by liposomes (modified from (Moudgil et al., 2023))

Based on the hypothesis, we followed the following objectives to carry out the study:

1. Optimization, Synthesis, and Characterization of the plain liposome.
2. Optimization, Synthesis, and Characterization of drug loaded liposomes.
3. Optimization, Synthesis, and Characterization of ligand tagged drug loaded liposomes against Breast cancer.
4. In vitro efficacy studies.

Chapter 2

Materials and Methods

2 Materials and Methods

2.1 Materials

Table 2.1 List of chemicals/materials used in the study and their sources

Name	Source
L-α Phosphatidylcholine (PC)	Sigma
CHOL	Sigma
DSPE-mPEG2000	Avanti polar lipids
DOPE	Sigma
Cholesteryl hemmisuccinate (CHEMS)	Sigma
1,2-Distearoyl-sn-glycero-3-Phosphoethanolamine polyethylene glycol-2000- FOL (DSPE-PEG2000-FOL)	Avanti polar lipids
1,2-distearoyl-sn-glycero-3-phosphoethanolamine-N-[carboxy(polyethylene glycol)-2000 (DSPE-PEG2000-COOH)	Avanti polar lipids
CET	Sigma
Chloroform	HiMedia
Methanol	HiMedia
CUR	Sigma
DOX	Sigma
Triton X 100	HiMedia
Sodium chloride	SRL
Disodium hydrogen phosphate	SRL
Potassium chloride	SRL
Potassium dihydrogen phosphate	SRL
1-Ethyl-3-(3-dimethylaminopropyl) carbodiimide (EDC)	Sigma
N-hydroxysuccinimide (NHS)	Sigma
Avanti mini hand extruder	Avanti
Whatman polycarbonate membranes	Whatman
Whatman filter discs	Whatman
Dialysis bags	Sigma
Round bottom flask (RBF)	Borosil
MCF-7 cell line	NCCS repository

MDA-MB-231 cell line	NCCS repository
Rosewell Park Memorial Institute- 1640 (RPMI-1640)	HiMedia
Dulbecco's Modified Eagle Medium (DMEM)	HiMedia
3-(4,5-Dimethylthiazol-2-yl)-2,5-Diphenyltetrazolium Bromide (MTT)	Sigma
Dimethyl sulfoxide (DMSO)	Sigma

2.2 Methods

2.2.1 Synthesis of plain liposomes

We synthesized liposomes using the thin film hydration technique using PC and CHOL (Mendez and Banerjee, 2017) (Zhang, 2017). Lipids solubilized in chloroform were added to an RBF, following which the solvent was removed under vacuum at 50 °C in a rotary evaporator, creating a lipid layer; the RBFs were kept in a vacuum desiccator for 3–4 h to ensure complete removal of chloroform traces. The lipid layer was hydrated at 60 °C for 1 h with phosphate buffer saline pH 7.4 (PBS), and the liposomal suspension was incubated overnight at 4 °C.

Liposomes were downsized by sonicating for 20 min in a water bath, then extruding through a 100 nm polycarbonate membrane using a mini hand extruder. These liposomes were stored at 4 °C till further use. PEGylated liposomes were synthesized using the same protocol by adding DSPE-mPEG2000, PC, and CHOL.

2.2.2 Synthesis of CUR liposomes

CUR dissolved in chloroform was added to an RBF with PC and CHOL in the thin film formation step (Schmitt et al., 2020) (Ding et al., 2017), and the organic solvent was removed on a rotary evaporator at 50 °C under 700 mm of Hg of vacuum and 270 RPM of rotation for 30 min. A thin lipid layer with CUR formed on the walls of the RBF was hydrated with PBS at 60 °C at 270 RPM rotation for 2 h. We observed that, as in plain liposomes that hydrated in 1 h, for the CUR liposomes, the layer was still attached to the walls at the end of 1 h, so we hydrated it for more time than the plain liposomes. The so-formed CUR liposomes were then stored at 4 °C overnight for aging.

The liposomes were then downsized by a 20 min sonication in the water bath followed by a mini hand extruder extrusion through a 100 nm polycarbonate membrane for the desired number of times. The liposomes so formed were then stored at 4 °C for further use. PEGylated curcumin liposomes were synthesized in the same fashion with DSPE-mPEG2000 added along with the lipids and curcumin in the thin film formation step.

2.2.3 Synthesis of DOX liposomes

DOX was loaded in the liposomes using a passive loading technique (Sesarman et al., 2018). Lipids in specific concentrations solubilized in chloroform were added to the RBF. The chloroform was then evaporated under a 700 mm Hg vacuum at 50 °C for 30 min in a rotary evaporator. The flasks were kept in a vacuum desiccator for 3-4 h to ensure the removal of trace chloroform. The formed lipid layer was then hydrated with PBS containing DOX (desired concentration) for 2 h at 270 RPM rotation. The developed DOX loaded liposomal suspension was then stored at 4 °C for aging. After storage, these liposomes were extruded at 60 °C and stored at 4 °C for further use.

2.2.4 Synthesis of CUR-DOX loaded liposomes

Dual loaded liposomes were synthesized by loading the drugs with the passive loading technique (Sesarman et al., 2018). The optimized concentration of CUR was added in the thin film formation step along with the lipids solubilized in chloroform in the RBF. CUR was incorporated in the lipid layer; the RBFs were then kept in the vacuum desiccator for 3-4 h to remove the traces of chloroform. The thin film was then hydrated with PBS containing DOX and hydrated with 2 h at 270 RPM. The formed liposomal suspension was then stored at 4 °C for aging. These liposomes were then extruded through 100 nm polycarbonate membranes and stored at 4 °C till further use.

2.2.5 Synthesis of FOL tagged liposomes

FOL tagged liposomes were formulated by the thin film hydration technique (Soe et al., 2018). 0.1 mole % of DSPE-PEG2000-FOL was added to the RBF along with the lipids in the thin film formation step, as mentioned in section 3.2.1. This FOL tagged lipid incorporated into the lipid layer was hydrated in the thin film hydration step.

For the Synthesis of FOL CUR liposomes, CUR was added as mentioned in section 3.2.2; for the Synthesis of FOL DOX liposomes, DOX was added as discussed in section 3.2.3; FOL CUR-DOX liposomes were prepared as per section 3.2.4.

2.2.6 Synthesis of CET tagged liposomes

CET was tagged to the liposomes after the synthesis of drug loaded liposomes (Burande et al., 2020). A 7: 3 molar ratio of PC and CHOL was used along with 1 mole % of DSPE-mPEG2000 and 0.1 mole % DSPE-PEG2000-COOH. The drugs were added per the earlier protocols, i.e., section 3.2.2 for CUR loading, section 3.2.3 for DOX liposomes, and section 3.2.4 for CUR-DOX loading. After the hydration step, the formed liposomes were stored at 4 °C for aging overnight.

The liposomes were extruded through a 100 nm polycarbonate membrane with 5 extrusion passes. 250 µl of the liposomal suspension with 1.5 mg EDC and 1 mg NHS were mixed with moderate stirring for 30 min at pH 7.4. Then 0.06 mg of CET was added to this mixture with light stirring for 4H at room temperature. This reaction mixture was ultra-centrifuged at 60,000 RPM for 2 h at 4 °C. The pellet was suspended in PBS for further use. The supernatant was stored for the analysis of % CET conjugation efficiency.

2.2.7 Synthesis of FOL-CET CUR-DOX liposomes

FOL-CET tagged liposomes were synthesized by adding 7: 3 molar ratio of PC and CHOL, 1 mole % of DSPE-mPEG2000, 0.05 % of DSPE-PEG2000-FOL and 0.05% of DSPE-PEG2000-COOH. The drugs were added per the earlier protocols, i.e., section 3.2.2 for CUR loading, section 3.2.3 for DOX liposomes, and section 3.2.4 for CUR-DOX loading. After the hydration step, the formed liposomes were stored at 4 °C for aging overnight. The liposomes were extruded through a 100 nm polycarbonate membrane with 5 extrusion passes. The ligation of CET was carried out as per section 3.2.5.

2.2.8 Synthesis of pH responsive liposomes

pH responsive liposomes were synthesized using the protocol mentioned above. The lipids used for the Synthesis are DOPE and CHEMS in a 7:3 molar ratio and 10 mg/ml concentration of each lipid. The FOL, CET, and FOL-CET tagged liposomes, and non-targeted CUR, DOX, and CUR-DOX liposomes were synthesized by the above mentioned methods.

2.3 Characterization of liposomes

2.3.1 Hydrodynamic diameter, PDI, and Zeta potential

The dynamic light scattering (DLS) technique elucidated the hydrodynamic diameter and the polydispersity index (PDI) values. The readings were taken on Malvern Zetasizer Pro (Malvern Panalytical, UK) at 25 °C (173 ° non-invasive backscattering angle). The zeta potential values were also recorded on the same instrument. All the samples were assessed in triplicate, and three independent measurements were recorded for each sample.

2.3.2 Removal of unencapsulated drug

As reported in other studies, the drug was removed during the extrusion step for CUR liposomes (Mahmud et al., 2016). Both unencapsulated CUR and DOX were removed twice by ultracentrifugation at 60 000 RPM for 2.5 h. The pellet contained drug loaded liposomes that were suspended in PBS; the supernatant contained the unencapsulated drug that was discarded.

2.3.3 Calculation of % EE

After the Removal of the unencapsulated drug, the % EE of the respective drug was calculated from the liposomal suspension – the calculation of the unencapsulated drug would not be appropriate since, as mentioned before, a significant portion of unencapsulated CUR is removed during extrusion that cannot be quantified thus, the proper calculation of % EE of the liposomal suspension is required. The liposomal suspension and 0.075 % of triton X-100 in 1:5 v/v ratio were mixed, and the absorbance was measured at 426 nm by a UV-Vis spectrophotometer.

The drug concentration encapsulated in the liposomes was calculated using the straight line equation obtained by plotting a standard curve of CUR and DOX in 0.075 % triton X-100. After the Calculation of the encapsulated drug, the % EE was calculated from the following formula:

$$\% \, EE \; = \; \frac{Concentration \; of \; encapsulated \; drug}{Total \; drug} \times 100$$

The concentration of encapsulated drug was calculated by preparing a standard curve of the drugs. Aliquots of CUR stock corresponding to 1, 2, 3, 4, 5, 6, 7, 8, 9, and 10 µg/ml of drug was mixed with 0.075 % triton X-100 in 1:5 v/v ratio. The absorbance of each concentration was measured at 426 nm, taking 0.075 % triton X-100 as blank. The straight line graph and equation (Figure 2.1) obtained after the analysis with an R^2 value of 0.9996 were used to quantify the liposome encapsulated drug.
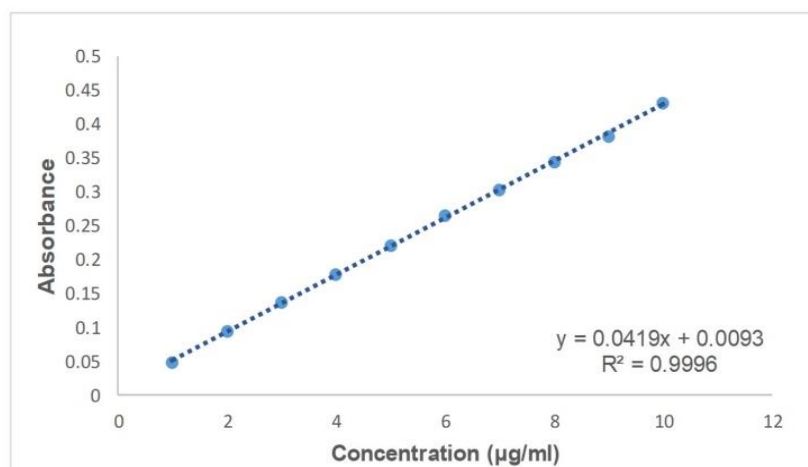
Figure 2.1 Standard curve of CUR in 0.075 % triton X-100

Aliquots of DOX stock corresponding to 2, 4, 6, 8, and 10 µg/ml of drug was mixed with 0.075 % triton X-100 in 1:5 v/v ratio. The absorbance of each concentration was measured at 480 nm, taking 0.075 % triton X-100 as blank. The straight line graph and equation obtained after the analysis with an R^2 value of 0.9994 were used to quantify the liposome encapsulated drug (Figure 2.2).
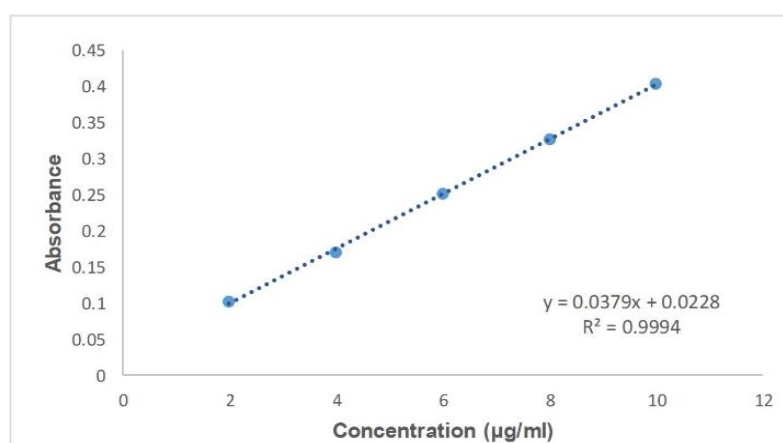
Figure 2.2 Standard curve of DOX in 0.075 % triton X-100

2.3.4 Calculation of percentage drug loading (% DL)

Liposomal formulations were lyophilized to form powder. The lyophilized formulations were then weighed to calculate % DL by the following formula:

$$\% \, DL \; = \; \frac{Weight \; of \; encapsulated \; drug}{Weight \; of \; drug \; loaded \; liposomes} \times 100$$

2.3.5 Morphology of Liposomes

The morphology of the particles was ascertained using the transmission electron microscopy (TEM) technique. The TEM images were recorded on Tecnai G2 20 S-Twin. The high-resolution transmission electron microscopy (HRTEM) images were recorded on JEOL-JEM-F200. Liposomal formulations diluted with deionized water/PBS were dropped on a 200 mesh carbon-coated copper grid, following which the samples were air-dried before analysis.

2.3.6 Fourier transform infrared spectroscopy (FTIR)

FTIR spectra were recorded to determine the presence of functional groups in the raw material (PC, CHOL, and DSPE-mPEG2000) and the liposomal formulations after synthesis. The liposomal formulations were freeze-dried for analysis. The infrared spectral profiles were recorded on Tensor 27 (Bruker) in the wavenumber range of 4000–600 cm^{-1}. Each sample was subjected to 40 runs.

2.3.7 Thermogravimetric analysis (TGA)

TGA was used to determine the thermal stability of raw materials and freeze-dried liposomal formulations. The TGA profiles were recorded on an STA 6000 system from Perkin Elmer. Approximately 5–10 mg of the sample was taken in an alumina crucible to conduct the experiments. The samples were analyzed in the 50–900 °C temperature range with a scanning rate of 10 °C /min in a nitrogen atmosphere (flow rate: 20 mL/min).

2.3.8 Differential scanning colorimetry (DSC)

The DSC technique was used to analyze the samples on DSC Q100 V8.2 Build 268. The samples (5–10 mg) were placed in a standard aluminum pan with a lid. The samples were scanned at 10 °C /min in a nitrogen atmosphere (flow rate: 50 mL/min). The data spanning the

temperature range from 0 °C to below the degradation onset temperature were recorded (as identified from TGA analysis).

2.3.9 Quantification of CET

After tagging CET to the liposomes, the particles were ultra-centrifuged at 60,000 RPM for 2 h, and the supernatant was collected to quantify the untagged CET. The percentage binding efficiency (% BE) of CET on the liposomal surface was calculated by the following formula:

$$\% \, BE \; = \; \frac{Initial \; weight \; of \; CET \; - \; Untagged \; CET}{Initial \; weight \; of \; CET} \times 100$$

The untagged CET was calculated from the straight line equation acquired from plotting a standard curve of bovine serum albumin (BSA) and determining the protein concentration by Bradford assay (Figure 2.3). Varied dilutions of BSA were made from the stock of 1 mg/ ml of BSA, i.e., 1,2,3,4 and 5 µg/ml. 500 µl Bradford reagent was added to 250 µl BSA dilution, and the reaction mixture was incubated for 5 min. The absorbance was read after 5 min by a UV-VIS spectrophotometer at 590 nm. The concentration of CET was calculated by the straight line equation.

The plotted data shows absorbance versus concentration with the fitted equation $y = 0.0611x + 0.3693$ and $R^2 = 0.9992$.
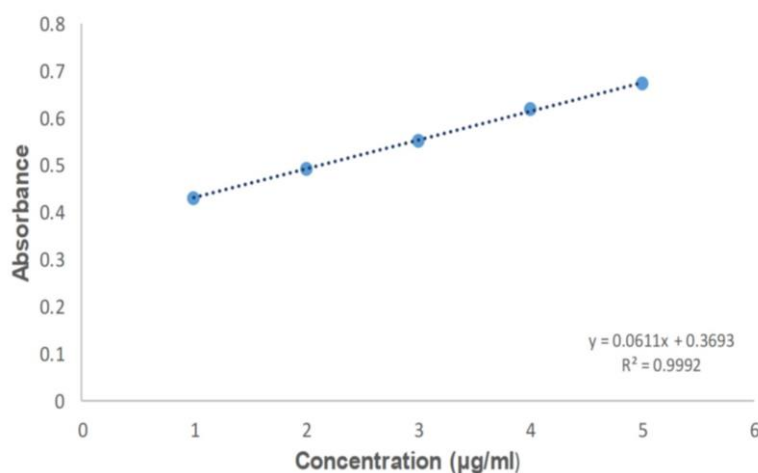
Figure 2.3 Standard curve of BSA

2.4 *In-vitro* studies

2.4.1 Stability studies

The stability of the liposomal formulations was tested at 4 °C. The hydrodynamic diameter, PDI, and zeta potential values were determined over time. These values were recorded every 15 days by withdrawing aliquots from the stock to identify changes occurring during storage.

For drug loaded formulations, the % EE was calculated when the liposomes were formulated and at the end of the experiment to determine the total drug retention. The liposomal formulations were ultra-centrifuged at 60,000 RPM for 2.5 h at 4 °C; the supernatant was used to determine the amount of drug leaked from the liposomes during storage. The following formula calculated the % drug retention:

$$\% \, Drug \, retention$$
$$= \frac{(Weight \, of \, encapsulated \, drug - Weight \, of \, unencapsulated \, drug}{Weight \, of \, encapsulated \, drug}$$
$$\times 100$$

2.4.2 Drug release studies

Drug release studies were carried out by dialysis method. 1 ml of liposomal suspension was placed in a dialysis bag immersed in 15 ml of recipient buffer formed with 30% methanol in PBS with two different pH of 5.5 and 7.4. This experimental setup was stirred at 100 RPM at 37 °C. 1 ml sample from the recipient buffer was withdrawn at predetermined time intervals of 30 min, 1, 2, 4, 8, 12, 24, 48, and 72 h; an equal amount of fresh recipient buffer was added to the experimental setup.

The drug concentration was determined by plotting a standard curve of the drugs in the recipient buffer and calculating the drug concentration from the straight line equation. The following formulas were used to determine the amount of drug released and the cumulative percentage of drug release (Ravindran Chandrasekaran et al., 2011):

$$Drug \, released \, (\frac{mg}{ml})$$
$$= \frac{Drug \, concentration \, \times Recipient \, buffer \, volume \, \times Dilution \, factor}{1000}$$

$$Cumulative\ drug\ release\ \% \ = \ \frac{Volume\ of\ sample\ withdrawn\ (ml)}{Bath\ volume\ (v)} \times P(t-1) + Pt$$

Pt is the percentage release at time't', and P (t-1) is the percentage release before to time't'.

The standard curve for CUR in the recipient buffer was prepared by forming aliquots of CUR stock corresponding to 1, 2, 3, 4, 5, 6, 7, 8, 9, and 10 µg/ml of drug in 30 % methanol in PBS (recipient buffer). The absorbance of each concentration was measured at 426 nm, with 30 % methanol in PBS as a blank. The straight line graph and equation obtained after the analysis with the R^2 value of 0.9961 were used to quantify the released drug (Figure 2.4).
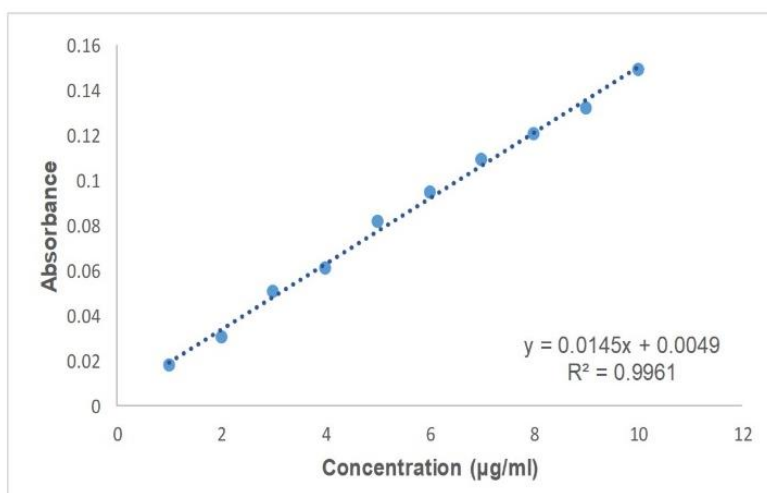
Figure 2.4 Standard curve of CUR in 30 % methanol in PBS

The standard curve for DOX in the recipient buffer was prepared by forming aliquots of DOX stock corresponding to 2, 4, 6, 8, and 10 µg/ml of drug in 30 % methanol in PBS (recipient buffer). The absorbance of each concentration was measured at 480 nm, taking 30% methanol in PBS as blank. The straight line graph and equation obtained after the analysis with the R^2 value of 0.9993 were used to quantify the released drug (Figure 2.5).
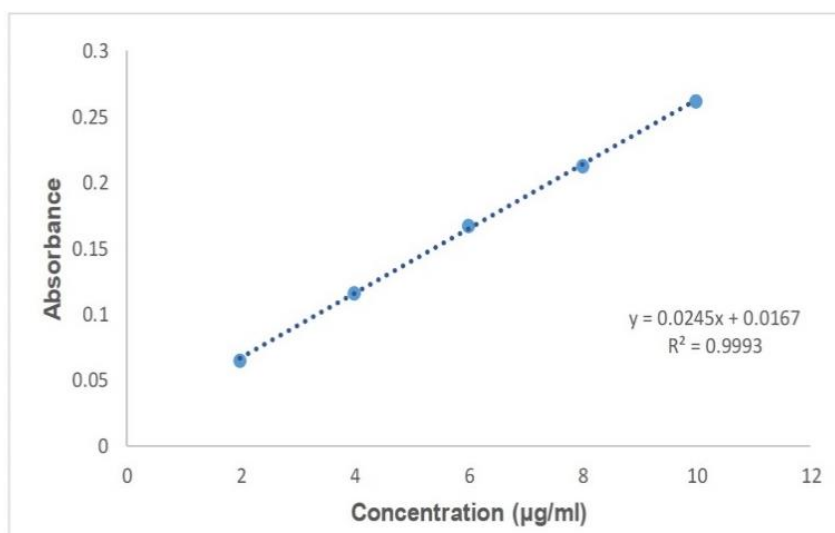
Figure 2.5 Standard curve of DOX in 30 % methanol in PBS

2.4.4 Cell viability assay

MCF-7 and MDA-MB-231 cells were seeded in a 96 well plate (4000 cells per well) and incubated for 24 h (Mahmud et al., 2016). We added 10% fetal bovine serum and pennicilin/streptomycin solution in the media. Thereafter, the cells were treated with plain DOX, plain CUR, and liposomal formulations at varied concentrations (1, 5, and 10 µM) and incubated at 37 °C for 48 h. After the incubation, 20 µl MTT (5 mg/ml) was added to each well and further incubated for 4 h at 37 °C. The formazan crystals formed were then dissolved by adding 100 µl DMSO, and the reading was taken at 570 nm on a Multiscan Go Thermo Scientific plate reader. The following formula then calculated the % cell viability:

$$\% \; Cell \; viability \; = \; \frac{100 \; \times Absorbance \; at \; 570 \; nm}{Absorbance \; at \; 570 \; nm}$$

We plotted a graph for % cell viability against drug concentrations and calculated the IC_{50} values using the KyPlot software.

2.4.3 Uptake analysis

MCF-7 and MDA-MB-231 cells were seeded in a 12 well plate at a density of 2×10^5 cells per well and incubated for 24 h (Pan et al., 2017). The cells were treated with 1 µM of DOX and 3 µM of CUR as plain drugs and in various liposomal formulations and incubated for 8 h. Thereafter, the media was removed, and the plates were washed with PBS twice. The cells

were harvested in PBS by mechanically scrapping from the plates and centrifuged at 3000 RPM for 3 min. The supernatant was removed, and the pellet was washed with deionized water and centrifuged at 3000 RPM for 3 min. The pellet was resuspended in deionized water and added to the Fluorescence activated cell sorting (FACS) tubes, and BD FACS ARIA III SORP, a FACS machine, recorded the % uptake.

2.5 Statistical Analysis

Data are presented as mean ± standard deviation calculated using Microsoft Office Excel. One-way ANOVA and the *t*-test were performed using GraphPad Prism, and the p-values ≤ 0.05 were considered statistically significant. FTIR spectra, and TGA and DSC thermograms, were plotted using Origin Pro 8.5 software. The IC_{50} values were calculated using KyPlot software and the FACS graphs were generated using Flowing software 2.

CHAPTER 3

Optimization, Synthesis, and Characterization of plain liposomes

3.1 Introduction

Laboratory scale techniques such as ether injection, ethanol injection, reverse-phase evaporation, and detergent removal (Chang et al., 2012) synthesize heterogeneous liposomes, expose drugs to organic solvents (that alter their biological and functional attributes), dilute the liposomes, and present difficulty in removing the organic solvents (Vemuri and Rhodes, 1995); the thin film hydration technique supersedes these shortcomings and is a popular approach (Laouini et al., 2012). These methods fabricate MLVs/ LUVs that require size reduction to create a homogenous population in a ~50–200 nm size range for biomedical applications (optimum for drug delivery) (Guimaraes et al., 2021). The risk of clearance by RES rises with the increase in particle size; thus, smaller particles are superior drug delivery vehicles (Brown and Khan, 2012). Nanoparticles extravasate through tumor vascular defects and accumulate through the EPR effect.

PDI and zeta potential values determine the monodispersity and stability of liposomes: a monodisperse population has PDI ≤ 0.3 (Danaei et al., 2018), and a highly stable population has zeta potential $\geq$ -30/+30. Zeta potential depends on the liposome's surface properties and is sensitive to the solvent's pH, viscosity, ionic strength, and temperature (Smith et al., 2017). Zeta potential values ranging from ± 0 - 10 mV, $\pm 10 - 20$ mV, $\pm 20 - 30$ mV, > 30 mV, and > 60 mV indicate unstable formulations, relative stability, moderate stability, good stability, and excellent stability, respectively of the formulations (Honary and Zahir, 2013) (Bhattacharjee, 2016). Thus, size, PDI, and zeta potential are the three cornerstones that should be optimized to formulate liposomes for drug delivery.

In this study, we identified and optimized process parameters of the thin film hydration technique and intrinsic factors to synthesize liposomes for drug delivery. We assessed rotation speed, vacuum pressure, and type and volume of organic solvent in the thin film formation step; rotation speed, hydrating medium, and hydration time in the thin film hydration step; number of extrusion passes, and number of polycarbonate membranes in the downsizing step. Intrinsic factors included the molar ratio and concentration of lipids. We characterized these liposomes by various analytical techniques. This all-inclusive study provides mechanistic insight into liposomal synthesis, specifies the role of every process and intrinsic factor, and helps modulate precise parameters to synthesize liposomes with desired specifications for varied applications.

3.2 Methods

We synthesized plain liposomes with a 1:1 molar ratio of PC: CHOL by the thin film hydration technique elaborated in Chapter 2, section 2.2.1, and optimized based on the hydrodynamic diameter, PDI, and zeta potential (Figure 3.1).

3.2.1 Factors affecting the thin film formation step

The rotation speed (30, 60, 120, 150, 240, and 270 RPM), vacuum pressure (100, 200, 300, 400, 500, 600, and 700 mm of Hg), organic solvents (chloroform, chloroform: methanol in 2:1 and 9:1 v/v ratios), volume of chloroform (2, 5, and 10 ml), and volume of RBF (50, 250 and 500 ml) were varied to study their effect on the nature of lipid layer. These layers were hydrated, and the liposomal suspensions were assessed for their size, PDI, and zeta potential without the downsizing step.

3.2.2 Factors affecting the thin film hydration step

Lipid layers were made with the optimized values from the thin film formation step. The hydration step was studied on three grounds: rotation speeds (30, 60, 90, 120, 240, and 270 RPM), hydrating mediums (PBS, deionized, and double distilled water), and hydration time (15, 30, 60, and 120 min). Liposomes were evaluated for size, PDI, and zeta potential by bypassing the downsizing step.

3.2.3 Factors affecting the downsizing step

The downsizing step was optimized for the number of extrusion passes (1, 5, 10, and 20) and the number of polycarbonate membranes (1 and 2) based on the size and PDI of the particles.

3.2.4 Intrinsic factors

The intrinsic factors were examined by varying PC and CHOL concentrations (10, 20, and 30 mg/mL) and the molar ratio of PC: CHOL (1:1, 3:2, 7:3, 4:1, 9:1, and 1:0). DSPE-mPEG2000 concentration (1, 3, and 5 mole % of lipids) was optimized for PEGylated liposomes.

3.2.5 Characterization of liposomes

Liposomes synthesized with the final optimized values of the process and intrinsic parameters were characterized for their hydrodynamic diameter, PDI, and zeta potential by DLS, the morphology by HRTEM and TEM, the functional groups by FTIR, and the thermal analysis

by TGA and DSC. The technical details of the analytical techniques are provided in Chapter 2, section 2.3.
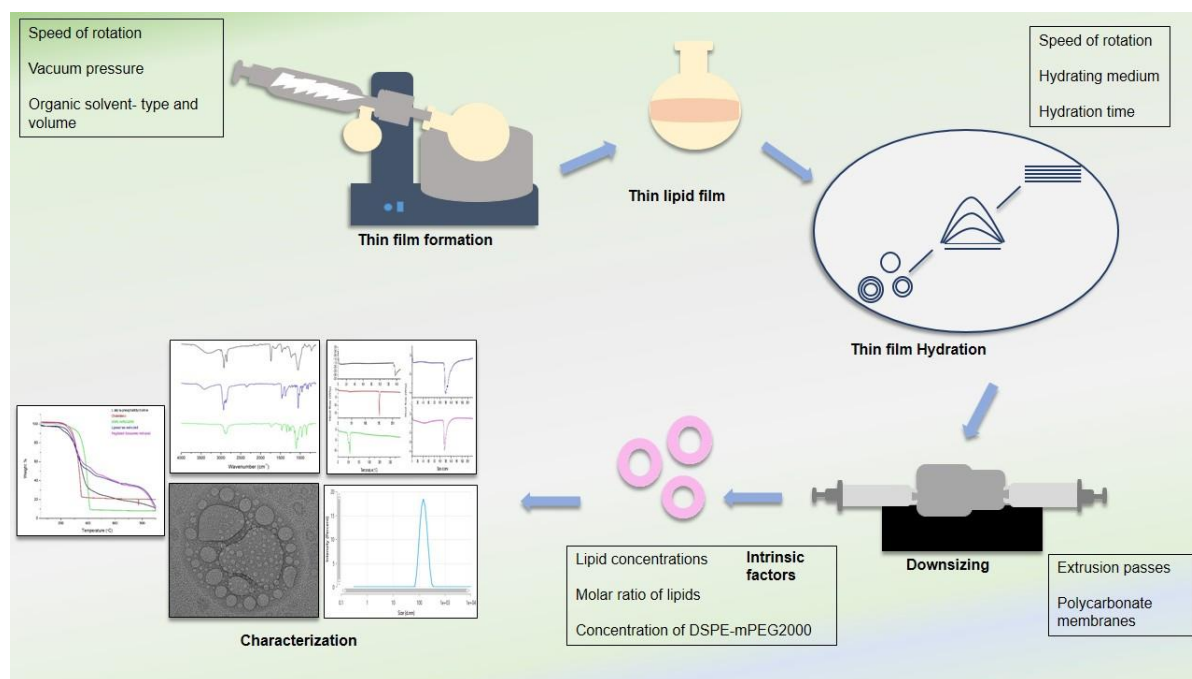
Figure 3.1 Overview of optimization of the process parameters of the thin film hydration technique, downsizing step and intrinsic factors, and characterization of liposomes

3.3 Results and Discussion

The thin film hydration method involves two steps: the organic solvent containing dissolved lipids is evaporated to form a lipid layer on the RBF wall in the thin film formation step; the lipid layer is hydrated with an aqueous solvent in the thin film hydration step. Successful hydration generates a turbid suspension, confirming the synthesis of liposomes, and a rise in turbidity indicates larger particles (Torchilin and Weissig, 2003). Incomplete hydration (with most of the layer attached to the RBF after hydration) also produces a less turbid suspension that signifies a low concentration of liposomes.

Identified parameters from the thin film hydration method, the downsizing step, and the intrinsic factors can affect the synthesis process and the particle specifications. We investigated the process parameters with a 1:1 molar ratio of lipids, as the advisable limit of CHOL to synthesize liposomes is $\leq 50\%$ (Yadav et al., 2017). We intended to optimize the process parameters to create a monodisperse population of smaller particles just after hydration to avoid severe downsizing steps.

3.3.1 Factors affecting the thin film formation step

We identified and investigated four process parameters in the thin film formation step: rotation speed, vacuum pressure, and organic solvent type and volume.

3.3.1.1 Rotation speed

We optimized the rotation speed (30, 60, 120, 150, 240, and 270 RPM) based on the lipid layer quality, ease of hydration, and liposomal specifications. The rotation speed significantly affected the nature of the lipid layer (Table 3.1): 30 and 60 RPM formed a non-uniform layer on the walls and bottom of the RBF that hydrated incompletely and yielded a non-turbid liposomal suspension; 120 and 150 RPM created a non-uniform layer on the walls and base of RBF that hydrated better, and produced a suspension with increased turbidity; 240 and 270 RPM formed a perfect ring-shaped and uniform layer on the RBF walls that hydrated completely and generated a highly turbid liposomal suspension. Thus, higher rotation speeds construct a uniform lipid layer on the RBF walls that hydrates smoothly and produces a highly turbid liposomal suspension –this confirms a lower lipid loss.

Table 3.1 Effect of rotation speed on the lipid layer in the thin film formation step

Rotation speed (RPM)	Nature of the lipid layer	Position of the lipid layer	Turbidity upon Hydration	Lipid layer after hydration
30	Non-Uniform	Bottom of the RBF	Non-turbid	Incompletely hydrated
60				
120			Slightly turbid	Incompletely hydrated
150		Uneven layer on the RBF wall		
240	Uniform	Ring-like layer on the RBF wall	Highly turbid	Completely hydrated
270				

The hydrodynamic diameter ranged from 212.86 ± 21.69 to 256.11 ± 4.54 nm, PDI from 0.34 ± 0.07 to 0.46 ± 0.1, and zeta potential from -20.55 ± 0.95 to -24.84 ± 0.68 mV with different rotation speeds (Table 3.2). The hydrodynamic diameter (ANOVA p value = 0.3461), PDI (ANOVA p value = 0.6146), and zeta potential (ANOVA p value = 0.1840) exhibited an insignificant change upon increasing the rotation speed (Figure 3.2). The size and PDI crossed

the mandates of drug delivery, i.e., > 200 nm and 0.3, respectively, and the zeta potential characterized the liposomes with moderate stability.

Table 3.2 Effect of rotation speed on hydrodynamic diameter, PDI, and zeta potential during thin film formation

Rotation speed (RPM)	Average Hydrodynamic Diameter (nm)	Average PDI	Average Zeta Potential (mV)
30	235.74 ± 12.01	0.45 ± 0.13	-20.55 ± 0.95
60	243.57 ± 58.62	0.43 ± 0.17	-21.95 ± 3.50
120	247.47 ± 7.77	0.46 ± 0.10	-21.30 ± 1.80
150	256.11 ± 4.54	0.41 ± 0.02	-23.58 ± 1.58
240	212.86 ± 21.69	0.34 ± 0.07	-24.84 ± 0.68
270	214.19 ± 21.76	0.34 ± 0.09	-22.51 ± 2.18

Figure 3.2 Effect of rotation speed on hydrodynamic diameter (a), PDI (b), and zeta potential (c) during thin film formation

The rotation speed significantly impacted the lipid layer. The lipid layer quality ascertains lipid homogeneity and ensures smooth hydration (Torchilin and Weissig, 2003). We optimized the 240 RPM rotation speed on the lipid layer's nature, hydration level, and suspension turbidity.

3.3.1.2 Vacuum pressure

Vacuum pressure also considerably affected the lipid layer (Figure 3.3) (Table 3.3): 100, 200, 300, and 400 mm of Hg vacuum pressure created a non-uniform and patchy layer in more than 30 min; 500 and 600 mm of Hg of vacuum pressure cast a uniform layer within 30 min; 700 mm of Hg of vacuum pressure formed the most uniform layer within 30 min that hydrated most

efficiently, and fabricated a highly turbid suspension. Thus, reduced pressure develops a thin and uniform layer that can hydrate effectively. We optimized 700 mm of Hg vacuum pressure based on the lipid layer uniformity and hydration level.

Table 3.3 Effect of vacuum pressure on the lipid layer

Vacuum pressure (mm of Hg)	Nature of the lipid layer	Time required for layer formation	Lipid layer after hydration
100	Non-uniform and	> 30 min	Non-uniform
200	patchy layer		hydration
300			
400			
500	Uniform layer	Within 30 min	Uniform hydration
600			
700	Most uniform layer		Most uniform hydration
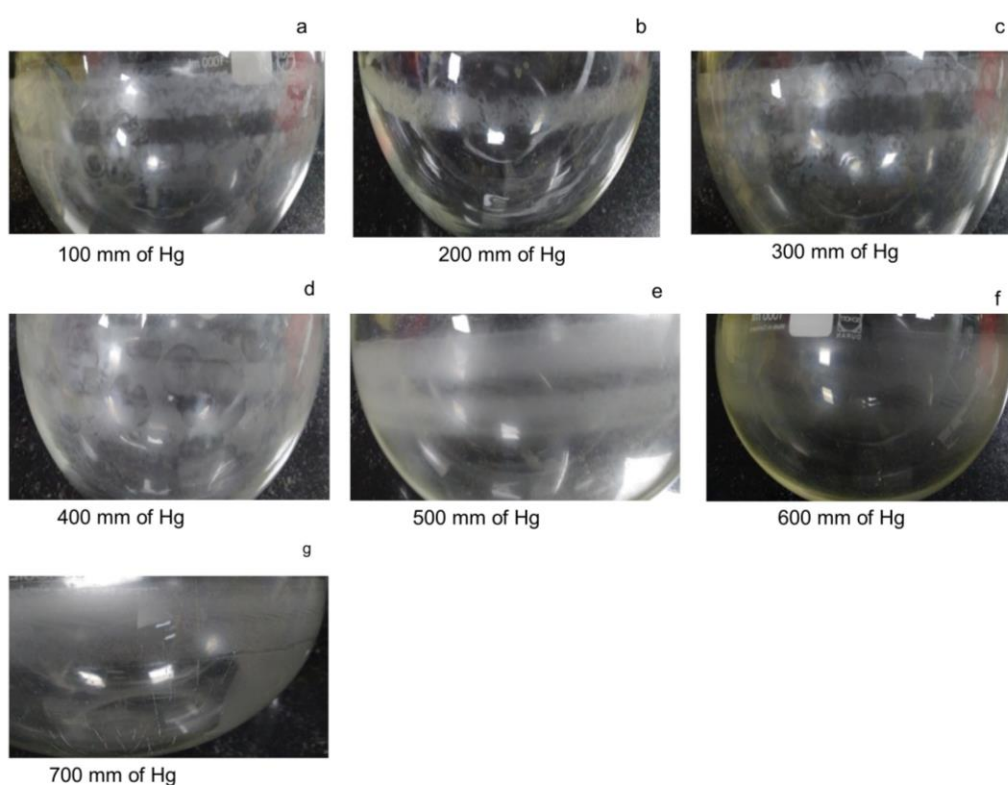
Figure 3.3 Effect of vacuum pressure on the lipid layer

3.3.1.3 Type of organic solvent

Chloroform and chloroform: methanol are the most widely used organic solvents for the synthesis of liposomes. Chloroform and 9:1 v/v ratio of chloroform: methanol constituted a uniform and thin lipid layer on the RBF walls that hydrated completely, but 2:1 v/v ratio of chloroform: methanol formed white crystals on the lipid layer that hydrated partially (Figure 3.4).

Chloroform as Organic
solvent

Chloroform: Methanol (2:1 v/v ratio)
as Organic solvent
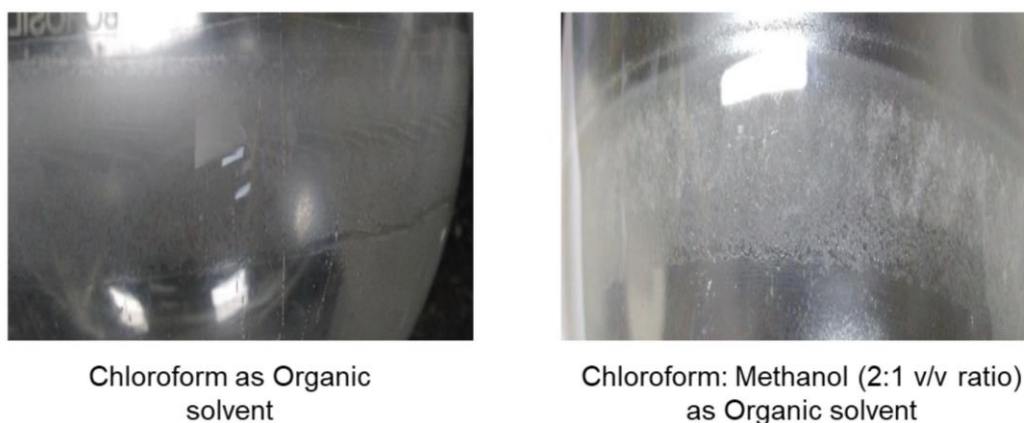
Figure 3.4 Effect of organic solvent on the lipid layer

The hydrodynamic diameter (ANOVA p value = 0.0275), PDI (ANOVA p value = 0.0096), and zeta potential (ANOVA p value = 0.0028) changed significantly with the change in the organic solvent -implying the relevance of organic solvent in affecting liposomal specifications. Chloroform as the organic solvent significantly reduced the hydrodynamic diameter (t-test p value = 0.0360 with chloroform: methanol 2:1 v/v ratio and p value = 0.0427 with chloroform: methanol 9:1 v/v ratio), PDI (t-test p value = 0.0149 with chloroform: methanol 2:1 v/v ratio) and zeta potential (t-test p value = 0.0087 with chloroform: methanol 2:1 v/v ratio and p value = 0.0006 with chloroform: methanol 9:1 v/v ratio) of liposomes (Table 3.4) (Figure 3.5).

CHOL formed crystals in the presence of methanol and incorporated poorly in the liposomes, resulting in variations in size, PDI, and zeta potential. Thus, it is advisable to use chloroform or a higher volume of chloroform with methanol. We optimized chloroform based on both the visual observations and liposomal specifications.

Table 3.4 Effect of organic solvent on the hydrodynamic diameter, PDI, and zeta potential of liposomes

Organic solvent	Average Hydrodynamic Diameter (nm)	Average PDI	Average Zeta Potential (mV)
Chloroform	212.86 ± 21.69	0.34 ± 0.07	-24.84 ± 0.68
Chloroform: Methanol (2:1)	409.54 ± 107.46	0.53 ± 0.03	-18.04 ± 2.36
Chloroform: Methanol (9:1)	277.87 ± 31.68	0.44 ± 0.03	-19.26 ± 0.69
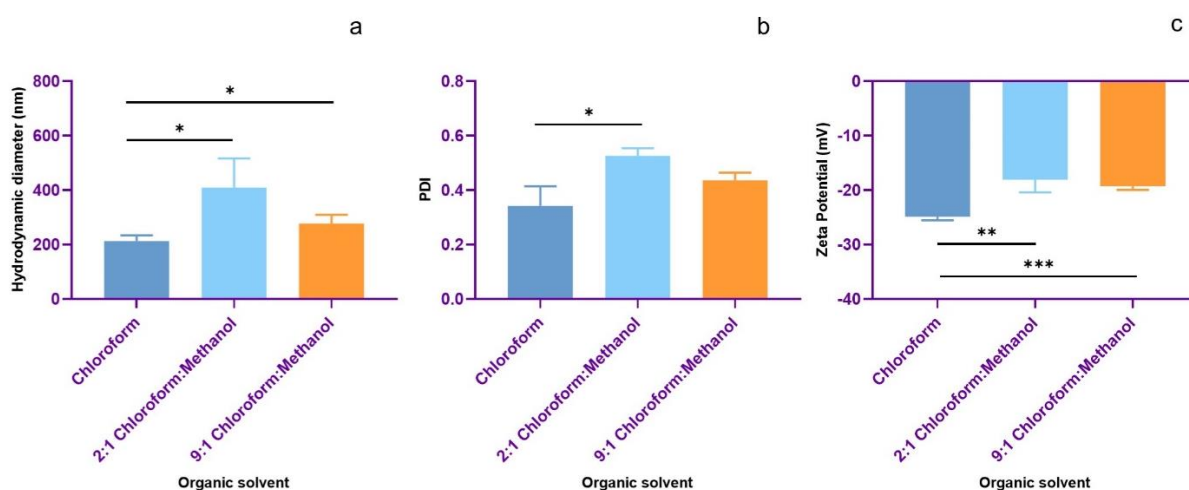
Figure 3.5 Effect of Organic solvent on hydrodynamic diameter (a), PDI (b), and zeta potential (c) on the lipid layer

3.3.1.4 Volume of organic solvent

The volume of chloroform created visual disparities in the lipid layer (Table 3.5): 2 ml chloroform constructed a uniform and thin layer that hydrated completely and generated a highly turbid liposomal suspension; 5 and 10 ml chloroform constituted a broad layer from the walls to the base of RBF that hydrated partially and produced a less turbid liposomal suspension. We optimized 2 ml chloroform to create a thin lipid lipid in the thin film formation step.

Table 3.5 Effect of volume of chloroform on the lipid layer

Volume of Organic solvent (ml)	Nature of the lipid layer	Turbidity upon Hydration	Layer after hydration
2	Uniform and thin layer on the RBF wall	Highly turbid	The majority of the lipid layer was hydrated
5 10	Broad layer on the RBF wall with encroachment to the base	Low turbidity	The majority of the layer attached to the RBF

3.3.1.5 Volume of RBF

We experimented with RBFs of varied volumes (500, 250, and 50 ml) and noted negligible changes in the nature of the lipid layer, level of hydration, and turbidity of the liposomal suspension; this resulted from the lower volume of chloroform optimized to create a thin and uniform lipid layer. With higher chloroform volumes, we noticed a thick, broad, and non-uniform layer in 50 ml RBFs and a broad and non-uniform layer in 250 and 500 ml RBFs that hydrated partially to yield a less turbid liposomal suspension.

A thin and uniform layer hydrates efficiently; thus, it is crucial to optimize factors impacting the lipid layer (Torchilin and Weissig, 2003). Particles obtained with a hydrodynamic diameter > 200 nm and PDI > 0.3 undergo downsizing, but we omitted the downsizing step to optimize liposomes with the lowest hydrodynamic diameter and PDI values.

3.3.2 Factors affecting the thin film hydration step

We investigated the thin film hydration step on the grounds of rotation speed, hydrating medium, and hydration time.

3.3.2.1 Rotation speed

Unlike the thin film formation step that influenced the nature of the lipid layer, the hydration step controlled the particle specifications. We noted a gradual and significant decrease in the hydrodynamic diameter (ANOVA p-value = < 0.0001) from 587.72 ± 32.69 to 212.86 ± 21.69 nm (Table 3.6) on increasing the rotation speed from 30 to 270 RPM -deeming this parameter

relevant in modulating particle specifications. The hydrodynamic diameter at 270 RPM was significantly lower than 30 (t-test p value = <0.0001), 60 (t-test p value = 0.0003), and 120 RPM (t-test p value = 0.0021).

Reduced speeds produced a heterogeneous population (PDI values > 0.3), and the polydispersity significantly decreased (ANOVA p-value = 0.0029) at higher rotation speeds; PDI at 270 RPM depreciated significantly than 30 (t-test p value = 0.0055), 60 (t-test p value = 0.0058) and 120 RPM (t-test p value = 0.0441).

The zeta potential defined the particles with moderate stability, but we observed a significant increase in the absolute zeta potential values for liposomes synthesized at 270 RPM than 30 (t-test p value = 0.0090) and 60 RPM (t-test p value = 0.0310). The elevated zeta potential values correspond to the insufficient hydration of the layers at 30 and 60 RPM, resulting in a diluted liposomal suspension. We optimized 270 RPM rotation speed based on the lowest hydrodynamic diameter and PDI.

Table 3.6 Effect of rotation speed on hydrodynamic diameter, PDI, and zeta potential of liposomes in the thin film hydration step

Rotation speed (RPM)	Average Hydrodynamic Diameter (nm)	Average PDI	Average Zeta potential (mV)
30	587.72±32.69	0.57±0.01	-22.89±0.23
60	588.99±51.84	0.9±0.16	-22.62±1.19
120	354.83±26.96	0.69±0.19	-24.96±0.75
240	282.07±80.22	0.47±0.1	-23.79±0.49
270	212.86±21.69	0.34±0.07	-24.84±0.67
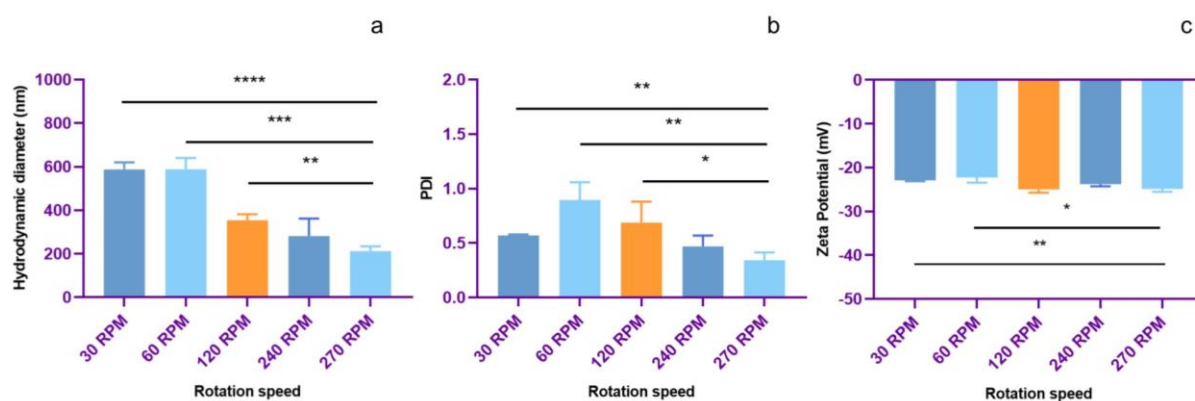
Figure 3.6 Effect of rotation speed on hydrodynamic diameter (a), PDI (b), and zeta potential (c) of liposomes in the thin film hydration step

Phospholipids fashion sheets in an aqueous solvent that enclose to reduce the energy gap between the hydrophobic and hydrophilic phases, and maintain a thermodynamic equilibrium; these spherical structures have higher stability due to low surface tension (Yadav et al.,2017). Hydrophobic interactions form liposomes; van der Waals forces strengthen the bilayer; hydrogen bonds and polar interactions between the aqueous solvent and lipid polar head groups stabilize the particles (Bozzuto and Molinari, 2015).

During hydration with an aqueous solvent, the outer lipid layers swell, and the solvent leaks into the subsequent inner layers that swell; vigorous agitation allows bilayer structures to form and suspend in the aqueous solvent (Lasic, 1988). The intensity of agitation influences the particle size; intense and vigorous hydration (higher rotation speeds) forms a smaller and homogenous population, as also corroborated in our study (Bellare, 1995).

3.3.2.2 Hydrating medium

We observed the impact of the hydrating solvent on liposomes: PBS hydrated the lipid layers completely in 1 h and formed a turbid liposomal suspension; deionized and doubled distilled water hydrated the lipid layers in 2 h to achieve equivalent turbidity and hydration -different molar ratios of lipids could be hydrated in lesser time.

The hydrodynamic diameter (ANOVA p value = 0.0027), PDI (ANOVA p value = 0.0241), and zeta potential (ANOVA p value = <0.0001) altered significantly on changing the hydrating medium. Liposomes in PBS were significantly smaller than in deionized water (t-test p value = 0.0160) and double distilled water (t-test p value = 0.0001) (Table 3.7). The PDI values also significantly lowered in PBS from deionized water (t-test p value = 0.0328) and double distilled water (t-test p value = 0.0150) (Figure 3.7).

PBS imparted moderate stability to the liposomes with a zeta potential of - 24.84 ± 0.68 mV and deionized, and double distilled water conferred excellent stability to the liposomes with a zeta potential of - 65.16 ± 3.57 (t-test p value = <0.0001) and - 59.77 ± 2.24 mV (t-test p value = <0.0001) respectively. This discrepancy corresponds to salts in PBS that lower the negative zeta potential (Sarkar and Bose, 2019). Despite moderate stability, we optimized PBS based on the reduced particle size and PDI values; PBS is also widely used because its ionic and osmotic potential is analogous to human blood. However, PEG provides stearic stability to stealth liposomes that overpowers this reduced electrical stability in PBS (Marjan and Allen, 1996).

Table 3.7 Effect of hydrating medium on the hydrodynamic diameter, PDI, and zeta potential of liposomes in the thin film hydration step

Rotation speed (RPM)	Average Hydrodynamic Diameter (nm)	Average PDI	Average Zeta Potential (mV)
PBS	212.86 ± 21.69	0.34 ± 0.07	-24.84 ± 0.68
Deionized water	416.8 ± 85.42	0.77 ± 0.22	-65.16 ± 3.57
Double distilled water	451.91 ± 19.07	0.91 ± 0.23	-59.77 ± 2.24
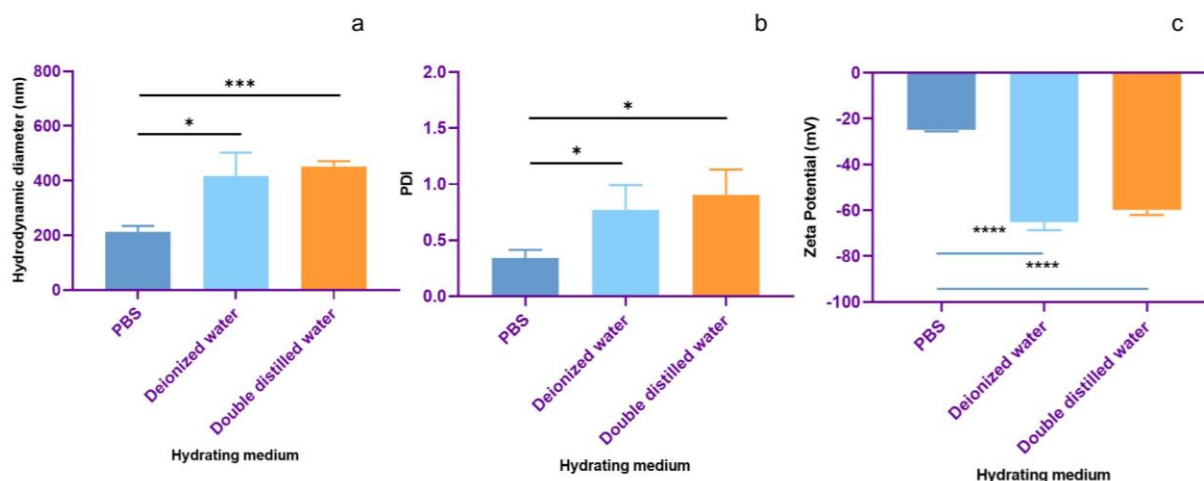
Figure 3.7 Effect of hydrating medium on the hydrodynamic diameter (a), PDI (b), and zeta potential (c) of the liposomes in the thin film hydration step

3.3.2.3 Hydration time

Hydration time notably varied the hydration levels and influenced the particle specifications: PBS partially hydrated the lipid layers under 15 and 30 min and produced non-turbid and

slightly turbid suspensions, respectively, but completely hydrated the lipid layers in 60 and 120 min and generated highly turbid suspension (Table 3.8).

Table 3.8 Effect of hydration time on the lipid layer and liposomal suspension

Hydration time (min)	Turbidity after hydration	Thin layer after hydration
15	Non-turbid suspension	The majority layer attached
30	Slightly turbid suspension	to the RBF
60	Highly turbid suspension	Majority layer hydrated
120		

The hydrodynamic diameter (ANOVA p value = 0.0437) and PDI (ANOVA p value = 0.0006) changed significantly on increasing the hydration time. The hydrodynamic diameter markedly reduced after 60 min compared to 15 min (t-test p-value = 0.0297), but remained unchanged after 30, 60, and 120 min. The PDI values diminished significantly after 60 min than 15 (t-test p value = 0.0077) and 30 min (t-test p value = 0.0376) (Table 3.9) (Figure 3.8), and the values remained unaltered for 60 and 120 min. The zeta potential characterized particles with moderate stability, and the unchanged values correspond to PBS.

The outer lipid layers impartially hydrate and swell in 15 and 30 min, hindering the solvent from breaching and percolating in the inner layers, culminating in a non-turbid or slightly turbid liposomal suspension, respectively. But the lipid layers entirely hydrated in 60 and 120 min producing a turbid liposomal suspension.

We optimized 60 min hydration time for plain liposomes based on the hydrodynamic diameter, PDI, level of hydration, and turbidity of the liposomal suspension. Hydration time should be sufficient to ensure complete hydration to constitute a smaller and homogenous liposomal suspension.

Table 3.9 Effect of hydration time on hydrodynamic diameter, PDI, and zeta potential of the liposomes in the thin film hydration step

Hydration time (min)	Average Hydrodynamic Diameter (nm)	Average PDI	Average Zeta Potential (mV)
15	326.59 ± 47.83	0.52 ± 0.02	-25.56 ± 1.49
30	272.66 ± 27.13	0.45 ± 0.03	-25.64 ± 1.22
60	232.94 ± 10.69	0.34 ± 0.06	-24.71 ± 2.03
120	238.42 ± 44.93	0.29 ± 0.05	-23.9 ± 1.74
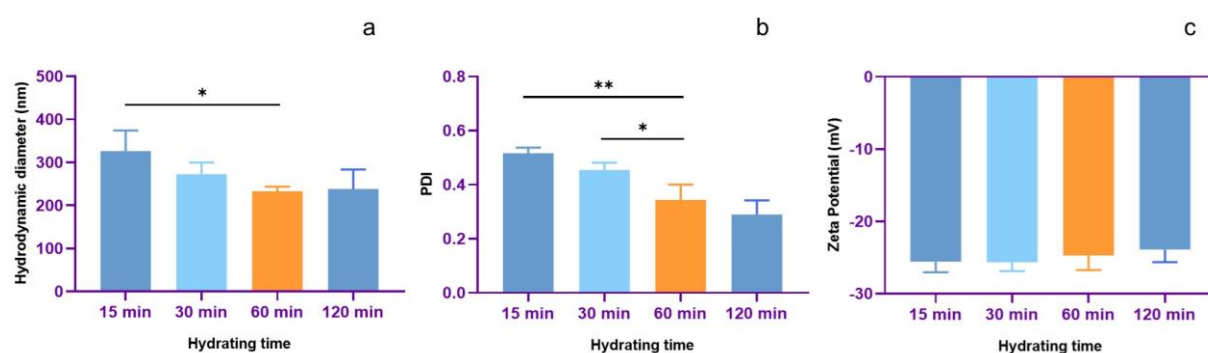
Figure 3.8 Effect of hydration time on hydrodynamic diameter (a), PDI (b), and zeta potential (c) of the liposomes in the thin film hydration step

Hydration speed determines the particle size and size distribution; different hydrating mediums impart varying levels of stability to the particles; hydration time affects the level of hydration, size, and PDI of the particles. Thus, optimizing the process parameters of the thin film hydration step is essential to control the particle specifications.

3.3.3 Factors affecting the downsizing step

Liposomes synthesized after the hydration step are unfit for drug delivery as the hydrodynamic diameter is > 200 nm and PDI > 0.3, and require downsizing by probe sonication, water bath sonication, or extrusion (Large et al., 2021). Probe sonication reduces the particle size but leaches titanium requiring an additional filtration step, and elevates the temperature adversely affecting the integrity of the liposomes (Ghatage et al., 2017). Water bath sonication decreases the particle sizes but generates a heterogeneous population -with high PDI values (Torchilin and Weissig, 2003). Extrusion significantly lowers the size and PDI, is reproducible, can be rapidly executed, and is gentler on the liposomes as compared to other techniques (Gim et al.,

2016). We sonicated the liposomes in a water bath before extrusion to downsize the particles in our study.

We optimized the extrusion process by varying the number of extrusion passes and the number of polycarbonate membranes. The hydrodynamic diameter significantly reduced from 161.69 ± 8.85 to 133.16 ± 8.07 nm (p-value = 0.02) for single and 163.43 ± 16.18 to 127.64 ± 3.62 nm (p-value = 0.02) for double polycarbonate membranes (Table 3.10) on increasing the extrusion passes from 1 to 20; the PDI values reduced significantly from 0.16 ± 0.02 to 0.06 ± 0.01 (p-value = 0.001) for single and 0.12 ± 0.02 to 0.06 ± 0.01 (p-value = 0.01) for double polycarbonate membranes on increasing the extrusion passes from 1 to 20. But, the size and PDI remained unchanged from 10 to 20 extrusion passes. We observed that increasing the number of polycarbonate membranes to 2 and the extrusion passes to 20 was unnecessary for size reduction (Figure 3.9) (Figure 3.10).

Our data confirms instances from the literature of synthesizing particles greater than 100 nm even after extrusion through 100 nm polycarbonate membranes (Gim et al., 2016). We optimized the process parameters that synthesized comparatively smaller liposomes just after the hydration step that effectively downsized through a 100 nm polycarbonate membrane; but with unoptimized process parameters, the thin film hydration technique synthesizes MLVs/LUVs that require a series of polycarbonate membranes of varied pore sizes for downsizing.

Table 3.10 Effect of extrusion passes and number of polycarbonate membranes on the hydrodynamic diameter and PDI of liposomes in the downsizing step

Extrusion passes	Polycarbonate membrane	Average Hydrodynamic diameter (nm)	Average PDI
1	1	161.69 ± 8.85	0.16 ± 0.02
5		148.21 ± 11.61	0.09 ± 0.01
10		133.94 ± 3.73	0.06 ± 0.01
20		133.16 ± 8.07	0.06 ± 0.01
1	2	163.43 ± 16.18	0.12 ± 0.02
5		137.76 ± 5.26	0.06 ± 0.01
10		137.78 ± 5.41	0.06 ± 0.02
20		127.64 ± 3.62	0.06 ± 0.01

Figure 3.9 Hydrodynamic diameter and PDI of liposomes on extruding the liposomes 1, 5, 10, and 20 times for a single polycarbonate membrane (a) and double polycarbonate membranes (b)
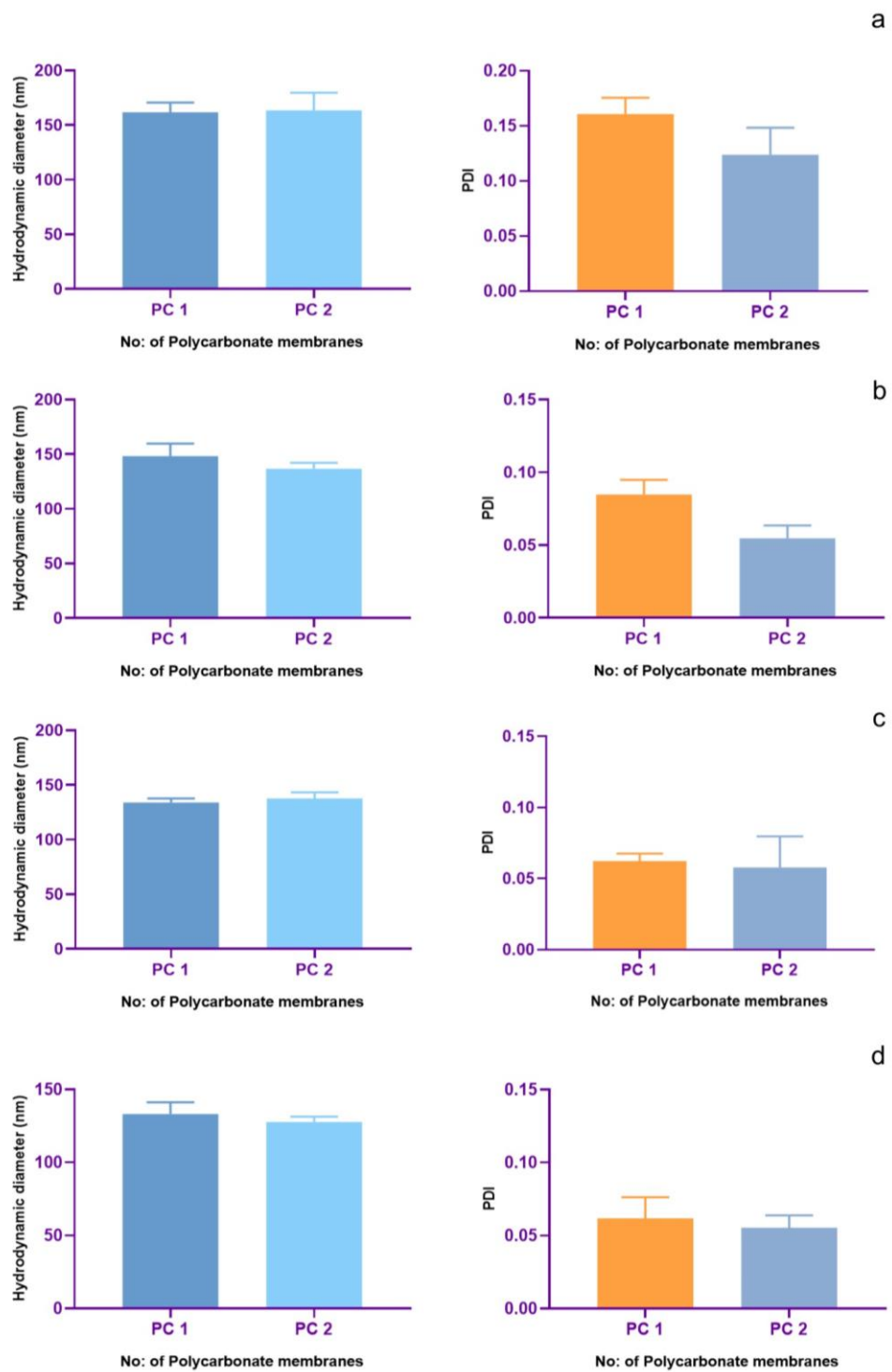
Figure 3.10 Hydrodynamic diameter and PDI of liposomes using 1 and 2 polycarbonate membranes and extruding for 1 (a), 5 (b), 11 (c), and 21 (d) extrusion passes

3.3.4 Effect of Intrinsic factors

Intrinsic factors include concentrations and molar ratios of lipids.

3.3.4.1 Lipid concentration

We investigated the process parameters using a 1:1 molar ratio of PC: CHOL with a 10 mg/ ml concentration of each lipid and 20 mg of total lipids. Upon varying the lipid concentration (10, 20, and 30 mg/ml), we observed disparity in the nature of the lipid layer and its hydration: 10 mg/ml concentration of lipids (amounting to 20 mg of total lipids) created a thin and uniform lipid layer on the RBF walls that hydrated readily within 1 h; but 20 and 30 mg/ ml of lipids (amounting to 40 and 60 mg of total lipids respectively) developed a thick lipid layer that partially hydrated in 1 h. Thus, higher lipid concentrations form thicker layers that hydrate incompletely.

3.3.4.2 Molar ratio of PC: CHOL

We modulated the PC: CHOL ratio (1:1, 3:2, 7:3, 4:1, 9:1, and 1:0) by reducing CHOL concentration from 50 % and equivalently increasing the PC concentration (Gregory Gregoriadis, 2010). The hydrodynamic diameter changed significantly (ANOVA p value = <0.0001) by depreciating the particle size on reducing CHOL concentration from 50 to 30% (t-test p value = 0.0109) and 30 to 0% (t-test p-value = 0.0384) (Figure 3.11) (Table 3.11). The effective downsizing generated a monodisperse (PDI < 0.3) population for all the molar ratios of lipids.

Lower CHOL concentrations (4:1 and 9:1) impart flexibility and induce fragility in the bilayers, decreasing the particle size; higher CHOL concentrations (1: 1 and 3:2) provide rigidity to the bilayers, increasing the particle size (Zarrabi et al., 2021). 7: 3 molar ratio of PC: CHOL characterized the liposomes with optimum size, PDI, and appropriate CHOL concentration for drug delivery. These outcomes coincide with previously reported studies (Briuglia and Rotella, 2015).

Table 3.11 Effect of PC: CHOL molar ratio on the hydrodynamic diameter and PDI of liposomes

Molar ratio of PC: CHOL	Average Hydrodynamic Diameter (nm)	Average PDI
1:1	149.67 ± 2.4	0.07 ± 0.01
3:2	145.16 ± 1.67	0.06 ± 0.02
7:3	129.57 ± 7.36	0.06 ± 0.03
4:1	122.62 ± 6.8	0.07 ± 0.02
9:1	120.19 ± 4.04	0.07 ± 0.01
1:0	113.6 ± 5.34	0.08 ± 0.001
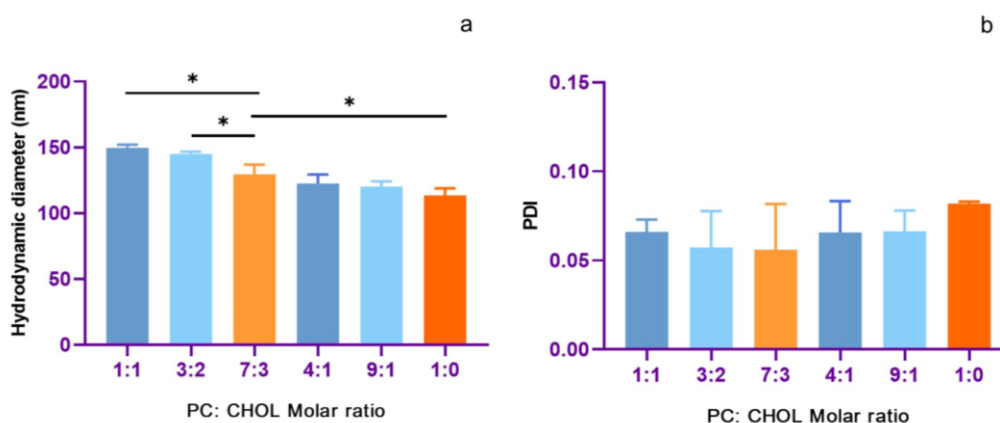
Figure 3.11 Effect of PC: CHOL molar ratio on the hydrodynamic diameter and PDI of liposomes

3.3.4.3 Concentration of DSPE-mPEG2000

We optimized the PEGylated liposomes by varying the concentration of DSPE-mPEG2000 (1, 3, and 5 mole % with respect to lipids). During synthesis, DSPE-mPEG2000 positions in either leaflet of the bilayer and can project outwards from the liposomal surface and into the internal aqueous core.

The hydrodynamic diameter (ANOVA p value = <0.0001) and PDI (ANOVA p value = 0.0310) changed significantly with unaltered zeta potential values. The particle size (t-test p-value = 0.0009 with 5 mole %) and PDI (t-test p value = 0.0391 with 3% and p value = 0.0053 with 5 mole %) reduced significantly (Figure 3.12) for 5 mole % DSPE-mPEG2000. The PDI values suggest monodispersity, and the zeta potential values changed to -7.55 ± 0.53, -5.02 ± 4.04,

and -6.63 ± 0.13 mV (neutral range) for 1, 3, and 5 mole % of DSPE-mPEG2000 respectively (Table 3.12).

Table 3.12 Effect of DSPE-mPEG2000 concentration on hydrodynamic diameter, PDI, and zeta potential of liposomes

DSPE-mPEG2000 (mole %)	Average Hydrodynamic Diameter (nm)	Average PDI	Average Zeta Potential (mV)
1	119.94±1.23	0.1±0.002	-7.55±0.53
3	118.03±1.19	0.07±0.02	-5.02±4.04
5	103.71±2.92	0.08±0.004	-6.63±0.13
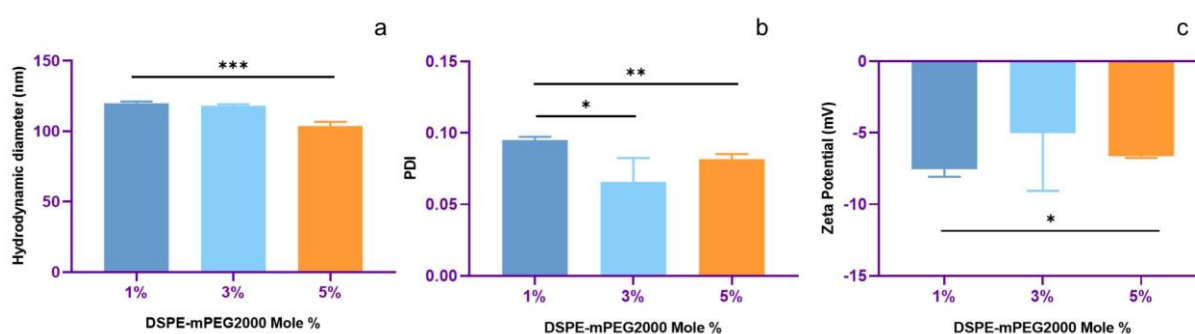
Figure 3.12 Effect of DSPE-mPEG2000 concentration on hydrodynamic diameter (a), PDI (b), and zeta potential (c) of liposomes

The optimization of the process and intrinsic parameters concludes: (a) high rotation speed (240 RPM), reduced vacuum pressure (700 mm of Hg), and less volume (2 ml) of chloroform as the organic solvent create a thin and uniform lipid layer; (b) high rotation speed during hydration (270 RPM) yields smaller particles, the hydrating medium governs the particle size and stability of the particles (PBS was optimized in our study), and the hydration time (1 h optimized) is crucial for complete hydration; (c) Extrusion through a 100 nm polycarbonate membrane with 10 passes effectively downsized the liposomes; (d) 10 mg/ml of lipids formed the most uniform layer, and 7:3 molar ratio of the PC: CHOL and 1 mole % of DSPE-mPEG2000 formulated liposomes with desired specifications. Liposomes formed with these optimized values were further characterized.

3.4 Characterization of liposomes

3.4.1 Hydrodynamic diameter, PDI, and zeta potential

The DLS graph recorded the hydrodynamic diameter and PDI for liposomes after hydration at 221.7 nm and 0.32, respectively, for liposomes after extrusion at 135.1 nm and 0.08, respectively, and for PEGylated liposomes at 133 nm and 0.07, respectively (Figure 3.13). A high-intensity peak at 244.3 nm and a low-intensity peak at 4205 nm for liposomes after hydration, and single sharp peaks for liposomes after extrusion (non-PEGylated and PEGylated) confirm the size and PDI disparity of the two formulations.

The zeta potential of -24.84 ± 0.67 mV characterizes the liposomes with moderate stability; PC, a neutral lipid, orients its choline head to project the phosphate groups from the bilayer towards the external aqueous environment to provide a negative zeta potential, that is also facilitated by CHOL (Fahmy, 2019) (Pamunuwa et al., 2016). The significant shift in zeta potential for the PEGylated liposomes to -8.36 ± 0.99 mV confirms the surface functionalization with PEG that shields and reduces the negative charge of PC –as also corroborated by other studies (Hardiansyah et al., 2017) (Dhule et al., 2014). The data highlights the substantial role of optimizing the process parameters to synthesize smaller liposomes just after the hydration step and the significance of downsizing to create a monodisperse population of smaller liposomes.
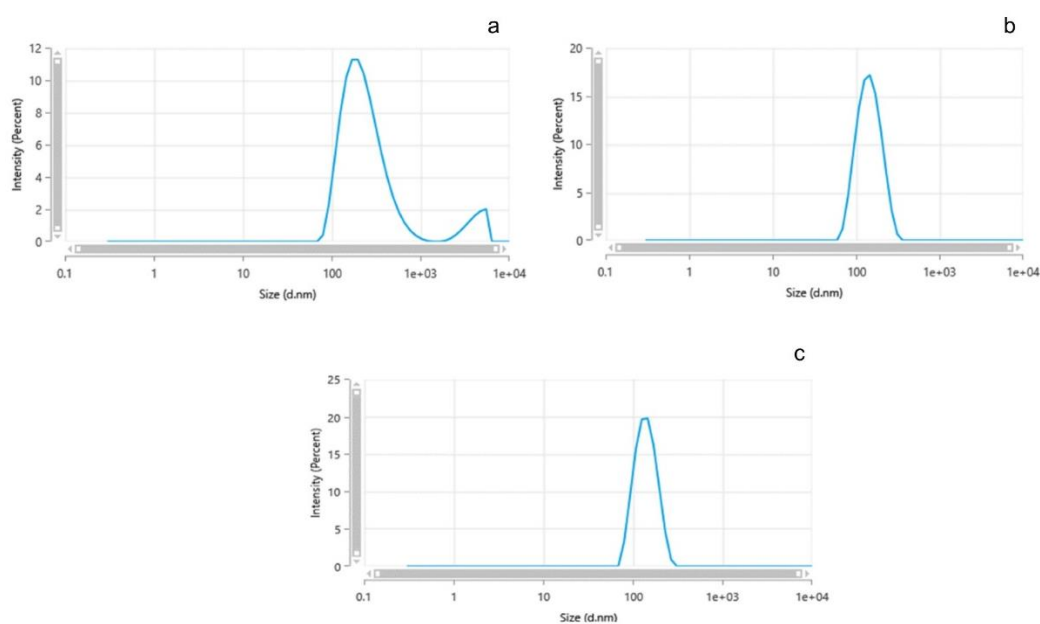
Figure 3.13 DLS graph for liposomes after hydration (a), after extrusion (b), and PEGylated liposomes (c)

Plain liposomes and PEGylated liposomes exhibited an insignificant change in the hydrodynamic diameter and PDI, but the absolute value of zeta potential changed significantly after PEGylating the liposomes (t-test p value = <0.0001) (Figure 3.14).
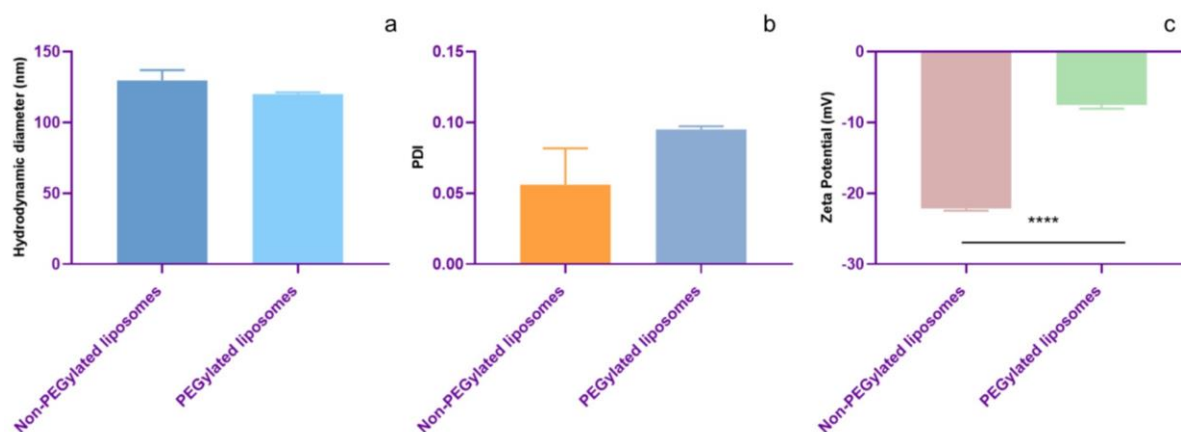
Figure 3.14 Comparison of hydrodynamic diameter (a), PDI (b), and zeta potential (c) of plain and PEGylated liposomes

3.4.2 Morphology of liposomes

The HRTEM images at 100 (Figure 3.15a) and 20 nm (Figure 3.15b) magnification show particles with spherical morphology and smooth surfaces. Certain oval and irregular structures accompany these spherical particles as the membrane reorganizes or deforms during the dehydration step of sample preparation (Chen et al., 2012). Particles might clump after casting the sample drop on the copper grid and air drying. A disparity in the image clarity in Figure 3.15c arises as it depicts samples diluted in PBS compared to the others in deionized water.
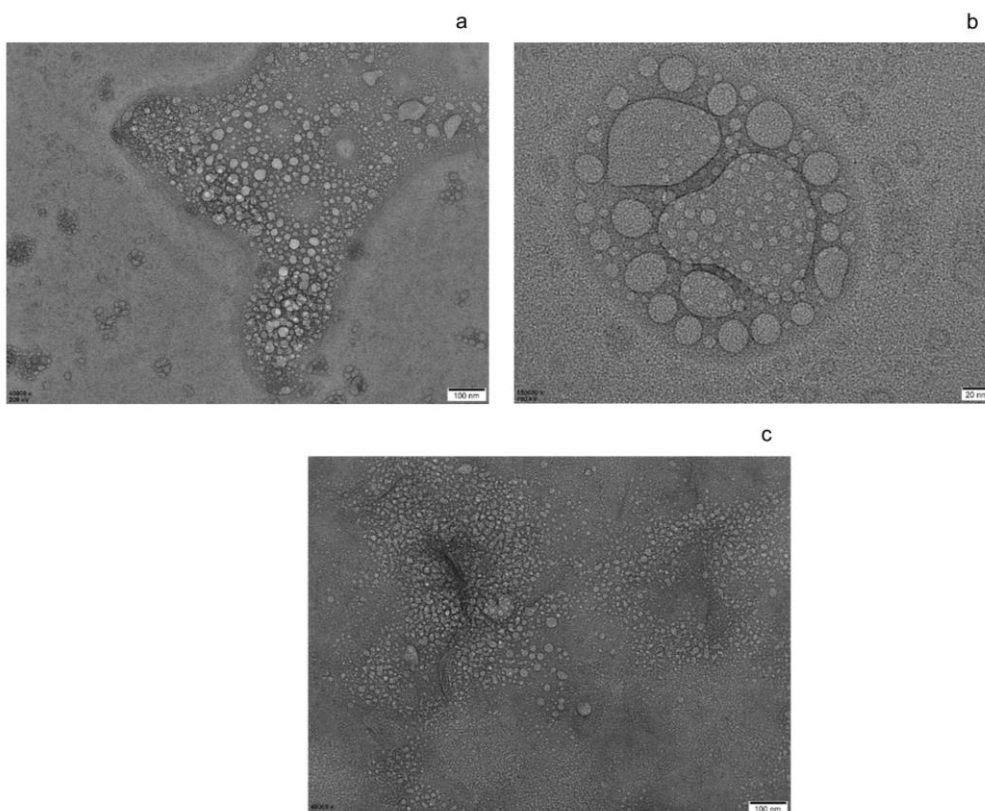
Figure 3.15 HRTEM images of liposomes in deionized water at 100 nm magnification (a), 20 nm magnification (b), and in PBS at 100 nm magnification (c)

Liposomes are dynamic structures that require an aqueous environment to persist, which is a major restraint while imaging with conventional electron microscopy techniques. The sample preparation method involves drying, staining, and fixation of liposomes that result in vesicle reorganization (Almgren et al., 2000). CryoTEM imaging overcomes these drawbacks by imaging the particles in their native environment; thus, it is suitable for liposome's sensitive and dynamic nature.

3.4.3 FTIR analysis

The FTIR spectral profiles (Figure 3.16) present the characteristic peaks of PC, CHOL, DSPE-mPEG2000, liposomes after hydration and extrusion, and PEGylated liposomes after hydration and extrusion. PC shows a broad peak at 3300 cm^{-1} corresponding to the OH stretching vibration; peaks at 2922 and 2853 cm^{-1} correspond to the antisymmetric and symmetric CH stretching vibrations, respectively; a prominent peak at 1736 cm^{-1} is for the C =O (ester) stretching vibration, at 1651 cm^{-1} for C=C stretching vibration, and at 1463 and 1377 cm^{-1} for CH$_2$ and CH$_3$ bending vibrations. The peaks for the head group appear at 1225 and 1057 cm^{-1}

for the PO_2^- antisymmetric and symmetric stretching vibrations, respectively. The peak at 829 cm^{-1} corresponds to the P-O stretching vibration (Aisha et al., 2014) (Li et al., 2020).

Characteristic peaks for CHOL appear at 2935, 2896, and 2859 cm^{-1} for the CH stretching vibration in methyl and cyclic hydrocarbons; peaks at 1461 and 1371 cm^{-1} correspond to CH bending and CH_2 and CH_3 bending vibrations, respectively (Li et al., 2020). The characteristic peaks for DSPE-mPEG2000 appear at 2916, 2885, 1736, 1467, 1240, and 1060 cm^{-1} for antisymmetric and symmetric CH stretching, C =O (ester) stretching, CH_2 bending, PO_2^- antisymmetric, and symmetric stretching, respectively (Haghiralsadat et al., 2017).

We compared the FTIR spectral profiles for liposomes after hydration and extrusion with PC (Figure 3.16b): a broad peak at approximately 3368 cm^{-1} corresponds to the OH stretching vibration; the peaks for the CH antisymmetric and symmetric stretching vibrations slightly shifted to 2924 and 2856 cm^{-1} respectively; the peak for C =O (ester) stretching vibration appear at 1736 cm^{-1}; the peaks for C=C stretching, CH_2 bending, and CH_3 bending vibration shifted to 1652, 1459 and 1372 cm^{-1} respectively. The peaks for the head group region shifted to 1229 cm^{-1} for PO_2^- antisymmetric vibration and 1060 and 1061 cm^{-1} for the symmetric stretching vibrations of liposomes after hydration and extrusion, respectively. The peak for P-O stretching shifted to 839 and 842 cm^{-1} for liposomes after hydration and extrusion (Istenič et al., 2016).

For PEGylated liposomes after hydration and extrusion (Figure 4c), a broad peak appears at approximately 3360 cm^{-1} representing the OH stretching vibration; the peaks for CH antisymmetric and symmetric stretching vibrations shifted to 2924 and 2856 cm^{-1} respectively; C =O (ester) stretching and C =C stretching vibration appear at 1736 and 1651 cm^{-1} respectively; the peaks corresponding to CH_2 bending vibrations shifted to 1459 and 1460 cm^{-1} formulation after hydration and after extrusion respectively; the peak for CH_3 bending vibration shifted to 1372 cm^{-1}. The PO_2^- antisymmetric and symmetric stretching vibrations shifted to 1228 and 1060 cm^{-1}, respectively, for the PEGylated liposomes after hydration and at 1228 and 1061 cm^{-1} respectively for PEGylated liposomes after extrusion. The peak for P-O stretching shifted to 842 and 859 cm^{-1} for liposomes after hydration and extrusion.

The spectral profiles of liposomes after hydration and after extrusion remain unchanged, and for the non-PEGylated and PEGylated liposomes. But, the shift in the hydrocarbon chain region and the head group region in the liposomes suggests the arrangement of the phospholipids to form bilayers after the incorporation of CHOL.
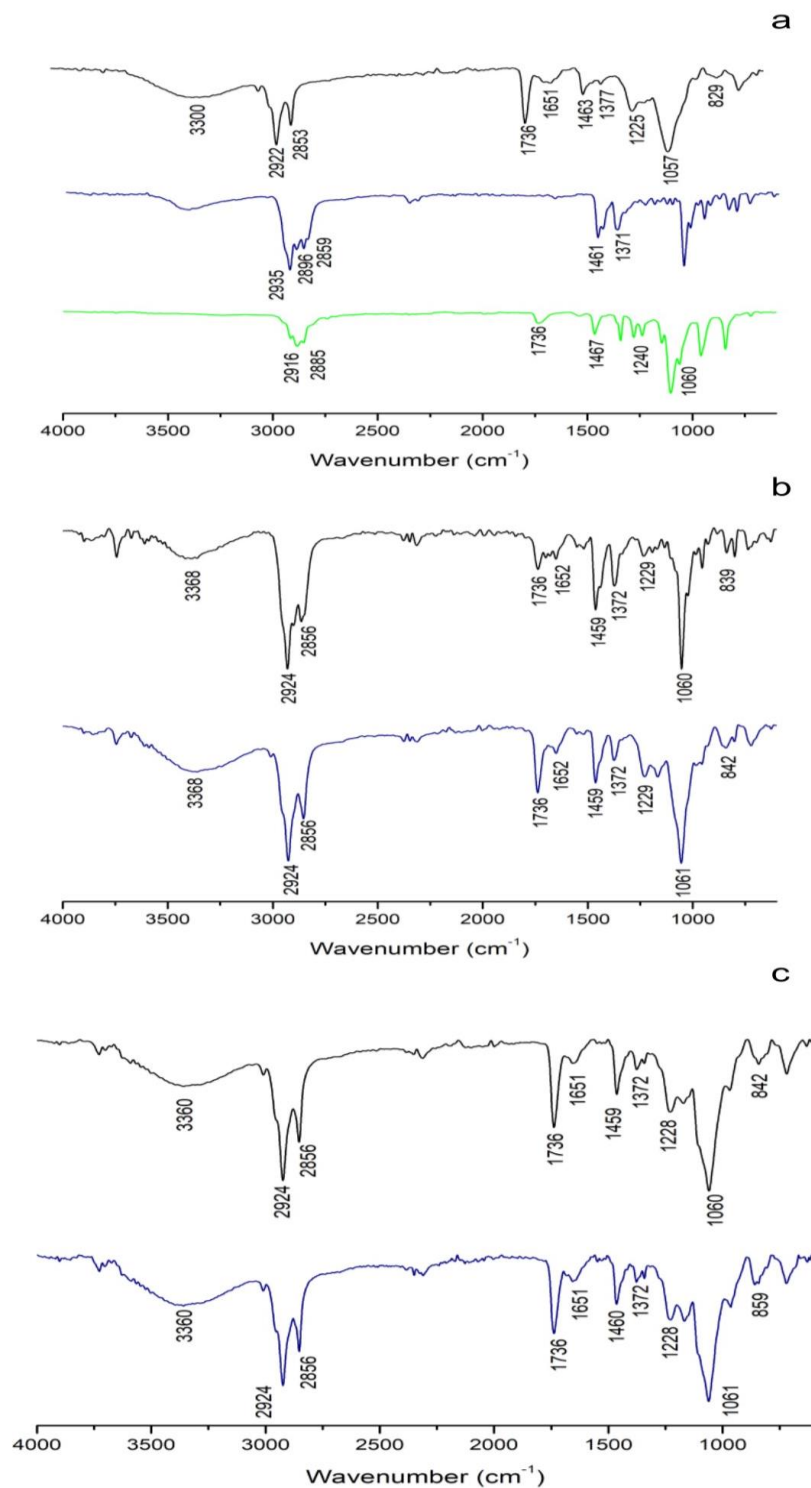
Figure 3.16 FTIR spectral profiles for PC (black), CHOL (blue), and DSPE-mPEG2000 (green) (a); hydrated liposomes (black) and extruded liposomes (blue) (b); hydrated PEGylated liposomes (black) and extruded PEGylated liposomes (blue) (c)

3.4.4 TGA analysis

TGA determines any chemical or physical fluctuations with respect to temperature. The TGA thermogram (Figure 3.17) exhibits the degradation onset temperature of PC at 182.46 °C (78.4% degradation), of CHOL at 249.76 °C (99.98% degradation), and of DSPE-mPEG2000 at 320.91 °C (98.92% degradation).

The degradation onset temperature increased to 240.78 °C (54.81% degradation) for non-PEGylated liposomes and 248.53 °C (56.55% degradation) for PEGylated liposomes compared to PC. This discrepancy in the thermal stability and degradation pattern of liposomes and the raw materials corresponds to liposomes held together with strong interactions. The results indicate that the bilayer structures are more stable than their components.
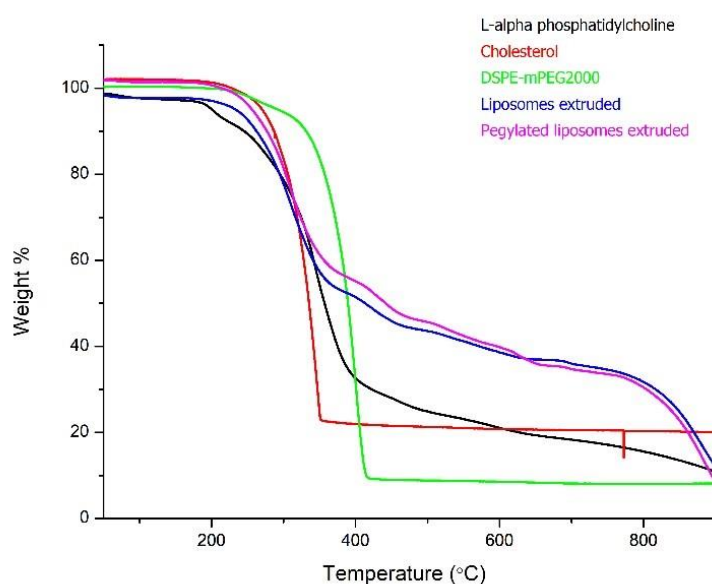
Figure 3.17 TGA thermogram of PC (black), CHOL (red), DSPE-mPEG2000 (green), non-PEGylated liposomes (blue), and PEGylated liposomes (magenta)

3.4.5 DSC analysis

The DSC thermogram displays an endotherm at 136.7 °C for PC and 151.59 °C for CHOL (Figure 3.18) (Jangde and Singh, 2016). The melting endotherm for non-PEGylayed liposomes shifted to 121.13 °C - concurred with previously reported results (Patel et al., 2009)- as the strong interactions severed in the bilayer structure (Niu et al., 2012).

DSPE-mPEG2000 exhibits an endotherm at 56.96 °C, and for PEGylated liposomes at 116.68 °C that verifies the strong bonds to form bilayer structures; the endotherm for DSPE-mPEG2000 disappears that substantiates successful functionalization of liposomes.
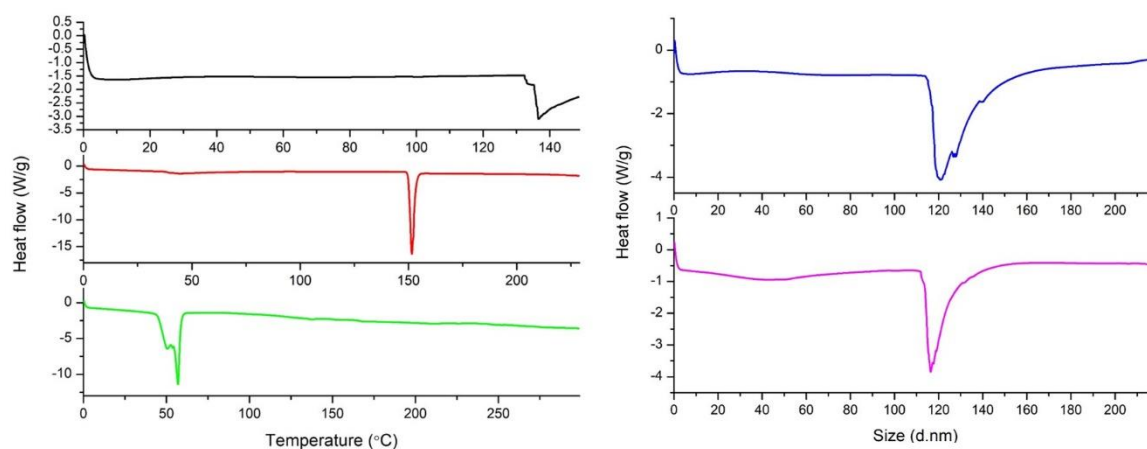
Figure 3.18 DSC thermogram of PC (black), CHOL (red), DSPE-mPEG2000 (green), non-PEGylated liposomes (blue), and PEGylated liposomes (magenta)

3.5 Conclusion

Liposomes were widely synthesized by the thin film hydration technique, and this study identifies and optimizes process parameters and intrinsic factors to synthesize liposomes for drug delivery. Higher rotation speed (240 RPM), reduced vacuum pressure (700 mm of Hg), and 2 ml chloroform in the thin film formation step created a thin and uniform lipid layer on the RBF walls that hydrated effectively and produced a highly turbid liposomal suspension. Higher rotation speed (270 RPM) in the hydration step synthesized smaller particles with low PDI, different hydrating mediums imparted varied levels of stability, and 1 h hydration time successfully hydrated the lipid layer to produce a monodisperse and smaller liposomal population. The downsizing parameters (extrusion passes and the number of polycarbonate membranes) significantly reduced the particle size. 10 mg/ml lipid concentrations created a thin and uniform lipid layer, a 7:3 molar ratio of PC: CHOL, and 1 mole % DSPE-mPEG2000 synthesized liposomes apt for drug delivery.

The analytical characterization techniques confirmed the synthesis of spherical particles with hydrodynamic diameter < 150 nm and PDI < 0.3; zeta potential values tagged the particles with moderate stability, and the decrease in the absolute negative zeta potential for PEGylated liposomes confirmed the successful functionalization by PEG; FTIR analysis corroborated the synthesis of liposomes; TGA and DSC analysis indicated high thermal stability; smaller

liposomes displayed higher storage stability than larger particles. Thus, this study facilitates the synthesis of liposomes for drug delivery or other applications by modulating the identified parameters to attain the desired specifications.

CHAPTER 4

Optimization, Synthesis, and Characterization of drug loaded liposomes

CHAPTER 4A

Optimization, Synthesis, and Characterization of CUR loaded liposomes

4.1A Introduction

CUR has a pleiotropic effect on cancer cells and acts as a chemosensitizer. The standard dose for the pharmacological activity of CUR is 8g/day, and studies report a dose of up to 10g/day that is non-toxic in humans (Ambreen *et al.*, 2020). The liposomal encapsulation of CUR increases its bioavailability by incorporating it in the lipid bilayer. CUR is a hydrophobic drug and attains a higher % EE by the passive loading mechanism. The biological activity of CUR is due to its polyphenols, conjugated double bonds, and hydroxy and methoxy groups.

We aspired to co-encapsulate CUR and DOX in a single liposomal particle to exploit the chemosensitizer behavior of CUR that would enhance the chemotherapeutic activity of DOX. During CUR loading, we optimized various parameters to formulate CUR loaded liposomes with size < 200 nm, PDI < 0.3, and the highest % EE for the drug. We simultaneously varied the CUR to lipid ratio (wt. / wt.) ratio with the PC: CHOL molar ratio to optimize particles with appropriate specifications with the highest % EE. In the downsizing step, we investigated the influence of sonication on reducing the particle size and PDI, as well as number of extrusion passes.

We optimized the concentration of DSPE-mPEG2000 and the number of extrusion passes while synthesizing PEGylated CUR liposomes. Liposomes with final optimized values were characterized by various analytical techniques: hydrodynamic diameter, PDI, and zeta potential by DLS; morphology by HRTEM; functional groups by FTIR; % EE and % DL; and thermal stability by TGA and DSC. This study allows us to examine the effects of different factors of drug loading while synthesizing liposomes.

4.2A Methods

4.2.1A Synthesis of CUR loaded liposomes

We synthesized CUR liposomes and PEGylated CUR liposomes by the protocol mentioned in Chapter 2, section 2.2.2 –via thin film hydration technique using PC, CHOL, and CUR loaded passively, and DSPE-mPEG2000 for PEGylated CUR liposomes. We varied the CUR: lipid (wt. / wt.) ratio, the PC: CHOL molar ratio, and the downsizing step to optimize a monodisperse population of small liposomes with a maximum % EE of CUR.

4.2.2A Optimization of CUR: lipid (wt. / wt.) ratio and PC: CHOL molar ratio

We varied CUR to lipid wt. / wt. ratios (1:10, 1:20, 1:30, 1:40, and 1:50) in tandem with PC: CHOL molar ratio (1:1, 3:2, 7:3, 4:1, and 9:1) to optimize CUR liposomes for apt size, PDI, and highest % EE.

4.2.3A Optimization of the downsizing step of CUR liposomes

We investigated the effect of sonication in the downsizing step and varied the number of extrusion passes (5 and 11) through a 100 nm polycarbonate membrane to achieve CUR liposomes fit for drug delivery.

4.2.4A Optimization of PEGylated CUR liposomes

We formulated PEGylated CUR liposomes with the optimized PC: CHOL molar ratio and CUR to lipid wt. / wt. ratio, and varied the DSPE-mPEG2000 concentrations (1, 3, and 5 mole % of lipids).

The downsizing step was optimized for the number of extrusion passes (5 and 11) through a 100 nm polycarbonate membrane.

4.2.5A Characterization of CUR loaded liposomes

We characterized the CUR loaded liposomes synthesized with the final optimized values for hydrodynamic diameter, PDI, and zeta potential by DLS, % EE for CUR concentration, % DL, morphology by HRTEM, functional groups by FTIR, and thermal stability by TGA and DSC.

4.3A Results and Discussion

We optimized the parameters to formulate particles in ~50-200 nm size range and PDI ≤ 0.3 (as per the drug delivery mandates) with maximum % EE for CUR.

4.3.1A Optimization of CUR: lipid (wt. / wt.) ratio and PC: CHOL molar ratio

We encapsulated CUR by the passive loading technique, a routinely practiced approach to achieve a high % EE of hydrophobic drugs. CUR, a hydrophobic drug, positions in the lipid bilayer; thus, the lipid concentration influences the concentration of the incorporated drug.

4.3.1.1A Effect on Hydrodynamic Diameter

The hydrodynamic diameter of all CUR liposomes was < 150 nm and suitable for drug delivery application (Table 4.1A).

Table 4.1A Average hydrodynamic diameter of CUR liposomes for different PC: CHOL molar ratio and CUR to lipid wt. /wt. ratio

CUR /lipid (wt. /wt.)	1:10	1:20	1:30	1:40	1:50
PC: CHOL molar ratio	**Average hydrodynamic diameter (nm)**				
1:1	138.74 ± 8.05	137.67 ± 6.79	138.47 ± 4.49	136.56 ± 3.57	129.04 ± 3.41
3:2	135.44 ± 5.61	129.48 ± 7.15	122.93 ± 1.49	126.02 ± 1.78	123.68 ± 4.43
7:3	136.27 ± 0.57	122.44 ± 2.36	122.93 ± 1.49	126.02 ± 1.78	123.68 ± 4.43
4:1	124.17 ± 2.50	109.68 ± 6.88	113.86 ± 2.18	103.37 ± 2.39	111.99 ± 3.44
9:1	96.93 ± 7.78	106.48 ± 3.98	102.25 ± 6.57	105.82 ± 7.89	114.97 ± 1.40

We recorded a significant change in the particle size (ANOVA p value = <0.0001) on varying the PC: CHOL molar ratios for each CUR: lipid wt. / wt. ratio (Figure 4.1A) -suggesting the significance of lipid molar ratios in affecting the particle size. For the highest CUR: lipid ratio (1:10), the particle size reduced significantly after 30 % CHOL (7:3) and after 40 % CHOL (3:2) for the other drug: lipid ratios. We noted comparable sizes of plain liposomes with 4:1, 9:1, and 7:3 PC: CHOL molar ratios (Chapter 3), but loading CUR significantly reduced the particle size with 4:1 and 9:1 PC: CHOL molar ratios than 7:3 PC: CHOL molar ratio. Thus, CUR affects the liposomal size.
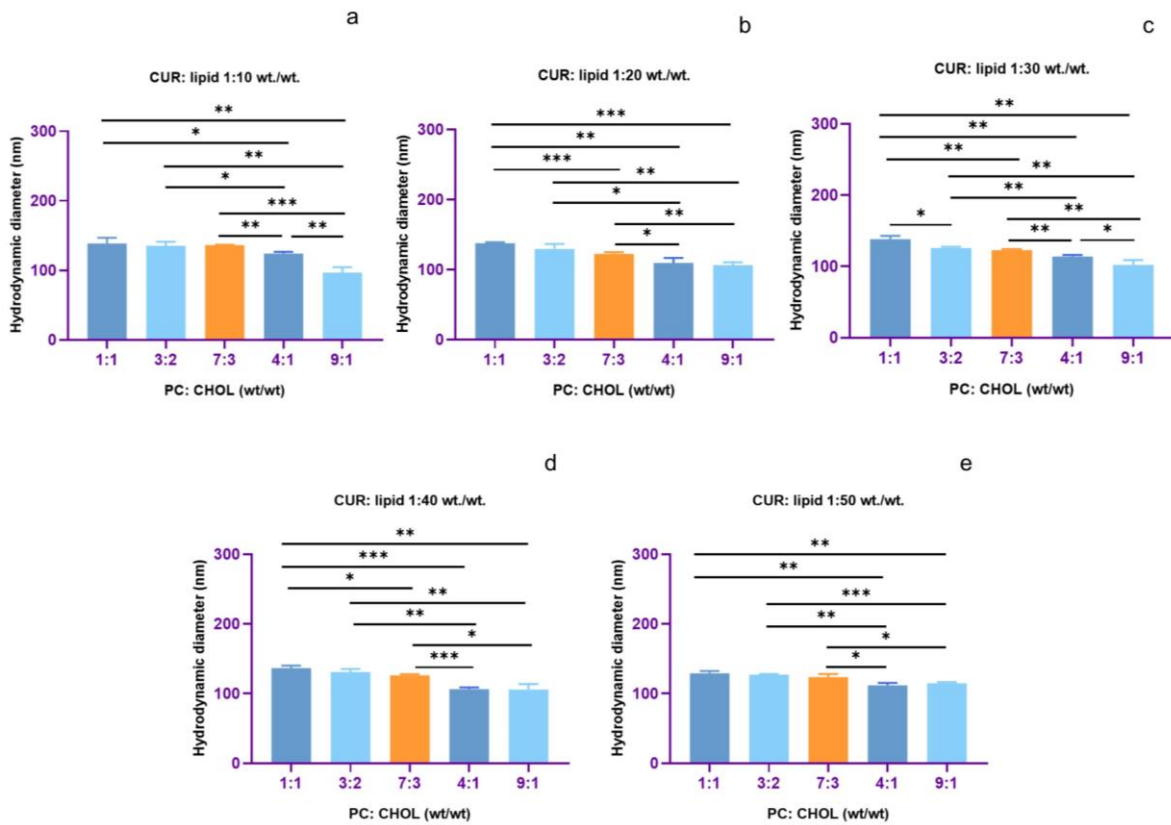
Figure 4.1A Hydrodynamic diameter of liposomes for different PC: CHOL molar ratios with 1:10 (a), 1:20 (b), 1:30 (c), 1:40 (d), and 1:50 (e) CUR: lipid wt. / wt. ratio

The hydrodynamic diameter of liposomes with 1:1 and 3:2 PC: CHOL molar ratios remained unaltered upon varying the drug: lipid ratios (Figure 4.2A) – the particle size remained unaffected by CUR concentration. But the size significantly changed for 7:3 (ANOVA p value = 0.0002), 4:1 (ANOVA p value = 0.0024), and 9:1 (ANOVA p value = 0.0469) PC: CHOL molar ratios on altering the drug concentrations. For 7:3 and 4:1 lipid ratios, we observed the largest liposomes for 1:10 CUR: lipid (wt. / wt.) ratio but 1:50 CUR: lipid (wt. / wt.) ratio for 9:1 lipid ratio. Upon increasing the phospholipid concentration, the particle size increased, as seen in other reports (Konatham *et al.* 2010).
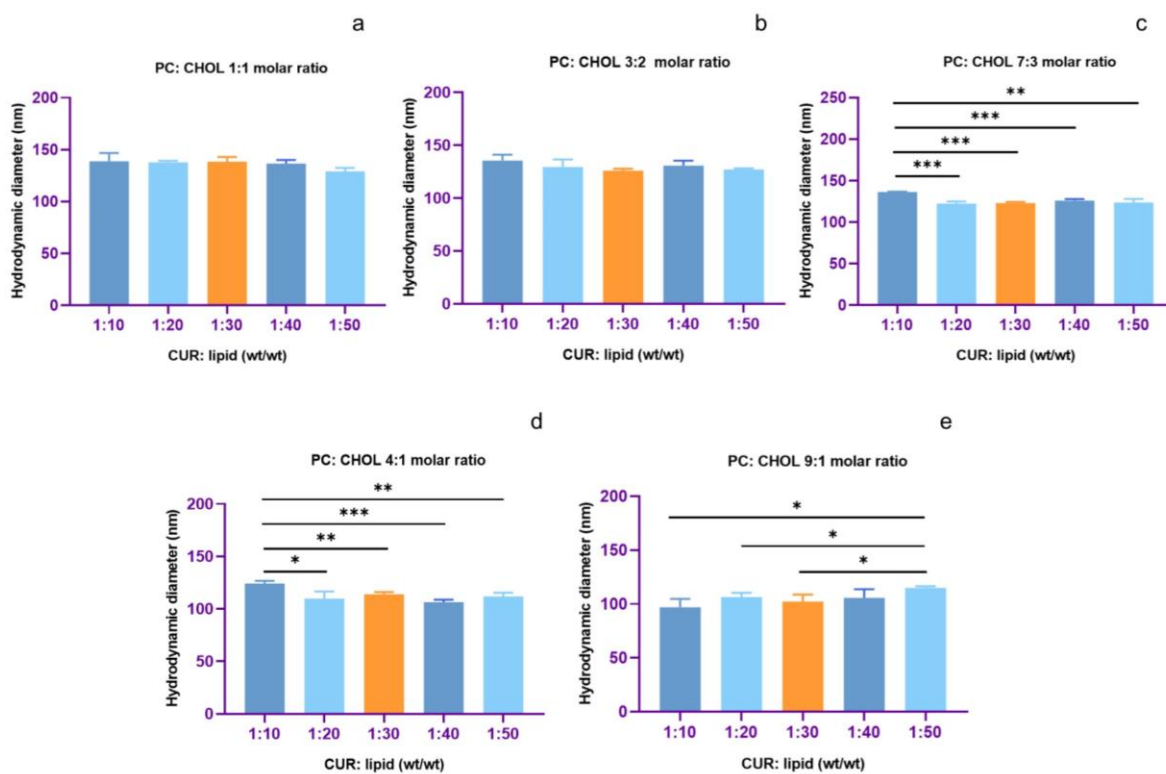
Figure 4.2A Hydrodynamic diameter of liposomes for different CUR: lipid (wt. / wt.) ratio for 1:1 (a), 3:2 (b), 7:3 (c), 4:1 (d), and 9:1 (e) PC: CHOL molar ratio

4.3.1.2 Effect on PDI

We recorded monodispersity for all the liposomal formulations with PDI values ranging from 0.11 ± 0.01 to 0.04 ± 0.01 (Table 4.2A); this attributed to the effective downsizing of the liposomes.

Table 4.2A Average PDI of CUR liposomes for different PC: CHOL molar ratio and CUR to lipid wt. /wt. ratio

CUR /lipid (wt. /wt.)	1:10	1:20	1:30	1:40	1:50
PC: CHOL molar ratio		Average PDI			
1:1	0.10 ± 0.04	0.08 ± 0.003	0.10 ± 0.01	0.04 ± 0.03	0.04 ± 0.01
3:2	0.09 ± 0.01	0.10 ± 0.01	0.07 ± 0.02	0.06 ± 0.01	0.06 ± 0.01
7:3	0.11 ± 0.01	0.10 ± 0.01	0.08 ± 0.03	0.05 ± 0.03	0.07 ± 0.02
4:1	0.08 ± 0.01	0.07 ± 0.02	0.06 ± 0.01	0.07 ± 0.01	0.08 ± 0.01
9:1	0.08 ± 0.01	0.09 ± 0.01	0.10 ± 0.01	0.09 ± 0.01	0.07 ± 0.02

The PDI of liposomes remained unaltered for all the CUR: lipid (wt. / wt.) ratios on varying the PC: CHOL molar ratios (Figure 4.3A) except for 1:30 CUR: lipid ratio (ANOVA p value = 0.0326). But, the PDI values below 0.12 suggest monodispersity of all the liposomal suspensions.
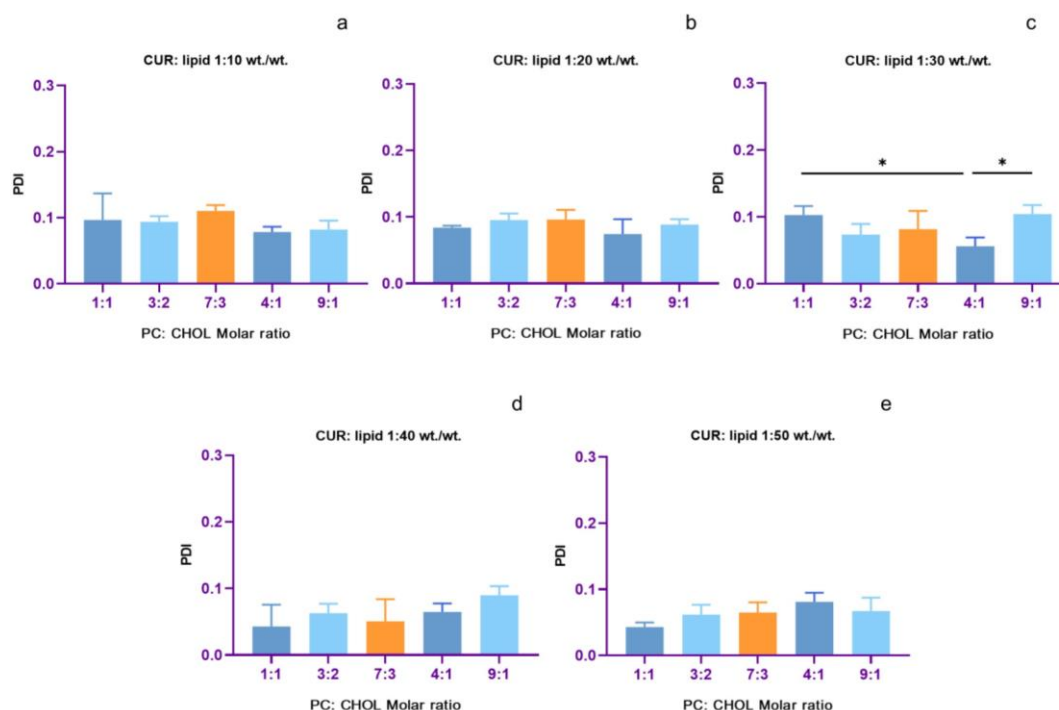
Figure 4.3A PDI of CUR liposomes for different PC: CHOL molar ratios with 1:10 (a), 1:20 (b), 1:30 (c), 1:40 (d), and 1:50 (e) CUR: lipid wt. / wt. ratios

The PDI values of liposomes with specific PC: CHOL molar ratio on varying the CUR: lipid (wt. / wt.) ratio recorded significant changes for 1:1 (ANOVA p value = 0.0279), 3:2 (ANOVA p value = 0.0212) and 7:3 (ANOVA p value = 0.0450) ratios (Figure 4.4A). But, the PDI for all the formulations is < 0.12, suggesting monodispersity of the population.
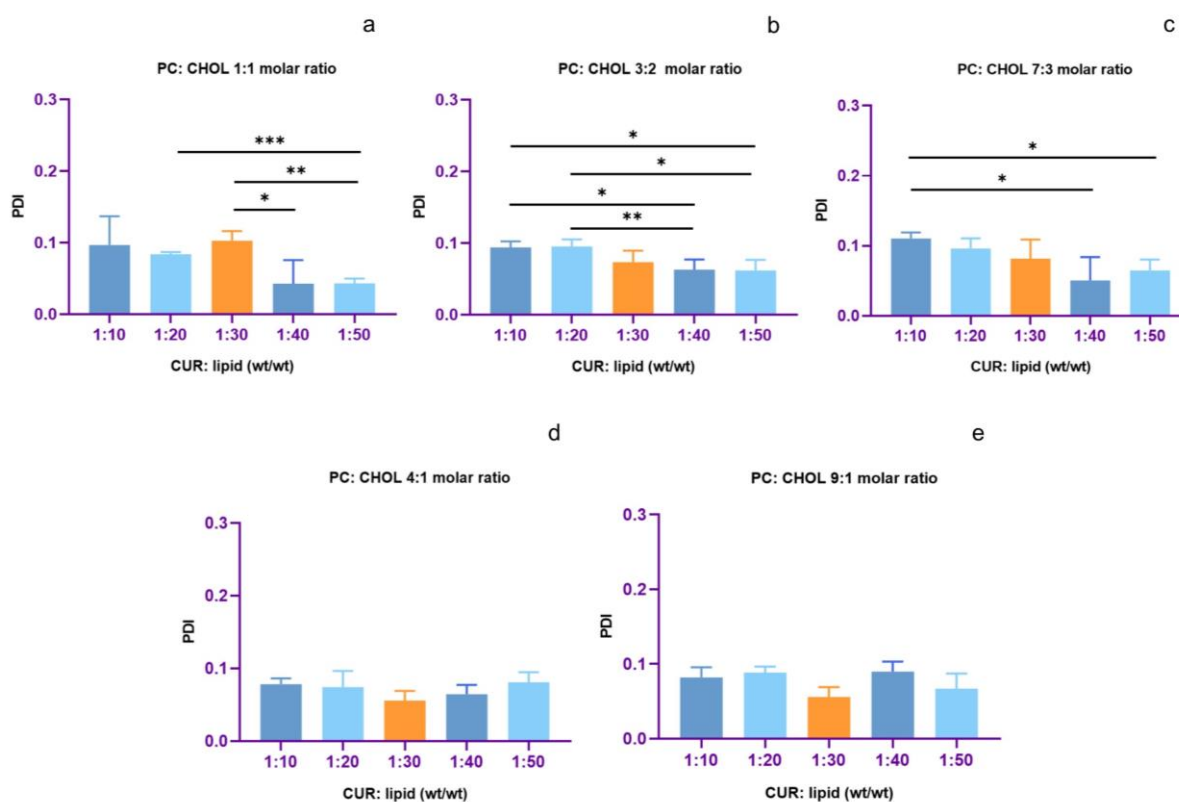
Figure 4.4A PDI of liposomes for different CUR: lipid (wt. / wt.) ratios for 1:1 (a), 3:2 (b), 7:3 (c), 4:1 (d), and 9:1 (e) PC: CHOL molar ratios

4.3.1.3 Effect on % EE

The % EE of CUR liposomes ranged from 24.76 ± 2.42 to 77.75 ± 2.83 %, suggesting the influence of PC: CHOL molar ratio and CUR: lipid (wt. / wt.) ratio (Table 4.3A).

Table 4.3A Average % EE of CUR for different PC: CHOL molar ratio and drug: to lipid (wt. / wt.) ratio

CUR/lipid (wt. /wt.)	1:10	1:20	1:30	1:40	1:50
PC: CHOL molar ratio			Average % EE		
1:1	35.98 ± 0.13	37.93 ± 6.79	52.93 ± 4.43	52.03 ± 2.77	53.29 ± 4.42
3:2	24.76 ± 2.42	47.20 ± 3.89	65.30 ± 2.46	51.67 ± 2.29	52.83 ± 7.66
7:3	37.73 ± 7.07	72.17 ± 3.05	76.15 ± 3.21	75.61 ± 3.21	77.75 ± 2.83
4:1	35.72 ± 2.12	43.00 ± 4.97	34.20 ± 2.88	42.48 ± 2.33	53.84 ± 6.80
9:1	47.83 ± 7.85	63.53 ± 3.37	59.30 ± 3.04	55.97 ± 1.88	53.00 ± 5.80

The % EE changed significantly for 1:10 (ANOVA p value = 0.0033), 1:20 (ANOVA p value = < 0.0001), 1:30 (ANOVA p value = < 0.0001), 1:40 (ANOVA p value = < 0.0001), and 1:50 (ANOVA p value = 0.0012) CUR: lipid ratios on varying the PC: CHOL molar ratios (Figure 4.5A). We recorded the lowest % EE for a 1:10 CUR: lipid ratio, indicating the saturation of liposomes with the highest CUR concentration. For 1:20, 1:30, 1:40, and 1:50 CUR: lipid ratios, the % EE increased till 7:3 PC: CHOL molar ratio and decreased thereafter.
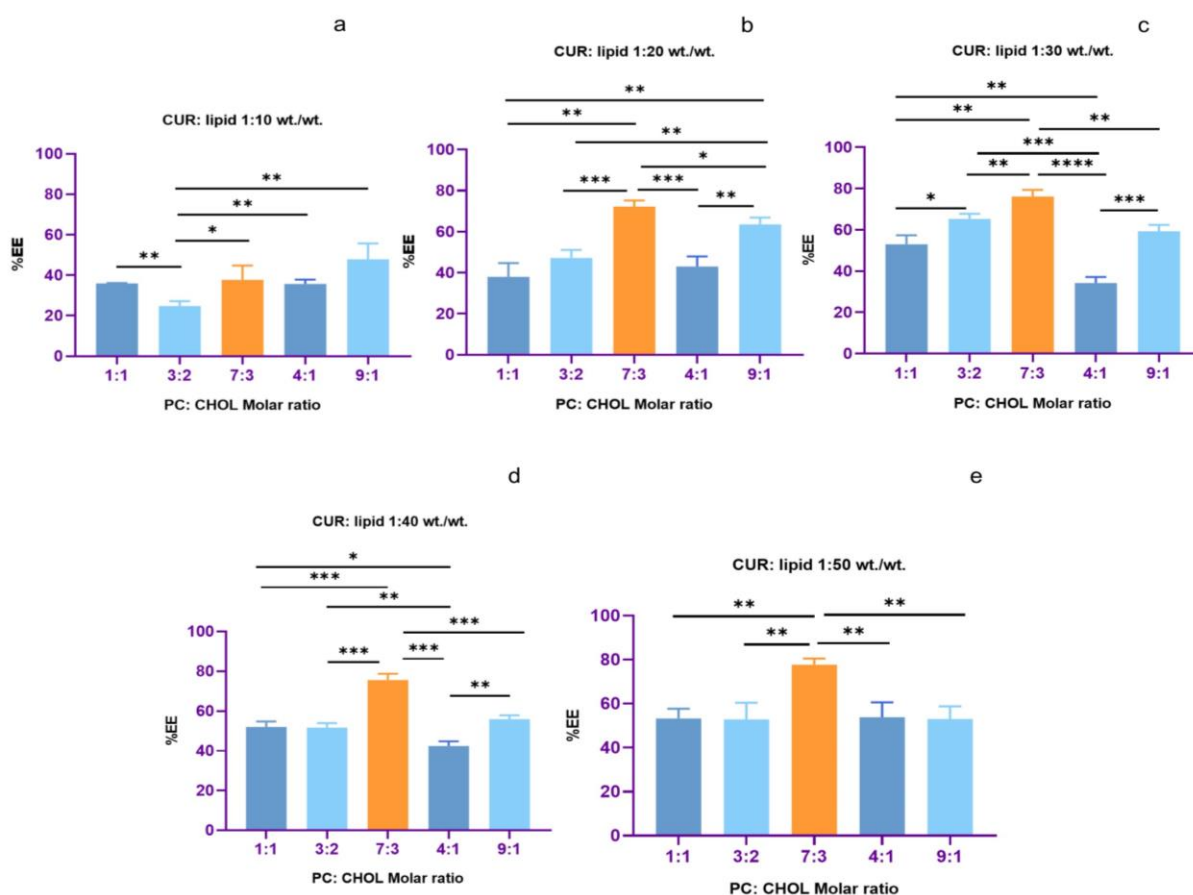
Figure 4.5A % EE of different PC: CHOL molar ratios with 1:10 (a), 1:20 (b), 1:30 (c), 1:40 (d), and 1:50 (e) CUR: lipid wt. / wt. ratios

Liposomes with 7:3 PC: CHOL molar ratio had higher % EE than 1:1 and 3:2 molar ratios (Figure 4.6A) even with smaller and comparable sizes, respectively; high CHOL concentrations (1:1 and 3:2 molar ratios) increase the bilayer rigidity resulting in lower CUR in the bilayer. Liposomes with lower CHOL concentrations (4:1 and 9:1) had lower % EE than 7:3, corresponding to increased membrane fluidity at lower CHOL concentrations, causing reduced drug retention and higher leakage.

PC: CHOL molar ratio of 9: 1 recorded higher % EE than the 4:1 ratio for 1:20 (t-test p value = 0.0041), 1:30 (t-test p value = 0.0005), and 1:40 (t-test p value = 0.0015) CUR: lipid ratios as at lower CHOL concentration (9:1); CUR acts as CHOL to stabilize the bilayer resulting in a higher drug encapsulation with equivalent sizes. At a 9:1 ratio, the competition between CUR and CHOL reduced, resulting in a higher % EE.

The % EE varied significantly on changing the CUR: lipid ratios for 1:1 (ANOVA p value = 0.0007), 3:2 (ANOVA p value = <0.0001), 7:3 (ANOVA p value = <0.0001), 4:1 (ANOVA p value = 0.0015) and 9:1 (ANOVA p value = 0.0245) PC: CHOL molar ratios (Figure 4.6A). We observed the highest % EE for the 7:3 PC: CHOL molar ratio (with CUR: lipids ratio of 1:20, 1:30, 1:40, and 1:50 ratio) and the lowest for the 1:1 PC: CHOL molar ratio. At higher CHOL concentrations (1:1 and 3:2 molar ratios), liposomes saturated with CUR at 1:10 and 1:20 CUR: lipid ratios.

The % EE remained unaltered for the 7:3 lipid ratio except for 1:10, suggesting drug saturation at higher drug concentration; the highest % EE in the 7:3 molar ratio of lipids corresponds to increased bilayer fluidity with a balanced rigidity incorporating higher CUR concentration with enhanced drug retention (Saengkrit *et al.* 2014) (Chen *et al.* 2012). Liposomes with lower CHOL concentrations (4:1 and 9:1) unfollowed this trend, and the lower % EE corresponded to the smaller particle size (Isacchi *et al.* 2012). Even though at lower CHOL levels (4:1 and 9:1), CUR acts as CHOL when incorporated in the bilayer to give rigidity, lower CHOL levels increase the bilayer flexibility, increasing the leakage of the drug from the bilayer (Choudhary *et al.* 2019) (Zarrabi *et al.* 2021).
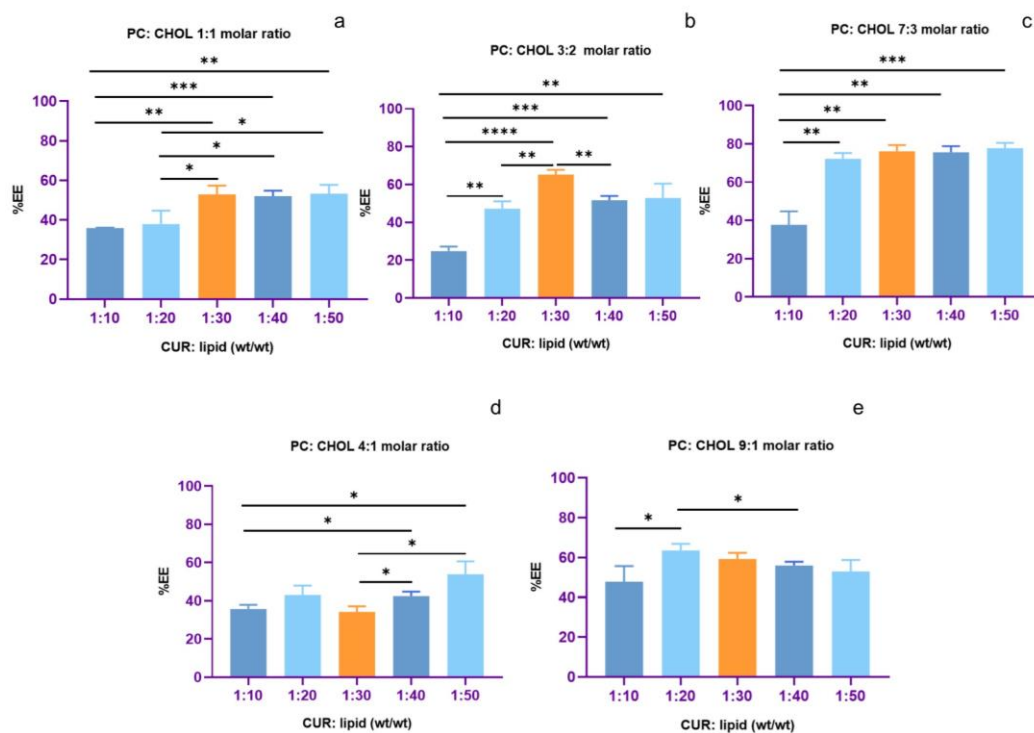
Figure 4.6A % EE with different CUR: lipid (wt. / wt.) ratios for 1:1 (a), 3:2 (b), 7:3 (c), 4:1 (d), and 9:1 (e) PC: CHOL molar ratios

CUR, due to its small size, incorporates in the defects created during the imperfect packing of the lipids (Hamano, Böttger, *et al.* 2019) and attains a trans bilayer orientation by forming hydrogen bonds with the phosphate groups of the lipids (Chen, *et al.* 2015); the location and orientation of CUR determine the particle size. CHOL and CUR actively compete for space in the bilayer and influence the drug's particle size and % EE (Choudhary *et al.* 2019); stronger competition occurs at higher CUR concentrations and weaker at lower concentrations.

Hydrophobic acyl chains of PC strongly interact with each other in reduced CHOL concentrations (4:1 and 9:1 lipid ratio), increasing the packing efficiency of liposomes and reducing drug incorporation. CUR decreases the hydrophobic interactions between the fatty acyl chains and perturbs the packing of the phospholipid bilayer (Hasan *et al.* 2016). Saturated fatty acids form a highly ordered lipid bilayer that reduces the hydration level and further depreciates the membrane fluidity. But, unsaturated fatty acyl chains form a comparatively less ordered lipid layer with high membrane fluidity (Hasan *et al.* 2014) (Hasan *et al.* 2016) – as PC in our study.

Liposomes accommodate an optimum CUR concentration without any structural changes in the bilayer, but higher concentrations induce structural changes by creating holes when the bilayer reorganizes and destabilizes, disrupting the phospholipid packing (Cheng *et al.* 2019) (Jin *et al.* 2016) (Arab-Tehrany *et al.* 2020).

The hydrodynamic diameter and PDI values for all the liposomal batches were within the mandates of drug delivery, and we optimized the 7: 3 molar ratio of lipids and 1:50 CUR: lipid (wt. / wt.) ratio based on the % EE.

4.3.2A Optimization of the downsizing step of CUR liposomes

We downsized the liposomes by sonicating them for 20 min in a water bath, then extruding them through a 100 nm polycarbonate membrane. We studied the influence of sonication and the number of extrusion passes in modulating the particle size, PDI, and % EE.

The hydrodynamic diameter and PDI of liposomes after hydration and sonication are higher than the drug delivery mandates (> 200 nm and > 0.3, respectively). But after extruding, irrespective of the sonication step, the particles have sizes < 150 nm and PDI < 0.1 (Table 4.4A).

Table 4.4A Effect of sonication on the hydrodynamic diameter (a), PDI (b), and % EE (c) of CUR liposomes

Downsizing protocol	Average Hydrodynamic diameter (nm)	Average PDI	Average % EE
After Hydration	248.31 ± 46.49	0.32 ± 0.06	
Hydration-Sonication	249.07 ± 34.64	0.33 ± 0.05	
Hydration-Sonication-Extrusion	128.37 ± 2.31	0.06 ± 0.03	77.75 ± 2.83
Hydration-Extrusion	120.79 ± 0.94	0.07 ± 0.02	76.49 ± 2.41

The particle size (ANOVA p value = 0.0007) and PDI (ANOVA p value = <0.0001) significantly reduced after the downsizing step with comparable specifications after sonication and after hydration (Figure 4.7A). We recorded equivalent size, PDI, and % EE of liposomes extruded directly after hydration and liposomes sonicated before extrusion. Sonication proved insignificant in our study but would be significant to downsize MLVs/ LUVs. We synthesized liposomes with the optimized process parameters (chapter 3) and achieved smaller particles after the hydration step. We intended to avert a stringent downsizing procedure as studies report loss of encapsulated CUR while downsizing the liposomes (Basnet *et al.* 2012).
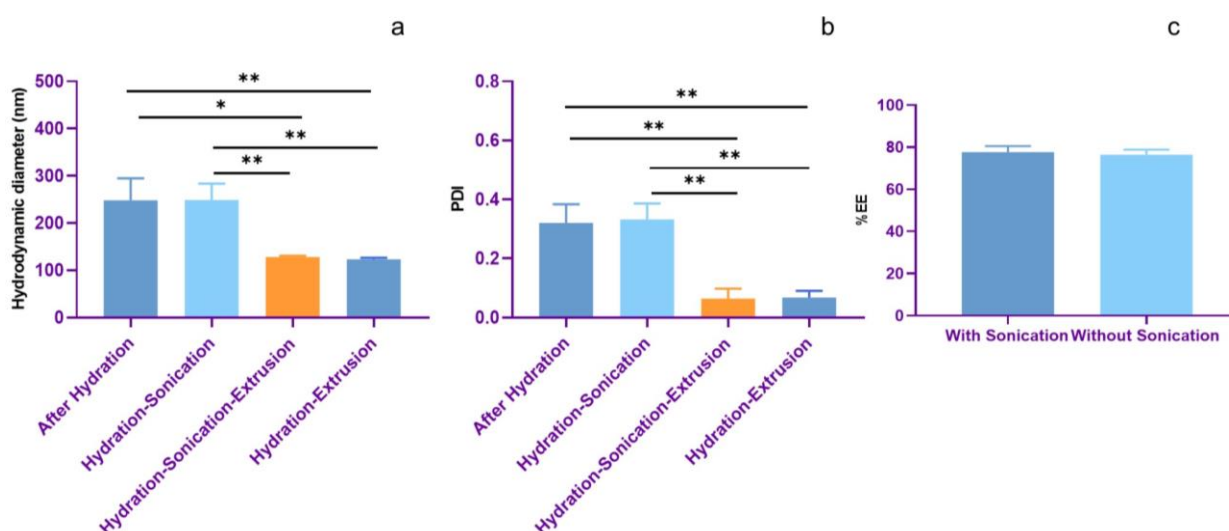
Figure 4.7A Effect of sonication on the hydrodynamic diameter (a), PDI (b), and % EE (c) of CUR liposomes

Extruding the liposomes significantly decreased the size and PDI after hydration, but the specifications remained unchanged for 5 and 11 extrusion passes (Table 4.5A) (Figure 4.8A).

Studies report the efficacy of extruding the liposomes for a smaller and monodisperse liposomal population with smaller values of the standard deviation of the CUR liposomes (Yeh *et al.* 2015).

Table 4.5A Effect of extrusion passes on the hydrodynamic diameter (a), PDI (b), and % EE (c) of CUR liposomes

Extrusion passes	Average Hydrodynamic diameter (nm)	Average PDI	Average % EE
5	117.66 ± 5.36	0.07 ± 0.01	75.95 ± 3.22
11	123.16 ± 3.27	0.07 ± 0.02	76.49 ± 2.41
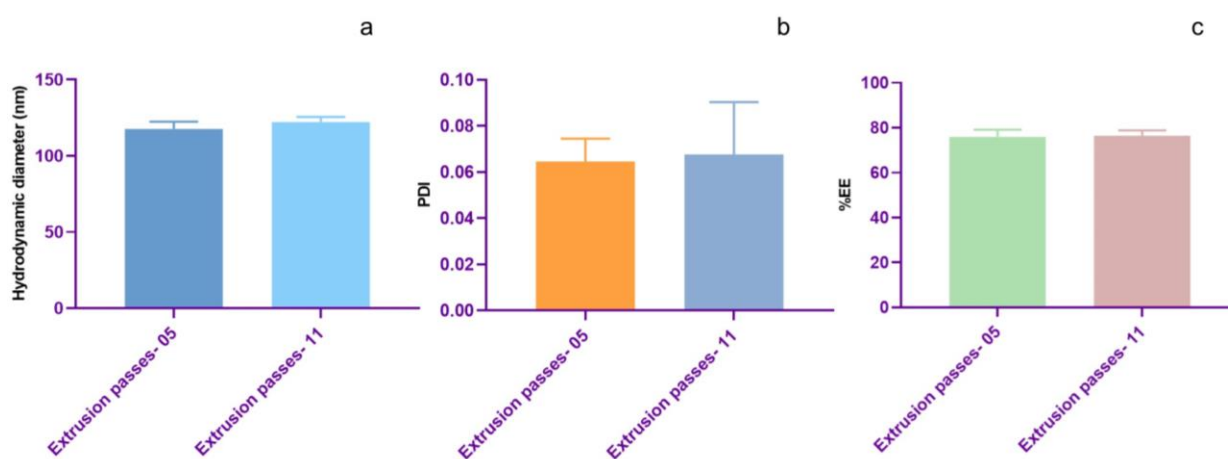
Figure 4.8A Effect of extrusion passes on the hydrodynamic diameter (a), PDI (b), and % EE (c) of CUR liposomes

The data suggested eliminating the sonication step and extruding the liposomes directly after hydration for 5 extrusion passes.

4.3.3A Optimization of PEGylated CUR liposomes

We synthesized PEGylated CUR liposomes with a 7: 3 molar ratio of PC: CHOL with a 1: 50 CUR: lipid (wt. / wt.) ratio and varied DSPE-mPEG2000 concentration (1, 3, and 5 mole %). The hydrodynamic diameter (ANOVA p value = 0.0053) and % EE (ANOVA p value = 0.0031) reduced significantly on increasing the concentration of DSPE-mPEG2000 from 1 to 5 mole %, but the PDI values indicated a monodisperse population (PDI $\leq$ 0.3) for all the formulations (Table 4.6A) (Figure 4.9A).

Liposomes with 1 mole % DSPE-mPEG2000 reported the highest size (t-test p value = 0.0273 with 3% and p value = 0.0008 with 5 mole %) and % EE (t-test p value = 0.0075 with 3 mole % and p value = 0.0070 with 5 mole %). The reduced particle size corresponds to PEG induced size reduction, where a higher concentration of PEG results in the collapse of the particles; the reduced particle size also corresponds to the decrease in the % EE.

Table 4.6A Effect of DSPE-mPEG2000 concentration on the hydrodynamic diameter, PDI, and % EE of PEGylated CUR liposomes

DSPE-mPEG2000 (mole % of lipids)	Average Hydrodynamic diameter (nm)	Average PDI	Average % EE
1	122.91 ± 0.65	0.06 ± 0.01	77.86 ± 2.61
3	108.57 ± 7.38	0.06 ± 0.02	66.49 ± 2.97
5	102.98 ± 3.68	0.08 ± 0.02	68.56 ± 1.79
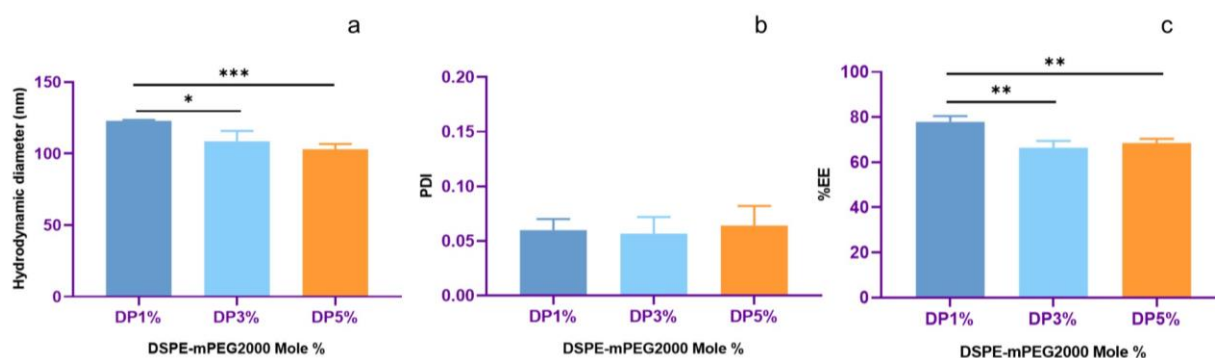
Figure 4.9A Effect of DSPE-mPEG2000 concentration on hydrodynamic diameter (a), PDI (b), and % EE (c) of PEGylated CUR liposomes

After hydration, we extruded the PEGylated CUR liposomes and varied the number of extrusion passes. The size, PDI, and % EE of liposomes after 5 and 11 extrusion passes showed insignificant change (Table 4.7A) (Figure 4.10A).

Table 4.7A Effect of extrusion passes on hydrodynamic diameter, PDI, and % EE of PEGylated CUR liposomes

Extrusion passes	Average Hydrodynamic diameter (nm)	Average PDI	Average % EE
5	118.19 ± 4.09	0.07 ± 0.02	77.86 ± 2.61
11	122.91 ± 0.65	0.06 ± 0.01	76.81 ± 2.93
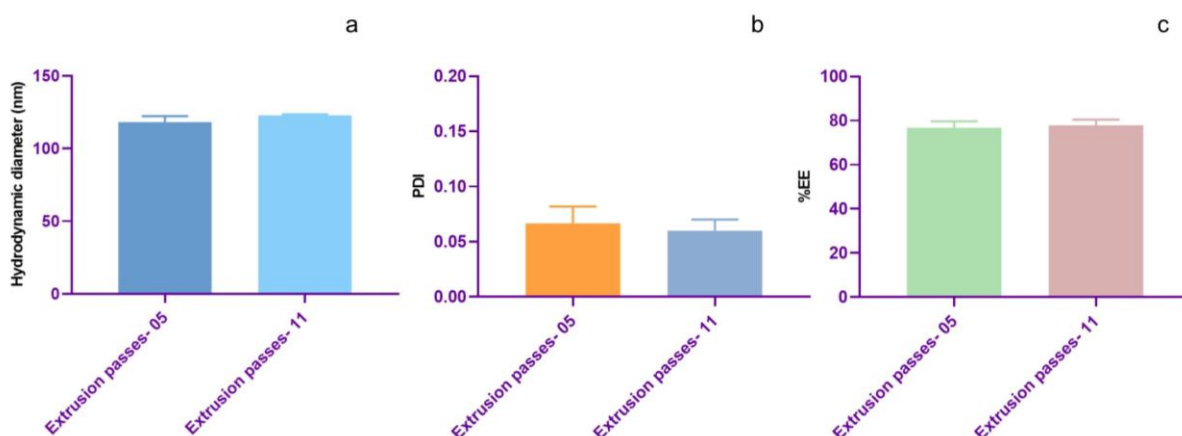
Figure 4.10A Effect of extrusion passes on hydrodynamic diameter (a), PDI (b), and % EE (c) of PEGylated CUR liposomes

We optimized a 7:3 molar ratio of lipids, a 1:50 drug to lipid ratio, excluded the sonication step after hydration, and 5 extrusion passes to synthesize CUR liposomes, and 1 mole % DSPE-mPEG2000 and 5 extrusion passes for PEGylated CUR liposomes based on the size, PDI and % EE.

4.4A Characterization of CUR loaded liposomes

We characterized the liposomes synthesized with the optimized values by analytical techniques.

4.4.1A Hydrodynamic diameter, PDI, and zeta potential

The DLS graph records the hydrodynamic diameter and PDI for CUR liposomes at 117.3 nm and 0.08, respectively, and for PEGylated CUR liposomes at 118 nm and 0.08 respectively. Single sharp peaks for both formulations confirm a smaller sized and monodisperse liposomal

population (Figure 4.11A). The zeta potential value significantly changed from -21.97 ± 2.99 mV for CUR liposomes to -10.08 ± 0.38 mV for PEGylated CUR liposomes.
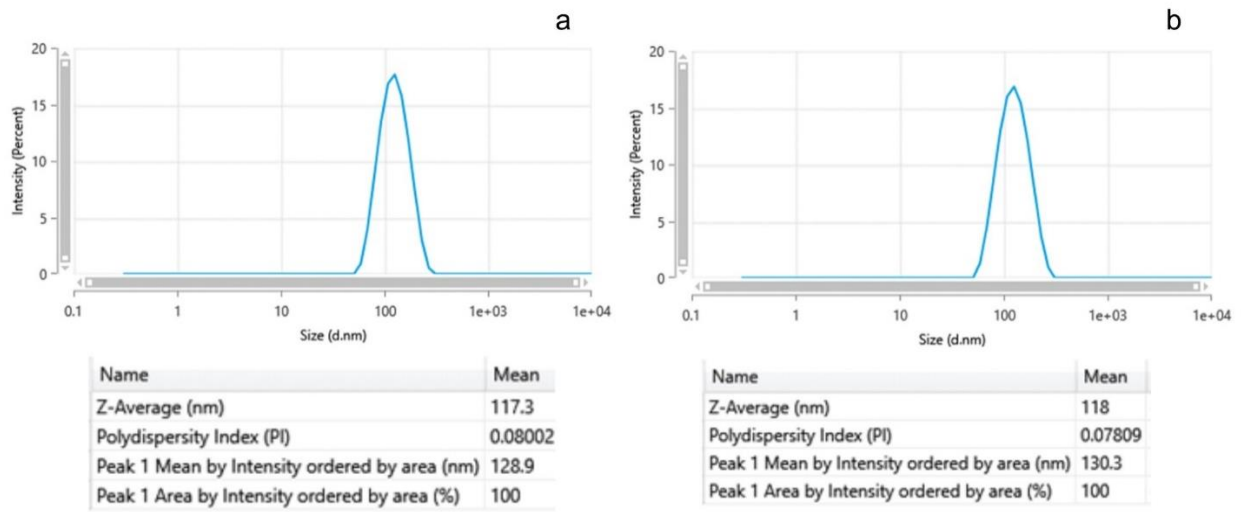
Figure 4.11A DLS graphs of CUR liposomes (a) and PEGylated liposomes (b)

The hydrodynamic diameter and PDI of CUR and PEGylated CUR liposomes showed an insignificant difference, but the statistically significant change in the zeta potential (t-test p value = 0.0024) confirms the surface functionalization of liposomes with PEG; PEG prevents liposomes from aggregating in a suspension that increases the colloidal stability (Hardiansyah *et al.* 2017) (Dhule *et al.* 2014) (Figure 4.12A).
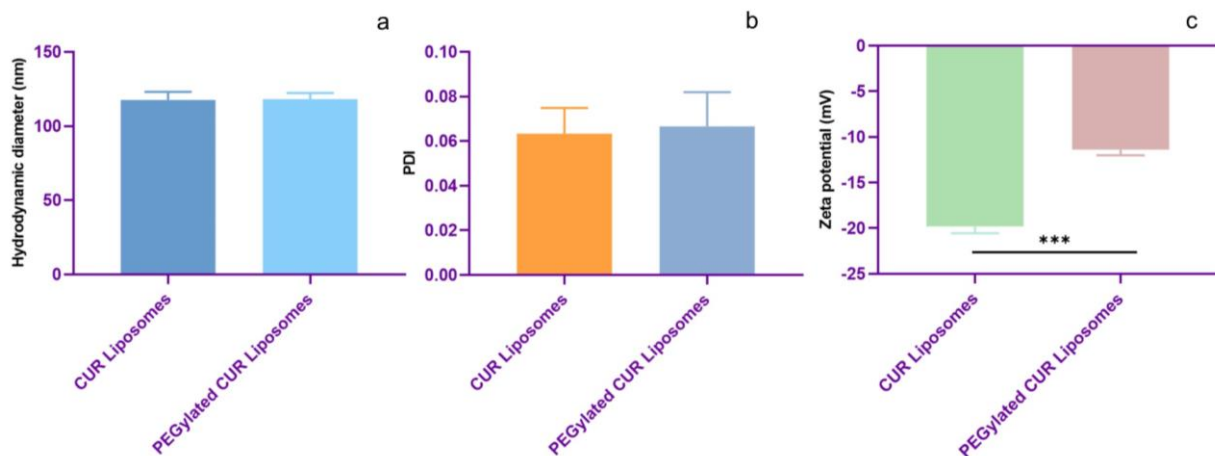
Figure 4.12A Comparative analysis of hydrodynamic diameter (a), PDI (b), and zeta potential (c) of CUR and PEGylated CUR liposomes

The sizes of the non-PEGylated and PEGylated liposomes were similar after CUR loading, suggesting that CUR interacts with the hydrophobic fatty acyl chains that compact the core of liposomes (Hasan *et al.* 2014). The PDI values remained unchanged and suggest a monodisperse population. The zeta potential values remain unaltered after CUR loading, suggesting that the liposomal surface remains untransformed after CUR loaded in the bilayer.

PEGylated liposomes followed a similar trend after incorporating CUR; although the PDI values reduced significantly (t-test p value = 0.0332), the values < 0.1 suggest a monodisperse population. Studies also report a change in the zeta potential (t-test p value = 0.0393) for the PEGylated liposomes, as observed in our study, corresponds to the changes in the liposomal surface after incorporating CUR (Jin *et al.* 2016) (Figure 4.13A). CUR positions in the bilayer formed by PC's unsaturated fatty acyl chains and the saturated fatty acyl chains of DSPE in the PEGylated liposomes; this might suggest the change in the zeta potential of the liposomes after CUR loading.
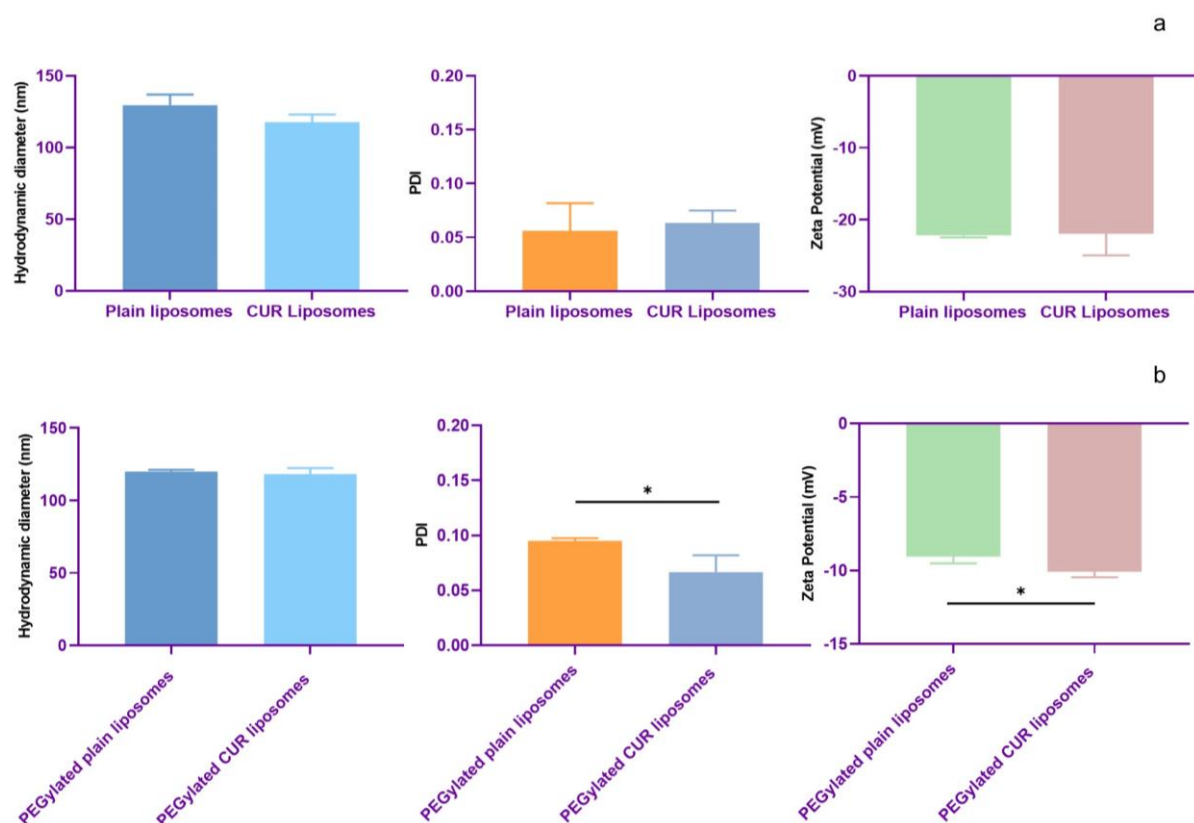
Figure 4.13A Comparative analysis of hydrodynamic diameter, PDI, and zeta potential of plain and CUR liposomes (a) and PEGylated plain liposomes and PEGylated CUR liposomes

4.4.2A % EE and % DL

We recorded statistically equivalent values of % EE of CUR in CUR and PEGylated CUR liposomes at 75.95 ± 3.22 and 77.86 ± 2.61 %, respectively, corresponding to equivalent sizes (Figure 4.14A). We calculated the % DL for CUR liposomes and PEGylated CUR liposomes at 3.64 ± 0.15 % and 3.21 ± 0.27 %, respectively, with statistical insignificance between the two. Li et al. reported similar % DL of 3.96 ± 0.32 % for CUR loaded liposomes (Li *et al.* 2020). Studies report the % DL for liposomes with hydrophobic drugs < 5 % (Hamano, *et al.* 2019), coinciding with our observations. We anticipated loss of CUR while extruding and during ultracentrifugation, as also observed in other studies.
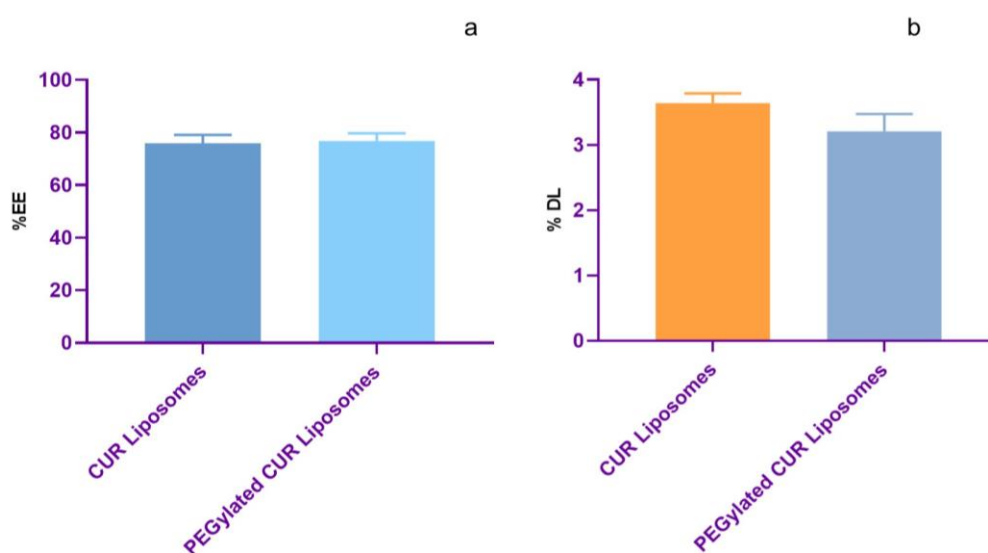
Figure 4.14A % EE and % DL of CUR and PEGylated CUR liposomes

4.4.3A Morphology of CUR loaded liposomes

The HRTEM images show spherical particles of CUR liposomes and PEGylated CUR liposomes with smooth surfaces. We observed oval and other irregular structures due to limitations in the sample preparation for conventional electron microscopy (Figure 4.15A) (discussed in Chapter 3). Studies report that particle size decreases due to contraction during drying (Li *et al.* 2020) (Hong *et al.* 2020). The particle size deduced in microscopy is smaller than the DLS size as we measure the hydrodynamic diameter in DLS (Ruttala and Ko 2015) – also observed in other studies.
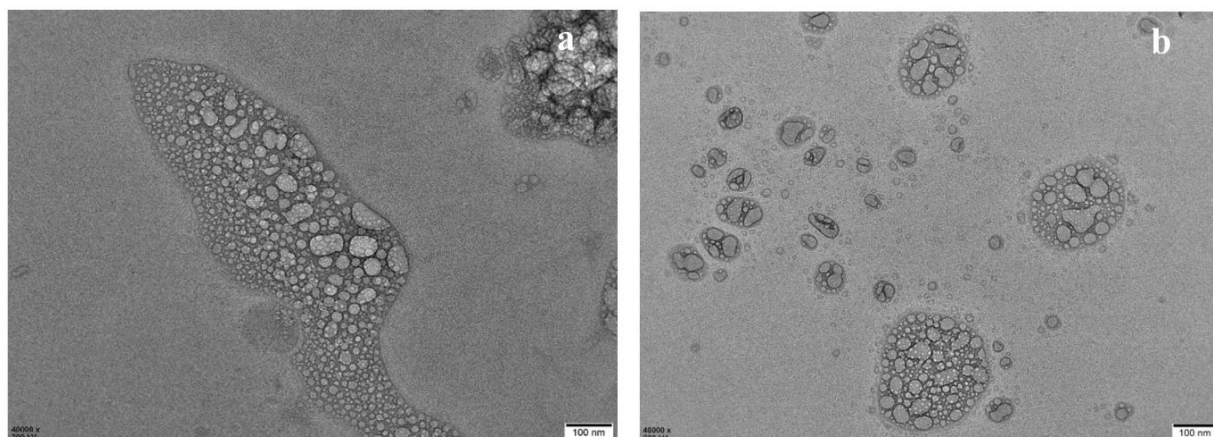
Figure 4.15A HRTEM images of CUR liposomes (a) and PEGylated CUR liposomes (b) at 100 nm magnification

4.4.4A FTIR analysis

The FTIR spectrum for plain CUR (Figure 4.16A) shows characteristic peaks for phenolic OH stretching at 3508 cm^{-1}, C=O stretching at 1627 cm^{-1}, C=C symmetric aromatic stretch at 1599 cm^{-1}, C=C stretching at 1503 cm^{-1}, aromatic enol in plane bending at 1426 cm^{-1}, CH in plane bending, enolic COH, and skeletal CCC at 1377 cm^{-1}, aromatic C-O stretch at 1274 cm^{-1}, asymmetric C-O-C stretch at 1026 cm^{-1}, CH overtone stretching, and C-O-C stretching at 1152 cm^{-1}, C-O, C-C and CCO stretching at 1116 cm^{-1}, CH out of plane bending of aromatic CCH and skeletal CCH at 858 cm^{-1}, and C=C-H stretch at 715 and 782 cm^{-1} (Hudiyanti *et al.* 2021) (Pu *et al.* 2019) (Li *et al.* 2018) (Aadinath *et al.* 2016) (Huang *et al.* 2019) (Ng *et al.* 2018).
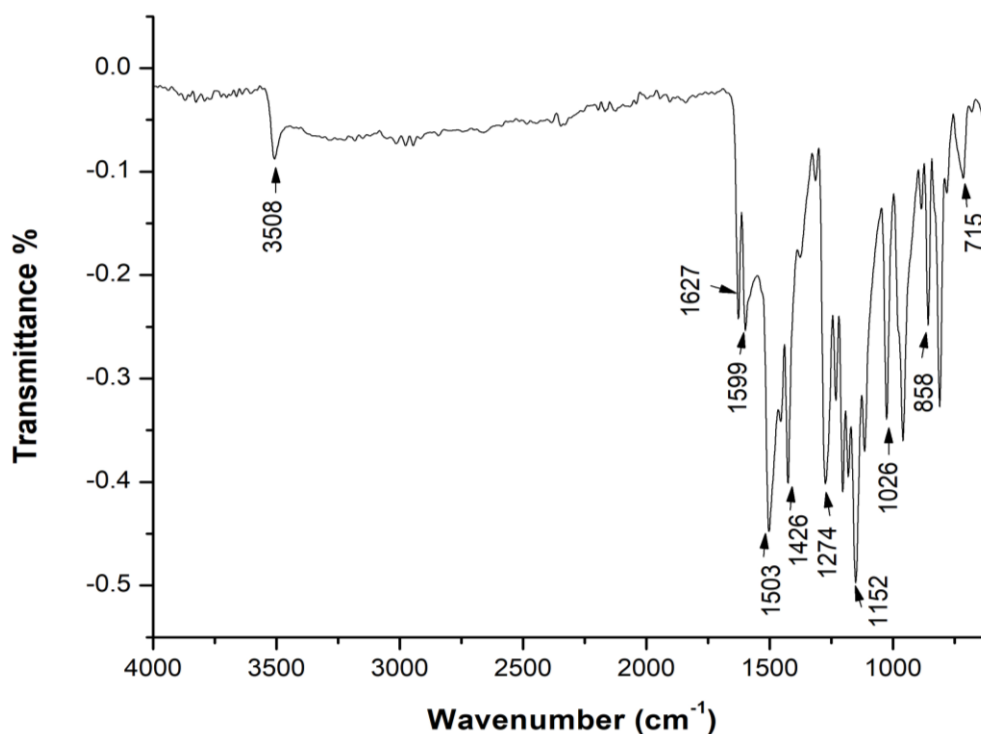
Figure 4.16A FTIR spectrum of plain CUR

We compared the FTIR spectra of CUR liposomes and PEGylated CUR liposomes with PC to determine deviations in the wavenumber after drug loading to comprehend the interaction between the drug and liposomal components and the location of CUR in the liposomes (Figure 4.17A).

In CUR liposomes, the OH stretching peak shifted from 3300 to 3417 cm⁻¹; the antisymmetric CH stretch shifted from 2922 to 2924 cm⁻¹ and the symmetric CH stretching from 2853 to 2856 cm⁻¹; the C=O (ester) stretching shifted from 1736 to 1735 cm⁻¹; the C=C stretching shifted from 1651 to 1648 cm⁻¹; the CH_2 bending shifted from 1463 to 1458 cm⁻¹; the CH_3 bending shifted from 1377 to 1373 cm⁻¹; the characteristic peaks for the head group region for antisymmetric PO^{2-} shifted from 1225 to 1226 cm⁻¹ and symmetric PO^{2-} remained unchanged at 1057 cm⁻¹, the P-O stretching shifted from 829 to 827 cm⁻¹.

In PEGylated CUR liposomes, the OH stretching shifted from 3300 to 3392 cm⁻¹; the antisymmetric CH stretch shifted from 2922 to 2924 cm⁻¹ and the symmetric CH stretching shifted from 2853 to 2856 cm⁻¹; the C=O (ester) stretching shifted from 1736 to 1735 cm⁻¹; the C=C stretch shifted from 1651 to 1647 cm⁻¹; the CH_2 bending shifted from 1463 to 1458 cm⁻¹; the CH_3 bending shifted from 1377 to 1373 cm⁻¹; the characteristic peaks for the head group

region for antisymmetric PO_2^- shifted from 1225 to 1226 cm^{-1} and symmetric PO_2^- remained unchanged at 1057 cm^{-1}, the P-O stretching shifted from 829 to 823 cm^{-1}.

The hydrogen bonds disintegrate to form new bonds between the phenolic OH of CUR and PC, corresponding to a shift in the OH stretching vibration (Hasan *et al.* 2016). The shift in the symmetric and antisymmetric CH stretch suggests a slight change in the order of the membrane. The FTIR spectra of CUR loaded liposomes resembled that of PC, with the characteristic peaks of CUR missing at 1627, 1599, 1503, 1426, 1152, 1116, 858, and 1026 cm^{-1} (Zarrabi *et al.* 2021).

The masking of CUR characteristic peaks indicates successful loading of CUR in the phospholipid interface with physical interactions and the absence of any chemical interactions as no new peaks emerge (Hudiyanti *et al.* 2021) (Li *et al.* 2018) (Aadinath *et al.* 2016) (Ng *et al.* 2018). CUR adopts a trans bilayer orientation with one phenoxy group towards the headgroup and water interface and the keto-enol and another phenoxy group toward the hydrophobic chain of the bilayer (Niu *et al.* 2012). This orientation protects the CUR's keto-enol group and stabilizes the liposome drug (Chen, *et al.* 2015).
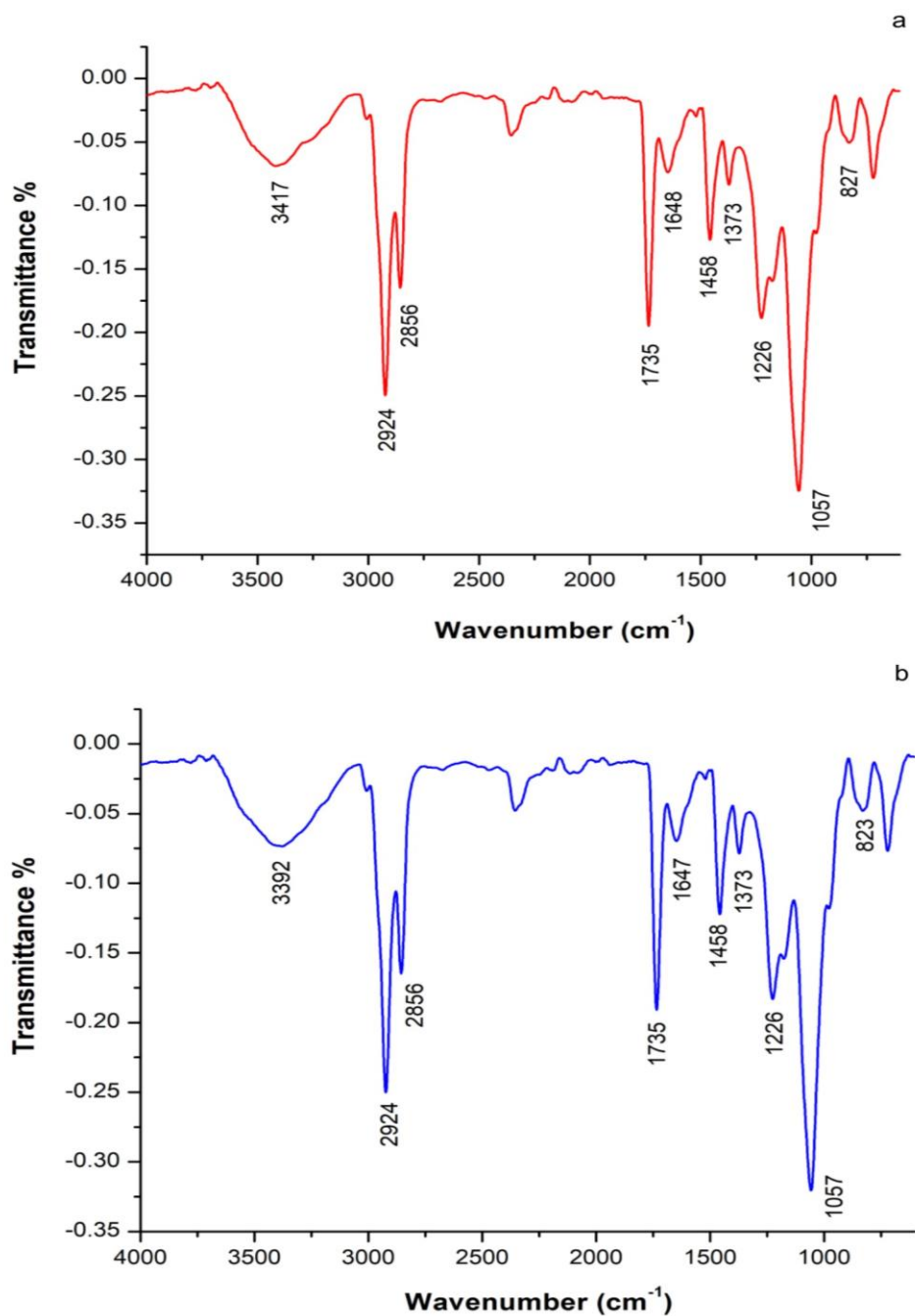
Figure 4.17A FTIR spectra CUR liposomes (a) and PEGylated CUR liposomes (b)

4.4.5A TGA analysis

The thermogram of plain CUR drug records the degradation onset temperature at 253.79 °C with 72.7% degradation. The degradation onset temperature for CUR liposomes shifted from 182.46 °C for PC and 240.78 °C for plain liposomes to 244.49 °C with 74.86% degradation; the degradation onset temperature for PEGylated CUR liposomes increased from 182.46 °C for PC and 248.53 °C for plain PEGylated liposomes to 260.7 °C with 77.88 % degradation

(Figure 4.18A). The thermograms suggest an increase in the thermal stability after CUR loading in the liposomes, corresponding to the high stability of the bilayer and compaction of the liposomal core.
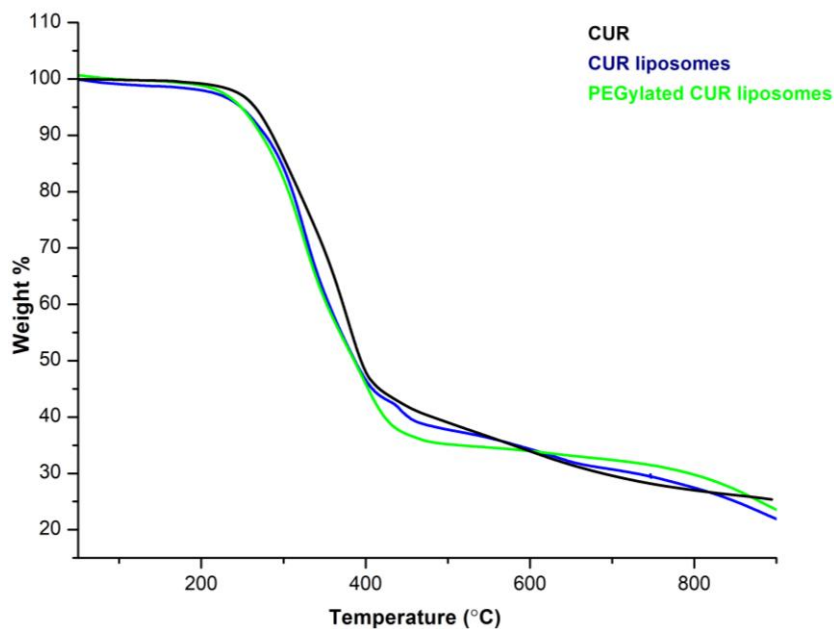
Figure 4.18A TGA thermogram of CUR (green), CUR liposomes (blue), and PEGylated CUR liposomes (red)

4.4.6A DSC analysis

We observed a sharp endotherm for plain CUR at 176.55 °C. The endotherm for CUR liposomes and PEGylated CUR liposomes broadened and occurred at 120.50 and 94.73 °C, respectively (Figure 4.19A). As seen in the FTIR spectra, CUR incorporates the bilayer interacting with the phosphate group of the head group region and the hydrophobic fatty acyl chain regions. CUR induces a dip in the packing of the phospholipids, which increases the hydration level. These bonds degrade by absorbing heat, resulting in a shift in the endotherm to lower temperatures (Niu *et al.* 2012).

The endotherm's broad nature confirms the drug's presence in the bilayer region (Campani *et al.*, 2020). The higher endotherm than the storage temperature suggests higher storage stability of the particles without undergoing a phase transition (Chaves *et al.* 2018). The sharp endotherm for plain CUR disappeared, confirming the successful loading of CUR in the liposomes (Gómez-Mascaraque *et al.* 2017).
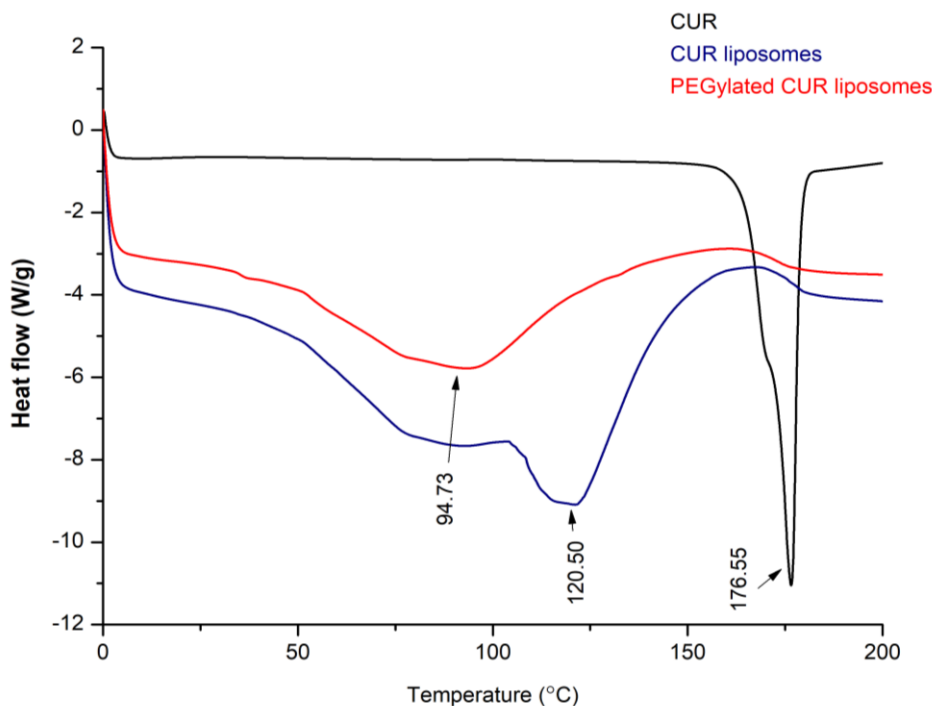
Figure 4.19A DSC thermogram of CUR (black), CUR liposomes (blue), and PEGylated CUR liposomes (green)

4.5A Conclusion

This study identifies and examines various parameters for synthesizing CUR liposomes and PEGylated CUR liposomes. We investigated various intrinsic factors such as the CUR: lipid (wt. wt.) ratio, the molar ratio of PC: CHOL, the concentration of DSPE-mPEG2000, and process parameters such as the importance of sonication and the number of extrusion passes in downsizing step. We optimized a 7: 3 molar ratio of PC: CHOL, 1: 50 wt. / wt. ratio of the CUR: lipids and excluded sonication with 5 extrusion passes in the downsizing step for CUR liposomes: 1 mole % DSPE-mPEG2000 and 5 extrusion passes for PEGylated CUR liposomes.

Upon characterization, we confirmed the hydrodynamic diameter, PDI, and zeta potential at 1117.66 ± 5.36 nm, 0.07 ± 0.01, and -21.97 ± 2.99 mV, respectively for CUR liposomes, and 118.19 ± 4.09 nm, 0.07 ± 0.02, and -10.08 ± 0.38 mV respectively for PEGylated CUR liposomes. We recorded the % EE and % DL of CUR liposomes at 75.95 ± 3.22 % and 3.64 ± 0.15 %, respectively, and for PEGylated CUR liposomes at 77.86 ± 2.61 % and 3.21 ± 0.27 % respectively.

HRTEM confirmed particles were spherical morphology and smooth surfaces. The FTIR analysis suggested the successful loading of CUR in the lipid bilayer of liposomes. TGA analysis showed high thermal stability with the degradation onset temperature for CUR liposomes at 244.49 °C and PEGylated CUR liposomes at 260.7 °C compared to 182.46 °C for PC. The DSC thermograms recorded a sharp endotherm for plain CUR at 176.55 °C and broad endotherms for CUR liposomes and PEGylated CUR liposomes at 120.50 and 94.73 °C respectively; this suggests the successful loading of CUR in the liposomes. Thus, the results indicate the synthesis of robust CUR loaded liposomes according to the drug delivery mandates.

CHAPTER 4B

Optimization, Synthesis, and Characterization of DOX loaded liposomes

4.1B Introduction

DOX, an anthracycline, is the primary chemotherapeutic drug clinically prescribed for breast cancer. It interacts with the enzyme topoisomerase II and creates double stranded breaks in DNA. The aglycone component of DOX incorporates between the adjacent base pairs of DNA, forming hydrophobic interactions and stabilizing the enzyme with hydrogen bonds between the sugar moieties of the bases and the chromophore region of the drug; this deforms and destabilizes the structure by stabilizing topoisomerase II.

DOX induces cardiotoxicity and accumulates nonspecifically, causing toxicities and myelosuppression. DOX has a small therapeutic window with a 10-12 min circulation half-life. Thus, incorporating DOX in liposomes alters the pharmacological and pharmacodynamics of the drug. It enhances its therapeutic potential by imparting a higher circulation time and bioavailability and reducing non-target accumulation.

We prepared DOX liposomes with the previously optimized values of 10 mg/ml concentration of PC and CHOL, a 7:3 molar ratio of PC: CHOL, and 1 mole % of DSPE-mPEG-2000 (for PEGylated DOX liposomes). We optimized DOX concentration and the number of extrusion passes in the downsizing step- we dropped sonication while optimizing CUR loaded liposomes. We characterized the DOX loaded liposomes synthesized by the final optimized values by various analytical techniques: hydrodynamic diameter, PDI, zeta potential, morphology, functional groups, % EE, % DL, and thermal stability. We aimed to synthesize liposomes with an appropriate size, PDI, and the highest % EE of DOX.

4.2B Methods

We synthesized DOX liposomes and PEGylated DOX liposomes by the protocol elaborated in Chapter 2, section 2.2.3 – DOX was loaded passively with a 7: 3 molar ratio of PC: CHOL, and 1 mole % DSPE-mPEG2000 (for PEGylated DOX liposomes). We examined the influence of DOX concentration and no: of extrusion passes to fabricate DOX loaded liposomes with size < 200 nm, PDI < 0.3, and highest % EE of DOX.

4.2.1B Optimization of DOX liposomes

We optimized the DOX concentration (0.05, 0.1, 0.2, and 0.4 mg) based on the hydrodynamic diameter, PDI, and % EE.

4.2.2B Optimization of the downsizing step of DOX liposomes

We extruded liposomes by varying the number of extrusion passes (5 and 11) through a 100 nm polycarbonate membrane - sonication was excluded from the downsizing protocol (as optimized in chapter 3A).

4.2.3B Synthesis and Optimization of PEGylated DOX Liposomes

PEGylated DOX liposomes were synthesized with the optimized drug concentration (0.1 mg) and 1 mole % of DSPE-mPEG2000. We optimized the number of extrusion passes (5 and 11) through a 100 nm polycarbonate membrane.

4.2.4B Characterization of DOX loaded liposomes

We characterized DOX liposomes and PEGylated DOX liposomes by various analytical techniques (Chapter 2, section 2.3): hydrodynamic diameter, PDI, and zeta potential by DLS; morphology by HRTEM; functional groups by FTIR; and thermal analysis by TGA and DSC.

4.3B Results and Discussion

We aimed to fabricate DOX liposomes and PEGylated DOX liposomes with hydrodynamic diameter < 200 nm, PDI <0.3, and high % EE of DOX.

4.3.1B Optimization of DOX concentration

We passively encapsulated DOX by dissolving it in PBS and adding it to the thin film hydration step, allowing the drug to position itself in the aqueous core. We investigated DOX concentration (0.05, 0.1, 0.2, and 0.4 mg) considering the liposome's optimized CUR concentration. We observed a significant change in the hydrodynamic diameter (ANOVA p value = < 0.0001), PDI (ANOVA p value = 0.0002), zeta potential (ANOVA p value = 0.0068), and % EE (ANOVA p value = < 0.0001) on varying the DOX concentration (Table 4.1B). We optimized 0.1 mg DOX based on the size, PDI, % EE, and the optimized CUR concentration.

When compared to liposomes with 0.1 mg DOX, liposomes with 0.4 mg DOX was significantly larger in hydrodynamic diameter (t-test p value = <0.0001) and PDI (t-test p value = 0.0045) corresponding to an aggregated liposomal formulation (Figure 4.1B); the % EE reduced significantly (t-test p value = 0.0017) attributing to the saturation of the liposomes with drugs.

Liposomes with 0.2 mg DOX were significantly larger (t-test p value = 0.0490) than liposomes with 0.1 mg with comparable PDI values, and a non-aggregated liposomal formulation but smaller than liposomes with 0.4 mg DOX (t-test p value = <0.0001) with lower PDI values (t-test p value = 0.0063) and comparable % EE. We recorded equivalent specifications of liposomes with 0.1 and 0.05 mg DOX.

We observed that the particle size decreased by lowering the drug concentration (Haghiralsadat, *et al.* 2017). The zeta potential of all the formulations characterized the particles with incipient stability. The % EE peaked at 0.1 mg and declined with increasing drug concentration, suggesting that the liposomes were saturated with DOX (Chen *et al.* 2019). Lower DOX concentration in the liposomal formulation is more economical to synthesize (Haghiralsadat, *et al.* 2017). Thus, 0.1 mg DOX is economical and lower than the encapsulated CUR concentration, allowing us to exploit CUR's chemosensitizer activity and DOX's high cytotoxicity activity.

Table 4.1B Effect of DOX concentration on hydrodynamic diameter, PDI, zeta potential, and % EE of DOX liposomes

DOX concentration (mg)	Average Hydrodynamic Diameter (nm)	Average PDI	Average Zeta Potential	Average % EE
0.4	288.44 ± 10.63	0.36 ± 0.08	-22.16 ± 1.18	32.71 ± 10.7
0.2	136.92 ± 4.45	0.10 ± 0.03	-20.13 ± 1.05	42.70 ± 1.11
0.1	123.31 ± 7.16	0.09 ± 0.01	-21.70 ± 0.18	79.44 ± 1.70
0.05	120.47 ± 0.93	0.09 ± 0.03	-16.44 ± 2.61	76.90 ± 9.54
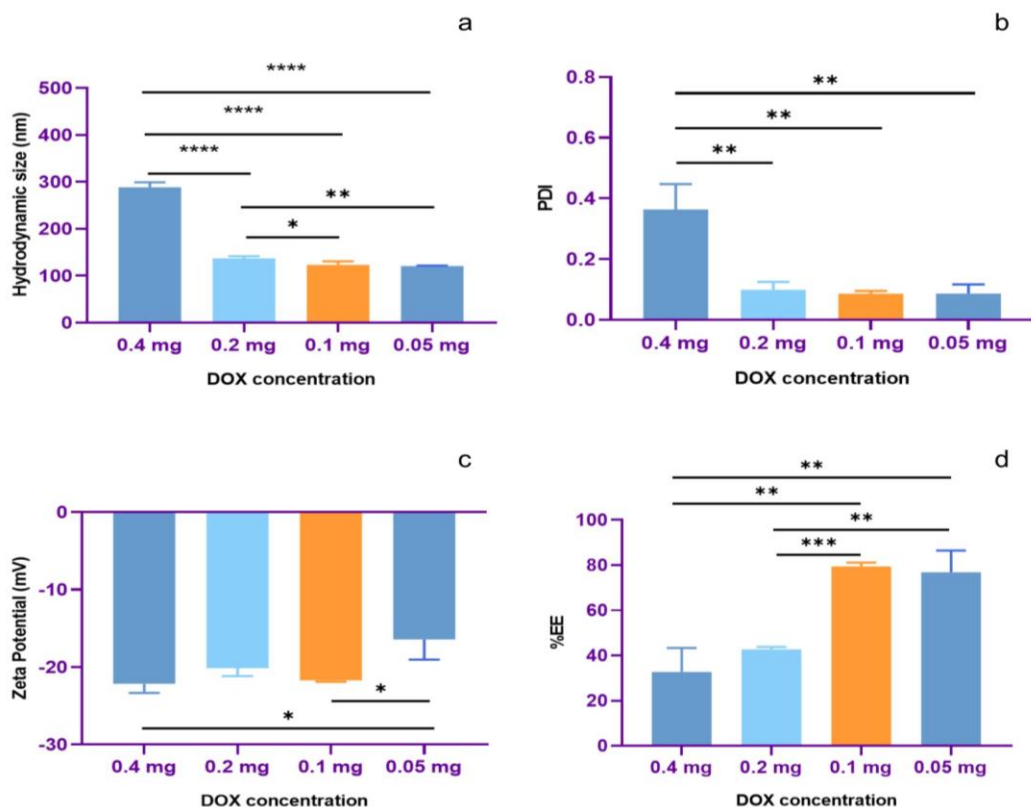
Figure 4.1B Effect of DOX concentration on hydrodynamic diameter (a), PDI (b), zeta potential (c), and % EE (d) of DOX liposomes

4.3.2B Optimization of downsizing step of DOX liposomes

On extruding DOX liposomes 5 and 11 times, the hydrodynamic diameter, PDI, zeta potential, and % EE remained unchanged; we optimized 5 extrusion passes to downsize the DOX liposomes (Table 4.2B) (Figure 4.2B).

Table 4.2B Effect of extrusion passes on hydrodynamic diameter, PDI, zeta potential, and % EE of DOX liposomes

	Average Hydrodynamic Diameter (nm)	Average PDI	Average Zeta potential	Average % EE
Extrusion passes 05	129.79 ± 5.07	0.08 ± 0.001	-20.49 ± 0.77	78.24 ± 7.59
Extrusion passes 11	123.31 ± 7.16	0.09 ± 0.01	-21.70 ± 0.18	79.44 ± 1.70
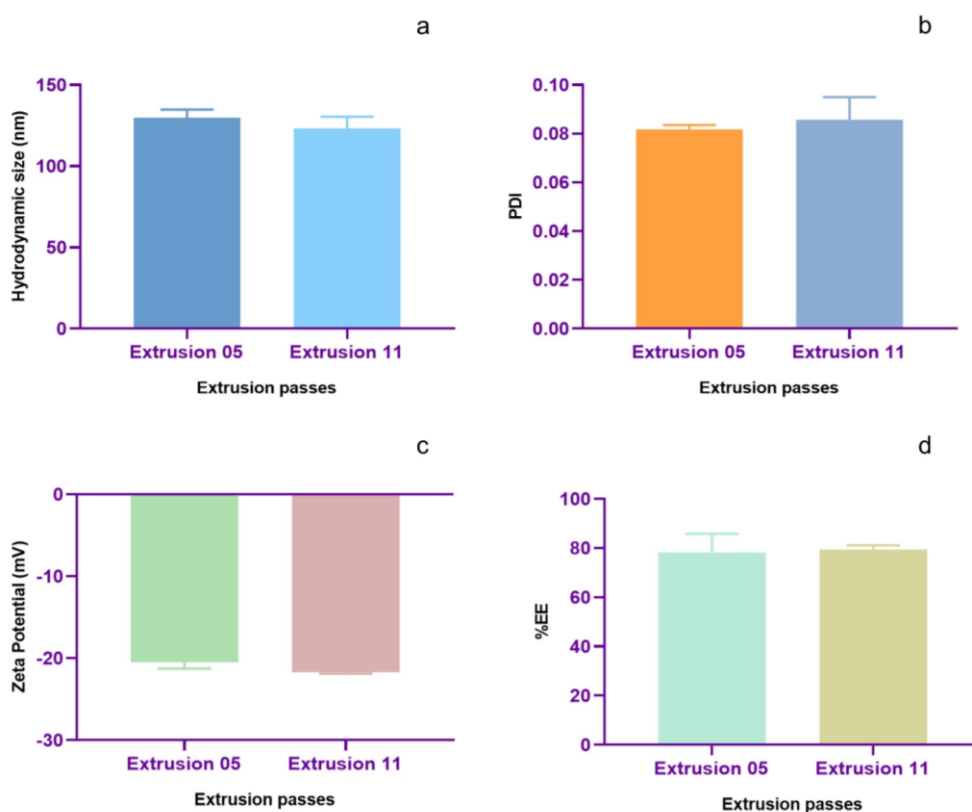
Figure 4.2B Effect of extrusion passes on hydrodynamic diameter (a), PDI (b), zeta potential (c), and % EE (d) of DOX liposomes

4.3.3B Synthesis of PEGylated DOX liposomes

We fabricated PEGylated DOX liposomes with 1 mole % of DSPE-mPEG2000, 7:3 molar ratio of PC: CHOL, and 0.1 mg DOX, and optimized the downsizing step by varying the number of extrusion passes (5 and 11 times) (Table 4.3B).

Table 4.3B Effect of extrusion passes on hydrodynamic diameter, PDI, zeta potential, and % EE of PEGylated DOX liposomes

	Average Hydrodynamic Diameter (nm)	Average PDI	Average Zeta potential	Average % EE
Extrusion passes 05	118.57 ± 5.01	0.08 ± 0.01	-9.25 ± 1.46	74.42 ± 2.17
Extrusion passes 11	110.4 ± 2.43	0.05 ± 0.01	-10.2 ± 1.58	76.17 ± 5.51

The hydrodynamic diameter, PDI, zeta potential, and % EE remained unchanged; thus, we optimized 5 extrusion passes for PEGylated DOX liposomes per the drug delivery mandates (Figure 4.3B).
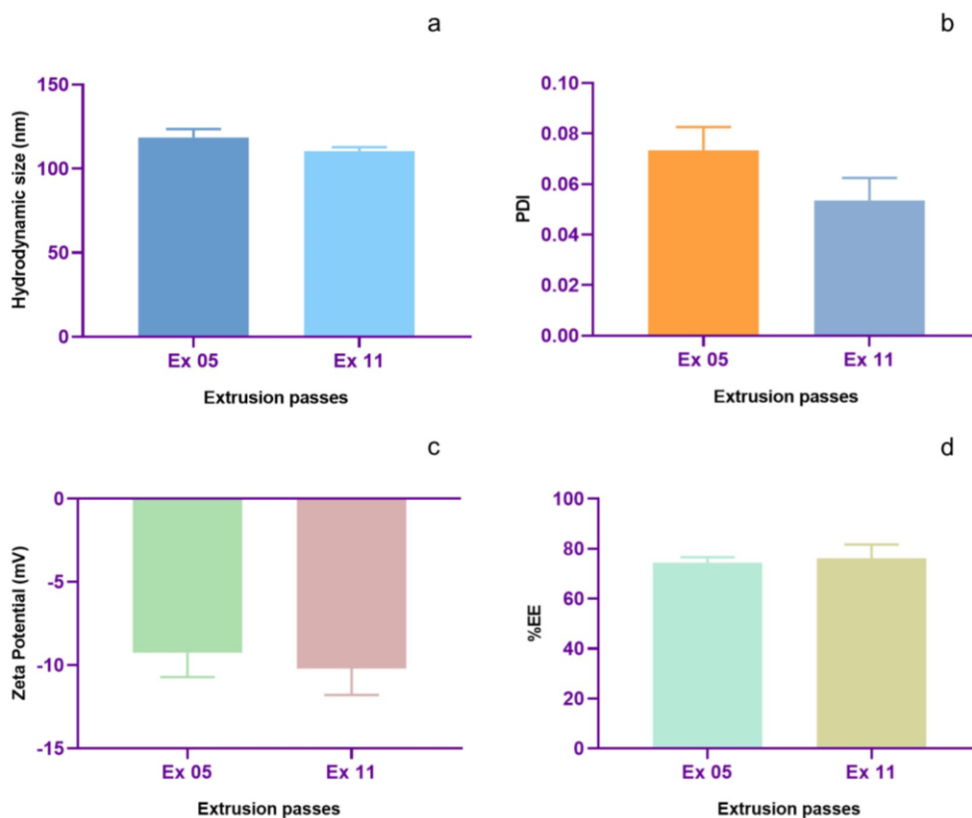
Figure 4.3B Effect of extrusion passes on hydrodynamic diameter (a), PDI (b), zeta potential (c), and % EE (d) of PEGylated DOX liposomes

4.4B Characterization of DOX loaded liposomes

We synthesized DOX loaded liposomes with the optimized values and characterized them by various analytical techniques.

4.4.1B Hydrodynamic diameter, PDI, and zeta potential

The DLS graph recorded the hydrodynamic diameter and PDI of DOX liposomes at 121.1 nm and 0.08, respectively, and for PEGylated DOX liposomes at 109.7 nm and 0.08, respectively (Figure 4.4B). The single sharp peaks for both formulations confirm a monodisperse population with smaller liposomes. We recorded the zeta potential of DOX liposomes at -20.49 ± 0.77 mV

with incipient stability and for PEGylated DOX liposomes at -9.25 ± 1.46 mV in the neutral range due to PEG functionalization of the liposomal surface.
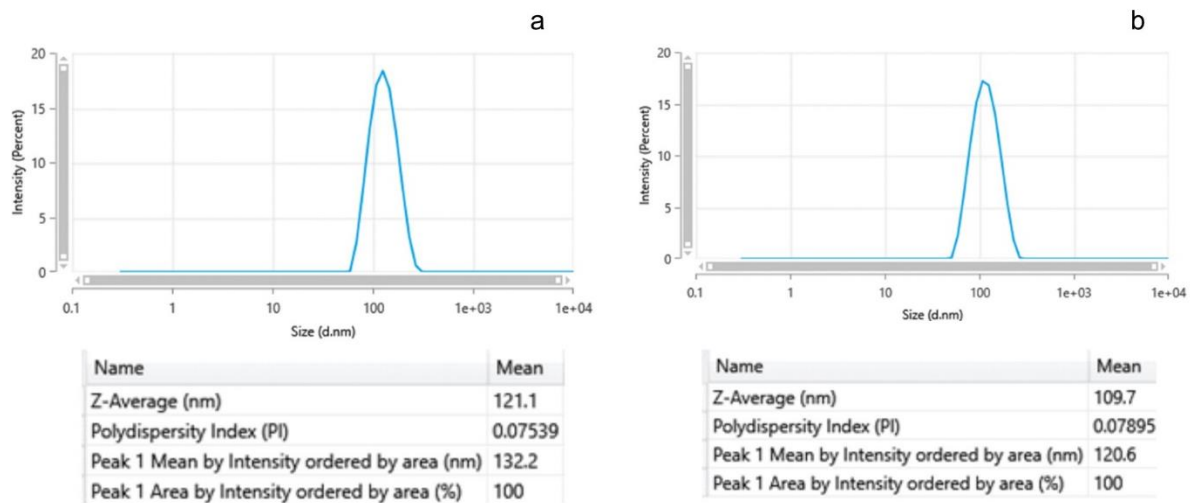
Figure 4.4B Hydrodynamic diameter and PDI of DOX liposomes (a) and PEGylated DOX liposomes (b)

The hydrodynamic diameter and PDI of DOX liposomes and PEGylated DOX liposomes were equivalent, corresponding to the effective downsizing of the particles. But the absolute zeta potential values reduced significantly (t-test p value = 0.0003) after functionalizing the liposomal surface with PEG that masks the charges on the surface (Figure 4.5B).
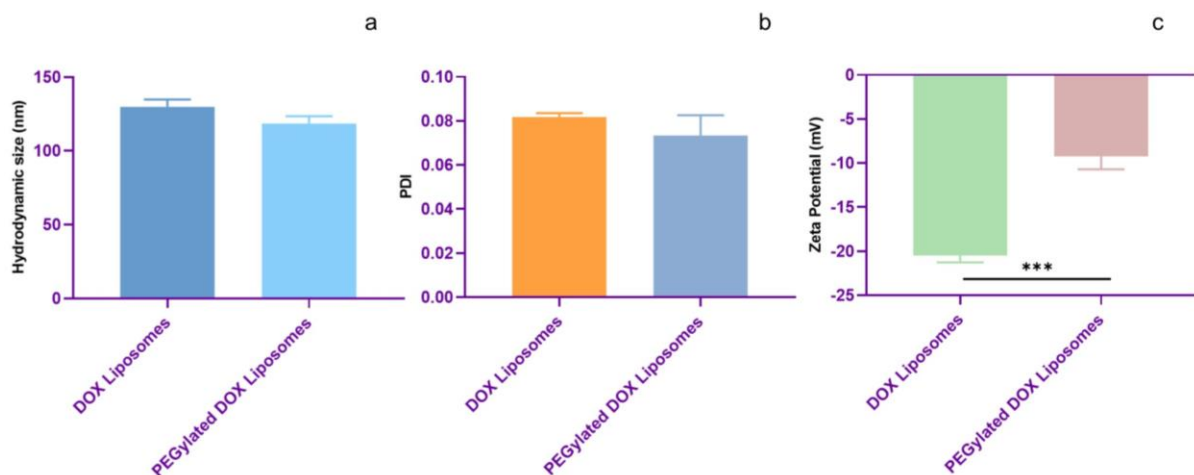
Figure 4.5B Comparison of hydrodynamic diameter (a), PDI (b), and zeta potential (c) of DOX and PEGylated DOX liposomes

We observed comparable particle size and PDI values for plain liposomes and DOX liposomes, but the zeta potential values (t-test p value = 0.0247) changed significantly after DOX loading. For plain PEGylated liposomes and PEGylated DOX liposomes, the hydrodynamic diameter and zeta potential remained equivalent with significantly lower PDI (t-test p value = 0.0222) values (Figure 4.6B).
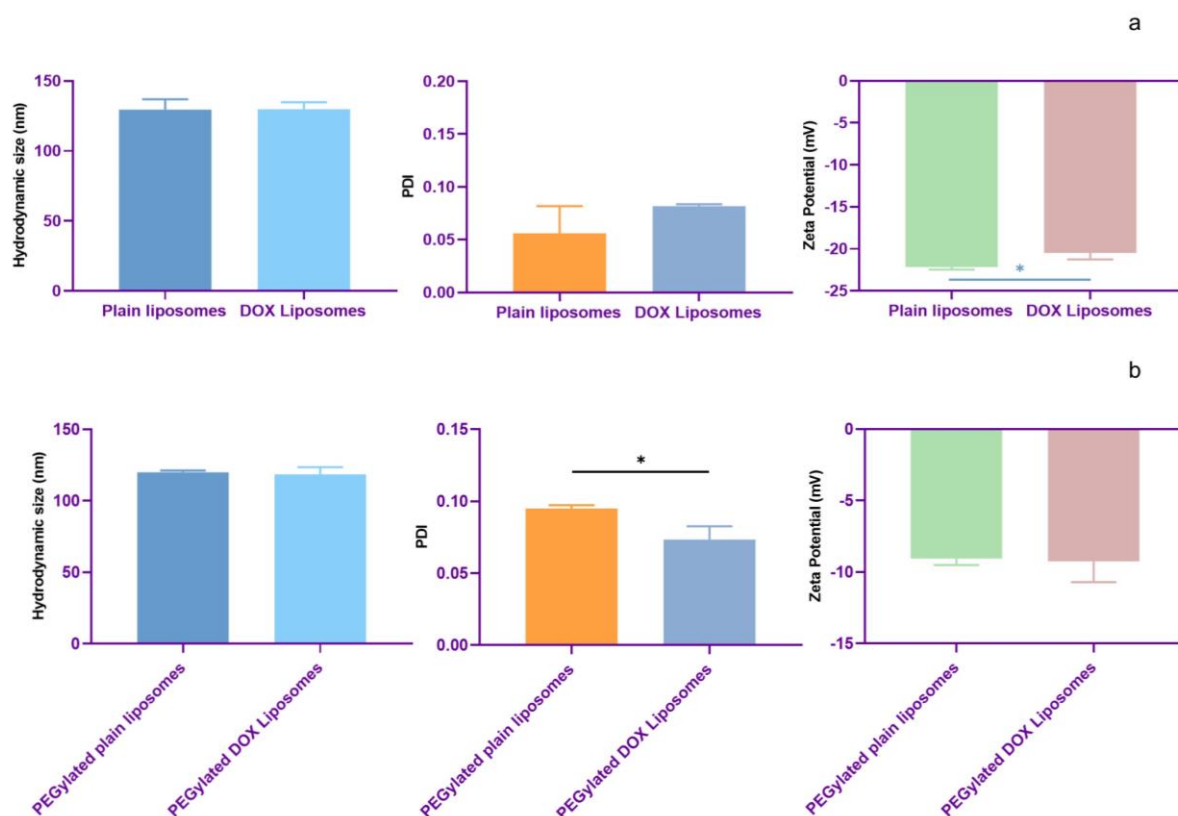
Figure 4.6B Comparative analysis of hydrodynamic diameter, PDI, and zeta potential of plain and DOX liposomes (a) and plain PEGylated and PEGylated DOX liposomes (b)

4.4.2B % EE and % DL

We calculated an equivalent % EE of DOX for DOX liposomes and PEGylated DOX liposomes at 78.24 ± 7.59 and 74.42 ± 2.17 %, respectively. We estimated an equivalent % DL for DOX liposomes and PEGylated DOX liposomes at 2.31 ± 0.21 and 2.51 ± 0.10 %, respectively (Figure 4.7B).
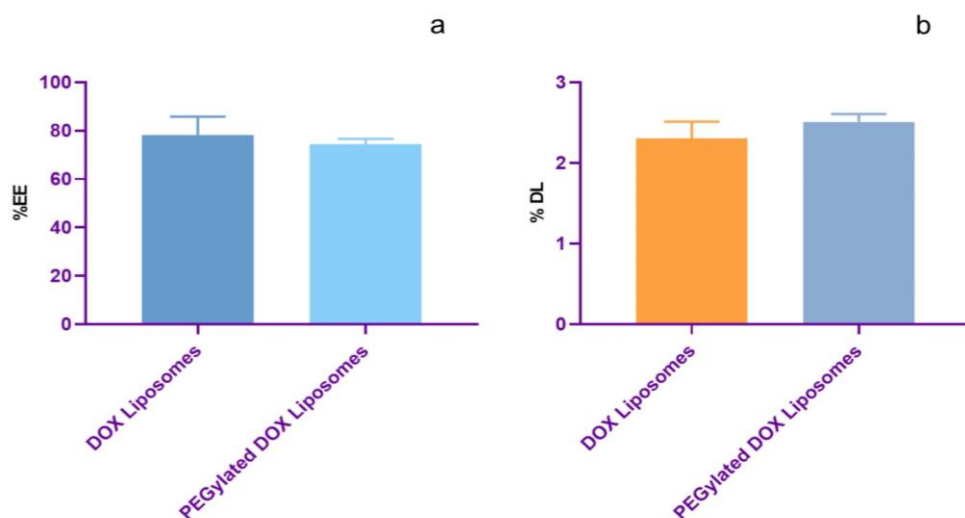
Figure 4.7B Comparison of % EE (a) and % DL (b) between DOX liposomes and PEGylated DOX liposomes

4.4.3B Morphology of DOX loaded liposomes

HRTEM images for DOX liposomes and PEGylated DOX liposomes show spherical structures with smooth surfaces (Figure 4.8B). We also observed irregular structures, a major limitation of imaging liposomes with conventional microscopy imaging (as discussed in Chapter 3).
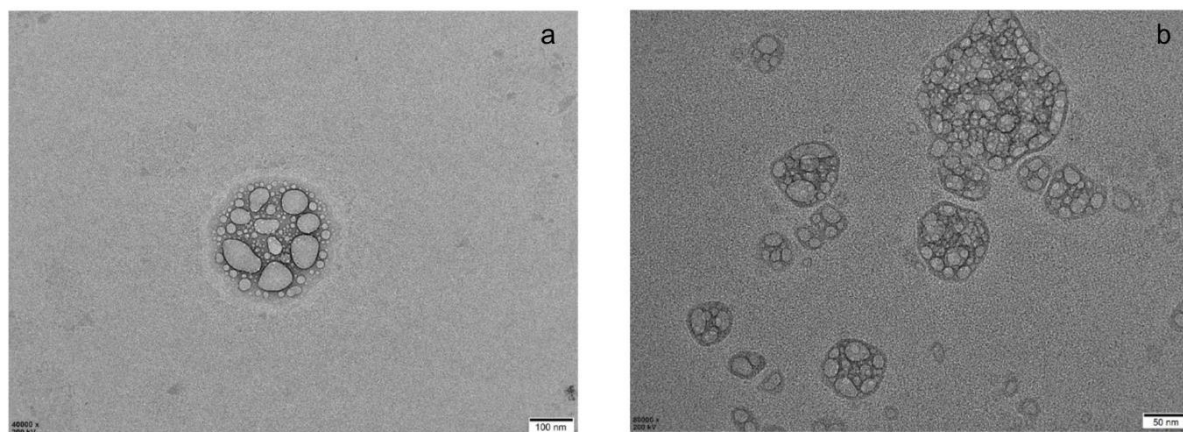
Figure 4.8B HRTEM image of DOX liposomes (a) and PEGylated DOX liposomes (b)

4.4.4B FTIR analysis

FTIR spectrum for plain DOX recorded characteristic peaks at 3523 cm^{-1} for N-H stretching, 3319 cm^{-1} for O-H stretching, 2899 cm^{-1} for C-H stretching, 1728 cm^{-1} for C=O cm^{-1} stretching,

1614 and 1581cm^{-1} for –NH stretching for amide group, 1407 cm^{-1} for C-C stretching, 1282 cm^{-1} for OH stretching, 1072 cm^{-1} for C-O stretching, 867 and 800 cm^{-1} for NH stretching, and 1521 cm^{-1} for the C=C aromatic ring (Figure 4.9B) (Jayakumar *et al.* 2012) (Unsoy *et al.* 2014) (Rahim *et al.* 2021) (Murugesan *et al.* 2020) (Yoncheva *et al.* 2020).
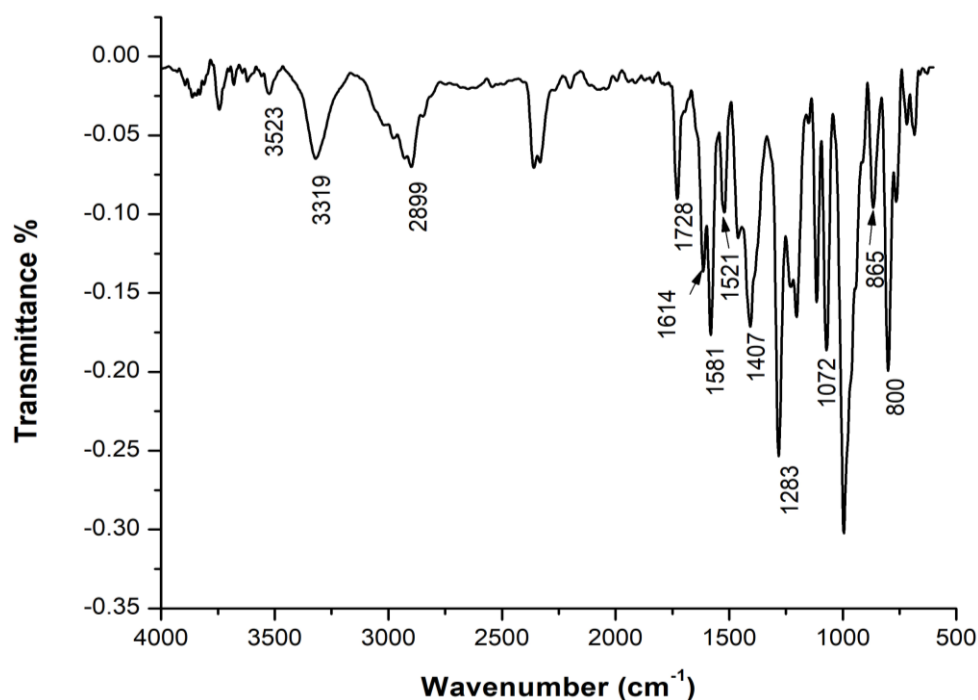
Figure 4.9B FTIR spectrum of plain DOX

We compared the FTIR spectra for DOX liposomes and PEGylated DOX liposomes with PC to determine drug loading, interaction between DOX and the liposomal components, and location of the drug in the liposomes (Figure 4.10B).

The FTIR spectra of DOX liposomes deviated from the spectra of PC: the OH stretching shifted from 3300 to 3392 cm^{-1} and also increased in intensity; the peaks for CH$_3$ antisymmetric and symmetric stretching remain unaltered at 2922 and 2852 cm^{-1}; the peak for C=O stretching shifted from 1736 to 1726 cm^{-1} and also reduced in intensity; the C=C stretching shifted from 1663 cm^{-1} to 1642 cm^{-1}; the CH$_2$ bending peak positioned at 1464 cm^{-1} and the CH$_3$ bending at 1378 cm^{-1}. The headgroup peak for PO^{2-} antisymmetric stretching remained unchanged at 1225 cm^{-1} but reduced in intensity, the peak for PO^{2-} symmetric stretching shifted from 1057 to 1051 cm^{-1}, and the P-O stretching shifted from 829 to 862 cm^{-1}.

The characteristic peaks for PEGylated DOX liposomes recorded a shift in the OH stretching to 3357 cm^{-1}; the CH antisymmetric and symmetric stretching wavenumbers at 2923 and 2856 cm^{-1}; the C=O stretch at 1735 cm^{-1}; the C=C stretching at 1648 cm^{-1}; the CH$_2$ bending peak at 1458 cm^{-1}; the CH$_3$ bending at 1371 cm^{-1}; the PO^{2-} antisymmetric stretching peak shifted at 1226 cm^{-1}; the asymmetric stretching shifted at 1056 cm^{-1}, the P-O stretching at 835 cm^{-1}.

The wavenumbers for the hydrocarbon chain region remained unaffected, and the unaltered CH2 stretching vibrations confirmed the constant number of gauche conformers after DOX loading (Abdullah *et al.* 2022). DOX's OH and NH stretching merged and shifted, suggesting weak hydrogen bonds (Abdullah *et al.* 2022). The peak for the head group region disappeared in DOX liposomes, indicating that DOX interacted with the head group of PC by hydrogen bonds, suggesting that DOX resides in the lipid-water interfacial region (Mady *et al.* 2012). But, the head group peak in the PEGylated DOX liposomes suggests that DOX could not interact with the head group in the interfacial region owing to PEG groups extending into the aqueous core.

The C=O stretching reduced in intensity in the DOX liposomes, suggesting that DOX physically interacted with the lipids of the inner leaflet of the bilayer, also explaining the shift in the C=C stretching as the C=O bonds are slightly submerged in the bilayer and DOX interacting with the bilayer changes the membrane fluidity. This trend disappeared in the PEGylated DOX liposomes due to PEG extending into the aqueous cavity (Deygen *et al.* 2016). The absence of any new peaks suggested the lack of any chemical interactions but only physical interactions such as weak dipole-dipole interactions, hydrogen bonds or van der Waals interactions implying the successful loading of DOX in the liposomes (Haghiralsadat, *et al.* 2017) (Ghosh *et al.* 2020) (Haghiralsadat *et al.* 2018).
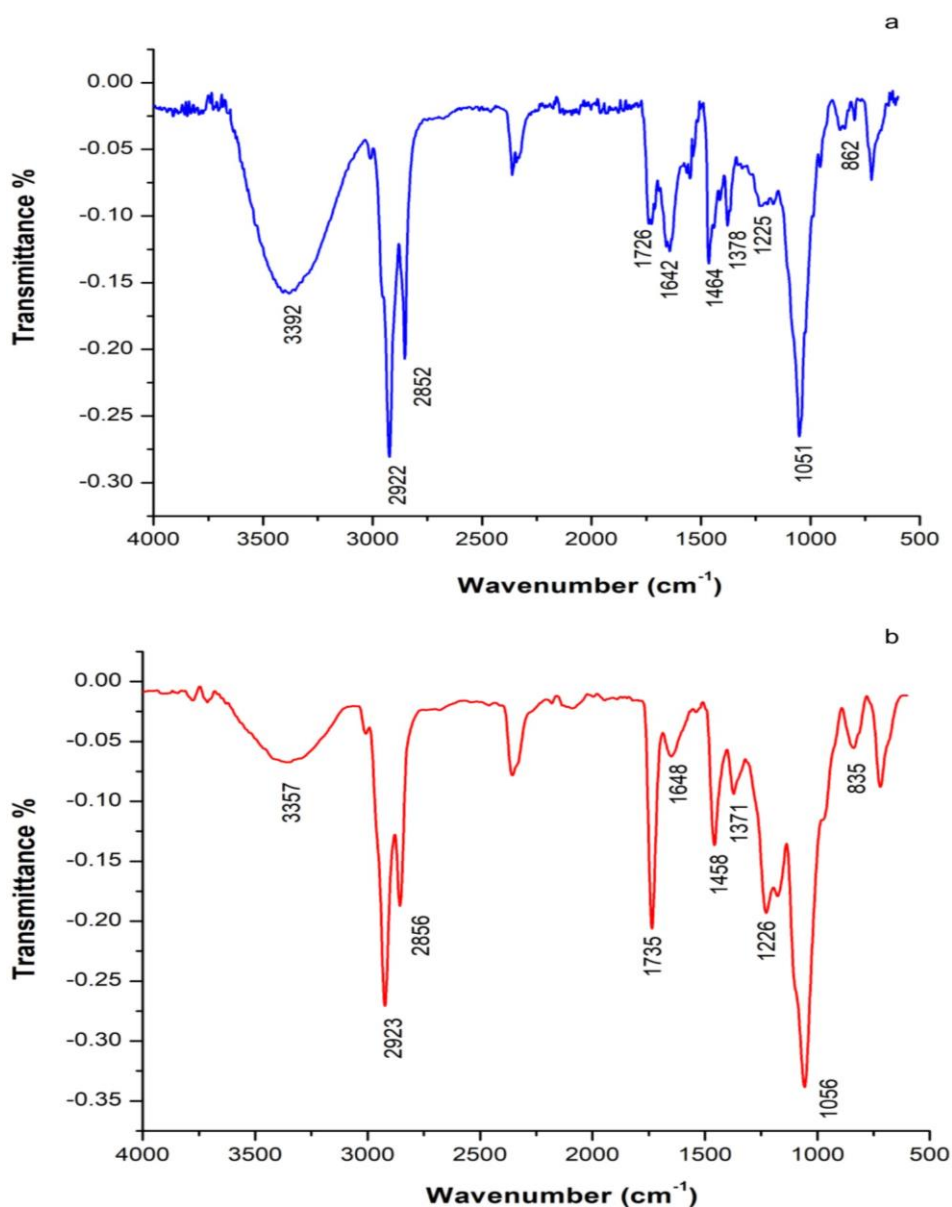
Figure 4.10B FTIR spectra of DOX liposomes (a) and PEGylated DOX liposomes (b)

4.4.5B TGA analysis

We recorded the degradation onset temperature for DOX at 213 °C with 55.27% degradation. The peak shifted from 182.46 °C for PC and 240.78 °C for plain liposomes to 227.67 °C for DOX liposomes with an initial 10.96% degradation corresponding to the removal of any water followed by a 57.9% degradation (Figure 4.11B). The degradation onset temperature for PEGylated DOX liposomes shifted from 182.46 °C for PC and 248.53 °C for plain PEGylated liposomes to 268.88 °C with an initial degradation of 4.05%, attributing to the removal of water followed by an 81.03% degradation.
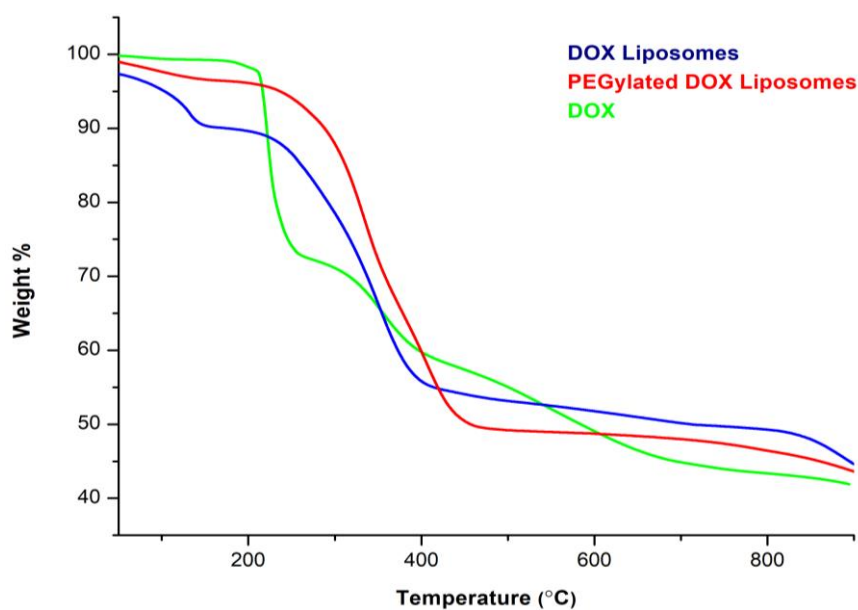
Figure 4.11B TGA thermogram of DOX (green), DOX liposomes (blue), and PEGylated DOX liposomes (red)

4.4.6B DSC analysis

We observed an endotherm for plain DOX at 50.44 °C. The endotherm for DOX liposomes and PEGylated DOX liposomes broadened and occurred at 104.97 and 84.17 °C, respectively (Figure 4.12B). As seen in the FTIR spectra, DOX resides in the aqueous cavity or the water-lipid interface with DOX interacting with the bilayer in the DOX liposomes, unlike the PEGylated DOX liposomes resulting in the broadening of the endotherm for the former formulation. Compared to the PC, the shift to lower temperatures suggests the synthesis of liposomes.

The endotherm for DOX disappeared in the liposomes, confirming the loading of the drug. The physical interactions are severed, resulting in a shift in the endotherm to lower temperatures (Niu *et al.* 2012). The endotherm's broad nature confirms the drug's presence in the bilayer region (Campani *et al.*, 2020). The higher endotherm than the storage temperature suggests higher storage stability of the particles without undergoing a phase transition (Chaves *et al.* 2018).
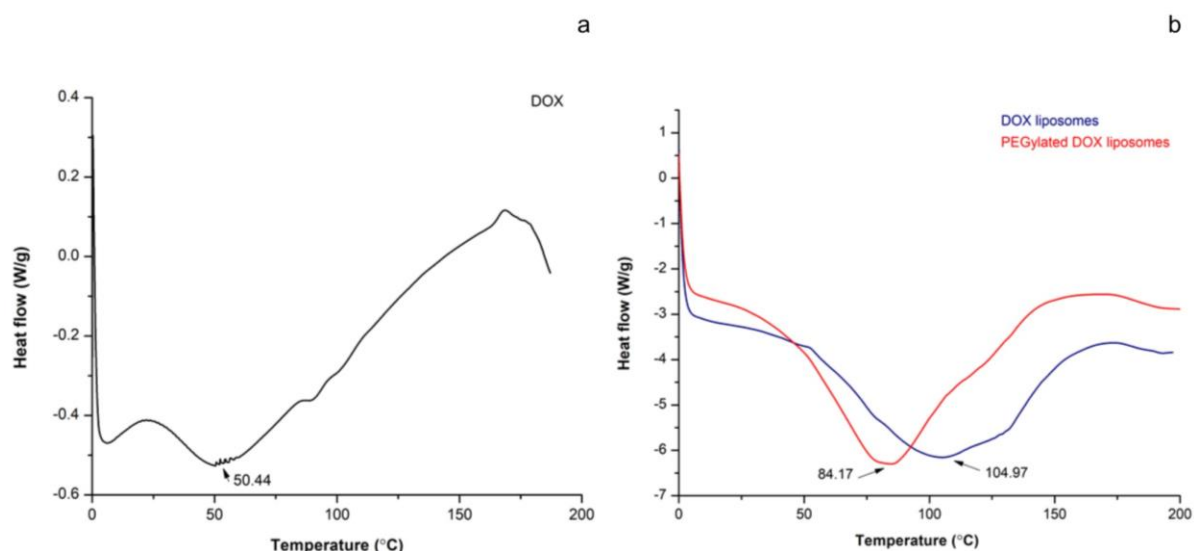
Figure 4.12B DSC thermogram of plain DOX (a), DOX liposomes (blue), and PEGylated DOX liposomes (red) (b)

4.5 B Conclusion

With this study, we prepared DOX loaded liposomes with a 10 mg/ml concentration of lipids, a 7: 3 molar ratio of PC: CHOL, and 1 mole % DSPE-mPEG2000. We optimized 0.1 mg DOX and 5 extrusion passes for both DOX liposomes and PEGylated DOX liposomes. The DOX liposomes had hydrodynamic diameter, PDI, and zeta potential of 129.79 ± 5.07 nm, 0.08 ± 0.001, and -20.49 ± 0.77 mV, respectively; for PEGylated DOX liposomes at 118.57 ± 5.01 nm in size, 0.07 ± 0.01 PDI and -9.25 ± 1.46 mV respectively.

We calculated the % EE and % DL for DOX liposomes at 78.24 ± 7.59 % and 2.31 ± 0.21 %, respectively, and for PEGylated DOX liposomes at 74.42 ± 2.17 % and 2.51 ± 0.10 % respectively. HRTEM determined particles with spherical morphology. FTIR analysis suggested a successful loading of DOX in the aqueous cavity and the water-lipid interface. The TGA and DSC analysis confirmed the successful loading of DOX and determined high stability for the formulations. Thus, the results suggest the synthesis of robust DOX loaded liposomes according to the drug delivery mandates.

CHAPTER 4C

Optimization, Synthesis, and Characterization of CUR-DOX loaded liposomes

4.1C Introduction

Breast cancer is a heterogeneous disease influenced by MDR that affects the therapeutic potential of drugs and requires higher dosages. Researchers explore the co-delivery of drugs to acknowledge the MDR in breast cancer cells by using a chemotherapeutic drug along with a chemosensitizer. Dual drugs loaded in a single particle are more effective than combination treatment of single drug loaded formulations as it ensures a constant ratio of drugs reaching the target site.

CUR has pleiotropic effects on cancer cells along with a chemosensitizer attribute. Studies suggest that CUR enhances the cytotoxic activity of DOX that otherwise has a poor therapeutic potential due to MDR. We prepared CUR-DOX loaded liposomes with a 7: 3 molar ratio of PC: CHOL, a 1: 50 (wt. / wt.) ratio of CUR: lipids, and 0.1 mg of DOX; for stealth liposomes, we added 1 mole % of DSPE-mPEG2000. We intentionally kept the concentration of CUR higher than DOX since DOX shows an effective chemotherapeutic effect at lower concentrations, and CUR would enhance the action of DOX, which shows a cytotoxic attribute on cancer cells at a comparatively higher concentration.

We synthesized CUR-DOX loaded liposomes with the final optimized values without undertaking any optimization process and characterized the liposomes by various analytical techniques. We deduced the hydrodynamic diameter, PDI, and zeta potential by DLS; morphology by HRTEM; functional groups by FTIR analysis; % EE and % DL; and thermal stability by TGA and DSC.

4.2C Methods

4.2.1C Synthesis of CUR-DOX liposomes

We fabricated CUR-DOX liposomes and PEGylated CUR-DOX liposomes as per the protocol established in Chapter 2, section 2.2.4 -with 7:3 PC: CHOL molar ratio and 1:50 CUR: lipid (wt. /wt.) ratio added in the thin film formation step, and 0.1 mg DOX in the thin film hydration step; PEGylated CUR-DOX liposomes were formulated with 1% DSPE-mPEG2000 added in the thin film formation step. We extruded the liposomes through a 100 nm polycarbonate membrane for 5 extrusion passes- as optimized in the previous chapters.

4.2.2C Characterization of CUR-DOX loaded liposomes

We characterized CUR-DOX liposomes and PEGylated CUR-DOX liposomes for hydrodynamic diameter, PDI, and zeta potential by DLS; the % EE and % DL; morphology by HRTEM imaging; functional groups by FTIR analysis; and thermal stability by TGA and DSC -details mentioned in Chapter 2, section 2.3.

4.3C Results and Discussion

We formulated CUR-DOX loaded liposomes by the optimized process parameters of liposomal synthesis (Chapter 3), PC: CHOL molar ratio, CUR concentration, and DSPE-mPEG2000 mole % (Chapter 4a), and DOX concentration (Chapter 4B).

4.3.1C Synthesis of CUR-DOX liposomes

We passively loaded CUR and DOX: CUR, a hydrophobic drug, attains a higher drug encapsulation by the passive loading technique; we passively loaded DOX to prevent the release of CUR that positions itself in the lipid bilayer and can diffuse out during DOX loading. Studies report a passive loading technique to load CUR in the bilayer region and DOX in the aqueous cavity of liposomes. We intended a higher CUR concentration than DOX, as it reverses MDR, is cytotoxic, and can synergistically assist DOX's uptake and chemotherapeutic activity.

The hydrodynamic diameter and PDI of CUR-DOX liposomes and PEGylated CUR-DOX liposomes align with the drug delivery mandates. 5 extrusion passes effectively reduced the particle size and PDI, synthesizing a monodisperse population of smaller particles, and the zeta potential characterized the particles with incipient stability for CUR-DOX liposomes and in a neutral range for PEGylated CUR-DOX liposomes (Table 4.1C).

Table 4.1C Hydrodynamic diameter, PDI, zeta potential, and % EE of CUR-DOX liposomes and PEGylated CUR-DOX liposomes

	Average Hydrodynamic diameter (nm)	Average PDI	Average zeta potential (mV)	Average % EE
CUR-DOX liposomes	125.4 ± 3.26	0.08 ± 0.02	-19.07 ± 3.03	**CUR:** 76.82 ± 3.9 **DOX:** 78.66 ± 2.49
PEGylated CUR-DOX liposomes	121.51 ± 0.82	0.09 ± 0.02	-10.20 ± 1.60	**CUR:** 77.57 ± 7.94 **DOX:** 73.32 ± 2.84

4.4C Characterization of CUR-DOX loaded liposomes

4.4.1C Hydrodynamic diameter, PDI, and zeta potential

The DLS graph recorded the hydrodynamic diameter and PDI for CUR-DOX liposomes at 116 nm and 0.07, respectively, and for PEGylated CUR-DOX liposomes at 121.1 nm and 0.09, respectively. The single sharp peaks correspond to a smaller sized and monodisperse population (Figure 4.1C). The negative zeta potential value of the PEGylated CUR-DOX liposomes significantly decreased from -19.07 ± 3.03 to -10.2 ± 1.6 mV, confirming that the PEG surface functionalized the liposomal surface.
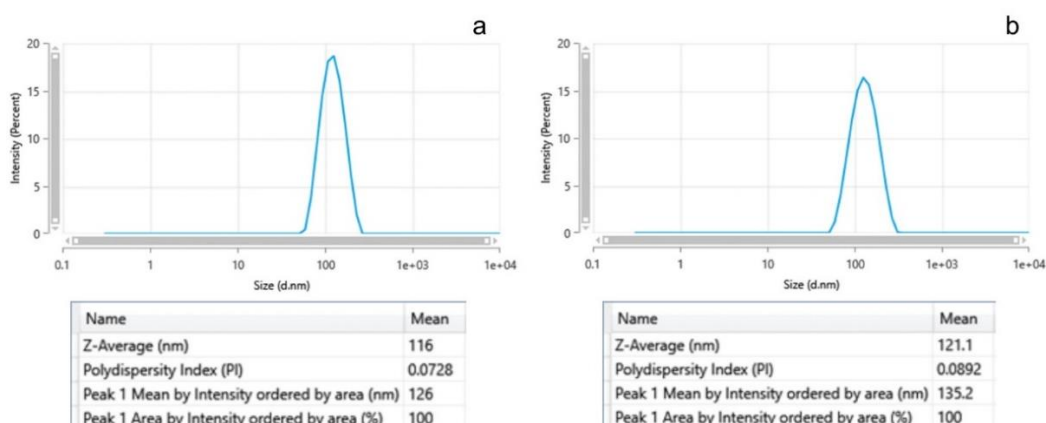
Figure 4.1C DLS graphs of CUR-DOX liposomes (a) and PEGylated CUR-DOX liposomes (b)

The hydrodynamic diameter and PDI of CUR-DOX liposomes and PEGylated CUR-DOX liposomes remained unchanged. But, a significant change in the zeta potential values (t-test p value = 0.0110) confirms that the PEG surface functionalized the liposomal surface (Figure 4.2C).
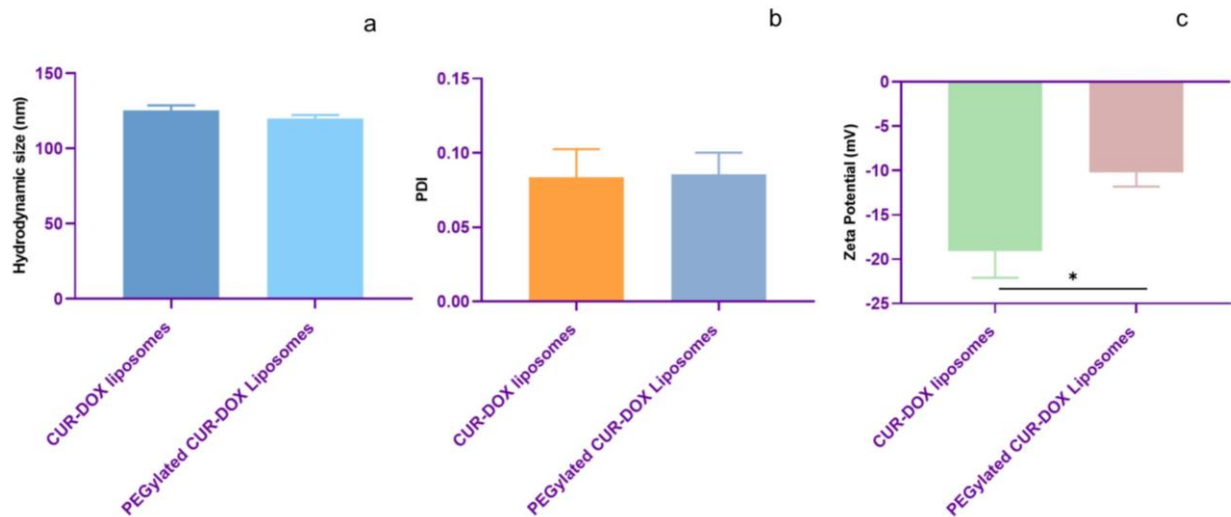
Figure 4.2C Comparative analysis of hydrodynamic diameter (a), PDI (b), and zeta potential (c) of CUR-DOX liposomes and PEGylated CUR-DOX liposomes

We compared plain liposomes with CUR-DOX liposomes and noted that the particle size, PDI, and zeta potential values remained unaltered; the sizes, PDI, and zeta potential of plain PEGylated and PEGylated CUR-DOX liposomes also stayed unchanged (Figure 4.3C).
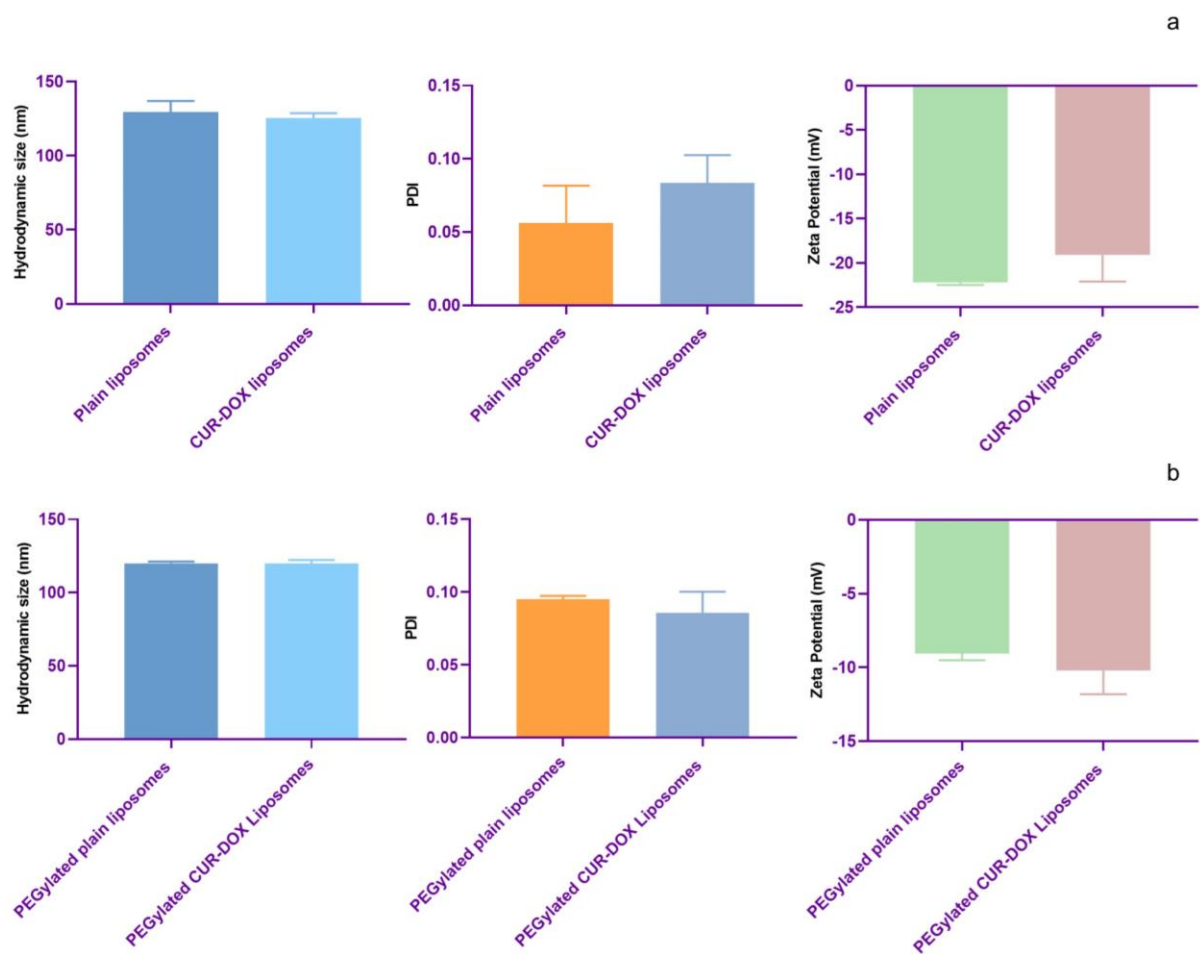
Figure 4.3C Comparative analysis of hydrodynamic diameter, PDI, and zeta potential of plain liposomes and CUR-DOX liposomes (a) and plain PEGylated liposomes and PEGylated CUR-DOX liposomes (b)

We compared CUR liposomes, DOX liposomes, and CUR-DOX liposomes and noted insignificant changes in the particle size, PDI, and zeta potential values for both non-PEGylated and PEGylated counterparts (Figure 4.4C); this corresponds to the effective downsizing of the liposomes by extrusion.
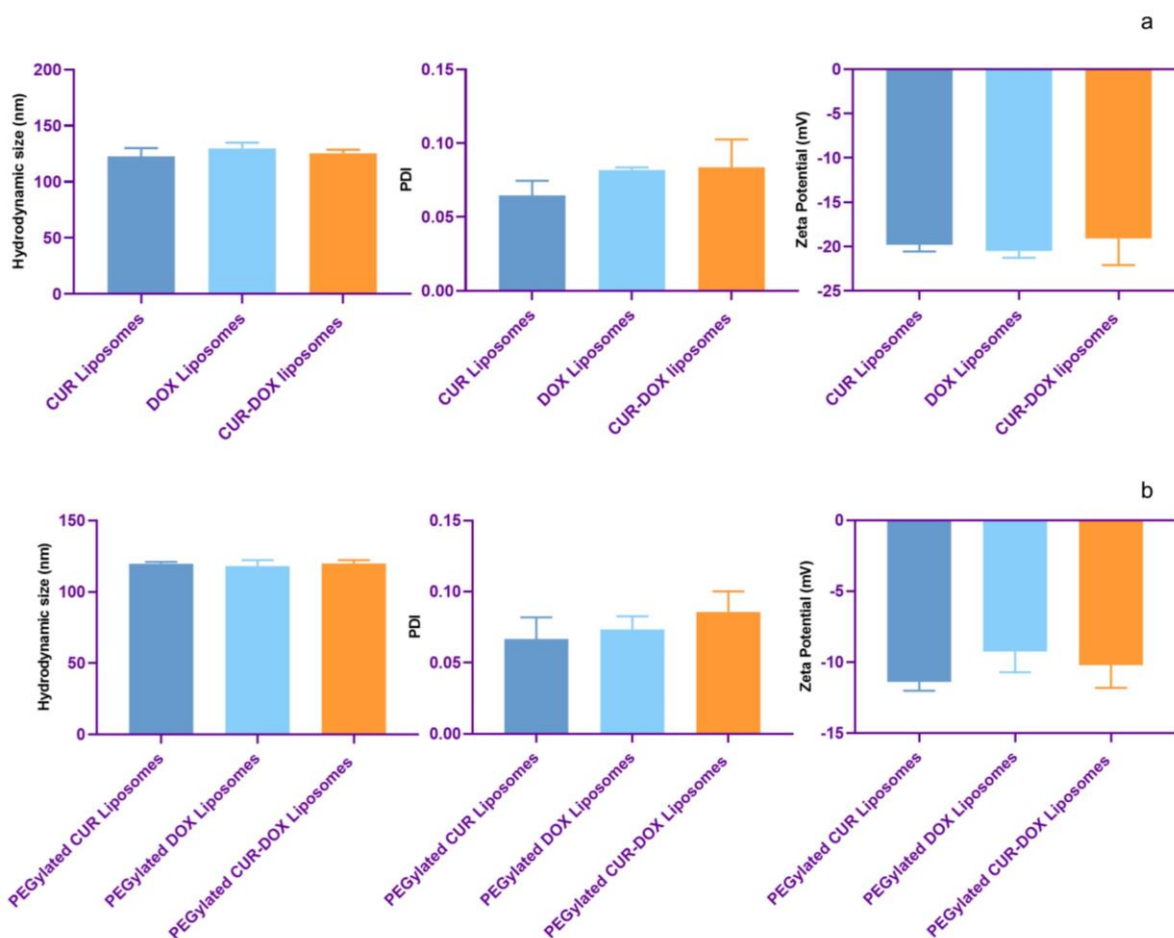
Figure 4.4C Comparative analysis of hydrodynamic diameter, PDI, and zeta potential of CUR liposomes, DOX liposomes and CUR-DOX liposomes (a) and PEGylated CUR liposomes, PEGylated DOX liposomes and PEGylated CUR-DOX liposomes (b)

4.4.2C % EE and % DL

We calculated an equivalent % EE of CUR in CUR-DOX liposomes and PEGylated CUR-DOX liposomes at 76.82 ± 3.9 and $77.57 \pm 7.95\%$ respectively, and for DOX at 78.66 ± 2.49 and 73.32 ± 2.84 % respectively. The % DL of CUR-DOX liposomes and PEGylated CUR-DOX liposomes were equivalent and calculated at 4.46 ± 0.30 and 4.25 ± 0.24 % respectively (Figure 4.5C).
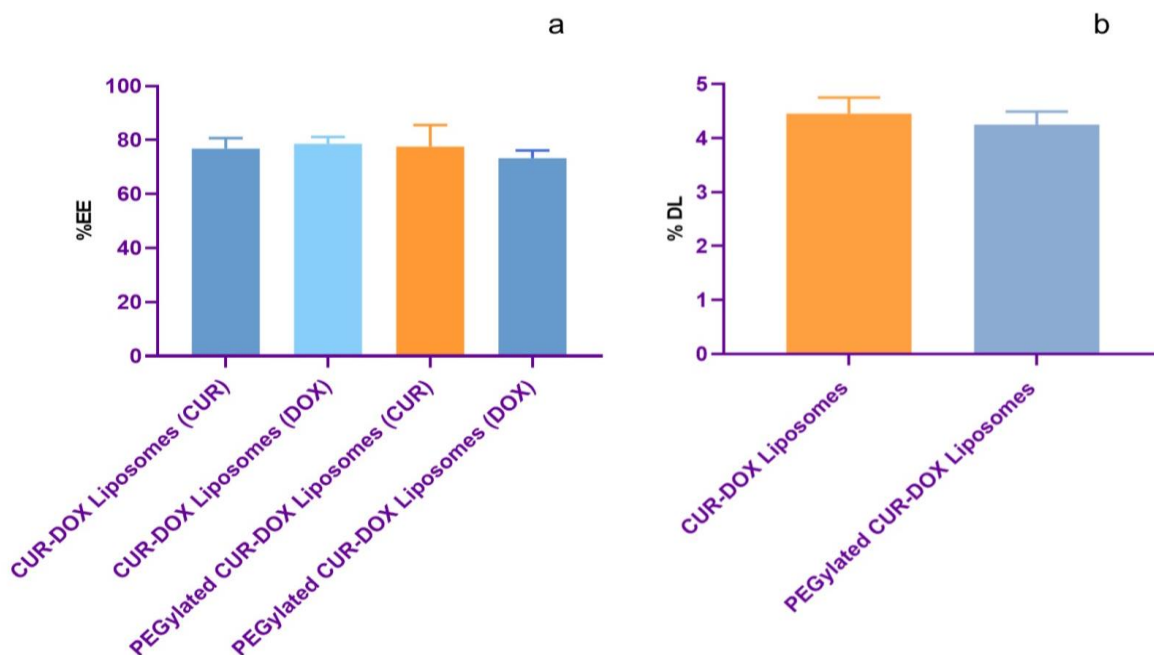
Figure 4.5C % EE and % DL of CUR-DOX and PEGylated CUR-DOX liposomes

We noted comparable % EE of all the single and dual drug loaded formulations suggesting the non-interference of either drug in the encapsulation of the other drug (Wang et al., 2011). But the % DL varied significantly (ANOVA p value = <0.0001) (Figure 4.6C): % DL for DOX liposomes was significantly lower than CUR liposomes (t-test p value = 0.0008), and CUR-DOX liposomes (t-test p value = 0.0005) corresponding to the less concentration of DOX loaded in the liposomes than CUR, and the % DL for CUR-DOX liposomes was significantly higher than CUR liposomes (t-test p value = 0.0135) attributing to the dual drug concentration than exceeds the single drug CUR.

We observed similar results for the PEGylated counterparts with comparable % EE but a significant change in the formulations' % DL (ANOVA p value = <0.0001). % DL for PEGylated DOX liposomes was significantly lower than PEGylated CUR liposomes (t-test p value = 0.0004), and CUR-DOX liposomes (t-test p value = 0.0003), and the % DL for PEGylated CUR-DOX liposomes was significantly higher than PEGylated CUR liposomes (t-test p value = 0.0038).
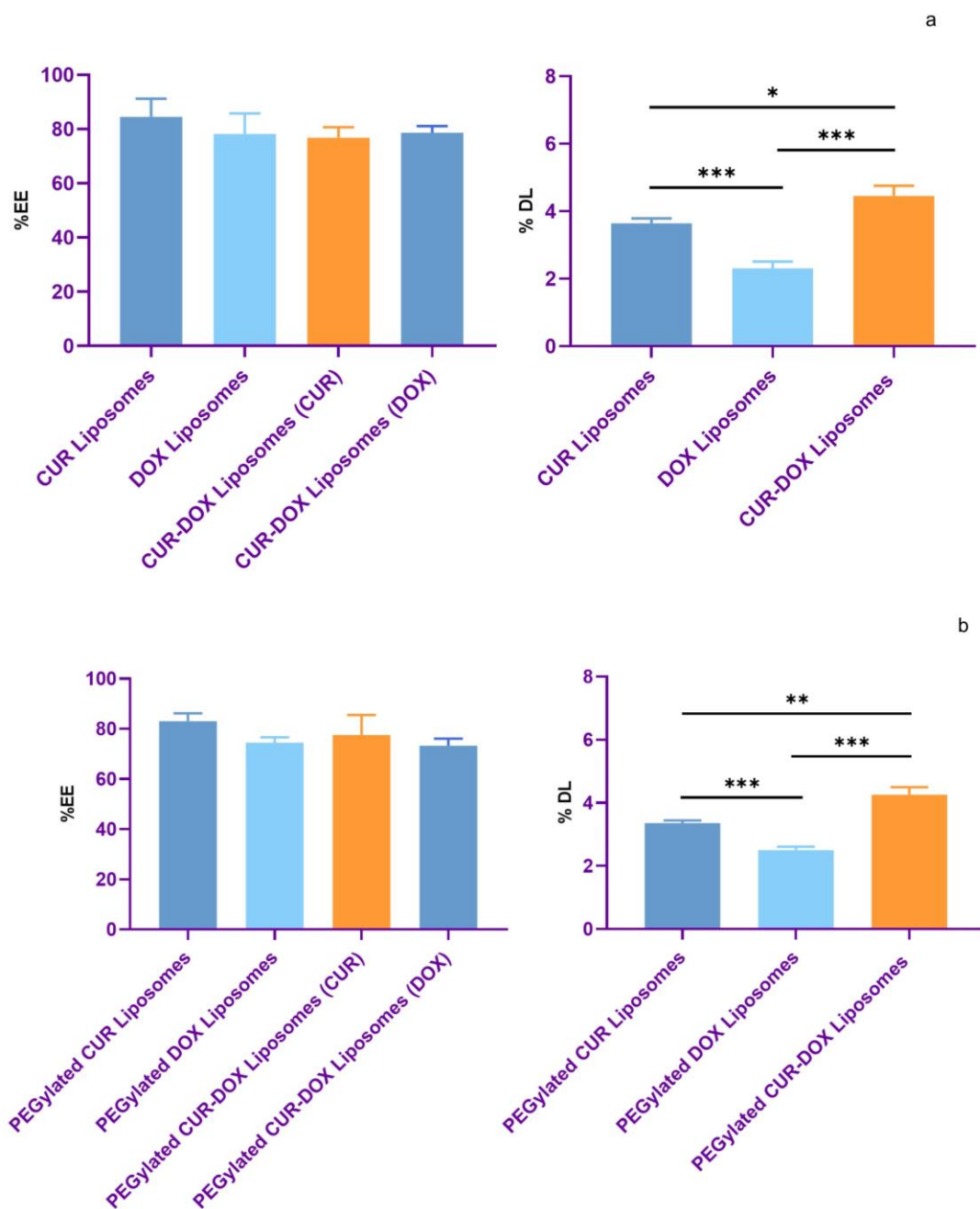
Figure 4.6C Comparison of % EE and % DL of CUR liposomes, DOX liposomes, and CUR-DOX liposomes (a), and PEGylated CUR liposomes, PEGylated DOX liposomes and PEGylated CUR-DOX liposomes (b)

4.4.3C Morphology of CUR-DOX loaded liposomes

The HRTEM images show spherical structures with smooth surfaces for CUR-DOX liposomes and PEGylated CUR-DOX liposomes (Figure 4.7C). Other irregular structures accompanied

and are common with imaging liposomes with conventional microscopy imaging (as discussed in Chapter 3).
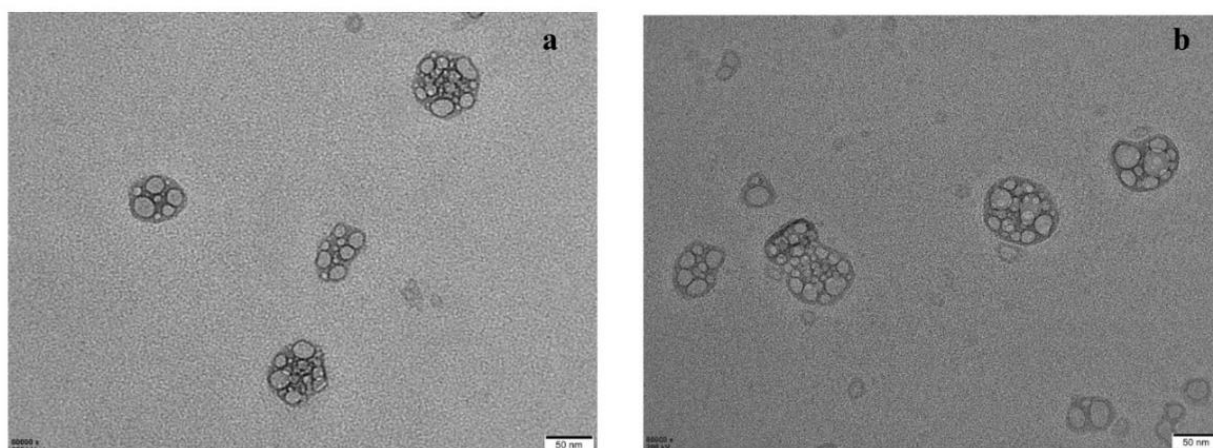
Figure 4.7C HRTEM of CUR-DOX liposomes (a) and PEGylated CUR-DOX liposomes (b)

4.4.4C FTIR analysis

We compared the FTIR spectra of CUR-DOX liposomes and PEGylated CUR-DOX liposomes with PC to examine if wavenumber deviated after drug loading, the drug-liposomal interactions, and the location of the drugs in the liposomes (Figure 4.8C).

For the CUR-DOX liposomes, the OH stretching peak shifted from 3300 to 3382 cm^{-1}; the antisymmetric CH stretching shifted from 2922 to 2924 cm^{-1}, and the CH symmetric stretching remained unaltered at 2853 cm^{-1}, suggesting an insignificant change in the order of the bilayer. The C=O (ester) stretching shifted from 1736 to 1739 cm^{-1}; the C=C stretching shifted from 1651 to 1642 cm^{-1}; the CH_2 and CH_3 bending remained unchanged at 1463 and 1377 cm^{-1} respectively. The characteristic peak of the PO_2^{-} antisymmetric stretching shifted from 1225 to 1222 cm^{-1} and reduced in intensity, as also seen for the DOX liposomes, and we noted the PO_2^{-} symmetric stretching at 1057 cm^{-1}. The P-O stretching shifted from 829 to 865 cm^{-1}.

For the PEGylated CUR-DOX liposomes, the OH stretching shifted to 3373 cm^{-1}. The CH antisymmetric stretching shifted to 2924 cm^{-1}, and the CH symmetric stretching remained unchanged at 2853 cm^{-1}. The carbonyl peak shifted to 1739 cm^{-1}. The C=C stretching shifted to 1648 cm^{-1}, the CH_2 bending vibration at 1463 cm^{-1}, and the CH_3 bending vibration at 1377

cm^{-1}. The characteristic peak of the PO$_2^{-}$ antisymmetric stretching appeared at 1222 cm^{-1}, the PO$_2^{-}$ symmetric stretching at 1057 cm^{-1}, and the P-O stretching at 823 cm^{-1}.

The shift in the OH stretching occurs when the hydrogen bonds disintegrate, and new bonds form between the phenolic OH of CUR and PC. The order of the bilayer remained unchanged after CUR and DOX loading. The C=O stretching shifted, suggesting that the drugs physically interact with the lipids, also corroborated by the shift in the C=C stretching of the bilayer -as the C=O bonds are slightly submerged in the bilayer, and any interaction changes the membrane fluidity.

The peak for the head group corresponding to PO$_2^{-}$ antisymmetric stretching disappeared for CUR-DOX liposomes, but the PO$_2^{-}$ symmetric stretching remained unchanged, indicating that DOX interacts with the head group region. The spectrum determines DOX positions in the interfacial region. In the PEGylated CUR-DOX liposomes, the PO$_2^{-}$ antisymmetric and symmetric stretching peaks remained unchanged compared to the DOX liposomes, as the PEG extensions in the aqueous activity hinder DOX from interacting with the lipid bilayer.

The FTIR spectra of both formulations mask the characteristic peaks of CUR and DOX that the drugs successfully incorporated in the liposomes. The absence of any new peaks suggests physical interactions such as weak dipole-dipole interactions, hydrogen bonds, or van der Waals interactions, and the absence of any chemical interactions.
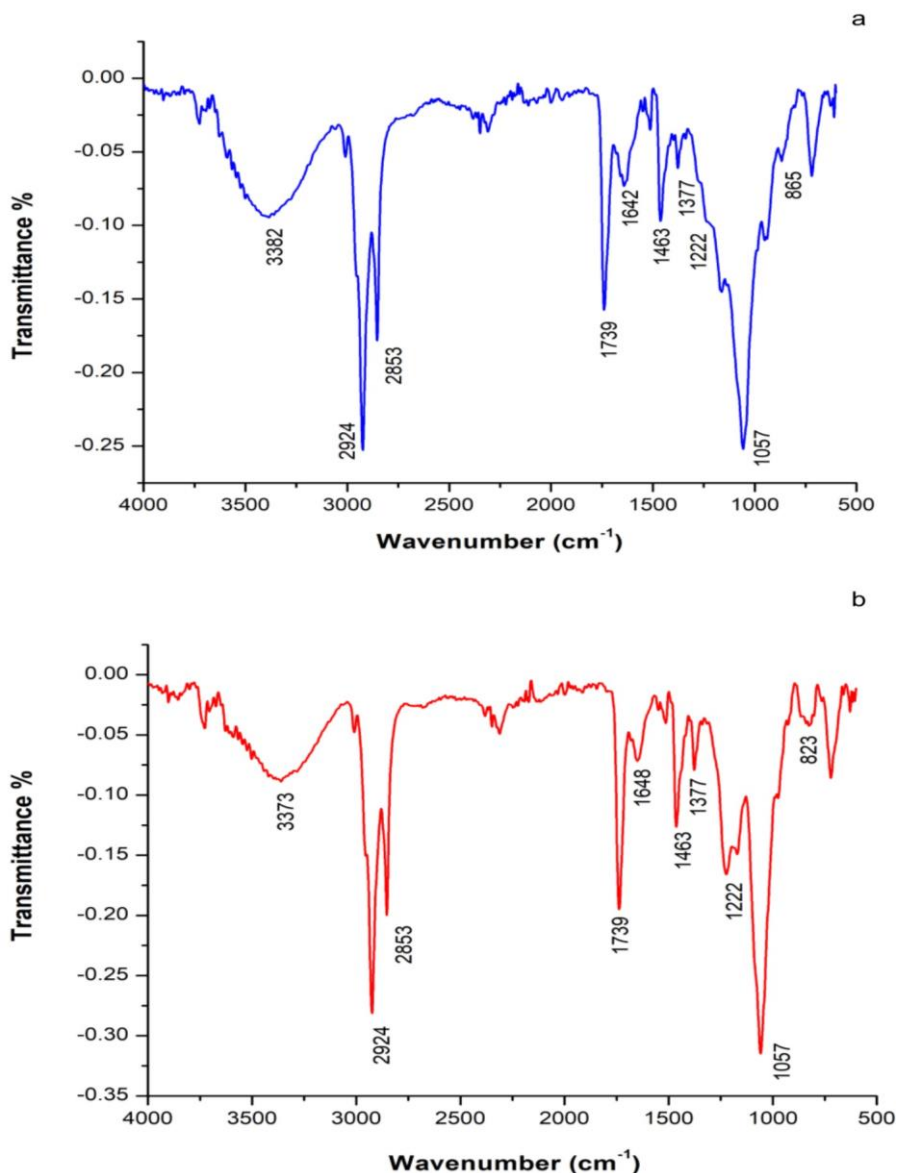
Figure 4.8C FTIR spectra of CUR-DOX liposomes (black) and PEGylated CUR-DOX liposomes (blue)

4.4.5C TGA analysis

The thermogram for CUR-DOX liposomes and PEGylated CUR-DOX liposomes determined the degradation onset temperature of 264.88 °C with 53.48% degradation and 254.61 °C with 76.6% degradation, respectively (Figure 4.9C).
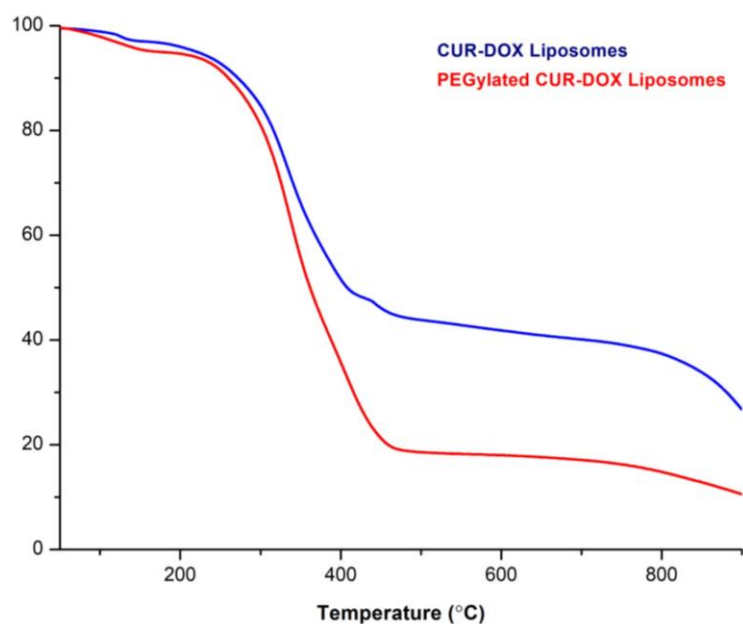
Figure 4.9C TGA thermogram of CUR-DOX (blue) and PEGylated CUR-DOX liposomes (red)

4.4.6C DSC analysis

We recorded an endotherm for CUR-DOX liposomes at 92.31 °C and for PEGylated CUR-DOX liposomes at 89.89 °C. The sharp endotherm for CUR at 176.55 °C and the endotherm for DOX at 50.44 °C disappeared, suggesting the successful loading of the drugs (Figure 4.10C). The endotherm for these formulations shifted to lower temperatures compared to PC, indicating the synthesis of liposomes due to disintegrating bonds between the liposomal components and the drugs.
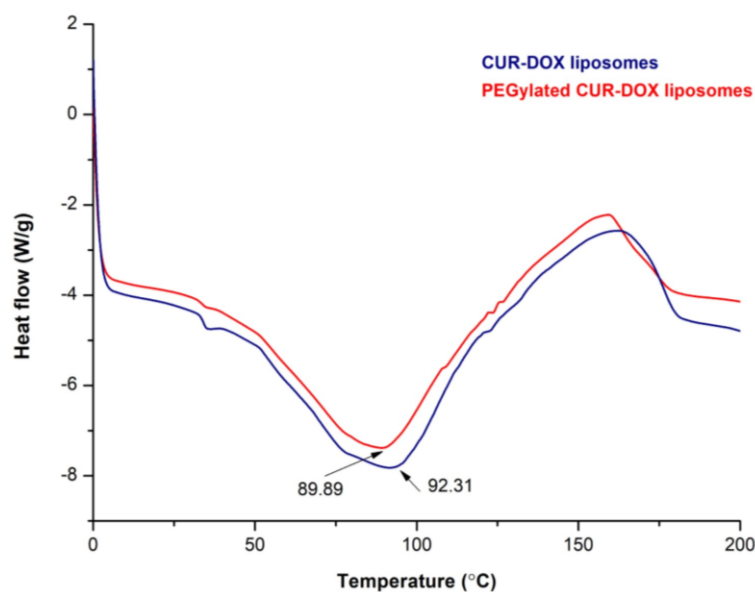
Figure 4.9C DSC thermogram of CUR-DOX (blue) and PEGylated CUR-DOX liposomes (red)

4.5C Conclusion

We prepared CUR-DOX loaded liposomes for drug delivery by incorporating both the drugs in a single particle. We synthesized these formulations by the final optimized values of 7: 3 molar ratio of PC and CHOL, 1: 50 (wt. / wt.) ratio of CUR: lipid, 0.1 mg DOX, and 1 mole % DSPE-mPEG2000. Upon characterizing, we confirmed the synthesis of CUR-DOX liposomes with the hydrodynamic diameter, PDI, and zeta potential at 117.36 ± 1.61 nm, 0.08 ± 0.004 and -19.07 ± 3.03 mV respectively, and for PEGylated CUR-DOX liposomes at 121.51 ± 0.82 nm, 0.09 ± 0.02, and -10.2 ± 1.6 mV respectively.

We calculated the % EE of CUR in CUR-DOX liposomes and PEGylated CUR-DOX liposomes at 76.82 ± 3.9 and 77.57 ± 7.95% respectively, and for DOX at 78.66 ± 2.49 and 73.32 ± 2.84 % respectively; and the % DL of CUR-DOX liposomes and PEGylated CUR-DOX liposomes at 4.46 ± 0.30 and 4.25 ± 0.24 % respectively. HRTEM confirmed spherical morphology for both formulations. FTIR analysis suggested the loading of CUR in the bilayer region and DOX in the aqueous cavity and the water lipid interface. The TGA analysis determined high thermal stability for the formulations, and the DSC analysis suggested the successful loading of the drugs in the liposomes. Thus, the results indicate the synthesis of robust CUR-DOX loaded liposomes according to the drug delivery mandates.

163

CHAPTER 5

Optimization, Synthesis, and Characterization of targeted drug loaded liposomes

CHAPTER 5A

Optimization, Synthesis, and Characterization of FOL tagged liposomes

5.1A Introduction

Normal cells uptake FOL by low affinity reduced FRs and have either under expressed or inaccessible high affinity FRs that are overexpressed on cancers of epithelial origin (Hartmann *et al.* 2007). The high affinity FRs have a $> 10^3$ times increased affinity for FOL, ensuring the FOL tagged liposomes to target and accumulate in the cancer cells selectively; FOL also has a higher affinity to FRs than folic acid, a synthetic form of Vitamin B9 (Zhao *et al.* 2008).

Breast cancer cells overexpressing FRs are associated with poor prognosis. The overexpression of FRs is a biomarker as a cohort study of 447 breast cancer patients reported that 80 % of TNBCs expressed FRs (Zhang *et al.* 2014) (O'Shannessy *et al.* 2012). TNBC, a highly metabolically active cancer subtype, overexpresses FRα to fulfill the hefty requirement of FOL to support these immensely proliferating cells (Nel *et al.*, 2023). MDA-MB-231 cells (TNBC) express FRs 1.76 times higher than the MCF-7 cells (hormone responsive) (Marshalek *et al.* 2016).
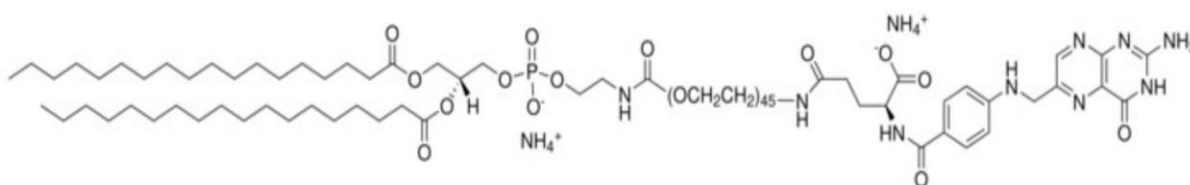
Figure 5.1A Structure of DSPE-PEG2000-FOL (Image source: www.sigmaaldrich.com)

We formulated liposomes by adding DSPE-PEG2000-FOL -where FOL is attached to a PEGylated lipid (Figure 5.1A) - and lipids with the optimized values of molar ratio, the concentration of DSPE-mPEG2000, and CUR and DOX. We optimized the number of extrusion passes to downsize the particles since adding a ligand can increase the particle size and PDI. We then characterized these particles for hydrodynamic diameter, PDI, zeta potential, % EE, % DL, morphology, and functional groups.

5.2A Methods

5.2.1A Synthesis of FOL tagged liposomes

FOL liposomes, FOL CUR liposomes, FOL DOX liposomes, and FOL CUR-DOX liposomes were synthesized by the protocol mentioned in Chapter 2, section 2.2.5 -with a 7:3 molar ratio of PC: CHOL, 1 mole % DSPE-mPEG2000, 0.1 mole % DSPE-mPEG2000-FOL, 1: 50 CUR: lipid ratio (wt. / wt.) ratio and 0.1 mg DOX for CUR, DOX and CUR-DOX liposomes. The downsizing step was optimized by varying the extrusion number (5 and 11) through a 100 nm polycarbonate membrane.

5.2.2A Characterization of FOL tagged liposomes

FOL-tagged liposomes were characterized for hydrodynamic diameter, PDI, zeta potential, % EE, % DL, morphology, and functional groups - Chapter 2, section 2.3.

5.3A Results and Discussion

5.3.1A Optimization of Plain FOL liposomes

During synthesis, the lipid DSPE-mPEG2000 incorporates in either bilayer leaflet with PEG chains extending from the liposomal surface and inwards into the aqueous core. We anticipated an increased size and PDI for FOL liposomes and optimized for the number of extrusion passes (5 and 11). The hydrodynamic diameter of the plain FOL liposomes was < 200 nm, and the PDI was < 0.3 (Table 5.1A).

Table 5.1A Hydrodynamic diameter and PDI of FOL liposomes after hydration and extrusion

	Average Hydrodynamic diameter (nm)	**Average PDI**
After Hydration	249.68 ± 17.37	0.36 ± 0.04
Extrusion passes-5	152.18 ± 16.54	0.17 ± 0.07
Extrusion passes- 11	126.29 ± 5.14	0.09 ± 0.02

The hydrodynamic diameter and PDI (ANOVA p value = <0.0001) changed significantly after extruding the particles (Figure 5.2A). After hydration, the hydrodynamic diameter decreased significantly after 5 (t-test p values = 0.0010), and 11 (t-test p value = 0.0003) extrusion passes; the particle size also reduced significantly from 5 to 11 extrusion passes (t-test p value =

0.0003). The PDI of liposomes after hydration decreased significantly after 5 (t-test p value = 0.0027) and 11 (t-test p value = 0.0003) extrusion passes; the PDI also reduced significantly from 5 to 11 extrusion passes (t-test p value = 0.0002). Thus, we optimized 11 extrusion passes for plain FOL liposomes.
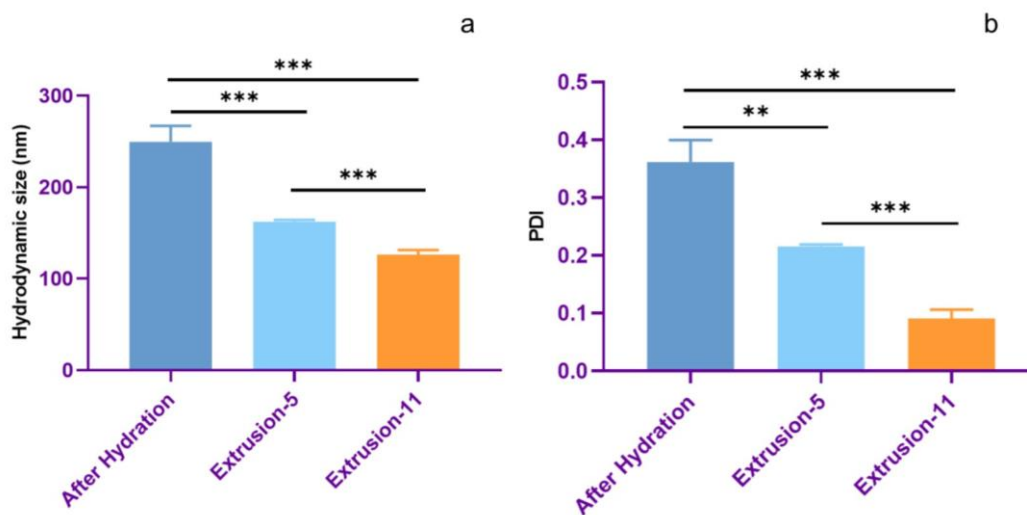
Figure 5.2A Hydrodynamic diameter (a) and PDI (b) of FOL liposomes after hydration and extrusion

5.3.2A Optimization of FOL CUR liposomes

We synthesized FOL CUR liposomes and optimized the number of extrusion passes (5 and 11). The particle size and PDI were < 150 nm and 0.3, respectively (Table 5.2A). The zeta potential in a neutral range corresponds to PEG and FOL on the liposomal surface, imparting stearic stability to the liposomes.

Table 5.2A Hydrodynamic diameter, PDI, zeta potential, and % EE of FOL CUR liposomes after hydration and extrusion

	Average Hydrodynamic diameter (nm)	Average PDI	Average Zeta potential (mV)	Average % EE
After Hydration	209.24 ± 25.75	0.42 ± 0.07		
Extrusion passes-5	151.04 ± 0.85	0.15 ± 0.01		77.30 ± 2.13
Extrusion passes- 11	131.24 ± 3.91	0.10 ± 0.05	-8.99 ± 1.37	78.40 ± 2.34

We noted a significant change in the hydrodynamic diameter (ANOVA p value = 0.0018) and PDI (ANOVA p value = 0.0003) after extruding the liposomes (Figure 5.3A). The hydrodynamic diameter of FOL CUR liposomes decreased significantly after 5 (t-test p value = 0.0174), and 11 (t-test p value = 0.066) extrusion passes, and from 5 to 11 (t-test p value = 0.0010) extrusion passes. The PDI of FOL CUR liposomes also reduced significantly after 5 (t-test p value = 0.0019), and 11 (t-test p value = 0.025) extrusion passes. We recorded an equivalent % EE of CUR after 5 and 11 extrusion passes. Thus, we optimized 11 extrusion passes for FOL CUR liposomes based on the hydrodynamic diameter.
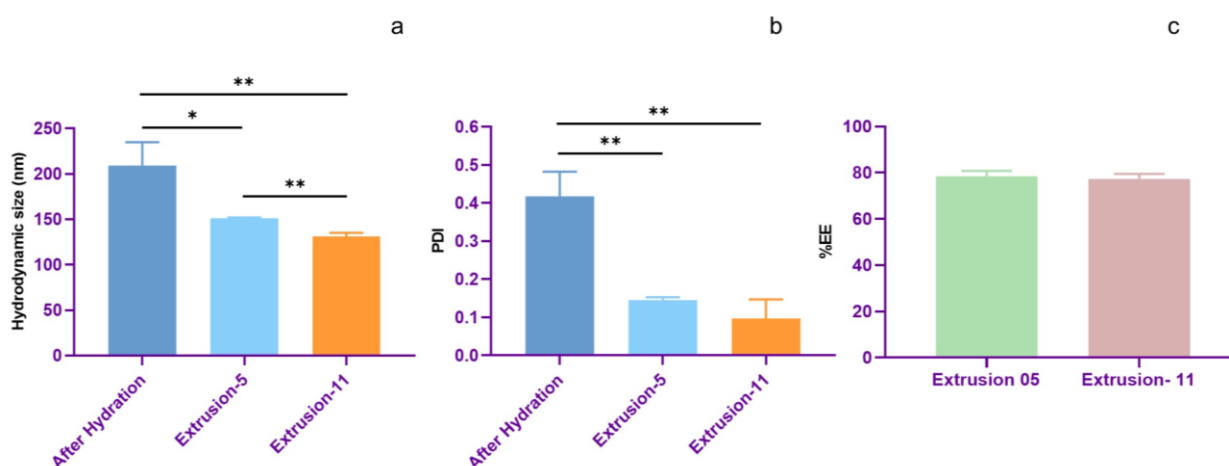
Figure 5.3A Hydrodynamic diameter, PDI, and % EE of FOL CUR liposomes after hydration and extrusion

5.3.3A Optimization of FOL DOX liposomes

We optimized the number of extrusion passes (5 and 11) and recorded the hydrodynamic diameter < 150 nm and PDI < 0.3 for the FOL DOX liposomes (Table 5.3A). The zeta potential in a neutral range corresponds to PEG and FOL on the liposomal surface, imparting stearic stability to the liposomes.

Table 5.3A Hydrodynamic diameter, PDI, zeta potential, and % EE of FOL DOX liposomes after hydration and extrusion

	Average Hydrodynamic diameter (nm)	Average PDI	Average Zeta potential (mV)	Average % EE
After Hydration	235.67 ± 22.50	0.34 ± 0.04		
Extrusion passes-5	144.42 ± 1.20	0.13 ± 0.01		78.93 ± 5.02
Extrusion passes- 11	128.38 ± 2.10	0.06 ± 0.01	-6.92 ± 0.41	79.47 ± 4.75

The hydrodynamic diameter (ANOVA p value = 0.0001) and PDI (ANOVA p value = <0.0001) of FOL DOX liposomes significantly changed after extruding the liposomes (Figure 5.4A). The particle size after hydration reduced significantly after 5 (t-test p value = 0.0022) and 11 (t-test p value = 0.0012) extrusion passes and from 5 to 11 (t-test p value = 0.0003) extrusion passes. The PDI after hydration also decreased significantly after 5 (t-test p value = 0.0014), and 11 (t-test p value = 0.0004) extrusion passes, and from 5 to 11 extrusion passes (t-test p value = 0.0004). The % EE for DOX was comparable after 5 and 11 extrusion passes. Thus, we optimized 11 extrusion passes for FOL DOX liposomes based on the hydrodynamic diameter and PDI with similar % EE.
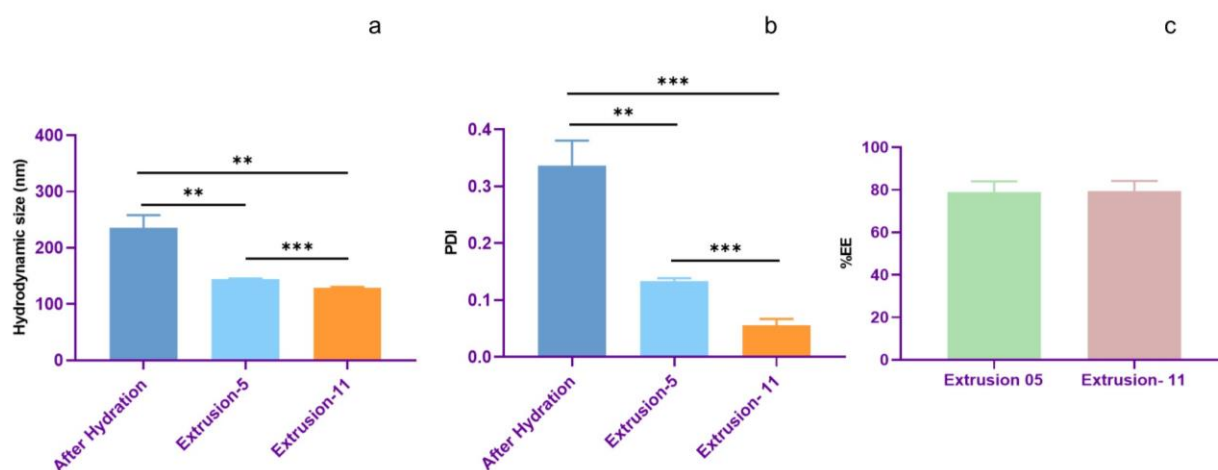
Figure 5.4A Hydrodynamic diameter, PDI, and % EE of FOL DOX liposomes after hydration and extrusion

5.3.4A Optimization of FOL CUR-DOX liposomes

We optimized the number of extrusion passes (5 and 11) and recorded the hydrodynamic diameter < 150 nm and PDI < 0.3 for the FOL CUR-DOX liposomes (Table 5.4A). The zeta potential in a neutral range corresponds to PEG and FOL on the liposomal surface, imparting stearic stability to the liposomes.

Table 5.4A Hydrodynamic diameter, PDI, zeta potential, and % EE of FOL CUR-DOX liposomes after hydration and extrusion

	Average Hydrodynamic diameter (nm)	Average PDI	Average Zeta potential (mV)	Average % EE
After Hydration	191.38 ± 6.37	0.29 ± 0.02		
Extrusion passes-5	140.17 ± 0.87	0.09 ± 0.004		**CUR:** 75.76 ± 3.56 **DOX:** 79.83 ± 2.34
Extrusion passes-11	129.44 ± 0.81	0.07 ± 0.01	-8.57 ± 0.35	**CUR:** 77.73 ± 3.50 **DOX:** 78.46 ± 3.26

The hydrodynamic diameter (ANOVA p value = <0.0001) and PDI (ANOVA p value = <0.0001) of FOL CUR-DOX liposomes changed significantly after extruding the liposomes

(Figure 5.5A). The hydrodynamic diameter of FOL CUR-DOX liposomes after hydration reduced significantly after 5 (t-test p value = 0.0002) and 11 (t-test p value = <0.0001) extrusion passes, and from 5 to 11 (t-test p value = <0.0001) extrusion passes.

The PDI also reduced significantly after 5 (t-test p value = 0.0001), and 11(t-test p value = 0.0001) extrusion passes and from 5 to 11 (t-test p value = 0.0057) extrusion passes. The % EE for CUR and DOX remained unaltered after 5 and 11 extrusion passes. Thus, we optimized 11 extrusion passes for FOL CUR-DOX liposomes based on the hydrodynamic diameter and PDI with equivalent % EE.
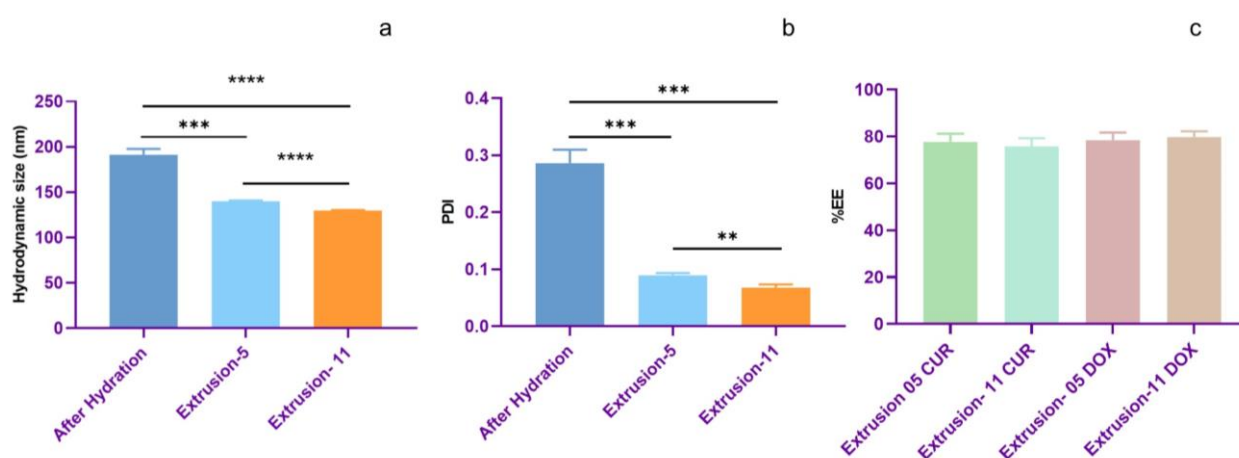
Figure 5.5A Hydrodynamic diameter, PDI, and % EE of FOL CUR-DOX liposomes after hydration and extrusion

5.4A Characterization of FOL tagged liposomes

5.4.1A Hydrodynamic diameter, PDI, and zeta potential

The DLS graph shows the hydrodynamic diameter, PDI, and zeta potential of FOL CUR liposomes at 126.4 nm, 0.1, and -8.99 ± 1.37 mV respectively; FOL DOX liposomes at 122.6 nm, 0.06 and -6.92 ± 0.41 mV respectively; and FOL CUR-DOX liposomes at 126.7 nm, 0.08 and -8.57 ± 0.35 mV respectively. The single sharp peaks for the three formulations suggest a monodisperse population with smaller sized liposomes (Figure 5.6A).
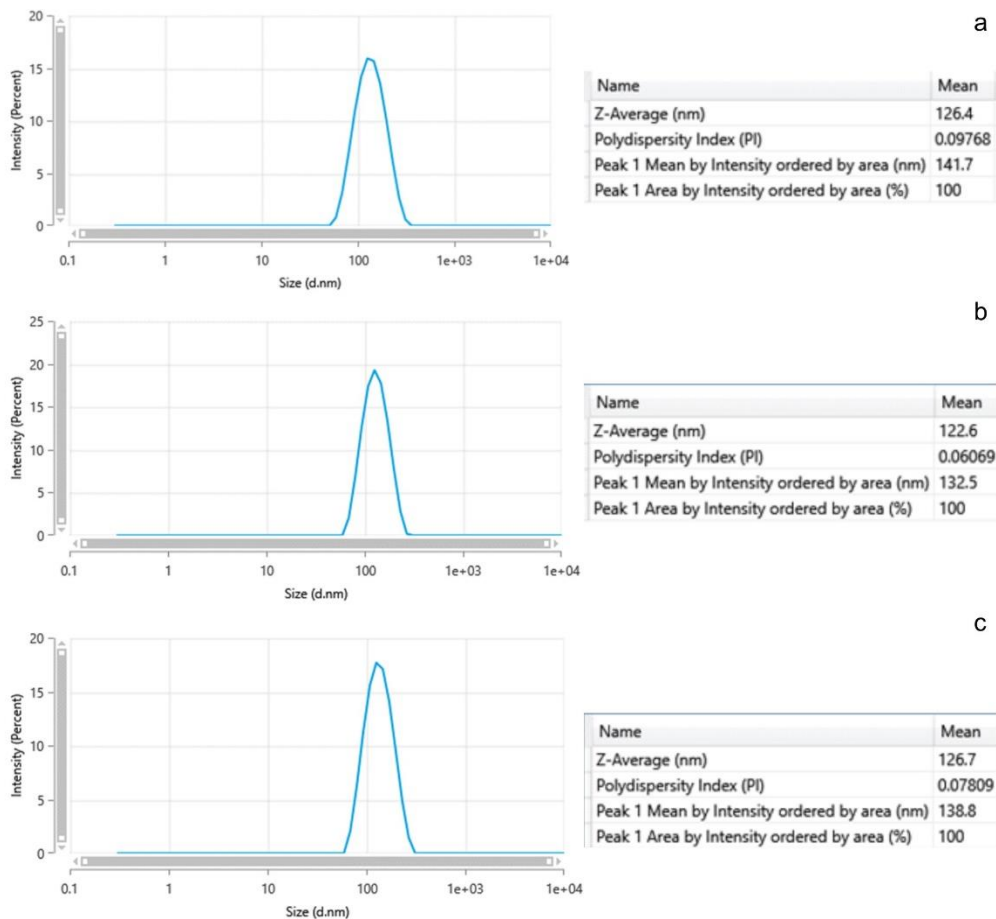
Figure 5.6A DLS graphs of FOL CUR liposomes (a), FOL DOX liposomes (b), and FOL CUR-DOX liposomes (c)

We compared the specifications of FOL CUR liposomes, FOL DOX liposomes, and FOL CUR-DOX liposomes and observed equivalent hydrodynamic diameter, PDI, and zeta potential values (Figure 5.7A). These results correspond to the effective downsizing of the particles after optimizing 11 extrusion passes for each formulation.
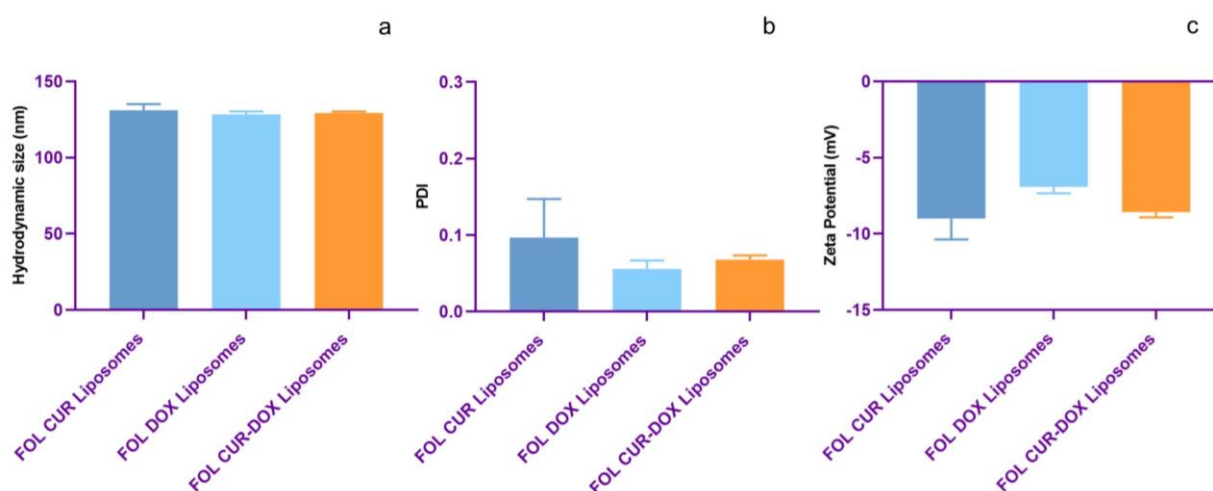
Figure 5.7A Comparison of hydrodynamic diameter (a), PDI (b), and zeta potential (c) of FOL CUR liposomes, FOL DOX liposomes and FOL CUR-DOX liposomes

We optimized 5 extrusion passes to downsize PEGylated CUR/DOX/CUR-DOX liposomes (in Chapter 4) and compared the specifications of FOL CUR/DOX/CUR-DOX liposomes downsized with 5 extrusion passes to determine any FOL induced structural changes after tagging the ligand (Figure 5.8A). We noted a statistically significant larger hydrodynamic diameter for FOL CUR liposomes (t-test p value = 0.0002) than PEGylated CUR liposomes, FOL DOX liposomes (t-test p value = 0.0002) than PEGylated DOX liposomes, and FOL CUR-DOX liposomes (t-test p value = 0.0001) than PEGylated CUR-DOX liposomes.

The PDI was also significantly higher for FOL CUR liposomes (t-test p value = 0.0014) than PEGylated CUR liposomes, and FOL DOX liposomes (t-test p value = 0.0006) than PEGylated DOX liposomes –although PDI for all the formulations was < 0.3. These results indicate that attaching FOL on the liposomal surface increased the particles' size and PDI, confirming the successful tagging of FOL on the particle surface.

174
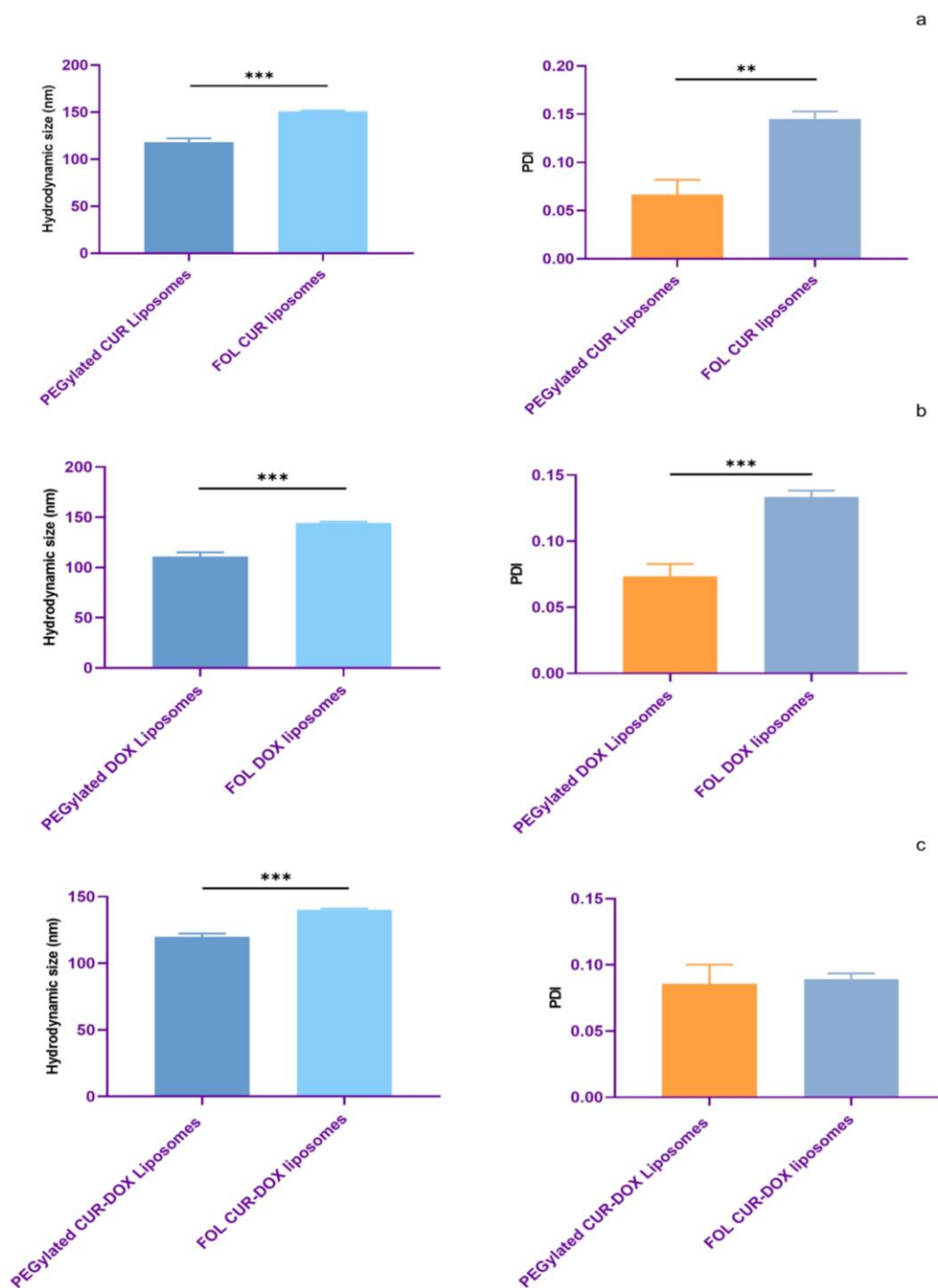
Figure 5.8A Comparison of hydrodynamic diameter and PDI after 5 extrusion passes of PEGylated CUR liposomes and FOL CUR liposomes (a), PEGylated DOX liposomes and FOL DOX liposomes (b), and PEGylated CUR-DOX liposomes and FOL CUR-DOX liposomes (c)

On comparing the FOL tagged liposomes with the optimized 11 extrusion passes (final formulation) with their PEGylated counterparts with the optimized 5 extrusion passes (Figure 5.9A), we noted that the FOL CUR liposomes were still significantly larger (t-test p value = 0.0289) with higher PDI (t-test p value = 0.0129) than PEGylated CUR liposomes, but the zeta

potential remained unchanged. The FOL DOX liposomes were significantly larger (t-test p value = 0.0115) than PEGylated DOX liposomes, and the PDI and zeta potential values remained unchanged. The FOL CUR-DOX liposomes were significantly larger (t-test p value = 0.0336) than PEGylated CUR-DOX liposomes, but the PDI and zeta potential values remained unchanged.

These observations again confirm the successful tagging of FOL on the liposomal surface and suggest that tagging FOL increased the particle size even after 11 extrusion passes.
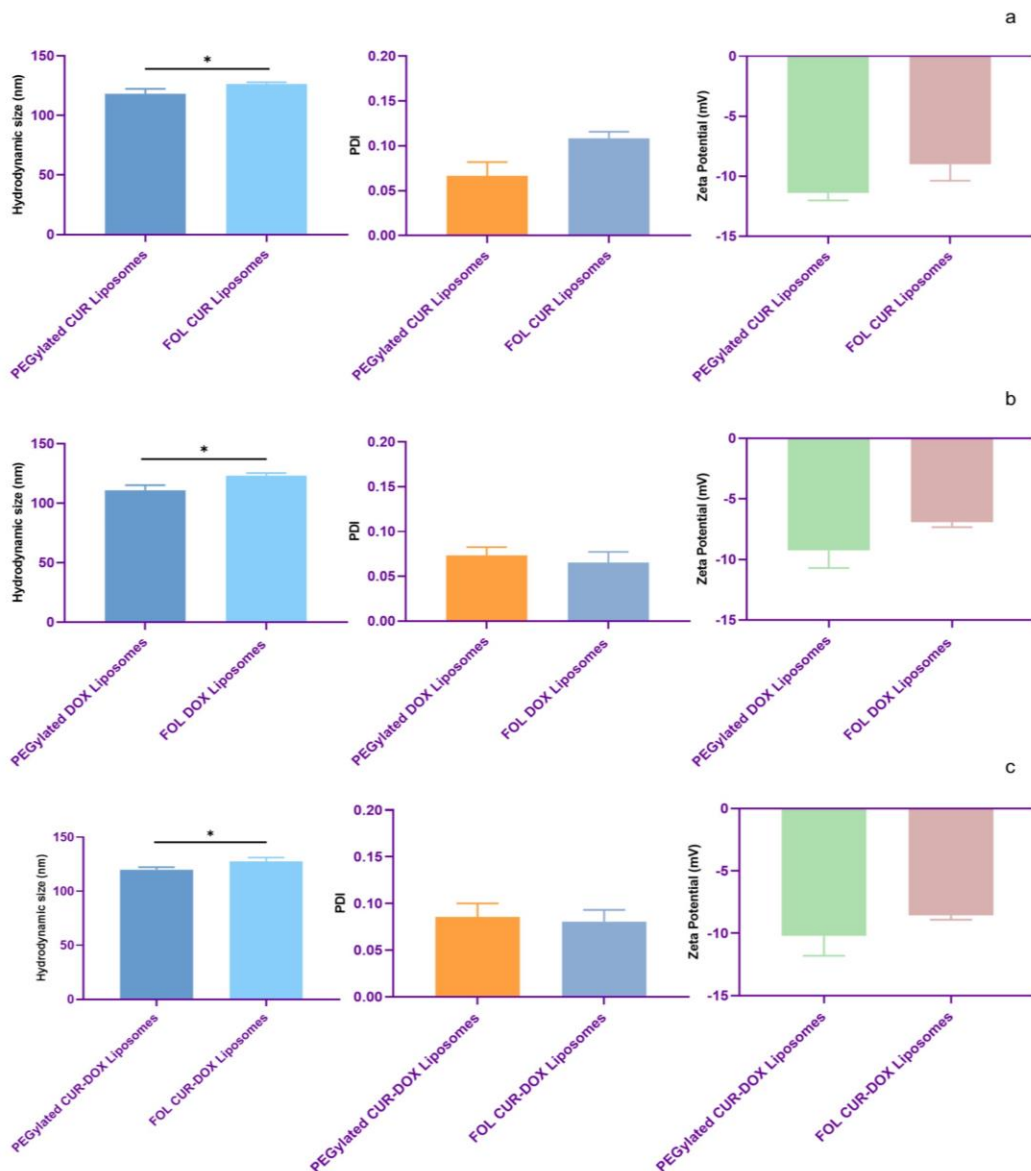
Figure 5.9A Comparison of hydrodynamic diameter, PDI, and zeta potential of PEGylated CUR liposomes and FOL CUR liposomes (a), PEGylated DOX liposomes and FOL DOX liposomes (b) and PEGylated CUR-DOX liposomes and FOL CUR-DOX liposomes (c)

5.4.2A % EE and % DL

We calculated the % EE of CUR and DOX in FOL tagged liposomes and the % DL (Table 5.5A).

Table 5.5A % EE and % DL of FOL tagged liposomes

Formulations	% EE	% DL
FOL CUR liposomes	78.40 ± 2.34	3.57±1.91
FOL DOX liposomes	79.47 ± 4.75	2.4±0.15
FOL CUR-DOX liposomes	**CUR:** 77.73 ± 3.50	4.49±0.18
	DOX: 78.46 ± 3.26	

The % EE remained unaltered for all the FOL tagged liposomes corresponding to a similar size range (Figure 5.10A). But the % DL (ANOVA p value = <0.0001) changed significantly: the % DL of FOL DOX liposomes was significantly less than FOL CUR liposomes (t-test p value = 0.0011) and FOL CUR-DOX liposomes (t-test p value = 0.0001) corresponding to a lower DOX concentration than CUR in the liposomes; % DL of FOL CUR-DOX liposomes was significantly higher (t-test p value = 0.0038) than FOL CUR liposomes attributing to both DOX and CUR in the liposomes.
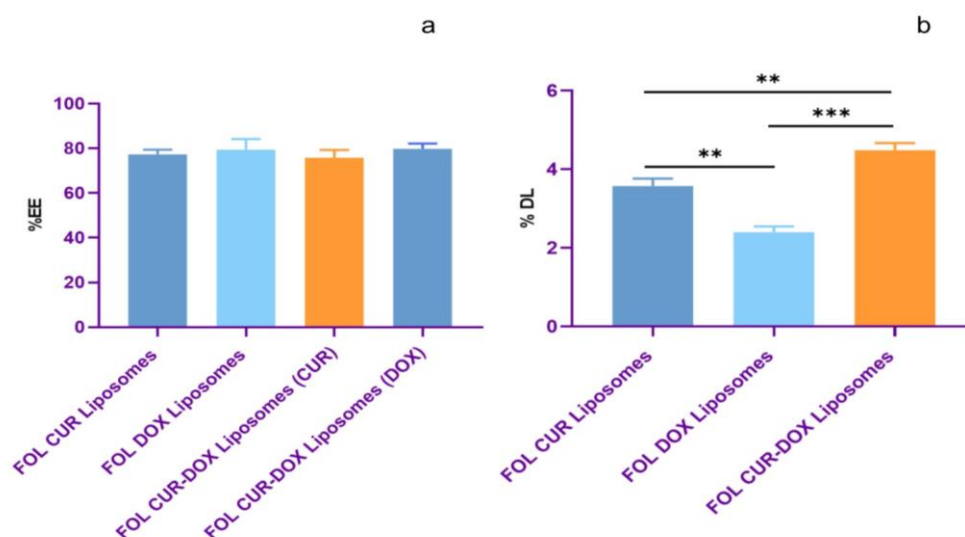
Figure 5.10A Comparison of % EE (a) and % DL (b) of FOL CUR liposomes, FOL DOX liposomes and FOL CUR-DOX liposomes

We recorded comparable % EE and % DL of the non-targeted liposomes and their FOL tagged counterparts (Figure 5.11A), suggesting the drug encapsulation in the liposomes remained unaffected by FOL on the liposomal surface; the insignificant change in the % DL corresponded to the lower concentrations of DSPE-mPEG2000-FOL used (0.1 mole %).
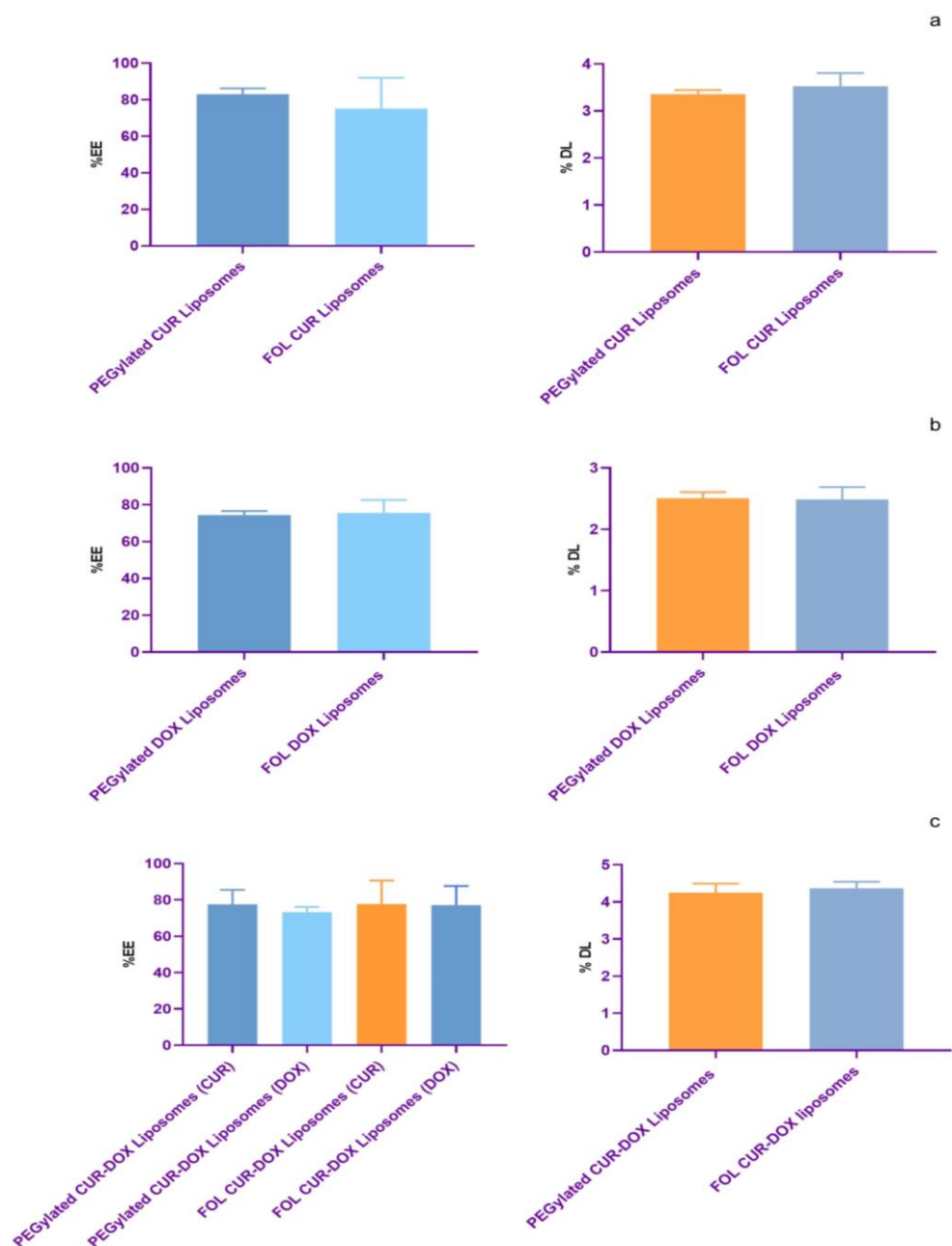
Figure 5.11A Comparison of % EE and % DL of PEGylated CUR liposomes and FOL CUR liposomes (a), PEGylated DOX liposomes and FOL DOX liposomes (b), and PEGylated CUR-DOX liposomes and FOL CUR-DOX liposomes (c)

5.4.3A Morphology of FOL tagged liposomes

The HRTEM images of the FOL liposomes determine spherical structures with smooth surfaces (Figure 5.12A). The smaller particles compared to their hydrodynamic diameter correspond to the hydrodynamic diameter measured by DLS measurements. The image shows approximately 60 nm sized particles – also observed in other studies (Pakdaman Goli *et al.* 2021). This size is appropriate for drug delivery applications. The irregular structures and artifacts are expected when we image liposomes with conventional electron microscopy (as discussed in Chapter 3).
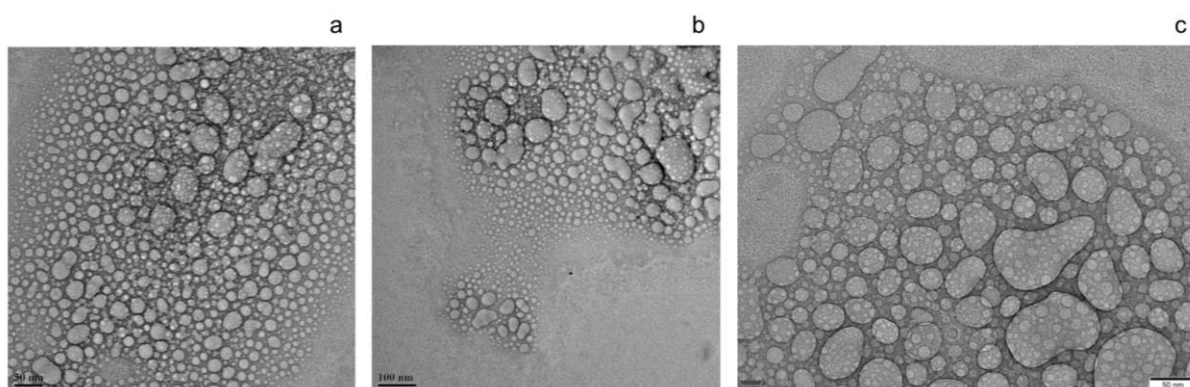
Figure 5.12A HRTEM images of FOL CUR liposomes (a), FOL DOX liposomes (b), and FOL CUR-DOX liposomes (c)

5.4.4A FTIR analysis

The characteristic peaks of pure folic acid (Figure 5.13A) occur at 3100 to 3540 cm^{-1} for OH stretching and NH of pterin ring,1689 cm^{-1} for C=O stretching, 1603 cm^{-1} for NH bending, and 1411 cm^{-1} for the OH deformation band of the phenyl ring (Raouf *et al.* 2014) (Venkatasubbu *et al.* 2013) (He *et al.* 2009).
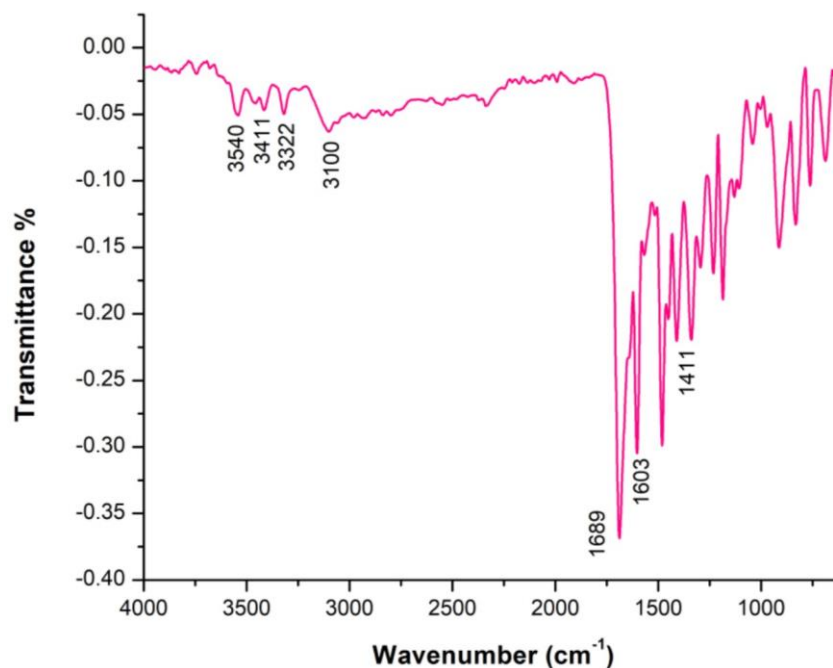
Figure 5.13A FTIR spectrum of Folic acid

For plain FOL liposomes (Figure 5.14A), the OH stretching of PC and the carboxyl moiety of FOL and the ring of FOL shifted from 3300 to 3344 cm^{-1} (Baskararaj *et al.* 2020) (Pakdaman Goli *et al.* 2021) indicating that FOL functionalizes the liposomal surface. We noted the antisymmetric and symmetric CH stretching at 2923 and 2856 cm^{-1}, respectively, and the C=O stretching at 1737 cm^{-1}. The C=C stretching overlapped with the amine group of the DSPE at 1652 cm^{-1} (Baskararaj *et al.* 2020), the CH$_2$ bending shifted from 1463 to 1459 cm^{-1}, and the CH3 bending shifted from 1377 to 1373 cm^{-1}. The peak for the head group region for PO^{2-} antisymmetric stretch shifted from 1225 to 1231 cm^{-1}, the PO^{2-} symmetric at 1057 cm^{-1}, and the peak for P-O stretching shifted from 829 to 838 cm^{-1}, respectively.
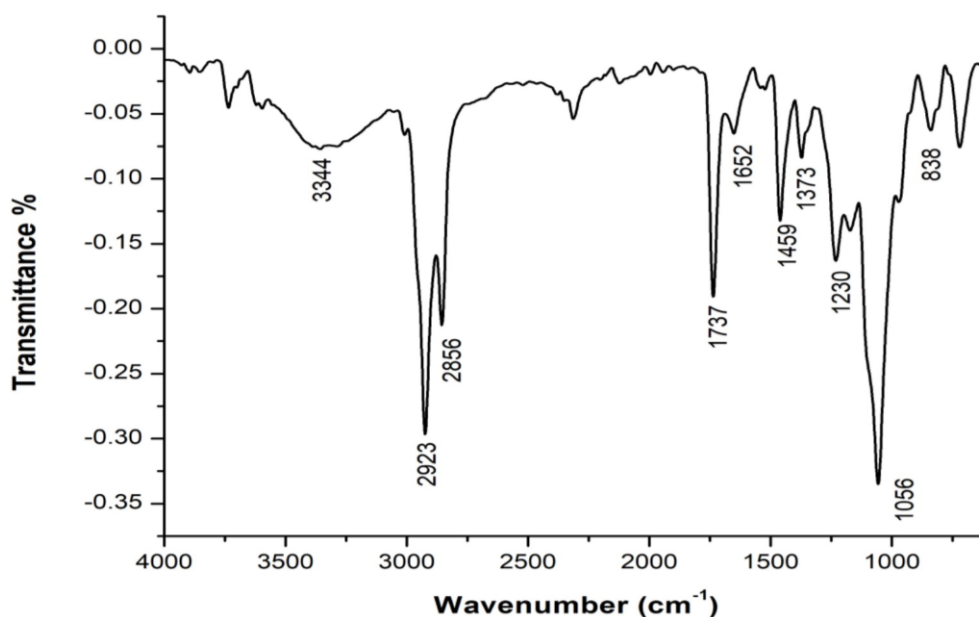
Figure 5.14A FTIR spectrum of plain FOL liposomes

For FOL CUR liposomes (Figure 5.15A), the OH stretching of PC, the carboxyl moiety of FOL, and the ring of FOL shifted from 3300 to 3359 cm^{-1}. The antisymmetric and symmetric CH stretching occurred at 2923 and 2853 cm^{-1}, respectively, the C=O stretching at 1737 cm^{-1}, and the C=C stretching overlapped with the amine group of the DSPE at 1652 cm^{-1}. The CH$_2$ bending occurred at 1463 cm^{-1}, and the CH$_3$ bending at 1377 cm^{-1}. The peak for the head group regions for PO$_2^{-}$ antisymmetric stretching shifted from 1225 to 1232 cm^{-1}, the PO$_2^{-}$ symmetric stretching occurred at 1059 cm^{-1}, and the P-O stretching shifted from 829 to 842 cm^{-1}.
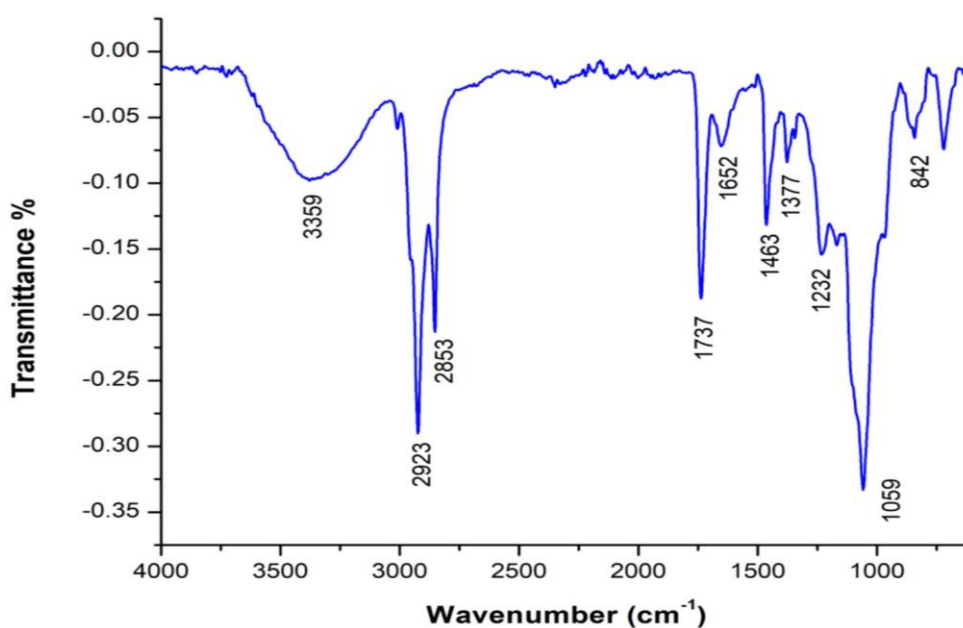
Figure 5.15A FTIR spectrum of FOL CUR liposomes

For the FOL DOX liposome (Figure 5.16A), the OH stretching of PC, the carboxyl moiety of FOL, and the ring of FOL shifted from 3300 to 3384 cm^{-1}. The antisymmetric and symmetric CH stretching occurred at 2923 and 2853 cm^{-1}, respectively, and the C=O stretching occurred at 1737 cm^{-1}. The C=C stretching occurred at 1650 cm^{-1}, the CH_2 bending 1463 cm^{-1}, and the CH3 bending at 1377 cm^{-1}. The peak for the head group regions for PO^{2-} antisymmetric stretching shifted from 1225 to 1230 cm^{-1}, the PO^{2-} symmetric stretching at 1060 cm^{-1}, and the P-O stretching shifted from 829 to 842 cm^{-1}.
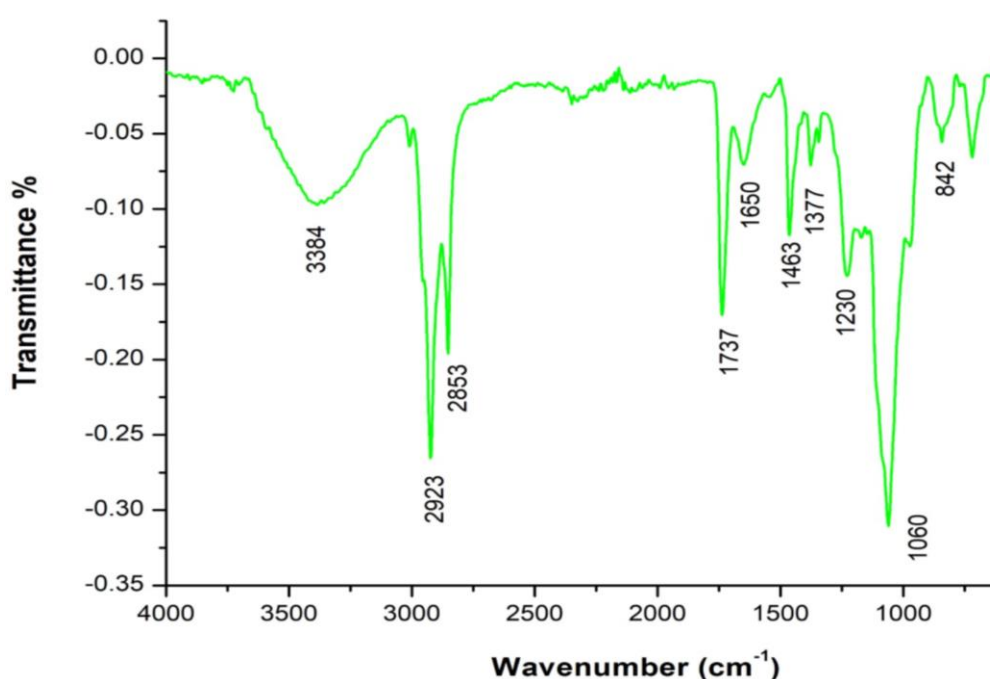
Figure 5.16A FTIR spectrum of FOL DOX liposomes

For the FOL CUR-DOX liposome (Figure 5.17A), the OH stretching of PC, the carboxyl moiety of FOL, and the ring of FOL shifted from 3300 to 3362 cm^{-1}. The antisymmetric and symmetric CH stretching occurred at 2923 and 2853 cm^{-1}, respectively, and the C=O stretching occurred at 1737 cm^{-1}. The C=C stretching occurred at 1650 cm^{-1}, the CH_2 bending 1463 cm^{-1}, and the CH_3 bending at 1377 cm^{-1}. The peak for the head group regions for PO^{2-} antisymmetric stretching shifted from 1225 to 1228 cm^{-1}, and for PO^{2-} symmetric stretching occurred at 1061 cm^{-1}, the P-O stretching shifted from 829 to 840 cm^{-1}.
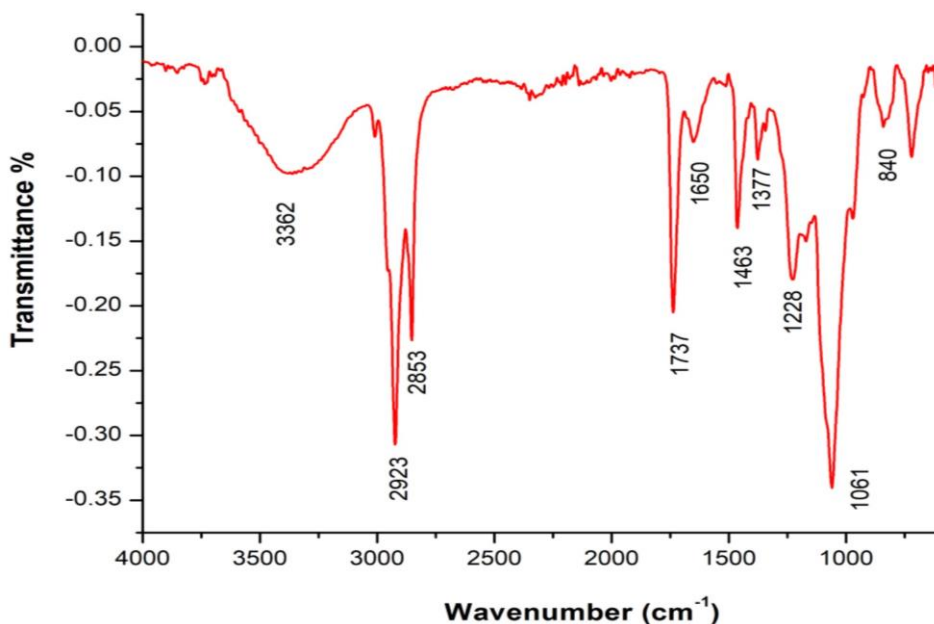
Figure 5.17A FTIR spectrum of FOL CUR-DOX liposomes

We noted a shift in the OH stretching peaks corresponding to FOL on the liposomal surface. The order of the bilayer and hydrocarbon region of the lipids remained unaltered. The major shift in the head group region occurs due to FOL attached to DSPE. The masking of the characteristic peaks of CUR and DOX suggests the successful loading of drugs inside the liposomes. The absence of new peaks confirms the presence of physical interactions rather than chemical bonds.

5.5A Conclusion

We synthesized FOL tagged liposomes with the previously optimized values of process parameters of liposomal synthesis by the thin film hydration technique, the molar ratio of the lipids, concentration of PC, CHOL, and DSPE-mPEG2000; concentration of CUR and DOX. We added 0.1 mole % of DSPE-PEG2000-FOL to tag FOL on the surface of liposomes. We optimized 11 extrusion passes to downsize the FOL tagged liposomes.

We observed that the particle size increased after tagging FOL compared to the non targeted liposomes. We recorded the hydrodynamic diameter, PDI, and zeta potential for FOL CUR liposomes at 131.24 ± 3.91 nm, 0.10 ± 0.05, and -8.99 ± 1.37 mV respectively; FOL DOX liposomes at 128.38 ± 2.10 nm, 0.06 ± 0.01, and -6.92 ± 0.41 mV respectively; and FOL CUR-DOX liposomes at 129.44 ± 0.81 nm, 0.07 ± 0.01 and -8.57 ± 0.35 mV respectively. The HRTEM images showed liposomes with a spherical morphology.

We noted the % EE and % DL of FOL CUR liposomes at 78.40 ± 2.34% and 3.57 ± 1.91%, respectively; FOL DOX liposomes at 79.47 ± 4.75% and 2.4 ± 0.15% respectively; and FOL CUR-DOX liposomes at 77.73 ± 3.50 for CUR and 78.46 ± 3.26% for DOX, and 4.49 ± 0.18% respectively. FTIR analysis hinted that FOL functionalizes the liposomal surface with the drugs encapsulated inside the liposomes. Thus, the results suggest the synthesis of robust FOL tagged and drug loaded liposomes according to the drug delivery mandates.

CHAPTER 5B

Optimization, Synthesis, and Characterization of CET tagged drug

loaded liposomes

5.1B Introduction

Approximately 80 % of TNBCs overexpress EGFR receptors, which engenders a poor prognosis. Tyrosine kinase inhibitors such as gefitinib and erlotinib and MAbs such as CET target these receptors (De Laurentiis et al., 2010). CET (ICM-225, ErbituxTM) is a 152 KDa chimeric MAb (human/murine) composed of two identical heavy chains of 449 amino acids and two identical light chains with 214 amino acids (Vincenzi et al., 2008).

CET has a higher binding affinity for EGFR receptors than its physiologic ligands (Baselga, 2001). CET binds and blocks the extracellular ligand binding domain of EGFR, preventing these receptors from forming dimers with other EGFR subtypes that hinder the intracellular tyrosine kinase domain from phosphorylating that block the subsequent signal transduction pathways (Brand et al., 2011). Studies report an anticancer effect of CET in TNBC patients with and without chemotherapy (Brand et al., 2011). When used with chemotherapy, CET sensitizes the cancer cells to the chemotherapeutic drugs and induces apoptosis by reducing Bcl-2 and increasing Bax (Gerber and Choy, 2010).

We synthesized CET tagged liposomes with the optimized values of the molar ratio of lipids, concentration of DSPE-mPEG2000, and CUR and DOX concentrations. We added 0.1 mole % of DSPE-PEG2000-COOH, causing the COOH groups to extend from the liposomal surface (Eloy et al., 2017) that binds to CET via carbodiimide coupling between the –COOH of DSPE-PEG2000-COOH and $-NH_2$ groups of CET (Deen et al., 1990). The COOH group, when treated with EDC and NHS, forms a sulfo-NHS ester that forms stable amide bonds with the primary amines on CET (Thorek et al., 2009). Although water soluble, EDC is unstable in water, so NHS enhances the stability of EDC (Keleştemur et al., 2017). We optimized the extrusion passes for the CET tagged liposomes and characterized the particles for hydrodynamic diameter, PDI, zeta potential, % EE, % DL, % BE of CET, and morphology.

5.2B Methods

5.2.1B Synthesis of CET tagged liposomes

Liposomes were synthesized by the protocol mentioned in Chapter 2, section 2.2.6 with a 7:3 molar ratio of PC: CHOL, 1 mole % of DSPE-mPEG2000, 1: 50 CUR: lipid (wt. / wt.) ratio, and 0.1 mg DOX.

5.2.2B Characterization of CET tagged liposomes

CET liposomes were characterized for hydrodynamic diameter, PDI, and zeta potential by DLS; % EE and % DL; % BE of CET by Bradford assay; and morphology by HRTEM.

5.3B Results and Discussion

5.3.1B Synthesis of CET CUR liposomes

We optimized the extrusion passes after attaching DSPE-PEG2000-COOH to synthesize a monodisperse population before ligating CET. The particle size and PDI were < 150 nm and 0.3, respectively (Table 5.1B).

Table 5.1B Hydrodynamic diameter and PDI of CUR liposomes- COOH after 5 and 11 extrusion passes

	Average Hydrodynamic diameter (nm)	Average PDI
Extrusion- 05	146.57 ± 1.89	0.07 ± 0.01
Extrusion- 11	131.53 ± 2.17	0.06 ± 0.02

The hydrodynamic diameter reduced significantly (t-test p value = 0.0008), but the PDI remained unaltered on increasing the number of extrusion passes from 5 to 11 (Figure 5.1B). We optimized 11 extrusion passes for the CUR loaded formulation.
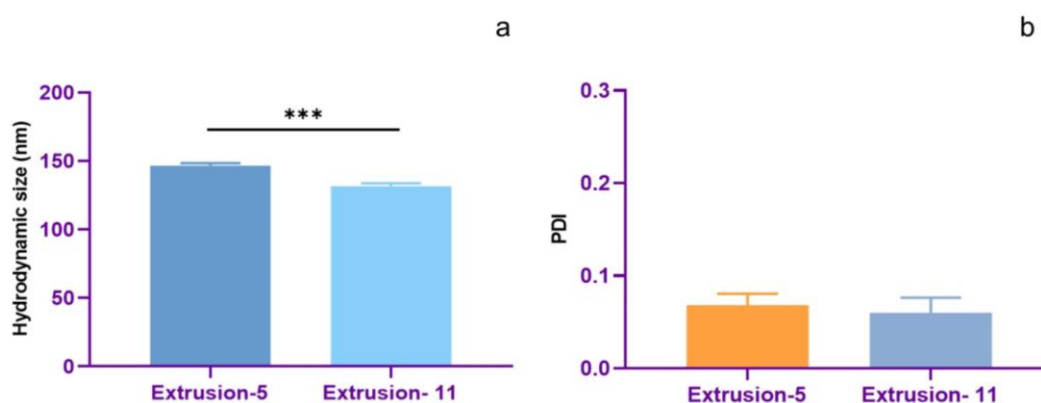
Figure 5.1B Hydrodynamic diameter (a) and PDI (b) of CUR liposomes- COOH after 5 and 11 extrusion passes

Upon attaching CET to the liposomes, we recorded the hydrodynamic diameter at 131.08 ± 0.72 nm and the PDI at 0.09 ± 0.01, confirming a monodisperse population of smaller liposomes. The zeta potential of -9.80 ± 0.50 in a neutral range corresponds to PEG and CET on the liposomal surface, imparting stearic stability to the liposomes.

After tagging CET to the liposomal surface, the hydrodynamic diameter remained unchanged, but the PDI increased significantly (t-test p value = 0.0411) (Figure 5.2B). CET is approximately 152 KDa, corresponding to roughly a radius of 3.6 nm; we anticipate that due to the small size of CET, the particle size remained unaltered, but tagging CET caused some structural changes, resulting in a higher PDI. Although the PDI values < 0.3 suggest a monodisperse population.
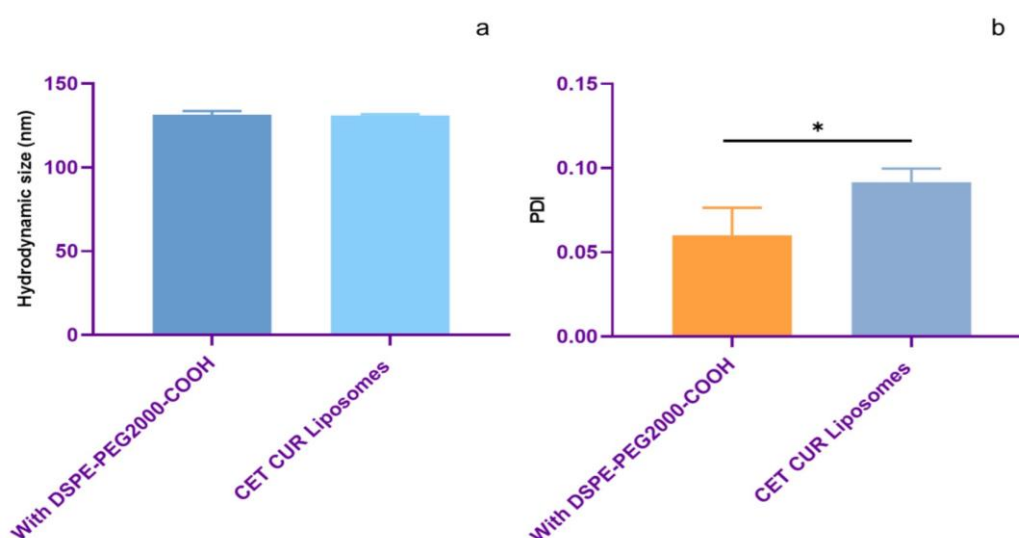
Figure 5.2B Comparison of hydrodynamic diameter (a) and PDI (b) of CET liposomes before and after tagging CET

5.3.2B Synthesis of CET DOX liposomes

We optimized the extrusion passes after attaching DSPE-PEG2000-COOH to synthesize a monodisperse population before ligating CET. The particle size and PDI were < 150 nm and 0.3, respectively (Table 5.2B).

Table 5.2B Hydrodynamic diameter and PDI of DOX liposomes-COOH after 5 and 11 extrusion passes

	Average Hydrodynamic diameter (nm)	Average PDI
Extrusion- 5	169.7 ± 0.66	0.20 ± 0.01
Extrusion- 11	135.56 ± 0.71	0.06 ± 0.01

The hydrodynamic diameter (t-test p value = < 0.0001) and PDI (t-test p value = < 0.0001) reduced significantly on increasing the number of extrusion passes from 5 to 11 (Figure 5.3B). We optimized 11 extrusion passes for the DOX loaded formulation.
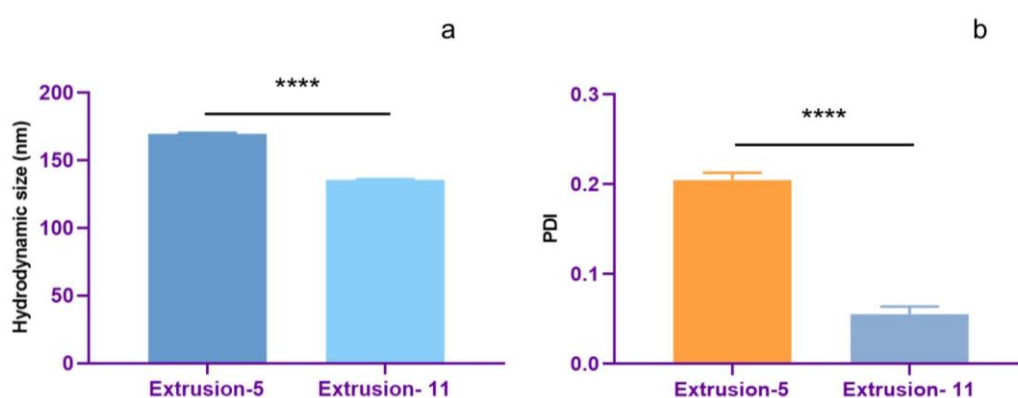
Figure 5.3B Hydrodynamic diameter (a) and PDI (b) of DOX liposomes- DP-COOH after 5 and 11 extrusion passes

Upon attaching CET to the liposomes, we recorded the hydrodynamic diameter at 141.49 ± 2.9 nm and the PDI at 0.12 ± 0.02, confirming a monodisperse population of smaller liposomes. The zeta potential of -9.16 ± 0.44 is in a neutral range corresponding to PEG and CET on the liposomal surface, imparting stearic stability to the liposomes.

After tagging CET to the liposomal surface, the hydrodynamic diameter (t-test p value = 0.0264) and PDI (t-test p value = 0.0058) increased significantly (Figure 5.4B). Although the PDI values < 0.3 suggest a monodisperse population.
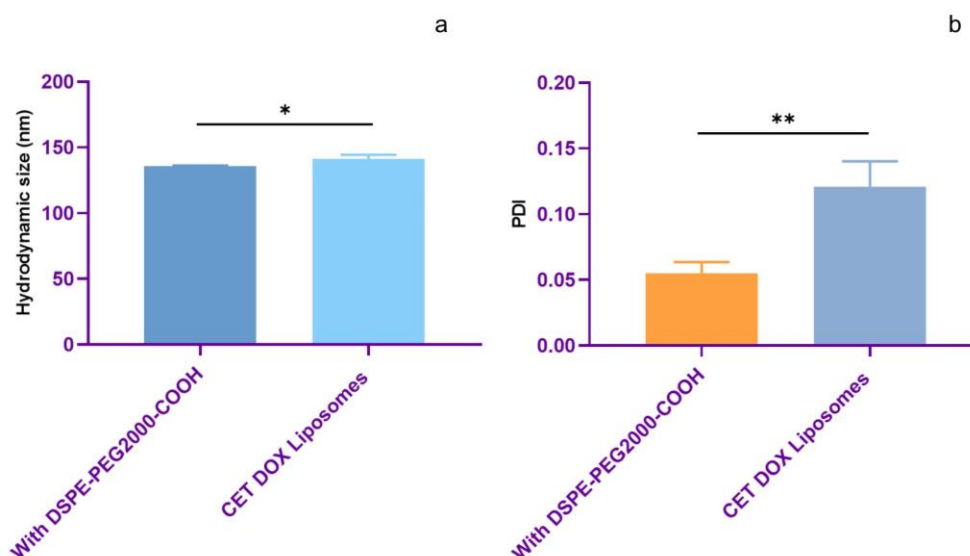
Figure 5.4B Comparison of hydrodynamic diameter (a) and PDI (b) of CET DOX liposomes before and after tagging CET

5.3.3B Synthesis of CET CUR-DOX liposomes

We optimized the extrusion passes after attaching DSPE-PEG2000-COOH to synthesize a monodisperse population before ligating CET. The particle size and PDI were < 150 nm and 0.3, respectively (Table 5.3B).

Table 5.3B Hydrodynamic diameter and PDI of CUR-DOX liposomes- DP-COOH after 5 and 11 extrusion passes

	Average Hydrodynamic diameter (nm)	Average PDI
Extrusion- 5	167.33 ± 2.64	0.18 ± 0.01
Extrusion- 11	126.1 ± 0.61	0.07 ± 0.01

The hydrodynamic diameter (t-test p value = < 0.0001) and PDI (t-test p value = 0.0003) reduced significantly on increasing the number of extrusion passes from 5 to 11 (Figure 5.5B). We optimized 11 extrusion passes for the CUR-DOX loaded formulation.
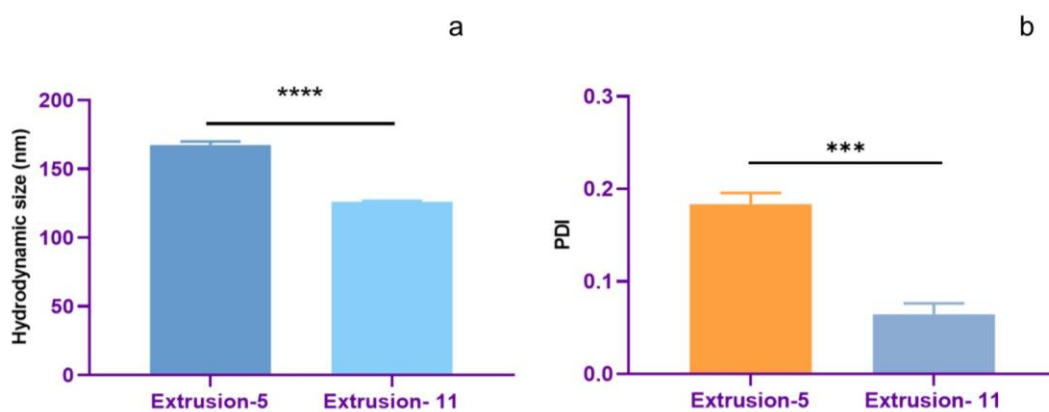
Figure 5.5B Hydrodynamic diameter (a) and PDI (b) of CUR-DOX liposomes- DP-COOH after 5 and 11 extrusion passes

Upon attaching CET to the liposomes, we recorded the hydrodynamic diameter at 126.43 ± 2.59 nm and the PDI at 0.13 ± 0.03, confirming a monodisperse population of smaller liposomes. The zeta potential of -10.14 ± 0.64 in a neutral range corresponds to PEG and CET on the liposomal surface, imparting stearic stability to the liposomes.

After tagging CET to the liposomal surface, the hydrodynamic diameter remained unchanged, but the PDI (t-test p value = 0.0399) increased significantly (Figure 5.6B). Although the PDI values < 0.3 suggest a monodisperse population.
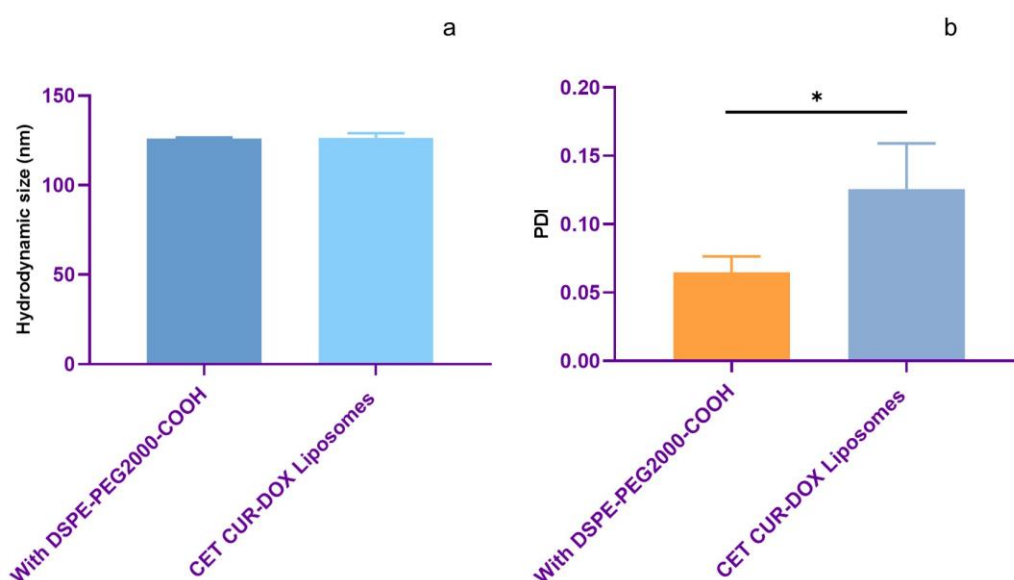
Figure 5.6B Comparison of hydrodynamic diameter (a) and PDI (b) of CET DOX liposomes before and after tagging CET

5.4B Characterization of CET tagged liposomes

5.4.1B Hydrodynamic diameter, PDI, and zeta potential

The DLS graph shows the hydrodynamic diameter and PDI of CET CUR liposomes at 130.1 nm and 0.1, respectively; CET DOX liposomes at 138.2 nm and 0.13, respectively; and CET CUR-DOX liposomes at 125.3 nm, 0.12 respectively (Figure 5.7B). The single sharp peaks for the three formulations suggest a monodisperse population with smaller sized liposomes.

a

Name	Mean	Standard Deviation	RSD	Minimum	Maximum
Z-Average (nm)	130.1	-	-	130.1	130.1
Polydispersity Index (PI)	0.104	-	-	0.104	0.104
Peak 1 Mean by Intensity ordered by area (nm)	147	-	-	147	147
Peak 1 Area by Intensity ordered by area (%)	100	-	-	100	100

b

Name	Mean	Standard Deviation	RSD	Minimum	Maximum
Z-Average (nm)	138.2	-	-	138.2	138.2
Polydispersity Index (PI)	0.1278	-	-	0.1278	0.1278
Peak 1 Mean by Intensity ordered by area (nm)	158.4	-	-	158.4	158.4
Peak 1 Area by Intensity ordered by area (%)	100	-	-	100	100

c

Name	Mean	Standard Deviation	RSD	Minimum	Maximum
Z-Average (nm)	125.3	-	-	125.3	125.3
Polydispersity Index (PI)	0.1182	-	-	0.1182	0.1182
Peak 1 Mean by Intensity ordered by area (nm)	143.7	-	-	143.7	143.7
Peak 1 Area by Intensity ordered by area (%)	100	-	-	100	100

Figure 5.7B DLS graph of CET CUR liposomes (a), CET DOX liposomes (b), and CET CUR-DOX liposomes (c)

After attaching CET to the drug loaded liposomes, we removed the untagged CET by ultracentrifugation and redispersed the pellet in PBS. To ensure a suspension of single particles, we passed the liposomes through a polycarbonate membrane.

Upon comparing the specifications of all the CET tagged liposomes, the particle size changed significantly (ANOVA p value = 0.0005) (Figure 5.8B). We noted CET DOX liposomes with the largest size than CET CUR liposomes (t-test p value = 0.0038) and CET CUR-DOX liposomes (t-test p value = 0.0026); the CET CUR liposomes were significantly larger than the CET CUR-DOX liposomes (t-test p value = 0.04). The PDI and zeta potential remained unchanged.
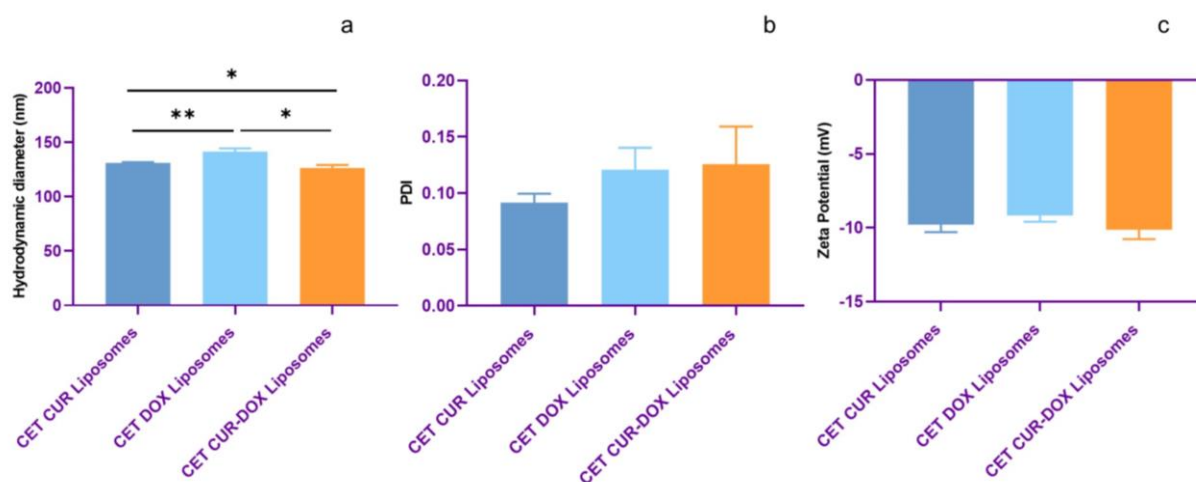
Figure 5.8B Comparison of hydrodynamic diameter (a), PDI (b), and zeta potential (c) of CET CUR liposomes, CET DOX liposomes and CET CUR-DOX liposomes

We compared the specifications of CET-tagged liposomes with those of their non-tagged counterparts (Figure 5.9B). The CET CUR liposomes were significantly larger than PEGylated CUR liposomes (t-test p value = 0.0058), CET DOX liposomes were significantly larger than PEGylated DOX liposomes (t-test p value = 0.0024), and CET CUR-DOX liposomes were significantly larger than PEGylated CUR-DOX liposomes (t-test p value = 0.0318). The PDI values remained unchanged except for higher values for CET DOX liposomes than PEGylated DOX liposomes (t-test p value = 0.0186); these unaltered values correspond to the extrusion of liposomes. The zeta potential values also remained unaltered. The increase in size corresponds to the CET tagging on the liposomal surface.
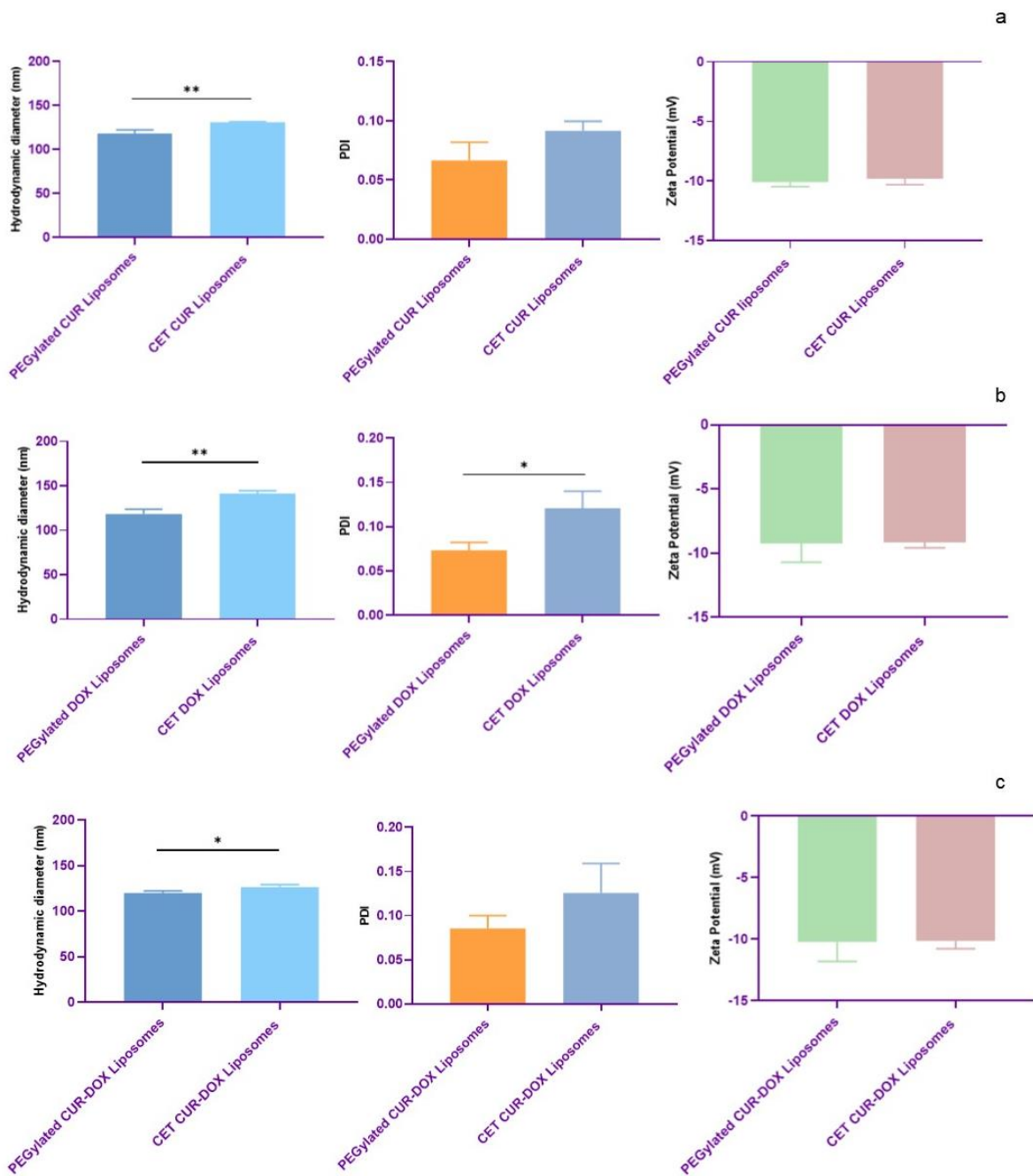
Figure 5.9B Comparison of hydrodynamic diameter, PDI, and zeta potential of PEGylated CUR and CET CUR liposomes (a), PEGylated DOX and CET DOX liposomes (b) and PEGylated CUR-DOX and CET CUR-DOX liposomes (c)

5.4.2B % EE

We calculated the % EE of CUR and DOX in CET tagged liposomes (Table 5.4).

Table 5.4 % EE of CET tagged liposomes

Formulations	% EE
CET CUR liposomes	79.49 ± 1.6
CET DOX liposomes	76.71 ± 3.18
CET CUR-DOX liposomes	**CUR:** 79.11 ± 2.22
	DOX: 75.22 ± 1.78

We recorded an equivalent % EE of CET tagged liposomes (Figure 5.10B). These results suggest that the drug retained in the liposomes during CET tagging and the comparable values correspond to particles in a similar size range.
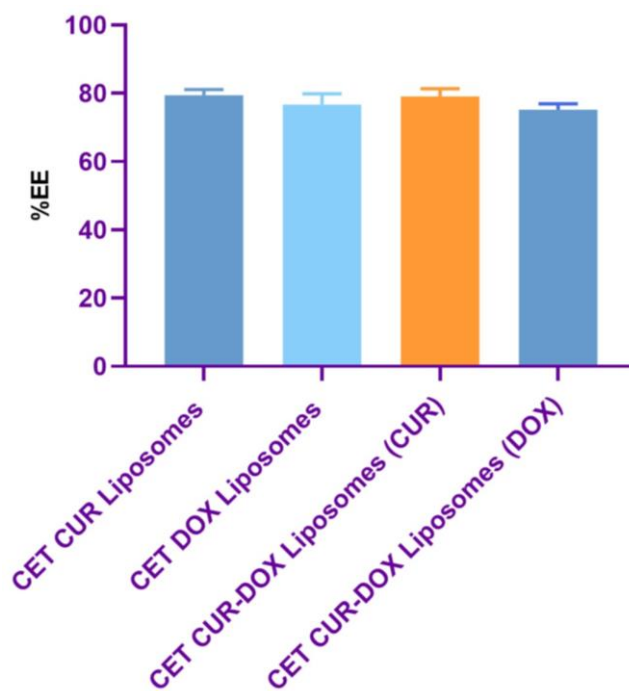
Figure 5.10B Comparison of % EE of CET tagged CUR, DOX, and CUR-DOX loaded liposomes

On comparing the CET tagged liposomes with their non-tagged counterparts, we noted equivalent % EEs, implying that the drug encapsulation remained unaffected by CET tagging (Figure 5.11B).
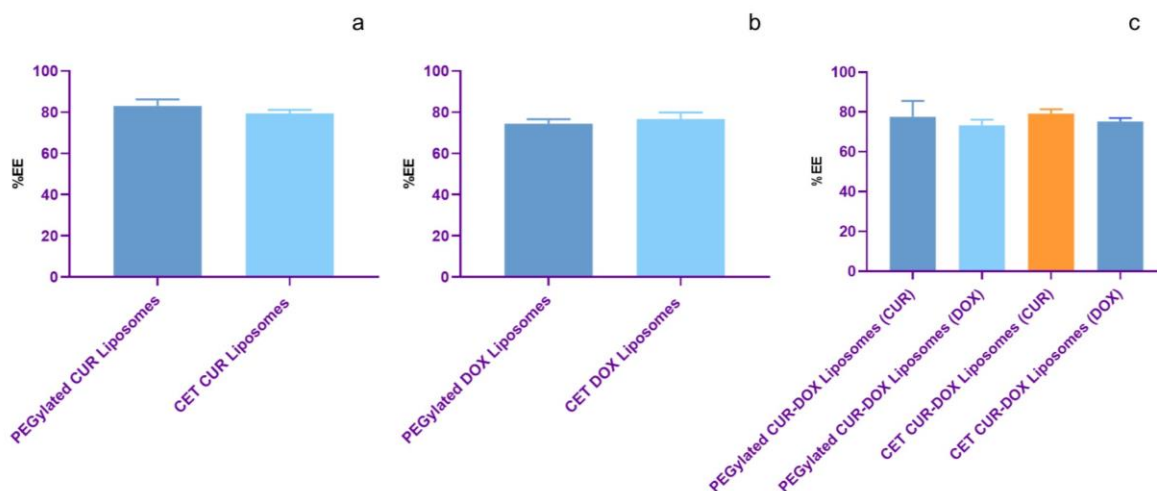
Figure 5.11B Comparison of % EE between non-targeted and CET tagged liposomes

5.4.3B Morphology of CET tagged liposomes

The HRTEM images for the three CET tagged formulations show spherical structures with smooth surfaces (Figure 5.12A). The images show smaller particles than the hydrodynamic diameter deduced by DLS.
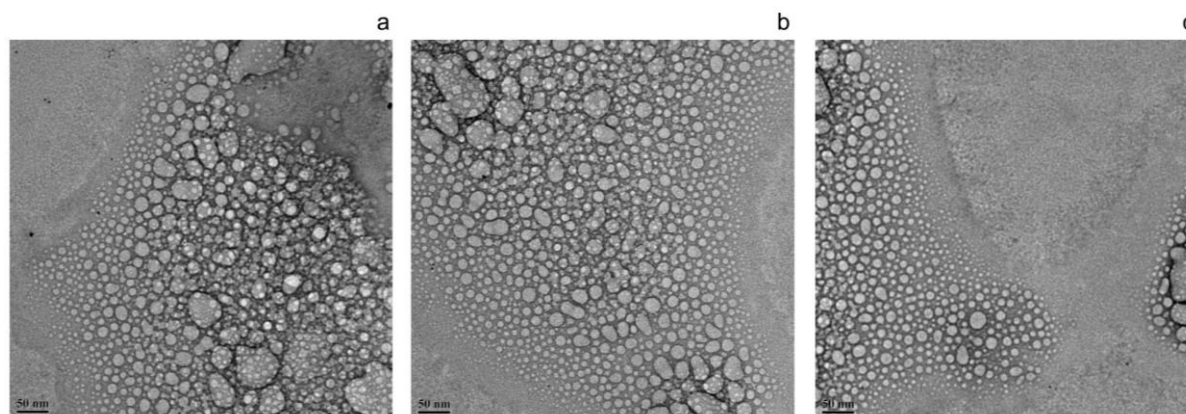
Figure 5.12B HRTEM/TEM images of CET tagged CUR (a), DOX (b), and CUR-DOX (c) liposomes

5.4.4B % BE of CET

We determined the % BE of CET by the Bradford assay at 87.11 ± 1.99 % for CET CUR liposomes, 85.86 ± 1.96 % for CET DOX liposomes, and 88.14 ± 1.72 % for CET CUR-DOX

liposomes. The CET concentrations on the liposomal surface were equivalent for all the CET tagged formulations (Figure 5.13B).
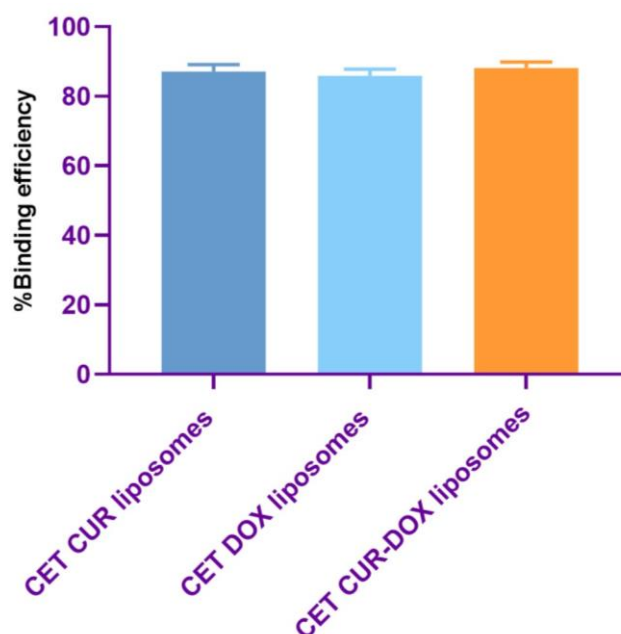
Figure 5.13B Comparison of %BE of CET on different CET tagged liposomes

5.5B Conclusion

We synthesized CET tagged liposomes with the previously optimized values of process parameters of liposomal synthesis by the thin film hydration technique, the molar ratio of the lipids, concentration of PC, CHOL, and DSPE-mPEG2000, the concentration of CUR and DOX. We added 0.1 mole % of DSPE-PEG2000-COOH to tag CET on the surface of liposomes by carbodiimide coupling. We optimized 11 extrusion passes to downsize the CET tagged liposomes.

We observed that the particle size increased after tagging CET compared to the non targeted liposomes. We recorded the hydrodynamic diameter, PDI, and zeta potential for CET CUR liposomes at 131.08 ± 0.72 nm, 0.09 ± 0.01 and -9.80 ± 0.50 mV respectively; CET DOX liposomes at 141.49 ± 2.9 nm, 0.12 ± 0.02, and -9.16 ± 0.44 mV respectively; and CET CUR-DOX liposomes at 126.43 ± 2.59 nm, 0.13 ± 0.03 and -10.14 ± 0.64 mV respectively. The HRTEM image showed liposomes with a spherical morphology.

We noted the % EE of CET CUR liposomes at 79.49 ± 1.6 %, CET DOX liposomes at 76.71 ± 3.18 %, and CET CUR-DOX liposomes at 79.11 ± 2.22 % for CUR and 75.22 ± 1.78 % for DOX. We calculated the % BE of CET at 87.11 ± 1.99 % for CET CUR liposomes, 85.86 ± 1.96 % for CET DOX liposomes, and 88.14 ± 1.72 % for CET CUR-DOX liposomes. Thus, the results suggest the synthesis of robust CET tagged and drug loaded liposomes according to the drug delivery mandates.

CHAPTER 5C

Optimization, Synthesis, and Characterization of FOL-CET tagged drug

loaded liposomes

5.1C Introduction

Studies report enhanced uptake and anticancer activity of dual targeted NPs by the cancer cells compared to single ligand targeted particles. The dual ligands increase the precision of the interaction and uptake of these particles since cancer cells have a heterogeneous expression of receptors on the cell surface. This mechanism also enhances the therapeutic efficacy of the encapsulated drugs. Amidst the absence of dual targeted liposomes to manage breast cancer, we synthesized FOL and CET tagged liposomes to target both the FRs and EGFR receptors that are overexpressed on the TNBC cells.

We synthesized liposomes with the optimized values of the liposomal components. In the thin film hydration step, we added both DSPE-PEG2000-FOL and DSPE-PEG2000-COOH, and the latter tagged CET by the EDC-NHS carbodiimide chemistry. We optimized the number of extrusion passes to downsize the particles and characterized for hydrodynamic diameter, PDI, zeta potential, % EE, % BE of CET, and morphology of the particles.

5.2C Methods

5.2.1C Synthesis of FOL-CET tagged liposomes

The FOL-CET tagged liposomes were synthesized by the protocol mentioned in Chapter 2 Section 2.2.7 using 7:3 molar ratio of PC: CHOL, 1 mole % DSPE-mPEG2000, 0.1 mole % DSPE-mPEG2000-FOL, 0.1 mole % DSPE-mPEG2000-COOH, 1: 50 CUR: lipid ratio (wt. / wt.) ratio and 0.1 mg DOX for CUR, DOX and CUR-DOX liposomes. The downsizing step was optimized by varying the extrusion number (5 and 11) through a 100 nm polycarbonate membrane.

5.2.2C Characterization of FOL-CET tagged liposomes

FOL-CET tagged liposomes were characterized for hydrodynamic diameter, PDI, and zeta potential by DLS; % EE and % DL; the morphology by HRTEM, and the %BE of CET by Bradford assay -as mentioned in Chapter 2, section 2.3.

5.3C Results and Discussion

5.3.1C Synthesis of FOL-CET CUR liposomes

We optimized the number of extrusion passes after attaching DSPE-mPEG2000-FOL and DSPE-PEG2000-COOH to synthesize a monodisperse population of smaller liposomes before ligating CET. The particle size and PDI were < 150 nm and 0.3, respectively (Table 5.1C).

Table 5.1C Hydrodynamic diameter and PDI of FOL CUR liposomes-COOH after 5 and 11 extrusion passes

	Average Hydrodynamic diameter (nm)	Average PDI
Extrusion- 5	148.20 ± 1.15	0.1 ± 0.001
Extrusion- 11	142.80 ± 0.15	0.11 ± 0.02

The hydrodynamic diameter reduced significantly (t-test p value = < 0.0001), but the PDI remained unaltered on increasing the number of extrusion passes from 5 to 11 (Figure 5.1C). We optimized 11 extrusion passes for the CUR loaded formulation.
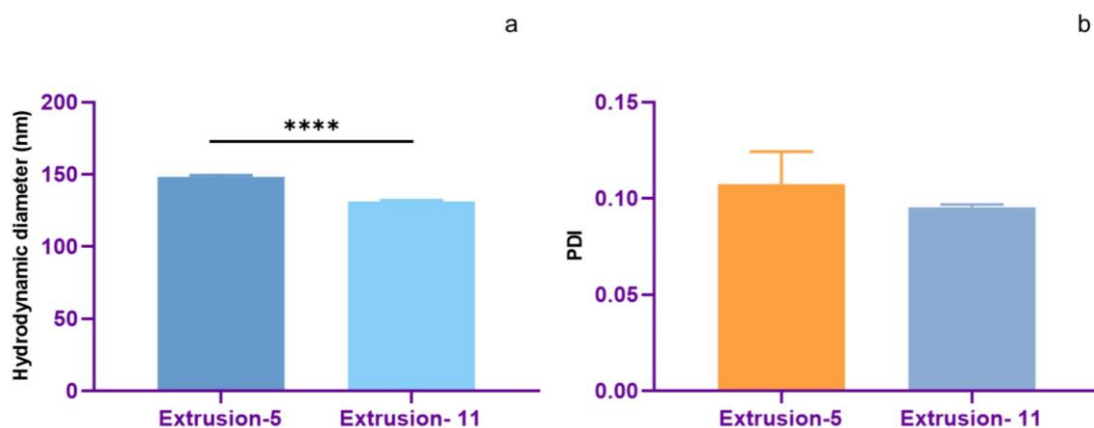
Figure 5.1C Hydrodynamic diameter (a) and PDI (b) of FOL CUR liposomes-COOH after 5 and 11 extrusion passes

Upon attaching CET to the liposomes, we recorded the hydrodynamic diameter at 130.90 ± 1.54 nm and the PDI at 0.08 ± 0.01, confirming a monodisperse population of smaller liposomes. The zeta potential of -9.71 $\pm$ 1.08 is in a neutral range corresponding to PEG, FOL, and CET on the liposomal surface, imparting stearic stability to the liposomes. After tagging CET to the liposomal surface, the hydrodynamic diameter remained unchanged, but the PDI

increased significantly (t-test p value = 0.0152) (Figure 5.2C). Although the PDI values < 0.3 suggest a monodisperse population.
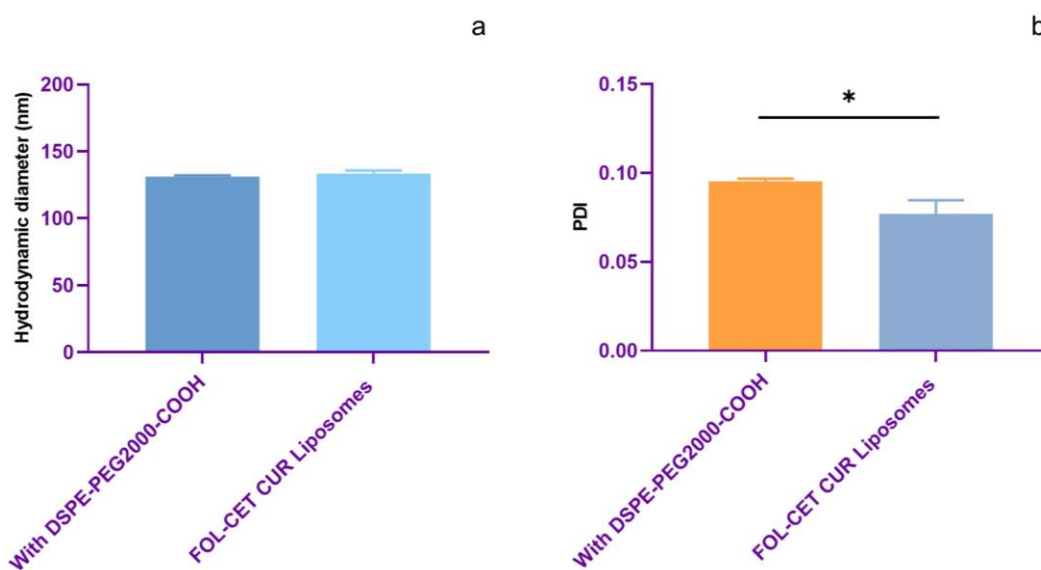
Figure 5.2C Comparison of hydrodynamic diameter (a) and PDI (b) of FOL-CET liposomes before and after tagging CET

5.3.2C Synthesis of FOL-CET DOX liposomes

We optimized the extrusion passes after attaching DSPE-mPEG2000-FOL and DSPE-PEG2000-COOH to synthesize a smaller sized and monodisperse population before ligating CET. The particle size and PDI were < 200 nm and 0.3, respectively (Table 5.2C).

Table 5.2B Hydrodynamic diameter and PDI of FOL DOX liposomes- DP-COOH after 5 and 11 extrusion passes

	Average Hydrodynamic diameter (nm)	Average PDI
Extrusion- 5	169.7 ± 0.66	0.20 ± 0.01
Extrusion- 11	135.56 ± 0.71	0.06 ± 0.01

The hydrodynamic diameter (t-test p value = < 0.0001) and PDI (t-test p value = 0.0081) reduced significantly on increasing the number of extrusion passes from 5 to 11 (Figure 5.3C). We optimized 11 extrusion passes for the DOX loaded formulation.
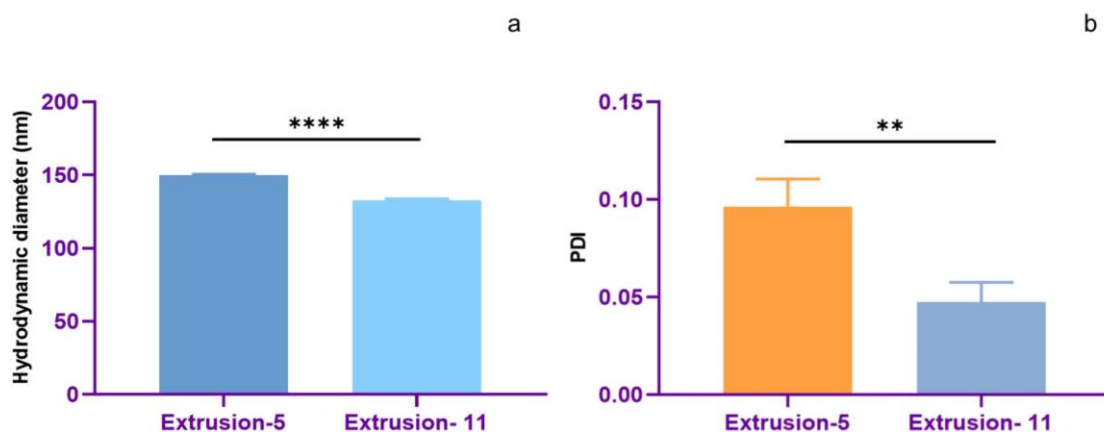
Figure 5.3C Hydrodynamic diameter (a) and PDI (b) of FOL DOX liposomes-COOH after 5 and 11 extrusion passes

Upon attaching CET to the liposomes, we recorded the hydrodynamic diameter at 129.57 ± 0.67 nm and the PDI at 0.10 ± 0.01, confirming a monodisperse population of smaller liposomes. The zeta potential of -10.45 ± 0.42 is in a neutral range corresponding to PEG and CET on the liposomal surface, imparting stearic stability to the liposomes. After tagging CET to the liposomal surface, the hydrodynamic diameter remained unchanged, but the PDI increased significantly (t-test p value = 0.0021) (Figure 5.4C). Although the PDI values < 0.3 suggest a monodisperse population.
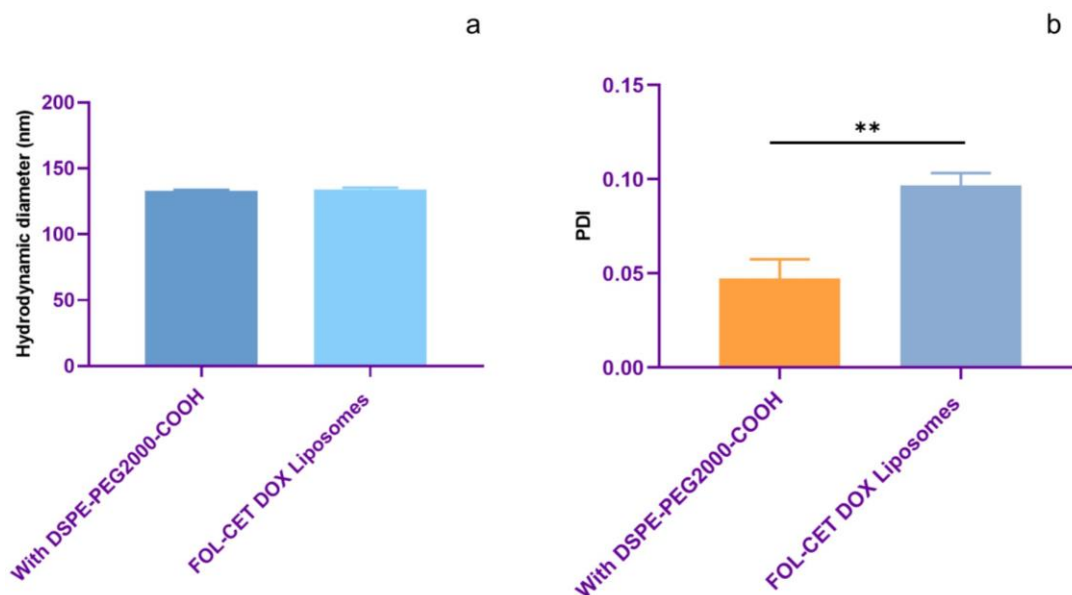
Figure 5.4C Comparison of hydrodynamic diameter (a) and PDI (b) of FOL-CET DOX liposomes before and after tagging CET

5.3.3C Synthesis of FOL-CET CUR-DOX liposomes

We optimized the extrusion passes after attaching DSPE-mPEG2000-FOL and DSPE-PEG2000-COOH to synthesize a monodisperse population before ligating CET. The particle size and PDI were < 150 nm and 0.3, respectively (Table 5.3C).

Table 5.3C Hydrodynamic diameter and PDI of CUR-DOX liposomes- DP-COOH after 5 and 11 extrusion passes

	Average Hydrodynamic diameter (nm)	Average PDI
Extrusion- 5	145.43 ± 0.75	0.06 ± 0.03
Extrusion- 11	122.8 ± 0.44	0.06 ± 0.01

The hydrodynamic diameter (t-test p value = < 0.0001) reduced significantly, but the PDI remained unaltered on increasing the number of extrusion passes from 5 to 11 (Figure 5.5C). We optimized 11 extrusion passes for the CUR-DOX loaded formulation.
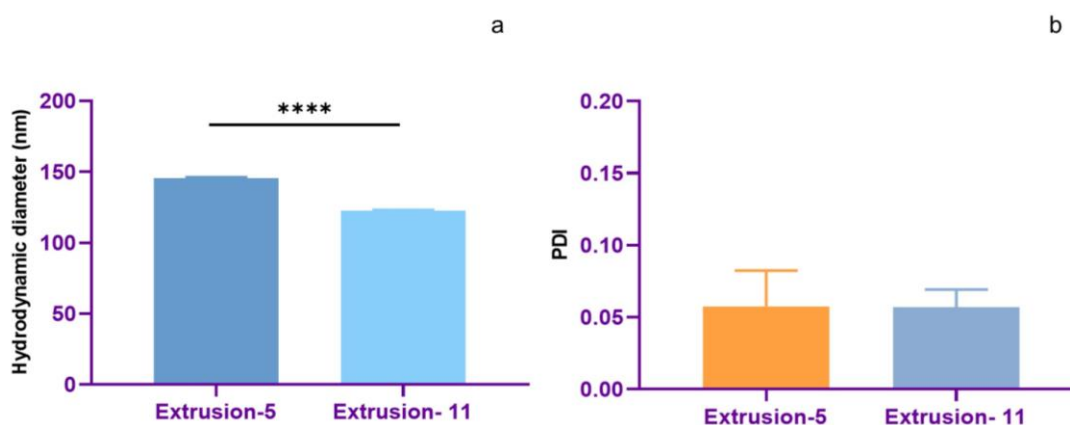
Figure 5.5C Hydrodynamic diameter (a) and PDI (b) of FOL CUR-DOX liposomes--COOH after 5 and 11 extrusion passes

Upon attaching CET to the liposomes, we recorded the hydrodynamic diameter at 131.38 ± 1.96 nm and the PDI at 0.14 ± 0.01, confirming a monodisperse population of smaller liposomes. The zeta potential of -10.86 ± 1.22 is in a neutral range corresponding to PEG and CET on the liposomal surface, imparting stearic stability to the liposomes. After tagging CET to the liposomal surface, the hydrodynamic diameter (t-test p value = 0.0018) and the PDI (t-test p value = 0.0013) increased significantly (Figure 5.6B). Although the PDI values < 0.3 suggest a monodisperse population.
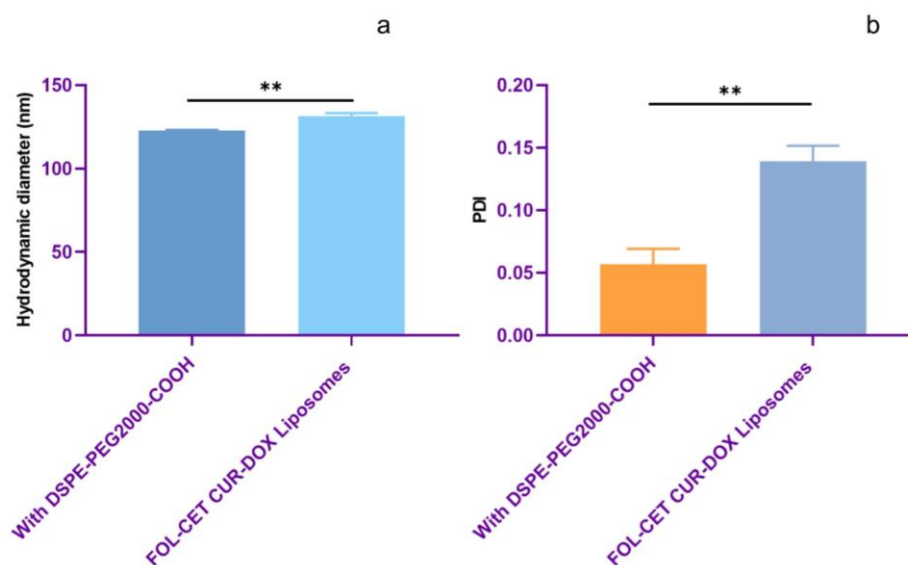
Figure 5.6B Comparison of hydrodynamic diameter (a) and PDI (b) of FOL-CET CUR-DOX liposomes before and after tagging CET

5.4C Characterization of FOL-CET tagged liposomes

5.4.1C Hydrodynamic diameter, PDI, and zeta potential

The DLS graph shows the hydrodynamic diameter and PDI of FOL-CET CUR liposomes at 131.7 nm and 0.06, respectively; FOL-CET DOX liposomes at 130.7 nm and 0.11, respectively; and FOL-CET CUR-DOX liposomes at 134.8 nm and 0.18 respectively (Figure 5.7C). The single sharp peaks for the three formulations suggest a monodisperse population with smaller sized liposomes.
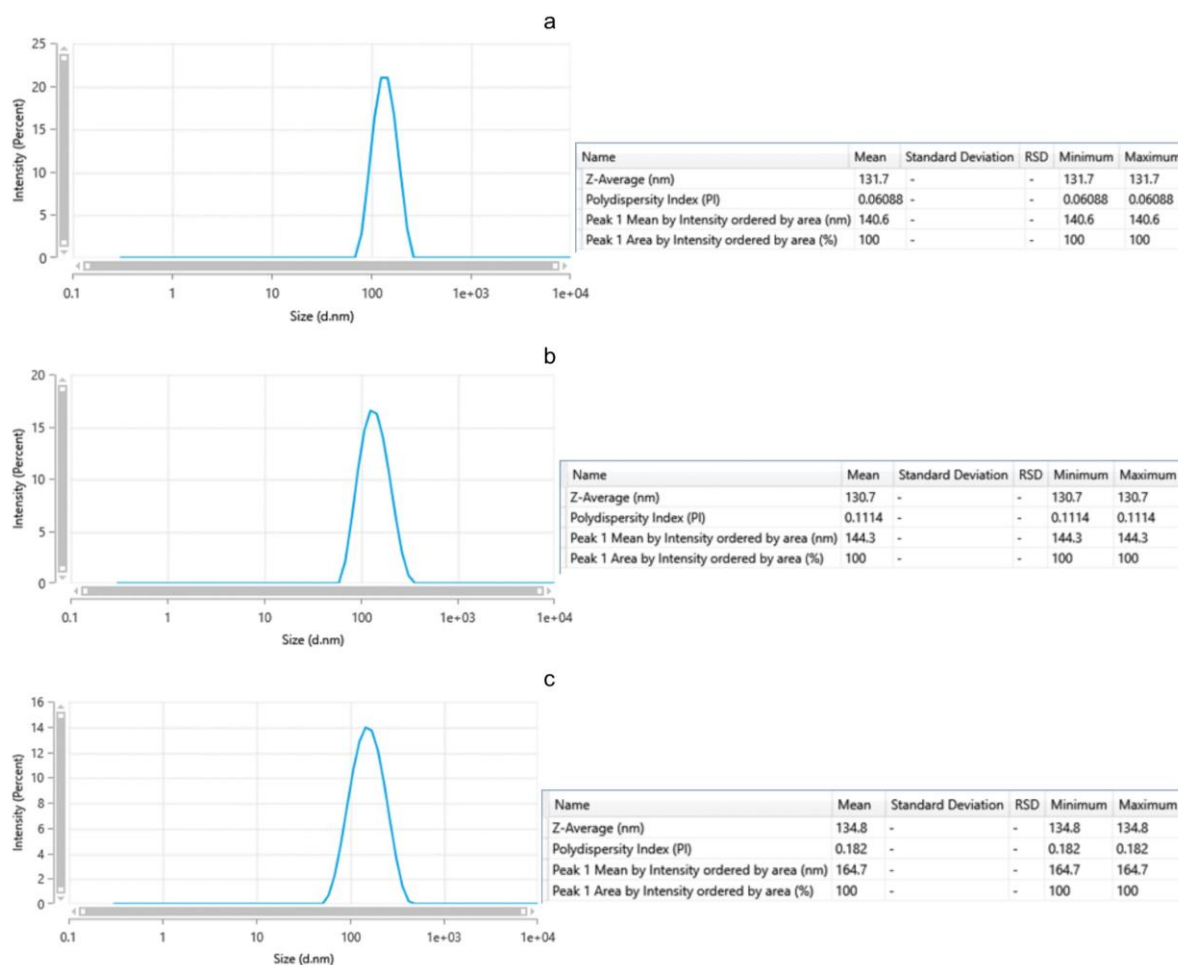
Figure 5.7C DLS graph of FOL-CET tagged CUR (a), DOX (b), and CUR-DOX (c) loaded liposomes

After attaching CET to the drug loaded liposomes, we removed the untagged CET by ultracentrifugation and redispersed the pellet in PBS. To ensure a suspension of single particles, we passed the liposomes through a polycarbonate membrane.

Upon comparing the specifications of all the FOL-CET tagged liposomes, we noted equivalent hydrodynamic diameters corresponding to both FOL and CET attached to the particle's surface (Figure 5.8C). But the PDI changed significantly (ANOVA p value = 0.0005): the PDI for the FOL-CET CUR-DOX liposomes was higher than FOL-CET CUR liposomes (t-test p value = 0.0019), and FOL-CET DOX liposomes (t-test p value = 0.0067), and the PDI for FOL-CET DOX was higher than FOL-CET CUR liposomes (t-test p value = 0.0281). However, the PDI values for all the formulations were lower than 0.3, indicating monodisperse populations. The zeta potential values remained unaltered and neutral to incipient stability owing to PEG, FOL, and CET tagged on the particle surface.
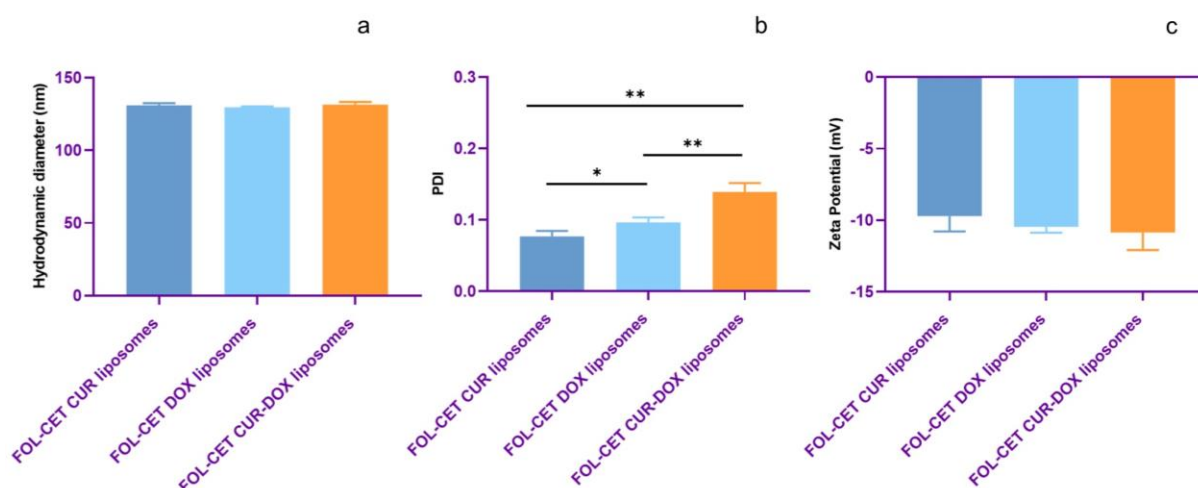
Figure 5.8B Comparison of hydrodynamic diameter (a), PDI (b) and zeta potential (c) of FOL-CET CUR liposomes, FOL-CET DOX liposomes and FOL-CET CUR-DOX liposomes

We compared the specifications of FOL-CET tagged liposomes with their non-tagged counterparts (Figure 5.9C). The PEGylated CUR liposomes were significantly smaller than FOL-CET CUR liposomes (t-test p value = 0.0073); the PEGylated DOX liposomes were significantly smaller than FOL-CET DOX liposomes (t-test p value = 0.0016) with lower PDI value (t-test p value = 0.0238); the PEGylated CUR-DOX liposomes were significantly smaller than the FOL-CET CUR-DOX(t-test p value = 0.0073) with lower PDI value (t-test p value = 0.0086). The zeta potential values remained unaltered. The increase in size and PDI corresponds to both FOL and CET tagging on the liposomal surface.
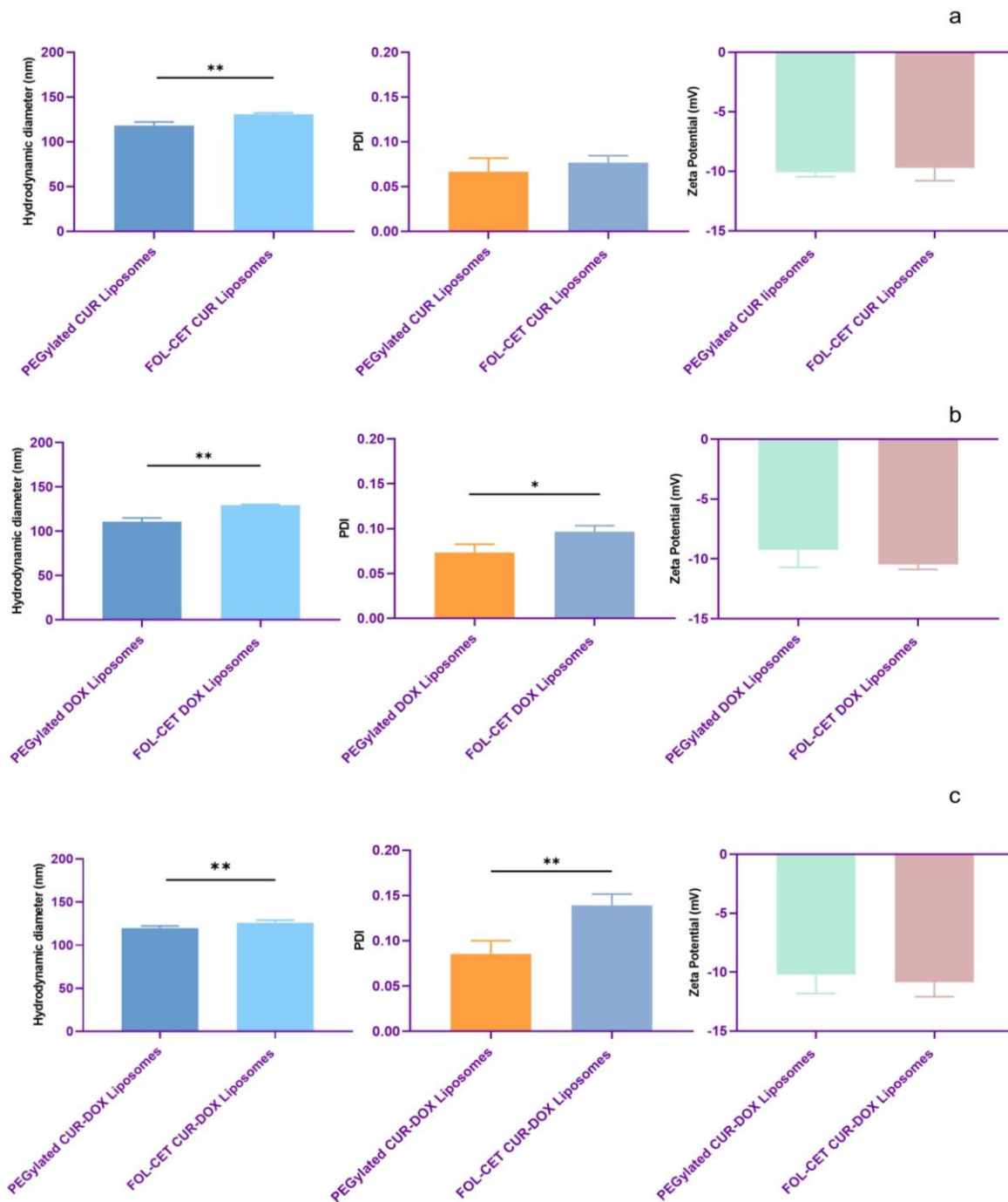
Figure 5.9C Comparison of hydrodynamic diameter, PDI, and zeta potential of PEGylated CUR and FOL-CET CUR liposomes (a), PEGylated DOX and FOL-CET DOX liposomes (b) and PEGylated CUR-DOX and FOL-CET CUR-DOX liposomes (c)

5.4.2C % EE

We calculated the % EE of CUR and DOX in FOL-CET tagged liposomes (Table 5.4).

Table 5.4C % EE of FOL-CET tagged liposomes

Formulations	% EE
FOL-CET CUR liposomes	79.29 ± 2.96
FOL-CET DOX liposomes	76.47 ± 2.20
FOL-CET CUR-DOX liposomes	**CUR:** 79.00 ± 3.65
	DOX: 76.77 ± 2.89

We calculated similar % EE of all the FOL-CET tagged liposomes (Figure 5.10B), suggesting that the drug encapsulation remained unaffected by FOL and CET tagging, the drug retained in the particles during tagging CET and the particles are in a similar size range.
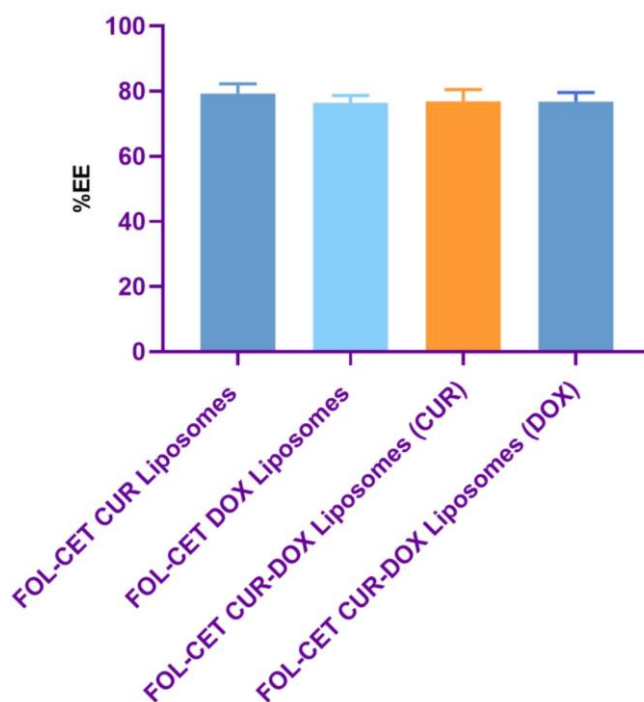
Figure 5.10C Comparison of % EE of FOL-CET tagged CUR, DOX, and CUR-DOX loaded liposomes

On comparing the FOL-CET tagged liposomes with their non-tagged counterparts, we noted equivalent % EEs, implying that the drug encapsulation remained unaffected by FOL and CET tagging (Figure 5.11C).
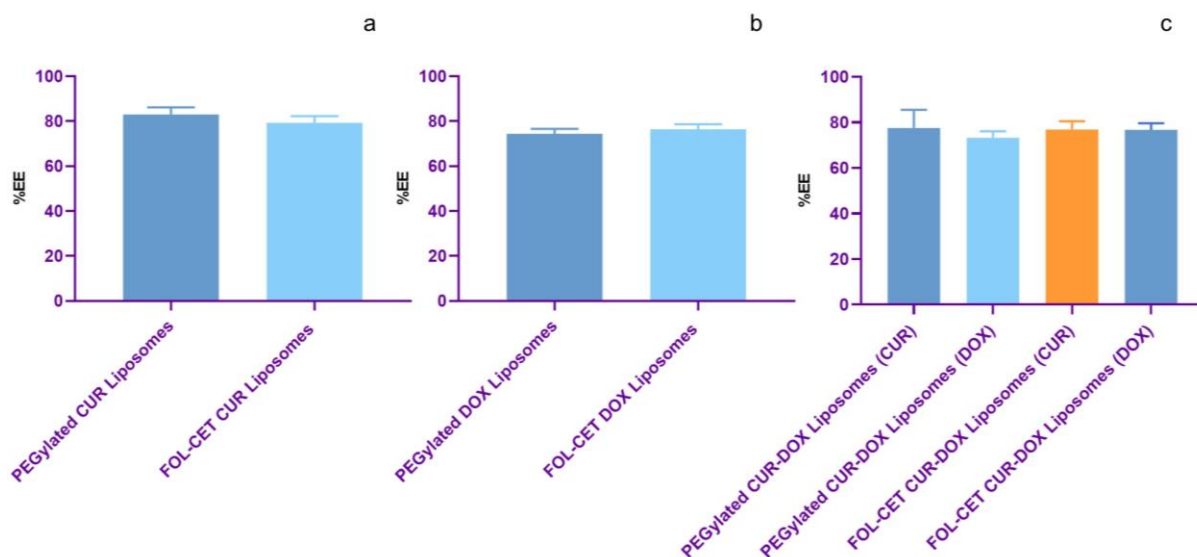
Figure 5.11C Comparison of % EE between non-targeted and FOL-CET tagged liposomes

5.4.3C Morphology of FOL-CET tagged liposomes

The HRTEM images for the three FOL-CET formulations show spherical structures with smooth surfaces (Figure 5.12C). The images show smaller particles than the hydrodynamic diameter deduced by DLS.
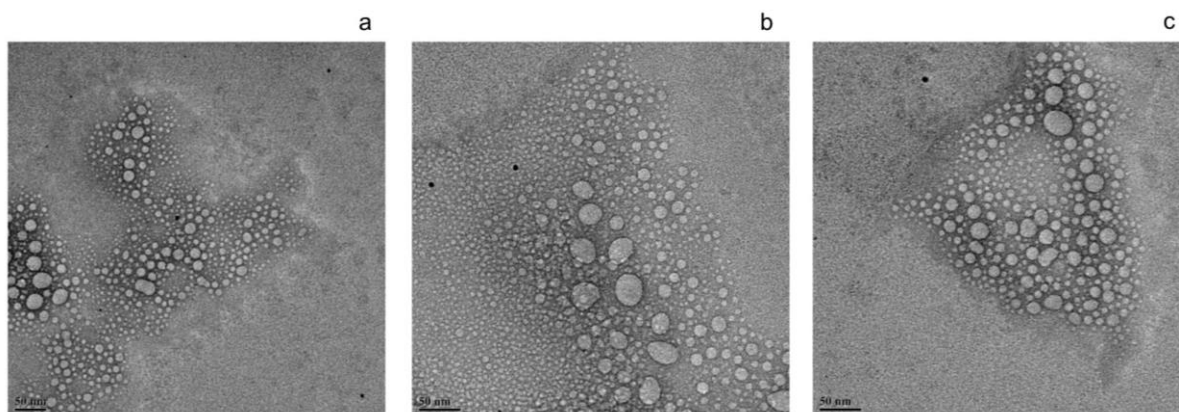
Figure 5.12C HRTEM/TEM images of FOL-CET tagged CUR (a), DOX (b) and CUR-DOX (c) liposomes

5.4.4C % BE of CET

We determined the equivalent % BE of CET by the Bradford assay at 87.55 ± 2.74 % for FOL-CET CUR liposomes, 86.96 ± 2.35 % for FOL-CET DOX liposomes, and 87.67 ± 1.34 % for FOL-CET CUR-DOX liposomes (Figure 5.13C).
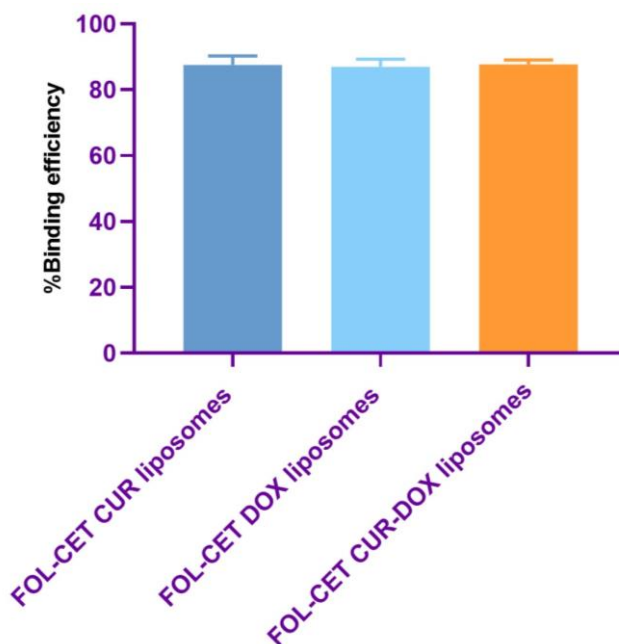
Figure 5.13C Comparison of %BE of CET on different FOL-CET tagged liposomes

5.5C Conclusion

We synthesized FOL-CET tagged liposomes with the previously optimized values of process parameters of liposomal synthesis by the thin film hydration technique; molar ratio of the lipids, concentration of PC, CHOL, and DSPE-mPEG2000; concentration of CUR and DOX. We added 0.1 mole % of DSPE-PEG2000-COOH to tag CET on the surface of liposomes by carbodiimide coupling and 0.1 mole % of DSPE-PEG2000-FOL. We optimized 11 extrusion passes to downsize the dual ligand tagged liposomes.

We observed that the particle size increased after the tagging of FOL and CET compared to the non targeted liposomes. We recorded the hydrodynamic diameter, PDI, and zeta potential for FOL-CET CUR liposomes at 130.90 ± 1.54 nm, 0.08 ± 0.01, and -9.71 ± 1.08 mV respectively; FOL-CET DOX liposomes at 129.57 ± 0.67 nm, 0.10 ± 0.01, and -10.45 ± 0.42mV

respectively; and FOL-CET CUR-DOX liposomes at 125.97 ± 3.11 nm, 0.14 ± 0.01 and -10.86 ± 1.22 mV respectively. The HRTEM image showed liposomes with spherical morphology.

We calculated the % EE of CUR in FOL-CET CUR liposomes at $79.29 \pm 2.96\%$, of DOX in FOL-CET DOX liposomes at 76.47 ± 2.20 %, and of CUR and DOX in FOL-CET CUR-DOX liposomes at 79.00 ± 3.65 % and 76.77 ± 2.89 % respectively. We calculated the %BE of CET for FOL-CET CUR liposomes at 87.55 ± 2.74 %, for FOL-CET DOX liposomes at 86.96 ± 2.35 %, and for FOL-CET CUR-DOX liposomes at 87.67 ± 1.34 %. Thus, the results suggest the synthesis of robust FOL-CET tagged and drug loaded liposomes according to the drug delivery mandates.

CHAPTER 6

Optimization, Synthesis, and Characterization of pH responsive liposomes

6.1 Introduction

Cytotoxic drugs enter the cells via simple diffusion and face P-gp receptors that engender MDR in breast cancer cells. Liposomes bypass these receptors as they undergo endocytosis and deliver drugs to the cytoplasm, overcoming MDR (Shen et al., 2008). After endocytosis, liposomes undergo the endosome-lysosome pathway, where the pH drops to $6 - 5$ in the early and late endosomes and $5 - 4$ in the lysosomes (Liu et al., 2020). The highly acidic environment in the lysosomes causes the liposomal components and the drugs to degrade and release slowly in the cytoplasm, reducing the drugs' therapeutic index (Chu et al., 1990). pH responsive liposomes supersede the conventional liposomes by displaying sensitivity to the pH of the endosomes triggering an endosomal escape and rapid release of the drug in the cytoplasm and circumventing the lysosomal stage (Yan and Ding, 2020) (Tang et al., 2019).

PC, a cylindrical shaped phospholipid, has an equal head group and acyl chain area and forms a lamellar phase in an aqueous medium pertinent to creating bilayers at physiological pH (Paliwal et al., 2015). But pH responsive liposomes are commonly fabricated with DOPE and CHEMS. DOPE has a minimally hydrated small head group region and a longer hydrophobic tail region, imparting a cone shape favoring a strong bond between the phosphate and amine groups of the lipid (Aghdam et al., 2019). This interaction allows an inverted hexagonal phase, a non-lamellar phase, to form above the phase transition temperature (Yuba, 2020).

CHEMS, a weakly acidic amphiphile, creates an electrostatic repulsion between its carboxylate groups and the phosphate groups of DOPE. These intermolecular interactions obstruct the hydrogen bonds between the neighboring DOPE molecules that favor bilayers (Santiago, 2013). But, when the carboxylic groups of CHEMS protonate in the acidic medium of endosomes, it negates the electrostatic repulsion, causing the DOPE to change its lamellar phase to an inverted hexagonal phase. This mechanism destabilizes the liposomes and triggers the release of the encapsulated drugs (Collins et al., 1990) (Jain et al., 2021) (Sudimack et al., 2002). Being an analog of CHOL, CHEMS also imparts stability to the bilayer, acting as an efficient stabilizer.

The endosomal escape of the drugs into the cytoplasm follows three proposed mechanisms. Firstly, the destabilizing pH responsive liposomes instigate the endosomal membrane to destabilize by forming pores and causing drug release (Paliwal et al., 2015). Secondly, the drug from the destabilizing pH responsive liposomes diffuses into the cytoplasm through the

endosomal membrane (Kanamala et al., 2019). Thirdly, the membranes of the liposomes and endosomes fuse to release the drug in the cytoplasm; liposomes might exhibit a net positive charge when protonated that fuses with the endosomal membrane with a net negative charge (Shi et al., 2002).

The RES rapidly removes the pH liposomes due to the unsaturated fatty acyl chains and a net negative charge of the lipid, but functionalizing the liposomal surface with PEG helps evade the immune system, enhancing the circulation time of the carrier (Zignani et al., 2000) (Sudimack et al., 2002). Studies report that pH responsive liposomes composed of DOPE, CHEMS, and DSPE-mPEG2000 are effectively internalized compared to the non-responsive liposomes as DOPE increases the hydrophobic nature, causing the liposomes to aggregate at the cell surface (Ferreira et al., 2013).

We synthesized pH responsive liposomes using the already optimized values for the non-responsive liposomes. We then characterized these particles for their hydrodynamic diameter, PDI, zeta potential, morphology, functional groups, % EE, % DL, and thermal stability.

6.2 Methods

We synthesized pH liposomes using a 7: 3 molar ratio of DOPE: CHEMS, 1 mole % of DSPE-mPEG2000, 1: 50 (wt. / wt.) ratio of CUR: lipids and 0.1 mg DOX- as elaborated in Chapter 2, section 2.2.8. FOL tagged liposomes were synthesized by adding 0.1 mole % of DSPE-PEG2000-FOL; CET tagged liposomes were synthesized by adding 0.1 mole % DSPE-PEG2000-COOH during the thin film formation step and later tagged with CET by the EDC-NHS carbodiimide chemistry; the same protocol synthesized FOL-CET pH liposomes.

6.2.1 Optimization of the downsizing step

The pH responsive liposomes were optimized for the number of extrusion passes (5, 11, and 21) to reduce the particle size and PDI to attain comparable specifications to the non-responsive counterparts.

6.2.2 Characterization of pH responsive liposomes

The pH responsive liposomes were characterized by various analytical techniques (chapter 2 Section 2.3): hydrodynamic diameter, PDI, and zeta potential values by DLS analysis; the

morphology by HRTEM/TEM imaging; % EE and % DL; %BE of CET by Bradford assay; functional groups by FTIR analysis; and thermal analysis by TGA and DSC.

6.3 Results and Discussion

6.3.1 Optimization of pH responsive plain liposomes

We optimized the number of extrusion passes for pH responsive plain liposomes and recorded the hydrodynamic diameter < 200 nm and PDI < 0.3 (Table 6.1).

Table 6.1 Hydrodynamic diameter and PDI of pH responsive plain liposomes before and after a series of extrusion passes

Formulations	Average Hydrodynamic diameter (nm)	Average PDI	Average Zeta potential (mV)
Extrusion- 5	158.13 ± 7.10	0.23 ± 0.08	
Extrusion- 11	137.08 ± 2.51	0.10 ± 0.01	-9.41 ±0.97
Extrusion- 21	128.13 ± 1.59	0.07 ± 0.02	

The hydrodynamic diameter of pH responsive liposomes decreased significantly after extrusion (ANOVA p value = 0.0004) (Figure 6.1). Comparing the particle specifications with 11 extrusion passes (as optimized for non-responsive liposomes), we noted that the particle size reduced significantly after 5 extrusion passes (t-test p value = 0.0083) and further after 21 extrusion passes (t-test p value = 0.0065). The PDI also reduced significantly (ANOVA p value = 0.0124) for particles after 11 extrusion passes than 5 extrusion passes (t-test p value = 0.0437) but remained unchanged after 21 extrusion passes. This trend is dissimilar to the non responsive liposomes, where the particle specifications remained unchanged after 10 extrusion passes, indicating larger pH responsive liposomes. These results suggest that the particle specifications also change when modulating the liposomal components.
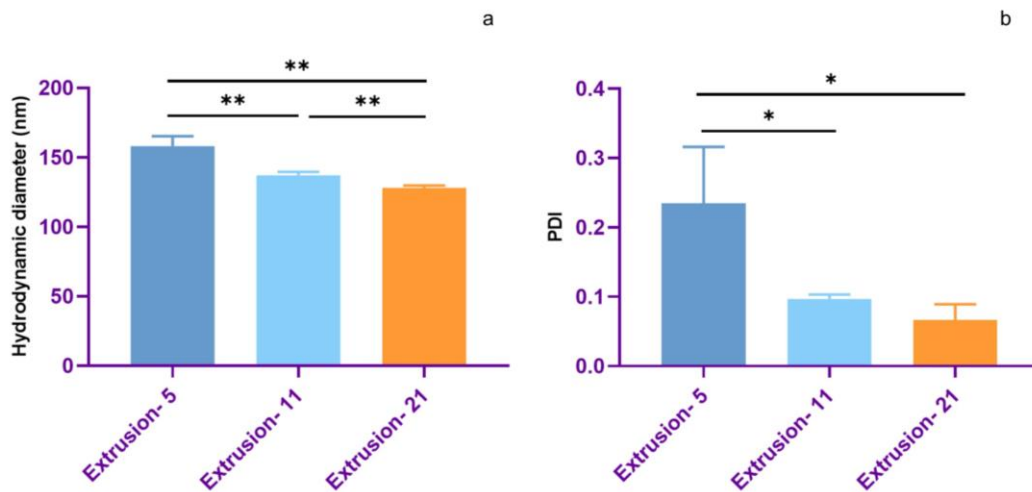
Figure 6.1 Hydrodynamic diameter and PDI of pH responsive plain liposomes after hydration and after a series of extrusion passes

On comparing the specifications of non responsive plain liposomes (optimized 10 extrusion passes) (Figure 6.2), we noted that the pH responsive plain liposomes (ANOVA p value = < 0.0001) with 11 (t-test p value = 0.0004) and 21 extrusion passes (t-test p value = 0.0021) were significantly larger. The PDI values remained unchanged, with values < 0.3 indicating monodisperse populations. The pH responsive liposomes' absolute zeta potential value reduced significantly (t-test p value = 0.0431).
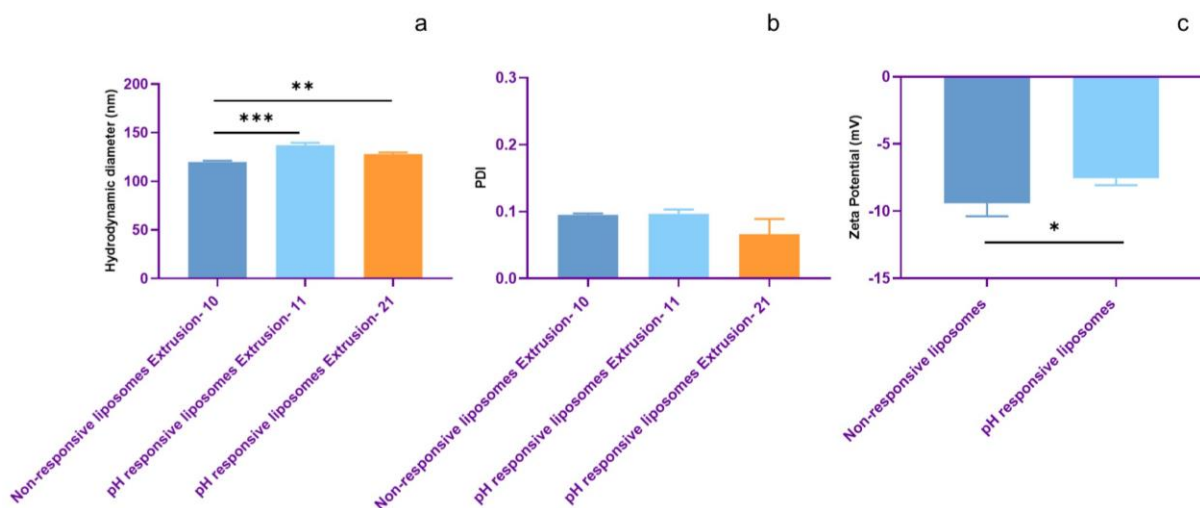
Figure 6.2 Comparative analysis of non responsive and pH responsive plain liposomes

6.3.2 Optimization of pH responsive CUR-DOX liposomes

CUR positions in the lipid bilayer in the pH responsive liposomes and DOX in the aqueous core. We recorded the particle size below 200 nm and the PDI values < 0.3, suggesting a monodisperse population of smaller sized particles (Table 6.2).

Table 6.2 Hydrodynamic diameter and PDI of pH responsive CUR-DOX liposomes after 5 and 11 extrusion passes

Formulations	Average Hydrodynamic diameter (nm)	Average PDI	Average Zeta Potential (mV)
Extrusion- 5	153.10 ± 5.93	0.10 ± 0.02	
Extrusion- 11	136.47 ± 2.58	0.08 ± 0.03	-11 ± 0.35

The particle size reduced significantly after 11 extrusion passes (t-test p value = 0.0119), but the PDI values remained unchanged (Figure 6.3). We optimized 11 extrusion passes to downsize pH responsive CUR-DOX liposomes.
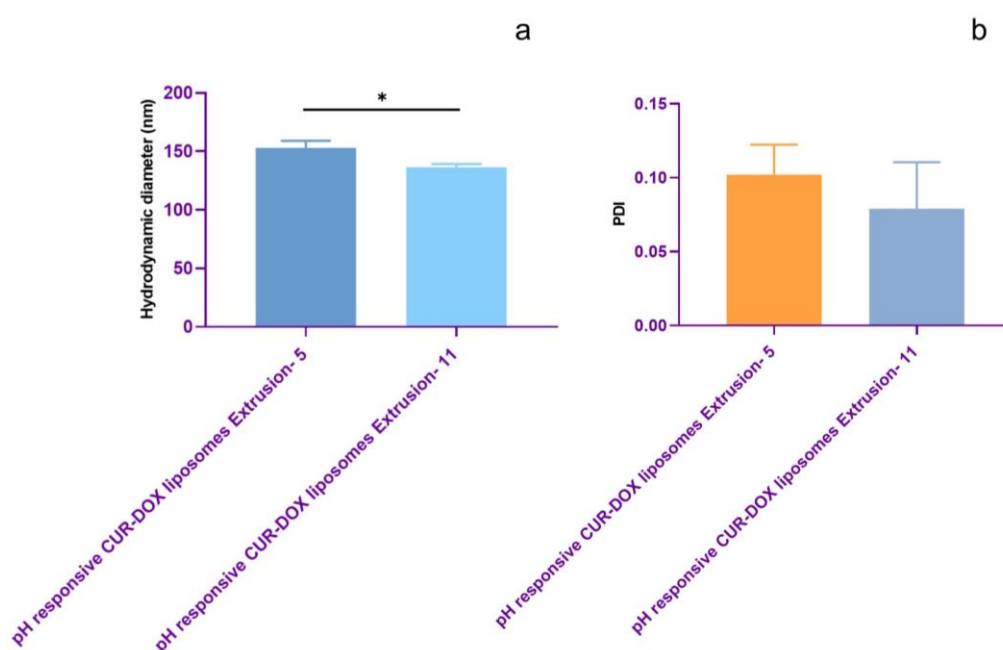
Figure 6.3 Hydrodynamic diameter and PDI of pH responsive CUR-DOX liposomes after 5 and 11 extrusion passes

Upon comparing the specifications with the non responsive liposomes with the optimized 5 extrusion passes, we recorded a larger size for pH responsive CUR-DOX liposomes (ANOVA p value = 0.0002) (Figure 6.4) with 5 (t-test p value = 0.0008) and 11 (t-test p value = 0.0014) extrusion passes. The PDI and zeta potential values remained unchanged for both formulations, corresponding to effective downsizing and PEGylation of the liposomal surface.
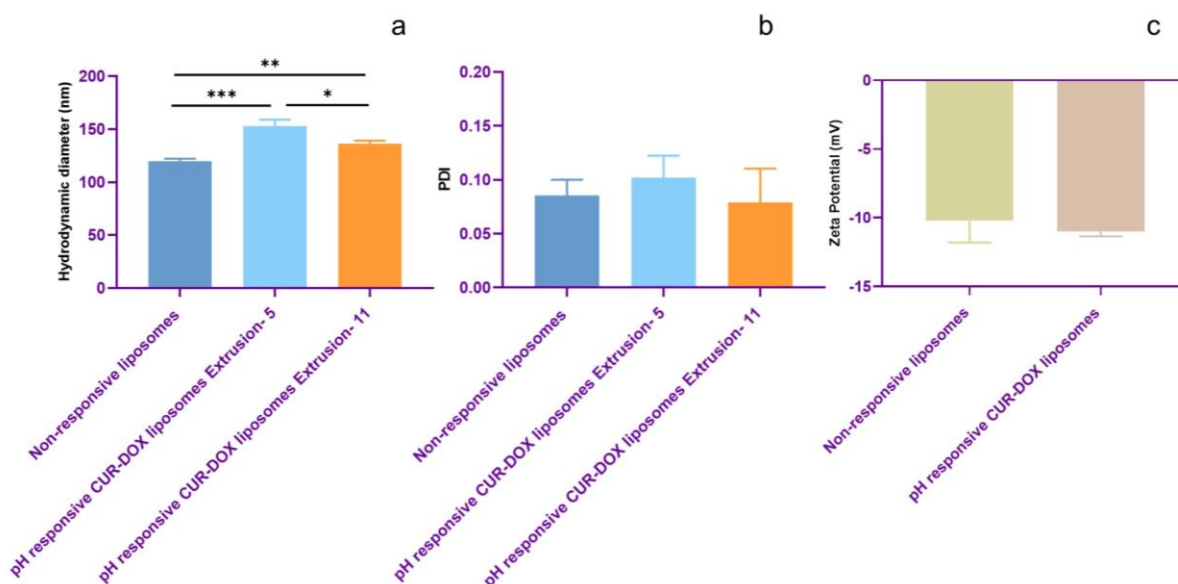
Figure 6.4 Comparative analysis of non-responsive and pH responsive CUR-DOX liposomes

6.3.3 Optimization of pH responsive FOL CUR-DOX liposomes

We recorded the particle size for pH responsive FOL CUR-DOX liposomes < 200 nm and PDI values < 0.3, suggesting monodisperse populations (Table 6.3).

Table 6.3 Hydrodynamic diameter and PDI of pH responsive FOL CUR-DOX liposomes after 5 and 11 extrusion passes

Formulations	Average Hydrodynamic diameter (nm)	Average PDI	Average Zeta Potential (mV)
Extrusion- 5	155.58 ± 1.59	0.14 ± 0.01	
Extrusion- 11	136.99 ± 4.70	0.11 ± 0.04	-8.54 ± 0.34

The particle size reduced significantly after 11 extrusion passes (t-test p value = 0.0029), but the PDI values remained unchanged (Figure 6.5). We optimized 11 extrusion passes to downsize pH responsive FOL CUR-DOX liposomes.
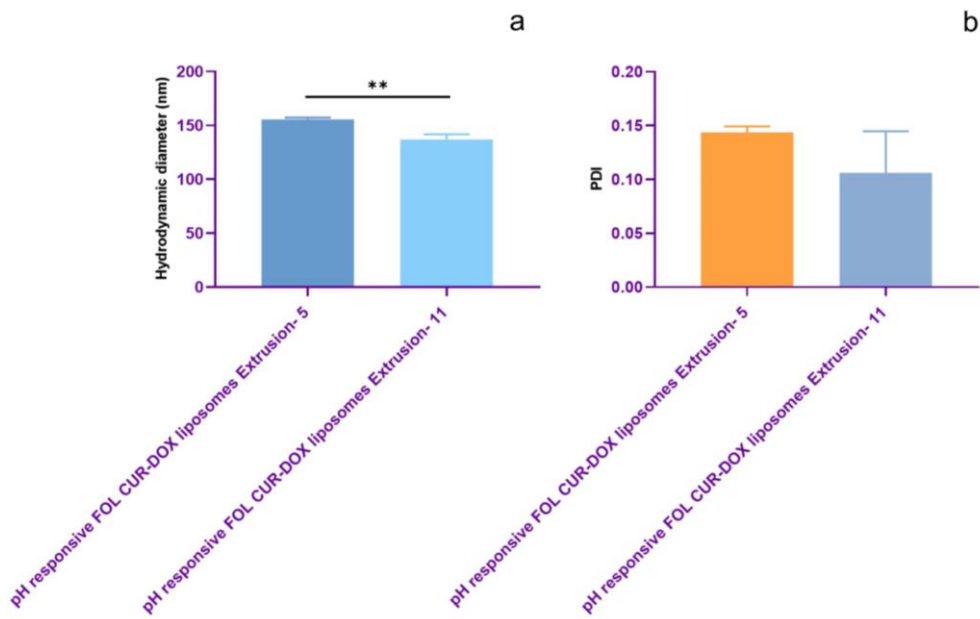
Figure 6.5 Hydrodynamic diameter and PDI of CUR-DOX pH liposomes after 5 and 11 extrusion passes

The hydrodynamic diameter, PDI, and zeta potential of non-responsive and pH responsive FOL CUR-DOX liposomes remained unchanged as we optimized 11 extrusion passes for both formulations (Figure 6.6).
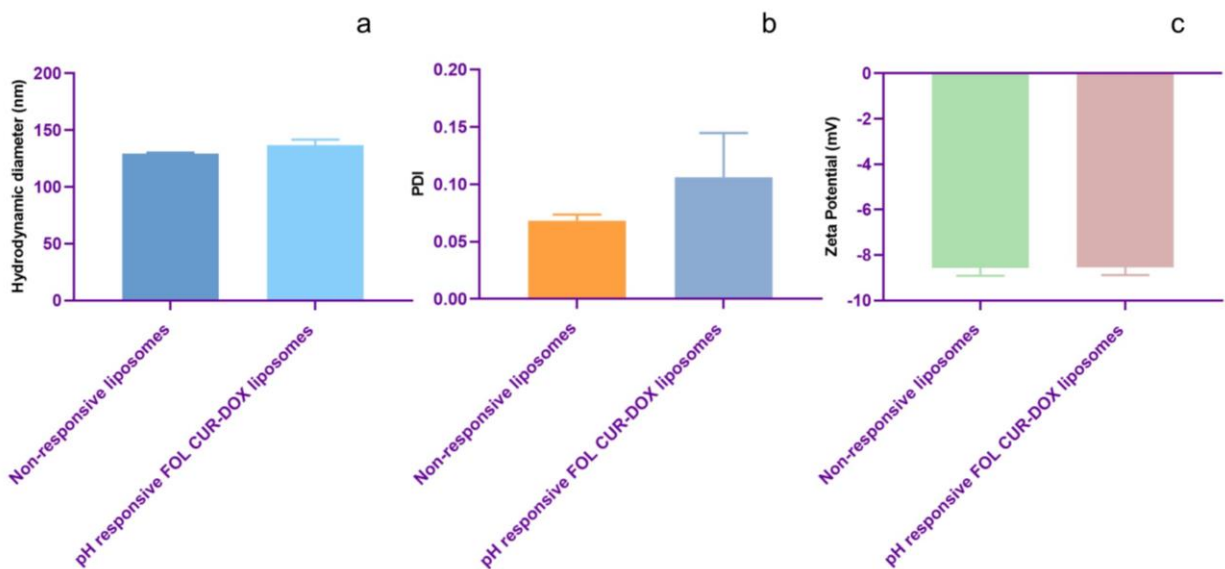
Figure 6.6 Comparative analysis of non-responsive and pH responsive FOL CUR-DOX liposomes

6.3.4 Optimization of pH responsive CET CUR-DOX liposomes

We synthesized pH responsive liposomes by adding DSPE-PEG2000-COOH in the thin film hydration step and attached CET after extruding the particles. We optimized the number of extrusion passes before tagging CET on the liposomal surface and recorded the particle size < 200 nm and PDI < 0.3 for both 5 to 11 extrusion passes (Table 6.4) (Figure 6.4).

Table 6.4 Hydrodynamic diameter and PDI of CUR-DOX pH liposomes-DSPE-PEG2000-COOH after 5 and 11 extrusion passes

Formulations	Average Hydrodynamic diameter (nm)	Average PDI
Extrusion- 5	149.27 ± 1.31	0.13 ± 0.03
Extrusion- 11	130.13 ± 0.84	0.06 ± 0.01

The particle size (t-test p value = < 0.0001) and PDI (t-test p value = 0.0171) reduced significantly after 11 extrusion passes (Figure 6.7). We optimized 11 extrusion passes for these formulations.
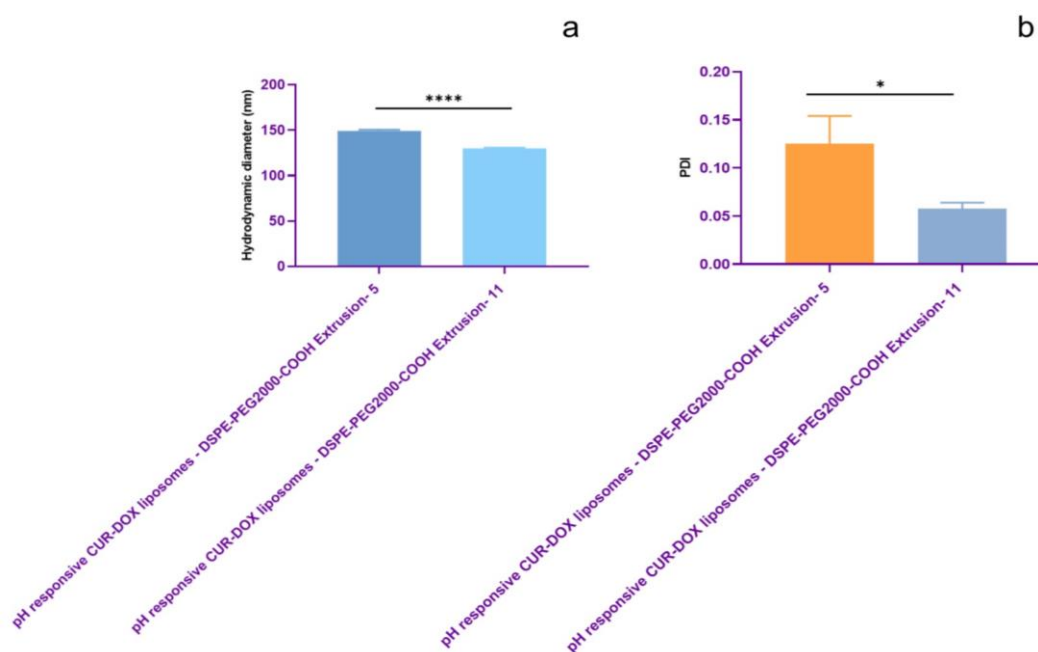
Figure 6.7 Hydrodynamic diameter and PDI of CUR-DOX pH liposomes-DSPE-PEG2000-COOH after 5 and 11 extrusion passes

After tagging CET, we recorded the hydrodynamic diameter at 157.72 ± 2.07 nm, PDI at 0.18 ± 0.01, and zeta potential at -8.26 ± 0.05 mV. This formulation was significantly larger (t-test p value $= < 0.0001$) than the non responsive counterparts with equivalent PDI values (Figure 6.8). The absolute value of zeta potential for pH responsive liposomes was lower (t-test p value $= 0.0034$).
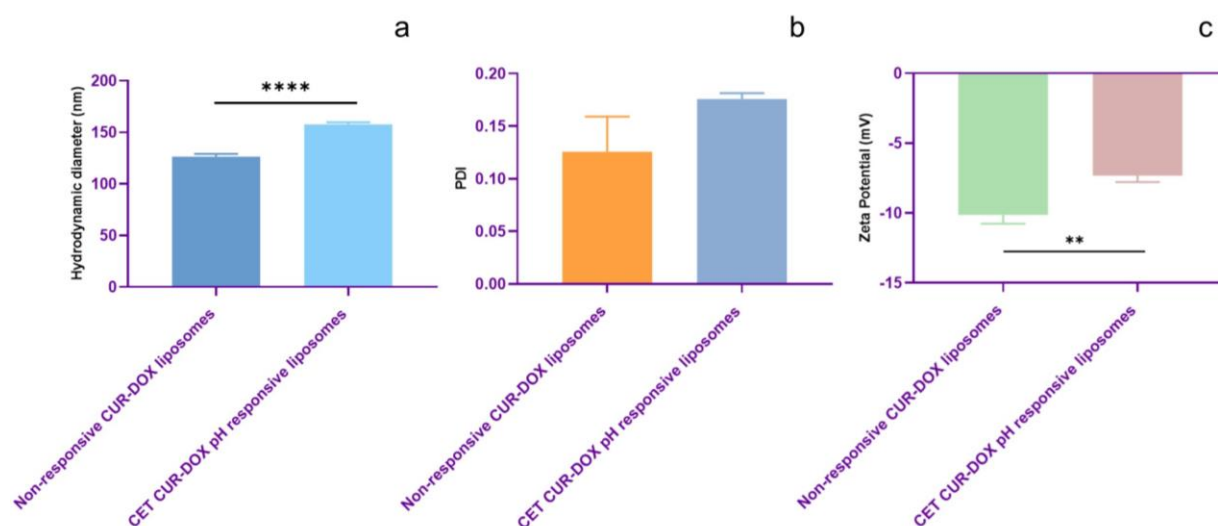
Figure 6.8 Comparative analysis of non-responsive and pH responsive CET CUR-DOX liposomes

6.3.5 Optimization of pH responsive FOL-CET CUR-DOX liposomes

We synthesized pH responsive liposomes by adding DSPE-PEG2000-COOH and DSPE-PEG2000-FOL in the thin film hydration step and attached CET after extruding the particles. We optimized the number of extrusion passes before tagging CET on the liposomal surface and recorded the particle size < 200 nm and PDI < 0.3 for both 5 to 11 extrusion passes (Table 6.5).

Table 6.5 Hydrodynamic diameter and PDI of pH responsive FOL CUR-DOX liposomes-DSPE-PEG2000-COOH after 5 and 11 extrusion passes

Formulations	Average Hydrodynamic diameter (nm)	Average PDI
Extrusion- 5	226.07 ± 1.60	0.24 ± 0.02
Extrusion- 11	124.07 ± 3.08	0.08 ± 0.02

The hydrodynamic diameter (t-test p value = < 0.0001) and PDI (t-test p value = 0.0003) reduced significantly from 5 to 11 extrusion passes (Figure 6.9). We optimized 11 extrusion passes for these formulations.
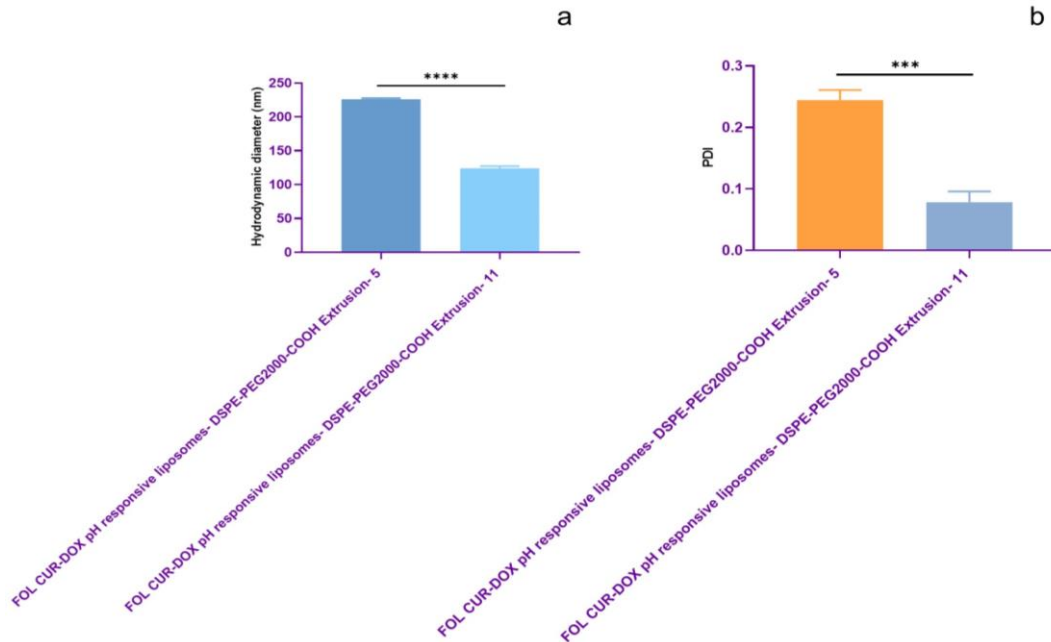
Figure 6.9 Hydrodynamic diameter and PDI of pH responsive FOL CUR-DOX liposomes-DSPE-PEG2000-COOH after 5 and 11 extrusion passes

After tagging CET, we recorded the hydrodynamic diameter at 163.21 ± 1.51 nm, PDI at 0.17 ± 0.001, and zeta potential at -9.63 ± 1.53 mV. We observed larger sizes (t-test p value = < 0.0001), higher PDI (t-test p value = 0.0202), and equivalent zeta potential values for pH responsive FOL-CET CUR-DOX liposomes than the non-responsive liposomes (Figure 6.10).
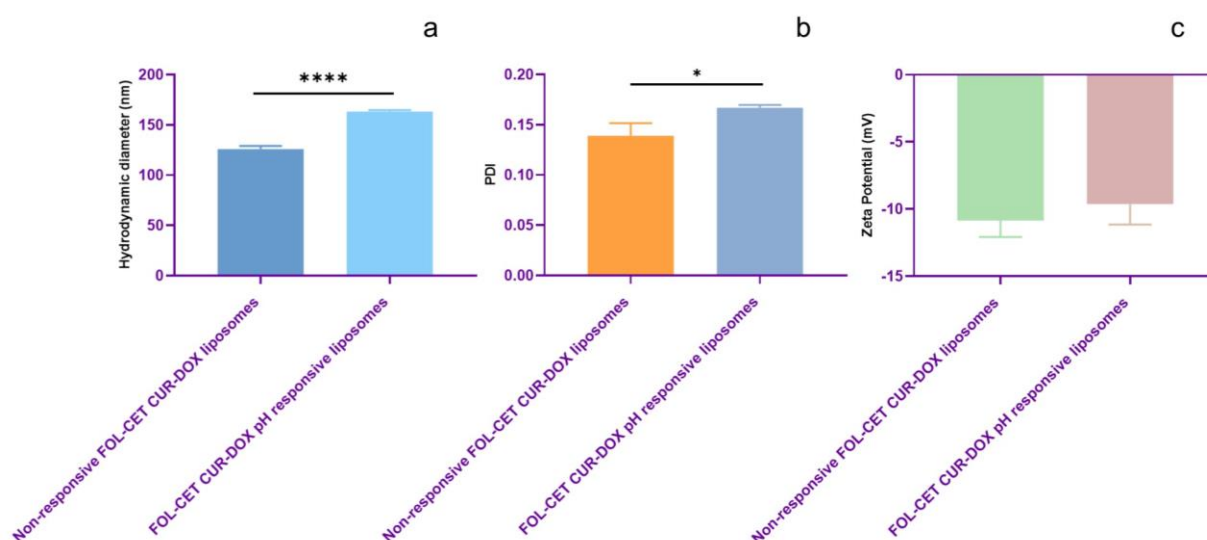
Figure 6.10 Comparative analysis of non-responsive and pH responsive FOL-CET CUR-DOX liposomes

6.4 Characterization of pH responsive liposomes

6.4.1 Hydrodynamic diameter, PDI, and zeta potential

The DLS graph shows the hydrodynamic diameter and PDI for pH responsive plain liposomes at 127.8 nm and 0.07, for pH responsive CUR-DOX liposomes at 142.4 nm and 0.07, respectively, for pH responsive FOL CUR-DOX pH liposomes at 137.9 nm and 0.12 respectively, for pH responsive CET CUR-DOX pH liposomes at 156 nm and 0.1843 respectively, and pH responsive FOL-CET CUR-DOX pH liposomes at 164.7 nm and 0.17 respectively. Single sharp peaks for all the formulations suggest a monodisperse population of smaller particles (Figure 6.11).
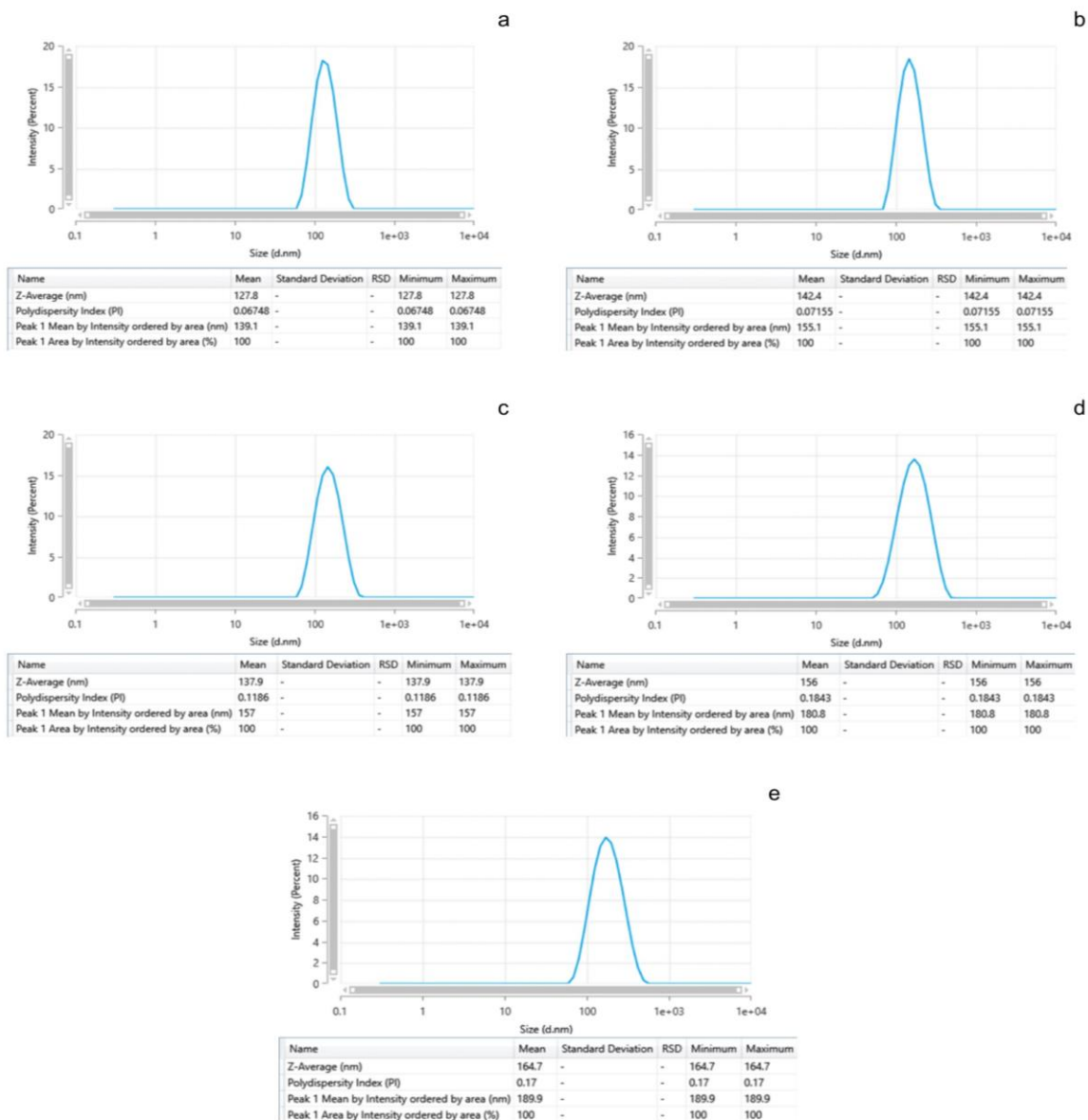
Figure 6.11 DLS graphs of pH responsive plain liposomes (a), pH responsive CUR-DOX liposomes (b), pH responsive FOL CUR-DOX liposomes (c), pH responsive CET CUR-DOX liposomes (d) and pH responsive FOL-CET CUR-DOX liposomes (e)

The optimized 1 mole % of DSPE-mPEG2000 is low enough for the pH liposomes to retain their responsive behaviour as higher PEG concentrations reduce the pH sensitivity of the liposomes (Roux et al., 2004).

On comparing all the pH responsive liposomes (ANOVA p value = < 0.0001) (Figure 6.12), we noted equivalent sizes of pH responsive CUR-DOX liposomes and pH responsive FOL CUR-DOX liposomes, but lower than CET tagged (t-test p value = 0.0005) and FOL-CET

tagged (t-test p value = 0.0001) liposomes; the FOL tagged liposomes were smaller than the CET tagged (t-test p value = 0.0022) and FOL-CET tagged (t-test p value = 0.0008) liposomes. The CET tagged liposomes were lower than the FOL-CET tagged liposomes (t-test p value = 0.0207). The larger size of CET and the largest size of FOL-CET tagged liposomes corresponds to the tagging of CET after liposomal synthesis and FOL in the latter formulation.

The PDI of these pH responsive liposomes also saw a significant change (ANOVA p value = 0.0039): the PDI of pH responsive CUR-DOX liposomes was lower than CET tagged (t-test p value = 0.0063) and FOL-CET tagged (t-test p value = 0.0085) liposomes; the PDI of FOL tagged liposomes was lower than the CET tagged liposomes (t-test p value = 0.0370). But, the values for all the formulations were < 0.3, suggesting monodisperse populations.
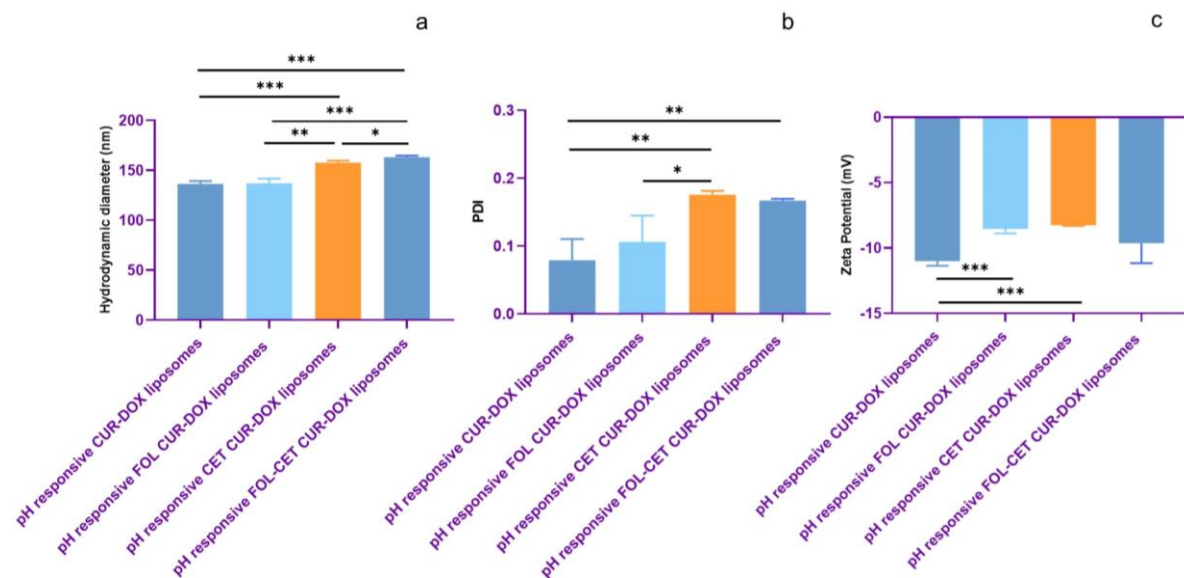
Figure 6.12 Comparative analysis of hydrodynamic diameter (a), PDI (b), and zeta potential (c) of all pH responsive liposomes

The zeta potential of the liposomes also changed (ANOVA p value = 0.0116): the absolute value for pH responsive CUR-DOX liposomes was higher than FOL tagged (t-test p value = 0.0010) and CET tagged (t-test p value = 0.0002). These zeta potential values are the neutral for all the pH responsive formulations corresponding to the PEGylation and ligand tagging on the liposomal surface.

6.4.2 % EE and % DL

We calculated the % EE (Table 6.6) and noted unchanged values for both CUR and DOX in all the pH responsive liposomes (Figure 6.13), corresponding to a similar size range for all the formulations.

Table 6.6 % EE of CUR and DOX in pH responsive liposomes

Formulations	Average % EE	
	CUR	**DOX**
pH responsive CUR-DOX liposomes	81.49 ± 2.95	79.77 ± 1.62
pH responsive FOL CUR-DOX liposomes	73.74 ± 2.51	74.70 ± 2.35
pH responsive CET CUR-DOX liposomes	77.22 ± 3.94	75.11 ± 2.91
pH responsive FOL-CET CUR-DOX liposomes	75.81 ± 3.16	76.89 ± 2.61
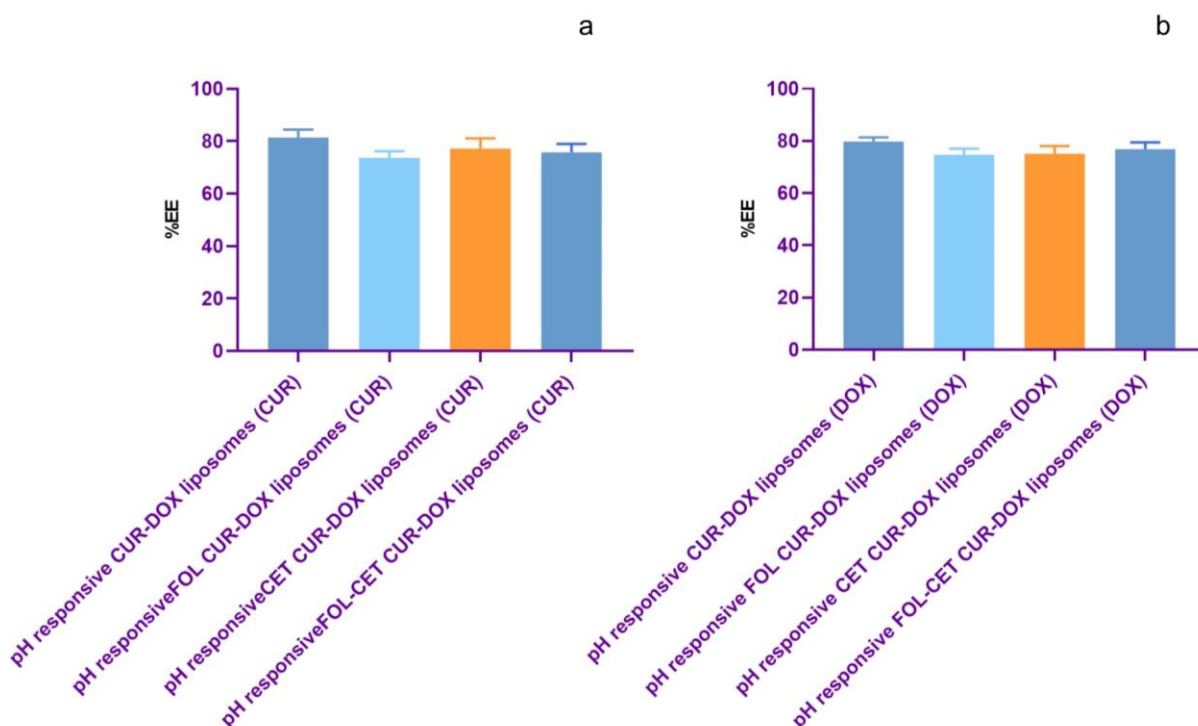
Figure 6.13 Comparison of % EE of CUR and DOX in different pH responsive liposomes

We observed a higher % EE for CUR (t-test p value = 0.0275) and DOX (t-test p value = 0.0268) in the pH responsive CUR-DOX liposomes than the non-responsive counterpart corresponding to its larger size (Figure 6.14). The % EE for CUR and DOX in FOL, CET, and

FOL-CET tagged pH responsive liposomes is comparable to the non-responsive liposomes corresponding to the equivalent sizes.
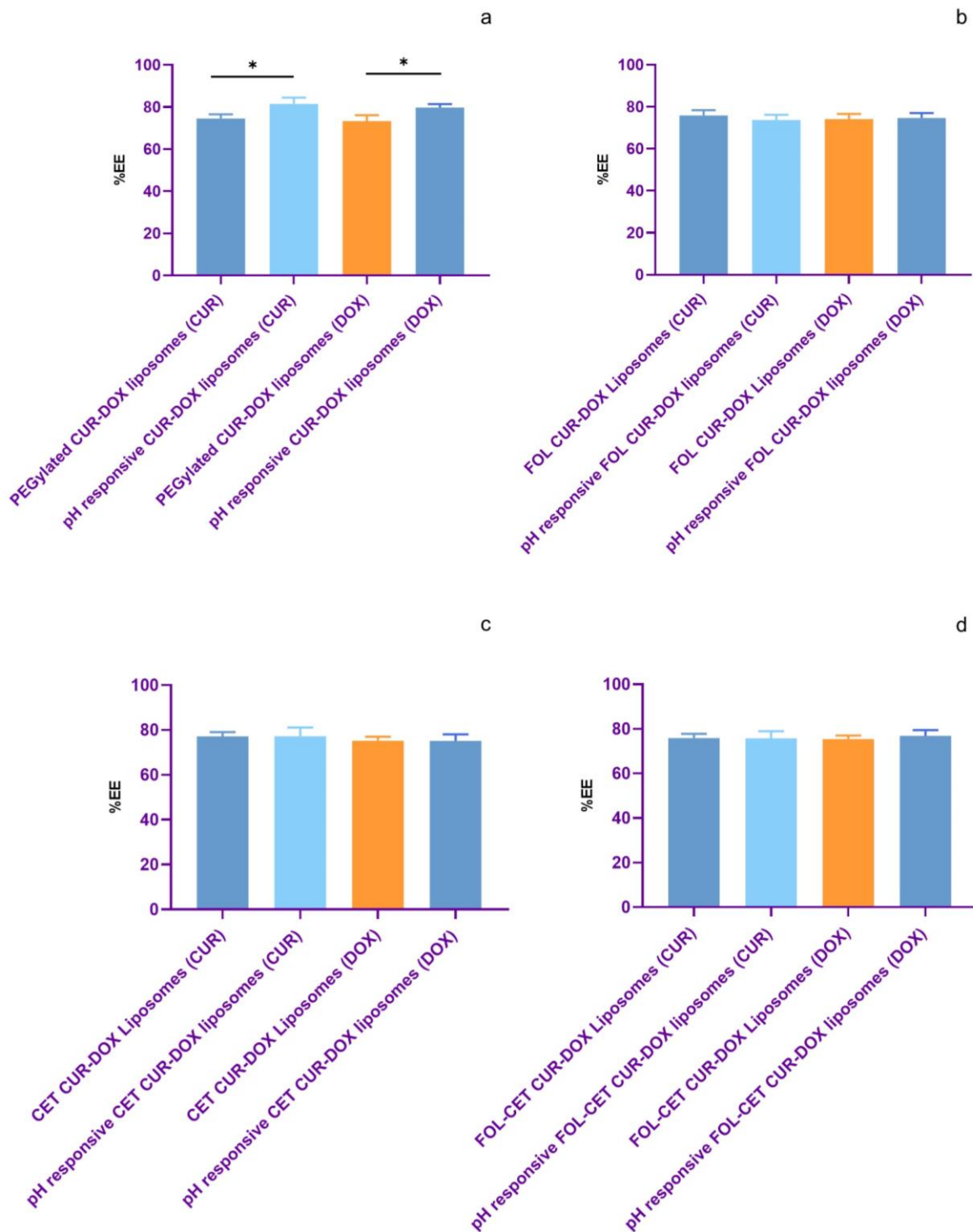
Figure 6.14 Comparison of % EE of CUR and DOX in non-responsive liposomes and pH responsive liposomes

We recorded the % DL for pH responsive CUR-DOX liposomes at 4.25 ± 0.47 % and for pH responsive FOL CUR-DOX liposomes at 4.56 ± 0.40 %; the % DL was equivalent to their non-responsive counterparts (Figure 6.15).
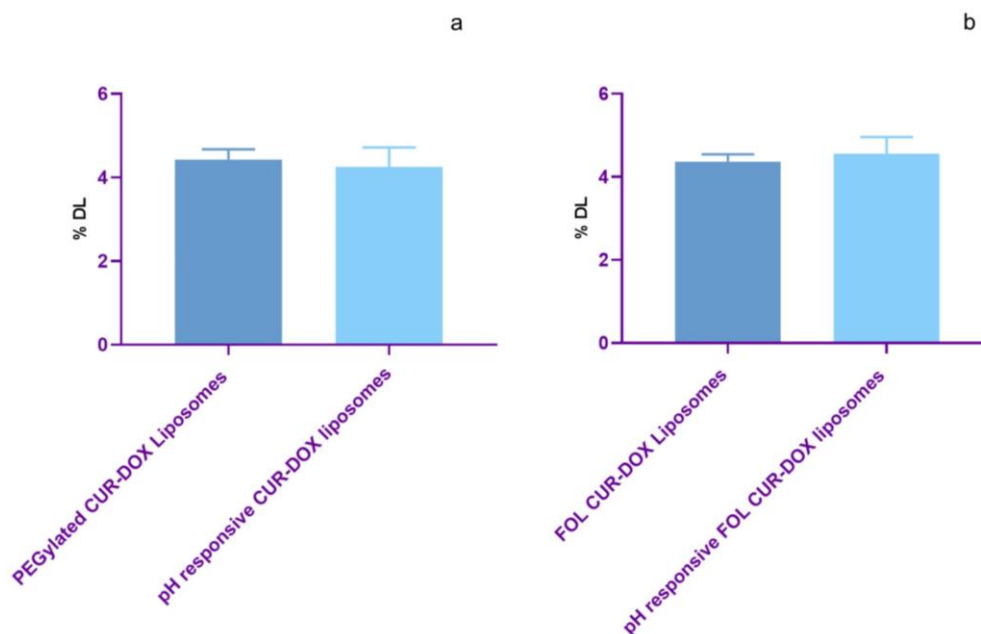
Figure 6.15 Comparison of % DL non-responsive and pH responsive CUR-DOX liposomes (a), and non-responsive and pH responsive FOL CUR-DOX liposomes

6.4.3 Morphology of pH liposomes

The pH responsive liposomes have a spherical morphology with smooth surfaces (Figure 6.16). The accompanying oval and other irregular structures occur due to limitations of the sample preparation for conventional electron microscopy. The particle size is smaller than deduced by the DLS analysis due to the determination of hydrodynamic diameter in the DLS that has a larger size than the original particle size (Ruttala and Ko, 2015) – such instances are also observed in other studies.
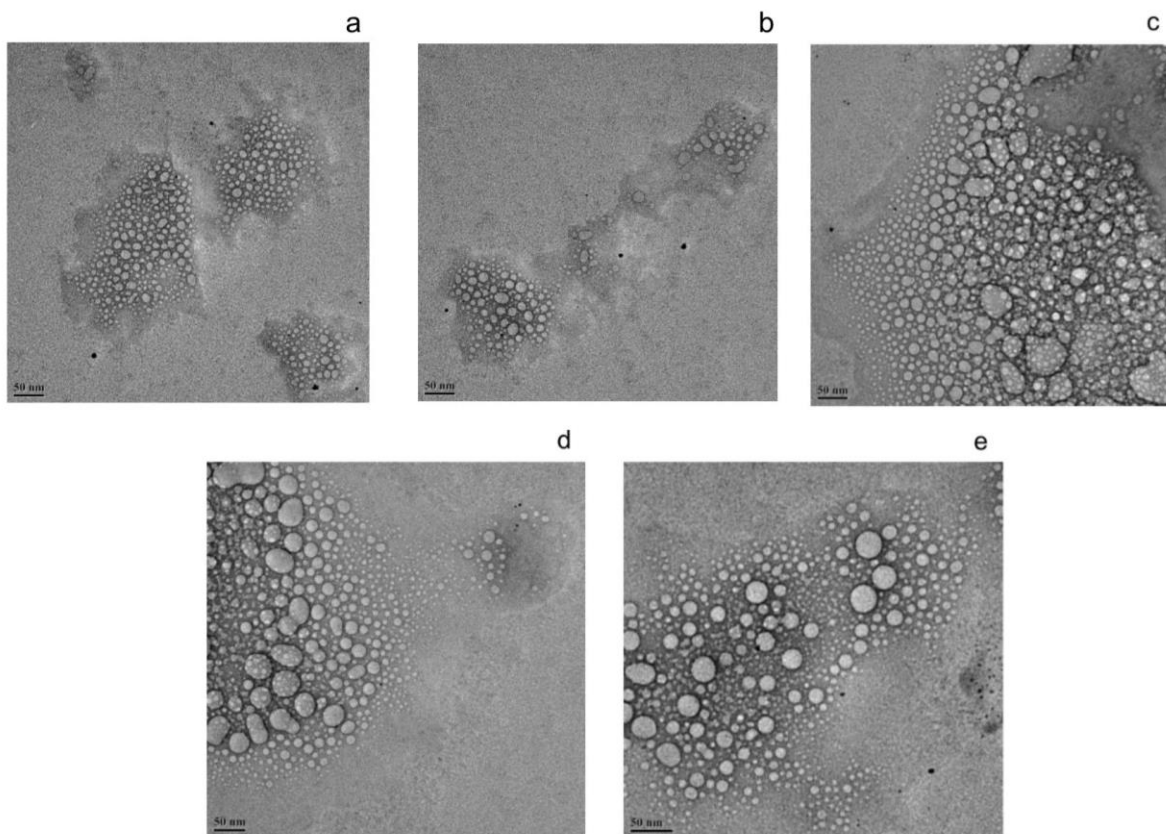
Figure 6.16 HRTEM images of Plain pH responsive liposomes (a), pH responsive CUR-DOX liposomes (b), pH responsive FOL CUR-DOX liposomes (c), pH responsive CET CUR-DOX liposomes (d), and pH responsive FOL-CET CUR-DOX liposomes (e)

6.4.4 FTIR analysis

We observed the characteristic peaks of DOPE (Figure 6.17) at 2919 and 2850 cm^{-1} for CH antisymmetric and symmetric stretching, respectively, 1733 cm^{-1} for C=O (ester) stretching, 1629 cm^{-1} for C=C stretching, 1463 cm^{-1} for CH$_2$ bending, 1378 cm^{-1} for CH$_3$ bending, 1232 and 1083 cm^{-1} for antisymmetric and symmetric PO^{2-} stretching. Characteristic peaks for CHEMS emerge at 2935, 2890, and 2865 cm^{-1} for the CH stretching vibration in methyl and cyclic hydrocarbons; peaks at 1465 and 1377 cm^{-1} correspond to CH bending, and CH$_2$ and CH$_3$ bending vibrations, respectively.
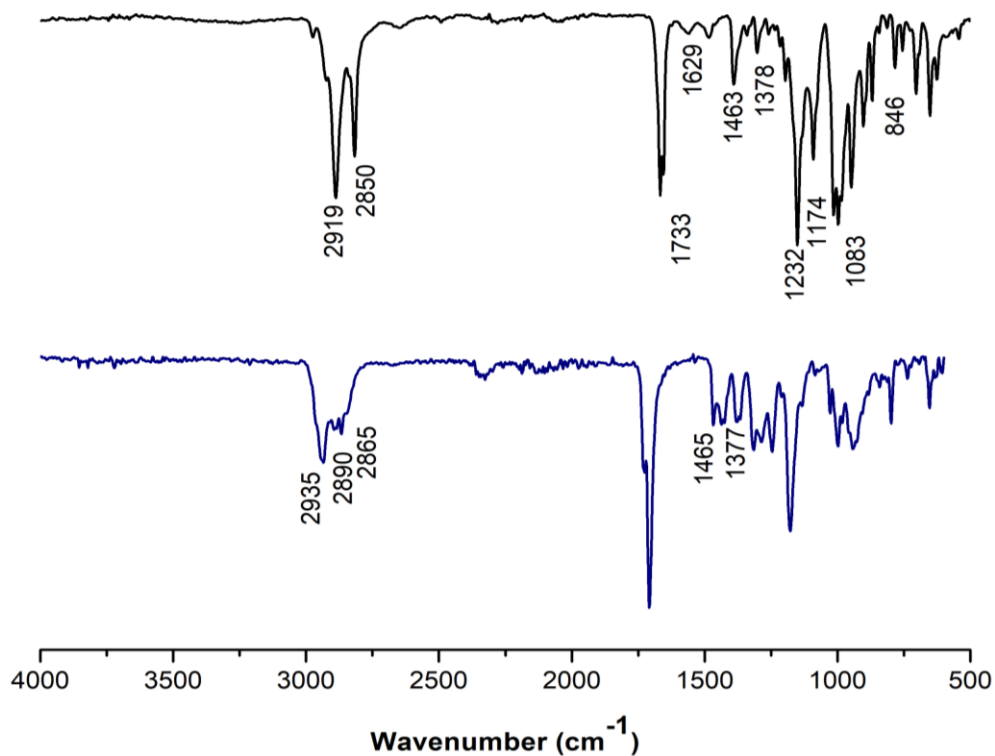
Figure 6.17 FTIR spectra of DOPE (black) and CHEMS (blue)

We compared the FTIR spectrum of pH responsive liposomes to DOPE (Figure 6.18). For plain pH responsive liposomes, we observed a shift for CH antisymmetric and symmetric stretching from 2919 and 2850 cm^{-1} to 2921 and 2852 cm^{-1}, respectively; C=O (ester) stretching from 1733 to 1735 cm^{-1}; C=C stretching from 1629 to 1627 cm^{-1}; CH$_2$ bending from 1463 to 1465 cm^{-1}; and CH3 bending at 1378 cm^{-1}. The antisymmetric and symmetric PO$_2$ stretching occurred at 1232 and 1083 cm^{-1}, and the P-O stretching at 821 cm^{-1}.

For pH responsive CUR-DOX liposomes, we observed a broad peak at 3429 cm^{-1} corresponding to the OH stretching of CUR and the NH stretching of DOPE; this was indistinctly visible in the spectra of DOPE and plain pH responsive liposomes. We noted a shift to 2923 and 2852 cm^{-1} for CH antisymmetric and symmetric stretching, respectively; 1735 cm^{-1} for C=O (ester) stretching; 1633 cm^{-1} for C=C stretching; 1465 cm^{-1} for CH$_2$ bending; and 1377 cm^{-1} for CH$_3$ bending. The peak at 1228 cm^{-1} corresponds to antisymmetric PO^{2-} stretching, 1070 cm^{-1} for symmetric PO^{2-} stretching, and the P-O stretching at 823 cm^{-1}.

The OH stretching of CUR and the NH stretching of DOPE for pH responsive FOL CUR-DOX liposomes shifted to 3421 cm^{-1}; the antisymmetric and symmetric CH stretching to 2923 and

2852 cm^{-1}; C=O stretching to 1735 cm^{-1}; C=C stretching to 1631 cm^{-1}; CH$_2$ bending at 1463 cm^{-1}; CH$_3$ bending to 1377 cm^{-1}. The peaks for the head group regions shifted to 1232 and 1074 cm^{-1}for the PO2- antisymmetric and symmetric stretching respectively and 825 cm^{-1} for P-O stretching.
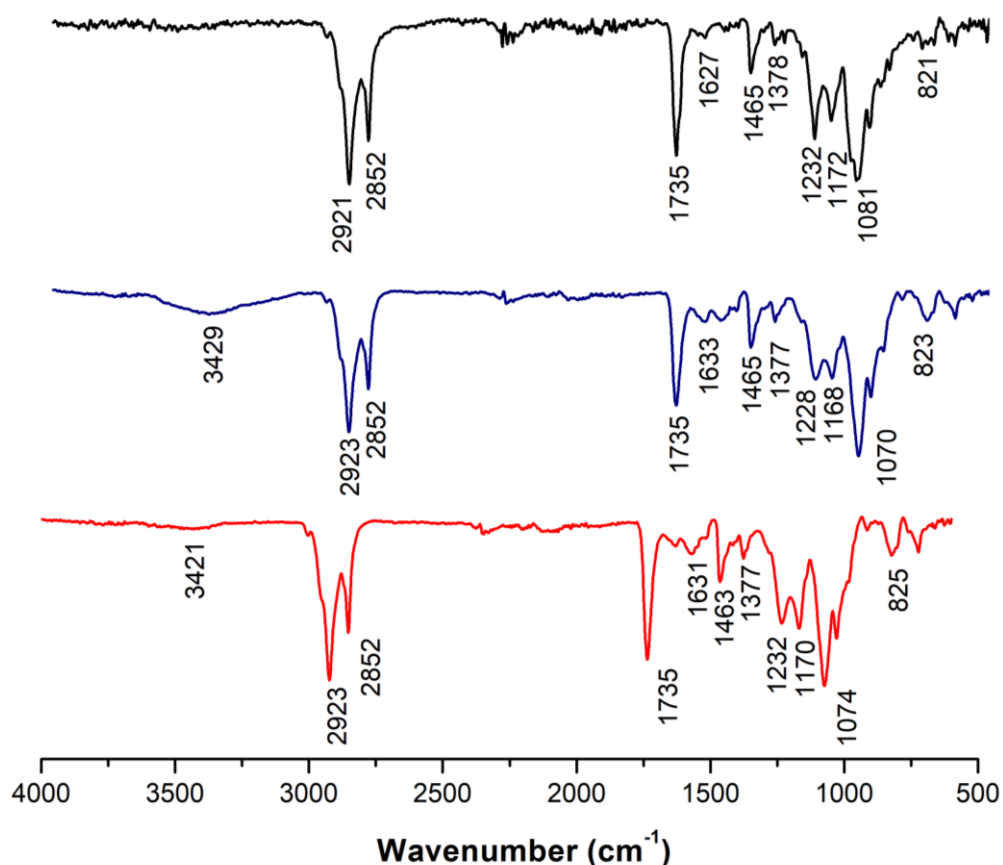
Figure 6.18 FTIR spectra of plain pH liposomes (black), pH CUR-DOX liposomes (blue), and pH FOL CUR-DOX liposomes (red)

The hydrogen bonds severe to form new bonds between the phenolic OH of CUR and DOPE, corresponding to an OH stretching vibration (Hasan *et al.* 2016c) and the overlapping of the NH stretching of DOPE. The characteristic peaks for CUR and DOX disappear, confirming that CUR positions in the lipid bilayer and DOX in the aqueous core (Zarrabi *et al.* 2021b). The absence of new peaks suggested the absence of any chemical interactions but only physical interactions such as weak dipole-dipole interactions, hydrogen bonds, or van der Waals interactions.

6.4.5 TGA analysis

We recorded the degradation onset temperature for DOPE at 247.38 °C with 87.83 % degradation and for CHEMS at 240.30 °C with 99.77 % degradation (Figure 6.19). After loading CUR and DOX in the liposomes, we saw a shift in the degradation onset temperature to 214.90 °C with 67.46 % degradation. This shift also indicates and confirms the loading of drugs in the liposomes.
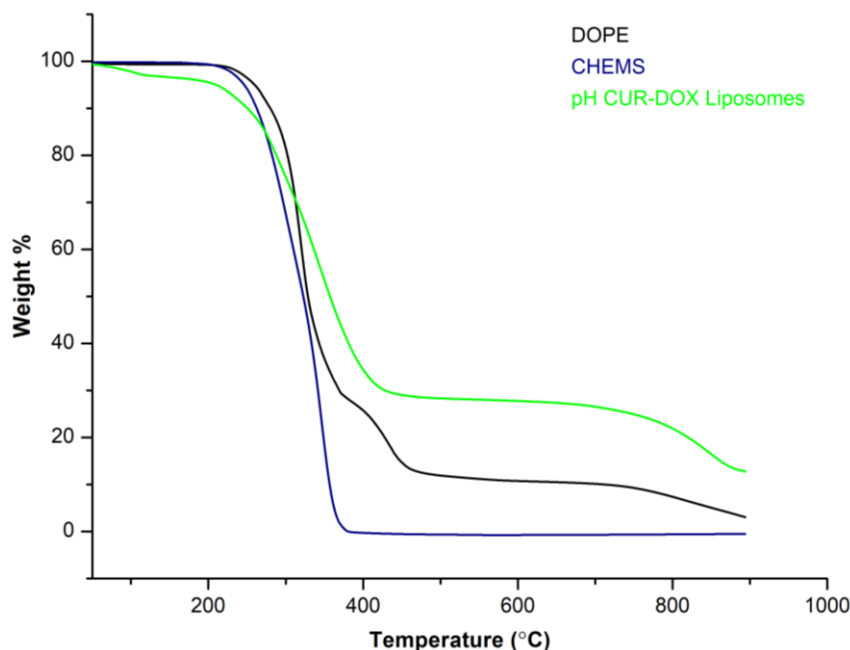
Figure 6.19 TGA thermogram of DOPE (black), CHEMS (blue), and pH CUR-DOX liposomes (green)

6.4.6 DSC analysis

We noted a sharp endotherm for DOPE at 123.08 °C and CHEMS at 184.15 °C (Figure 6.20). After loading CUR and DOX in the liposomes, we witnessed a shift to 110.90 °C for the pH responsive CUR-DOX liposomes. The endotherm's broad nature confirms the drug's presence in the bilayer region (Campani et al., 2020). The endotherms corresponding to CHEMS, for CUR at 176.55 ° C and for DOX at 50.44 ° C, disappear, suggesting the formation of liposomes and loading of drugs.

On correlating these results with the FTIR, we understand that when CUR positions in the bilayer, it interacts with the phosphate group of the head group region and the hydrophobic

fatty acyl chain regions; DOX also creates changes to the bilayer after incorporating in the aqueous core or lipid interface inducing a dip in the endotherm temperature. This occurs when the bonds degrade and correspond to an endotherm at lower temperatures (Niu et al., 2012). A higher endotherm than the storage temperature suggests higher stability without phase transition (Chaves et al., 2018).
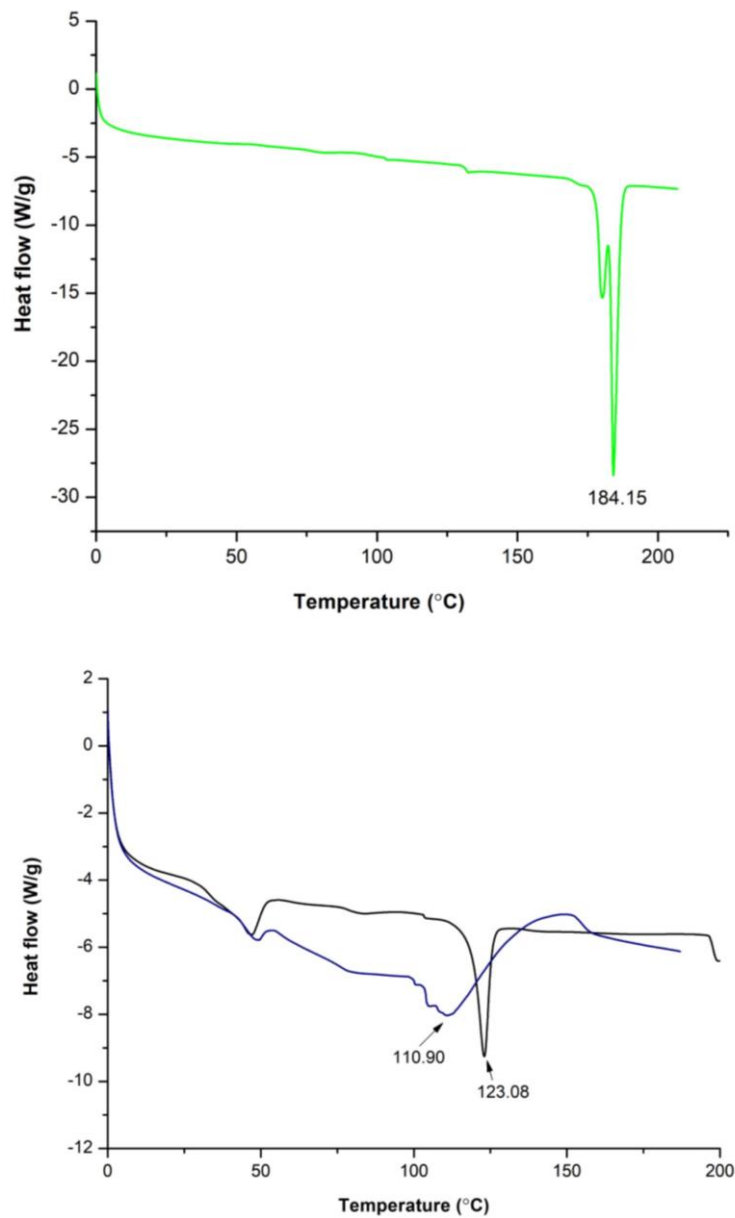
Figure 6.20 DSC thermogram of CHEMS (green), DOPE (black), and pH CUR-DOX liposomes (blue)

6.5 Conclusion

We synthesized the pH responsive liposomes by the optimized values of the process parameters of the thin film hydration technique and the intrinsic factors of molar ratio of the lipids, concentration of PC, CHOL, and DSPE-mPEG2000; concentration of CUR and DOX. We added 0.1 mole % of DSPE-PEG2000-COOH to tag CET on the surface of liposomes by carbodiimide coupling and 0.1 mole % of DSPE-PEG2000-FOL.

We optimized 11 extrusion passes for pH responsive CUR-DOX liposomes and recorded the hydrodynamic diameter, PDI and zeta potential at 136.47 ± 2.58 nm, 0.08 ± 0.03 and -11 ± 0.35 mV; pH responsive FOL CUR-DOX liposomes at 136.99 ± 4.70 nm, 0.11 ± 0.04 and -8.54 ± 0.34 mV; pH responsive CET CUR-DOX liposomes at 157.72 ± 2.07 nm, 0.18 ± 0.01 and -8.26 ± 0.05 mV; pH responsive FOL-CET CUR-DOX liposomes at 163.21 ± 1.51 nm, 0.17 ± 0.001 and -9.63 ± 1.53 mV. We calculated the % EE of CUR for pH responsive CUR-DOX liposomes, pH responsive FOL CUR-DOX liposomes, pH responsive CET CUR-DOX liposomes, and pH responsive FOL-CET CUR-DOX liposomes at 81.49 ± 2.95, 73.74 ± 2.51, 77.22 ± 3.94 and 75.81 ± 3.16 % respectively; for DOX at 79.77 ± 1.62, 74.70 ± 2.35, 75.11 ± 2.91 and 76.89 ± 2.61 % respectively.

HRTEM confirmed spherical morphology for all the formulations. FTIR analysis suggested the loading of CUR in the bilayer region, DOX in the aqueous cavity and the water lipid interface, and FOL on the liposomal surface. The TGA analysis determined high thermal stability for the formulations, and the DSC analysis suggested the successful loading of the drugs in the liposomes. Thus, the results indicate the synthesis of robust pH responsive liposomes according to the drug delivery mandates.

CHAPTER 7

In vitro efficacy studies

7.1 Introduction

In vitro studies are pertinent to establish the efficacy of the formulations on cancer cell lines. MCF-7 stands for "Michigan Cancer Foundation-7" and was first derived from the pleural effusion of a 69 years old white female (Lee et al., 2015). It is a less aggressive and non-invasive Luminal A model with ER+ and PR+ status (Comşa et al., 2015). MCF-7 cells proliferate by estrogen and progesterone mechanisms where estrogen binds to ERα receptors and progesterone to PRs, upon endocytosis, act as transcription factors and bind to estrogen response elements and progesterone response elements respectively to modulate gene expression (Trabert et al., 2019) (Tian et al., 2018).

MDA-MB-231 cell lines were first established in 1973 from the pleural effusion of a 51 years old Caucasian female, a TNBC model with p53 mutation (Huang et al., 2020). It is an aggressive and invasive cell line. About 80 % of TNBC cells overexpress EGFR receptors, also linked to a poor prognosis (Kathryn et al., 2012). Studies report 1.76 times higher expression of FRs in MDA-MB-231 than in the MCF-7 cells (Marshalek et al., 2016).

We investigated the stability of the liposomal formulations during storage over a period of time; high colloidal stability at physiological conditions suggests a higher blood circulation time and increased drug retention. This study also highlights any structural changes over time. Secondly, we examined the release profiles for both CUR and DOX from different liposomal formulations. Drug release from nanoformulations occurs by diffusion, erosion, or swelling of the formulation.

We correlated the drug release kinetics to various kinetic models: *in zero order*, the drug release is independent of the drug concentration and shows a constant release whereas in *first order* kinetics, the release depends on the drug concentration; in *higuchi* model, drug release occurs by diffusion; in *Korsmeyer-Peppas* model, the release occurs either by swelling or diffusion or both, and the first 60% of the release by almost all the formulations follow this model; in *Hixon-Crowell* model, the release occurs by dissolution where the surface area and the size of the formulation change; in *Hopfenberg* model, the drug release occurs from spheres or cylindrical formulations after erosion of the formulations; in *Baker-Lonsdale* model, the drug releases in a controlled manner through spherical matrixes; *makoid-banakar* model is a diffusion based model where the drug releases from a matrix in a controlled manner; in *Peppas-Sahlin* model, an extension of the Korsmeyer-Peppas model, the drug releases by diffusion

from a polymeric matrix; in *weibull* model, the drug shows prolonged drug release, and followed by mostly all the nanoformulations; in *gompertz* model, the drug exhibits an initial rapid release (Dash et al., 2010) (Singh and Pilani, 2021) (Jain and Jain, 2016) (Heredia et al., 2022).

After treating them with various liposomal formulations, we checked for the cell viability of the MCF-7 and MDA-MB-231 cells. We calculated the IC_{50} values and compared the anticancer effect of the formulations with plain drugs and other formulations. We then investigated the cellular uptake of various liposomal formulations after 8 h of incubation. These studies would establish the efficacy of different liposomal formulations.

7.2 Methods

We synthesized liposomes using the protocol and optimized values mentioned in the prior chapters and investigated the stability, drug release, cell viability, and uptake mentioned in Chapter 2, Section 2.4.

7.3 Results and Discussion

7.3.1 Stability studies

7.3.1.1 Stability studies for Plain liposomes

We studied the stability of the non-PEGylated and PEGylated liposomes formed after 5 and 10 extrusion passes (Figure 7.1). The non-PEGylated liposomes formed by 5 extrusion passes were stable till week 4. They aggregated after that, and liposomes with 10 extrusion passes were stable till week 7 and aggregated and precipitated after week 5, leaving smaller particles in the suspension.

PEGylated liposomes with 5 extrusion passes were stable till 6 weeks, and particles with 10 extrusion passes recorded stability till 7 weeks; both the formulations showed precipitation after 5 weeks with smaller particles in suspension. The PDI values for all the formulations were < 0.3, and the zeta potential values reflected moderate/incipient stability for all the formulations during storage. The fluctuations in the size, PDI, and zeta potential occur due to the dynamic nature of liposomes. The data suggest higher storage stability for smaller liposomes (extrusion passes 10).
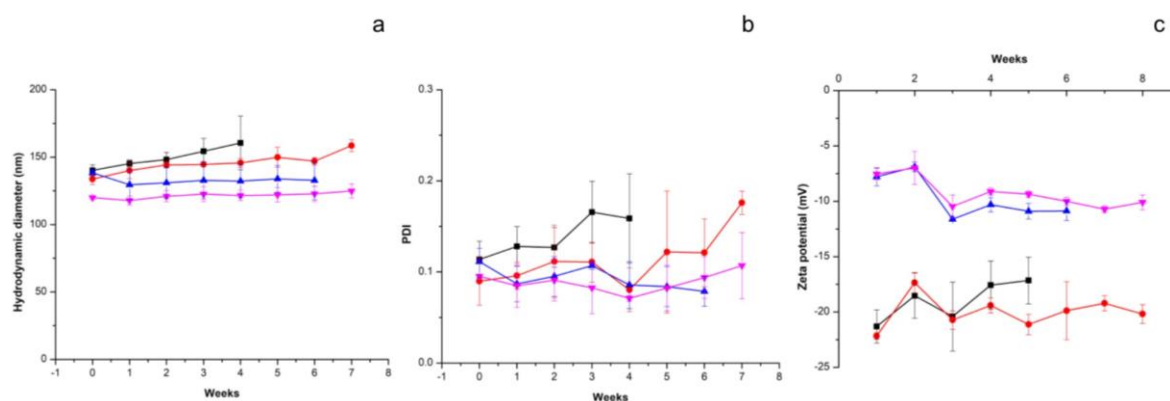
Figure 7.1 Hydrodynamic diameter (a), PDI (b), and zeta potential (c) of liposomes with 5 extrusion passes (black) and 10 extrusion passes (red), and PEGylated liposomes after 5 extrusion passes (blue) and 10 extrusion passes (pink) during storage

7.3.1.2 Stability Studies of CUR loaded liposomes

We studied the stability of CUR liposomes and PEGylated CUR liposomes for 3 months and observed clear suspensions without any precipitate or aggregates during storage. The average particle size < 200 nm mark and PDI values < 0.3 suggest that liposomes maintained their structural integrity and monodispersity (Figure 7.2). Fluctuations in the specifications correspond to the dynamic nature of the liposomes. The zeta potential values indicate moderate stability for CUR liposomes and a neutral range of the PEGylated CUR liposomes; variations in the absolute zeta potential values correspond to the dynamic nature of the liposomes and the drug release from the particles.

At the end of 3 months, the CUR liposomes and PEGylated CUR liposomes retained 62.88 ± 3.50 and 66.70 ± 1.90 % of CUR respectively. We noted higher stability than Wang et al., who observed an increase in size from 168.04 ± 1.78 nm to 268.77 ± 3.36 nm over 28 days with a 59.14% drug retention for liposomal formulations synthesized with similar lipids (Wang et al., 2021). Lower temperatures protract the colloidal stability as the particles cannot access the activation energy to hydrolyze lipids, which would otherwise be faster at higher temperatures (Jin et al., 2016).
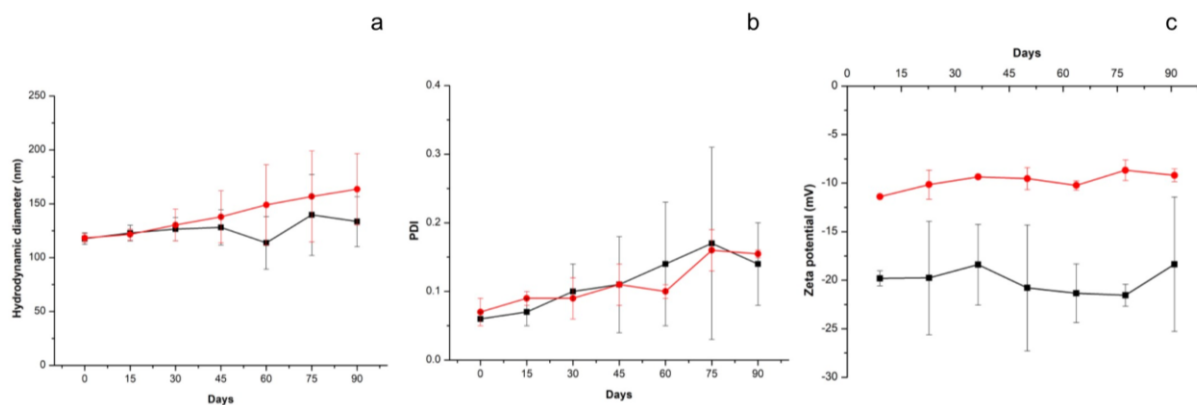
Figure 7.2 Hydrodynamic diameter (a), PDI (b), and zeta potential (c) of CUR liposomes (black) and PEGylated CUR liposomes (red) during storage

7.3.1.3 Stability Studies of DOX loaded liposomes

DOX liposomes and PEGylated DOX liposomes were stable for 3 months with clear suspensions without any precipitate or aggregates during storage. The average particle size < 200 nm and PDI values < 0.3 suggest that the particles maintained smaller sizes and a monodisperse nature (Figure 7.3). The zeta potential values depict moderate stability for DOX liposomes and a neutral range of PEGylated DOX liposomes, and variations over time occur due to the dynamic nature of the liposomes and drug release from the liposomes.

The DOX liposomes and PEGylated DOX liposomes retained 65.03 ± 2.72 and 71.08 ± 1.30 % DOX respectively till 3 months. We recorded excellent colloidal stability with decent drug retention for 3 months.
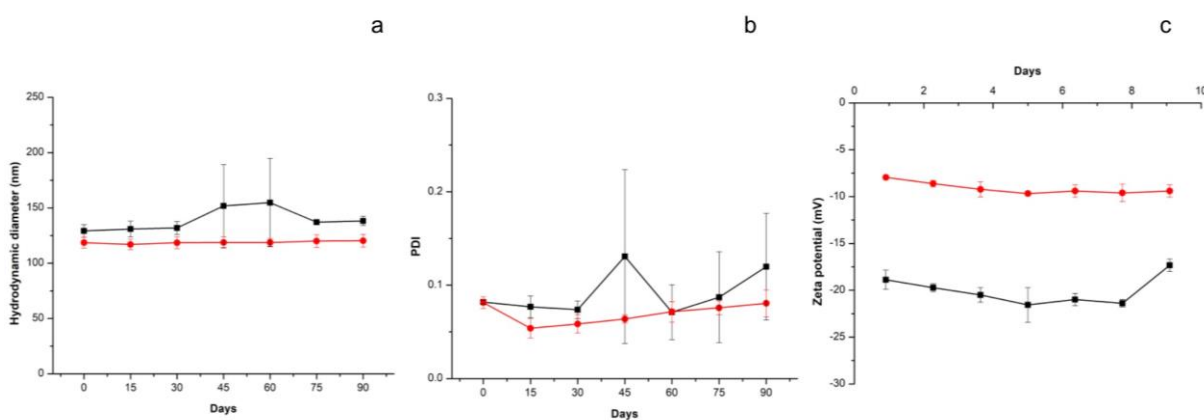
Figure 7.3 Hydrodynamic diameter (a), PDI (b), and zeta potential (c) of DOX liposomes (black) and PEGylated DOX liposomes (red) during storage

7.3.1.4 Stability studies of CUR-DOX loaded liposomes

CUR-DOX liposomes and PEGylated CUR-DOX liposomes were stable till 3 months and had clear suspension without any aggregates at the bottom of the storage vials. The average particle size was < 200 nm, and the PDI values were < 0.3 throughout the storage conditions, implying that the liposomes maintained their structural integrity over 3 months (Figure 7.4). Fluctuations in specifications correspond to the dynamic nature of the liposomes. The zeta potential values also marked moderate stability for CUR-DOX liposomes and values in a neutral range for PEGylated CUR-DOX liposomes; any variations suggest the drug release from the liposomes over time.

The CUR-DOX liposomes retained 63.94 ± 2.81 % of CUR and 69.36 ± 3.55 % of DOX; the PEGylated CUR-DOX liposomes retained 69.06 ± 2.91 % CUR and 70.38 ± 4.57 % DOX till 3 months. The data indicates excellent stability for these formulations over 3 months.
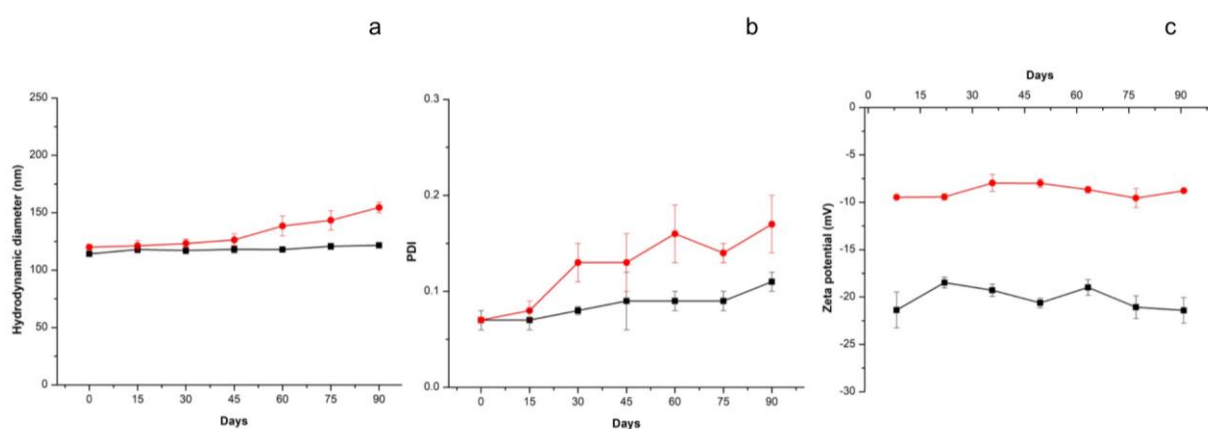
Figure 7.4 Hydrodynamic diameter (a), PDI (b), and zeta potential (c) of CUR-DOX liposomes (black) and PEGylated CUR-DOX liposomes (red) during storage

7.3.1.5 Stability Studies of FOL tagged liposomes

The FOL CUR liposomes, FOL DOX liposomes, and FOL CUR-DOX liposomes showed stability till 3 months with clear suspensions without any precipitates seen at the bottom of the storage vials. The average particle size < 200 nm mark and the PDI values < 0.3 suggest that

the liposomes maintained structural integrity during storage even after functionalizing the surface with FOL (Figure 7.5). The zeta potential values remained in the neutral range corresponding to the functionalized liposomal surface and varied over time, resulting from drug release during storage.

The FOL CUR liposomes retained 67.25 ± 3.70 % of CUR, the FOL DOX liposomes retained 70.25 ± 5.61 % DOX, and the FOL CUR-DOX liposomes retained 66.05 ± 3.84 % CUR and 69.86 ± 4.23% DOX till 3 months. These formulations exhibited excellent stability over 3 months that remained unaffected by FOL on the particle surface corresponding to the stearic hindrance created by the PEG chains and FOL.
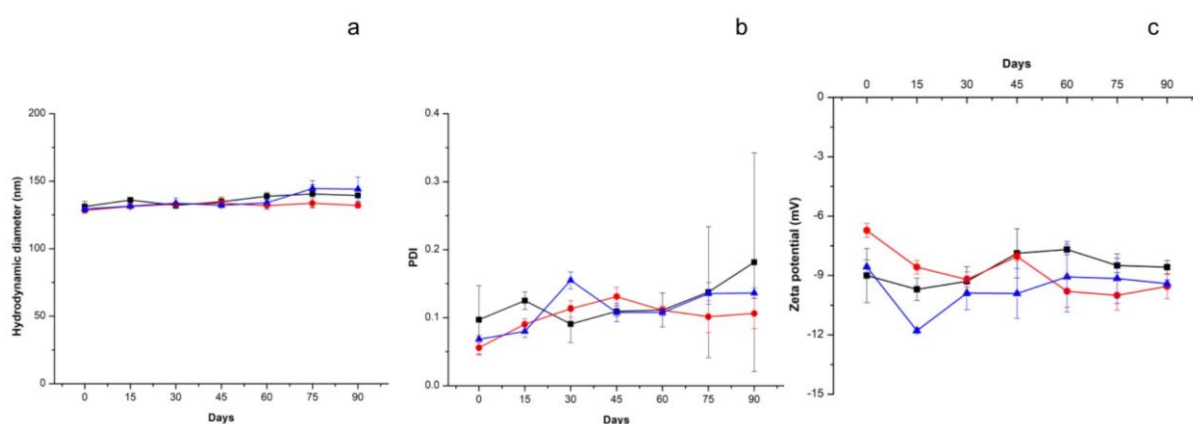
Figure 7.5 Hydrodynamic diameter (a), PDI (b), and zeta potential (c) of FOL CUR liposomes (black) and FOL DOX liposomes (red), and FOL CUR-DOX liposomes (blue) during storage

7.3.1.6 Stability Studies of CET tagged liposomes

The CET CUR liposomes, CET DOX liposomes, and CET CUR-DOX liposomes showed clear suspensions without any aggregates during 3 months. The average particle size < 200 nm mark and the PDI values < 0.3 state excellent stability of the formulations even after functionalizing the surface with CET (Figure 7.6). The zeta potential values maintained a neutral range corresponding to PEGylation and CET tagging on the particle surface, and variations hint toward drug release from the liposomes during storage.

The CET CUR liposomes retained 62.80 ± 6.45 % CUR, the CET DOX liposomes retained 64.77 ± 5.50 % DOX, and the CET CUR-DOX liposomes retained 64.21 ± 4.48 % CUR and 65.91 ± 5.19 %DOX till 3 months. The data suggest excellent stability for these formulations.
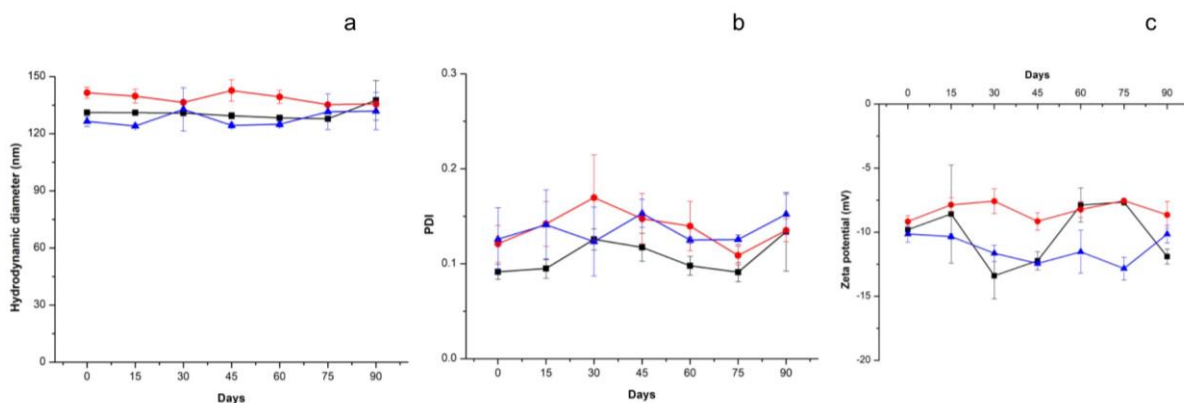
Figure 7.6 Hydrodynamic diameter (a), PDI (b), and zeta potential (c) of CET CUR liposomes (black) and CET DOX liposomes (red), and CET CUR-DOX liposomes (blue) during storage

7.3.1.7 Stability Studies of FOL-CET tagged liposomes

The FOL-CET CUR liposomes, FOL-CET DOX liposomes, and FOL-CET CUR-DOX liposomes were stable till 3 months and had clear suspensions without aggregates at the bottom of the storage vials. The average particle size was < 200 nm and the PDI values were < 0.3, suggesting that the liposomes maintained structural integrity during storage after functionalizing the surface with FOL and CET (Figure 7.7). The absolute zeta potential values in the neutral range correspond to PEGylating and dual ligands on the liposomal surface. Liposomes are dynamic, resulting in drug release during the storage conditions.

FOL-CET CUR liposomes retained 64.56 ± 5.51 % CUR, FOL-CET DOX liposomes retained $62.88 \pm 4.50\%$ DOX, and FOL-CET CUR-DOX liposomes retained 64.66 ± 3.32 % CUR and $63.44 \pm 5.39\%$ DOX till 3 months. The data indicates excellent stability of the liposomes till 3 months.
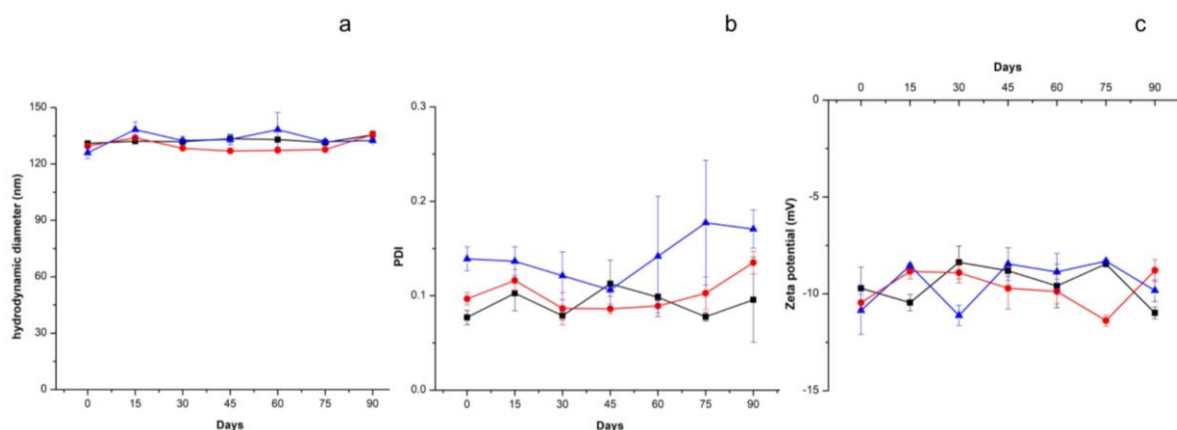
Figure 7.7 Hydrodynamic diameter (a), PDI (b), and zeta potential (c) of FOL-CET CUR liposomes (black) and FOL-CET DOX liposomes (red), and FOL-CET CUR-DOX liposomes (blue) during storage

7.3.1.8 Stability Studies of pH responsive liposomes

The pH responsive liposomes, namely pH responsive CUR-DOX liposomes, pH responsive FOL CUR-DOX liposomes, pH responsive CET CUR-DOX liposomes, and pH responsive FOL-CET CUR-DOX liposomes were stable till 3 months. The pH responsive plain liposomes aggregated after 30 days, leaving a clear suspension with smaller sized particles. The formulations maintained an average particle size of < 200 nm and PDI values of < 0.3 (Figure 7.8). The absolute zeta potential values in the neutral range correspond to PEGylating the liposomal surface.

We recorded the CUR retention during storage of 60.58 ± 2.64, 63.74 ± 3.61, 62.56 ± 4.38, and $61.67 \pm 3.47\%$ for pH CUR-DOX liposomes, pH FOL CUR-DOX liposomes, pH CET CUR-DOX liposomes and pH FOL-CET CUR-DOX liposomes respectively; we recorded the DOX retention at 63.99 ± 1.31, 62.81 ± 4.14, 63.03 ± 2.52, and $61.88 \pm 2.95\%$ for pH CUR-DOX liposomes, pH FOL CUR-DOX liposomes, pH CET CUR-DOX liposomes and pH FOL-CET CUR-DOX liposomes respectively. The data suggests excellent stability of all the drug loaded pH responsive liposomes and equivalent to the non responsive liposomes.
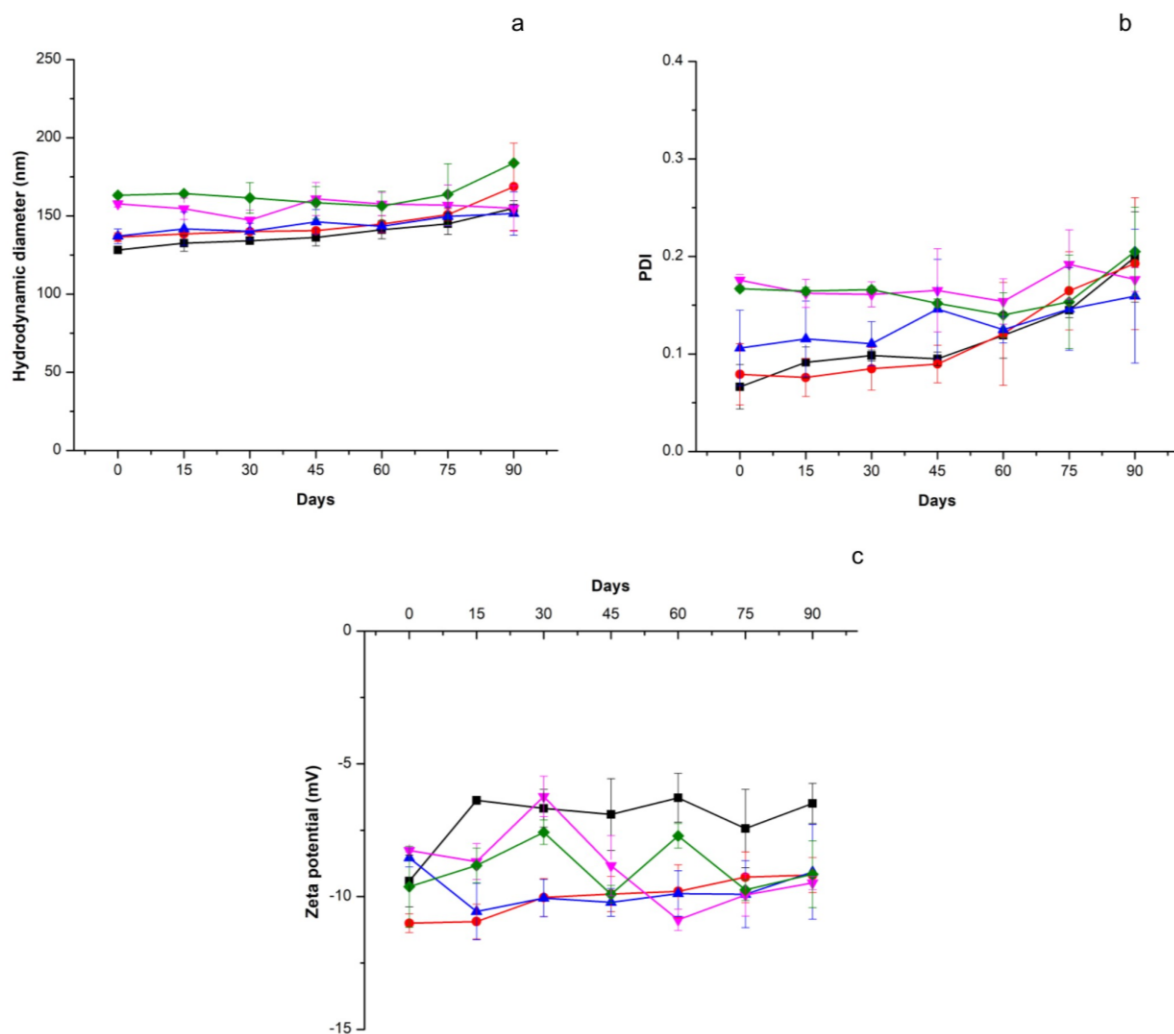
Figure 7.8 Hydrodynamic diameter (a), PDI (b), and zeta potential (c) of pH plain liposomes (black), pH CUR-DOX liposomes (red), pH FOL CUR-DOX liposomes (blue), and pH FOL-CET CUR-DOX liposomes during storage

The 7: 3 molar ratio of PC: CHOL supports the excellent stability of the formulations till 3 months, as 30 % CHOL imparts stability to the liposomes to maintain their structural integrity. Secondly, PEGylating the liposomal surface created a hydration sheath around the particles, forming a steric barrier that prevented the liposomes from aggregating. Thirdly, the smaller particle size also prevented aggregations and increased stability. Lastly, we maintained ambient storage conditions of 4 ° C and protected all the formulations from light for 3 months.

7.3.2 Drug release studies

Liposomes release the encapsulated drugs by three primary mechanisms: desorption of the drugs adsorbed on the liposomal surface when the particles come in contact with the release medium; the encapsulated drugs diffuse out of the liposomes; liposomes degrade and release the encapsulated drugs (Wei et al., 2020). We used a recipient buffer of 30 % methanol in PBS to solubilize CUR (as it is hydrophobic) as it is poorly soluble in PBS.

7.3.2.1 CUR release studies

CUR showed an accelerated release in pH 7.4 and 5.5, with 66.38 and 79.82% after 12 h, 78.29 and 88.35 % after 24 h, and 86.61 and 93.49 % after 72 h respectively (Figure 7.9). The liposomal formulations engendered a biphasic release of an initial exponential followed by a sustained and prolonged release. In release mediums of pH 7.5 and 5.5, CUR liposomes released 39.54 and 56.66 % CUR after 12 h, 49.33 and 65.63 % after 24 h, and 61.75 and 78.95 % after 72 h; the PEGylated CUR liposomes released 33.89 and 49.56 % after 12 h, 41.87 and 58.44 % after 24 h, and 52.76 and % after 72 h in pH 7.4; % after 24 h, and 71.75 % after 72 h in pH 5.5.

CUR release from CUR-DOX liposomes in 7.4 and 5.5 pH showed 40.11 and 58.28 % release after 12 h, 50.42 and 66.37 % release after 24 h, and 62.13 and 79.31 % release after 72 h, respectively; CUR release from PEGylated CUR-DOX liposomes in 7.4 and 5.5 pH showed 30.89 % and 47.73 % release after 12 h, 40.43 % and 56.7 % release after 24 h, and 54.15 % and 68.87 % release after 72 h respectively.

CUR from the CUR solution diffuses through the dialysis membrane. It shows an accelerated release, but the liposome's biphasic release ensures an initial rapid release, exposing the cancer cells to a higher drug concentration followed by a sustained release to perpetuate the drug's efficacy (Ding et al., 2017). The slower release profile of CUR corresponds to the movement of CUR from the lipid bilayer and out of the dialysis membrane (Chen et al., 2015). The initial rapid release corresponds to the drug release from the outer leaflet of the bilayer and the subsequent sustained release to the deeper located drug in the inner lipid leaflet (Chang et al., 2015).
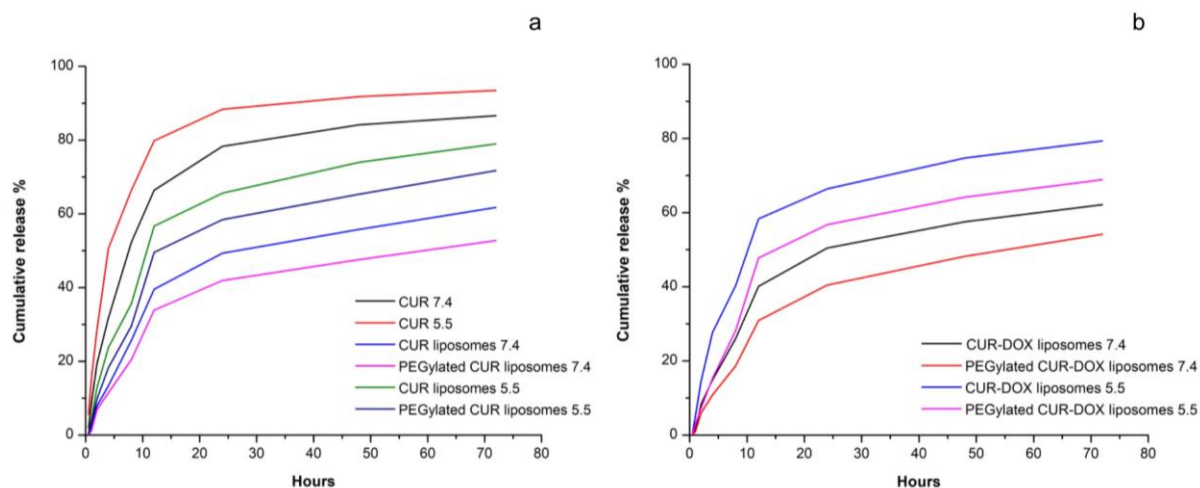
Figure 7.9 Release profile of CUR from CUR liposomes and PEGylated CUR liposomes in a release medium of pH 7.4 and 5.5

We selected the best fit drug release model based on the R^2 values > 0.95, Akaike Information Criterion (AIC) < 50, and Model Selection Criterion (MSC) > 3. Based on the R^2 values, all the formulations followed the Peppas-Sahlin, Weibull, and Gompertz model, suggesting drug release by diffusion. But the R^2, AIC, and MSC values suggest Gompertz as the best fit model for releasing CUR from the CUR liposomes, PEGylated CUR liposomes, CUR-DOX liposomes and PEGylated CUR-DOX liposomes (Table 7.1).

Table 7.1 Drug release models for CUR from CUR liposomes, PEGylated CUR liposomes, CUR-DOX liposomes and PEGylated CUR-DOX liposomes in a release medium of pH 7.4 and 5.5

Formulations	Release Kinetic models	R^2	AIC	MSC
CUR 7.4	Zero order	0.1849	81.9290	-0.0178
	First order	0.9442	57.7908	2.6642
	Higuchi	0.8189	68.3892	1.4866
	Korsmeyer-Peppas	0.8714	66.1095	1.7399
	Hixon-Crowell	0.8706	65.3637	1.8228
	Hopfenberg	0.9362	59.7964	2.4414
	Baker-Lonsdale	0.9311	59.6906	2.4532
	Makoid-Banakar	0.9746	52.1244	3.2938
	Peppas-Sahlin	0.9661	54.7259	3.0048

	Weibull	0.9798	50.0433	3.5251
	Gompertz	0.9936	39.1123	4.7396
CUR 5.5	Zero order	-0.3011	86.6671	-0.4855
	First order	0.9729	51.8237	3.3860
	Higuchi	0.6450	74.9781	0.8133
	Korsmeyer-Peppas	0.8308	69.1070	1.4657
	Hixon-Crowell	0.7194	72.8592	1.0488
	Hopfenberg	0.9690	53.8261	3.1635
	Baker-Lonsdale	0.8789	65.3010	1.8885
	Makoid-Banakar	0.9586	57.0386	2.8066
	Peppas-Sahlin	0.9515	58.4738	2.6471
	Weibull	0.9856	47.5493	3.8610
	Gompertz	0.9944	38.3767	4.8801
CUR liposomes 7.4	Zero order	0.5786	70.0877	0.6419
	First order	0.8116	62.8402	1.4472
	Higuchi	0.9189	55.2526	2.2902
	Korsmeyer-Peppas	0.9112	56.8665	2.1109
	Hixon-Crowell	0.7432	65.6304	1.1372
	Hopfenberg	0.7846	64.8449	1.2244
	Baker-Lonsdale	0.9337	53.4424	2.4914
	Makoid-Banakar	0.9731	46.7318	3.2370
	Peppas-Sahlin	0.9653	49.0226	2.9825
	Weibull	0.9731	46.7454	3.2355
	Gompertz	0.9862	40.1442	3.9690
CUR liposomes 5.5	Zero order	0.4423	77.0017	0.3617
	First order	0.8901	62.3869	1.9855
	Higuchi	0.8899	62.4022	1.9838
	Korsmeyer-Peppas	0.8955	62.7310	1.9473
	Hixon-Crowell	0.8267	66.4800	1.5308
	Hopfenberg	0.8743	64.3894	1.7630
	Baker-Lonsdale	0.9321	58.0476	2.4677
	Makoid-Banakar	0.9695	52.2448	3.1124
	Peppas-Sahlin	0.9620	54.2286	2.8920

	Weibull	0.9737	50.9297	3.2586
	Gompertz	0.9878	43.3998	4.0952
PEGylated CUR liposomes 7.4	Zero order	0.5939	66.9572	0.6790
	First order	0.7740	61.6835	1.2650
	Higuchi	0.9199	52.3493	2.3021
	Korsmeyer-Peppas	0.9111	54.0866	2.1091
	Hixon-Crowell	0.7185	63.6599	1.0454
	Hopfenberg	0.7417	63.6851	1.0426
	Baker-Lonsdale	0.9311	50.9902	2.4531
	Makoid-Banakar	0.9708	44.6623	3.1562
	Peppas-Sahlin	0.9632	46.7625	2.9229
	Weibull	0.9685	45.3601	3.0787
	Gompertz	0.9795	40.8948	3.5749
PEGylated CUR liposomes 5.5	Zero order	0.5197	73.9694	0.5112
	First order	0.8475	63.6470	1.6582
	Higuchi	0.9038	59.5005	2.1189
	Korsmeyer-Peppas	0.8996	60.6787	1.9880
	Hixon-Crowell	0.7637	67.5857	1.2205
	Hopfenberg	0.8256	65.6486	1.4358
	Baker-Lonsdale	0.9289	56.7834	2.4208
	Makoid-Banakar	0.9666	51.3968	3.0193
	Peppas-Sahlin	0.9583	53.3769	2.7993
	Weibull	0.9680	50.9997	3.0634
	Gompertz	0.9837	44.3075	3.8070
CUR-DOX liposomes 7.4	Zero order	0.5638	70.6576	0.6074
	First order	0.8111	63.1261	1.4442
	Higuchi	0.9169	55.7388	2.2650
	Korsmeyer-Peppas	0.9101	57.2360	2.0986
	Hixon-Crowell	0.7390	66.0345	1.1210
	Hopfenberg	0.7840	65.1291	1.2216
	Baker-Lonsdale	0.9339	53.6732	2.4945
	Makoid-Banakar	0.9771	45.5354	3.3987
	Peppas-Sahlin	0.9695	48.1252	3.1110

	Weibull	0.9759	45.9955	3.3476
	Gompertz	**0.9876**	**39.3933**	**4.0812**
CUR-DOX liposomes 5.5	Zero order	0.3498	78.2386	0.2083
	First order	0.8727	63.5616	1.8391
	Higuchi	0.8691	63.8163	1.8108
	Korsmeyer-Peppas	0.8902	63.0287	1.8983
	Hixon-Crowell	0.8073	67.2944	1.4243
	Hopfenberg	0.8545	65.5635	1.6166
	Baker-Lonsdale	0.9299	58.1870	2.4362
	Makoid-Banakar	0.9677	52.6281	3.0539
	Peppas-Sahlin	0.9609	54.3595	2.8615
	Weibull	0.9771	49.5448	3.3965
	Gompertz	**0.9922**	**39.2393**	**4.5415**
PEGylayed CUR-DOX liposomes 7.4	Zero order	0.6839	64.9216	0.9296
	First order	0.8397	58.8086	1.6088
	Higuchi	0.9434	49.4383	2.6499
	Korsmeyer-Peppas	0.9354	51.4352	2.4281
	Hixon-Crowell	0.7932	61.1030	1.3539
	Hopfenberg	0.8168	60.8103	1.3864
	Baker-Lonsdale	0.9460	49.0130	2.6972
	Makoid-Banakar	0.9803	41.3348	3.5503
	Peppas-Sahlin	0.9752	43.4255	3.3180
	Weibull	0.9804	41.2874	3.5556
	Gompertz	**0.9901**	**34.5063**	**4.3090**
PEGylayed CUR-DOX liposomes 5.5	Zero order	0.5487	73.1362	0.5733
	First order	0.8451	63.5120	1.6427
	Higuchi	0.9011	59.4758	2.0911
	Korsmeyer-Peppas	0.8923	61.0381	1.9175
	Hixon-Crowell	0.7664	67.2074	1.2321
	Hopfenberg	0.8228	65.5218	1.4193
	Baker-Lonsdale	0.9208	57.4754	2.3134
	Makoid-Banakar	0.9677	50.7991	3.0552
	Peppas-Sahlin	0.9576	53.2515	2.7827

Weibull	0.9635	51.9159	2.9311
Gompertz	0.9811	45.3604	3.6595

7.3.2.2 DOX release studies

DOX from the plain DOX solution in 7.4 and 5.5 pH showed an accelerated release of 72.77 and 82.41 % after 12 h, 79.06 and 83.70 % after 24 h, and 87.42 and 94.50 % release after 72 h respectively (Figure 7.10). The liposomal formulations observed a biphasic release with an initial increased release followed by a sustained and prolonged release. DOX from DOX liposomes in 7.4 and 5.5 pH showed 13.97 and 21.28 % release after 12 h, 16.28 and 23.88 % after 24 h, and 20.60 and 31.99 % after 72 h respectively; DOX from PEGylated DOX liposomes in 7.4 and 5.5 pH showed 11.56 % and 16.45 % release after 12 h, 13.89 and 19.32 % after 24 h, and 18.03 % and 26.33 % after 72 h respectively.

DOX release from CUR-DOX liposomes in 7.4 and 5.5 pH showed 14.53 and 22.84 % release after 12 h, 16.84 and 26.31 % after 24 h, and 21.75 and 32.44 % after 72 h; DOX release from PEGylated CUR-DOX liposomes in 7.4 and 5.5 pH showed 12.43 % and 17.66 % release after 12 h, 14.66 and 20.54 % after 24 h, and 18.52 and 27.65 % after 72 h.

The slower release profile of DOX from the liposomes compared to DOX solution and CUR results from the diffusion of DOX from the deeper seated aqueous core of liposomes; the drug release patterns of both CUR and DOX also correspond to the 30 % CHOL that stabilizes the particles (Chen et al., 2019).
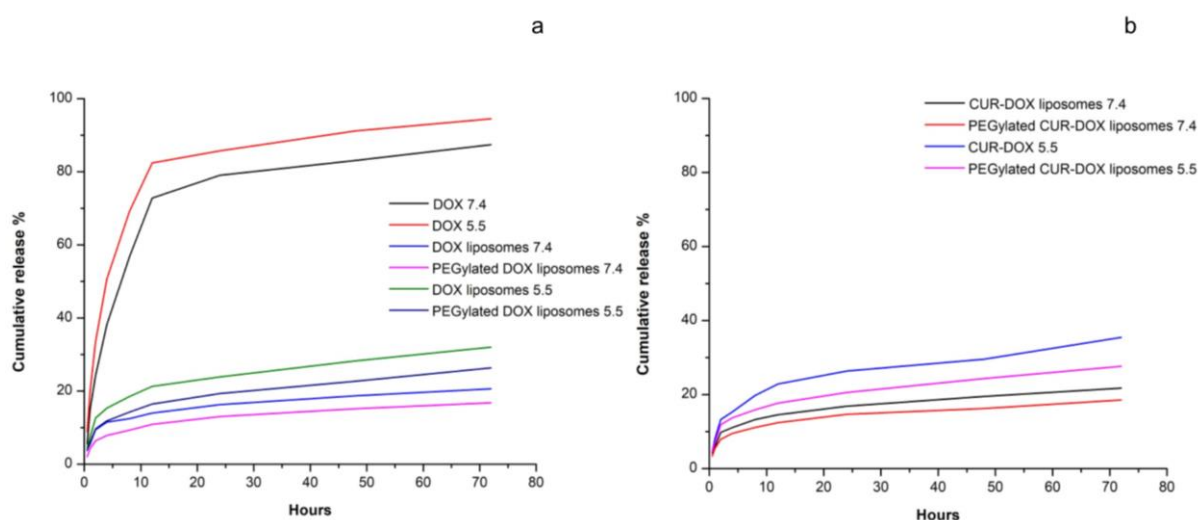
Figure 7.10 Release profile of DOX from DOX liposomes and PEGylated DOX liposomes in a release medium of pH 7.4 and 5.5

Based on the R^2 values, all the formulations follow the Korsmeyer-Peppas, Makoid-Banakar, Peppas-Sahlin, Weibull, and Gompertz models, suggesting drug release by diffusion. Based on the R^2, AIC, and MSC values, we found Weibull to be the best fit model for the release of DOX (Table 7.2).

Figure 7.2 Release models for DOX from DOX liposomes, PEGylated DOX liposomes, CUR-DOX liposomes and PEGylated CUR-DOX liposomes in a release medium of pH 7.4 and 5.5

Formulations	Release Kinetic models	R^2	AIC	MSC
DOX 7.4	Zero order	-0.1260	83.8446	-0.3409
	First order	0.9169	60.3921	2.2650
	Higuchi	0.7242	71.1827	1.0660
	Korsmeyer-Peppas	0.8614	65.7894	1.6653
	Hixon-Crowell	0.7697	69.5603	1.2463
	Hopfenberg	0.9049	62.3968	2.0422
	Baker-Lonsdale	0.9224	59.7674	2.3344
	Makoid-Banakar	0.9654	53.9228	2.9838
	Peppas-Sahlin	0.9590	55.4408	2.8151
	Weibull	0.9674	53.3853	3.0435
	Gompertz	0.9872	44.3629	4.0460
DOX 5.5	Zero order	-0.5336	87.2104	-0.6498
	First order	0.9589	54.6272	2.9705
	Higuchi	0.5715	75.7344	0.6253
	Korsmeyer-Peppas	0.8405	67.6412	1.5245
	Hixon-Crowell	0.6236	74.5687	0.7548
	Hopfenberg	0.9531	56.6299	2.7480
	Baker-Lonsdale	0.8500	66.2894	1.6747
	Makoid-Banakar	0.9541	57.0398	2.7024
	Peppas-Sahlin	0.9506	57.7013	2.6290
	Weibull	0.9833	47.9356	3.7140
	Gompertz	0.9905	42.2212	4.3490

DOX liposomes 7.4	Zero order	-0.7709	57.2058	-0.7937
	First order	-0.6180	56.3932	-0.7034
	Higuchi	0.5775	44.3074	0.6394
	Korsmeyer-Peppas	0.9680	21.8919	3.1301
	Hixon-Crowell	-0.6691	56.6732	-0.7345
	Hopfenberg	-0.8499	58.3967	-0.9260
	Baker-Lonsdale	0.6224	43.2970	0.7517
	Makoid-Banakar	0.9812	17.7011	3.5957
	Peppas-Sahlin	0.9847	15.8307	3.8035
	Weibull	0.9915	10.5549	4.3897
	Gompertz	0.9885	12.6405	4.1580
DOX liposomes 5.5	Zero order	-0.3908	63.7400	-0.5521
	First order	-0.1825	62.2797	-0.3898
	Higuchi	0.7015	49.8897	0.9868
	Korsmeyer-Peppas	0.9576	33.1297	2.8490
	Hixon-Crowell	-0.2519	62.7934	-0.4469
	Hopfenberg	-0.3520	64.2834	-0.6125
	Baker-Lonsdale	0.7558	48.0824	1.1876
	Makoid-Banakar	0.9677	31.2786	3.0547
	Peppas-Sahlin	0.9720	30.0052	3.1962
	Weibull	0.9903	20.5013	4.2522
	Gompertz	0.9847	23.9696	3.8668
PEGylated DOX liposomes 7.4	Zero order	-0.3780	53.4151	-0.5429
	First order	-0.2684	52.6689	-0.4599
	Higuchi	0.7135	39.2782	1.0279
	Korsmeyer-Peppas	0.9660	20.8926	3.0707
	Hixon-Crowell	-0.3049	52.9245	-0.4884
	Hopfenberg	-0.4499	54.6710	-0.6824
	Baker-Lonsdale	0.7425	38.3186	1.1345
	Makoid-Banakar	0.9767	18.1059	3.3804
	Peppas-Sahlin	0.9798	16.8301	3.5221
	Weibull	0.9931	7.1424	4.5985
	Gompertz	0.9857	13.1049	3.9361

PEGylated DOX liposomes 5.5	Zero order	-0.2416	59.0199	-0.4386
	First order	-0.0903	57.8504	-0.3087
	Higuchi	0.7639	44.0805	1.2213
	Korsmeyer-Peppas	0.9751	24.6430	3.3810
	Hixon-Crowell	-0.1406	58.2563	-0.3538
	Hopfenberg	-0.2466	59.8538	-0.5313
	Baker-Lonsdale	0.8011	42.5392	1.3925
	Makoid-Banakar	0.9792	23.6090	3.4959
	Peppas-Sahlin	0.9822	22.2368	3.6484
	Weibull	0.9942	12.0791	4.7770
	Gompertz	0.9908	15.6370	4.3817
CUR-DOX liposomes 7.4	Zero order	-0.8503	58.1796	-0.8376
	First order	-0.6863	57.3444	-0.7448
	Higuchi	0.5443	45.5686	0.5637
	Korsmeyer-Peppas	0.9657	23.0776	3.0627
	Hixon-Crowell	-0.7411	57.6325	-0.7768
	Hopfenberg	-0.9276	59.3461	-0.9672
	Baker-Lonsdale	0.5933	44.5455	0.6773
	Makoid-Banakar	0.9729	21.5938	3.2275
	Peppas-Sahlin	0.9768	20.1651	3.3863
	Weibull	0.9907	11.9978	4.2938
	Gompertz	0.9843	16.0748	3.8408
CUR-DOX liposomes 5.5	Zero order	-0.6152	65.3833	-0.7017
	First order	-0.3668	63.8806	-0.5347
	Higuchi	0.6241	52.2629	0.7562
	Korsmeyer-Peppas	0.9534	34.2763	2.7547
	Hixon-Crowell	-0.4501	64.4128	-0.5938
	Hopfenberg	-0.5625	65.8829	-0.7572
	Baker-Lonsdale	0.6929	50.4445	0.9582
	Makoid-Banakar	0.9790	27.6934	3.4861
	Peppas-Sahlin	0.9826	26.0025	3.6740
	Weibull	0.9888	22.0621	4.1118
	Gompertz	0.9874	22.4850	4.0648

PEGylayed CUR-DOX liposomes 7.4	Zero order	-0.8622	55.2497	-0.8440
	First order	-0.7255	54.5634	-0.7677
	Higuchi	0.5415	42.6357	0.5576
	Korsmeyer-Peppas	0.9672	19.6847	3.1077
	Hixon-Crowell	-0.7713	54.7989	-0.7939
	Hopfenberg	-0.9725	56.5656	-0.9902
	Baker-Lonsdale	0.5828	41.7850	0.6521
	Makoid-Banakar	0.9759	17.5440	3.3455
	Peppas-Sahlin	0.9798	15.9296	3.5249
	Weibull	0.9949	3.6116	4.8936
	Gompertz	0.9853	12.4622	3.9102
PEGylayed CUR-DOX liposomes 5.5	Zero order	-0.5988	61.4133	-0.6915
	First order	-0.4079	60.2688	-0.5643
	Higuchi	0.6350	48.1191	0.7857
	Korsmeyer-Peppas	0.9673	27.1913	3.1110
	Hixon-Crowell	-0.4715	60.6669	-0.6085
	Hopfenberg	-0.6094	62.2712	-0.7868
	Baker-Lonsdale	0.6878	46.7133	0.9419
	Makoid-Banakar	0.9688	27.3884	3.0891
	Peppas-Sahlin	0.9724	26.2981	3.2102
	Weibull	0.9904	16.8175	4.2636
	Gompertz	0.9832	21.2316	3.7732

7.3.2.3 Release studies from pH responsive liposomes

CUR release from pH responsive CUR-DOX liposomes in pH 7.4 and 5.5 records 38.23 and 81.10 % after 12 h, 47.84 and 90.15 % after 24 h, and 57.25 and 94.97 % after 72 h, respectively. DOX release from pH responsive CUR-DOX liposomes in pH 7.4 and 5.5 records 13.41 and 34.07 % after 12 h, 15.63 and 39.64 % after 24 h, and 20.31 and 49.2 % after 72 h, respectively (Figure 7.11).
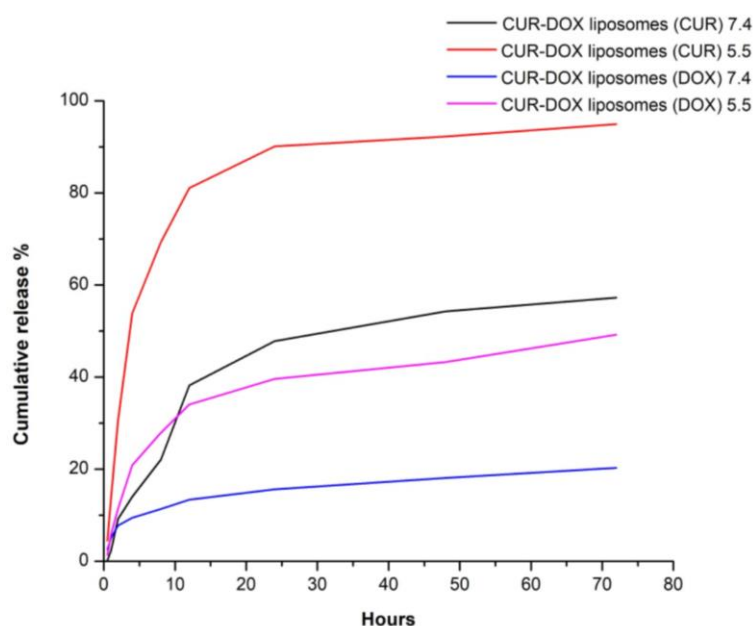
Figure 7.11 Release profile of CUR and DOX from pH responsive liposomes

Based on the R^2 values, all the formulations follow the Korsmeyer-Peppas, Makoid-Banakar, Peppas-Sahlin, Weibull, and Gompertz models, suggesting the release of drugs by diffusion. Based on the R^2, AIC, and MSC values, all the formulations follow the Gompertz model for CUR release and the Weibull model for DOX release (Table 7.3).

Table 7.3 Release models of CUR and DOX from pH responsive liposomes

Formulations		Release Kinetic models	R^2	AIC	MSC
pH CUR-DOX liposomes 7.4	CUR	Zero order	0.5431	69.7274	0.5610
		First order	0.7752	63.3423	1.2704
		Higuchi	0.9107	55.0328	2.1937
		Korsmeyer-Peppas	0.9048	56.4045	2.0413
		Hixon-Crowell	0.7054	65.7780	0.9998
		Hopfenberg	0.7431	65.3442	1.0480
		Baker-Lonsdale	0.9288	52.9992	2.4197
		Makoid-Banakar	0.9767	44.3600	3.3796
		Peppas-Sahlin	0.9693	46.8324	3.1049
		Weibull	0.9605	49.1143	2.8513
		Gompertz	0.9776	43.4045	3.4857

pH CUR-DOX liposomes 5.5	Zero order	-0.3273	87.2821	-0.5054
	First order	0.9761	51.1208	3.5125
	Higuchi	0.6217	75.9853	0.7498
	Korsmeyer-Peppas	0.8128	70.4492	1.3649
	Hixon-Crowell	0.6960	74.0155	0.9687
	Hopfenberg	0.9727	53.1237	3.2900
	Baker-Lonsdale	0.8513	67.5790	1.6838
	Makoid-Banakar	0.9450	60.0337	2.5222
	Peppas-Sahlin	0.9369	61.2834	2.3833
	Weibull	0.9863	47.5075	3.9140
	Gompertz	0.9972	32.6985	5.5594
pH CUR-DOX DOX liposomes 7.4	Zero order	-0.7709	57.2058	-0.7937
	First order	-0.6180	56.3932	-0.7034
	Higuchi	0.5775	44.3074	0.6394
	Korsmeyer-Peppas	0.9680	21.8919	3.1301
	Hixon-Crowell	-0.6691	56.6732	-0.7345
	Hopfenberg	-0.8499	58.3967	-0.9260
	Baker-Lonsdale	0.6224	43.2970	0.7517
	Makoid-Banakar	0.9812	17.7011	3.5957
	Peppas-Sahlin	0.9847	15.8307	3.8035
	Weibull	0.9958	4.9494	5.0941
	Gompertz	0.9868	14.6360	4.0178
pH CUR-DOX liposomes 5.5	Zero order	0.1675	70.1872	-0.0388
	First order	0.4306	66.7687	0.3410
	Higuchi	0.8374	55.4867	1.5945
	Korsmeyer-Peppas	0.9065	51.3093	2.0587
	Hixon-Crowell	0.3440	68.0435	0.1993
	Hopfenberg	0.3491	68.7712	0.1185
	Baker-Lonsdale	0.8865	52.2548	1.9536
	Makoid-Banakar	0.9587	44.5702	2.8075
	Peppas-Sahlin	0.9571	44.9116	2.7696
	Weibull	0.9790	38.4997	3.4820
	Gompertz	0.9782	38.2235	3.5127

We observed a comparatively slower release of drugs from the PEGylated liposomes than the non-PEGylated counterparts, as PEG chains impart stearic stability to the liposomes, hindering the drug release from the liposomes. Secondly, the drug is released faster in an acidic medium (pH 5.5) due to the pH gradient; the head groups of the lipids also protonate in an acidic medium that modifies the liposome's surface charge and alters the liposome's structural integrity.

The drugs released faster from the pH responsive liposomes than the non responsive counterparts, confirming the pH sensitive attribute of the liposomes (Zhao et al., 2016). The carboxylic groups of CHEMS protonate in an acidic medium that reduces the electrostatic repulsion between the neighboring DOPE, resulting in the lamellar phase transforming to an inverted hexagonal phase that destabilizes the bilayer and releases the drug from the liposomes (Karanth et al., 2007).

7.3.3 Cell Viability Studies

We studied the cell viability of MCF-7 and MDA-MB-231 cells by MTT assay after 48 h of treatment with plain drugs and liposomal formulations.

7.3.3.1 Cell viability studies in MCF-7 cell line

We recorded 2.88 times lower IC_{50} value of plain DOX than DOX liposomes (t-test p values = 0.0029) and 3.77 times lower than CUR-DOX liposomes (t-test p values = 0.0148), but equivalent for both liposomal formulations. The IC_{50} value of plain CUR was 2.15 times lower than CUR liposomes (t-test p values = 0.0323) but comparable to CUR-DOX liposomes that showed 2.65 times lower IC_{50} than CUR liposomes (t-test p values = 0.0295) (Table 7.4) (Figure 7.12). The IC_{50} of DOX in FOL CUR-DOX liposomes was 3.37 times higher than plain DOX (t-test p values = 0.0014) but equivalent to DOX liposomes and CUR-DOX liposomes. The IC_{50} of CUR in FOL CUR-DOX liposomes was similar to plain CUR and CUR-DOX liposomes but 2.61 times lower than CUR liposomes (t-test p values = 0.0220).

The IC_{50} of DOX in the CET CUR-DOX liposomes was equivalent to the plain DOX and 1.81 times lower than DOX liposomes (t-test p values = 0.0397), 2.37 times than CUR-DOX liposomes (t-test p values = 0.0432), and 2.11 times that FOL CUR-DOX liposomes (t-test p values = 0.0150). But the IC_{50} of CUR in CET CUR-DOX liposomes was 2.56 times lower

than plain CUR (t-test p values = 0.0015), 5.51 times than CUR liposomes (t-test p values = 0.0085), and 2.11 times than FOL CUR-DOX liposomes (t-test p values = 0.0148), but equivalent to CUR-DOX liposomes.

The IC_{50} of DOX in FOL-CET CUR-DOX liposomes was equivalent to the plain DOX and CET CUR-DOX liposomes and 2.58 times lower than DOX liposomes (t-test p values = 0.0046), 3.38 times than CUR-DOX liposomes (t-test p values = 0.0177), and 3.02 times than FOL CUR-DOX liposomes (t-test p values = 0.0021). But the IC_{50} of CUR in FOL-CET CUR-DOX liposomes was 3.67 times lower than plain CUR (t-test p values = <0.0001), 7.89 times than CUR liposomes (t-test p values = 0.0063), 2.98 times than CUR-DOX liposomes (t-test p values = 0.0483), and 3.03 times than FOL CUR-DOX liposomes (t-test p values = 0.0021), and equivalent to CET CUR-DOX liposomes.

The IC_{50} of pH CUR-DOX liposomes was 2.29 times higher than plain DOX (t-test p values = <0.0001) but equivalent to CUR-DOX liposomes; the IC_{50} of CUR in pH responsive CUR-DOX liposomes was 1.78 times lower than plain CUR (t-test p values = <0.0001), and 1.44 times than CUR-DOX liposomes (t-test p values = 0.0112). The IC_{50} of DOX in pH FOL CUR-DOX liposomes was 5.42 times higher than plain DOX (t-test p values = <0.0001) and 1.61 times than FOL CUR-DOX liposomes (t-test p values = 0.0030); the IC_{50} of CUR in pH FOL CUR-DOX liposomes was 1.33 times higher than plain CUR (t-test p values = 0.0007), and 1.61 times than FOL CUR-DOX liposomes (t-test p values = 0.0030).

The IC_{50} of DOX in pH CET CUR-DOX liposomes was 5.10 higher than the plain DOX (t-test p values = <0.0001) and 1.67 times than CET CUR-DOX liposomes (t-test p values = 0.0009); the IC_{50} of CUR in pH CET CUR-DOX liposomes was 1.25 times higher than plain CUR (t-test p values = 0.0172) and 3.20 times than CET CUR-DOX liposomes (t-test p values = 0.0009). The IC_{50} of DOX in pH FOL-CET CUR-DOX liposomes was 1.63 times higher than plain DOX (t-test p values = 0.0294) and equivalent to FOL-CET CUR-DOX liposomes, but the IC_{50} of CUR in pH FOL-CET CUR-DOX liposomes was 2.51 times lower than plain CUR (t-test p values = 0.0003) and equivalent to FOL-CET CUR-DOX liposomes.

The IC_{50} of DOX and CUR in pH responsive CUR-DOX liposomes was 2.36 times lower than pH FOL CUR-DOX liposomes, 2.23 times pH responsive CET CUR-DOX liposomes, but 1.41 times higher than pH responsive FOL-CET CUR-DOX liposomes. The IC_{50} of pH responsive FOL CUR-DOX liposomes was equivalent to pH responsive CET CUR-DOX liposomes and

3.33 times higher than pH responsive FOL-CET CUR-DOX liposomes that had 3.13 times lower IC50 than pH responsive CET CUR-DOX liposomes.

In the MCF-7 cell lines, the anticancer efficacy of DOX in CET CUR-DOX liposomes and FOL-CET CUR-DOX liposomes was equivalent to plain DOX. But, the anticancer efficacy of CUR in CET CUR-DOX liposomes and FOL-CET CUR-DOX liposomes was higher than in plain CUR. The anticancer activity of FOL CUR-DOX liposomes, DOX liposomes, and CUR-DOX liposomes was equivalent, but the CET CUR-DOX liposomes and FOL-CET CUR-DOX liposomes showed increased efficacy than the rest liposomal formulations. The anticancer activity of CUR in FOL CUR-DOX liposomes was equivalent to CUR-DOX liposomes. But, the CET CUR-DOX liposomes and FOL-CET CUR-DOX liposomes showed increased efficacy compared to the rest of the liposomal formulations.

DOX showed reduced anticancer activity for all the pH-responsive liposomes compared to plain DOX and non-responsive liposomes. But CUR in pH responsive CUR-DOX liposomes and pH responsive FOL-CET CUR-DOX liposomes shower higher activity than plain CUR. Only the pH responsive CUR-DOX liposomal formulation was more efficacious than its non-responsive counterpart, and the pH responsive FOL-CET CUR-DOX liposomes were equivalent to their non-responsive counterparts.

Table 7.4 IC_{50} values of DOX and CUR of various formulations in MCF-7 cells

	MCF-7	
	DOX	CUR
Plain DOX	1.05 ± 0.02	
Plain CUR		12.85 ± 0.45
DOX Liposomes	3.02 ± 0.53	
CUR Liposomes		27.64 ± 7.94
CUR-DOX Liposomes	3.96 ± 1.23	10.43 ± 4.23
FOL CUR-DOX Liposomes	3.53 ± 0.54	10.61 ± 1.63
CET CUR-DOX Liposomes	1.17 ± 0.19	3.50 ± 0.57
FOL-CETCUR-DOX Liposomes	1.67 ± 0.57	5.02 ± 1.70
pH CUR-DOX Liposomes	2.40 ± 0.08	7.22 ± 0.23
pH FOL CUR-DOX Liposomes	5.69 ± 0.20	17.07 ± 0.62

pH CET CUR-DOX Liposomes	5.36 ± 0.45	16.07 ± 1.35
pH FOL-CET CUR-DOX Liposomes	1.71 ± 0.34	5.13 ± 1.04
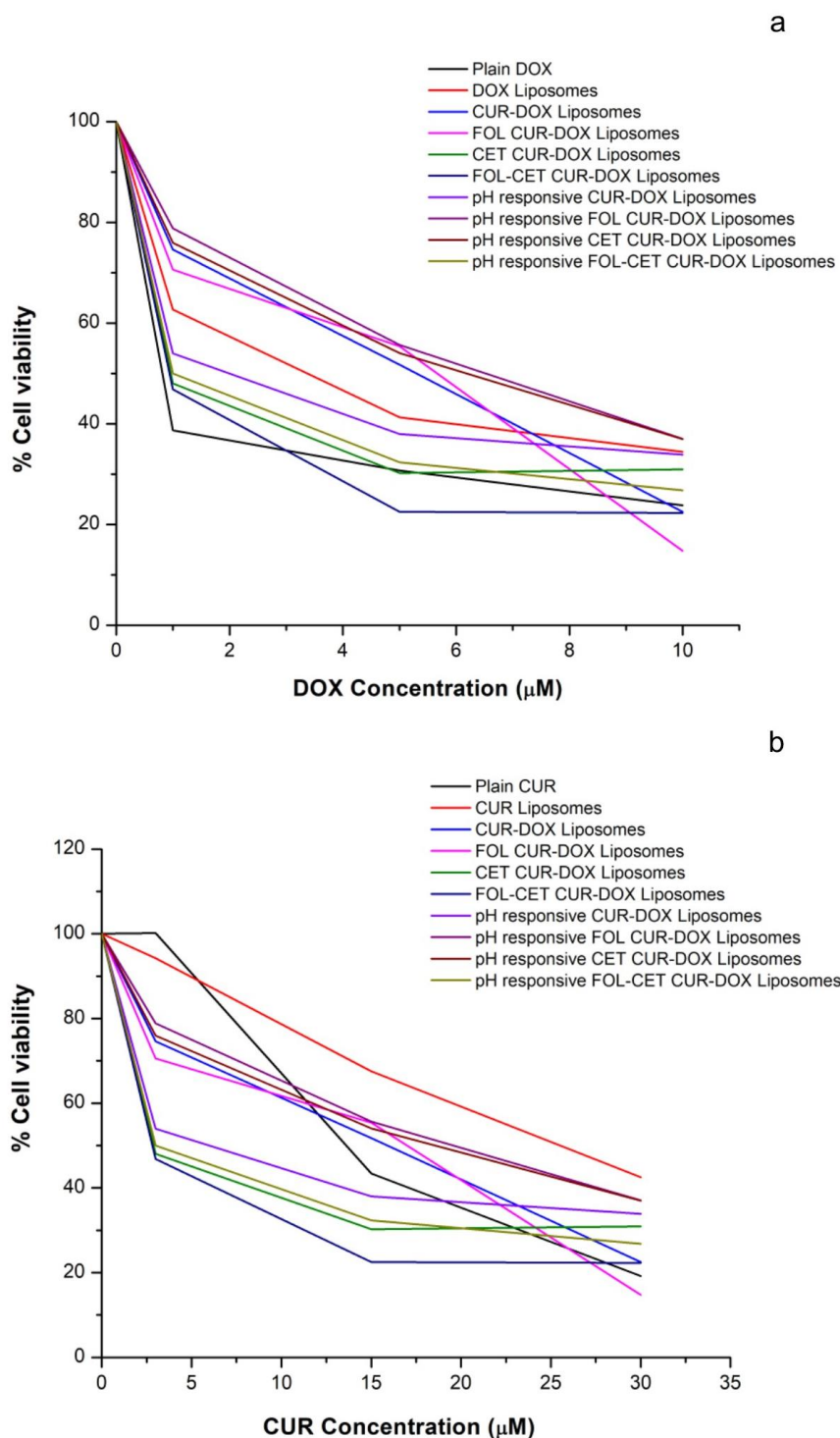
Figure 7.12 % viability of MCF-7 cells at different concentrations of DOX (a) and CUR (b)

7.3.3.2 Cell viability studies in MDA-MB-231 cell line

The IC_{50} of plain DOX was significantly lower (t-test p value = <0.0001) in the MCF-7 cells as MDA-MB-231 cells are aggressive and multi drug resistant thanMCF-7 that have a lower P-gp expression (Table 7.5) (Figure 7.13) (Lv et al., 2016). The IC_{50} value for plain DOX was 2.12 times lower than DOX liposomes (t-test p values = <0.0001) and 1.65 times than CUR-DOX liposomes (t-test p values = 0.0131) that had the IC_{50} 1.28 times lower than DOX liposomes (t-test p values = 0.0465). The IC_{50} of plain CUR was 4.63 times lower than CUR liposomes (t-test p values = <0.0001) and 1.68 times than CUR-DOX liposomes (t-test p values = 0.0165) that had IC_{50} 2.75 times lower than CUR liposomes (t-test p values = 0.0004).

The IC_{50} value of DOX in FOL CUR-DOX liposomes was 1.79 times higher than plain DOX (t-test p values = 0.0007) but 1.18 times lower than DOX liposomes (t-test p values = 0.0354), and equivalent to the CUR-DOX liposomes. The IC_{50} of CUR in FOL CUR-DOX liposomes was 1.83 times higher than plain CUR (t-test p values = 0.0018), 2.53 times lower than CUR liposomes (t-test p values = 0.0003), and equivalent to CUR-DOX liposomes.

The IC_{50} of DOX in CET CUR-DOX liposomes was1.76 times higher than plain DOX (t-test p values = 0.0269) but equivalent to DOX liposomes, CUR-DOX liposomes, and FOL CUR-DOX liposomes. But the IC_{50} of CUR in CET CUR-DOX liposomes was 1.80 times higher than plain CUR (t-test p values = 0.0290), 2.58 times higher than CUR liposomes (t-test p values = 0.0008), and equivalent to CUR-DOX liposomes and FOL CUR-DOX liposomes.

The IC_{50} of DOX in the FOL-CET CUR-DOX liposomes was equivalent to the plain DOX and 2.11 times lower than DOX liposomes (t-test p values = <0.0001), 1.64 times than CUR-DOX liposomes (t-test p values = 0.0134), 1.79 times than FOL CUR-DOX liposomes (t-test p values = 0.0007) and 1.75 times than CET CUR-DOX liposomes (t-test p values = 0.0274). The IC_{50} of CUR in FOL-CET CUR-DOX liposomes was equivalent to plain CUR and 4.52 times lower than CUR liposomes (t-test p values = <0.0001), 1.65 times than CUR-DOX liposomes (t-test p values = 0.0134), 1.79 times than FOL CUR-DOX liposomes (t-test p values = 0.0007), and 1.76 times than CET CUR-DOX liposomes (t-test p values = 0.0274).

The IC_{50} of DOX in pH CUR-DOX liposomes was 1.29 times lower than plain DOX (t-test p values = 0.0336) and 2.13 times than CUR-DOX liposomes (t-test p values = 0.0059); the IC_{50} of CUR in pH CUR-DOX liposomes was equivalent to plain CUR but 2.13 times lower than

CUR-DOX liposomes (t-test p values = 0.0059). The IC_{50} of DOX in pH FOL CUR-DOX liposomes was 1.24 times lower than plain DOX (t-test p values = 0.0033), 2.23 times than FOL CUR-DOX liposomes (t-test p values = 0.0003); the IC_{50} of CUR in pH FOL CUR-DOX liposomes was equivalent to plain CUR and 2.23 times lower than FOL CUR-DOX liposomes (t-test p values = 0.0003).

The IC_{50} of DOX and CUR in pH CET CUR-DOX liposomes was equivalent to plain drugs and CET CUR-DOX. The IC_{50} of pH FOL-CET CUR-DOX liposomes was 1.63 times lower than the plain DOX (t-test p values = 0.0044) and 1.63 times than FOL-CET CUR-DOX liposomes (t-test p values = 0.0043); the IC_{50} of CUR in pH FOL-CET CUR-DOX liposomes 1.59 times lower than plain CUR (t-test p values = 0.0201) and 1.63 times than FOL-CET CUR-DOX liposomes (t-test p values = 0.0043).

The IC_{50} of DOX and CUR in pH responsive CUR-DOX liposomes was equivalent to pH responsive FOL CUR-DOX liposomes and pH responsive FOL-CET CUR-DOX liposomes, 1.60 times lower than pH responsive CET CUR-DOX liposomes. The IC_{50} of pH responsive FOL CUR-DOX liposomes was 1.54 times lower than pH responsive CET CUR-DOX liposomes and 1.31 times higher than pH responsive FOL-CET CUR-DOX liposomes. The IC_{50} of pH responsive FOL-CET CUR-DOX liposomes was 2.02 times lower than pH responsive CET CUR-DOX liposomes.

In MDA-MB-231 cell lines, the anticancer efficacy of DOX in FOL-CET CUR-DOX liposomes was equivalent to plain DOX and higher than the other liposomal formulations. The anticancer efficacy of CUR in FOL-CET CUR-DOX liposomes was comparable to plain CUR and higher than the different liposomal formulations. But, the anticancer efficacy of the pH responsive formulations was higher than plain DOX except for pH responsive CET CUR-DOX liposomes and higher than their non-responsive counterparts.

Table 7.5 IC$_{50}$ values of DOX and CUR of various liposomal formulations in MDA-MB-231 cells

	MDA-MB-231	
	DOX	**CUR**
Plain DOX	4.86 ± 0.23	
Plain CUR		14.29 ± 1.93
DOX Liposomes	10.30 ± 0.56	
CUR Liposomes		66.14 ± 5.42
CUR-DOX Liposomes	8.02 ± 1.27	24.08 ± 3.80
FOL CUR-DOX Liposomes	8.72 ± 0.68	26.15 ± 2.03
CET CUR-DOX Liposomes	8.86 ± 1.86	25.67 ± 5.59
FOL-CETCUR-DOX Liposomes	4.88 ± 0.23	14.63 ± 0.70
pH CUR-DOX Liposomes	6.03 ± 0.96	18.09 ± 2.89
pH FOL CUR-DOX Liposomes	3.91 ± 0.13	11.74 ± 0.38
pH CET CUR-DOX Liposomes	3.76 ± 0.55	11.29 ± 1.66
pH FOL-CET CUR-DOX Liposomes	2.99 ± 0.51	8.97 ± 1.52
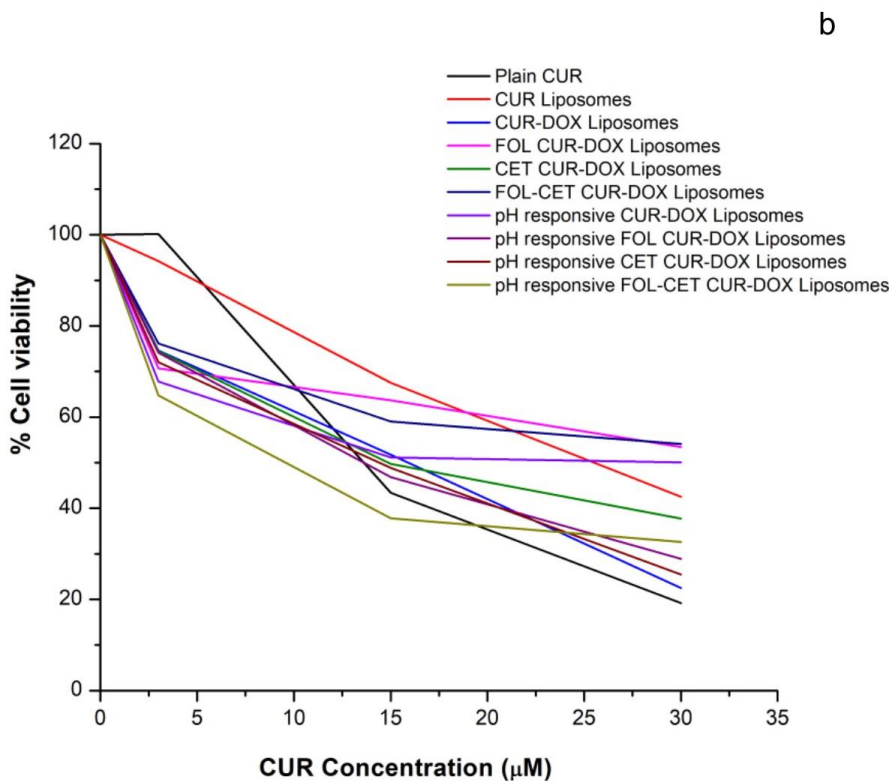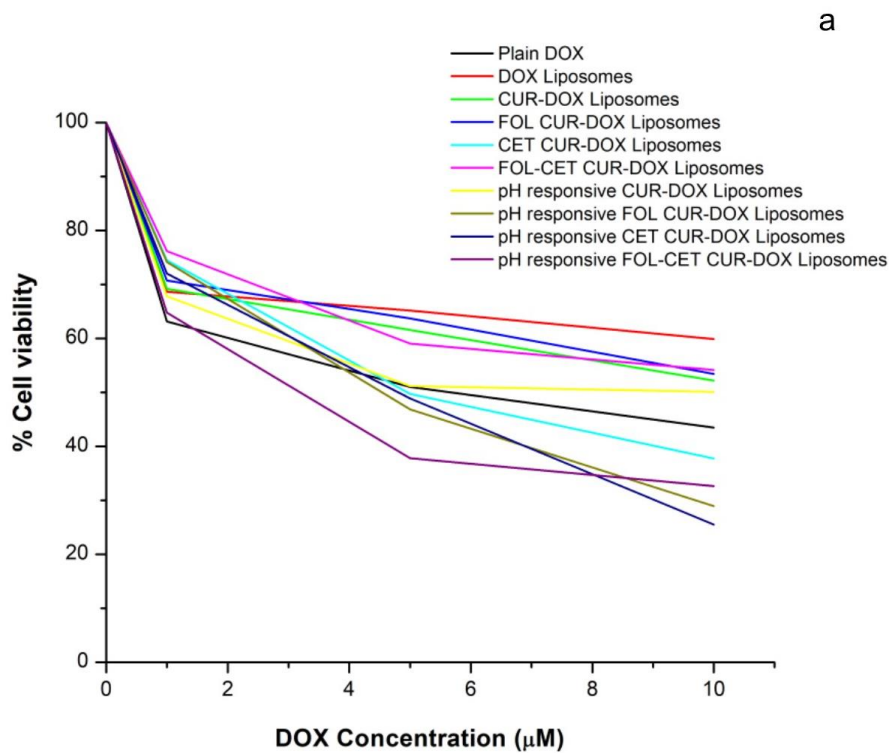
Figure 7.13 % viability of MDA-MB-231 cells at different concentrations of DOX (a) and CUR (b)

Even with a higher uptake of single drug liposomes, CUR-DOX liposomes, and FOL CUR-DOX liposomes than the plain drug (elaborated in section 7.3.4), the lower anticancer activity

corresponds to a slower drug release from the liposomes or degradation of the drugs in the lysosomes or slower release from the lysosomes compared to the faster uptake of plain drugs via diffusion; various studies reported a similar trend (Wu et al., 2007) (Yang et al., 2021) (Cai et al., 2014) (Xie et al., 2018). Also, the liposomal formulations engender sustained release of the drugs (Paliwal et al., 2016). Fahmy et al. (2019) (Fahmy, 2019), Wang et al. (Wang et al., 2008), and Yeh et al. (2015) (Yeh et al., 2015) observed a similar trend.

The increased efficacy of the dual drug loaded liposomes than the single drug loaded liposomes suggests that CUR acted as a chemosensitizer to enhance the uptake and activity of DOX and also exhibited its inherent cytotoxic potential (Zhou et al., 2017) (Zhao et al., 2014); these trends were also reported by previously published studies (Sesarman et al., 2018) (Wang et al., 2011) (Cui et al., 2017) (Guo et al., 2014). The increased anticancer efficacy of the dual targeted liposomes compared to the single targeted liposomes could result from a higher rate of internalization and accumulation in the cells and a controlled and prolonged release of the drugs.

The higher anticancer activity of the pH responsive liposomes in MDA-MB-231 cells corresponds to the triggered endosomal escape of the drugs in the cytoplasm by evading the lysosomal phase (Paliwal et al., 2012) (Kanamala et al., 2016) (Straubinger et al., 1985). The increased activity of the pH responsive liposomes in the MDA-MB-231 cells corresponds to their aggressive nature and higher metabolic activity than the MCF-7 cells. These cells consume high glucose concentrations to generate energy and liberate increased CO_2 and lactic acid –Warburg effect (Potter et al., 2016).

To maintain the physiologic intracellular pH, these cancer cells expel the lactic acid and CO_2 by active transport, making the extracellular environment acidic. But, these highly proliferating cancer cells get handicapped by the increasing energy demand and excessive active transport of the by-products; burdened by these mechanisms, the cancer cells cannot regulate the intracellular pH effectively (Swietach et al., 2014). This mechanism could also engender varied intracellular effects or anticancer activity of the liposomal formulations in different cell lines.

7.3.4 Cellular Uptake Studies

7.3.4.1 Cellular uptake in the MCF-7 cells

In the MCF-7 cells, DOX liposomes (39.70%) showed a lower uptake than the plain DOX (57.93%), and both the plain CUR (7.83%) and CUR liposomes (8.62%) showed equivalent but considerably lower uptake (Table 7.6) (Figure 7.14). This observation explains the lower anticancer potential of these liposomal formulations than plain DOX and CUR. We observed a heterogeneous cell population for CUR-DOX liposomes (73.03 % DOX and 22.54 % DOX+CUR), for FOL CUR-DOX liposomes (78.50 % DOX and 19.53 % DOX+CUR); despite higher uptake by these cells a lower anticancer efficacy than DOX could result from degradation of the drug in the lysosomes or slower release of the drugs in the cytoplasm. Plain drugs diffuse in the cells by passive diffusion, but the multi-drug resistant cells expel the drugs. Also, we ascertained the uptake studies after 8 h of treatment and checked the cell viability after 48 h of treatment.

A comparatively reduced uptake of the CET CUR-DOX liposomes (35.09 % DOX and 10.80 % DOX+CUR) corresponds to the reduced expression of EGFR receptors on the MCF-7 cells. The FOL-CET CUR-DOX liposomes showed a significantly higher uptake than CET tagged liposomes (60.39 % DOX and 8.44 % DOX+CUR), corresponding to both FOL and CET mediated uptake.

The pH CUR-DOX liposomes (82.32 % DOX and 6.56 % DOX+CUR) and pH FOL CUR-DOX liposomes (91.80 % DOX) showed a higher uptake than plain drugs. The higher uptake of both CUR and DOX in the non-responsive counterparts suggests a higher anticancer efficacy than the pH responsive liposomes. The reduced uptake of the pH CET CUR-DOX liposomes (39.02 % DOX and 13.85 % DOX+CUR) corresponds to the low expression of EGFR receptors. The pH FOL-CET CUR-DOX liposomes also showed a lower uptake (45.46 % DOX and 11.50 % DOX+CUR) than plain DOX and the non-responsive counterpart. This reduced uptake of the pH responsive liposomes by the MCF-7 cells also contributes to the lower anticancer efficacy than the non-responsive liposomes. The higher uptake of the FOL tagged liposomes than the CET tagged liposomes corresponds to the higher FRs than EGFRs on the MCF-7 cells.

Table 7.6 FACS analysis of liposomal formulations in MCF-7 cells

	Lower left quadrant-Unstained cells (%)	Lower right quadrant-DOX (%)	Upper left quadrant-CUR (%)	Upper right quadrant-CUR-DOX (%)
Plain DOX	42.02	57.93		
Plain CUR	91.95		7.83	
DOX Liposomes	60.24	39.70		
CUR Liposomes	91.34		8.62	
CUR-DOX Liposomes	4.41	73.03		22.54
FOL CUR-DOX Liposomes	1.95	78.50	0.01	19.53
CET CUR-DOX Liposomes	53.57	35.09		10.80
FOL-CET CUR-DOX Liposomes	31.09	60.39		8.44
pH CUR-DOX Liposomes	11.10	82.32		6.56
pH FOL CUR-DOX Liposomes	8.20	91.80		
pH CET CUR-DOX Liposomes	46.72	39.02		13.85
pH FOL-CET CUR-DOX Liposomes	42.87	45.46		11.50

Figure 7.14 FACS analysis of liposomal formulations in MCF-7 cells with unstained cells in the lower left quadrant, cells with DOX in the lower right quadrant, cells with CUR in the upper left quadrant and cells with dual drugs in the upper right quadrant

7.3.4.2 Cellular uptake in MDA-MB-231 cells

In the MDA-MB-231 cells, DOX liposomes (84.28 %) showed a comparatively higher uptake than plain DOX (54.57 %), but both CUR liposomes (0.27 %) and plain CUR (0.31 %) showed negligible uptake. All cells showed DOX uptake after the CUR-DOX liposomes (100 %) and FOL CUR-DOX liposomes (99.46 %) treatment (Table 7.7) (Figure 7.15).

Unlike in MCF-7 cells, CET CUR-DOX liposomes (63.42 % DOX and 34.92 % DOX+CUR) and FOL-CET CUR-DOX liposomes (57.44 % DOX and 36.84 % DOX+CUR) showed higher uptake in the MDA-MB-231 cells corresponding to a higher expression of EGFR and FRs on the surface of the MDA-MB-231. The heterogeneous cell population of both DOX and CUR, along with a comparatively higher uptake, explains the higher anticancer activity of these formulations.

The pH responsive CUR-DOX liposomes (82.32 % DOX and 6.56 % DOX+CUR) and pH responsive FOL CUR-DOX liposomes (99.96 % DOX) showed a higher uptake than plain DOX and similar to their non-responsive counterparts. The pH responsive CET CUR-DOX liposomes (67.65 % DOX and 29.14 % DOX+CUR) and pH responsive FOL-CET CUR-DOX liposomes (61.83 % DOX and 33.02 % DOX+CUR) showed a higher uptake than plain DOX and similar to their non-responsive counterparts. Despite an equivalent uptake of the pH responsive and non-responsive liposomes in the MDA-MB-231 cells, the former formulations have a higher anticancer efficacy that corresponds to the pH susceptible nature of the liposomes.

Table 7.5 FACS analysis of liposomal formulations in MDA-MB-231 cells

	Lower left quadrant-Unstained cells (%)	Lower right quadrant-DOX (%)	Upper left quadrant-CUR (%)	Upper right quadrant-CUR-DOX (%)
Plain DOX	45.35	54.57		
Plain CUR			0.27	
DOX Liposomes	15.68	84.28		
CUR Liposomes			0.31	
CUR-DOX Liposomes	0.00	100		
FOL CUR-DOX Liposomes	0.00	99.46		0.04
CET CUR-DOX Liposomes	1.65	63.42		34.92
FOL-CET CUR-DOX Liposomes	5.72	57.44		36.84
pH CUR-DOX Liposomes	11.10	82.32		6.56
pH FOL CUR-DOX Liposomes	0.03	99.96		0.01
pH CET CUR-DOX Liposomes	3.21	67.65		29.14
pH FOL-CET CUR-DOX Liposomes	5.14	61.83		33.02

Figure 7.15 FACS analysis of liposomal formulations in MDA-MB-231 cells with unstained cells in the lower left quadrant, cells with DOX in the lower right quadrant, cells with CUR in the upper left quadrant, and cells with dual drugs in the upper right quadrant

7.4 Conclusion

The in vitro efficacy studies defined the robust efficacy of the liposomal formulations synthesized. The stability studies established the stability of all the non-targeted and targeted drug loaded liposomal formulations for 3 months with 60-70 % drug retention. The drug release analysis established a slower release profile when compared to the plain drugs but an increased drug release in the acidic environment and higher release by the pH liposomes. The CUR release followed the Gompertz model, and the DOX release followed the Weibull model.

The cell viability assay established higher anticancer efficacy of the pH responsive FOL-CET CUR-DOX liposomes in the MDA-MB-231 than MCF-7 cells; these pH responsive liposomes were more efficacious than their non responsive counterparts. In the MCF-7 cells, the non-responsive liposomes exhibited a higher proficiency than their non responsive counterparts; the efficacy of the FOL-CET CUR-DOX liposomes was equivalent to that of the plain drugs. The uptake studies showed higher levels of the ligand tagged liposomes in both the MCF-7 and MDA-MB-231 cell lines. The CET tagged liposomes showed higher uptake in the MDA-MB-231 cells than the MCF-7 cell lines owing to a higher EGFR expression on the former cell line.

The *in vitro* efficacy studies confirm the robust nature of the liposomes and higher anticancer efficacy.

CHAPTER 8

Conclusions & Future prospects

8.1 Conclusions

We synthesized liposomes using the thin film hydration technique and identified various process parameters and intrinsic factors. We optimized 240 RPM rotation speed, 700 mm of Hg vacuum pressure, and 2 ml chloroform in the thin film formation step; 270 RPM rotation speed, PBS as an aqueous solvent, and 1 h hydration time in the thin film hydration step; a single 100 nm polycarbonate membrane and 10 extrusion passes in the downsizing step; 10 mg/ml lipids, a 7:3 molar ratio of PC: CHOL, and 1 mole % DSPE-mPEG2000 as intrinsic factors.

The analytical characterization techniques confirmed the synthesis of spherical particles with hydrodynamic diameter, PDI, and zeta potential values of 129.57 ± 7.36, 0.06 ± 0.03, and -24.84 ± 0.67 mV, respectively, for plain liposomes, and 119.94 ± 1.23, 0.1 ± 0.002, and -8.36 ± 0.99 mV respectively for PEGylated liposomes. The electron microscopy elucidated the spherical morphology of the particles, FTIR analysis corroborated the synthesis of liposomes, and TGA and DSC analysis indicated high thermal stability.

We optimized a 7: 3 molar ratio of PC: CHOL, 1: 50 wt. / wt. ratio of the CUR: lipids and excluded sonication with 5 extrusion passes in the downsizing step for CUR liposomes: 1 mole % DSPE-mPEG2000 and 5 extrusion passes for PEGylated CUR liposomes. We recorded the hydrodynamic diameter, PDI, and zeta potential at 1117.66 ± 5.36 nm, 0.07 ± 0.01, and -21.97 ± 2.99 mV, respectively, for CUR liposomes, and 118.19 ± 4.09 nm, 0.07 ± 0.02, and -10.08 ± 0.38 mV respectively for PEGylated CUR liposomes. We recorded the % EE and % DL of CUR liposomes at 75.95 ± 3.22 % and 3.64 ± 0.15 %, respectively, and for PEGylated CUR liposomes at 77.86 ± 2.61 % and 3.21 ± 0.27 % respectively. The electron microscopy elucidated the spherical morphology of the particles, FTIR analysis corroborated the loading of CUR in the lipid bilayer, and TGA and DSC analysis indicated high thermal stability with successful loading of CUR in the liposomes.

We optimized 0.1 mg DOX and 5 extrusion passes for both DOX liposomes and PEGylated DOX liposomes. The DOX liposomes had hydrodynamic diameter, PDI, and zeta potential of 129.79 ± 5.07 nm, 0.08 ± 0.001, and -20.49 ± 0.77 mV, respectively; for PEGylated DOX liposomes at 118.57 ± 5.01 nm in size, 0.07 ± 0.01 PDI and -9.25 ± 1.46 mV respectively. We calculated the % EE and % DL for DOX liposomes at 78.24 ± 7.59 % and 2.31 ± 0.21 %, respectively, and for PEGylated DOX liposomes at 74.42 ± 2.17 % and 2.51 ± 0.10 %

respectively. The electron microscopy elucidated the spherical morphology of the particles, FTIR analysis corroborated the loading of DOX in the aqueous core or the water-lipid interface, and TGA and DSC analysis indicated high thermal stability with successful loading of DOX in the liposomes.

We recorded the hydrodynamic diameter, PDI, and zeta potential at 117.36 ± 1.61 nm, 0.08 ± 0.004, and -19.07 ± 3.03 mV, respectively, for CUR-DOX liposomes and at 121.51 ± 0.82 nm, 0.09 ± 0.02, and -10.2 ± 1.6 mV respectively for PEGylated CUR-DOX liposomes. We calculated the % EE of CUR in CUR-DOX liposomes and PEGylated CUR-DOX liposomes at 76.82 ± 3.9 and 77.57 ± 7.95% respectively, and for DOX at 78.66 ± 2.49 and 73.32 ± 2.84 % respectively; and the % DL of CUR-DOX liposomes and PEGylated CUR-DOX liposomes at 4.46 ± 0.30 and 4.25 ± 0.24 % respectively. The electron microscopy elucidated the spherical morphology of the particles, FTIR analysis corroborated the loading of CUR in the lipid bilayer and DOX in the aqueous core or the water-lipid interface, and TGA and DSC analysis indicated high thermal stability with successful loading of both drugs in the liposomes.

We tagged FOL on the liposomal surface and recorded the hydrodynamic diameter, PDI, and zeta potential for FOL CUR liposomes at 131.24 ± 3.91 nm, 0.10 ± 0.05, and -8.99 ± 1.37 mV, respectively; FOL DOX liposomes at 128.38 ± 2.10 nm, 0.06 ± 0.01, and -6.92 ± 0.41 mV respectively; and FOL CUR-DOX liposomes at 129.44 ± 0.81 nm, 0.07 ± 0.01 and -8.57 ± 0.35 mV respectively. We noted the % EE and % DL of FOL CUR liposomes at 78.40 ± 2.34% and 3.57 ± 1.91%, respectively; FOL DOX liposomes at 79.47 ± 4.75% and 2.4 ± 0.15% respectively; and FOL CUR-DOX liposomes at 77.73 ± 3.50 for CUR and 78.46 ± 3.26% for DOX, and 4.49 ± 0.18% respectively. The electron microscopy elucidated the spherical morphology of the particles, FTIR analysis corroborated the loading of CUR in the lipid bilayer and DOX in the aqueous core or the water-lipid interface, and FOL on the liposomal surface.

We tagged CET on the liposomal surface and noted the hydrodynamic diameter, PDI, and zeta potential for CET CUR liposomes at 131.08 ± 0.72 nm, 0.09 ± 0.01, and -9.80 ± 0.50 mV, respectively; CET DOX liposomes at 141.49 ± 2.9 nm, 0.12 ± 0.02, and -9.16 ± 0.44 mV respectively; and CET CUR-DOX liposomes at 126.43 ± 2.59 nm, 0.13 ± 0.03 and -10.14 ± 0.64 mV respectively. We noted the % EE of CET CUR liposomes at 79.49 ± 1.6%, CET DOX liposomes at 76.71 ± 3.18 %, and CET CUR-DOX liposomes at 79.11 ± 2.22% for CUR and 75.22 ± 1.78% for DOX. We calculated the %BE of CET at 87.11 ± 1.99 % for CET CUR

liposomes, 85.86 ± 1.96 % for CET DOX liposomes, and 88.14 ± 1.72 % for CET CUR-DOX liposomes. The electron microscopy elucidated the spherical morphology of the particles.

We fabricated FOL and CET dual tagged liposomes. DLS elucidated the hydrodynamic diameter, PDI, and zeta potential for FOL-CET CUR liposomes at 130.90 ± 1.54 nm, 0.08 ± 0.01, and -9.71 ± 1.08 mV, respectively; FOL-CET DOX liposomes at 129.57 ± 0.67 nm, 0.10 ± 0.01, and -10.45 ± 0.42mV respectively; and FOL-CET CUR-DOX liposomes at 125.97 ± 3.11 nm, 0.14 ± 0.01 and -10.86 ± 1.22 mV respectively. We calculated the % EE of CUR in FOL-CET CUR liposomes at 79.29 ± 2.96%, of DOX in FOL-CET DOX liposomes at 76.47 ± 2.20 %, and of CUR and DOX in FOL-CET CUR-DOX liposomes at 79.00 ± 3.65 % and 76.77 ± 2.89 % respectively. We calculated the %BE of CET for FOL-CET CUR liposomes at 87.55 ± 2.74 %, for FOL-CET DOX liposomes at 86.96 ± 2.35 %, and for FOL-CET CUR-DOX liposomes at 87.67 ± 1.34 %. The electron microscopy elucidated the spherical morphology of the particles.

We optimized 11 extrusion passes for pH responsive CUR-DOX liposomes and recorded the hydrodynamic diameter, PDI and zeta potential at 136.47 ± 2.58 nm, 0.08 ± 0.03 and -11 ± 0.35 mV; pH responsive FOL CUR-DOX liposomes at 136.99 ± 4.70 nm, 0.11 ± 0.04 and -8.54 ± 0.34 mV; pH responsive CET CUR-DOX liposomes at 157.72 ± 2.07 nm, 0.18 ± 0.01 and -8.26 ± 0.05 mV; pH responsive FOL-CET CUR-DOX liposomes at 163.21 ± 1.51 nm, 0.17 ± 0.001 and -9.63 ± 1.53 mV. We calculated the % EE of CUR for pH responsive CUR-DOX liposomes, pH responsive FOL CUR-DOX liposomes, pH responsive CET CUR-DOX liposomes, and pH responsive FOL-CET CUR-DOX liposomes at 81.49 ± 2.95, 73.74 ± 2.51, 77.22 ± 3.94 and 75.81 ± 3.16 % respectively; for DOX at 79.77 ± 1.62, 74.70 ± 2.35, 75.11 ± 2.91 and 76.89 ± 2.61 % respectively. The electron microscopy elucidated the spherical morphology of the particles, FTIR analysis corroborated the loading of CUR in the lipid bilayer and DOX in the aqueous core or the water-lipid interface, and FOL on the liposomal surface.

The stability studies established excellent stability of all the non-targeted and targeted drug loaded liposomal formulations for 3 months with 60-70 % drug retention. The formulations showed a biphasic drug release with CUR following the Gompertz drug release model and DOX the Weibull model. The cell viability assay established higher anticancer efficacy of the pH responsive FOL-CET CUR-DOX liposomes in the MDA-MB-231 than MCF-7 cells; these pH responsive liposomes were more efficacious than their non responsive counterparts. The uptake studies showed higher levels of the ligand tagged liposomes in both the MCF-7 and

MDA-MB-231 cell lines. The *in vitro* efficacy studies confirm the robust nature of the liposomes and higher anticancer efficacy.

Our study is a proof of concept and concurs with the hypothesis that the FOL-CET CUR-DOX liposomes exhibit a heightened cellular uptake and better anticancer potential than the plain drugs (CUR and DOX), with a higher activity in the MDA-MB-231 than MCF-7 cell lines. The pH responsive counterparts were more efficacious than the non responsive counterparts in the MDA-MB-231 cell line.

8.2 Future prospects

This proof of concept study highlights the anticancer efficacy of the FOL-CET CUR-DOX liposomes and their pH-responsive counterpart in the MDA-MB-231 cell lines compared to the MCF-7 cells. Building on these grounds, we propose this study's future roadmap.

- We can optimize the ratio of CUR and DOX loaded in the liposomes based on the cell viability assay to achieve drug concentrations that can further increase the anticancer efficacy of the formulations.
- We can optimize the concentration of the ligands attached to the liposomal surface based on the cellular uptake and cell viability assays. This will ensure the formulations' heightened cellular uptake and subsequent anticancer potential.
- After optimizing the drug and ligand concentrations, we can carry out other *in vitro* assays, such as receptor specific assays, determining the uptake mechanism of the liposomes, cell cycle analysis, cell apoptosis assay, etc. These assays support the efficacy of the final optimized formulation.
- After gathering evidence of the anticancer potential of these formulations, we can investigate the efficacy in the *in vivo* assays to determine the tumor inhibition, nonspecific accumulation, accumulation in the tumor, pharmacokinetics and pharmacodynamics, etc.
- We can use these formulations for precision medicine/ personalized treatment to prevent and treat cancer based on every patient's genetics and medical condition.
- We can develop vehicles for precision medicine or other pathologies using the optimized values of the process parameters and the intrinsic factors.

BIBLIOGRAPHY

Aadinath, W., Bhushani, A., Anandharamakrishnan, C., 2016. Synergistic radical scavenging potency of curcumin-in-β-cyclodextrin-in-nanomagnetoliposomes. Mater. Sci. Eng. C. 64, 293–302. https://doi.org/10.1016/j.msec.2016.03.095

Abd-Ellatef, G.E.F., Gazzano, E., Chirio, D., Hamed, A.R., Belisario, D.C., Zuddas, C., Peira, E., Rolando, B., Kopecka, J., Marie, M.A.S., Sapino, S., Fahmy, S.R., Gallarate, M., Abdel-Hamid, A.H.Z., Riganti, C., 2020. Curcumin-loaded solid lipid nanoparticles bypass p-glycoprotein mediated doxorubicin resistance in triple negative breast cancer cells. Pharm. 12, 96. https://doi.org/10.3390/pharmaceutics12020096

Al Mutairi, A.A., Mady, M.M., 2022. Biophysical Characterization of (DOX-NPTM): FTIR and DSC Studies. J. Adv. Phys. 20, 2347–3487. https://doi.org/10.24297/jap.v20i.9194

Abuhanoğlu, G., Özer, A., 2014. Radiation sterilization of new drug delivery systems. Interv. Med. Appl. Sci. 6, 51–60. https://doi.org/10.1556/imas.6.2014.2.1

Abri Aghdam, M., Bagheri, R., Mosafer, J., Baradaran, B., Hashemzaei, M., Baghbanzadeh, A., de la Guardia, M., Mokhtarzadeh, A., 2019. Recent advances on thermosensitive and pH-sensitive liposomes employed in controlled release. J. Control. Release. 315, 1–22. https://doi.org/10.1016/j.jconrel.2019.09.018

Ahmad, M.Z., Alkahtani, S.A., Akhter, S., Ahmad, F.J., Ahmad, J., Akhtar, M.S., Mohsin, N., Abdel-Wahab, B.A., 2016. Progress in nanotechnology-based drug carrier in designing of curcumin nanomedicines for cancer therapy: Current state-of-the-art. J. Drug Target. 24, 273–293. https://doi.org/10.3109/1061186x.2015.1055570

Aisha, A.F.A., Majid, A.M.S.A., Ismail, Z., 2014. Preparation and characterization of nano liposomes of Orthosiphon stamineus ethanolic extract in soybean phospholipids. BMC Biotechnol. 14, 1–11. https://doi.org/10.1186/1472-6750-14-23

Akbarzadeh, A., Rezaei-Sadabady, R., Davaran, S., Joo, S.W., Zarghami, N., Hanifehpour, Y., Samiei, M., Kouhi, M., Nejati-Koshki, K., 2013. Liposome: Classification, preparation, and applications. Nanoscale Res. Lett. 8, 1–9. https://doi.org/10.1186/1556-276x-8-102

Allen, T.M., Cullis, P.R., 2013. Liposomal drug delivery systems : From concept to clinical applications. Adv. Drug Deliv. Rev. 65, 36–48. https://doi.org/10.1016/j.addr.2012.09.037

Almgren, M., Edwards, K., Karlsson, G., 2000. Cryo transmission electron microscopy of liposomes and related structures. Colloids Surf. A Physicochem. Eng. Asp. 174, 3–21. https://doi.org/10.1016/S0927-7757(00)00516-1

Ambreen, G., Duse, L., Tariq, I., Ali, U., Ali, S., Pinnapireddy, S.R., Bette, M., Bakowsky, U., Mandic, R., 2020. Sensitivity of Papilloma Virus-Associated Cell Lines to Photodynamic Therapy with Curcumin-Loaded Liposomes. Cancers 12, 3278. https://doi.org/10.3390/cancers12113278

Andreea, G., Pegza, R., Lascu, L., Bondari, S., Stoica, Z., Bondari, A., 2011. The role of imaging techniques in diagnosis of breast cancer. Curr. Health Sci.J. 37, 55–61.

Arab-Tehrany, E., Elkhoury, K., Francius, G., Jierry, L., Mano, J.F., Kahn, C., Linder, M., 2020. Curcumin Loaded Nanoliposomes Localization by Nanoscale Characterization. Int. J. Mol. Sci. 21, 7276. https://doi.org/10.3390/ijms21197276

Assanhou, A.G., Li, W., Zhang, L., Xue, L., Kong, L., Sun, H., Mo, R., Zhang, C., 2015. Reversal of multidrug resistance by co-delivery of paclitaxel and lonidamine using a TPGS and hyaluronic acid dual-functionalized liposome for cancer treatment. Biomater. 73, 284–295. https://doi.org/10.1016/j.biomaterials.2015.09.022

Barbosa, M. V., Monteiro, L.O.F., Carneiro, G., Malagutti, A.R., Vilela, J.M.C., Andrade, M.S., Oliveira, M.C., Carvalho-Junior, A.D., Leite, E.A., 2015. Experimental design of a liposomal lipid system: A potential strategy for paclitaxel-based breast cancer treatment. Colloids Surf. B. 136, 553–561. https://doi.org/10.1016/j.colsurfb.2015.09.055

Barenholz, Y., 2001. Liposome application: problems and prospects. Curr Opin Colloid Interface Sci. 6, 66–77. https://doi.org/10.1016/S1359-0294(00)00090-X

Basakran, N.S., 2015. CD44 as a potential diagnostic tumor marker. Saudi Med. J. 36, 273–279. https://doi.org/10.15537/smj.2015.3.9622

Baselga, J., 2001. The EGFR as a target for anticancer therapy - Focus on cetuximab. Eur. J. Cancer. 37, 16–22. https://doi.org/10.1016/s0959-8049(01)00233-7

Baskararaj, S., Panneerselvam, T., Govindaraj, S., Arunachalam, S., Parasuraman, P., Pandian, S.R.K., Sankaranarayanan, M., Mohan, U.P., Palanisamy, P., Ravishankar, V., Kunjiappan, S., 2020. Formulation and characterization of folate receptor-targeted PEGylated liposome encapsulating bioactive compounds from Kappaphycus alvarezii for cancer therapy. 3 Biotech. 10, 1–18. https://doi.org/10.1007/S13205-020-2132-7/metrics

Basnet, P., Hussain, H., Tho, I., Skalko-Basnet, N., 2012. Liposomal Delivery System Enhances Anti-Inflammatory Properties of Curcumin. J. Pharm. Sci. 101, 598–609. https://doi.org/10.1002/jps.22785

Behzadi, S., Serpooshan, V., Tao, W., Hamaly, M.A., Alkawareek, M.Y., Dreaden, E.C., Brown, D., Alkilany, A.M., Farokhzad, O.C., Mahmoudi, M., 2017. Cellular uptake of nanoparticles: Journey inside the cell. Chem. Soc. Rev. 46, 4218–4244. https://doi.org/10.1039/c6cs00636a

Belfiore, L., Saunders, D.N., Ranson, M., Thurecht, K.J., Storm, G., Vine, K.L., 2018. Towards clinical translation of ligand-functionalized liposomes in targeted cancer therapy: Challenges and opportunities. J. Control. Release 277, 1–13. https://doi.org/10.1016/j.jconrel.2018.02.040

Beltrán-Gracia, E., López-Camacho, A., Higuera-Ciapara, I., Velázquez-Fernández, J.B., Vallejo-Cardona, A.A., 2019. Nanomedicine review: Clinical developments in liposomal applications. Cancer Nanotechnol. 10, 1–40. https://doi.org/10.1186/s12645-019-0055-y

Bellare, R.M.W. and J.R., 1995. Manufacture of liposomes: A review. Curr. Sci. 68, 715–724. https://doi.org/https://www.jstor.org/stable/24096654

Berger, C.M., Gaume, X., Bouvet, P., 2015. The roles of nucleolin subcellular localization in cancer. Biochimie. 113, 78–85. https://doi.org/10.1016/j.biochi.2015.03.023

Beuttler, J., Rothdiener, M., Müller, D., Frejd, F.Y., Kontermann, R.E., 2009. Targeting of epidermal growth factor receptor (EGFR)-expressing tumor cells with sterically stabilized affibody liposomes (SAL). Bioconjug. Chem. 20, 1201–1208.

https://doi.org/10.1021/bc900061v

Bhattacharyya, S., Khan, J.A., Curran, G.L., Robertson, J.D., Bhattacharya, R., Mukherjee, P., 2011. Efficient delivery of gold nanoparticles by dual receptor targeting. Adv. Mater. 23, 5034–5038. https://doi.org/10.1002/adma.201102287

Bhattacharjee, S., 2016. DLS and zeta potential – What they are and what they are not? J. Control. Release. 235, 337–351. https://doi.org/10.1016/j.jconrel.2016.06.017

Bobo, D., Robinson, K.J., Islam, J., Thurecht, K.J., Corrie, S.R., 2016. Nanoparticle-Based Medicines: A Review of FDA-Approved Materials and Clinical Trials to Date. Pharm. Res. 33, 2373–2387. https://doi.org/10.1007/s11095-016-1958-5

Bonté, F., Juliano, R.L., 1986. Interactions of liposomes with serum proteins. Chem. Phys. Lipids. 40, 359–372. https://doi.org/10.1016/0009-3084(86)90079-4

Bozzuto, G., Molinari, A., 2015. Liposomes as nanomedical devices. Int. J. Nanomedicine. 10, 975–999. https://doi.org/10.2147/ijn.S68861

Brand, F.X., Ravanel, N., Gauchez, A.S., Pasquier, D., Payan, R., Fagret, D., Mousseau, M., 2006. Prospect for anti-Her2 receptor therapy in breast cancer. Anticancer Res. 26, 463–470.

Brand, T.M., Iida, M., Wheeler, D.L., 2011. Molecular mechanisms of resistance to the EGFR monoclonal antibody cetuximab. Cancer Biol. Ther. 11, 777–792. https://doi.org/10.4161/cbt.11.9.15050

Bray, F., Ferlay, J., Soerjomataram, I., Siegel, R.L., Torre, L.A., Jemal, A., 2018. Global cancer statistics 2018: GLOBOCAN estimates of incidence and mortality worldwide for 36 cancers in 185 countries. CA. Cancer J. Clin. 68, 394–424. https://doi.org/10.3322/caac.21492

Briuglia, M., Rotella, C., 2015. Influence of cholesterol on liposome stability and on in vitro drug release. Drug Deliv. Transl. Res. 5, 231–242. https://doi.org/10.1007/s13346-015-0220-8

Brown, S., Khan, D.R., 2012. The Treatment of Breast Cancer Using Liposome Technology.

J. Drug Deliv. 2012, 212965. https://doi.org/10.1155/2012/212965

Bulbake, U., Doppalapudi, S., Kommineni, N., Khan, W., 2017. Liposomal formulations in clinical use: An updated review. Pharm. 9, 1–33. https://doi.org/10.3390/pharmaceutics9020012

Burande, A.S., Viswanadh, M.K., Jha, A., Mehata, A.K., Shaik, A., Agrawal, N., Poddar, S., Mahto, S.K., Muthu, M.S., 2020. EGFR Targeted Paclitaxel and Piperine Co-loaded Liposomes for the Treatment of Triple Negative Breast Cancer. AAPS PharmSciTech. 21, 1–12. https://doi.org/10.1208/S12249-020-01671-7

Burns, K.A., Korach, K.S., 2012. Estrogen receptors and human disease: An update. Arch. Toxicol. 86, 1491–1504. https://doi.org/10.1007/s00204-012-0868-5

Campani, V., Scotti, L., Silvestri, T., Biondi, M., De Rosa, G., 2020. Skin permeation and thermodynamic features of curcumin-loaded liposomes. J. Mater. Sci. Mater. Med. 31, 1–8. https://doi.org/10.1007/S10856-019-6351-6

Cai, D., Gao, W., He, B., Dai, W., Zhang, H., Wang, X., Wang, J., Zhang, X., Zhang, Q., 2014. Hydrophobic penetrating peptide PFVYLI-modified stealth liposomes for doxorubicin delivery in breast cancer therapy. Biomater. 35, 2283–2294. https://doi.org/10.1016/j.biomaterials.2013.11.088

Cao, J., Wang, R., Gao, N., Li, M., Tian, X., Yang, W., Ruan, Y., Zhou, C., Wang, G., Liu, X., Tang, S., Yu, Y., Liu, Y., Sun, G., Peng, H., Wang, Q., 2015. A7RC peptide modified paclitaxel liposomes dually target breast cancer. Biomater. Sci. 3, 1545–1554. https://doi.org/10.1039/c5bm00161g

Cardoso, F., Kyriakides, S., Ohno, S., Penault-Llorca, F., Poortmans, P., Rubio, I.T., Zackrisson, S., Senkus, E., 2019. Early breast cancer: ESMO Clinical Practice Guidelines for diagnosis, treatment and follow-up. Ann. Oncol. 30, 1194–1220. https://doi.org/10.1093/annonc/mdz173

Cella, D., Peterman, A., Hudgens, S., Webster, K., Socinski, M.A., 2003. Measuring the side effects of taxane therapy in oncology: The Functional Assessment of Cancer Therapy–taxane (FACT-taxane). Cancer. 98, 822–831. https://doi.org/10.1002/cncr.11578

Chang, H.-I., Cheng, M.-Y., Yeh, and M.-K., 2012. Clinically-Proven Liposome-Based Drug Delivery: Formulation, Characterization and Therapeutic Efficacy. Open Access Sci. Reports 1, 1–8. https://doi.org/10.4172/scientificreports.559

Chang, H.I., Yeh, M.K., 2012. Clinical development of liposome-based drugs: Formulation, characterization, and therapeutic efficacy. Int. J. Nanomedicine. 7, 49–60. https://doi.org/10.2147/ijn.S26766

Chaves, M.A., Oseliero Filho, P.L., Jange, C.G., Sinigaglia-Coimbra, R., Oliveira, C.L.P., Pinho, S.C., 2018. Structural characterization of multilamellar liposomes coencapsulating curcumin and vitamin D3. Colloids Surf. A Physicochem. Eng. Asp. 549, 112–121. https://doi.org/10.1016/l.jcolsurfa.2018.04.018

Chen, H., Wu, J., Sun, M., Guo, C., Yu, A., Cao, F., Zhao, L., Tan, Q., Zhai, G., 2012. N-trimethyl chitosan chloride-coated liposomes for the oral delivery of curcumin. J. Liposome Res. 22, 100–109. https://doi.org/10.3109/08982104.2011.621127

Chen, X., Zou, L.Q., Niu, J., Liu, W., Peng, S.F., Liu, C.M., 2015. The Stability, Sustained Release and Cellular Antioxidant Activity of Curcumin Nanoliposomes. Mol. 20, 14293–14311. https://doi.org/10.3390/molecules200814293

Chang, H.-I., Cheng, M.-Y., Yeh, and M.-K., 2012. Clinically-Proven Liposome-Based Drug Delivery: Formulation, Characterization and Therapeutic Efficacy. Open Access Sci. Reports 1, 1–8. https://doi.org/10.4172/scientificreports.559

Chang, M., Lu, S., Zhang, F., Zuo, T., Guan, Y., Wei, T., Shao, W., Lin, G., 2015. RGD-modified pH-sensitive liposomes for docetaxel tumor targeting. Colloids Surf. B. 129, 175–182. https://doi.org/10.1016/j.colsurfb.2015.03.046

Chen, Y., Wu, Q., Zhang, Z., Yuan, L., Liu, X., Zhou, L., 2012. Preparation of Curcumin-Loaded Liposomes and Evaluation of Their Skin Permeation and Pharmacodynamics. Mol. 17, 5972–5987. https://doi.org/10.3390/molecules17055972

Chen, C., Ke, J., Edward Zhou, X., Yi, W., Brunzelle, J.S., Li, J., Yong, E.L., Xu, H.E., Melcher, K., 2013. Structural basis for molecular recognition of folic acid by folate receptors. Nat. 500, 486–489. https://doi.org/10.1038/nature12327

Chen, H., Ahn, R., Van Den Bossche, J., Thompson, D.H., O'Halloran, T. V., 2009. Folate-mediated intracellular drug delivery increases the anticancer efficacy of nanoparticulate formulation of arsenic trioxide. Mol. Cancer Ther. 8, 1955–1963. https://doi.org/10.1158/1535-7163.MCT-09-0045

Chen, H., Liu, L., Ma, A., Yin, T., Chen, Z., Liang, R., Qiu, Y., Zheng, M., Cai, L., 2021. Noninvasively immunogenic sonodynamic therapy with manganese protoporphyrin liposomes against triple-negative breast cancer. Biomater. 269, 120639. https://doi.org/10.1016/j.biomaterials.2020.120639

Chen, Y., Cheng, Y., Zhao, P., Zhang, S., Li, M., He, C., Zhang, X., Yang, T., Yan, R., Ye, P., Ma, X., Xiang, G., 2018. Co-delivery of doxorubicin and imatinib by pH sensitive cleavable PEGylated nanoliposomes with folate-mediated targeting to overcome multidrug resistance. Int. J. Pharm. 542, 266–279. https://doi.org/10.1016/j.ijpharm.2018.03.024

Chen, Z., Xu, X.H., 2016. Roles of nucleolin: Focus on cancer and anti-cancer therapy. Saudi Med. J. 37, 1312–1318. https://doi.org/10.15537/smj.2016.12.15972

Chen, L., Alrbyawi, H., Poudel, I., Arnold, R.D., Babu, R.J., 2019. Co-delivery of Doxorubicin and Ceramide in a Liposomal Formulation Enhances Cytotoxicity in Murine B16BL6 Melanoma Cell Lines. AAPS PharmSciTech. 20, 1–10. https://doi.org/10.1208/S12249-019-1316-0

Chen, X., Zou, L.Q., Niu, J., Liu, W., Peng, S.F., Liu, C.M., 2015. The Stability, Sustained Release and Cellular Antioxidant Activity of Curcumin Nanoliposomes. Mol. 20, 14293–14311. https://doi.org/10.3390/molecules200814293

Cheng, C., Wu, Z., McClements, D.J., Zou, L., Peng, S., Zhou, W., Liu, W., 2019. Improvement on stability, loading capacity and sustained release of rhamnolipids modified curcumin liposomes. Colloids Surf. B. 183, 110460. https://doi.org/10.1016/j.colsurfb.2019.110460

Chiani, M., Norouzian, D., Shokrgozar, M.A., Azadmanesh, K., Najmafshar, A., Mehrabi, M.R., Akbarzadeh, A., 2018. Folic acid conjugated nanoliposomes as promising carriers for targeted delivery of bleomycin. Artif. Cells, Nanomed. Biotechnol. 46, 757–763.

https://doi.org/10.1080/21691401.2017.1337029

Cho, K., Wang, X., Nie, S., Chen, Z., Shin, D.M., 2008. Therapeutic Nanoparticles for Drug Delivery in Cancer. Clin. Cancer Res. 14, 1310–1316. https://doi.org/10.1158/1078-0432.CCR-07-1441

Choi, J.Y., Thapa, R.K., Yong, C.S., Kim, J.O., 2016. Nanoparticle-based combination drug delivery systems for synergistic cancer treatment. J. Pharm. Investig. 46, 325–339. https://doi.org/10.1007/s40005-016-0252-1

Choudhary, V., Shivakumar, H., Ojha, H., 2019. Curcumin-loaded liposomes for wound healing: Preparation, optimization, in-vivo skin permeation and bioevaluation. J. Drug Deliv. Sci. Technol. 49, 683–691. https://doi.org/10.1016/j.jddst.2018.12.008

Chu, C.J., Dijkstra, J., Lai, M.Z., Hong, K., Szoka, F.C., 1990. Efficiency of Cytoplasmic Delivery by pH-Sensitive Liposomes to Cells in Culture. Pharm. Res. An Off. J. Am. Assoc. Pharm. Sci. 7, 824–834. https://doi.org/10.1023/A:1015908831507

Collins, D., Litzinger, D.C., Huang, L., 1990. Structural and functional comparisons of pH-sensitive liposomes composed of phosphatidylethanolamine and three different diacylsuccinylglycerols. BBA - Biomembr. 1025, 234–242. https://doi.org/10.1016/0005-2736(90)90102-T

Comşa, Ş., Cîmpean, A.M., Raica, M., 2015. The story of MCF-7 breast cancer cell line: 40 Years of experience in research. Anticancer Res. 35, 3147–3154.

Cotlar, A.M., Dubose, J.J., Rose, D.M., 2003. History of surgery for breast cancer: radical to the sublime. Curr. Surg. 60, 329–337. https://doi.org/10.1016/S0149-7944(02)00777-8

Cui, T., Sihao, Z., Sun, H., 2017. Co-delivery of doxorubicin and pH-sensitive curcumin prodrug by transferrin-targeted nanoparticles for breast cancer treatment. Oncol. Rep. 37, 1253–1260. https://doi.org/10.3892/or.2017.5345

Danaei, M., Dehghankhold, M., Ataei, S., Hasanzadeh Davarani, F., Javanmard, R., Dokhani, A., Khorasani, S., Mozafari, M.R., 2018. Impact of Particle Size and Polydispersity Index on the Clinical Applications of Lipidic Nanocarrier Systems. Pharm. 10, 57.

https://doi.org/10.3390/pharmaceutics10020057

Dang, Y., Guan, J., 2020. Nanoparticle-based drug delivery systems for cancer therapy. Smart Mater. Med. 1, 10–19. https://doi.org/10.1016/j.smaim.2020.04.001

Daraee, H., Etemadi, A., Kouhi, M., Alimirzalu, S., Akbarzadeh, A., 2016. Application of liposomes in medicine and drug delivery. Artif. Cells, Nanomed. Biotechnol. 44, 381–391. https://doi.org/10.3109/21691401.2014.953633

Dash, S., Murthy, P.N., Nath, L., Chowdhury, P., 2010. Kinetic modeling on drug release from controlled drug delivery systems. Acta Pol. Pharm. - Drug Res. 67, 217–223.

David Mankoff, J.C., 2016. Clinical and Translational Molecular Imaging of Breast Cancer. J. Nucl. Med. 57, 9-16.https://doi.org/10.2967/jnumed.115.157834

Deen, C., Claassen, E., Gerritse, K., Zegers, N.D., Boersma, W.J.A., 1990. A novel carbodiimide coupling method for synthetic peptides. Enhanced anti-peptide antibody responses. J. Immunol. Methods. 129, 119–125. https://doi.org/10.1016/0022-1759(90)90428-x

De Laurentiis, M., Cianniello, D., Caputo, R., Stanzione, B., Arpino, G., Cinieri, S., Lorusso, V., De Placido, S., 2010. Treatment of triple negative breast cancer (TNBC): Current options and future perspectives. Cancer Treat. Rev. 36, S80–S86. https://doi.org/10.1016/s0305-7372(10)70025-6

De Oliveira Silva, J., Fernandes, R.S., Ramos Oda, C.M., Ferreira, T.H., Machado Botelho, A.F., Martins Melo, M., de Miranda, M.C., Assis Gomes, D., Dantas Cassali, G., Townsend, D.M., Rubello, D., Oliveira, M.C., de Barros, A.L.B., 2019. Folate-coated, long-circulating and pH-sensitive liposomes enhance doxorubicin antitumor effect in a breast cancer animal model. Biomed. Pharmacother. 118, 109323. https://doi.org/10.1016/j.biopha.2019.109323

Delma, K.L., Lechanteur, A., Evrard, B., Semdé, R., Piel, G., 2021. Sterilization methods of liposomes: Drawbacks of conventional methods and perspectives. Int. J. Pharm. 597, 120271. https://doi.org/10.1016/j.ijpharm.2021.120271

Deng, C., Zhang, Quan, Jia, Mengdi, Zhao, Jin, Sun, Xun, Gong, Tao, Zhang Deng, Z.C., Jia, M, Zhao, J, Sun, X, Gong, T, Zhang, Z., Zhang, Q, 2019. Tumors and Their Microenvironment Dual-Targeting Chemotherapy with Local Immune Adjuvant Therapy for Effective Antitumor Immunity against Breast Cancer. Adv. Sci. 6, 1801868. https://doi.org/10.1002/advs.201801868

Dewhirst, M.W., Secomb, T.W., 2017. Transport of drugs from blood vessels to tumour tissue. Nat. Rev. Cancer 17, 738–750. https://doi.org/10.1038/nrc.2017.93

Deygen, I.M., Seidl, C., Kölmel, D.K., Bednarek, C., Heissler, S., Kudryashova, E. V., Bräse, S., Schepers, U., 2016. Novel Prodrug of Doxorubicin Modified by Stearoylspermine Encapsulated into PEG-Chitosan-Stabilized Liposomes. Langmuir. 32, 10861–10869. https://doi.org/10.1021/acs.langmuir.6b01023

Dhule, S.S., Penfornis, P., He, J., Harris, M.R., Terry, T., John, V., Pochampally, R., 2014. The combined effect of encapsulating curcumin and C6 ceramide in liposomal nanoparticles against osteosarcoma. Mol. Pharm. 11, 417–427. https://doi.org/10.1021/mp400366r

Ding, T., Li, T., Wang, Z., Li, J., 2017. Curcumin liposomes interfere with quorum sensing system of Aeromonas sobria and in silico analysis. Sci. Reports. 7, 1–16. https://doi.org/10.1038/s41598-017-08986-9

Doello, K., Ortiz, R., Alvarez, P.J., Melguizo, C., Cabeza, L, Prados, J., 2018. Latest in Vitro and in Vivo Assay, Clinical Trials and Patents in Cancer Treatment using Curcumin: A Literature Review. Nutr. Cancer. 70, 569–578. https://doi.org/10.1080/01635581.2018.1464347

Dorjsuren, B., Chaurasiya, B., Ye, Z., Liu, Y., Li, W., Wang, C., Shi, D., Evans, C.E., Webster, T.J., Shen, Y., 2020. Cetuximab-Coated Thermo-Sensitive Liposomes Loaded with Magnetic Nanoparticles and Doxorubicin for Targeted EGFR-Expressing Breast Cancer Combined Therapy. Int. J. Nanomedicine. 15, 8201. https://doi.org/10.2147/ijn.s261671

Dou, Y., Hynynen, K., Allen, C., 2017. To heat or not to heat: Challenges with clinical translation of thermosensitive liposomes. J. Control. Release. 249, 63–73. https://doi.org/10.1016/j.jconrel.2017.01.025

Drescher, S., van Hoogevest, P., 2020. The Phospholipid Research Center: Current Research in Phospholipids and Their Use in Drug Delivery. Pharm. 12, 1235. https://doi.org/10.3390/pharmaceutics12121235

Drugs Approved for Breast Cancer - NCI; https://www.cancer.gov/about-cancer/treatment/drugs/breast

Dua, J.S., Rana, A.C., Bhandari, A.K., 2012. Liposome: methods of preparation and applications. Int. J. Pharm. Stud. Res. 3, 14–20. https://doi.org/https://doi.org/10.3390/ijms19010195

Duan, J., Mansour, H.M., Zhang, Y., Deng, X., Chen, Y., Wang, J., Pan, Y., Zhao, J., 2012. Reversion of multidrug resistance by co-encapsulation of doxorubicin and curcumin in chitosan/poly(butyl cyanoacrylate) nanoparticles. Int. J. Pharm. 426, 193–201. https://doi.org/10.1016/j.ijpharm.2012.01.020

Dumitrescu, R.G., Shields, P.G., 2005. The etiology of alcohol-induced breast cancer. Alcohol. 35, 213–225. https://doi.org/10.1016/j.alcohol.2005.04.005

Düzgüneş, N., Nir, S., 1999. Mechanisms and kinetics of liposome-cell interactions. Adv. Drug Deliv. Rev. 40, 3–18. https://doi.org/10.1016/S0169-409x(99)00037-x

Ellis, H., Mahadevan, V., 2013. Anatomy and physiology of the breast. Surg. (United Kingdom) 31, 11–14. https://doi.org/10.1016/j.mpsur.2012.10.018

Elmore, J.G., Armstrong, K., Lehman, C.D., Fletcher, S.W., 2005. Screening for Breast Cancer. JAMA. 293, 1245–1256. https://doi.org/10.1001/jama.293.10.1245

Eloy, J.O., Petrilli, R., Trevizan, L.N.F., Chorilli, M., 2017. Immunoliposomes: A review on functionalization strategies and targets for drug delivery. Colloids Surf. B. 159, 454–467. https://doi.org/10.1016/j.colsurfb.2017.07.085

Fahmy, H.M., 2019. In vitro study of the cytotoxicity of thymoquinone/curcumin fluorescent liposomes. Naunyn. Schmiedebergs. Arch. Pharmacol. 392, 1465–1476. https://doi.org/10.1007/s00210-019-01688-1

Fan, Y., Zhang, Q., 2013. Development of liposomal formulations: From concept to clinical

investigations. Asian J. Pharm. Sci. 8, 81–87. https://doi.org/10.1016/j.ajps.2013.07.010

Feinleib, M., 1968. Breast cancer and artificial menopause: A cohort study. J. Natl. Cancer Inst. 41, 315–329. https://doi.org/10.1093/jnci/41.2.315

Feng, T., Wei, Y., Lee, R.J., Zhao, L., 2017. Liposomal curcumin and its application in cancer. Int. J. Nanomedicine. 12, 6027–6044. https://doi.org/10.2147/ijn.S132434

Feng, Y., Spezia, M., Huang, S., Yuan, C., Zeng, Z., Zhang, L., Ji, X., Liu, W., Huang, B., Luo, W., Liu, B., Lei, Y., Du, S., Vuppalapati, A., Luu, H.H., Haydon, R.C., He, T.C., Ren, G., 2018. Breast cancer development and progression: Risk factors, cancer stem cells, signaling pathways, genomics, and molecular pathogenesis. Genes Dis. 5, 77–106. https://doi.org/10.1016/j.gendis.2018.05.001

Fernandez-Garcia, B., Eiró, N., Marín, L., González-Reyes, S., González, L.O., Lamelas, M.L., Vizoso, F.J., 2014. Expression and prognostic significance of fibronectin and matrix metalloproteases in breast cancer metastasis. Histopathol. 64, 512–522. https://doi.org/10.1111/his.12300

Ferreira, D.D.S., Lopes, S.C.D.A., Franco, M.S., Oliveira, M.C., 2013. pH-sensitive liposomes for drug delivery in cancer treatment. Ther. Deliv. 4, 1099–1123. https://doi.org/10.4155/tde.13.80

Fujiki, H., Watanabe, T., Suganuma, M., 2014. Cell-surface nucleolin acts as a central mediator for carcinogenic, anti-carcinogenic, and disease-related ligands. J. Cancer Res. Clin. Oncol. 140, 689–699. https://doi.org/10.1007/s00432-014-1587-5

Fujiwara, A., Hoshino, T., Westley, J.W., 1985. Anthracycline Antibiotics. Crit. Rev. Biotechnol. 3, 133–157. https://doi.org/10.3109/07388558509150782

Fulfager, A.D., Yadav, K.S., 2021. Understanding the implications of co-delivering therapeutic agents in a nanocarrier to combat multidrug resistance (MDR) in breast cancer. J. Drug Deliv. Sci. Technol. 62, 102405. https://doi.org/10.1016/j.jddst.2021.102405

Gabizon, A., Martin, F., 1997. Polyethylene glycol-coated (pegylated) liposomal doxorubicin. Rationale for use in solid tumours. Drugs. 54, 15–21. https://doi.org/10.2165/00003495-

199700544-00005

Gandhi, R., Khatri, N., Baradia, D., Vhora, I., Misra, A., 2016. Surface-modified Epirubicin-HCl liposomes and its in vitro assessment in breast cancer cell-line: MCF-7. Drug Deliv. 23, 1152–1162. https://doi.org/10.3109/10717544.2014.999960

Gao, J., Liu, W., Xia, Y., Li, W., Sun, J., Chen, H., Li, B., Zhang, D., Qian, W., Meng, Y., Deng, L., Wang, H., Chen, J., Guo, Y., 2011. The promotion of siRNA delivery to breast cancer overexpressing epidermal growth factor receptor through anti-EGFR antibody conjugation by immunoliposomes. Biomater. 32, 3459–3470. https://doi.org/10.1016/j.biomaterials.2011.01.034

Garg, T., AK Goyal, 2014. Liposomes: targeted and controlled delivery system. Drug Deliv. Lett. 4, 62–71.

Gazzano, E., Rolando, B., Chegaev, K., Salaroglio, I.C., Kopecka, J., Pedrini, I., Saponara, S., Sorge, M., Buondonno, I., Stella, B., Marengo, A., Valoti, M., Brancaccio, M., Fruttero, R., Gasco, A., Arpicco, S., Riganti, C., 2018. Folate-targeted liposomal nitrooxy-doxorubicin: An effective tool against P-glycoprotein-positive and folate receptor-positive tumors. J. Control. Release. 270, 37–52. https://doi.org/10.1016/j.jconrel.2017.11.042

Geddes, D.T., 2007. Inside the Lactating Breast: The Latest Anatomy Research. J. Midwifery Women's Heal. 52, 556–563. https://doi.org/10.1016/j.jmwh.2007.05.004

Gerber, D.E., Choy, H., 2010. Cetuximab in combination therapy: From bench to clinic. Cancer Metastasis Rev. 29, 171–180. https://doi.org/10.1007/s10555-010-9215-6

Ghatage, T., Jadhav, S., Kore, V., 2017. A Review on Stealth Liposomes: Novel Drug Delivery System. Int. J. Sci. Eng. Technol. Res. 6, 2744–2750

Ghoncheh, M., Pournamdar, Z., Salehiniya, H., 2016. Incidence and mortality and epidemiology of breast cancer in the world. Asian Pacific J. Cancer Prev. 17, 43–46. https://doi.org/10.7314/apjcp.2016.17.S3.43

Ghosh, S., Lalani, R., Maiti, K., Banerjee, S., Patel, V., Bhowmick, S., Misra, A., 2020.

Optimization and efficacy study of synergistic vincristine coloaded liposomal doxorubicin against breast and lung cancer. Futur. Med. 15, 2585–2607. https://doi.org/10.2217/nnm-2020-0169

Ong, S.G.M., Chitneni, M., Lee, K.S., Ming, L.C., Yuen, K.H., 2016. Evaluation of Extrusion Technique for Nanosizing Liposomes. Pharm. 8, 36. https://doi.org/10.3390/pharmaceutics8040036

Glick, S.J., 2007. Breast CT. Annu. Rev. Biomed. Eng. 9, 501–526. https://doi.org/10.1146/annurev.bioeng.9.060906.151924

Gómez-Mascaraque, L.G., Casagrande Sipoli, C., de La Torre, L.G., López-Rubio, A., 2017. Microencapsulation structures based on protein-coated liposomes obtained through electrospraying for the stabilization and improved bioaccessibility of curcumin. Food Chem. 233, 343–350. https://doi.org/10.1016/j.foodchem.2017.04.133

Gradishar, W.J., Anderson, B.O., Balassanian, R., Blair, S.L., Burstein, H.J., Cyr, A., Elias, A.D., Farrar, W.B., Forero, A., Giordano, S.H., Goetz, M.P., Goldstein, L.J., Isakoff, S.J., Lyons, J., Kelly Marcom, P., Mayer, I.A., McCormick, B., Moran, M.S., O'Regan, R.M., Patel, S.A., Pierce, L.J., Reed, E.C., Salerno, K.E., Schwartzberg, L.S., Sitapati, A., Smith, K.L., Smith, M. Lou, Soliman, H., Somlo, G., Telli, M.L., Ward, J.H., Kumar, R., Shead, D.A., 2018. Clinical practice guidelines in oncology. JNCCN J. Natl. Compr. Cancer Netw. 16, 310–320. https://doi.org/10.6004/jnccn.2018.0012

Gregoriadis, G., 1991. Overview of liposomes. J. Antimicrob. Chemother. 28, 39–48. https://doi.org/10.1093/jac/28

Gregoriadis, G., Florence, A.T., 1993. Liposomes in Drug Delivery: Clinical, Diagnostic and Ophthalmic Potential. Drugs. 45, 15–28. https://doi.org/10.2165/00003495-199345010-00003

Gregoriadis, G., Perrie, Y., 2010. Liposomes. eLS. https://doi.org/10.1002/9780470015902.A0002656.pub2

Gubernator, J., 2011. Active methods of drug loading into liposomes: Recent strategies for stable drug entrapment and increased in vivo activity. Expert Opin. Drug Deliv. 8, 565–

580. https://doi.org/10.1517/17425247.2011.566552

Gucalp, A., Traina, T.A., Eisner, J.R., Parker, J.S., Selitsky, S.R., Park, B.H., Elias, A.D., Baskin-Bey, E.S., Cardoso, F., 2019. Male breast cancer: a disease distinct from female breast cancer. Breast Cancer Res. Treat. 173, 37–48. https://doi.org/10.1007/s10549-018-4921-9

Guimaraes, D., Cavaco-paulo, A., Nogueira, E., 2021. Design of liposomes as drug delivery system for therapeutic applications. Int. J. Pharm. 601, 120571. https://doi.org/10.1016/j.ijpharm.2021.120571

Guo, P., Yang, J., Jia, D., Moses, M.A., Auguste, D.T., 2016. ICAM-1-targeted, Lcn2 siRNA-encapsulating liposomes are potent anti-angiogenic agents for triple negative breast cancer. Theranostics. 6, 1–13. https://doi.org/10.7150/thno.12167

Guo, P., Yang, J., Liu, D., Huang, L., Fell, G., Huang, J., Moses, M.A., Auguste, D.T., 2019. Dual complementary liposomes inhibit triple-negative breast tumor progression and metastasis. Sci. Adv. 5, 1–15. https://doi.org/10.1126/sciadv.aav5010

Guo, P., You, J.O., Yang, J., Moses, M.A., Auguste, D.T., 2012. Using breast cancer cell CXCR4 surface expression to predict liposome binding and cytotoxicity. Biomater. 33, 8104–8110. https://doi.org/10.1016/j.biomaterials.2012.07.043

Guo, Q., Li, X., Yang, Y., Wei, J., Zhao, Q., Luo, F., Qian, Z., 2014. Enhanced 4T1 breast carcinoma anticancer activity by co-delivery of doxorubicin and curcumin with core-shell drug-carrier based on heparin modified poly(l-lactide) grafted polyethylenimine cationic nanoparticles. J. Biomed. Nanotechnol. 10, 227–237. https://doi.org/10.1166/jbn.2014.1785

Guo, Z., He, B., Yuan, L., Dai, W., Zhang, H., Wang, X., Wang, J., Zhang, X., Zhang, Q., 2015. Dual targeting for metastatic breast cancer and tumor neovasculature by EphA2-mediated nanocarriers. Int. J. Pharm. 493, 380–389. https://doi.org/10.1016/j.ijpharm.2015.05.051

Haeri, A., Zalba, S., ten Hagen, T.L.M., Dadashzadeh, S., Koning, G.A., 2016. EGFR targeted thermosensitive liposomes: A novel multifunctional platform for simultaneous tumor

targeted and stimulus responsive drug delivery. Colloids Surf. B. 146, 657–669. https://doi.org/10.1016/j.colsurfb.2016.06.012

Haghiralsadat, F., Amoabediny, G., Helder, M.N., Naderinezhad, S., Sheikhha, M.H., Forouzanfar, T., Zandieh-doulabi, B., 2017. A comprehensive mathematical model of drug release kinetics from nano-liposomes, derived from optimization studies of cationic PEGylated liposomal doxorubicin formulations for drug-gene delivery. Artif. Cells Nanomed Biotechnol. 46, 169- 177.https://doi.org/10.1080/21691401.2017.1304403

Haghiralsadat, F., Amoabediny, G., Sheikhha, M.H., Forouzanfar, T., Arough, J.M., Helder, M.N., Zandieh-Doulabi, B., 2017. A Novel Approach on Drug Delivery:Investigation of A New Nano-Formulation of LiposomalDoxorubicin and Biological Evaluation of EntrappedDoxorubicin on Various Osteosarcoma Cell Lines. Cell J. 19, 65. https://doi.org/10.22074/cellj.2017.4502

Haghiralsadat, F., Amoabediny, G., Sheikhha, M.H., Zandieh-doulabi, B., Naderinezhad, S., Helder, M.N., Forouzanfar, T., 2017. New liposomal doxorubicin nanoformulation for osteosarcoma: Drug release kinetic study based on thermo and pH sensitivity. Chem. Biol. Drug Des. 90, 368–379. https://doi.org/10.1111/cbdd.12953

Hai, L., He, D., He, X., Wang, K., Yang, X., Liu, J., Cheng, H., Huang, X., Shangguan, J., 2017. Facile fabrication of a resveratrol loaded phospholipid@reduced graphene oxide nanoassembly for targeted and near-infrared laser-triggered chemo/photothermal synergistic therapy of cancer in vivo. J. Mater. Chem. B. 5, 5783–5792. https://doi.org/10.1039/c7tb01600j

Hait, W.N., Yang, J.-M., 2005. Clinical Management of Recurrent Breast Cancer: Development of Multidrug Resistance (MDR) and Strategies to Circumvent it. Semin. Oncol. 32, 16–21. https://doi.org/10.1053/j.seminoncol.2005.09.011

Halka, B., Stark, A., 1995. Breast cancer: cause and prevention. Lancet. 346, 883–887. https://doi.org/10.1016/S0140-6736(95)92713-1

Hamano, N., Böttger, R., Lee, S.E., Yang, Y., Kulkarni, J.A., Ip, S., Cullis, P.R., Li, S.D., 2019. Robust microfluidic technology and new lipid composition for fabrication of curcumin-loaded liposomes: effect on the anticancer activity and safety of cisplatin. Mol. Pharm.

16, 3957–3967. https://doi.org/10.1021/acs.molpharmaceut.9b00583

Harbeck, N., Penault-Llorca, F., Cortes, J., Gnant, M., Houssami, N., Poortmans, P., Ruddy, K., Tsang, J., Cardoso, F., 2019. Breast cancer. Nat. Rev. Dis. Prim. 5. https://doi.org/10.1038/s41572-019-0111-2

Hardiansyah, A., Yang, M.C., Liu, T.Y., Kuo, C.Y., Huang, L.Y., Chan, T.Y., 2017. Hydrophobic Drug-Loaded PEGylated Magnetic Liposomes for Drug-Controlled Release. Nanoscale Res. Lett. 12, 1–11. https://doi.org/10.1186/S11671-017-2119-4

Hare, J.I., Lammers, T., Ashford, M.B., Puri, S., Storm, G., Barry, S.T., 2017. Challenges and strategies in anti-cancer nanomedicine development: An industry perspective. Adv. Drug Deliv. Rev. 108, 25–38. https://doi.org/10.1016/j.addr.2016.04.025

Harini, L., Srivastava, S., Gnanakumar, G.P., Karthikeyan, B., Ross, C., Krishnakumar, V., Kannan, V.R., Sundar, K., Kathiresan, T., 2019. An ingenious non-spherical mesoporous silica nanoparticle cargo with curcumin induces mitochondria-mediated apoptosis in breast cancer (MCF-7) cells. Oncotarget. 10, 1193–1208. https://doi.org/10.18632/oncotarget.26623

Harrington, K.J., Syrigos, K.N., Vile, R.G., 2002. Liposomally targeted cytotoxic drugs for the treatment of cancer. J. Pharm. Pharmacol. 54, 1573–1600. https://doi.org/10.1211/0022357002243

Harris, A.L., Nicholson, S., Richard, J., Sainsbury, C., Farndon, J., Wright, C., 1989. Epidermal growth factor receptors in breast cancer: Association with early relapse and death, poor response to hormones and interactions with neu. J. Steroid Biochem. 34, 123–131. https://doi.org/10.1016/0022-4731(89)90072-1

Hartmann, L.C., Keeney, G.L., Lingle, W.L., Christianson, T.J.H., Varghese, B., Hillman, D., Oberg, A.L., Low, P.S., 2007. Folate receptor overexpression is associated with poor outcome in breast cancer. Int. J. Cancer. 121, 938–942. https://doi.org/10.1002/ijc.22811

Hasan, M., Belhaj, N., Benachour, H., Barberi-Heyob, M., Kahn, C.J.F., Jabbari, E., Linder, M., Arab-Tehrany, E., 2014. Liposome encapsulation of curcumin: Physico-chemical characterizations and effects on MCF7 cancer cell proliferation. Int. J. Pharm. 461, 519–

528. https://doi.org/10.1016/j.ijpharm.2013.12.007

Hasan, M., Ben Messaoud, G., Michaux, F., Tamayol, A., Kahn, C.J.F., Belhaj, N., Linder, M., and Arab-Tehrany, E., 2016. Chitosan-coated liposomes encapsulating curcumin: Study of lipid-polysaccharide interactions and nanovesicle behavior. RSC Adv. 6, 45290–45304. https://doi.org/10.1039/c6ra05574e

He, L., Gu, J., Lim, L.Y., Yuan, Z.X., Mo, J., 2016. Nanomedicine-mediated therapies to target breast cancer stem cells. Front. Pharmacol. 7, 221834. https://doi.org/10.3389/fphar.2016.00313/bibtex

He, Y.Y., Wang, X.C., Jin, P.K., Zhao, B., and Fan, X., 2009. Complexation of anthracene with folic acid studied by FTIR and UV spectroscopies. Spectrochimica Acta A Mol Biomol Spectrosc. 72, 876–879. https://doi.org/10.1016/j.saa.2008.12.021

Heredia, N.S., Vizuete, K., Flores-Calero, M., Katherine Pazmiño, V., Pilaquinga, F., Kumar, B., Debut, A., 2022. Comparative statistical analysis of the release kinetics models for nanoprecipitated drug delivery systems based on poly(lactic-co-glycolic acid). PLoS One. 17, 1–28. https://doi.org/10.1371/journal.pone.0264825

Honary, S., Zahir, F., 2013. Effect of Zeta Potential on the Properties of Nano-Drug Delivery Systems - A Review (Part 2). Trop. J. Pharm. Res. 12, 265–273. https://doi.org/10.4314/tjpr.v12i2.20

Hong, S.C., Park, K.M., Hong, C.R., Kim, J.C., Yang, S.H., Yu, H.S., Paik, H.D., Pan, C.H., Chang, P.S., 2020. Microfluidic assembly of liposomes dual-loaded with catechin and curcumin for enhancing bioavailability. Colloids Surf. A Physicochem. Eng. Asp. 594, 124670. https://doi.org/10.1016/j.colsurfa.2020.124670

Hortobágyi, G.N., 1997. Anthracyclines in the treatment of cancer. An overview. Drugs. 54, 1–7. https://doi.org/10.2165/00003495-199700544-00003

Hsu, J.L., Hung, M.C., 2016. The role of HER2, EGFR, and other receptor tyrosine kinases in breast cancer. Cancer Metastasis Rev. 35, 575–588. https://doi.org/10.1007/s10555-016-9649-6

Huang, M., Liang, C., Tan, C., Huang, S., Ying, R., Wang, Y., Wang, Z., and Zhang, Y., 2019. Liposome co-encapsulation as a strategy for the delivery of curcumin and resveratrol. Food Funct. 10 (10), 6447–6458. https://doi.org/10.1039/c9fo01338e

Huang, B., Warner, M., Gustafsson, J.Å., 2015. Estrogen receptors in breast carcinogenesis and endocrine therapy. Mol. Cell. Endocrinol. 418, 240–244. https://doi.org/10.1016/j.mce.2014.11.015

Huang, Z., Yu, P., Tang, J., 2020. Characterization of triple-negative breast cancer MDA-MB-231 cell spheroid model. Onco. Targets. Ther. 13, 5395–5405. https://doi.org/10.2147/ott.s249756

Hudiyanti, D., Al Khafiz, M.F., Anam, K., Siahaan, P., and Suyati, L., 2021. Assessing encapsulation of curcumin in cocoliposome: In vitro study. Open Chem. 19, 358–366. https://doi.org/10.1515/chem-2021-0036

Hunter, D.J., Sc, D., 2018. Oral Contraceptives and the Small Increased Risk of Breast Cancer.NEJM. 2276–2277. https://doi.org/10.1056/nejme1709636

Iacoviello, L., Bonaccio, M., Gaetano, G. De, Donati, M.B., 2020. Epidemiology of breast cancer, a paradigm of the ¨common soil ¨hypothesis. Semin. Cancer Biol. 72, 4–10. https://doi.org/10.1016/j.semcancer.2020.02.010

Inglut, C.T., Sorrin, A.J., Kuruppu, T., Vig, S., Cicalo, J., Ahmad, H., Huang, H.C., 2020. Immunological and Toxicological Considerations for the Design of Liposomes. Nanomater. 10, 190. https://doi.org/10.3390/nano10020190

International Agency for Research on Cancer, 2020. Time Trend in Breast and Cervix Cancer of Women in India.Globocan 361, 2

International agency for research on cancer, W. health organization, 2021. Breast cancer overtakes lung cancer as leading cause of cancer worldwide. IARC showcases key research projects to address breast cancer. Press release.https://gco.iarc.fr/today

Isacchi, B., Bergonzi, M.C., Grazioso, M., Righeschi, C., Pietretti, A., Severini, C., and Bilia, A.R., 2012. Artemisinin and artemisinin plus curcumin liposomal formulations: Enhanced

antimalarial efficacy against Plasmodium berghei-infected mice. Eur J Pharm Biopharm. 80, 528–534. https://doi.org/10.1016/j.ejpb.2011.11.015

Istenič, K., Cerc Korošec, R., Poklar Ulrih, N., 2016. Encapsulation of (-)-epigallocatechin gallate into liposomes and into alginate or chitosan microparticles reinforced with liposomes. J. Sci. Food Agric. 96, 4623–4632. https://doi.org/10.1002/jsfa.7691

Jadia, R., Kydd, J., Piel, B., Rai, P., 2018. Liposomes Aid Curcumin's Combat with Cancer in a Breast Tumor Model. Oncomedicine. 3, 94–109. https://doi.org/10.7150/oncm.27938

Jafari, S., Soleimani, M., Salehi, R., 2019. Nanotechnology-based combinational drug delivery systems for breast cancer treatment. Int. J. Polym. Mater. Polym. Biomater. 68, 859–869. https://doi.org/10.1080/00914037.2018.1517348

Jain, S., Deore, S.V., Ghadi, R., Chaudhari, D., Kuche, K., Katiyar, S.S., 2021. Tumor microenvironment responsive VEGF-antibody functionalized pH sensitive liposomes of docetaxel for augmented breast cancer therapy. Mater. Sci. Eng. C. 121, 111832. https://doi.org/10.1016/j.msec.2020.111832

Jain, K.K., 2005. Nanotechnology-based drug delivery for cancer. Technol. Cancer Res. Treat. 4, 407–416. https://doi.org/10.1177/153303460500400408

Jain, A., Jain, S.K., 2016. In vitro release kinetics model fitting of liposomes: An insight. Chem. Phys. Lipids. 201, 28–40. https://doi.org/10.1016/j.chemphyslip.2016.10.005

Jangde, R., Singh, D., 2016. Preparation and optimization of quercetin-loaded liposomes for wound healing, using response surface methodology. Artif. Cells, Nanomed Biotechnol. 44, 635–641. https://doi.org/10.3109/21691401.2014.975238

Jasra, S., Anampa, J., 2018. Anthracycline Use for Early Stage Breast Cancer in the Modern Era: a Review. Curr. Treat. Options Oncol. 19, 1-17. https://doi.org/10.1007/S11864-018-0547-8

Jayakumar, R., Nair, A., Rejinold, N.S., Maya, S., and Nair, S. V., 2012. Doxorubicin-loaded pH-responsive chitin nanogels for drug delivery to cancer cells. Carbohydr Polym. 87, 2352–2356. https://doi.org/10.1016/j.carbpol.2011.10.040

Jesinger, R.A., 2014. Breast Anatomy for the Interventionalist. Tech. Vasc. Interv. Radiol. 17, 3–9. https://doi.org/10.1053/j.tvir.2013.12.002

Ji, J.-L., Huang, X.-F., Zhu, H.-L., 2012. Curcumin and its Formulations: Potential Anti-Cancer Agents. Anticancer. Agents Med. Chem. 12, 210–218. https://doi.org/10.2174/187152012800228733

Jin, H.H., Lu, Q., Jiang, J.G., 2016. Curcumin liposomes prepared with milk fat globule membrane phospholipids and soybean lecithin. J. Dairy Sci. 99, 1780–1790. https://doi.org/10.3168/jds.2015-10391

Junttila, M.R., De Sauvage, F.J., 2013. Influence of tumour micro-environment heterogeneity on therapeutic response. Nature. 501, 346–354. https://doi.org/10.1038/nature12626

Kathryn, J.C., Sireesha V, G., Stanley, L., 2012. Triple Negative Breast Cancer Cell Lines: One Tool in the Search for Better Treatment of Triple Negative Breast Cancer. Breast Dis. 32, 35–48. https://doi.org/10.3233/bd-2010-0307

Kanamala, M., Palmer, B.D., Jamieson, S.M.F., Wilson, W.R., Wu, Z., 2019. Dual pH-sensitive liposomes with low pH-triggered sheddable PEG for enhanced tumor-targeted drug delivery. Nanomed. 14, 1971–1989. https://doi.org/10.2217/nnm-2018-0510

Kanamala, M., Wilson, W.R., Yang, M., Palmer, B.D., Wu, Z., 2016. Mechanisms and biomaterials in pH-responsive tumour targeted drug delivery: A review. Biomater. 85, 152–167. https://doi.org/10.1016/j.biomaterials.2016.01.061

Kang, C., Yuan, X., Li, F., Pu, P., Yu, S., Shen, C., Zhang, Z., Zhang, Y., 2010. Evaluation of folate-PAMAM for the delivery of antisense oligonucleotides to rat C6 glioma cells in vitro and in vivo. J. Biomed. Mater. Res. 93, 585–594. https://doi.org/10.1002/jbm.a.32525

Karanth, H., Murthy, R.S.R., 2007. pH-Sensitive liposomes-principle and application in cancer therapy. J. Pharm. Pharmacol. 59, 469–483. https://doi.org/10.1211/jpp.59.4.0001

Keleştemur, S., Altunbek, M., Culha, M., 2017. Influence of EDC/NHS coupling chemistry on stability and cytotoxicity of ZnO nanoparticles modified with proteins. Appl. Surf. Sci.

403, 455–463. https://doi.org/10.1016/j.apsusc.2017.01.235

Kelsey, J.L., Gammon, M.D., John, E.M., 1993. Reproductive and hormonal risk factors. Epidemiol. Rev. 15, 36–47. https://doi.org/10.1093/oxfordjournals.epirev.a036115

Kim, D.M., Kim, M., Park, H. Bin, Kim, K.S., Kim, D.E., 2019. Anti-MUC1/CD44 Dual-Aptamer-Conjugated Liposomes for Cotargeting Breast Cancer Cells and Cancer Stem Cells. ACS Appl. Bio Mater. 2, 4622–4633. https://doi.org/10.1021/acsabm.9B00705

Kim, M.W., Jeong, H.Y., Kang, S.J., Jeong, I.H., Choi, M.J., You, Y.M., Im, C.S., Song, I.H., Lee, T.S., Lee, J.S., Lee, A., Park, Y.S., 2019. Anti-EGF Receptor Aptamer-Guided Co-Delivery of Anti-Cancer siRNAs and Quantum Dots for Theranostics of Triple-Negative Breast Cancer. Theranostics. 9, 852. https://doi.org/10.7150/thno.30228

Klevos, G.A., Ezuddin, N.S., Vinyard, A., Ghaddar, T., Gort, T., Almuna, A., Abisch, A., Welsh, C.F., 2017. A Breast Cancer Review: Through the Eyes of the Doctor, Nurse, and Patient. J. Radiol. Nurs. 36, 158–165. https://doi.org/10.1016/j.jradnu.2017.07.001

Kneidl, B., Peller, M., Winter, G., Lindner, L.H., Hossann, M., 2014. Thermosensitive liposomal drug delivery systems: state of the art review. Int. J. Nanomed. 9, 4387–4398. https://doi.org/10.2147/ijn.s49297

Konduri, S., Singh, M., Bobustuc, G., Rovin, R., Kassam, A., 2020. Epidemiology of male breast cancer. Breast. 54, 8–14. https://doi.org/10.1016/j.breast.2020.08.010

Kong, L., Chen, Q., Campbell, F., Snaar-Jagalska, E., Kros, A., 2020. Light-Triggered Cancer Cell Specific Targeting and Liposomal Drug Delivery in a Zebrafish Xenograft Model. Adv. Healthc. Mater. 9, 1901489. https://doi.org/10.1002/adhm.201901489

Konatham, S., Nyathani, H.K., Bonepally, C.R., Yeannameneni, P.K., and Aukunuru, J., 2010. Liposomal delivery of curcumin to liver. Turk J Pharm Sci. 7, 89–98.

Krasnici, S., Werner, A., Eichhorn, M.E., Schmitt-Sody, M., Pahernik, S.A., Sauer, B., Schulze, B., Teifel, M., Michaelis, U., Naujoks, K., Dellian, M., 2003. Effect of the surface charge of liposomes on their uptake by angiogenic tumor vessels. Int. J Cancer. 105, 561–567. https://doi.org/10.1002/ijc.11108

Krishnamurti, U., Silverman, J.F., 2014. HER2 in breast cancer: A review and update. Adv. Anat. Pathol. 21, 100–107. https://doi.org/10.1097/pap.0000000000000015

Kumar, N., Patni, P., Agarwal, A., Khan, M.A., Parashar, N., 2015. Prevalence of molecular subtypes of invasive breast cancer: A retrospective study. Med. J. Armed Forces India. 71, 254–258. https://doi.org/10.1016/j.mjafi.2015.04.006

Lamprou, E., Mourtas, S., Mantzari, M., Marazioti, A., Gkartziou, F., Antimisiaris, S.G., 2020. Folic Acid—Targeted Doxorubicin Drug Delivery System for Triple-Negative Breast Cancer Treatment. Proc. 78, 4. https://doi.org/10.3390/iecp2020-08660

Large, D.E., Abdelmessih, R.G., Fink, E.A., Auguste, D.T., 2021. Liposome composition in drug delivery design, synthesis, characterization, and clinical application. Adv. Drug Deliv. Rev. 176, 113851. https://doi.org/10.1016/j.addr.2021.113851

Lasic, D.D., 1995. Applications of liposomes, Handbook of Biological Physics. Elsevier Masson SAS. https://doi.org/10.1016/S1383-8121(06)80027-8

Lasic, D.D., 1988. The mechanism of vesicle formation. Biochem. J. 256, 1–11. https://doi.org/10.1042/BJ2560001

Laouini, A., Sfar, S., Charcosset, C., Fessi, H., Lyon, C.P.E., Bat, G., Novembre, B., Cedex, F.-V., 2012. Preparation , Characterization and Applications of Liposomes : State of the Art. J. Colloid Sci. Biotechnol. 1, 147–168. https://doi.org/10.1166/jcsb.2012.1020

Lee, M.K., 2019. Clinical usefulness of liposomal formulations in cancer therapy: lessons from the experiences of doxorubicin. J. Pharm. Investig. 49, 203–214. https://doi.org/10.1007/s40005-018-0398-0

Lee, W.H., Loo, C.Y., Young, P.M., Traini, D., Mason, R.S., Rohanizadeh, R., 2014. Recent advances in curcumin nanoformulation for cancer therapy. Expert Opin. Drug Deliv. 11, 1183–1201. https://doi.org/10.1517/17425247.2014.916686

Lee, A. V., Oesterreich, S., Davidson, N.E., 2015. MCF-7 Cells - Changing the Course of Breast Cancer Research and Care for 45 Years. J. Natl. Cancer Inst. 107, 1–4. https://doi.org/10.1093/jnci/djv073

Lemaine, V., Simmons, P.S., 2013. The adolescent female: Breast and reproductive embryology and anatomy. Clin. Anat. 26, 22–28. https://doi.org/10.1002/ca.22167

Li, Z., Huang, Y., Peng, S., Chen, X., Zou, L., Liu, W., Liu, C., 2020. Liposomes consisting of pluronic F127 and phospholipid: Effect of matrix on morphology, stability and curcumin delivery. J. Dispers. Sci. Technol. 41, 207–213. https://doi.org/10.1080/01932691.2018.1562353

Li, C., Wang, Xiaodong, Yang, L., Du, Y., Jin, Q., Wang, S., Wang, Xiaoli, 2021. Use of mitoxantrone hydrochloride liposome for treating breast cancer.UA20230078702A1. United States

Li, J., Wang, X., Zhang, T., Wang, C., Huang, Z., Luo, X., Deng, Y., 2015. A review on phospholipids and their main applications in drug delivery systems. Asian J. Pharm. Sci. 10, 81-98. https://doi.org/10.1016/j.ajps.2014.09.004

Li, M., Du, C., Guo, N., Teng, Y., Meng, X., Sun, H., Li, S., Yu, P., Galons, H., 2019. Composition design and medical application of liposomes. Eur. J. Med. Chem. 164, 640–653. https://doi.org/10.1016/j.ejmech.2019.01.007

Li, M., Shi, K., Tang, X., Science, M., Wei, J., Science, M., Cun, X., Long, Y., Zhang, Z., He, Q., 2018. Synergistic tumor microenvironment targeting and blood – brain barrier penetration via a pH-responsive dual-ligand strategy for enhanced breast cancer and brain metastasis therapy. Nanomedicine Nanotechnology, Biol. Med. 14, 1833–1843. https://doi.org/10.1016/j.nano.2018.05.008

Li, R., Lin, Z., Zhang, Q., Zhang, Y., Liu, Y., Lyu, Y., Li, X., Zhou, C., Wu, G., Ao, N., and Li, L., 2020. Injectable and in Situ-Formable Thiolated Chitosan-Coated Liposomal Hydrogels as Curcumin Carriers for Prevention of in Vivo Breast Cancer Recurrence. ACS Appl. Mater. Interfaces. 12, 17936-19748. https://doi.org/10.1021/acsami.9b21528

Li, Z. ling, Peng, S. feng, Chen, X., Zhu, Y. qing, Zou, L. qiang, Liu, W., and Liu, C. mei, 2018. Pluronics modified liposomes for curcumin encapsulation: Sustained release, stability and bioaccessibility. Food Res. Int. 108, 246–253. https://doi.org/10.1016/j.foodres.2018.03.048

Lian, T., Ho, R.J.Y., 2001. Trends and Developments in Liposome Drug Delivery Systems. J. Pharm. Sci. 90, 667–680. https://doi.org/10.1002/jps.1023

Lila, A.S.A., Ishida, T., 2017. Liposomal delivery systems: Design optimization and current applications. Biol. Pharm. Bull. 40, 1–10. https://doi.org/10.1248/bpb.b16-00624

Limasale, Y.D.P., Tezcaner, A., Özen, C., Keskin, D., Banerjee, S., 2015. Epidermal growth factor receptor-targeted immunoliposomes for delivery of celecoxib to cancer cells. Int. J. Pharm. 479, 364–373. https://doi.org/10.1016/j.ijpharm.2015.01.016

Lin, Y.L., Tsai, N.M., Chen, C.H., Liu, Y.K., Lee, C.J., Chan, Y.L., Wang, Y.S., Chang, Y.C., Lin, C.H., Huang, T.H., Wang, C.C., Chi, K.H., Liao, K.W., 2019. Specific drug delivery efficiently induced human breast tumor regression using a lipoplex by non-covalent association with anti-tumor antibodies. J. Nanobiotechnology. 17, 1–11. https://doi.org/10.1186/s12951-019-0457-3

Liu, D., Chen, Z., 2013. The effect of curcumin on breast cancer cells. J. Breast Cancer. 16, 133–137. https://doi.org/10.4048/jbc.2013.16.2.133

Liu, J., Sun, Y., Liu, X., Yang, Y., Widjaya, A.S., Long, Z., Jiang, Y., 2020. Efficiency of Different Treatment Regimens Combining Anti-tumor and Anti-inflammatory Liposomes for Metastatic Breast Cancer. AAPS PharmSciTech 21, 1–12. https://doi.org/10.1208/S12249-020-01792-z

Liu, C.G., Han, Y.H., Kankala, R.K., Wang, S. Bin, Chen, A.Z., 2020. Subcellular performance of nanoparticles in cancer therapy. Int. J. Nanomedicine. 15, 675–704. https://doi.org/10.2147/ijn.S226186

Love, M., 2013. Bailey and Love's Short practice of surgery.

Lv, L., Qiu, K., Yu, X., Chen, C., Qin, F., Shi, Y., Ou, J., Zhang, T., Zhu, H., Wu, J., Liu, C., Li, G., 2016. Amphiphilic copolymeric micelles for doxorubicin and curcumin co-delivery to reverse multidrug resistance in breast cancer. J. Biomed. Nanotechnol. 12, 973–985. https://doi.org/10.1166/jbn.2016.2231

M Román, M J Quintana, J Ferrer, M.S.& X.C., 2017. Cumulative risk of breast cancer

screening outcomes according to the presence of previous benign breast disease and family history of breast cancer : supporting personalised screening. Br. J. Cancer. 116, 1480–1485. https://doi.org/10.1038/bjc.2017.107

Ma, W., Guo, Q., Li, Y., Wang, X., Wang, J., Tu, P., 2017. Co-assembly of doxorubicin and curcumin targeted micelles for synergistic delivery and improving anti-tumor efficacy. Eur. J. Pharm. Biopharm. 112, 209–223. https://doi.org/10.1016/j.ejpb.2016.11.033

Macmahon, B., Cole, P., Brown, J., 1973. Etiology of human breast cancer: A review. J. Natl. Cancer Inst. 50, 21–42. https://doi.org/10.1093/jnci/50.1.21

Madni, M.A., Sarfraz, M., Rehman, M., Ahmad, M., Akhtar, N., Ahmad, S., Tahir, N., Ijaz, S., Al-Kassas, R., Löbenberg, R., 2014. Liposomal Drug Delivery: A Versatile Platform for Challenging Clinical Applications. J. Pharm. Pharm. Sci. 17, 401–426. https://doi.org/10.18433/j3cp55

Mady, M.M., Shafaa, M.W., Abbase, E.R., Fahium, A.H., 2012. Interaction of Doxorubicin and Dipalmitoylphosphatidylcholine Liposomes. Cell Biochem. Biophys. 62, 481–486. https://doi.org/10.1007/S12013-011-9334-x

Mahmud, M., Piwoni, A., Filiczak, N., Janicka, M., Gubernator, J., 2016. Long-circulating curcumin-loaded liposome formulations with high incorporation efficiency, stability and anticancer activity towards pancreatic adenocarcinoma cell lines in vitro. PLoS One 11, 1–23. https://doi.org/10.1371/journal.pone.0167787

Maherani, B., Arab-Tehrany, E., R. Mozafari, M., Gaiani, C., Linder, M., 2011. Liposomes: A Review of Manufacturing Techniques and Targeting Strategies. Curr. Nanosci. 7, 436–452. https://doi.org/10.2174/157341311795542453

Malam, Y., Loizidou, M., Seifalian, A.M., 2009. Liposomes and nanoparticles: nanosized vehicles for drug delivery in cancer. Trends Pharmacol. Sci. 30, 592–599. https://doi.org/10.1016/j.tips.2009.08.004

Maleki Dizaj, S., Alipour, M., Dalir Abdolahinia, E., Ahmadian, E., Eftekhari, A., Forouhandeh, H., Rahbar Saadat, Y., Sharifi, S., Zununi Vahed, S., 2022. Curcumin nanoformulations: Beneficial nanomedicine against cancer. Phyther. Res. 36, 1156–1181.

https://doi.org/10.1002/ptr.7389

Malhotra, G.K., Zhao, X., Band, H., Band, V., 2010. Histological, molecular and functional subtypes of breast cancers. Cancer Biol. Ther. 10, 955–960. https://doi.org/10.4161/cbt.10.10.13879

Maloney, S.M., Hoover, C.A., Morejon-Lasso, L. V., Prosperi, J.R., 2020. Mechanisms of Taxane Resistance. Cancers.12, 3323.https://doi.org/10.3390/cancers12113323

Mamot, C., Drummond, D.C., Noble, C.O., Kallab, V., Guo, Z., Hong, K., Kirpotin, D.B., Park, J.W., 2005. Epidermal Growth Factor Receptor – Targeted Immunoliposomes Significantly Enhance the Efficacy of Multiple Anticancer Drugs In vivo. Cancer Res. 65, 11631–11638. https://doi.org/10.1158/0008-5472.can-05-1093

Mamot, C., Ritschard, R., Wicki, A., Küng, W., Schuller, J., Herrmann, R., Rochlitz, C., 2012. Immunoliposomal delivery of doxorubicin can overcome multidrug resistance mechanisms in EGFR-overexpressing tumor cells. J. drug target. 20, 422–432. https://doi.org/10.3109/1061186x.2012.680960

Mansfield, C.M., 1993. A review of the etiology of breast cancer. J. Natl. Med. Assoc. 85, 217–221.

Marjan, J.M.J., Allen, T.M., 1996. Long circulating liposomes: Past, present and future. Biotechnol. Adv. 14, 151–175. https://doi.org/10.1016/0734-9750(96)00007-9

Markman, M., 2003. Managing taxane toxicities. Support. Care Cancer. 11, 144–147. https://doi.org/10.1007/S00520-002-0405-9

Marshalek, J.P., Sheeran, P.S., Ingram, P., Dayton, P.A., Witte, R.S., and Matsunaga, T.O., 2016. Intracellular delivery and ultrasonic activation of folate receptor-targeted phase-change contrast agents in breast cancer cells in vitro. J. Control. Release. 243, 69–77. https://doi.org/10.1016/j.jconrel.2016.09.010

Masuda, H., Zhang, D., Bartholomeusz, C., Doihara, H., Hortobagyi, G.N., Ueno, N.T., 2012. Role of epidermal growth factor receptor in breast cancer. Breast Cancer Res. Treat. 136, 331–345. https://doi.org/10.1007/s10549-012-2289-9

Matusewicz, L., Filip-psurska, B., Psurski, M., Tabaczar, S., Podkalicka, J., Wietrzyk, J., Ziółkowski, P., Czogalla, A., 2019. EGFR-targeted immunoliposomes as a selective delivery system of simvastatin , with potential use in treatment of triple-negative breast cancers. Int. J. Pharm. 569, 118605. https://doi.org/10.1016/j.ijpharm.2019.118605

Maughan, K.L., Lutterbie, M.A., Ham, P.S., 2010. Treatment of Breast Cancer. Am. Fam. Physician. 81, 1339–1346.

McCready, T., Littlewood, D., Jenkinson, J., 2005. Breast self-examination and breast awareness: A literature review. J. Clin. Nurs. 14, 570–578. https://doi.org/10.1111/j.1365-2702.2004.01108.x

Meier, R., Henning, T.D., Boddington, S., Tavri, S., Arora, S., Piontek, G., Rudelius, M., Corot, C., Daldrup-Link, H.E., 2010. Breast cancers: MR imaging of folate-receptor expression with the folate-specific nanoparticle p1133. Radiology. 255, 527–535. https://doi.org/10.1148/radiol.10090050

Mendez, R., Banerjee, S., 2017. Sonication-based basic protocol for liposome synthesis, Methods in Molecular Biology. Humana Press Inc. https://doi.org/10.1007/978-1-4939-6996-8_21

Miller, C.R., Bondurant, B., McLean, S.D., McGovern, K.A., O'Brien, D.F., 1998. Liposome-cell interactions in vitro: Effect of liposome surface charge on the binding and endocytosis of conventional and sterically stabilized liposomes. Biochem. 37, 12875–12883. https://doi.org/10.1021/bi980096y

Miller, E.R., Wilson, C., Chapman, J., Flight, I., Nguyen, A., Fletcher, C., Ramsey, I., 2018. Connecting the dots between breast cancer , obesity and alcohol consumption in middle-aged women : ecological and case control studies. BMC Public Health. 18, 460–473. https://doi.org/10.1186/s12889-018-5357-1

Minnelli, C., Cianfruglia, L., Laudadio, E., Galeazzi, R., Pisani, M., Crucianelli, E., Bizzaro, D., Armeni, T., Minnelli, C., Cianfruglia, L., Laudadio, E., Galeazzi, R., 2017. Selective induction of apoptosis in MCF7 cancercell by targeted liposomes functionalized with mannose-6-phosphate. J. Drug Target. 26, 242-251. https://doi.org/10.1080/1061186x.2017.1365873

Mishra, D.K., Shandilya, R., Mishra, P.K., 2018. Lipid based nanocarriers: a translational perspective. Nanomedicine Nanotechnology, Biol. Med. 14, 2023–2050. https://doi.org/10.1016/j.nano.2018.05.021

Mitchell, M.J., Jain, R.K., Langer, R., 2017. Engineering and physical sciences in oncology : challenges and opportunities. Nat. Publ. Gr. 17, 659–675. https://doi.org/10.1038/nrc.2017.83

Momenimovahed, Z., Salehiniya, H., 2019. Epidemiological characteristics of and risk factors for breast cancer in the world. Breast Cancer Targets Ther. 11, 151–164. https://doi.org/10.2147/bctt.s176070

Monteiro, L.O.F., Fernandes, R.S., Oda, C.M.R., Lopes, S.C., Townsend, D.M., Cardoso, V.N., Oliveira, M.C., Leite, E.A., Rubello, D., de Barros, A.L.B., 2018. Paclitaxel-loaded folate-coated long circulating and pH-sensitive liposomes as a potential drug delivery system: A biodistribution study. Biomed. Pharmacother. 97, 489–495. https://doi.org/10.1016/j.biopha.2017.10.135

Moorthi, C., Manavalan, R., Kathiresan, K., 2011. Nanotherapeutics to Overcome Conventional Cancer Chemotherapy Limitations. J. Pharm. Pharm. Sci. 14, 67–77. https://doi.org/10.18433/j30c7d

Moudgil, A., Jaiswal, N., Gajbhiye, K.R., Gajbhiye, V., Pawar, A.T., Chaudhari, B.P., 2022. Hypoxia mediated targeted nanomedicine for breast cancer. Target. Nanomedicine Breast Cancer Ther. 369–406. https://doi.org/10.1016/b978-0-12-824476-0.00013-9

Moudgil, A., Salve, R., Gajbhiye, V., Chaudhari, B.P., 2023. Challenges and emerging strategies for next generation liposomal based drug delivery: An account of the breast cancer conundrum. Chem. Phys. Lipids 250, 105258. https://doi.org/110.1016/j.chemphyslip.2022.105258

Mufamadi, M.S., Pillay, V., Choonara, Y.E., Toit, L.C. Du, Modi, G., Naidoo, D., Ndesendo, V.M.K., 2011. A Review on Composite Liposomal Technologies for Specialized Drug Delivery. J. Drug Deliv. 2011, 1–19. https://doi.org/10.1155/2011/939851

Muthu, M.S., Kulkarni, S.A., Raju, A., Feng, S.S., 2012. Theranostic liposomes of TPGS

coating for targeted co-delivery of docetaxel and quantum dots. Biomater. 33, 3494–3501. https://doi.org/10.1016/j.biomaterials.2012.01.036

Murugesan, K., Srinivasan, P., Mahadeva, R., Gupta, C.M., Haq, W., 2020. Tuftsin-bearing liposomes co-encapsulated with doxorubicin and curcumin efficiently inhibit eac tumor growth in mice. Int. J. Nanomedicine. 15, 10547–10559. https://doi.org/10.2147/ijn.s276336

Naksuriya, O., Okonogi, S., Schiffelers, R.M., Hennink, W.E., 2014. Curcumin nanoformulations: A review of pharmaceutical properties and preclinical studies and clinical data related to cancer treatment. Biomater. 35, 3365–3383. https://doi.org/10.1016/j.biomaterials.2013.12.090

Nazari, S.S., Mukherjee, P., 2018. An overview of mammographic density and its association with breast cancer. Breast Cancer. 25, 259–267. https://doi.org/10.1007/s12282-018-0857-5

Nazeer, N., Panicker, J.T., 2019. A Review on Surface Modified Sterically Stabilized Liposomes. Int. J. Innov. Sci. Res. Technol. 4, 795–801.

Needham, D., Hristova, K., Mcintosh, T.J., Dewhirst, M., Wu, N., Lasic, D.D., 1992. Polymer-grafted liposomes: Physical basis for the "stealth" property. J. Liposome Res. 2, 411–430. https://doi.org/10.3109/08982109209010218

Nel, J., Elkhoury, K., Velot, É., Bianchi, A., Acherar, S., Francius, G., Tamayol, A., Grandemange, S., and Arab-Tehrany, E., 2023. Functionalized liposomes for targeted breast cancer drug delivery. Bioact. Mater. 24, 401–437. https://doi.org/10.1016/j.bioactmat.2022.12.027

Ng, Z.Y., Wong, J.Y., Panneerselvam, J., Madheswaran, T., Kumar, P., Pillay, V., Hsu, A., Hansbro, N., Bebawy, M., Wark, P., Hansbro, P., Dua, K., and Chellappan, D.K., 2018. Assessing the potential of liposomes loaded with curcumin as a therapeutic intervention in asthma. Colloids Surf. B. 172, 51–59. https://doi.org/10.1016/j.colsurfb.2018.08.027

Nguyen, V. Du, Min, H.K., Kim, C.S., Han, J., Park, J.O., Choi, E., 2019. Folate receptor-targeted liposomal nanocomplex for effective synergistic photothermal-chemotherapy of

breast cancer in vivo. Colloids Surf. B. 173, 539–548. https://doi.org/10.1016/j.colsurfb.2018.10.013

Niu, Y., Ke, D., Yang, Q., Wang, X., Chen, Z., An, X., Shen, W., 2012. Temperature-dependent stability and DPPH scavenging activity of liposomal curcumin at pH 7.0. Food Chem. 135, 1377–1382. https://doi.org/10.1016/j.foodchem.2012.06.018

Nounou, M.I., Elamrawy, F., Ahmed, N., Abdelraouf, K., Goda, S., Syed-sha-qhattal, H., 2015. Breast Cancer : Conventional Diagnosis and Treatment Modalities and Recent Patents and Technologies. Breast Cancer: Basic Clin Res. 9, 17–34. https://doi.org/10.4137/bcbcr.s29420

O'Driscoll, L., Clynes, M., 2006. Biomarkers and Multiple Drug Resistance in Breast Cancer. Curr. Cancer Drug Targets. 6, 365–384. https://doi.org/10.2174/156800906777723958

O'Shannessy, D.J., Somers, E.B., Maltzman, J., Smale, R., Fu, Y.S., 2012. Folate receptor alpha (FRA) expression in breast cancer: Identification of a new molecular subtype and association with triple negative disease. Springerplus. 1, 1–9. https://doi.org/10.1186/2193-1801-1-22

Ogiso, T., Yamaguchi, T., Iwaki, M., Tanino, T., Miyake, Y., 2001. Effect of positively and negatively charged liposomes on skin permeation of drugs. J. Drug Target. 9, 49–59. https://doi.org/10.3109/10611860108995632

Ojima, I., Lichtenthal, B., Lee, S., Wang, C., Wang, X., 2016. Taxane anticancer agents: A patent perspective. Expert Opin. Ther. Pat. 26, 1–20. https://doi.org/10.1517/13543776.2016.1111872

Oshiro, C., Marsh, S., McLeod, H., Carrillo, M.W., Klein, T., Altman, R., 2009. Taxane Pathway. Pharmacogenet. Genomics. 19, 979. https://doi.org/10.1097/fpc.0b013e3283335277

Ouhtit, A., Rizeq, B., Saleh, H.A., Rahman, M.D.M., Zayed, H., 2018. Novel CD44-downstream signaling pathways mediating breast tumor invasion. Int. J. Biol. Sci. 14, 1782–1790. https://doi.org/10.7150/ijbs.23586

Page, D.L., 2003. Special types of invasive breast cancer, with clinical implications. Am. J. Surg. Pathol. 27, 832–835. https://doi.org/10.1097/00000478-200306000-00016

Pakdaman Goli, P., Bikhof Torbati, M., Parivar, K., Akbarzadeh Khiavi, A., Yousefi, M., 2021. Preparation and evaluation of gemcitabin and cisplatin-entrapped Folate-PEGylated liposomes as targeting co-drug delivery system in cancer therapy. J. Drug Deliv. Sci. Technol. 65, 102756. https://doi.org/10.1016/j.jddst.2021.102756

Paliwal, S.R., Paliwal, R., Vyas, S.P., 2015. A review of mechanistic insight and application of pH-sensitive liposomes in drug delivery. Drug Deliv. 22, 231–242. https://doi.org/10.3109/10717544.2014.882469

Paliwal, S.R., Paliwal, R., Agrawal, G.P., Vyas, S.P., 2016. Hyaluronic acid modified pH-sensitive liposomes for targeted intracellular delivery of doxorubicin. J. Liposome Res. 26, 276–287. https://doi.org/10.3109/08982104.2015.1117489

Paliwal, S.R., Paliwal, R., Pal, H.C., Saxena, A.K., Sharma, P.R., Gupta, P.N., Agrawal, G.P., Vyas, S.P., 2012. Estrogen-anchored pH-sensitive liposomes as nanomodule designed for site-specific delivery of doxorubicin in breast cancer therapy. Mol. Pharm. 9, 176–186. https://doi.org/10.1021/mp200439z

Pamunuwa, G., Karunaratne, V., Karunaratne, D.N., 2016. Effect of lipid composition on in vitro release and skin deposition of curcumin encapsulated liposomes. J. Nanomater. 2016. https://doi.org/10.1155/2016/4535790

Pan, G., Jia, T. ting, Huang, Q. xia, Qiu, Y. yan, Xu, J., Yin, P. hao, Liu, T., 2017. Mesoporous silica nanoparticles (MSNs)-based organic/inorganic hybrid nanocarriers loading 5-Fluorouracil for the treatment of colon cancer with improved anticancer efficacy. Colloids Surf. B Biointerfaces 159, 375–385. https://doi.org/10.1016/J.colsurfb.2017.08.013

Panahi, Y., Farshbaf, M., Mohammadhosseini, M., Mirahadi, M., Khalilov, R., Saghfi, S., Akbarzadeh, A., 2017. Recent advances on liposomal nanoparticles: synthesis, characterization and biomedical applications. Artif. Cells, Nanomed Biotechnol. 45, 788–799. https://doi.org/10.1080/21691401.2017.1282496

Pandey, H., Rani, R., Agarwal, V., 2016. Liposome and Their Applications in Cancer Therapy.

Braz. Arch. Biol. Technol. 59, 16150477. https://doi.org/http://dx.doi.org/10.1590/1678-4324-2016150477

Pandya, S., Moore, R.G., 2011. Breast development and anatomy. Clin. Obstet. Gynecol. 54, 91–95. https://doi.org/10.1097/grf.0b013e318207ffe9

Paolino, D., Licciardi, M., Celia, C., Giammona, G., Fresta, M., Cavallaro, G., 2012. Folate-targeted supramolecular vesicular aggregates as a new frontier for effective anticancer treatment in in vivo model. Eur. J. Pharm. Biopharm. 82, 94–102. https://doi.org/10.1016/j.ejpb.2012.06.001

Papahadjopoulos, D., 1996. Fate of liposomes in vivo: A brief introductory review. J. Liposome Res. 6, 3–17. https://doi.org/10.3109/08982109609037199

Patel, R., Patel, H., Baria, A., 2009. Formulation and Evaluation of Liposomes of Ketoconazole. Int. J. Drug Deliv. Technol. 1, 16–23. https://doi.org/10.25258/ijddt.v1i2.8839

Pillai, G., 2014. Nanomedicines for Cancer Therapy: An Update of FDA Approved and Those under Various Stages of Development. SOJ Pharm. Pharm. Sci. 1.https://doi.org/10.15226/2374-6866/1/2/00109

Pinamonti, M., Zanconati, F., 2018. Normal Breast. Monogr. Clin. Cytol. 24, 20–24. https://doi.org/10.1159/000479764

Polyak, K., 2011. Heterogeneity in breast cancer. J. Clin. Invest. 121, 3786–3788. https://doi.org/10.1172/jci60534

Potter, M., Newport, E., Morten, K.J., 2016. The Warburg effect: 80 years on. Biochem. Soc. Trans. 44, 1499–1505. https://doi.org/10.1042/bst20160094

Pradhan, A., Mishra, S., Basu, S.M., Surolia, A., Giri, J., Srivastava, R., Panda, D., 2021. Targeted nanoformulation of C1 inhibits the growth of KB spheroids and cancer stem cell-enriched MCF-7 mammospheres. Colloids Surf. B. 202, 111702. https://doi.org/10.1016/j.colsurfb.2021.111702

Prasad, R., Jain, N.K., Yadav, A.S., Chauhan, D.S., Devrukhkar, J., Kumawat, M.K., Shinde,

S., Gorain, M., Thakor, A.S., Kundu, G.C., Conde, J., Srivastava, R., 2020. Liposomal nanotheranostics for multimode targeted in vivo bioimaging and near-infrared light mediated cancer therapy. Commun. Biol. 3, 1-14. https://doi.org/10.1038/s42003-020-1016-z

Prasad, R., Yadav, A.S., Gorain, M., Chauhan, D.S., Kundu, G.C., Srivastava, R., Selvaraj, K., 2019. Graphene Oxide Supported Liposomes as Red Emissive Theranostics for Phototriggered Tissue Visualization and Tumor Regression. ACS Appl. Bio Mater. 2, 3312–3320. https://doi.org/10.1021/acsabm.9b00335

Prasad, S., Tyagi, A.K., Aggarwal, B.B., 2014. Recent developments in delivery, bioavailability, absorption and metabolism of curcumin: The golden pigment from golden spice. Cancer Res. Treat. 46, 2–18. https://doi.org/10.4143/crt.2014.46.1.2

Prat, A., Pineda, E., Adamo, B., Galván, P., Fernández, A., Gaba, L., Díez, M., Viladot, M., Arance, A., Muñoz, M., 2015. Clinical implications of the intrinsic molecular subtypes of breast cancer. The Breast. 24, 26–35. https://doi.org/10.1016/j.breast.2015.07.008

Provenzano, E., Ulaner, G.A., Chin, S.F., 2018. Molecular Classification of Breast Cancer. PET Clin. 13, 325–338. https://doi.org/10.1016/j.cpet.2018.02.004

Pu, Y., Zhang, H., Peng, Y., Fu, Q., Yue, Q., Zhao, Y., Guo, L., Wu, Y., 2019. Dual-targeting liposomes with active recognition of GLUT5 and $\alpha v\beta 3$ for triple-negative breast cancer. Eur. J. Med. Chem. 183, 111720. https://doi.org/10.1016/j.ejmech.2019.111720

Pu, C., Tang, W., Li, X., Li, M., and Sun, Q., 2019. Stability enhancement efficiency of surface decoration on curcumin-loaded liposomes: Comparison of guar gum and its cationic counterpart. Food Hydrocoll. 87, 29–37. https://doi.org/10.1016/j.foodhyd.2018.07.039

Puri, A., 2013. Phototriggerable Liposomes: Current Research and Future Perspectives. Pharm. 6, 1–25. https://doi.org/10.3390/pharmaceutics6010001

Qiu, Y., Yu, Q., Liu, Y., Tang, J., Wang, X., Lu, Z., Xu, Z., He, Q., 2018. Dual Receptor Targeting Cell Penetrating Peptide Modified Liposome for Glioma and Breast Cancer Postoperative Recurrence Therapy. Pharm. Res. 35, 1-15. https://doi.org/10.1007/s11095-018-2399-0

Rabbani, A., Finn, R.M., Ausió, J., 2005. The anthracycline antibiotics: antitumor drugs that alter chromatin structure. BioEssays. 27, 50–56. https://doi.org/10.1002/bies.20160

Rahim, M.A., Madni, A., Tahir, N., Jan, N., Shah, H., Khan, S., Ullah, R., Bari, A., and Khan, M.S., 2021. Mild hyperthermia responsive liposomes for enhanced in vitro and in vivo anticancer efficacy of doxorubicin against hepatocellular carcinoma. Pharm. 13, 1310. https://doi.org/10.3390/pharmaceutics13081310

Rahman, M., Beg, S., Verma, A., Kazmi, I., Ahmed, F.J., Kumar, V., Anwar, F., Akhter, S., 2019. Liposomes as Anticancer Therapeutic Drug Carriers Systems: More than a Tour de Force. Curr. Nanomedicine. 10, 178–185. https://doi.org/10.2174/2468187309666190618171332

Ramsay, D.T., Kent, J.C., Hartmann, R.A., Hartmann, P.E., 2005. Anatomy of the lactating human breast redefined with ultrasound imaging. J. Anat. 206, 525–534. https://doi.org/10.1111/J.1469-7580.2005.00417.x

Rastegar, R., Akbari Javar, H., Khoobi, M., Dehghan Kelishadi, P., Hossein Yousefi, G., Doosti, M., Hossien Ghahremani, M., Shariftabrizi, A., Imanparast, F., Gholibeglu, E., Gholami, M., 2018. Evaluation of a novel biocompatible magnetic nanomedicine based on beta-cyclodextrin, loaded doxorubicin-curcumin for overcoming chemoresistance in breast cancer. Artif. Cells, Nanomed Biotechnol. 46, 207–216. https://doi.org/10.1080/21691401.2018.1453829

Raouf, A.L.M., Hammud, K.K., Mohammed, J.M., and Al-Dulimyi, E.M.K., 2014. Qualitative and Quantitative Determination of Folic acid in Tablets by FTIR Spectroscopy. IJAPBC. 3, 773–780.

Ravindran Chandrasekaran, A., Yoke Jia, C., Sheau Theng, C., Muniandy, T., Muralidharan, S., Arumugam Dhanaraj, S., 2011. Invitro studies and evaluation of metformin marketed tablets-Malaysia. J. Appl. Pharm. Sci. 2011, 214–217.

Reis-Filho, J.S., Pusztai, L., 2011. Gene expression profiling in breast cancer: classification, prognostication, and prediction. Lancet. 378, 1812–1823. https://doi.org/10.1016/S0140-6736(11)61539-0

Reynolds, P., 2013. Smoking and breast cancer. J. Mammary Gland Biol. Neoplasia. 18, 15–23. https://doi.org/10.1007/s10911-012-9269-x

Riaz, M.K., Riaz, M.A., Zhang, X., Lin, C., Wong, K.H., Chen, X., Id, G.Z., Lu, A., Yang, Z., 2018. Surface Functionalization and Targeting Strategies of Liposomes in Solid Tumor Therapy : A Review. Int. J. Mol. Sci. 19, 195. https://doi.org/https://doi.org/10.3390/ijms19010195

Rivankar, S., 2014. An overview of doxorubicin formulations in cancer therapy. J. Cancer Res. Ther. 10, 853–858. https://doi.org/10.4103/0973-1482.139267

Rojas, K., Stuckey, A., 2016. Breast Cancer Epidemiology and Risk Factors. Clin. Obstet. Gynecol. 59, 651–672. https://doi.org/10.1097/grf.0000000000000239

Roux, E., Passirani, C., Scheffold, S., Benoit, J.P., Leroux, J.C., 2004. Serum-stable and long-circulating, PEGylated, pH-sensitive liposomes. J. Control. Release. 94, 447–451. https://doi.org/10.1016/j.jconrel.2003.10.024

Rowinsky, E.K., 1997. The development and clinical utility of the taxane class of antimicrotubule chemotherapy agents. Annu. Rev. Med. 48, 353–374. https://doi.org/10.1146/annurev.med.48.1.353

Rozencweig, M., Goldfarb, R., Forenza, S., 2015. Non-pegylated liposomal doxorubicin combinations for the treatment of triple negative breast cancer. US20150250723A1. United States

Rubin, I., Yarden, Y., 2001. The basic biology of HER2. Ann. Oncol. 12, S3–S8. https://doi.org/10.1093/annonc/12.suppl_1.S3

Rupen Shah, Kelly Rosso, S.D.N., 2014. Pathogenesis, prevention, diagnosis and treatment of breast cancer. World J. Clin. Oncol. 5, 283- 298. https://doi.org/10.5306/wjco.v5.i3.283

Ruttala, H.B. and Ko, Y.T., 2015. Liposomal co-delivery of curcumin and albumin/paclitaxel nanoparticle for enhanced synergistic antitumor efficacy. Colloids Surf. B. 128, 419–426. https://doi.org/10.1016/j.colsurfb.2015.02.040

Sabzi, A., Rahmani, A., Edalati, M., Kahroba, H., Dadpour, M.R., Salehi, R., Zarebkohan, A.,

2020. Targeted co-delivery of curcumin and doxorubicin by citric acid functionalized Poly (ε-caprolactone) based micelle in MDA-MB-231 cell. Colloids Surf. B. 194, 111225. https://doi.org/10.1016/j.colsurfb.2020.111225

Saengkrit, N., Saesoo, S., Srinuanchai, W., Phunpee, S., and Ruktanonchai, U.R., 2014. Influence of curcumin-loaded cationic liposome on anticancer activity for cervical cancer therapy. Colloids Surf. B. 114, 349–356. https://doi.org/10.1016/j.colsurfb.2013.10.005

Sainsbury, J.R.C., Anderson, T.J., Morgan, D.A.L., Dixon, J.M., 1994. ABC of Breast Diseases: Breast Cancer. The BMJ 309, 1150–1153. https://doi.org/10.1136/bmj.309.6962.1150

Sakar, F., Özer, A.Y., Erdogan, S., Ekizoglu, M., Kart, D., Özalp, M., Colak, S., Zencir, Y., 2017. Nano drug delivery systems and gamma radiation sterilization. Pharm. Dev. Technol. 22, 775–784. https://doi.org/10.3109/10837450.2016.1163393

Salem, M., Rohani, S., Gillies, E.R., 2014. Curcumin, a promising anti-cancer therapeutic: A review of its chemical properties, bioactivity and approaches to cancer cell delivery. RSC Adv. 4, 10815–10829. https://doi.org/10.1039/c3ra46396f

Samad, A., Sultana, Yasmin, Aqil, Mohd, Sultana, Y, Aqil, M, 2007. Liposomal drug delivery systems: an update review. Curr. Drug Deliv. 4, 297–305. https://doi.org/10.2174/156720107782151269

Sandhu, G.S., Erqou, S., Patterson, H., Mathew, A., 2016. Prevalence of Triple-Negative Breast Cancer in India: Systematic Review and Meta-Analysis. J. Glob. Oncol. 2, 412–421. https://doi.org/10.1200/jgo.2016.005397

Santiago, M., 2013. pH-sensitive liposomes for drug delivery in cancer treatment. Ther. Deliv. 4, 1099–1123. https://doi.org/10.4155/tde.13.80

Sargazi2, S.J.· A.B.· Z.K.· G., 2022. Co-delivery of doxorubicin and curcumin to breast cancer cells by a targeted delivery system based on NiTa core-shell metal-organic framework coated with folic acid-activated chitosan nanoparticles. J. Iran. Chem. Soc.19, 4287- 4298. https://doi.org/10.1007/s13738-022-02604-w

Sarkar, N., Bose, S., 2019. Liposome-Encapsulated Curcumin-Loaded 3D Printed Scaffold for Bone Tissue Engineering. ACS Appl. Mater. Interfaces. 11, 17184–17192. https://doi.org/10.1021/acsami.9b01218

Satsangi, A., Roy, S.S., Satsangi, R.K., Tolcher, A.W., Vadlamudi, R.K., Goins, B., Ong, J.L., 2015. Synthesis of a novel, sequentially active-targeted drug delivery nanoplatform for breast cancer therapy. Biomater. 59, 88–101. https://doi.org/10.1016/j.biomaterials.2015.03.039

Saul, J.M., Annapragada, A. V., Bellamkonda, R. V., 2006. A dual-ligand approach for enhancing targeting selectivity of therapeutic nanocarriers. J. Control. Release. 114, 277–287. https://doi.org/10.1016/j.jconrel.2006.05.028

Schmitt, C., Lechanteur, A., Cossais, F., Bellefroid, C., Arnold, P., Lucius, R., Held-Feindt, J., Piel, G., Hattermann, K., 2020. Liposomal encapsulated curcumin effectively attenuates neuroinflammatory and reactive astrogliosis reactions in glia cells and organotypic brain slices. Int. J. Nanomedicine. 15, 3649–3667. https://doi.org/10.2147/ijn.S245300

Schnitt, S.J., 2010. Classification and prognosis of invasive breast cancer : from morphology to molecular taxonomy. Mod. Pathol. 23, S60–S64. https://doi.org/10.1038/modpathol.2010.33

Schroeder, A., Kost, J., Barenholz, Y., 2009. Ultrasound, liposomes, and drug delivery: principles for using ultrasound to control the release of drugs from liposomes. Chem. Phys. Lipids. 162, 1–16. https://doi.org/10.1016/j.chemphyslip.2009.08.003

Seitz, H.K., Pelucchi, C., Bagnardi, V., Vecchia, C. La, 2012. Epidemiology and Pathophysiology of Alcohol and Breast Cancer : Update 2012. Alcohol Alcohol. 47, 204–212. https://doi.org/10.1093/alcalc/ags011

Senapati, S., Mahanta, A.K., Kumar, S., Maiti, P., 2018. Controlled drug delivery vehicles for cancer treatment and their performance. Signal Transduct. Target. Ther. 3, 1–19. https://doi.org/10.1038/s41392-017-0004-3

Sesarman, A., Tefas, L., Sylvester, B., Licarete, E., Rauca, V., Luput, L., Patras, L., Banciu, M., Porfire, A., 2018. Anti-angiogenic and anti-inflammatory effects of long-circulating

liposomes co-encapsulating curcumin and doxorubicin on C26 murine colon cancer cells. Pharmacol. Rep. 70, 331–339. https://doi.org/10.1016/j.pharep.2017.10.004

Sercombe, L., Veerati, T., Moheimani, F., Wu, S.Y., Sood, A.K., Hua, S., 2015. Advances and challenges of liposome assisted drug delivery. Front. Pharmacol. 6, 1-13.https://doi.org/10.3389/fphar.2015.00286

Shah, R., Rosso, K., David Nathanson, S., 2014. Pathogenesis, prevention, diagnosis and treatment of breast cancer. World J. Clin. Oncol. 5, 283. https://doi.org/10.5306/wjco.v5.i3.283

Shailesh, S., Neelam, S., Sandeep, K., Gd, G., 2009. Liposomes : A review 2. J. Pharm. Res. 2,1163–1167.

Shanle, E.K., Xu, W., 2010. Selectively targeting estrogen receptors for cancer treatment. Adv. Drug Deliv. Rev. 62, 1265–1276. https://doi.org/10.1016/j.addr.2010.08.001

Sharma, A., Sharma, U.S., 1997. Liposomes in drug delivery: progress and limitations. Int. J. Pharm. 154, 123- 140. x

Sharma, A., Srivastava, B., Vijay, S.K., N, M.D., K, S.A., 2010. Liposomes: Present prospective and future challenges. Artic. Int. J. Curr. Pharm. Rev. Res. 1.

Shen, Y., Tang, H., Radosz, M., Van Kirk, E., Murdoch, W.J., 2008. pH-responsive nanoparticles for cancer drug delivery, in: Methods in Molecular Biology. Humana Press, pp. 183–216. https://doi.org/10.1007/978-1-59745-210-6_10/cover

Sheena, T.S., Balaji, P., Venkatesan, R., Akbarsha, M.A., Jeganathan, K., 2018. Functional evaluation of doxorubicin decorated polymeric liposomal curcumin: A surface tailored therapeutic platform for combination chemotherapy. New J. Chem. 42, 16608–16619. https://doi.org/10.1039/c8nj02406e

Shi, J., Kantoff, P.W., Wooster, R., Farokhzad, O.C., 2016. Cancer nanomedicine: progress, challenges and opportunities. Nat. Rev. Cancer. 17, 20–37. https://doi.org/10.1038/nrc.2016.108

Shi, G., Guo, W., Stephenson, S.M., Lee, R.J., 2002. Efficient intracellular drug and gene

delivery using folate receptor-targeted pH-sensitive liposomes composed of cationic/anionic lipid combinations. J. Control. Release. 80, 309–319. https://doi.org/10.1016/s0168-3659(02)00017-2

Shindikar, A., Singh, A., Nobre, M., Kirolikar, S., 2016. Curcumin and Resveratrol as Promising Natural Remedies with Nanomedicine Approach for the Effective Treatment of Triple Negative Breast Cancer. J. Oncol. 2016, 1-13. https://doi.org/10.1155/2016/9750785

Singh, B., Mundlamuri, R., Friese, T., Mundrigi, A., Handt, S., Loewe, T., 2017. Benchmarking of Sterilizing grade filters with liposome Filtration. PDA J. Pharm. Sci. Technol. 72, 223–235. https://doi.org/10.5731/pdajpst.2017.007757

Singh, R.P., Gangadharappa, H. V., Mruthunjaya, K., 2017. Phospholipids: Unique carriers for drug delivery systems. J. Drug Deliv. Sci. Technol. 39, 166–179. https://doi.org/10.1016/j.jddst.2017.03.027

Singh, V., Saunders, C., Wylie, L., Bourke, A., 2008. New diagnostic techniques for breast cancer detection. Futur. Oncol. 4, 501–513. https://doi.org/10.2217/14796694.4.4.501

Singh, M., Pilani, S., 2021. In vitro Drug Release Characterization Models. Int. J. Pharm. Stud. Res. 2, 77–84.

Singletary, S.E., 2003. Rating the Risk Factors for Breast Cancer. Ann. Surg. 237, 474–482. https://doi.org/10.1097/01.sla.0000059969.64262.87

Smith, M.C., Crist, R.M., Clogston, J.D., Mcneil, S.E., 2017. Zeta potential : a case study of cationic, anionic, and neutral liposomes. Anal. Bioanal. Chem. 409, 5779–5787. https://doi.org/10.1007/s00216-017-0527-z

Sneider, A., Jadia, R., Piel, B., VanDyke, D., Tsiros, C., Rai, P., 2016. Engineering Remotely Triggered Liposomes to Target Triple Negative Breast Cancer. Oncomedicine. 2, 1–13. https://doi.org/10.7150/oncm.17406

Soe, Z.C., Thapa, R.K., Ou, W., Gautam, M., Nguyen, H.T., Jin, S.G., Ku, S.K., Oh, K.T., Choi, H.G., Yong, C.S., Kim, J.O., 2018. Folate receptor-mediated celastrol and

irinotecan combination delivery using liposomes for effective chemotherapy. Colloids Surf. B. 170, 718–728. https://doi.org/10.1016/j.colsurfb.2018.07.013

Sohail, M.F., Javed, I., Hussain, S.Z., Sarwar, S., Akhtar, S., Nadhman, A., Batool, S., Irfan Bukhari, N., Saleem, R.S.Z., Hussain, I., Shahnaz, G., 2016. Folate grafted thiolated chitosan enveloped nanoliposomes with enhanced oral bioavailability and anticancer activity of docetaxel. J. Mater. Chem. B. 4, 6240–6248. https://doi.org/10.1039/c6tb01348a

Soleimani, A., Mirzavi, F., Nikoofal-Sahlabadi, S., Nikpoor, A.R., Taghizadeh, B., Barati, M., Soukhtanloo, M., Jaafari, M.R., 2022. CD73 downregulation by EGFR-targeted liposomal CD73 siRNA potentiates antitumor effect of liposomal doxorubicin in 4T1 tumor-bearing mice. Sci. Rep. 12, 1–17. https://doi.org/10.1038/s41598-022-14392-7

Song, J.L., Chen, C., Yuan, J.P., Sun, S.R., 2016. Progress in the clinical detection of heterogeneity in breast cancer. Cancer Med. 5, 3475–3488. https://doi.org/10.1002/cam4.943

Song, X., Zhang, M., Dai, E., Medicine, Y.L.-M., 2019, U., 2019. Molecular targets of curcumin in breast cancer. Mol. Med. Rep. 19, 23–29. https://doi.org/10.3892/mmr.2018.9665

Speth, P.A.J., van Hoesel, Q.G.C.M., Haanen, C., 1988. Clinical Pharmacokinetics of Doxorubicin. Clin. Pharmacokinet. 15, 15–31. https://doi.org/10.2165/00003088-198815010-00002

Stathopoulos, G.P., Boulikas, T., 2012. Lipoplatin Formulation Review Article. J. Drug Deliv. 2012, 1–10. https://doi.org/10.1155/2012/581363

Storm, G., Crommelin, D.J.A., 1998. Liposomes: quo vadis? Pharm. Sci. Techn. Today. 1, 19–31. https://doi.org/10.1016/S1461-5347(98)00007-8

Straubinger, R.M., Düzgünes, N., Papahadjopoulos, D., 1985. pH-sensitive liposomes mediate cytoplasmic delivery of encapsulated macromolecules. FEBS Lett. 179, 148–154. https://doi.org/10.1016/0014-5793(85)80210-6

Su, Y., Burnouf, P., Chuang, K., Chen, B., Cheng, T., Roffler, S.R., 2017. Conditional internalization of PEGylated nanomedicines by PEG engagers for triple negative breast cancer therapy. Nat. Commun. 8, 1–12. https://doi.org/10.1038/ncomms15507

Subbaram, S., Dipersio, C.M., 2011. Integrin α3β1 as a breast cancer target. Expert Opin. Ther. Targets. 15, 1197–1210. https://doi.org/10.1517/14728222.2011.609557

Sudimack, J.J., Guo, W., Tjarks, W., Lee, R.J., 2002. A novel pH-sensitive liposome formulation containing oleyl alcohol. Biochim. Biophys. Acta - Biomembr. 1564, 31–37. https://doi.org/10.1016/S0005-2736(02)00399-1

Sun, L., Deng, X., Yang, X., Li, Z., Wang, Z., Li, L., Wu, Q., Peng, F., Liu, L., Gong, C., 2014. Co-delivery of doxorubicin and curcumin by polymeric micelles for improving antitumor efficacy on breast carcinoma. RSC Adv. 4, 46737–46750. https://doi.org/10.1039/c4ra07453j

Sun, M., Su, X., Ding, B., He, X., Liu, X., Yu, A., Lou, H., Zhai, G., 2012. Advances in nanotechnology-based delivery systems for curcumin. Nanomed. 7, 1085–1100. https://doi.org/10.2217/nnm.12.80

Suri, S.S., Fenniri, H., Singh, B., 2007. Nanotechnology-based drug delivery systems. J. Occup. Med. Toxicol. 2, 1–6. https://doi.org/10.1186/1745-6673-2-16

Swietach, P., Vaughan-Jones, R.D., Harris, A.L., Hulikova, A., 2014. The chemistry, physiology and pathology of pH in cancer. Philos. Trans. R. Soc. B Biol. Sci. 369, 20130099. https://doi.org/10.1098/rstb.2013.0099

Taherian, A., Li, X., Liu, Y., Haas, T.A., 2011. Differences in integrin expression and signaling within human breast cancer cells. BMC Cancer. 11, 293–307. https://doi.org/10.1186/1471-2407-11-293

Tang, M., Svirskis, D., Leung, E., Kanamala, M., Wang, H., Wu, Z., 2019. Can intracellular drug delivery using hyaluronic acid functionalised pH-sensitive liposomes overcome gemcitabine resistance in pancreatic cancer? J. Control. Release. 305, 89–100. https://doi.org/10.1016/j.jconrel.2019.05.018

Tang, H., Chen, X., Rui, M., Sun, W., Chen, J., Peng, J., Xu, Y., 2014. Effects of surface displayed targeting ligand GE11 on liposome distribution and extravasation in tumor. Mol. Pharm. 11, 3242–3250. https://doi.org/10.1021/MP5001718

Tang, J., Howard, C.B., Mahler, S.M., Thurecht, K.J., Huang, L., Xu, Z.P., 2018. Enhanced delivery of siRNA to triple negative breast cancer cells in vitro and in vivo through functionalizing lipid-coated calcium phosphate nanoparticles with dual target ligands. Nanoscale. 10, 4258–4266. https://doi.org/10.1039/c7nr08644j

Teifel, M., Michaelis, U., Sauer, B., Bartelheim, K., Brunner, C., 2016. Use of cationic liposomes, which includes paclitaxel.DK2286794T3. Denmark

Thakur, K.K., Bordoloi, D., Kunnumakkara, A.B., 2018. Alarming Burden of Triple-Negative Breast Cancer in India. Clin. Breast Cancer. 18, e393–e399. https://doi.org/10.1016/j.clbc.2017.07.013

Thomas, E., Menon, J.U., Owen, J., Skaripa-Koukelli, I., Wallington, S., Gray, M., Mannaris, C., Kersemans, V., Allen, D., Kinchesh, P., Smart, S., Carlisle, R., Vallis, K.A., 2019. Ultrasound-mediated cavitation enhances the delivery of an EGFR-targeting liposomal formulation designed for chemo-radionuclide therapy. Theranostics. 9, 5595–5609. https://doi.org/10.7150/thno.34669

Thomas, H., Coley, H.M., 2003. Overcoming multidrug resistance in cancer: An update on the clinical strategy of inhibiting P-glycoprotein. Cancer Control. 10, 159–165. https://doi.org/10.1177/107327480301000207

Thorek, D.L.J., Elias, D.R., Tsourkas, A., 2009. Comparative analysis of nanoparticle-antibody conjugations: Carbodiimide versus click chemistry. Mol. Imaging. 8, 221–229. https://doi.org/10.2310/7290.2009.00021

Thorn, C.F., Oshiro, C., Marsh, S., Hernandez-Boussard, T., McLeod, H., Klein, T.E., Altman, R.B., 2011. Doxorubicin pathways: pharmacodynamics and adverse effects. Pharmacogenet. Genomics. 21, 440. https://doi.org/10.1097/fpc.0b013e32833ffb56

Tian, J.M., Ran, B., Zhang, C.L., Yan, D.M., Li, X.H., 2018. MDA-MB-231. Brazilian J. Med. Biol. Res. https://doi.org/10.1590/1414-431x20175612

Torácica, A. de la P., Morphol, A. y M.-I.J., 2006. Anatomy of the thoracic wall, axilla and breast. Int. J. Morphol.24, 691-704.

Torchilin, V., 2011. Tumor delivery of macromolecular drugs based on the EPR effect. Adv. Drug Deliv. Rev. 63, 131–135. https://doi.org/10.1016/j.addr.2010.03.011

Torchilin, V.P., 2014. Multifunctional, stimuli-sensitive nanoparticulate systems for drug delivery. Nat. Publ. Gr. 13, 813–827. https://doi.org/10.1038/nrd4333

Torchilin, V.P., Weissig, V., 2003. Liposomes : a practical approach, in: Liposomes. Oxford University Press, p. 396.

Torre, L.A., Bray, F., Siegel, R.L., Ferlay, J., 2015. Global Cancer Statistics , 2012. CA Cancer J Clin. 65, 87–108. https://doi.org/10.3322/caac.21262.

Trabert, B., Sherman, M.E., Kannan, N., Stanczyk, F.Z., 2019. Progesterone and breast cancer. Endocr. Rev. 41, 320–344. https://doi.org/10.1210/endrev/bnz001

Tsang, J.Y.S., Tse, G.M., 2020. Molecular Classification of Breast Cancer. Adv. Anat. Pathol. 27, 27–35. https://doi.org/10.1097/pap.0000000000000232

Turashvili, G., Brogi, E., 2017. Tumor heterogeneity in breast cancer. Front. Med. 4, 322799 https://doi.org/10.3389/fmed.2017.00227

Unsoy, G., Khodadust, R., Yalcin, S., Mutlu, P., and Gunduz, U., 2014. Synthesis of Doxorubicin loaded magnetic chitosan nanoparticles for pH responsive targeted drug delivery. Eur. J. Pharm. Sci. 62, 243–250. https://doi.org/10.1016/j.ejps.2014.05.021

Vaidya, A., Wang, H., Qian, V., Gilmore, H., Lu, Z.R., 2020. Overexpression of Extradomain-B Fibronectin is Associated with Invasion of Breast Cancer Cells. Cells. 9, 1–19. https://doi.org/10.3390/cells9081826

Van Der Meel, R., Oliveira, S., Altintas, I., Heukers, R., Pieters, E.H.E., Van Bergen En Henegouwen, P.M.P., Storm, G., Hennink, W.E., Kok, R.J., Schiffelers, R.M., 2013. Inhibition of tumor growth by targeted anti-EGFR/IGF-1R nanobullets depends on efficient blocking of cell survival pathways. Mol. Pharm. 10, 3717–3727. https://doi.org/10.1021/mp400212v

Van Deventer, P. V., Graewe, F.R., 2016. The Blood Supply of the Breast Revisited. Plast. Reconstr. Surg. 137, 1388–1397. https://doi.org/10.1097/prs.0000000000002048

Vaněk, Z., Tax, J., Komersová, I., Sedmera, P., Vokoun, J., 1977. Anthracyclines. Folia Microbiol. 22, 139–159. https://doi.org/10.1007/bf02881640

Vemuri, S., Rhodes, C.T., 1995. Preparation and characterization of liposomes as therapeutic delivery systems: a review. Pharm. Acta Helv. 70, 95–111. https://doi.org/10.1016/0031-6865(95)00010-7

Venkatasubbu, G.D., Ramasamy, S., Avadhani, G.S., Ramakrishnan, V., and Kumar, J., 2013. Surface modification and paclitaxel drug delivery of folic acid modified polyethylene glycol functionalized hydroxyapatite nanoparticles. Powder Technol. 235, 437–442. https://doi.org/10.1016/j.powtec.2012.11.003

Viale, G., 2012. The current state of breast cancer classification. Ann. Oncol. 23, 207–210. https://doi.org/10.1093/annonc/mds326

Videira, M., Reis, R.L., Brito, M.A., 2014. Deconstructing breast cancer cell biology and the mechanisms of multidrug resistance. Biochim. Biophys. Acta - Rev. Cancer 1846, 312–325. https://doi.org/10.1016/j.bbcan.2014.07.011

Vigevani, A., Williamson, M.J., 1981. Doxorubicin. Anal. Profiles drug Subst. 9, 245–274. https://doi.org/10.1016/s0099-5428(08)60143-4

Vikas, Mehata, A.K., Suseela, M.N.L., Behera, C., Kumari, P., Mahto, S.K., Muthu, M.S., 2022. Chitosan-alginate nanoparticles of cabazitaxel: Design, dual-receptor targeting and efficacy in lung cancer model. Int. J. Biol. Macromol. 221, 874–890. https://doi.org/10.1016/j.ijbiomac.2022.09.053

Vikas, Viswanadh, M.K., Mehata, A.K., Sharma, V., Priya, V., Varshney, N., Mahto, S.K., Muthu, M.S., 2021. Bioadhesive chitosan nanoparticles: Dual targeting and pharmacokinetic aspects for advanced lung cancer treatment. Carbohydr. Polym. 274, 118617. https://doi.org/10.1016/j.carbpol.2021.118617

Vinay, K., Abul, A., Jon, A., 2012. Robins and Corton Pathologic Basis of Disease, Saunders

Elsevier.

Vincenzi, B., Schiavon, G., Silletta, M., Santini, D., Tonini, G., 2008. The biological properties of cetuximab. Crit. Rev. Oncol. Hematol. 68, 93–106. https://doi.org/10.1016/j.critrevonc.2008.07.006

Vishvakrama, P., Sharma, S., 2014. liposomes: an overview. J. Drug Deliv. Ther. 0, 47–55. https://doi.org/10.22270/jddt.v0i0.843

Vogel, V.G., 2015. Epidemiology of Breast Cancer, Fifth Edit. ed, The Breast. Elsevier Inc. https://doi.org/10.1016/B978-0-323-35955-9.00015-5

Voinea, M., Simionescu, M., 2002. Designing of 'intelligent' liposomes for efficient delivery of drugs. J. Cell. Mol. Med. 6, 465–474. https://doi.org/10.1111/J.1582-4934.2002.TB00450.x

Vuong, D., Simpson, P.T., Green, B., Cummings, M.C., Lakhani, S.R., 2014. Molecular classification of breast cancer. Virchows Arch. 465, 1–14. https://doi.org/10.1007/S00428-014-1593-7

Wagner, A., Vorauer-Uhl, K., 2011. Liposome Technology for Industrial Purposes. J. Drug Deliv. 2011, 1–9. https://doi.org/10.1155/2011/591325

Waks, A.G., Winer, E.P., 2019. Breast Cancer Treatment: A Review. JAMA. 321, 288–300. https://doi.org/10.1001/jama.2018.19323

Wang, L., 2017. Early Diagnosis of Breast Cancer. Sensors. 17, 1572. https://doi.org/10.3390/s17071572

Wang, S., Hüttmann, G., Scholzen, T., Zhang, Z., Vogel, A., Hasan, T., Rahmanzadeh, R., 2016. A light-controlled switch after dual targeting of proliferating tumor cells via the membrane receptor EGFR and the nuclear protein Ki-67. Sci. Reports. 6, 1–9. https://doi.org/10.1038/srep27032

Wang, Y., Yu, J., Cui, R., Lin, J., Ding, X., 2016. Curcumin in Treating Breast Cancer: A Review. J. Lab. Autom. 21, 723–731. https://doi.org/10.1177/2211068216655524

Wang, H., Hu, L.D., Li, C., Zhang, J., Zhang, T., 2011. Increase of therapeutic activity of doxorubicin by long circulating liposomes in combination with curcumin. Pharmazie. 66, 871–874. https://doi.org/10.1691/ph.2011.1057

Wang, C., Han, Z., Wu, Y., Lu, X., Tang, X., Xiao, J., Li, N., 2021. Enhancing stability and anti-inflammatory properties of curcumin in ulcerative colitis therapy using liposomes mediated colon-specific drug delivery system. Food Chem. Toxicol. 151, 112123. https://doi.org/10.1016/j.fct.2021.112123

Wang, D., Veena, M.S., Stevenson, K., Tang, C., Ho, B., Suh, J.D., Duarte, V.M., Faull, K.F., Mehta, K., Srivatsan, E.S., Wang, M.B., 2008. Liposome-encapsulated curcumin suppresses growth of head and neck squamous cell carcinoma in vitro and in xenografts through the inhibition of nuclear factor κB by an AKT-independent pathway. Clin. Cancer Res. 14, 6228–6236. https://doi.org/10.1158/1078-0432.ccr-07-5177

Wei, Y., Davis, J., Bina, W.F., 2012. Ambient air pollution is associated with the increased incidence of breast cancer in US. Int. J. Environ. Health Res. 22, 12–21. https://doi.org/10.1080/09603123.2011.588321

Wei, X.Q., Zhu, J.F., Wang, X.B., Ba, K., 2020. Improving the Stability of Liposomal Curcumin by Adjusting the Inner Aqueous Chamber pH of Liposomes. ACS Omega. 5, 1120–1126. https://doi.org/10.1021/acsomega.9b03293

Weigelt, B., Geyer, F.C., Reis-Filho, J.S., 2010. Histological types of breast cancer: How special are they? Mol. Oncol. 4, 192–208. https://doi.org/10.1016/j.molonc.2010.04.004

Weigelt, B., Horlings, H.M., Kreike, B., Hayes, M.M., Hauptmann, M., Wessels, L.F.A., De Jong, D., Van De Vijver, M.J., Van't Veer, L.J., Peterse, J.L., 2008. Refinement of breast cancer classification by molecular characterization of histological special types. J. Pathol. 216, 141–150. https://doi.org/10.1002/path.2407

Wen, C., Fu, L., Huang, J., Dai, Y., Wang, B., Xu, G., Wu, L., Zhou, H., 2019. Curcumin reverses doxorubicin resistance via inhibition the efflux function of ABCB4 in doxorubicin-resistant breast cancer cells. Mol. Med. Rep. 19, 5162–5168. https://doi.org/10.3892/mmr.2019.10180

Wind, N.S., Holen, I., 2011. Multidrug Resistance in Breast Cancer: From In Vitro Models to Clinical Studies . Int. J. Breast Cancer. 2011, 1–12. https://doi.org/10.4061/2011/967419

Winters, S., Martin, C., Murphy, D., Shokar, N.K., 2017. Breast Cancer Epidemiology, Prevention, and Screening. Prog. Mol. Biol. Transl. Sci. 151, 1–32. https://doi.org/10.1016/bs.pmbts.2017.07.002

Wu, J., Lee, A., Lu, Y., Lee, R.J., 2007. Vascular targeting of doxorubicin using cationic liposomes. Int. J. Pharm. 337, 329–335. https://doi.org/10.1016/j.ijpharm.2007.01.003

Xie, H., Feng, S., Farag, M.A., Sun, P., Shao, P., 2021. Synergistic cytotoxicity of erianin, a bisbenzyl in the dietetic Chinese herb Dendrobium against breast cancer cells. Food Chem. Toxicol. 149, 111960. https://doi.org/10.1016/j.fct.2020.111960

Xie, Q., Deng, W., Yuan, X., Wang, H., Ma, Z., Wu, B., Zhang, X., 2018. Selenium-functionalized liposomes for systemic delivery of doxorubicin with enhanced pharmacokinetics and anticancer effect. Eur. J. Pharm. Biopharm. 122, 87–95. https://doi.org/10.1016/j.ejpb.2017.10.010

Yadav, D., Sandeep, K., Pandey, D., Dutta, R.K., 2017. Liposomes for Drug Delivery. J. Biotechnol. Biomater. 07. https://doi.org/10.4172/2155-952x.1000276

Yallapu, M.M., Jaggi, M., Chauhan, S.C., 2012. Curcumin nanoformulations: A future nanomedicine for cancer. Drug Discov. Today. 17, 71–80. https://doi.org/10.1016/j.drudis.2011.09.009

Yan, Y., Ding, H., 2020. Ph-responsive nanoparticles for cancer immunotherapy: A brief review. Nanomater. 10, 1–15. https://doi.org/10.3390/nano10081613

Yang, K.K., Kong, M., Wei, Y.N., Liu, Y., Cheng, X.J., Li, J., Park, H.J., Chen, X.G., 2013. Folate-modified-chitosan-coated liposomes for tumor-targeted drug delivery. J. Mater. Sci. 48, 1717–1728. https://doi.org/10.1007/s10853-012-6930-0

Yang, M., Yu, L., Guo, R., Dong, A., Lin, C., Zhang, J., 2018. A modular coassembly approach to all-in-one multifunctional nanoplatform for synergistic codelivery of doxorubicin and curcumin. Nanomaterials. 8, 1–18. https://doi.org/10.3390/nano8030167

Yang, Y., Zhao, Z., Xie, C., Zhao, Y., 2020. Dual-targeting liposome modified by glutamic hexapeptide and folic acid for bone metastatic breast cancer. Chem. Phys. Lipids. 228, 104882. https://doi.org/10.1016/j.chemphyslip.2020.104882

Yang, Y., Zuo, S., Li, L., Kuang, X., Li, J., Sun, B., Wang, S., He, Z., Sun, J., 2021. Iron-doxorubicin prodrug loaded liposome nanogenerator programs multimodal ferroptosis for efficient cancer therapy. Asian J. Pharm. Sci. 16, 784–793. https://doi.org/10.1016/j.ajps.2021.05.001

Yared, J.A., Tkaczuk, K.H.R., 2012. Update on taxane development: New analogs and new formulations. Drug Des. Devel. Ther. 6, 371–384. https://doi.org/10.2147/dddt.s28997

Yeh, C.C., Su, Y.H., Lin, Y.J., Chen, P.J., Shi, C.S., Chen, C.N., Chang, H.I., 2015. Evaluation of the protective effects of curcuminoid (Curcumin and bisdemethoxycurcumin)-loaded liposomes against bone turnover in a cell-based model of osteoarthritis. Drug Des. Devel. Ther. 9, 2285–2300. https://doi.org/10.2147/dddt.s78277

Yoncheva, K., Tzankov, B., Yordanov, Y., Spassova, I., Kovacheva, D., Frosini, M., Valoti, M., and Tzankova, V., 2020. Encapsulation of doxorubicin in chitosan-alginate nanoparticles improves its stability and cytotoxicity in resistant lymphoma L5178 MDR cells. J. Drug Deliv Sci Technol. 59, 101870. https://doi.org/10.1016/j.jddst.2020.101870

Yuan, J.D., ZhuGe, D.L., Tong, M.Q., Lin, M.T., Xu, X.F., Tang, X., Zhao, Y.Z., Xu, H.L., 2018. pH-sensitive polymeric nanoparticles of mPEG-PLGA-PGlu with hybrid core for simultaneous encapsulation of curcumin and doxorubicin to kill the heterogeneous tumour cells in breast cancer. Artif. Cells Nanomed Biotechnol. 46, 302–313. https://doi.org/10.1080/21691401.2017.1423495

Yuan, Y., Cai, T., Xia, X., Zhang, R., Chiba, P., Cai, Y., 2016. Nanoparticle delivery of anticancer drugs overcomes multidrug resistance in breast cancer. Drug Deliv. 23, 3350–3357. https://doi.org/10.1080/10717544.2016.1178825

Yuba, E., 2020. Development of functional liposomes by modification of stimuli-responsive materials and their biomedical applications. J. Mater. Chem. B. 8, 1093–1107. https://doi.org/10.1039/c9tb02470k

Yue, G., Wang, C., Liu, B., Wu, M., Huang, Y., Guo, Y., Ma, Q., 2020. Liposomes co-delivery system of doxorubicin and astragaloside IV co-modified by folate ligand and octa-arginine polypeptide for anti-breast cancer. RSC Adv. 10, 11573–11581. https://doi.org/10.1039/c9ra09040a

Zarrabi, Ali, Zarepour, Atefeh, Khosravi, Arezoo, Alimohammadi, Zahra, Thakur, V.K., Zarrabi, A ;, Zarepour, A ;, Khosravi, A ;, Alimohammadi, Z ;, Bhattarai, N., 2021. Synthesis of Curcumin Loaded Smart pH-Responsive Stealth Liposome as a Novel Nanocarrier for Cancer Treatment. Fibers. 9, 19. https://doi.org/10.3390/fib9030019

Zhang, H., 2017. Thin-film hydration followed by extrusion method for liposome preparation. Methods Mol. Biol. 1522, 17–22. https://doi.org/10.1007/978-1-4939-6591-5_2

Zhang, Z., Wang, J., Tacha, D.E., Li, P., Bremer, R.E., Chen, H., Wei, B., Xiao, X., Da, J., Skinner, K., Hicks, D.G., Bu, H., Tang, P., 2014. Folate Receptor α Associated With Triple-Negative Breast Cancer and Poor Prognosis. Arch. Pathol. Lab. Med. 138, 890–895. https://doi.org/10.5858/arpa.2013-0309-oa

Zhao, J., Stenzel, M.H., 2018. Entry of nanoparticles into cells: The importance of nanoparticle properties. Polym. Chem. 9, 259–272. https://doi.org/10.1039/c7py01603d

Zhao, X., Li, H., Lee, R.J., 2008. Targeted drug delivery via folate receptors. Expert Opin. Drug Deliv. 5, 309–319. https://doi.org/10.1517/17425247.5.3.309

Zhao, X., Chen, Q., Liu, W., Li, Y., Tang, H., Liu, X., Yang, X., 2014. Codelivery of doxorubicin and curcumin with lipid nanoparticles results in improved efficacy of chemotherapy in liver cancer. Int. J. Nanomedicine. 10, 257–270. https://doi.org/10.2147/ijn.s73322

Zhao, Y., Ren, W., Zhong, T., Zhang, S., Huang, D., Guo, Y., Yao, X., Wang, C., Zhang, W.Q., Zhang, X., Zhang, Q., 2016. Tumor-specific pH-responsive peptide-modified pH-sensitive liposomes containing doxorubicin for enhancing glioma targeting and anti-tumor activity. J. Control. Release. 222, 56–66. https://doi.org/10.1016/j.jconrel.2015.12.006

Zhou, S., Li, J., Xu, H., Zhang, S., Chen, X., Chen, W., Yang, S., Zhong, S., Zhao, J., Tang, J., 2017. Liposomal curcumin alters chemosensitivity of breast cancer cells to Adriamycin

via regulating microRNA expression. Gene. 622, 1–12. https://doi.org/10.1016/j.gene.2017.04.026

Zignani, M., Drummond, D.C., Meyer, O., Hong, K., Leroux, J.C., 2000. In vitro characterization of a novel polymeric-based pH-sensitive liposome system. Biochim. Biophys. Acta - Biomembr. 1463, 383–394. https://doi.org/10.1016/S0005-2736(99)00234-5

ABSTRACT

Name of the student: **Aliesha Moudgil**   Registration No: **10BB18J26025**
Faculty of Study: **Biological Sciences**   Year of Submission: **2023**
AcSIR academic centre/ CSIR Lab: **CSIR- National Chemical Laboratory, Pune**
Name of the Supervisor: **Dr. Bhushan P. Chaudhari**
Title of the thesis: **Synthesis and evaluation of unique liposomal formulations as a targeted drug delivery system for the management of breast cancer**

Breast cancer bagged 2.3 million of 19.3 million new cancer cases reported worldwide in 2020. Nanotechnological interventions supersede chemotherapy by increasing the bioavailability and pharmacokinetics of the drug and reducing non-specific accumulation, and the injectable dose. We synthesized curcumin (CUR) and doxorubicin (DOX) loaded liposomes surface functionalized with folate (FOL) and cetuximab (CET) against the folate receptors and epidermal growth factor receptors overexpressed on the triple negative breast cancer (TNBC) subtype.

We identified process parameters of the thin film hydration technique of liposomal synthesis and optimized 240 RPM rotation speed, 700 mm of Hg vacuum pressure, and 2 ml chloroform in the thin film formation step; 270 RPM rotation speed, PBS as an aqueous solvent, and 1 h hydration time in the thin film hydration step; 100 nm polycarbonate membrane and 10 extrusion passes in the downsizing step; 10 mg/ml lipids, 7: 3 molar ratio of phospholipid and cholesterol, and 1 mole % of 1, 2 stearoyl-sn-glycerol- phosphoethanolamine- polyethylene glycol (2000) (DSPE-mPEG2000) as intrinsic factors.

We optimized 1: 50 CUR: lipid ratio (wt. /wt.), 7:3 molar ratio of phospholipid and cholesterol, 1 mole % of DSPE-mPEG2000 and 5 extrusion passes for CUR liposomes, and 0.1 mg DOX and 5 extrusion passes for DOX liposomes. We surface functionalized the liposomal surface with FOL and CET to formulate single and dual tagged liposomes. We synthesized the pH responsive counterparts with the optimized values of the process parameters and intrinsic factors. Upon characterizing all the single and dual drug loaded liposomes, actively targeted formulations and pH responsive liposomes, we obtained a monodisperse population of spherical particles with size < 200 nm, CUR loaded successfully in the lipid bilayer and DOX in the aqueous core or water-lipid interface, FOL and CET tagged on the liposomal surface.

The *in-vitro* efficacy studies established excellent storage stability of 3 months for all the formulations. Both drugs exhibited a biphasic release pattern with CUR following the Gompertz model and DOX the Weibull model. The liposomal formulations displayed a higher uptake efficiency in the MCF-7 and MDA-MB-231 cell lines than the plain drugs. In the MDA-MB-231 cells, the non-responsive FOL-CET CUR-DOX liposomes exhibited an efficacy equivalent to the plain drugs. However, the pH-responsive counterpart was more effective than the MCF-7 cell line. Our results concur with the hypothesis that the combination of CUR and DOX and FOL and CET showed an enhanced anticancer potential in TNBC over the hormone-responsive cell lines.

Details of Publications

Research Article Emanating from thesis

1. **Moudgil, A.,** Chaudhari, B.P., 2023. Understanding Critical Aspects of Liposomal Synthesis for Designing the Next Generation Targeted Drug Delivery Vehicle. ChemistrySelect 8, 20230. https://doi.org/10.1002/slct.202302435

Other Research Articles

2. **Moudgil, A.,** Varma, S., Shinde, M.D., Vamkudoth, K.R., Sarkar, D.M., Shende, R.A., Amalnerkar, D., Chaudhari, B.P., 2022c. One-pot concurrent biosynthesis of biphasic CuxO (cuprous and cupric oxide) nanoparticles using leaf extract of Eichhornia crassipes and investigation of their potent healthcare applications. Emergent Mater. 2022 52 5, 323–333. https://doi.org/10.1007/s42247-022-00347-1

3. **Moudgil, A.,** Deval, A.S., Dharne, M.S., Sarkar, D.M., Choudhari, A.S., Chaudhari, B.P., 2021. Eichhornia crassipes Mediated Bioinspired Synthesis of Crystalline Nano Silver as an Integrated Medicinal Material: A Waste to Value Approach. J. Clust. Sci. 32, 391–404. https://doi.org/10.1007/s10876-020-01797-5

Review Articles

4. **Moudgil, A.,** Salve, R., Gajbhiye, V., Chaudhari, B.P., 2023. Challenges and emerging strategies for next generation liposomal based drug delivery: An account of the breast cancer conundrum. Chem. Phys. Lipids 250, 105258. https://doi.org/110.1016/j.chemphyslip.2022.105258

Book Chapters

5. **Moudgil, A.,** Jaiswal, N., Gajbhiye, K.R., Gajbhiye, V., Pawar, A.T., Chaudhari, B.P., 2022a. Hypoxia mediated targeted nanomedicine for breast cancer. Target. Nanomedicine Breast Cancer Ther. 369–406. https://doi.org/10.1016/B978-0-12-824476-0.00013-9

6. **Moudgil, A.,** Shende, R.A., Pawar, A.T., Gajbhiye, K.R., Gajbhiye, V., Chaudhari, B.P., 2022b. Quantum dots based vehicles for controlled drug release in conjunction with bio-

imaging, in: Stimuli-Responsive Nanocarriers. Academic Press, 197–236. https://doi.org/10.1016/B978-0-12-824456-2.00016-3

7. **Moudgil, A.,** Chaudhari, B.P., 2019. Fungi the crucial contributors for nanotechnology: A green chemistry perspective, in: Advancing Frontiers in Mycology and Mycotechnology: Basic and Applied Aspects of Fungi. Springer Singapore, 279–298. https://doi.org/10.1007/978-981-13-9349-5_11

Poster Presentation

1. **Moudgil, A.,** Chaudhari, B.P., Liposomal drug delivery system for breast cancer: Strike and Counterstrike. National science day celebration held during February, 2021 at CSIR-National Chemical Laboratory, Pune, India.

ChemistrySelect

Research Article
doi.org/10.1002/slct.202302435

**Chemistry
Europe**
European Chemical
Societies Publishing

Understanding Critical Aspects of Liposomal Synthesis for Designing the Next Generation Targeted Drug Delivery Vehicle

Aliesha Moudgil[a, b] and Bhushan P. Chaudhari*[a, b]

We identified process parameters of the thin film hydration technique and intrinsic factors to synthesize liposomes for drug delivery. The thin film formation step impacted the nature of the lipid layer, and we optimized 240 RPM rotation speed, 700 mm of Hg vacuum pressure, and 2 ml of chloroform as the organic solvent. The hydration step controlled the particle specifications, and we optimized 270 RPM rotation speed, PBS as the hydrating medium, and 1 h hydration time. We obtained a comparatively smaller liposomal population with a lower size distribution just after hydrating the lipid layer that required milder downsizing steps −10 extrusion passes through a single polycarbonate membrane. The intrinsic factors including the concentrations and molar ratio of lipids affected the synthesis steps and the particle specifications. Characterization of liposomes by analytical techniques confirmed the synthesis of a monodisperse population with hydrodynamic diameter < 150 nm, moderate stability, spherical morphology, and high thermal and storage stability. This comprehensive study defines the role of every parameter, provides a mechanistic insight into synthesis that is supported by experimental data, and helps tune specific parameters to synthesize liposomes for drug delivery or any application with desired specifications.

Introduction

Dr. Alec D. Bangham and R. W. Horne discovered some bilayer structures upon negatively staining dry phospholipids in 1961.[1] Today these structures are known as liposomes, a name coined by Gerald Weismann,[2] and Gregory Gregordiadis was the first to explore them as drug delivery vehicles.[3] Phospholipids constitute a major portion with cholesterol (CHOL) as a secondary component to form a lipid bilayer that self-encloses into spherical structures;[4] the bilayer region incorporates hydrophobic drugs, and the enclosed aqueous unit or the water-lipid interface incorporates hydrophilic drugs.[5] These conventional liposomes transformed into stealth liposomes by ligating hydrophilic polymers such as polyethylene glycol (PEG) on the surface of liposomes – PEGylated liposomes.[6] This creates a stearic barrier that evades opsonization, escapes the reticuloendothelial system (RES), prolongs the blood circulation time, and reduces the clearance rates.[7] Stealth liposomes are remodeled to targeted liposomes by functionalizing the surfaces with ligands (such as antibodies, peptides, carbohydrates, and folic acid) that have high affinity towards receptors overexpressed on the target cells.[8] This approach of active targeting allows liposomes to accumulate in the tumor cells in large numbers.[9]

[a] A. Moudgil, Dr. B. P. Chaudhari
     Biochemical Sciences Division
     CSIR-National Chemical Laboratory
     Dr. Homi Bhabha Road, Pashan, Pune – 411008, India
     bp.chaudhari@ ncl.res.in

[b] A. Moudgil, Dr. B. P. Chaudhari
     Academy of Scientific and Innovative Research (AcSIR)
     Ghaziabad – 201002, India
     bp.chaudhari@ ncl.res.in

Laboratory scale techniques such as ether injection, ethanol injection, reverse-phase evaporation, and detergent removal techniques synthesize heterogeneous liposomes, expose drugs to organic solvents (that alters their biological and functional attributes), dilute the liposomes, and present difficulty in the removal of organic solvents;[10,11] the thin film hydration technique overcomes these shortcomings and is a popular approach.[12] These methods fabricate multilamellar vesicles (MLVs)/large unilamellar vesicles (LUVs) that require size reduction to create a homogenous population in a ~50–200 nm size range for biomedical applications (optimum for drug delivery).[13] The risk of clearance by RES rises with an increase in the particle size, thus smaller particles are superior drug delivery vehicles.[14] These particles can extravasate through tumor vascular defects and accumulate through an enhanced permeation and retention (EPR) effect.

Liposomes are also characterized by polydispersity index (PDI) and zeta potential: PDI for drug delivery vehicles should be less than 0.3 for a monodisperse population;[15] zeta potential depends on the surface properties of liposomes and is sensitive to variations in the pH, viscosity, ionic strength, and temperature of the solvent.[16] Zeta potential values ranging from ±0–10 mV, ±10–20 mV, ±20–30 mV, >30 mV, and >60 mV indicate unstable formulations, relative stability, moderate stability, good stability, and excellent stability respectively of the formulations.[17,18] Thus, size, PDI, and zeta potential – the three cornerstones – should be optimized to formulate liposomes for drug delivery.

In this study, we identified and optimized process parameters of the thin film hydration technique and intrinsic factors to synthesize liposomes for drug delivery. We assessed rotation speed, vacuum pressure, and type and volume of organic solvent in the thin film formation step; rotation speed,

ChemistrySelect

Research Article
doi.org/10.1002/slct.202302435

Chemistry Europe
European Chemical
Societies Publishing

hydrating medium, and hydration time in the thin film hydration step; number of extrusion passes, and number of polycarbonate membranes in the downsizing step. Intrinsic factors included the molar ratio and concentration of lipids. We characterized these liposomes by various analytical techniques. This all-inclusive study provides mechanistic insight into liposomal synthesis, specifies the role of every process and intrinsic factor, and helps modulate precise parameters to synthesize liposomes with desired specifications for varied applications.

Results and Discussion

The thin film hydration method involves two steps: organic solvent containing dissolved lipids is evaporated to form a lipid layer on the walls of the round bottom flask (RBF) in the thin film formation step; the lipid layer is hydrated with an aqueous solvent in the thin film hydration step. Successful hydration generates a turbid suspension confirming the synthesis of liposomes, and a rise in turbidity indicates larger particles.[19] Incomplete hydration (with most of the layer attached to the flask after hydration) also produces a less turbid suspension that signifies a low concentration of liposomes.

Identified parameters from the thin film hydration method, the downsizing step, and the intrinsic factors can affect the synthesis process and the particle specifications. We investigated the process parameters with a 1:1 molar ratio of lipids, as the advisable limit of CHOL to synthesize liposomes is $\leq 50\%$.[20] We intended to optimize the process parameters to create a monodisperse population of smaller particles just after the hydration step to avoid severe downsizing steps.

Synthesis of Liposomes

Factors affecting the thin film formation step

In our study, the rotation speed considerably affected the nature of the lipid layer: 30 and 60 RPM formed a non-uniform layer on the walls and bottom of the RBF that hydrated incompletely, and generated a non-turbid liposomal suspension; 120 and 150 RPM created a non-uniform layer on the walls and the base of the RBF that hydrated better, and produced a suspension with increased turbidity; 240 and 270 RPM formed a perfect ring-shaped and uniform layer on the RBF walls that hydrated completely, and achieved a highly turbid liposomal suspension. Thus, higher rotation speeds construct uniform lipid layers on the RBF walls that hydrate smoothly and produce a highly turbid liposomal suspension – this confirms a lower lipid loss.

The hydrodynamic diameter and PDI ranged from 212.86 ± 21.69 to 256.11 ± 4.54 nm, and 0.34 ± 0.07 to 0.46 ± 0.1 respectively; the zeta potential values indicated moderate stability and spanned from -20.55 ± 0.95 to -24.84 ± 0.68 mV (Table 1). We optimized 240 RPM rotation speed based on the nature of the lipid layer, the level of hydration, and the turbidity of the

suspension, as the DLS analysis showed insignificant change in the particle specifications.

Vacuum pressure also substantially affected the lipid layer (Figure 1a–g): 100, 200, 300, and 400 mm of Hg vacuum pressure created a non-uniform and patchy layer in more than 30 min; 500 and 600 mm of Hg of vacuum pressure cast a uniform layer within 30 min; 700 mm of Hg of vacuum pressure formed the most uniform layer within 30 min that hydrated most easily, and yielded a highly turbid suspension. Thus, reduced vacuum pressure develops a thin and uniform layer that can hydrate effectively.

Chloroform and 9:1 v/v ratio of chloroform: methanol constituted a uniform and thin lipid layer on the RBF walls that hydrated successfully; but the 2:1 v/v ratio of chloroform: methanol formed white crystals on the lipid layer that hydrated partially (Figure 1h). The Dynamic light scattering (DLS) analysis (Table 1) shows that the hydrodynamic diameter (p-value = 0.04) and PDI (p value = 0.02) significantly reduced with chloroform over the other two solvents, and the zeta potential tags all liposomes with moderate stability. CHOL formed crystals in the presence of methanol, and incorporated poorly in the liposomes, resulting in variations in size and PDI. Thus, it is advised to use chloroform or a higher volume of chloroform with methanol.
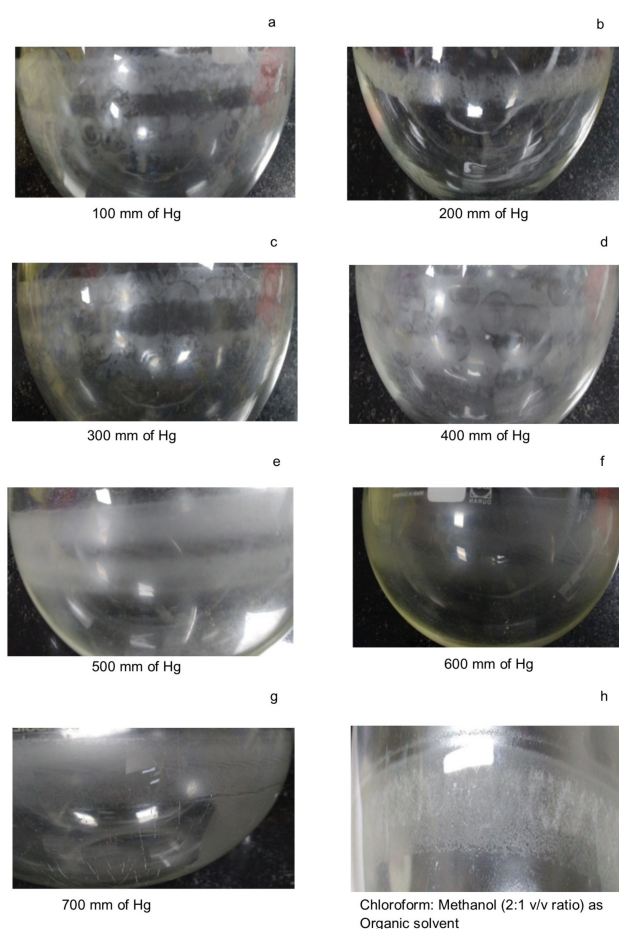

Figure 1. Effect of vacuum pressure (a–g) and 2:1 v/v ratio of chloroform:methanol (h) on the formation of lipid layers.

ChemistrySelect

Research Article
doi.org/10.1002/slct.202302435

Chemistry
Europe
European Chemical
Societies Publishing

Table 1. Factors affecting the thin film formation and hydration step.			
Thin film formation- Rotation Speed			
Rotation Speed (RPM)	Average Hydrodynamic Diameter (nm)	Average PDI	Average Zeta Potential (mV)
30	235.74 ± 12.01	0.45 ± 0.13	−20.55 ± 0.95
60	243.57 ± 58.62	0.43 ± 0.17	−21.95 ± 3.50
120	247.47 ± 7.77	0.46 ± 0.10	−21.30 ± 1.80
150	256.11 ± 4.54	0.41 ± 0.02	−23.58 ± 1.58
240	212.86 ± 21.69	0.34 ± 0.07	−24.84 ± 0.68
270	214.19 ± 21.76	0.34 ± 0.09	−22.51 ± 2.18
Thin film formation – Type of Organic Solvent			
Chloroform	212.86 ± 21.69	0.34 ± 0.07	−24.84 ± 0.68
Chloroform:Methanol (2:1)	409.54 ± 107.46	0.53 ± 0.03	−18.04 ± 2.36
Chloroform:Methanol (9:1)	277.87 ± 31.68	0.44 ± 0.03	−19.26 ± 0.69
Thin film hydration – Rotation speed			
30	587.72 ± 32.69	0.57 ± 0.01	−22.89 ± 0.23
60	588.99 ± 51.84	0.90 ± 0.16	−22.62 ± 1.19
120	354.83 ± 26.96	0.69 ± 0.19	−24.96 ± 0.75
240	282.07 ± 80.22	0.47 ± 0.10	−23.79 ± 0.49
270	212.86 ± 21.69	0.34 ± 0.07	−24.84 ± 0.67
Thin film hydration – Hydrating medium			
PBS	212.86 ± 21.69	0.34 ± 0.07	−24.84 ± 0.68
Deionized water	416.80 ± 85.42	0.77 ± 0.22	−65.16 ± 3.57
Double distilled water	451.91 ± 19.07	0.91 ± 0.23	−59.77 ± 2.24
Thin film hydration – Hydration time			
15	326.59 ± 47.83	0.52 ± 0.02	−25.56 ± 1.49
30	272.66 ± 27.13	0.45 ± 0.03	−25.64 ± 1.22
60	232.94 ± 10.69	0.34 ± 0.06	−24.71 ± 2.03
120	238.42 ± 44.93	0.29 ± 0.05	−23.90 ± 1.74

The volume of chloroform also created visible differences: 2 mL chloroform constituted a uniform and thin layer that hydrated completely, and generated a highly turbid liposomal suspension; 5 and 10 ml chloroform developed a broad layer from the walls to the base of the RBF that hydrated partially, and produced a less turbid liposomal suspension.

We experimented with RBFs of varied volumes (500, 250, and 50 ml), and noted negligible changes in the nature of the lipid layer, level of hydration, and turbidity of the liposomal suspension; this was attributed to the lower volume of chloroform optimized to create a thin and uniform lipid layer. With higher chloroform volumes, we noticed a thick, broad, and non-uniform layer in 50 ml RBFs, and a broad and non-uniform layer in 250 and 500 ml RBFs that hydrated partially to yield a less turbid liposomal suspension.

A thin and uniform layer hydrates efficiently, thus it is crucial to optimize factors impacting the lipid layer.[19] Particles obtained with a hydrodynamic diameter > 200 nm and PDI > 0.3 can be downsized, but we omitted the downsizing step to optimize liposomes with the lowest hydrodynamic diameter and PDI values.

Factors affecting the thin film hydration step

Unlike the thin film formation step that influenced the nature of the lipid layer, the hydration step controlled the particle specifications. We noted a gradual and significant decrease in the hydrodynamic diameter (p-value = < 0.0001) from 587.72 ± 32.69 to 212.86 ± 21.69 nm (Table 1) on increasing the rotation speed from 30 to 270 RPM. Reduced speeds produced a heterogeneous population (PDI values > 0.3), and the polydispersity significantly decreased (p-value = 0.0029) at higher rotation speeds. The zeta potential values defined all the particles with moderate stability.

Phospholipids form sheets in an aqueous solvent that enclose to reduce the energy gap between the hydrophobic and hydrophilic phases, and maintain a thermodynamic equilibrium; these spherical structures have higher stability due to low surface tension.[20] Hydrophobic interactions form liposomes; van der Waals forces keep the hydrocarbon chains together, and strengthen the bilayer; hydrogen bonds and polar interactions between the aqueous solvent and lipid polar head groups stabilize the particles.[5]

ChemistrySelect

Research Article
doi.org/10.1002/slct.202302435

Chemistry Europe
European Chemical
Societies Publishing

During hydration with an aqueous solvent, the outer lipid layers swell, and the solvent leaks into the subsequent inner layers that also swell; vigorous agitation during this process allows bilayer structures to form and suspend in the aqueous solvent.[21] The intensity of agitation influences the particle size; intense and vigorous hydration (higher rotation speeds) forms a smaller and homogenous population, as also corroborated in our study.[22]

We observed the impact of the hydrating solvent on liposomes: phosphate buffer saline (pH 7.4) (PBS) hydrated the lipid layers completely in 1 h, and formed a turbid liposomal suspension; deionized and doubled distilled water hydrated the lipid layers in 2 h to achieve equivalent turbidity and hydration – different molar ratios of lipids could be hydrated in lesser time. Liposomes formed in PBS were significantly smaller (p value = 0.0027) with lower PDI values (p value = 0.0241) (Table 1).

PBS imparted moderate stability to the liposomes with a zeta potential of -24.84 ± 0.68 mV and deionized and double distilled water conferred excellent stability to the liposomes with a zeta potential of -65.16 ± 3.57 and -59.77 ± 2.24 mV respectively. This discrepancy corresponds to the presence of salts in PBS that lower the negative zeta potential.[23] We optimized PBS based on the reduced particle size and PDI values despite moderate stability; PBS is also widely used because its ionic potential and osmotic potential are analogous to the human blood. However, PEG provides stearic stability to stealth liposomes that overpowers this reduced electrical stability in PBS.[24]

The hydration time illustrated a considerable variation in the hydration level, and the particle specifications: 15 and 30 min of hydration produced non-turbid and slightly turbid suspensions respectively due to the partial hydration of just the outer lipid layers; 60 and 120 min produced highly turbid suspension due to the complete hydration of the lipid layer. The hydrodynamic diameter (p-value = 0.03) and PDI (p-value = 0.01) values significantly reduced with 60 min of hydration (Table 1), and the zeta potential values presented moderate stability -as all the layers were hydrated with PBS. Sufficient hydration time ensures complete hydration and fabricates a homogenous suspension of smaller liposomes.

Hydration speed determines the particle size and size distribution; different hydrating mediums impart varying levels of stability to the particles; hydration time affects the level of hydration, size, and PDI of the particles. Thus, it is essential to optimize the process parameters of the thin film hydration step to control the particle specifications.

Factors affecting the downsizing step

Liposomes synthesized after the hydration step are unfit for drug delivery as the hydrodynamic diameter is > 200 nm and PDI > 0.3, and require downsizing by probe sonication, water bath sonication, or extrusion.[25] Probe sonication reduces the particle size but leaches titanium that requires an additional filtration step, and elevates the temperature that adversely affects the integrity of the liposomes.[26] Water bath sonication decreases the particle sizes but generates a heterogeneous population -with high PDI values.[19] Extrusion significantly lowers the size and PDI, is reproducible, can be rapidly executed, and is gentler on the liposomes as compared to other techniques.[27] We sonicated the liposomes in a water bath before extrusion to downsize the particles in our study.

We optimized the extrusion process by varying the number of extrusion passes, and the number of polycarbonate membranes. The hydrodynamic diameter significantly reduced from 161.69 ± 8.85 to 133.16 ± 8.07 nm (p-value = 0.02) for single, and 163.43 ± 16.18 to 127.64 ± 3.62 nm (p-value = 0.02) for double polycarbonate membranes (Table 2) on increasing the extrusion passes from 1 to 20; the PDI values reduced significantly from 0.16 ± 0.02 to 0.06 ± 0.01 (p-value = 0.001) for single and 0.12 ± 0.02 to 0.06 ± 0.01 (p-value = 0.01) for double polycarbonate membranes on increasing the extrusion passes from 1 to 20. But the size and PDI remained unchanged from 10 to 20 extrusion passes. We observed that increasing the number of polycarbonate membranes to 2, and the extrusion passes to 20 was unnecessary for size reduction.

Our data confirms instances from the literature of synthesizing particles greater than 100 nm even after extrusion through 100 nm polycarbonate membranes.[27] We optimized the process parameters that synthesized comparatively smaller liposomes just after the hydration step that were easily downsized through a 100 nm polycarbonate membrane; but with unoptimized process parameters, the thin film hydration technique synthesizes MLVs/LUVs that require a series of polycarbonate membranes of varied pore sizes for downsizing.

Effect of Intrinsic factors

Intrinsic factors include the concentrations and molar ratio of the lipids. We investigated the process parameters using a 1:1 molar ratio of L alpha phosphatidylcholine (PC): CHOL with a 10 mg/ ml concentration of each lipid, and 20 mg of total lipids. Upon varying the lipid concentration (10, 20, and 30 mg/ml), we observed disparity in the nature of the lipid layer and its hydration: 10 mg/ml concentration of lipids (amounting to 20 mg of total lipids) created a thin and uniform lipid layer on

Table 2. Factors affecting the downsizing step of liposomes.

Extrusion passes	Polycarbonate membranes	Average Hydrodynamic Diameter (nm)	Average PDI
1	1	161.69 ± 8.85	0.16 ± 0.02
5		148.21 ± 11.61	0.09 ± 0.01
10		133.94 ± 3.73	0.06 ± 0.01
20		133.16 ± 8.07	0.06 ± 0.01
1	2	163.43 ± 16.18	0.12 ± 0.02
5		137.76 ± 5.26	0.06 ± 0.01
10		137.78 ± 5.41	0.06 ± 0.02
20		127.64 ± 3.62	0.06 ± 0.01

ChemistrySelect

Research Article
doi.org/10.1002/slct.202302435

Chemistry Europe
European Chemical
Societies Publishing

the RBF walls that hydrated readily within 1 h; but 20 and 30 mg/ ml of lipids (amounting to 40 and 60 mg of total lipids respectively) developed a thick lipid layer that partially hydrated in 1 h. Thus, higher lipid concentrations form thicker layers that hydrate incompletely.

Upon varying the PC: CHOL ratio (1:1, 3:2, 7:3, 4:1, 9:1, and 1:0) – the ratios exhibit a decrease in the CHOL concentration from 50% and an equivalent increase in the PC concentration –[28] the hydrodynamic diameter significantly decreased on lowering the CHOL concentration from 50 to 30% (p-value = 0.01), and from 30 to 0% (p-value = 0.04) (Figure 2a). We recorded hydrodynamic diameters of 149.67 ± 2.4, 145.16 ± 1.67, 129.57 ± 7.36, 122.62 ± 6.80, 120.19 ± 4.04 and 113.6 ± 5.34 nm for 1:1, 3:2, 7:3, 4:1, 9:1 and 1:0 molar ratios respectively.

CHOL at lower concentrations (4:1 and 9:1) imparts flexibility and induces fragility in the bilayers decreasing the particle size; at higher concentrations (1:1 and 3:2), CHOL provides rigidity to the bilayers increasing the particle size.[29] All the batches were monodisperse with PDI < 0.1 due to the effective downsizing. The 7:3 molar ratio of PC: CHOL characterized the liposomes with optimum size, PDI, and appropriate CHOL concentration for drug delivery; these outcomes coincide with previously reported studies and are beneficial for higher drug encapsulation.[30]

We optimized the PEGylated liposomes by varying the concentration of 1, 2-distearoyl-sn-glycero-3-phosphoethanolamine-*N*-[methoxy (polyethylene glycol)-2000] (DSPE-mPEG2000) (1, 3, and 5 mole% with respect to lipids). During synthesis, DSPE-mPEG2000 incorporates in either leaflet of the bilayer and can project outwards from the liposomal surface and into the internal aqueous core. The particle size decreased significantly (p-value = 0.001) on increasing the DSPE-mPEG2000 concentration from 1 and 3% to 5% (Figure 2b); we recorded the hydrodynamic diameter at 119.94 ± 1.23, 118.03 ± 1.19 and 103.71 ± 2.92 nm for 1, 3 and 5 mole% respectively. The PDI values suggest monodispersity, and the zeta potential values changed to -7.55 ± 0.53, -5.02 ± 4.04, and -6.63 ± 0.13 mV for 1, 3 and 5 mole% of DSPE-mPEG2000.

The optimization of the process and intrinsic parameters concludes: (a) high rotation speed (240 RPM), reduced vacuum pressure (700 mm of Hg), and less volume (2 ml) of chloroform as the organic solvent create a thin and uniform lipid layer; (b) high rotation speed during hydration (270 RPM) yields smaller particles, the hydrating medium governs the particle size and stability of the particles (PBS was optimized in our study), and the hydration time (1 h optimized) is crucial for complete hydration; (c) Extrusion through a 100 nm polycarbonate membrane with 10 passes effectively downsized the liposomes; (d) 10 mg/ml of lipids formed the most uniform layer, and 7:3 molar ratio of the PC: CHOL and 1 mole% of DSPE-mPEG2000 formulated liposomes with desired specifications. Liposomes formed with these optimized values were further characterized.

Characterization of Liposomes

Hydrodynamic diameter, PDI, and Zeta potential

The DLS graph recorded the hydrodynamic diameter and PDI for liposomes after hydration at 221.7 nm and 0.32 respectively, for liposomes after extrusion at 135.1 nm and 0.08 respectively, and for PEGylated liposomes at 133 nm and 0.07 respectively (Figure 2). A high-intensity peak at 244.3 nm and a low-intensity peak at 4205 nm for liposomes after hydration, and single sharp peaks for liposomes after extrusion (non-PEGylated and PEGylated) confirm the size and PDI disparity of the two formulations.

The zeta potential of -24.84 ± 0.67 mV characterizes the liposomes with moderate stability; PC, a neutral lipid, orients its choline head to project the phosphate groups from the bilayer towards the external aqueous environment to provide a negative zeta potential, that is also facilitated by CHOL.[31,32] The significant shift in zeta potential for the PEGylated liposomes to -8.36 ± 0.99 mV confirms the surface functionalization with PEG that shields and reduces the negative charge of PC – as also corroborated by other studies.[33,34] The data highlights the substantial role of optimizing the process parameters to synthesize smaller liposomes just after the hydration step, and the significance of downsizing to create a monodisperse population of smaller liposomes.
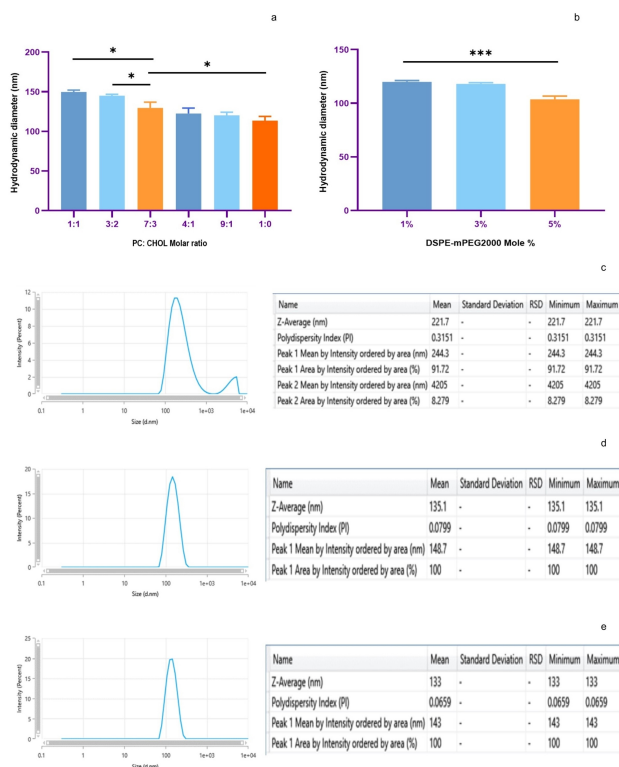

Figure 2. Effect of the molar ratio of PC and CHOL (a) and DSPE-mPEG2000 concentration (b) on the size of liposomes; DLS graph for liposomes after hydration (c), liposomes after extrusion (d), and PEGylated liposomes (e).

ChemistrySelect

Research Article
doi.org/10.1002/slct.202302435

Chemistry Europe
European Chemical
Societies Publishing

Morphology of Liposomes

The high-resolution transmission electron microscopy (HRTEM) images at 100 (Figure 3a) and 20 nm (Figure 3b) magnification show particles with spherical morphology and smooth surfaces. These spherical particles are accompanied by oval and irregular structures that occur due to membrane reorganization or deformation during the dehydration step of sample preparation.[35] Clumping of particles might occur after the sample drop is cast on the copper grid and air dried. A disparity in the image clarity in Figure 3c arises as the samples are diluted in PBS compared to the other samples in deionized water.

Liposomes are dynamic structures that require an aqueous environment to persist which is a major restraint while imaging

with conventional electron microscopy techniques. The sample preparation method involves drying, staining, and fixation of liposomes that result in vesicle reorganization.[36] CryoTEM imaging overcomes these drawbacks by imaging the particles in their native environment, thus is suitable for the sensitive and dynamic nature of liposomes.

Fourier transform infrared spectroscopy (FTIR)

The FTIR spectral profiles (Figure 4) present the characteristic peaks of PC, CHOL, DSPE-mPEG2000, liposomes after hydration and extrusion, and PEGylated liposomes after hydration and extrusion). PC shows a broad peak at 3300 cm^{-1} corresponding to the OH stretching vibration; peaks at 2922 and 2853 cm^{-1} correspond to the antisymmetric and symmetric CH stretching vibrations, respectively; a prominent peak at 1736 cm^{-1} is for the C=O (ester) stretching vibration, at 1651 cm^{-1} for C=C stretching vibration, and at 1463 and 1377 cm^{-1} for CH$_2$ and CH$_3$ bending vibrations. The peaks for the head group appear at 1225 and 1057 cm^{-1} for the PO$_2^-$ antisymmetric and symmetric stretching vibrations, respectively. The peak at 829 cm^{-1} corresponds to the P–O stretching vibration.[37,38]

Characteristic peaks for CHOL appear at 2935, 2896, and 2859 cm^{-1} for the CH stretching vibration in methyl and cyclic hydrocarbons; peaks at 1461 and 1371 cm^{-1} correspond to CH bending and CH$_2$ and CH$_3$ bending vibrations, respectively.[39] The characteristic peaks for DSPE-mPEG2000 appear at 2916, 2885, 1736, 1467, 1240, and 1060 cm^{-1} for antisymmetric and symmetric CH stretching, C=O (ester) stretching, CH$_2$ bending, PO$_2^-$ antisymmetric, and symmetric stretching, respectively.[40]

We compared the FTIR spectral profiles for liposomes after hydration and extrusion with PC (Figure 4b): a broad peak at approximately 3368 cm^{-1} corresponds to the OH stretching vibration; the peaks for the CH antisymmetric and symmetric stretching vibrations slightly shifted to 2924 and 2856 cm^{-1} respectively; the peak for C=O (ester) stretching vibration appear at 1736 cm^{-1}; the peaks for C=C stretching, CH$_2$ bending, and CH$_3$ bending vibration shifted to 1652, 1459 and 1372 cm^{-1} respectively. The peaks for the head group region shifted to 1229 cm^{-1} for PO$_2^-$ antisymmetric vibration, and to 1060 and 1061 cm^{-1} for the symmetric stretching vibrations of liposomes after hydration and extrusion respectively. The peak for P–O stretching shifted to 839 and 842 cm^{-1} for liposomes after hydration and extrusion.[41]

For PEGylated liposomes after hydration and extrusion (Figure 4c), a broad peak appears at approximately 3360 cm^{-1} representing the OH stretching vibration; the peaks for CH antisymmetric and symmetric stretching vibrations shifted to 2924 and 2856 cm^{-1} respectively; C=O (ester) stretching and C=C stretching vibration appear at 1736 and 1651 cm^{-1} respectively; the peaks corresponding to CH$_2$ bending vibrations shifted to 1459 and 1460 cm^{-1} formulation after hydration and after extrusion; for the peak for CH$_3$ bending vibration shifted to 1372 cm^{-1}. The PO$_2^-$ antisymmetric and symmetric stretching vibrations shifted to 1228 and 1060 cm^{-1}, respectively, for the PEGylated liposomes after hydration and at 1228 and
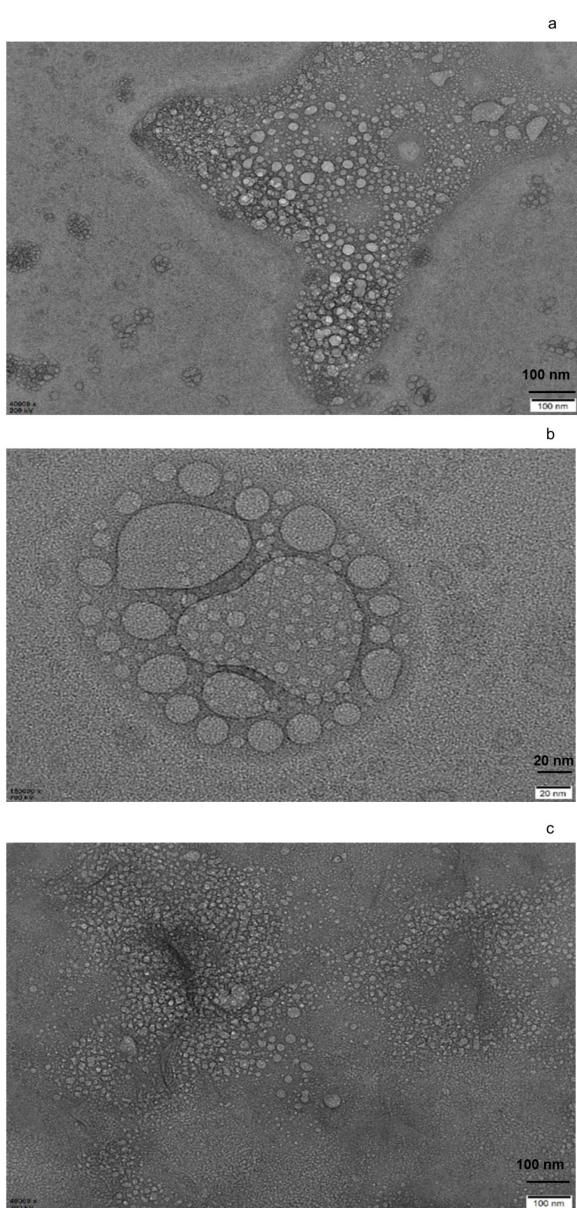

Figure 3. HRTEM images of liposomes at 100 nm magnification (a), at 20 nm magnification (b), and liposomes in PBS at 100 nm magnification (c).

ChemistrySelect

Research Article
doi.org/10.1002/slct.202302435

Chemistry Europe
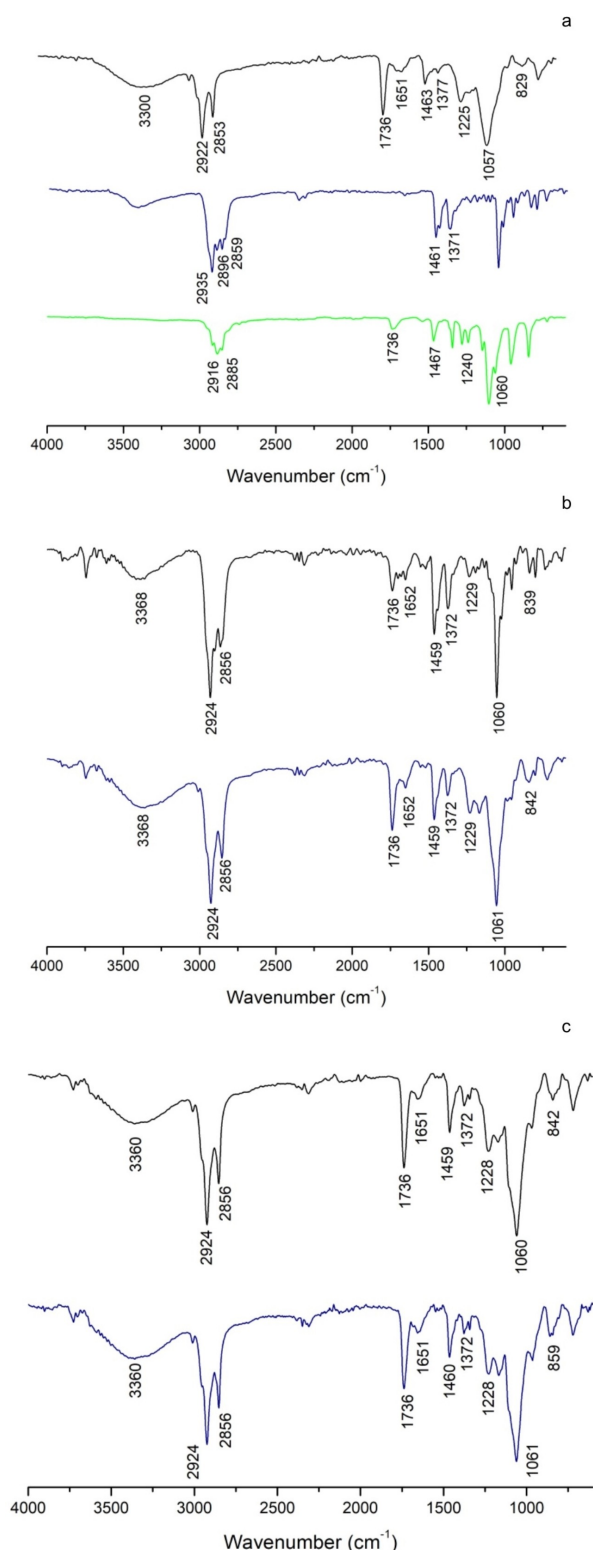European Chemical
Societies Publishing

Figure 4. FTIR spectral profiles of PC (black), CHOL (blue), and DSPE-mPEG2000 (green) (a); hydrated liposomes (black) and extruded liposomes (blue) (b); hydrated PEGylated liposomes (black) and extruded PEGylated liposomes (blue) (c).

$1061 \ cm^{-1}$ respectively for PEGylated liposomes after extrusion. The peak for P–O stretching shifted to 842 and $859 \ cm^{-1}$ for liposomes after hydration and extrusion.

The spectral profiles of liposomes after hydration and after extrusion remain unchanged, and for the non-PEGylated and PEGylated liposomes. But the shift in the hydrocarbon chain region and the head group region in the liposomes suggests the arrangement of the phospholipids to form bilayers after the incorporation of CHOL.

Thermal stability

Thermogravimetric analysis (TGA) and Differential scanning calorimetry (DSC) analyses determine any chemical or physical changes in the samples with respect to temperature. The TGA thermogram (Figure 5a) shows the degradation onset temperature of PC at 182.46 °C (78.4% degradation), for CHOL at 249.76 °C (99.98% degradation), and for DSPE-mPEG2000 at 320.91 °C (98.92% degradation).

The degradation onset temperature increased to 240.78 °C (54.81% degradation) for non-PEGylated liposomes and 248.53 °C (56.55% degradation) for PEGylated liposomes when compared to PC. This discrepancy in the thermal stability and degradation pattern of liposomes and the raw materials corresponds to the synthesis of liposomes that are held together with strong interactions. The results indicate that the bilayer structures are more stable than their components.

The DSC thermogram shows an endotherm at 136.7 °C for PC, at 151.59 °C for CHOL, and at 56.96 °C for DSPE-mPEG2000 (Figure 5b).[42] The melting endotherm for liposomes shifted to 121.13 °C and for PEGylated liposomes to 116.68 °C -that concurs with the previously reported results.[43] This shift to lower temperatures corresponds to the breaking of bonds in the bilayer and confirms the synthesis of liposomes.[44] The endotherm for DSPE-mPEG2000 disappears in the PEGylated liposomes, implying a successful functionalization of the liposomes with PEG.

Stability studies

We studied the stability of non-PEGylated and PEGylated liposomes formed through 5 and 10 extrusion passes (Figure 6). The non-PEGylated liposomes formed by 5 extrusion passes were stable till week 4 and aggregated thereafter. Non-PEGylated liposomes with 10 extrusion passes were stable till week 7, but the particles aggregated and precipitated after week 5 leaving smaller particles in the suspension.

PEGylated liposomes with 5 extrusion passes were stable till 6 weeks, and particles with 10 extrusion passes recorded stability till 7 weeks; both the formulations showed precipitation after 5 weeks with smaller particles in suspension. The PDI values for all the formulations were under 0.3, and the zeta potential values reflected moderate stability for all the formulations during storage. The fluctuations in the size, PDI, and zeta potential occur due to the dynamic nature of
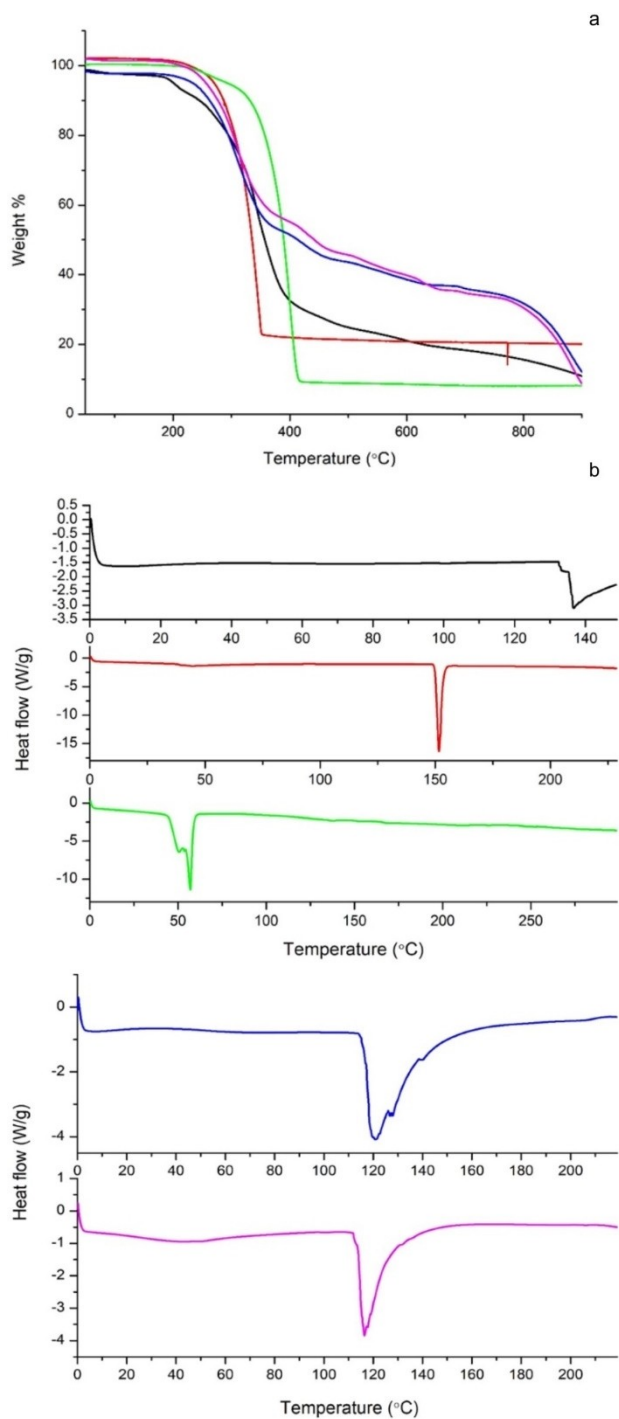
ChemistrySelect

Research Article
doi.org/10.1002/slct.202302435

Chemistry Europe
European Chemical
Societies Publishing

Figure 5. TGA thermograms for PC (black), CHOL (red), DSPE-mPEG2000 (green), liposomes (blue), and PEGylated liposomes (magenta) (a), and DSC thermogram of PC (black), CHOL (red), DSPE-mPEG2000 (green), liposomes (blue) and PEGylated liposomes (magenta) (b).
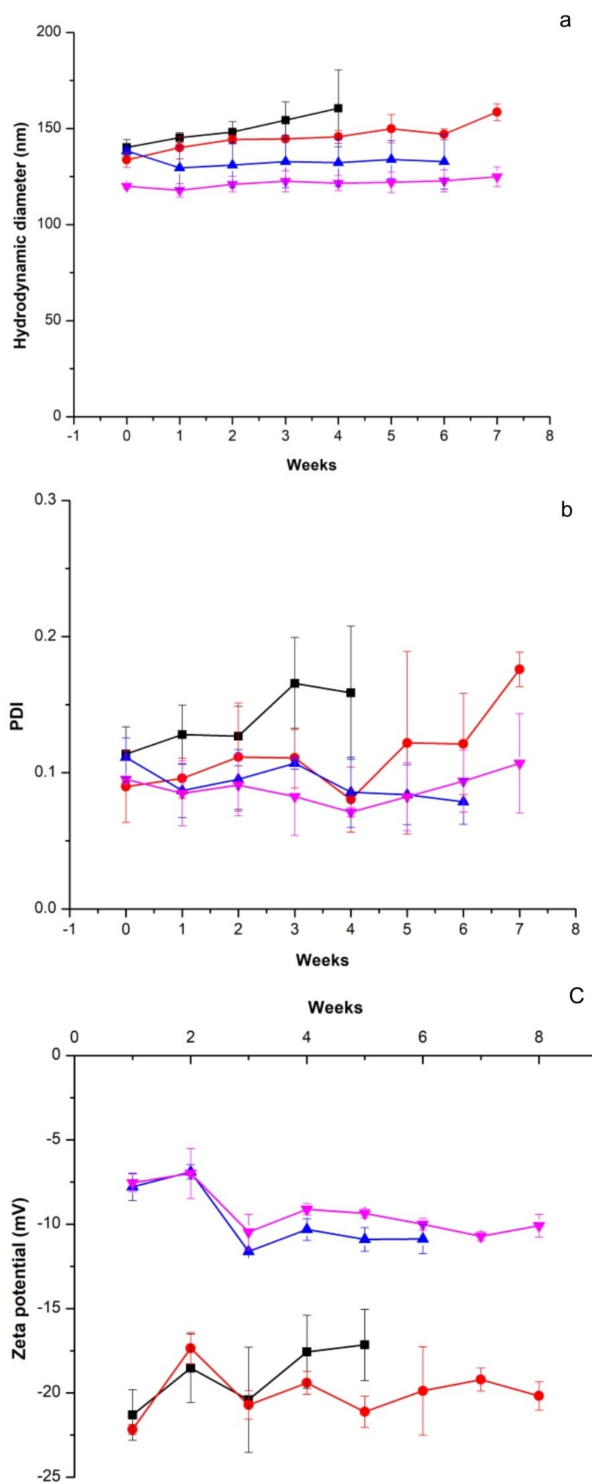

Figure 6. Stability studies of liposomes with 5 extrusion passes (blue) and 10 extrusion passes (orange), PEGylated liposomes with 5 extrusion passes (grey) and 10 extrusion passes (yellow).

liposomes. The data suggest lower storage stability for larger liposomes (extrusion passes 5).

Conclusions

Liposomes were widely synthesized by the thin film hydration technique, and this study identifies and optimizes process parameters and intrinsic factors to synthesize liposomes for

ChemistrySelect

Research Article
doi.org/10.1002/slct.202302435

Chemistry Europe
European Chemical
Societies Publishing

drug delivery. Higher rotation speed (240 RPM), reduced vacuum pressure (700 mm of Hg), and 2 ml chloroform in the thin film formation step created a thin and uniform lipid layer on the RBF walls that hydrated effectively and produced a highly turbid liposomal suspension. Higher rotation speed (270 RPM) in the hydration step synthesized smaller particles with low PDI, different hydrating mediums imparted varied levels of stability, and 1 h hydration time successfully hydrated the lipid layer to produce a monodisperse and smaller liposomal population. The downsizing parameters (extrusion passes and the number of polycarbonate membranes) significantly reduced the particle size. 10 mg/ml lipid concentrations created a thin and uniform lipid layer, a 7:3 molar ratio of PC:CHOL, and 1 mole% DSPE-mPEG2000 synthesized liposomes apt for drug delivery.

The analytical characterization techniques confirmed the synthesis of spherical particles with hydrodynamic diameter < 150 nm and PDI < 0.3; zeta potential values tagged the particles with moderate stability, and the decrease in the negative zeta potential for PEGylated liposomes confirmed the successful functionalization by PEG; FTIR analysis corroborated the synthesis of liposomes; TGA and DSC analysis indicated high thermal stability; smaller liposomes displayed higher storage stability than larger particles. Thus, this study facilitates the synthesis of liposomes for drug delivery or other applications by modulating the identified parameters to attain the desired specifications.

Experimental Section

Materials

PC from soybean and CHOL were purchased from Sigma-Aldrich, DSPE-mPEG2000 from Avanti Polar Lipids-Sigma-Aldrich, and Avanti mini hand extruder from Avanti polar lipids.

Synthesis of Liposomes

Liposomes were synthesized with a 1:1 molar ratio of PC:CHOL (10 mg/ml each) by the thin film hydration technique.[45] Lipids solubilized in chloroform were added to an RBF, and the solvent was removed under vacuum at 50 °C in a rotary evaporator to create a lipid layer; the RBFs were kept in a vacuum desiccator for 3–4 h to ensure complete removal of chloroform traces. The lipid layer was hydrated at 60 °C for 1 h with PBS, and the liposomal suspension was incubated overnight at 4 °C. Liposomes were subsequently downsized by sonicating for 20 min in a water bath followed by extrusion through a 100 nm polycarbonate membrane using a mini hand extruder. These liposomes were stored at 4 °C till further use. PEGylated liposomes were synthesized by the same protocol by adding DSPE-mPEG2000 along with PC and CHOL.

Factors affecting the thin film formation step

The rotation speed (30, 60, 120, 150, 240, and 270 RPM), vacuum pressure (100, 200, 300, 400, 500, 600, and 700 mm of Hg), organic solvents (chloroform, chloroform:methanol in 2:1 and 9:1 v/v ratios), and volume of chloroform (2, 5, and 10 ml) were varied to study their effect on the nature of lipid layer. These layers were

hydrated and the liposomal suspensions were assessed for their size, PDI, and zeta potential without the downsizing step.

Factors affecting the thin film hydration step

Lipid layers were made with the optimized values from the thin film formation step and the hydration was studied on three grounds: rotation speeds (30, 60, 90, 120, 240, and 270 RPM), hydrating mediums (PBS, deionized, and double distilled water), and hydration time (15, 30, 60, and 120 min). Liposomes were evaluated for size, PDI, and zeta potential by bypassing the downsizing step.

Factors affecting the downsizing step

The downsizing step was optimized for the number of extrusion passes (1, 5, 10, and 20), and the number of polycarbonate membranes (1 and 2) based on the size and PDI of the particles.

Intrinsic factors

The intrinsic factors were examined by varying PC and CHOL concentrations (10, 20, and 30 mg/mL), and the molar ratio of PC:CHOL (1:1, 3:2, 7:3, 4:1, 9:1, and 1:0). DSPE-mPEG2000 concentration (1, 3, and 5 mole% of lipids) was optimized for PEGylated liposomes.

Characterization of Liposomes

We recorded the hydrodynamic diameter, PDI, and zeta potential by DLS technique on Malvern Zetasizer Pro (Malvern Panalytical, UK) at 25 °C (173° non-invasive backscattering angle). All the samples were assessed in triplicate, and three independent measurements were recorded for each sample. The morphology of liposomes was ascertained by HRTEM on JEOL-JEM-F200. Liposomal formulations diluted with deionized water/PBS were dropped on a 200 mesh carbon-coated copper grid, and the samples were air-dried before analysis. FTIR spectra were recorded to determine the presence of functional groups in the raw materials (PC, CHOL, and DSPE-mPEG2000) and freeze-dried liposomal formulations. The infrared spectral profiles were recorded on Tensor 27 (Bruker) in the wavenumber range of 4000–600 cm^{-1}. Each sample was subjected to 40 runs.

TGA and DSC techniques were used to determine the thermal stability of raw materials and freeze-dried liposomal formulations. The TGA profiles were recorded on an STA 6000 system, Perkin Elmer. Approximately 5–10 mg sample was taken in an alumina crucible and analyzed from 50–900 °C with a scanning rate of 10 °C/min in a nitrogen atmosphere (flow rate: 20 mL/min). DSC thermograms were obtained on DSC Q100 V8.2 Build 268. Approximately 5–10 mg sample was placed in a standard aluminum pan with a lid and scanned from 0 °C to below the degradation onset temperature (as identified from TGA analysis) at 10 °C/min in a nitrogen atmosphere (flow rate: 50 mL/min). The stability of the liposomal formulations was tested at 4 °C by recording the hydrodynamic diameter, PDI, and zeta potential values weekly by withdrawing aliquots to identify changes occurring during storage.

Statistical analysis

Data are presented as mean ± standard deviation calculated using Microsoft Office Excel. One-way ANOVA and the *t*-test were performed using GraphPad Prism, and the p-values ≤ 0.05 were

[1] J. Dua, A. Rana, A. Bhandari, *Int J Pharm Stud Res.* **2012**, *3*, 14–20.
[2] M. Riaz, M. Riaz, X. Zhang, C. Lin, K. Wong, X. Chen, G. Zhang, A. Lu, Z. Yang, *Int. J. Mol. Sci.* **2018**, *19*, 195–222.
[3] T. Allen, P. Cullis, *Adv. Drug Delivery Rev.* **2013**, *65*, 36–48.
[4] H. Pandey, R. Rani, V. Agarwal, *Braz. Arch. Biol. Technol.* **2016**, *59*, e16150477.
[5] G. Bozzuto, A. Molinari, *Int. J. Nanomed.* **2015**, *10*, 975–999.
[6] M. Mufamadi, V. Pillay, Y. Choonara, L. Toit, G. Modi, D. Naidoo, V. Ndesendo, *J. Drug Delivery.* **2011**, *2011*, 1–19.
[7] A. Gabizon, F. Martin, *Drugs.* **1997**, *54*, 15–21.
[8] L. Sercombe, T. Veerati, F. Moheimani, S. Wu, A. Sood, S. Hua, *Front. Pharmacol.* **2015**, *6*, DOI: https://doi.org/10.3389/fphar.2015.00286.
[9] M. Li, C. Du, N. Guo, Y. Teng, X. Meng, H. Sun, S. Li, P. Yu, H. Galons, *Eur. J. Med. Chem.* **2019**, *164*, 640–653.
[10] H. Chang, M. Cheng, M. Yeh, *Open Access Sci. Reports.* **2012**, *1*, 195–202.
[11] S. Vemuri, C. Rhodes, *Pharm. Acta Helv.* **1995**, *70*, 95–111.
[12] A. Laouini, C. Jaafar-Maalej, I. Limayem-Blouza, S. Sfar, C. Charcosset, H. Fessi, *J. Colloid. Sci. Biotechnol.* **2012**, *1*, 147–168.
[13] D. Guimaraes, A. Cavaco-paulo, E. Nogueira, *Int. J. Pharm.* **2021**, *601*, 120571–120585.
[14] S. Brown, D. Khan, *J. Drug Delivery.* **2012**, *2012*, 1–6.
[15] M. Danaei, M. Dehghankhold, S. Ataei, F. Davarani, R. Javanmard, A. Dokhani, S. Khorasani, M. Mozafari, *Pharmaceutica* **2018**, *10*, 57–73.
[16] M. Smith, R. Crist, J. Clogston, S. Mcneil, *Anal. Bioanal. Chem.* **2017**, *409*, 5779–5787.
[17] S. Honary, F. Zahir, *Trop. J. Pharm. Res.* **2013**, *12*, 265–273.
[18] S. Bhattacharjee, *J. Controlled Release.* **2016**, *235*, 337–351.
[19] V. P. Torchilin, V. Torchilin, V. Weissig, *Liposomes: a practical approach*, Oxford University Press **2003**, p. 396.
[20] D. Yadav, K. Sandeep, D. Pandey, R. Dutta, *J. Biotechnol. Biomater.* **2017**, *7*, 1000276–1000282.
[21] D. Lasic, *Biochem. J.* **1988**, *256*, 1–11.
[22] R. Watve, J. Bellare, *Curr. Sci.* **1995**, *68*, 715–24.
[23] N. Sarkar, S. Bose, *ACS Appl. Mater. Interfaces.* **2019**, *11*, 17184–17192.
[24] J. Marjan, T. Allen, *Biotechnol. Adv.* **1996**, *14*, 151–75.
[25] D. Large, R. Abdelmessih, E. Fink, D. Auguste, *Adv. Drug Delivery Rev.* **2021**, *176*, 113851–113864.
[26] T. Ghatage, S. Jadhav, V. Kore, *Int. J. Sci. Eng. Technol. Res.* **2017**, *6*, 2744–2750.
[27] S. Ong, M. Chitneni, K. Lee, L. Ming, K. Yuen, *Pharmaceutica* **2016**, *8*, 36–47.
[28] G. Gregoriadis, Y. Perrie, *eLife.* **2010**, ■■■*Dear Author, if the journal has volumes, please add the journal number*■■■, DOI: https://doi.org/10.1002/9780470015902.a0002656.pub2.
[29] A. Zarrabi, A. Zarepour, A. Khosravi, Z. Alimohammadi, V. Thakur, *Fibers.* **2021**, *9*, 19–35.
[30] M. Briuglia, C. Rotella, A. McFarlane, D. Lamprou, *Drug Delivery Transl. Res.* **2015**, *5*, 231–242.
[31] H. Fahmy, *Naunyn-Schmiedeberg's Arch. Pharmacol.* **2019**, *392*, 1465–1476.
[32] G. Pamunuwa, V. Karunaratne, D. Karunaratne, *J. Nanomater.* **2016**, *2016*, 1–9.
[33] A. Hardiansyah, M. Yang, T. Liu, C. Kuo, L. Huang, T. Chan, *Nanoscale Res. Lett.* **2017**, *12*, 1–11.
[34] S. Dhule, P. Penfornis, J. He, M. Harris, T. Terry, V. John, R. Pochampally, *Mol. Pharmaceutics.* **2014**, *11*, 417–427.
[35] Y. Chen, Q. Wu, Z. Zhang, L. Yuan, X. Liu, L. Zhou, *Molecules.* **2012**, *17*, 5972–87.
[36] M. Almgren, K. Edwards, G. Karlsson, *Colloids Surf. A* **2000**, *174*, 3–21.
[37] A. Aisha, A. Majid, Z. Ismail, *BMC Biotechnol.* **2014**, *14*, 1–11.
[38] Z. Li, Y. Huang, S. Peng, X. Chen, L. Zou, W. Liu, C. Liu, *J. Dispersion Sci. Technol.* **2020**, *41*, 207–213.
[39] D. Hudiyanti, M. Khafiz, K. Anam, P. Siahaan, L. Suyati, *Open Chemistry* **2021**, *19*, 358–366.
[40] F. Haghiralsadat, G. Amoabediny, M. Helder, S. Naderinezhad, M. Sheikhha, T. Forouzanfar, B. Zandieh-doulabi, *Artif. Cells, Nanomed., Biotechnol.* **2018**, *46*, 169–177.
[41] K. Istenič, R. Korošec, N. Ulrih, *J. Sci. Food Agric.* **2016**, *96*, 4623–4632.
[42] R. Jangde, D. Singh, *Artif. Cells, Nanomed., Biotechnol.* **2016**, *44*, 635–641.
[43] R. Patel, H. Patel, A. Baria, *Int. J. Drug Delivery Technol.* **2009**, *1*, 16–23.
[44] Y. Niu, D. Ke, Q. Yang, X. Wang, Z. Chen, X. An, W. Shen, *Food Chem.* **2012**, *135*, 1377–1382.
[45] H. Zhang, *Liposomes. Methods in Molecular Biology*, (Eds: D'Souza G), Humana press, New York **2017**, pp. 17–22.

Manuscript received: June 22, 2023

RESEARCH ARTICLE
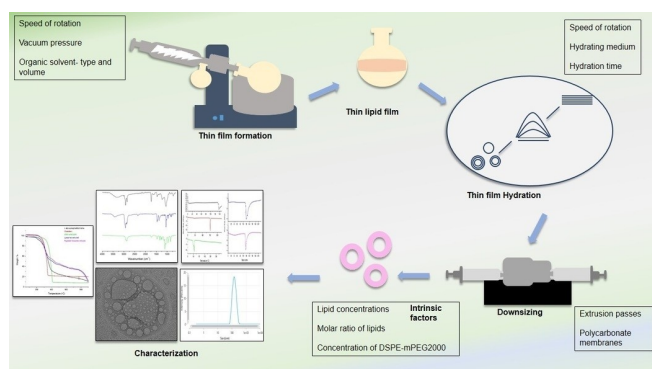
A. Moudgil, Dr. B. P. Chaudhari*

1 – 11

Understanding Critical Aspects of Liposomal Synthesis for Designing the Next Generation Targeted Drug Delivery Vehicle

We optimized multiple process paramters and certain intrinsic factors to develop liposomes for drug delivery; liposomes were also characterized by various analytical techniques. This study provides a mechanistic insight into the synthesis method, ascertains roles to every factor, and allows modification of appropriate parameters to synthesize liposomes with desired specificatio

---

🐦 **## SPACE RESERVED FOR IMAGE AND LINK**

Share your work on social media! *ChemistrySelect* has added Twitter as a means to promote your article. Twitter is an online microblogging service that enables its users to send and read short messages and media, known as tweets. Please check the pre-written tweet in the galley proofs for accuracy. If you, your team, or institution have a Twitter account, please include its handle @username. Please use hashtags only for the most important keywords, such as #catalysis, #nanoparticles, or #proteindesign. The ToC picture and a link to your article will be added automatically, so the **tweet text must not exceed 250 characters**. This tweet will be posted on the journal's Twitter account (follow us @ChemistrySelect) upon publication of your article in its final form. We recommend you to re-tweet it to alert more researchers about your publication, or to point it out to your institution's social media team.

ORCID (Open Researcher and Contributor ID)

Please check that the ORCID identifiers listed below are correct. We encourage all authors to provide an ORCID identifier for each coauthor. ORCID is a registry that provides researchers with a unique digital identifier. Some funding agencies recommend or even require the inclusion of ORCID IDs in all published articles, and authors should consult their funding agency guidelines for details. Registration is easy and free; for further information, see http://orcid.org/.

Aliesha Moudgil
Dr. Bhushan P. Chaudhari http://orcid.org/0000-0003-1064-3563

Author Contributions

Aliesha Moudgil: Data curation:Lead; Formal analysis:Lead; Methodology:Lead; Software:Lead; Writing – original draft:Lead
Bhushan Pradosh Chaudhari: Conceptualization:Lead; Supervision:Lead; Writing – review & editing:Lead